

**CRANFIELD UNIVERSITY**

**SCHOOL OF ENGINEERING**

**PhD THESIS**

**Academic Year 2005-2006**

**V. A. PACHIDIS**

**Gas Turbine Advanced Performance  
Simulation**

**Supervisor: P. Pilidis**

**January 2006**

© Cranfield University 2006. All rights reserved. No part of this publication may be reproduced without the written permission of the copyright owner.

**Dedicated to my father Anastasio, my mother  
Theodosia and my sister Marisa**



## **ABSTRACT**

Current commercial 'state of the art' engine simulation software is of a low fidelity. Individual component performance characteristics are typically represented via non-dimensional maps with empirical adjustments for off-design effects. Component non-dimensional characteristics are usually obtained through the averaging of experimental readings from rig test analyses carried out under nominal operating conditions.

In those cases where actual component characteristics are not available and default maps are used instead, conventional simulation tools can offer a good prediction of the performance of the whole engine close to design point, but can deviate substantially at off-design and transient conditions. On the other hand, even when real component characteristics are available, zero-dimensional engine cycle simulation tools can not predict the performance of the engine at other than nominal conditions satisfactorily. Low-fidelity simulation tools are generally incapable of analyzing the performance of individual engine components in detail, or capturing complex physical phenomena such as inlet flow distortion.

Although the available computational power has increased exponentially over the last two decades, a detailed, three-dimensional analysis of an entire propulsion system still seems to be so complex and computationally intensive as to remain cost-prohibitive. For this reason, alternative methods of integrating different types and levels of analysis are necessary. The integration of simulation codes that model at different levels of fidelity into a single simulation provides the opportunity to reduce the overall computing resource needed, while retaining the desired level of analysis in specific engine components.

The objective of this work was to investigate different simulation strategies for communicating the performance characteristics of an isolated gas turbine engine component, resolved from a detailed, high-fidelity analysis, to an engine system analysis carried out at a lower level of resolution. This would allow component-level, complex physical processes to be captured and analyzed in the context of the whole engine performance, at an affordable computing resource and time.

More specifically, this work identified and thoroughly investigated several advanced simulation strategies in terms of their actual implementation and potential, by looking into relative changes in engine performance after integrating into the basic, non-dimensional cycle analysis, the performance characteristics of i) two-dimensional Streamline Curvature (SLC) and ii) three-dimensional Computational Fluid Dynamics (CFD), engine component models.

In the context of this work, several case studies were carried out, utilising different two-dimensional and three-dimensional component geometries, under different operating conditions, such as different types and extents of compressor inlet pressure distortion and turbine inlet temperature distortion. More importantly, this research effort established the necessary methodology and technology required for a full, two-dimensional engine cycle analysis at an affordable computational resource.

## **ACKNOWLEDGEMENTS**

The completion of this work has been a significant milestone in my academic and professional career. Therefore, I would like to acknowledge the help of all the people who have contributed to the successful conclusion of this research work.

First of all, I would like to express my gratitude to my supervisor Professor Pericles Pilidis for his guidance and inspiration throughout all the years of my studies. Without his continuous encouragement and technical support it would have been very difficult to conclude this work.

My gratitude is also extended to Professor Joao R. Barbosa for his friendly advice and help that has been proven invaluable to the development of robust streamline curvature software.

In the context of this work and over the years this author had the opportunity and the privilege to collaborate with a number of people.

Particular thanks to my good friend and colleague Ioannis Templalexis for his significant help and technical advice during the development of the compressor streamline curvature software. His humour and good will really saved the day through desperate times.

I would also like to acknowledge the help of all the Thermal Power MSc and visiting students who have directly or in-directly contributed to this work.

Bueno Fredericko  
Charalambous Nikolaos  
Ghisu Tiziano  
Guindeuil Geoffrey  
Iurisci Giuseppe  
Melloni Leonardo  
Nantua Nikolas  
Talhouarn Fabian  
Zilli Andrea

Last but not least, it would have been an omission if I did not thank my family and loved ones for their continuous support, patience and confidence in my abilities. Their personal sacrifices over the years have been a continuous motivation in my life and work.

Vassilios Pachidis  
Cranfield University  
14<sup>th</sup> of January 2006

# **NOTATION**

## Abbreviations

0D	Zero-Dimensional, Non-Dimensional
1D	One-Dimensional
2D	Two-Dimensional
3D	Three-Dimensional
AOA	Angle Of Attack
AVDR	Axial Velocity Density ratio
BPCM	Blade Passage Choke Margin
CFD	Computational Fluid Dynamics
CLA	Centre Line Average
CMF	Corrected Mass Flow
DCA	Double Circular Arc
GT	Gross Thrust
HBR	High Bypass Ratio
HP	High Pressure
IGV	Inlet Guide Vane
ISA	International Standard Atmosphere
LBR	Low Bypass Ratio
LP	Low Pressure
NDMF	Non Dimensional Mass Flow
NT	Net Thrust
PDI	Pressure Distortion Index
PR	Pressure Ratio
RANS	Reynolds Averaged Navier Stokes
SFC	Specific Fuel Consumption
SLC	Streamline Curvature
SLS	Sea Level Static
SM	Surge Margin
TET	Turbine Entry Temperature

## Latin Symbols

A	Cross-sectional area
B	Blockage factor
C	Constant, Speed of sound
D	Diffusion factor
F	Blade forces, Interaction loss factor
H	Enthalpy, Boundary layer shape factor
L	Diffuser length
M	Mach number
N	Rotational speed, Number of
P	Pressure
Q	Mass flow function
R	Air constant



S	Entropy
T	Temperature
U	Blade speed
V	Absolute velocity, Volume
W	Relative velocity, Width
b	Diffuser width
c	Blade chord
e	Unit vector
h	Distance, Blade height, Altitude
i	Incidence angle
j	Number of computational node, Streamline number
k	Blade angle, Constant
l	Length
m	Meridional direction
n	Direction normal to a surface, Reynolds number exponent
q	Dynamic head
r	Cylindrical coordinate in radial direction
s	Direction tangent to the blade leading and trailing edge surfaces, Pitch distance, Characteristic distance
t	Time, Thickness
u	First derivative of the potential function with respect to the x-direction, Internal energy
v	First derivative of the potential function with respect to the y-direction, Prandtl–Meyer function
w	Cylindrical coordinate in tangential (whirl) direction
x	X-direction
y	Y-direction
z	Z-direction or cylindrical coordinate in axial direction

### *Greek Symbols*

$\Delta$	Change
$\Phi$	Potential flow function
$\alpha$	Air absolute angle, Streamline curvature, Speed of sound
$\beta$	Air relative angle
$\gamma$	Ratio of specific heats, Sweep angle
$\delta$	Deviation angle, Boundary layer displacement thickness
$\varepsilon$	Slope angle, Flow deflection angle
$\zeta$	Stagger angle
$\eta$	Efficiency
$\theta$	Camber angle, Boundary layer / wake momentum thickness
$\mu$	Viscosity
$\rho$	Density
$\sigma$	Solidity
$\tau$	Flow turning angle, Torque
$\phi$	Diffuser semi-angle
$\psi$	Diffuser swirl angle
$\omega$	Angular speed, Loss factor

Superscripts

-	Average conditions
'	Relative conditions
*	Minimum loss conditions
→	Vector quantity

Subscripts

$\infty$	Free stream conditions
o	Total thermodynamic conditions
1	Inlet plane
2	Outlet plane
BS	Before Shock
C	Compressor
CL	Camber Line
H	Hub
HP	High Pressure
LE	Leading Edge
LP	Low Pressure
PS	Pressure Surface
R	Relative, Ratio
Re	Reynolds
SS	Suction Surface
T	Tip, Turbine
TE	Trailing Edge
aero	Aerodynamic
blade_max	Blade Maximum
cl	Centre Line
cr	Critical
csd	Constant Section Duct
diff	Diffuser
dwstr	Downstream
eng	Engine face
geom	Geometrical
isent	Isentropic
lip	Intake lip
m	Meridional direction
mag	Magnification
prof	Profile
r	Radial direction
s	Stalling
sc	Sonic Conditions
sec	Secondary
sh	Shock, Shape
throat	Blade passage throat
tot	Total
upstr	Upstream

w	Whirl direction
z	Axial direction

*Full Symbols*

$C_D$	Drag coefficient
$C_F$	Skin friction coefficient
$C_L$	Lift coefficient
$C_p$	Specific heat under constant pressure
$D_{eq}$	Equivalent diffusion factor
$R_c$	Radius of curvature
$Re$	Reynolds number
$Q$	Heat rate
$r_b$	Leading edge radius
$(K_\delta)_{sh}$	Factor affecting deviation with respect to the thickness distribution around the leading edge
$(K_\delta)_t$	Factor affecting deviation with respect to the thickness to chord ratio
$(K_i)_{sh}$	Factor affecting incidence with respect to the thickness distribution around the leading edge
$(K_i)_t$	Factor affecting incidence with respect to the thickness to chord ratio
$(\delta_0)_{10}$	Deviation for the reference 10 percent thickness to chord ratio NACA 65-series blade
$\delta_c$	Tip clearance
$(i_0)_{10}$	Minimum-loss incidence for a reference NACA-65 cascade of zero camber and 10 per cent thickness to chord ratio
$k_B$	Blockage factor
$k_i$	Constant
$\lambda_{contr}$	Entry contraction ratio
$\lambda_{diff}$	Diffuser area ratio

# **LIST OF CONTENTS**

<b><i>Chapter I - Introduction</i></b> .....	<b>18</b>
1.1. Background.....	18
1.2. Advanced Performance Simulation.....	20
1.3. CFD versus Through-Flow Analysis.....	22
 <b><i>Chapter II - Project Objectives</i></b> .....	 <b>24</b>
2.1. Long-Term Research.....	24
2.2. Thesis Objectives.....	24
 <b><i>Chapter III - Thesis Structure</i></b> .....	 <b>27</b>
 <b><i>Chapter IV - Literature Review</i></b> .....	 <b>29</b>
4.1. 0D Gas Turbine Performance Simulation Software.....	29
4.2. High-Fidelity Gas Turbine Performance Simulation.....	31
4.2.1. NASA Numerical Propulsion System Simulation (NPSS).....	31
4.2.2. NASA-Pratt & Whitney 1D Compressor Simulation.....	32
4.2.3. NASA-GE Multi-Fidelity Turbofan Engine Simulation.....	34
4.2.4. Cranfield Rolls-Royce UTC 2D Fan Radial Profile Simulation.....	35
4.2.5. MTU Low-Bypass Fan Model.....	37
4.2.6. Discussion of Published Literature.....	38
4.2.7. Author's Publications.....	39
4.3. Turbomachine Through-Flow Analysis Methods.....	40
4.3.1. Characteristics of the Turbomachine Flow Field.....	40
4.3.2. General Through-Flow Modelling Assumptions.....	41
4.3.3. Classification of Through-Flow Methods.....	43
4.3.4. Development of Through-Flow Analysis Methods.....	45
4.3.5. Through-Flow Method Limitations.....	47
4.3.6. Comparison of Through-Flow Analysis Methods.....	48
 <b><i>Chapter V - 2D Compressor Flow Modelling</i></b> .....	 <b>49</b>
5.1. Compressor Streamline Curvature Equations.....	49
5.2. Continuity of Mass Flow.....	58
5.3. Calculation of Velocity Triangles.....	60
5.4. Calculation of Thermodynamic Properties.....	62
5.5. Calculation of Streamline Properties.....	70
5.6. Calculation of Incidence Angle.....	74
5.7. Calculation of Deviation Angle.....	79



5.8. Blade Passage Choking.....	86
5.9. Prediction of Stall.....	91
5.10. Calculation of Compressor End-Wall Boundary Layer.....	96
5.11. Calculation of Blade Losses.....	101
5.11.1. Calculation of Profile Losses.....	102
5.11.2. Loss due to Reynolds Effects.....	108
5.11.3. Calculation of Shock Losses.....	111
5.11.4. Calculation of Secondary Losses.....	116
 <i>Chapter VI - 2D Intake and Duct Flow Modelling.....</i>	 121
6.1. Intake Streamline Curvature Equations.....	121
6.2. Calculation of Intake Pressure Recovery.....	123
6.2.1. Calculation of Lip Pressure Recovery Loss.....	125
6.2.2. Calculation of Diffuser Pressure Recovery Loss.....	133
6.2.3. Calculation of Entry-Diffuser Interaction Loss.....	137
6.2.4. Effect of Incidence Angle on Pressure Recovery.....	141
6.2.5. Effect of Choking on Pressure Recovery.....	148
6.3. Calculation of Intake End-Wall Boundary Layer.....	152
 <i>Chapter VII - 2D SLC Algorithm Implementation.....</i>	 156
7.1. Software Programming Features.....	156
7.1.1. Programming Requirements.....	156
7.1.2. Software Design.....	158
7.1.3. Program Unit Notation.....	159
7.2. 2D Compressor SLC Algorithm.....	161
7.2.1. 2D Compressor SLC Software Capability.....	161
7.2.2. 2D Compressor SLC Algorithm Execution.....	162
7.2.3. Display Messages.....	169
7.3. 2D Intake SLC Algorithm.....	169
7.3.1. 2D Intake SLC Software Capability.....	169
7.3.2. 2D Intake SLC Algorithm Execution.....	170
7.3.3. Display Messages.....	173
7.4. Numerical Methods and Convergence Stability.....	174
 <i>Chapter VIII - 2D SLC Software Validation.....</i>	 176
8.1. 2D Compressor SLC Software Validation.....	176
8.1.1. Initial Comparison against Experimental Data.....	177
8.1.2. Loss Model Adaptation.....	179
8.1.3. Final Comparison against Experimental Data.....	184
8.1.4. 2D Profile Comparison against Experimental Data.....	188
8.2. 2D Intake SLC Software Validation.....	191
8.2.1. Validation of Inviscid Flow in Conical Ducts.....	191
8.2.2. Validation of Viscous Flow in Annular Intakes.....	194



<i>Chapter IX - High-Fidelity Engine Performance Simulation</i> .....	197
9.1. Advanced Performance Simulation Strategies.....	197
9.1.1. The De-Coupled Approach.....	198
9.1.2. The Iterative Approach.....	200
9.1.3. The Fully Integrated Approach.....	204
9.2. 2D SLC Gas Turbine Performance Simulation.....	206
9.2.1. Simulation Tools and Software Integration.....	206
9.2.2. Effect of 2D SLC Fan Characteristic.....	214
9.2.3. Effect of 2D SLC Intake Characteristic.....	225
9.2.4. Effect of 2D SLC Fan Inlet Total Pressure Distortion.....	229
9.3. 3D CFD Gas Turbine Performance Simulation.....	235
9.3.1. Effect of 3D CFD Intake Characteristic.....	235
9.3.2. Effect of 3D CFD Fan Inlet Total Pressure Distortion.....	254
9.3.3. Effect of 3D CFD Turbine Inlet Total Temperature Distortion.....	286
 <i>Chapter X - Conclusions and Future Work</i> .....	 303
10.1. Achievements.....	303
10.2. Main Conclusions.....	304
10.3. Recommendations for Future Work.....	309
 <i>References</i> .....	 315
 <i>Appendix A - 0D Performance Simulation Software Matrix</i> .....	 329
<i>Appendix B - Sign Convention and Velocity Triangles</i> .....	331
<i>Appendix C - Double Circular Arc Blade Geometry</i> .....	332
<i>Appendix D - 2D Compressor SLC Software Flow Chart</i> .....	333
<i>Appendix E - 2D Intake SLC Software Flow Chart</i> .....	340
<i>Appendix F - Two-Stage Compressor Geometry</i> .....	345
<i>Appendix G - Intake Geometry</i> .....	351
<i>Appendix H - 2D Profile Comparison</i> .....	353
<i>Appendix I - 2D SLC Intake Performance</i> .....	361
<i>Appendix J - PYTHIA Engine Input Data Files</i> .....	373

## ***LIST OF FIGURES***

### *Chapter I - Introduction*

**Figure 1.1.1: Software integration for advanced engine performance analysis..... 19**

### *Chapter IV - Literature Review*

**Figure 4.2.4.1: Sample fan outlet radial profiles.....35**  
**Figure 4.2.4.2: 0D fan model (Two fan maps).....36**  
**Figure 4.2.4.3: 2D fan model (Fan radial-profile map)..... 37**  
**Figure 4.3.1.1: Flow phenomena in axial-flow blade rows..... 41**  
**Figure 4.3.1.2: Meridional section of a 2-stage axial flow compressor..... 41**  
**Figure 4.3.2.1: S1 and S2 control surfaces..... 42**  
**Figure 4.3.3.1: 2-stage fan geometry with calculated streamlines.....44**  
**Figure 4.3.3.2: Finite volume elements for a 3D flow field computation.....44**

### *Chapter V - 2D Compressor Flow Modelling*

**Figure 5.1.1: Coordinate system..... 52**  
**Figure 5.5.1: Streamline curvature grid..... 71**  
**Figure 5.6.1: Blade maximum thickness to chord ratio correction for zero-camber reference minimum-loss incidence angle.....76**  
**Figure 5.6.2: Reference minimum-loss incidence angle for zero camber deduced from low-speed-cascade data of 10-per-cent-thick NACA 65 series blades..... 77**  
**Figure 5.6.3: Reference minimum-loss incidence angle slope factor deduced from low-speed-cascade data of NACA 65 series blades.....77**  
**Figure 5.7.1: Blade maximum thickness to chord ratio correction for zero-camber reference minimum-loss deviation angle..... 83**  
**Figure 5.7.2: Reference minimum-loss deviation angle for zero camber deduced from low-speed-cascade data of 10-percent-thick NACA 65 series blades..... 84**  
**Figure 5.8.1: Typical sketch of choked flow in a blade passage..... 86**  
**Figure 5.9.1: Compressor characteristic..... 92**  
**Figure 5.9.2: Blade passage – diffuser passage equivalence..... 94**  
**Figure 5.10.1: Solution nodes and auxiliary points along the end-wall boundary layer edges..... 100**  
**Figure 5.11.1.1: Estimated variation of wake momentum thickness with minimum-loss equivalent diffusion factor for DCA subsonic rotors..... 107**  
**Figure 5.11.3.1: Flow turning angle calculation..... 113**  
**Figure 5.11.4.1: Griepentrog's secondary loss factor variation with geometric parameter..... 119**



## Chapter VI - 2D Intake and Duct Flow Modelling

Figure 6.2.1.1: Lip loss factor for rounded lips at zero incidence.....	131
Figure 6.2.1.2: Lip loss boundary at zero incidence.....	132
Figure 6.2.1.3: Factor allowing for datum interaction effects between entry and diffuser.....	132
Figure 6.2.2.1: Diffuser loss factor $k_1$ variation with semi-angle.....	136
Figure 6.2.2.2: Diffuser loss factor $k_2$ variation with area ratio.....	136
Figure 6.2.3.1: Diffuser loss magnification factor $N_1$ for attached entry flow.....	139
Figure 6.2.3.2: Diffuser loss magnification factor $N_2$ for attached entry flow.....	140
Figure 6.2.3.3: Diffuser loss magnification factor $N_3$ for separated entry flow.....	140
Figure 6.2.3.4: Diffuser loss magnification factor $N_4$ for separated entry flow.....	141
Figure 6.2.4.1: Effective critical area ratio for circular lips at incidence.....	146
Figure 6.2.4.2: Effective critical area ratio for elliptical lips at incidence.....	147
Figure 6.2.4.3: $k_{inc}$ factor for circular lips at incidence.....	147
Figure 6.2.4.4: $k_{inc}$ factor for elliptical lips at incidence.....	148
Figure 6.2.5.1: Inlet choking Mach number for attached lip flow.....	151
Figure 6.2.5.2: Increment in choking Mach number due to lip flow separation.....	152

## Chapter VII - 2D SLC Algorithm Implementation

Figure 7.1.3.1: Example of program unit notation.....	160
---	-----

## Chapter VIII - 2D SLC Software Validation

Figure 8.1.1: Geometry comparison between the NASA experimental compressor and the SLC compressor model used in the analysis.....	177
Figure 8.1.1.1: Initial comparison with experimental results for the first stage – Pressure Ratio vs Corrected Mass Flow.....	178
Figure 8.1.1.2: Initial comparison with experimental results for the first stage – Isentropic Efficiency vs Corrected Mass Flow.....	179
Figure 8.1.2.1: Experimental variation of wake momentum thickness with suction-surface diffusion ratio.....	180
Figure 8.1.2.2: Wake momentum thickness variation with equivalent diffusion ratio for data points at angles of attack greater than minimum loss.....	180
Figure 8.1.2.3: Representative variation of wake momentum thickness with equivalent diffusion ratio at minimum-loss angle of attack used in calculations of cascade loss variations.....	182
Figure 8.1.2.4: Estimated variation of wake momentum thickness with minimum loss equivalent diffusion ratio.....	182
Figure 8.1.2.5: Adaptation with experimental results – Blade wake momentum thickness scaling factor matrix.....	183
Figure 8.1.3.1: Final comparison with experimental results for the first stage – Pressure Ratio vs Corrected Mass Flow.....	184
Figure 8.1.3.2: Final comparison with experimental results for the first stage – Isentropic Efficiency vs Corrected Mass Flow.....	185

<b>Figure 8.1.3.3: Final comparison with experimental results for both stages – Pressure Ratio vs Corrected Mass Flow.....</b>	<b>185</b>
<b>Figure 8.1.3.4: Final comparison with experimental results for both stages – Isentropic Efficiency vs Corrected Mass Flow.....</b>	<b>186</b>
<b>Figure 8.1.3.5: Profile of compressor inlet tip total pressure distortion.....</b>	<b>187</b>
<b>Figure 8.1.3.6: Tip pressure distortion effect – Pressure ratio vs Corrected Mass Flow.....</b>	<b>187</b>
<b>Figure 8.1.3.7: Tip pressure distortion effect – Isentropic Efficiency vs Corrected Mass Flow.....</b>	<b>188</b>
<b>Figure 8.2.1.1: Calculated streamlines in a conical convergent duct.....</b>	<b>192</b>
<b>Figure 8.2.1.2: Calculated streamlines in a conical divergent duct.....</b>	<b>192</b>
<b>Figure 8.2.1.3: Calculated streamlines in a conical convergent-divergent duct.....</b>	<b>194</b>
<b>Figure 8.2.2.1: Typical 2D SLC intake model with engine cone and pre-entry stream tube.....</b>	<b>195</b>
<b>Figure 8.2.2.2: Comparison between 1D ESDU data and averaged 2D SLC results – Intake Pressure Recovery vs Intake Throat Mach Number.....</b>	<b>195</b>

## *Chapter IX - High-Fidelity Engine Performance Simulation*

<b>Figure 9.1.1.1: De-coupled high-fidelity analysis flow chart.....</b>	<b>198</b>
<b>Figure 9.1.1.2: De-coupled high-fidelity analysis schematic diagram.....</b>	<b>199</b>
<b>Figure 9.1.2.1: Iterative scaling of default component characteristics in order to establish the actual component operating point.....</b>	<b>201</b>
<b>Figure 9.1.2.2: Iterative high-fidelity analysis flow chart.....</b>	<b>202</b>
<b>Figure 9.1.2.3: Iterative high-fidelity analysis schematic diagram.....</b>	<b>203</b>
<b>Figure 9.1.3.1: Fully integrated high-fidelity analysis flow chart.....</b>	<b>205</b>
<b>Figure 9.1.3.2: Fully integrated high-fidelity analysis schematic diagram.....</b>	<b>205</b>
<b>Figure 9.2.1.1: Single-stage 2D SLC compressor model.....</b>	<b>207</b>
<b>Figure 9.2.1.2: Single-stage LP compressor design point and overall performance – Pressure Ratio vs Corrected Mass Flow.....</b>	<b>208</b>
<b>Figure 9.2.1.3: Single-stage LP compressor design point and overall performance – Isentropic Efficiency vs Corrected Mass Flow.....</b>	<b>208</b>
<b>Figure 9.2.1.4: 2D SLC intake model and pre-entry stream tube.....</b>	<b>209</b>
<b>Figure 9.2.1.5: Cranfield’s gas turbine performance simulation and diagnostics software.....</b>	<b>210</b>
<b>Figure 9.2.1.6: PYTHIA’s engine modelling and simulation environment.....</b>	<b>211</b>
<b>Figure 9.2.1.7: Schematic representation of PYTHIA’s model of the notional, two-spool, LBR, mixed-exhaust, military turbofan engine.....</b>	<b>212</b>
<b>Figure 9.2.2.1: PYTHIA’s scaled default map for LP compressor and equilibrium running line.....</b>	<b>215</b>
<b>Figure 9.2.2.2: SLC derived map for LP compressor and equilibrium running line.....</b>	<b>215</b>
<b>Figure 9.2.2.3: Comparison of engine performance obtained with PYTHIA’s default fan map and 2D SLC fan map – Gross Thrust vs Turbine Entry Temperature.....</b>	<b>216</b>
<b>Figure 9.2.2.4: Comparison of engine performance obtained with PYTHIA’s default fan map and 2D SLC fan map – Fuel Flow vs Turbine Entry Temperature.....</b>	<b>217</b>
<b>Figure 9.2.2.5: Comparison of engine performance obtained with PYTHIA’s default fan map and 2D SLC fan map – Specific Fuel Consumption vs Turbine Entry Temperature.....</b>	<b>217</b>



<b>Figure 9.2.2.6:</b> Comparison between the PYTHIA scaled default fan map and the SLC high-fidelity map.....	<b>218</b>
<b>Figure 9.2.2.7:</b> Comparison of engine performance obtained with PYTHIA's default fan map and 2D SLC fan map – Fan Relative Rotational Speed vs Turbine Entry Temperature.....	<b>219</b>
<b>Figure 9.2.2.8:</b> Comparison of engine performance obtained with PYTHIA's default fan map and 2D SLC fan map – Corrected Engine Mass Flow vs Turbine Entry Temperature.....	<b>219</b>
<b>Figure 9.2.2.9:</b> Comparison between the equilibrium running lines established through the de-coupled and iterative high-fidelity simulation strategies.....	<b>220</b>
<b>Figure 9.2.2.10:</b> Comparison between the equilibrium running lines established through the de-coupled and fully integrated high-fidelity simulation strategies.....	<b>222</b>
<b>Figure 9.2.2.11:</b> Comparison of engine performance obtained with the manually integrated 2D SLC fan map and the fully integrated 2D SLC fan model – Gross Thrust vs Turbine Entry Temperature.....	<b>223</b>
<b>Figure 9.2.2.12:</b> Comparison of engine performance obtained with the manually integrated 2D SLC fan map and the fully integrated 2D SLC fan model – Fuel Flow vs Turbine Entry Temperature.....	<b>223</b>
<b>Figure 9.2.2.13:</b> Comparison of engine performance obtained with the manually integrated 2D SLC fan map and the fully integrated 2D SLC fan model – Specific Fuel Consumption vs Turbine Entry Temperature.....	<b>224</b>
<b>Figure 9.2.3.1:</b> Comparison of engine performance obtained with different lip geometries – Intake Pressure Recovery vs Turbine Entry Temperature.....	<b>227</b>
<b>Figure 9.2.3.2:</b> Comparison of engine performance obtained with different lip geometries – Gross Thrust vs Turbine Entry Temperature.....	<b>228</b>
<b>Figure 9.2.3.3:</b> Comparison of engine performance obtained with different lip geometries – Fuel Flow vs Turbine Entry Temperature.....	<b>228</b>
<b>Figure 9.2.3.4:</b> Comparison of engine performance obtained with different lip geometries – Specific Fuel Consumption vs Turbine Entry Temperature.....	<b>229</b>
<b>Figure 9.2.4.1:</b> LP compressor inlet radial total pressure profiles.....	<b>230</b>
<b>Figure 9.2.4.2:</b> Effect of radial inlet total pressure distortion on LP compressor map – Pressure Ratio vs Corrected Mass Flow.....	<b>231</b>
<b>Figure 9.2.4.3:</b> Effect of radial inlet total pressure distortion on LP compressor map – Isentropic Efficiency vs Corrected Mass Flow.....	<b>231</b>
<b>Figure 9.2.4.4:</b> Effect of LP compressor radial inlet total pressure distortion on engine performance – Gross Thrust vs Turbine Entry Temperature.....	<b>233</b>
<b>Figure 9.2.4.5:</b> Effect of LP compressor radial inlet total pressure distortion on engine performance – Fuel Flow vs Turbine Entry Temperature.....	<b>233</b>
<b>Figure 9.2.4.6:</b> Effect of LP compressor radial inlet total pressure distortion on engine performance – Specific Fuel Consumption vs Turbine Entry Temperature.....	<b>234</b>
<b>Figure 9.3.1.1:</b> PYTHIA HBR turbofan engine 0D model (CFM56-5B2).....	<b>236</b>
<b>Figure 9.3.1.2:</b> 3D CFD model based on the CFM56-5B2 intake geometry.....	<b>237</b>
<b>Figure 9.3.1.3:</b> CFD-generated HBR turbofan engine full intake characteristic map.....	<b>239</b>
<b>Figure 9.3.1.4:</b> Pressure recovery effect on HBR turbofan engine performance – Turbine Entry Temperature vs Gross Thrust.....	<b>240</b>
<b>Figure 9.3.1.5:</b> Pressure recovery effect on HBR turbofan engine performance – Turbine Entry Temperature vs Momentum Drag.....	<b>240</b>
<b>Figure 9.3.1.6:</b> Pressure recovery effect on HBR turbofan engine performance – Turbine Entry Temperature vs Net Thrust.....	<b>241</b>

<b>Figure 9.3.1.7: Pressure recovery effect on HBR turbofan engine performance – Turbine Entry Temperature vs Specific Fuel Consumption.....</b>	<b>241</b>
<b>Figure 9.3.1.8: CFD-generated HBR turbofan engine partial intake characteristic map.....</b>	<b>243</b>
<b>Figure 9.3.1.9: CFD model of the CFM56-5B2 intake in a ‘small’ flow domain....</b>	<b>244</b>
<b>Figure 9.3.1.10: Convergence history using a ‘small’ flow domain.....</b>	<b>245</b>
<b>Figure 9.3.1.11: CFD model of the CFM56-5B2 intake in a ‘big’ flow domain.....</b>	<b>245</b>
<b>Figure 9.3.1.12: Convergence history using a ‘big’ flow domain.....</b>	<b>246</b>
<b>Figure 9.3.1.13: Convergence history using a ‘big’ flow domain and intake outlet static pressure correction.....</b>	<b>246</b>
<b>Figure 9.3.1.14: Pressure recovery effect on HBR turbofan engine performance – Flight Mach number vs Gross Thrust.....</b>	<b>247</b>
<b>Figure 9.3.1.15: Pressure recovery effect on HBR turbofan engine performance – Flight Mach number vs Momentum Drag.....</b>	<b>248</b>
<b>Figure 9.3.1.16: Pressure recovery effect on HBR turbofan engine performance – Flight Mach number vs Net Thrust.....</b>	<b>248</b>
<b>Figure 9.3.1.17: Pressure recovery effect on HBR turbofan engine performance – Flight Mach number vs Specific Fuel Consumption.....</b>	<b>249</b>
<b>Figure 9.3.1.18: Convergence history using a ‘big’ flow domain for mass flow matching.....</b>	<b>251</b>
<b>Figure 9.3.1.19: Pressure recovery effect on HBR turbofan engine performance – Altitude vs Gross Thrust.....</b>	<b>252</b>
<b>Figure 9.3.1.20: Pressure recovery effect on HBR turbofan engine performance – Altitude vs Momentum Drag.....</b>	<b>252</b>
<b>Figure 9.3.1.21: Pressure recovery effect on HBR turbofan engine performance – Altitude vs Net Thrust.....</b>	<b>253</b>
<b>Figure 9.3.1.22: Pressure recovery effect on HBR turbofan engine performance – Altitude vs Specific Fuel Consumption.....</b>	<b>253</b>
<b>Figure 9.3.2.1: Schematic representation of PYTHIA’s model of a two-spool, LBR, mixed-exhaust, military turbofan engine.....</b>	<b>256</b>
<b>Figure 9.3.2.2: EJ200 2D schematic diagram and 3D CFD LP compressor model.</b>	<b>258</b>
<b>Figure 9.3.2.3: Meridional view of the first stage of the LP compressor.....</b>	<b>258</b>
<b>Figure 9.3.2.4: LP compressor first stage rotor computational mesh.....</b>	<b>260</b>
<b>Figure 9.3.2.5: LP compressor first stage stator computational mesh.....</b>	<b>260</b>
<b>Figure 9.3.2.6: LP compressor first stage geometry and computational mesh.....</b>	<b>260</b>
<b>Figure 9.3.2.7: Stage passage inlet boundary conditions plane.....</b>	<b>263</b>
<b>Figure 9.3.2.8: Typical contours of radial, circumferential and stratified inlet total pressure distortions.....</b>	<b>263</b>
<b>Figure 9.3.2.9: Passage inlet subdivision into several regions for the modelling of non-uniform total pressure profiles.....</b>	<b>264</b>
<b>Figure 9.3.2.10: Longer passage downstream of first stage and outlet boundary conditions plane.....</b>	<b>265</b>
<b>Figure 9.3.2.11: Effect of a lower total pressure region at the tip on meridional velocity distribution.....</b>	<b>266</b>
<b>Figure 9.3.2.12: Displacement and attenuation of the distorted region through the compressor stage.....</b>	<b>267</b>
<b>Figure 9.3.2.13: CFD derived LP compressor first stage characteristic for uniform inlet conditions – Pressure Ratio vs Corrected Mass Flow.....</b>	<b>273</b>
<b>Figure 9.3.2.14: CFD derived LP compressor first stage characteristic for uniform inlet conditions – Isentropic Efficiency vs Corrected Mass Flow.....</b>	<b>273</b>



<b>Figure 9.3.2.15:</b> Circumferential inlet total pressure variation with time step.....	<b>274</b>
<b>Figure 9.3.2.16:</b> Stratified distortion total pressure variation at stage inlet.....	<b>275</b>
<b>Figure 9.3.2.17:</b> Effect of stratified inlet total pressure distortion on LP compressor stage characteristic – Pressure Ratio vs Corrected Mass Flow.....	<b>276</b>
<b>Figure 9.3.2.18:</b> Effect of stratified inlet total pressure distortion on LP compressor stage characteristic – Isentropic Efficiency vs Corrected Mass Flow.....	<b>276</b>
<b>Figure 9.3.2.19:</b> Effect of inlet stratified distortion on LBR military engine performance – Gross Thrust vs Turbine Entry Temperature.....	<b>278</b>
<b>Figure 9.3.2.20:</b> Effect of inlet stratified distortion on LBR military engine performance – Net Thrust vs Turbine Entry Temperature.....	<b>278</b>
<b>Figure 9.3.2.21:</b> Effect of inlet stratified distortion on LBR military engine performance – Fuel Flow vs Turbine Entry Temperature.....	<b>279</b>
<b>Figure 9.3.2.22:</b> Effect of inlet stratified distortion on LBR military engine performance – Specific Fuel Consumption vs Turbine Entry Temperature.....	<b>280</b>
<b>Figure 9.3.2.23:</b> Radial distortion total pressure variation at stage inlet.....	<b>280</b>
<b>Figure 9.3.2.24:</b> Effect of radial inlet total pressure distortion on LP compressor stage characteristic – Pressure Ratio vs Corrected Mass Flow.....	<b>281</b>
<b>Figure 9.3.2.25:</b> Effect of radial inlet total pressure distortion on LP compressor stage characteristic – Isentropic Efficiency vs Corrected Mass Flow.....	<b>282</b>
<b>Figure 9.3.2.26:</b> Effect of inlet radial distortion on LBR military engine performance – Gross Thrust vs Turbine Entry Temperature.....	<b>284</b>
<b>Figure 9.3.2.27:</b> Effect of inlet radial distortion on LBR military engine performance – Net Thrust vs Turbine Entry Temperature.....	<b>284</b>
<b>Figure 9.3.2.28:</b> Effect of inlet radial distortion on LBR military engine performance – Fuel Flow vs Turbine Entry Temperature.....	<b>285</b>
<b>Figure 9.3.2.29:</b> Effect of inlet radial distortion on LBR military engine performance – Specific Fuel Consumption vs Turbine Entry Temperature.....	<b>285</b>
<b>Figure 9.3.3.1:</b> Schematic representation of PYTHIA’s model of the two-spool LBR mixed-exhaust military turbofan engine.....	<b>290</b>
<b>Figure 9.3.3.2:</b> EJ200 2D schematic diagram and 3D CFD HP turbine model.....	<b>291</b>
<b>Figure 9.3.3.3:</b> HP turbine stator and rotor blades.....	<b>291</b>
<b>Figure 9.3.3.4:</b> HP turbine stator and rotor blade stacking.....	<b>292</b>
<b>Figure 9.3.3.5:</b> LBR military turbofan HP turbine computational mesh.....	<b>293</b>
<b>Figure 9.3.3.6:</b> HP turbine radial total temperature distortion inlet profile.....	<b>295</b>
<b>Figure 9.3.3.7:</b> Meridional view of the hot spot temperature profile.....	<b>296</b>
<b>Figure 9.3.3.8:</b> Hot spot temperature profile over 1/20 <sup>th</sup> of annulus area.....	<b>297</b>
<b>Figure 9.3.3.9:</b> Conventional design - Hot spot aligned to NGV mid-passage (unclocked position).....	<b>297</b>
<b>Figure 9.3.3.10:</b> Managed hot streak design - Hot spot aligned to NGV LE (clocked position).....	<b>298</b>
<b>Figure 9.3.3.11:</b> 3D CFD HP turbine characteristic for two constant speed lines – Non Dimensional Mass Flow vs Stage Overall Pressure Ratio.....	<b>299</b>
<b>Figure 9.3.3.12:</b> 3D CFD HP turbine characteristic for two constant speed lines – Stage Isentropic Efficiency vs Stage Overall Pressure Ratio.....	<b>299</b>
<b>Figure 9.3.3.13:</b> Design point HP turbine performance comparison for inlet total temperature distortion conditions against uniform inlet conditions – Non-Dimensional Mass Flow vs Stage Pressure Ratio.....	<b>301</b>
<b>Figure 9.3.3.14:</b> Design point HP turbine performance comparison for inlet total temperature distortion conditions against uniform inlet conditions – Stage Isentropic Efficiency vs Stage Pressure Ratio.....	<b>301</b>

## ***LIST OF TABLES***

### *Chapter V - 2D Compressor Flow Modelling Using SLC*

<b>Table 5.4.1: <math>C_p</math> polynomial function constants for dry air.....</b>	<b>63</b>
---	-----------

### *Chapter VII - 2D SLC Algorithm Implementation*

<b>Table 7.1.3.1: Codeword structure for program unit notation.....</b>	<b>159</b>
<b>Table 7.1.3.2: Codeword structure for variable nomenclature.....</b>	<b>161</b>

### *Chapter VIII - 2D SLC Software Validation*

<b>Table 8.1.1: Two-stage compressor design overall parameters.....</b>	<b>176</b>
<b>Table 8.1.3.1: Stage comparison between NASA TP 1493 and NASA TP 1294 fans.....</b>	<b>186</b>
<b>Table 8.2.1.1: Sample 2D SLC data compared against PYTHIA's 1D data for a convergent duct.....</b>	<b>193</b>
<b>Table 8.2.1.2: Sample 2D SLC data compared against PYTHIA's 1D data for a divergent duct.....</b>	<b>193</b>

### *Chapter IX - High-Fidelity Engine Performance Simulation*

<b>Table 9.2.1.1: First stage design compressor performance.....</b>	<b>207</b>
<b>Table 9.2.1.2: Notional engine design performance parameters.....</b>	<b>212</b>
<b>Table 9.2.2.1: Number of required iterations per equilibrium running line operating point.....</b>	<b>221</b>
<b>Table 9.3.1.1: CFM56-5B2 turbofan engine performance data.....</b>	<b>236</b>
<b>Table 9.3.2.1: Two-shaft, LBR, military turbofan engine design performance parameters.....</b>	<b>257</b>
<b>Table 9.3.2.2: LP compressor first stage geometric characteristics.....</b>	<b>259</b>
<b>Table 9.3.2.3: Results for different magnitudes of inlet stratified total pressure distortion.....</b>	<b>269</b>
<b>Table 9.3.2.4: Results for different types of distortion with the same extent and the same distortion magnitude.....</b>	<b>270</b>
<b>Table 9.3.2.5: Results for different types of distortion with similar inlet average total pressure drops.....</b>	<b>271</b>
<b>Table 9.3.3.1: Two-shaft, LBR, military turbofan engine design performance parameters.....</b>	<b>290</b>
<b>Table 9.3.3.2: LBR military turbofan HP turbine performance.....</b>	<b>291</b>
<b>Table 9.3.3.3: LBR military turbofan HP turbine grid resolution.....</b>	<b>293</b>
<b>Table 9.3.3.4: LBR military turbofan HP turbine inflow boundary conditions.....</b>	<b>295</b>
<b>Table 9.3.3.5: HP turbine performance comparison for inlet total temperature distortion conditions against uniform inlet conditions.....</b>	<b>300</b>



**Table 9.3.3.6: HP turbine efficiency comparison for inlet total temperature distortion conditions against uniform inlet conditions..... 300**

**CHAPTER I****INTRODUCTION**

This chapter discusses the reasons and considerations that led to the undertaking of this particular research activity and explains the concept of 'Gas Turbine Advanced Performance Simulation'.

**1.1. Background**

The cost of research, development and implementation of new technology in gas turbine systems is becoming prohibitively expensive. The global competition in the commercial gas turbine industry has initiated pioneering research for the reduction of development costs and time and the improvement of engine performance, efficiency and reliability. One of the main contributors to the high development cost is the need to perform many large-scale hardware tests.

Design and development costs could potentially be reduced by replacing some of the large-scale tests, currently required for product development, with high-resolution, highly integrated component-system computational simulations. A more extensive use of sophisticated simulation tools, would certainly save a large portion of the costs directly associated with testing, and also enable the effects of design changes to be studied in detail, before a commitment to a final design is made. In other words, by simulating gas turbine systems, in sufficient detail early in the design process, critical design and cost issues can be identified and resolved on time, before hardware is built.

Moreover, the recent rapid development of gas turbine diagnostic techniques such as non-linear gas path analysis, fuzzy logic, neural networks and genetic algorithms, demands more accurate engine models (higher level of fidelity) and shorter simulation times. During engine diagnosis, using any of the above techniques, an engine model is required to run off-design hundreds or even thousands of times. For the time being however, 'high-fidelity simulation' and 'faster simulation' are two contradictory concepts.

Current commercial 'state of the art' engine simulation software is of a low fidelity, in that there is no axial, radial or circumferential resolution within given engine component models. In these zero-dimensional cycle simulations, individual component performance characteristics are typically represented via non-dimensional, look-up tables (maps) of experimental or default data, with empirical adjustments for off-design effects, such as variable geometry, Reynolds effects, gamma correction and clearances. In addition, non-dimensional characteristics usually refer to component nominal operating conditions.

In those cases where actual component characteristics are not available and default characteristics are used instead, conventional zero-dimensional simulation tools can offer a good prediction of the performance of the whole engine close to design point, but can deviate substantially at off-design and transient conditions. On the other hand,



even when real component characteristics are available, conventional engine cycle simulation tools can not predict the performance of the engine at other than nominal conditions satisfactorily, since individual component characteristics are usually established during component rig tests under nominal conditions.

Conventional low-fidelity gas turbine performance simulation tools can offer a good prediction of the performance of a whole engine under nominal conditions but are incapable of analyzing the performance of individual engine components in detail, or capturing complex physical phenomena such as inlet flow distortion. On the other hand, direct numerical analysis has the ability to carry out computations at different levels of resolution and predict the performance of individual engine components under various operating conditions satisfactorily, but does not offer whole engine performance prediction.

Sometimes a detailed engine component simulation is sufficient to determine the performance characteristics of that component (e.g. fan). The presence of other upstream or downstream engine components (compressor, bypass duct, etc.) however, also affects the flow conditions and hence, effects from these components must also be considered. For this reason, using an isolated simulation of one component alone may not be sufficient. The remaining engine components must be included in the simulation to account for inter-component effects.

One may think that the obvious answer to the above mentioned issues is the three-dimensional analysis of the whole engine system. By modeling the entire geometry of a propulsion system at the highest level of resolution, all the information necessary to assess engine life, reliability and performance could perhaps be collected. Two issues, however, prevent this from being a practical solution. Firstly, for a complete three-dimensional system simulation, the amount and level of detailed information needed as boundary and initial conditions would be extremely difficult to obtain. Secondly, the computational time and cost will be extremely high for effective and practical use in an industrial or academic research environment.

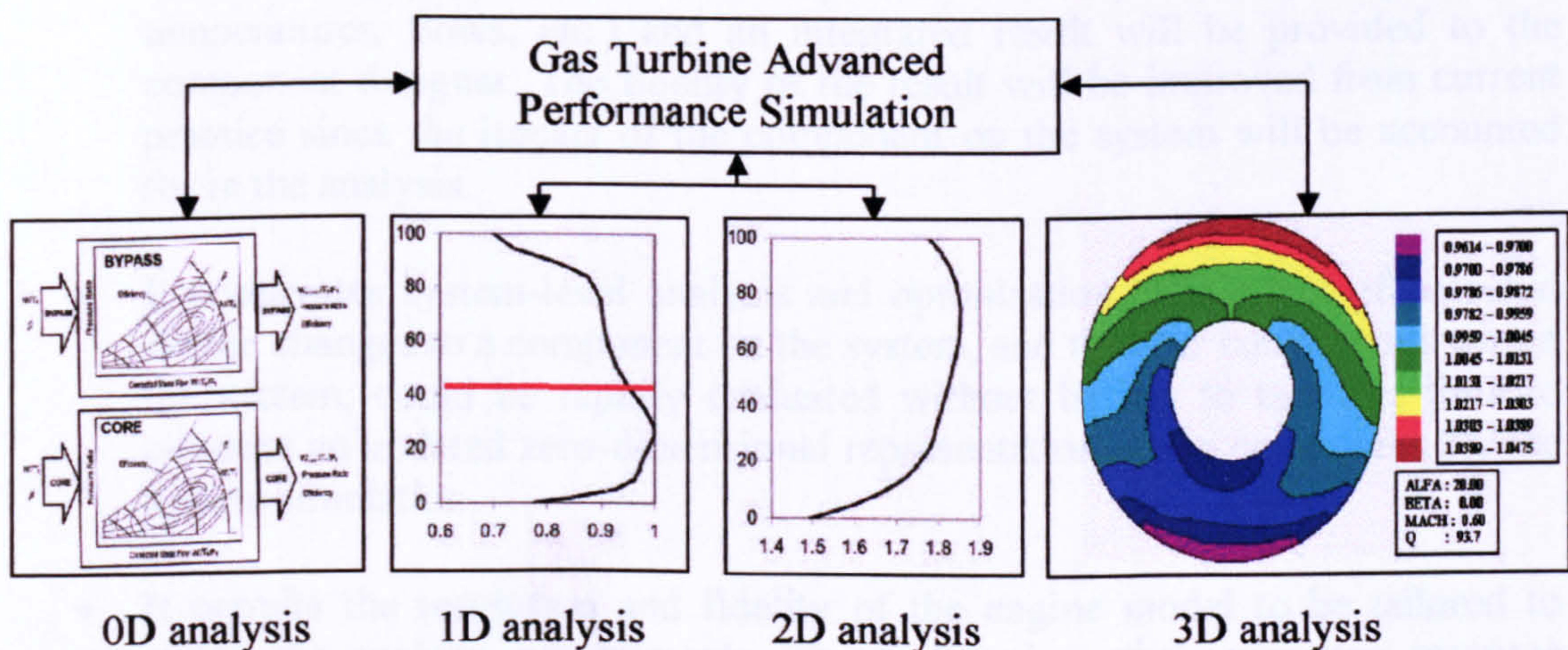


Figure 1.1.1: Software integration for advanced engine performance analysis

Although the available computational power has increased exponentially over the last two decades, a detailed analysis of an entire propulsion system still seems to be so



complex and computationally intensive as to remain cost-prohibitive. For this reason, a method (or methods) of integrating different types and levels of analysis is necessary. The integration of simulation codes that model at different levels of fidelity into a single simulation provides the opportunity to reduce the overall computing effort needed while retaining the desired level of analysis in specific engine components (Figure 1.1.1). The following section explains the concept of ‘Gas Turbine Advanced Performance Simulation’ and discusses its advantages in more detail.

## ***1.2. Advanced Performance Simulation***

By integrating a higher fidelity component simulation within a low-fidelity system simulation, it is possible to ‘zoom in’ on the relevant flow physics taking place in any given component. Such a scheme would allow a designer to quickly and efficiently determine the effects of component design changes on the operation of both the component as well as the entire propulsion system. This type of detailed analysis would be performed, for example, to study the effects of a new fan blade design, or inlet flow distortion, or tip treatment modifications on engine response, at an affordable computational cost and time.

‘Gas Turbine Advanced Performance Simulation’ basically involves the execution of a higher order component analysis code and the results from this analysis being used to adjust the zero-dimensional component performance characteristics within the system simulation. By utilizing data from a more predictive, physics-based, higher order analysis code, complete cycle simulations can be refined to more closely model and predict the complex physical processes taking place in an engine. This capability provides multiple benefits to the engine design and development process:

- It enables potential component designs to be more fully and rapidly evaluated in the context of the overall engine performance. The concept will automatically provide accurate component boundary conditions (pressures, temperatures, flows, etc.) and an integrated result will be provided to the component designer. The fidelity of the result will be improved from current practice since the impact of the component on the system will be accounted for in the analysis.
- It accelerates system-level analysis and optimisation. The effect of potential design changes to a component on the system, and to other components within the system, could be rapidly evaluated without having to take the time to generate an updated zero-dimensional representation of the component for the system simulation.
- It permits the resolution and fidelity of the engine model to be tailored to match the analysis requirements. This will reduce the computing resource requirements since high-fidelity analysis is applied only to the components of interest where the increased resolution is required to support a particular analysis.

- And generally, the engine system simulation will become more predictive, since component performance characteristics will be derived from physics-based, first-principle analysis codes. This will increase design confidence prior to commitment to hardware.

From the onset of this work, four different methods were identified for carrying out 'Advanced Performance Simulation'. These methods can be applied to all engine components and involve different levels of complexity and hence, applicability:

#### The De-Coupled Approach

This is a manual approach to high-fidelity analysis. Several zero-dimensional engine cycle simulations are carried out for a range of flight conditions and a range of engine power settings to generate an approximate database of different component operating conditions. The high-fidelity component model takes information generated by the corresponding, baseline, non-dimensional representation of the same component and uses that data as boundary conditions. After several high-fidelity runs, a new component map is generated. The operating characteristics of the high-fidelity component model are integrated back into the zero-dimensional cycle model via the component characteristic map, generated from the averaged, high-fidelity flow solutions.

#### The Iterative Approach

This is a semi-manual approach to high-fidelity analysis. This approach couples and partially integrates the high-fidelity component model with the low-fidelity cycle analysis in that there is no automatic link between them. It requires matching the correct component operating point via an iterative execution of the low-fidelity cycle and the higher fidelity component model. A partial component characteristic map can be also generated for use at a later stage without iteration. The non-dimensional cycle program is used primarily to reduce the parameter space that has to be examined by the higher order component in the program.

#### The Fully Integrated Approach

This is a fully automated approach. The non-dimensional cycle program basically provides the backbone where non-dimensional and high-fidelity engine components are linked. It takes all the non-dimensional cycle information from the entire engine and uses it as boundary conditions (initial guesses) to the high fidelity component models until the correct component operating point is established. Execution of the cycle program and the high-fidelity component simulations is done iteratively and in a parallel fashion, with the high-fidelity components passing the necessary (high-fidelity or averaged back to non-dimensional) information to the next component or the engine cycle at real-time. The fully integrated approach has the potential to develop into a real-time, full two-dimensional or three-dimensional cycle simulation, provided that all component representations are of high-fidelity.

#### The 'Jump-Start' Approach

Another approach would be to use medium-fidelity (i.e. two-dimensional) component models as an intermediate simulation. This has the advantage of not requiring as much execution time as a three-dimensional simulation when less accuracy is needed. In addition, it would be possible to use the solution from the medium-fidelity simulation



to ‘jump-start’ a higher-fidelity (i.e. three-dimensional) solution, thus shortening the execution time of the higher-fidelity simulation.

The first three methods are discussed explicitly and in much more detail in *Chapter IX - High-Fidelity Engine Performance Simulation*. The last method (‘jump-start’) is simply an indirect approach which derives from the combination of the other three.

### ***1.3. CFD versus Through-Flow Analysis***

This particular section discusses the author’s view on how ‘Advanced Performance Simulation’ could actually be implemented in practice.

Reynolds-Averaged Navier-Stokes (RANS) Computational Fluid Dynamics (CFD) analysis has been used for quite some time with various degrees of success to simulate the flow field inside isolated engine components. It has offered over the years promising results and will probably become the standard in high-resolution gas turbine modelling and performance simulation in the future.

For the time being however, it seems that CFD analysis suffers from certain drawbacks that prevent its widespread application, at least as far as advanced engine performance analysis is concerned. For example, it can not satisfy requirements such as whole engine performance simulation, within a realistic amount of time and computational resource and the use of a single computational platform. The integration of just two high-fidelity CFD component models into the same low-fidelity cycle would require extremely long execution times and probably the use of distributed or parallel computing architecture.

CFD analysis also suffers from the fact that it requires a very high amount of manual intervention. Robust CFD models usually take a long time to set up, i.e. produce an accurate geometry, generate a grid, carry out a grid independence study, run CFD, calibrate and improve the initial model and so on.

Moreover, commercially available CFD tools do not allow in-house empiricism and expertise to be incorporated in the flow-field solution in the form of deviation and loss models, and in those cases where CFD results differ from experiments there is really little the user can do in order to identify the source of the inaccuracy and calibrate the model.

CFD analysis seems to be unable to provide a sufficiently accurate, real-time engine performance prediction required in many cases, for example when running diagnostics. For the above reasons, a high-fidelity CFD analysis would perhaps be more appropriate for the de-coupled and iterative types of advanced simulation which both involve the generation of a standard component characteristic map that can be used at a later stage by a zero-dimensional cycle analysis. Since the maps can be generated at any time before the actual cycle analysis, the CFD component representations may as well be three-dimensional.

The de-coupled and iterative approaches to ‘Advanced Performance Simulation’, allow selected components to be simulated in detail individually, and be integrated

into a low-fidelity engine simulation at a latter stage and at an affordable computational cost. In cases where the fidelity levels are too far apart however, (e.g. a three-dimensional CFD component model and a non-dimensional engine simulation code) a different problem arises. A large portion of the performance data can be 'lost' due to extensive averaging required to pass information from one code to the other, in the form of a non-dimensional map. That can have the effect of certain averaged flow phenomena 'appearing' exaggerated or underestimated in the whole engine performance analysis.

Let us consider for example, the case of an engine cycle with a high-fidelity model of a single-stage fan and a non-dimensional model of a booster, simulated at conditions of severe fan inlet pressure distortion. In reality, the location and type of the distortion leaving the fan would influence the performance of the booster. In this case however, the non-dimensional model can only receive a single, averaged value of fan outlet total pressure which may result in a different booster performance and hence engine performance.

The fully integrated type of analysis has the potential to overcome this problem by linking together several high-fidelity components. As mentioned before, using three-dimensional CFD analysis would result in a high computational demand. On the other hand, a flexible, two-dimensional through-flow analysis code, based on a fast and robust computational technique, could provide a fairly accurate representation of the flow field, as well as the ability to study complex phenomena and their effects on engine performance, in a more cost- and time-effective manner than CFD.

Although the detailed, three-dimensional CFD analysis of an entire propulsion system is still impractical and cost-prohibitive for the reasons mentioned before, a two-dimensional through-flow analysis of the whole engine would be quite feasible even with today's computational tools.

Incorporating in-house expertise, two-dimensional through-flow component models could be used directly by an engine simulation code, to provide a more accurate performance prediction for individual engine components, based on the actual component geometry. A full, two-dimensional engine analysis program, could avoid the errors associated with the averaging of performance data altogether, and could overcome the long execution times, complexity and impracticality associated with the use of three-dimensional CFD software. Moreover, if such a requirement arises, it could still provide an even more accurate prediction when combined with CFD models of the same or higher resolution according to the 'jump-start' approach mentioned above.

The following chapters are focused on supporting the views discussed above.



## CHAPTER II

# **PROJECT OBJECTIVES**

This chapter describes briefly the long-term ambition of this research effort and then focuses on the objectives and milestones that had to be achieved in the context of this particular work.

### ***2.1. Long-Term Research***

Research certainly never stops and hopefully researchers will continue to pursue this or similar research efforts long after the completion of this particular activity. The long-term objective of this work is the development of a sophisticated simulation tool that will enable in the future the performance simulation of an entire propulsion system, at the highest level of resolution and at an affordable computational and financial expense. This will allow multidisciplinary processes and component interactions, currently observable only in expensive, large-scale engine tests, to be captured and analysed in the context of the whole engine performance, life and reliability. By being able to simulate the performance of full gas turbine systems in detail, early in the design process, critical design and cost issues will be identified and resolved on time and design and development costs will be considerably reduced.

As mentioned previously, despite the large increase in computational power over the last two decades, a three-dimensional analysis of an entire propulsion system still remains quite impractical and cost-prohibitive in terms of complexity and computational resources.

### ***2.2. Thesis Objectives***

The objective of this work was to investigate different simulation strategies for communicating the performance characteristics of an isolated gas turbine engine component, resolved from a detailed, high-fidelity analysis, to an engine system analysis carried out at a lower level of resolution. This would allow component-level, complex physical processes to be captured and analyzed in the context of the whole engine performance, at an affordable computing resource and time.

In the context of this study, the first three methods of advanced performance simulation, identified in *Chapter I - Introduction* as de-coupled, iterative and fully integrated, were to be thoroughly investigated in terms of their actual implementation and potential. The last method ('jump-start'), being simply an indirect approach which derives from the combination of the other three, was not to be attempted for obvious reasons.



### Primary Objectives

The primary objective of this work was the investigation of the three simulation strategies, utilising 2D engine component models based on a well-established through-flow analysis method. For the reasons discussed in *Chapter I - Introduction*, this approach was identified as the most promising and the one with the larger potential to lead to a two-dimensional through-flow analysis of the entire engine system, at an affordable computing resource, in the short or medium term.

For the purposes of the primary objective, Streamline Curvature (SLC) was selected as the method to carry out the through-flow analysis. Streamline curvature methods have continued to receive refinements over the years and are still considered by industry as ‘state of the art software’, capable of providing an accurate, quick and inexpensive solution compared to the full, three-dimensional CFD methods. The reasons for selecting streamline curvature as the through-flow analysis method are discussed in more detail in *Chapter IV - Literature Review*.

In the context of the primary objective, basic cold-section engine components (i.e. intake, conical duct, annular duct and compressor) were to be modelled in two dimensions in order to take part in the subsequent engine advanced simulation studies. This demanded the development of robust SLC software. A *2D Intake SLC Software* was to be developed to handle the performance of intakes and ducts, and a *2D Compressor SLC Software* was to be developed to handle the performance of compressors.

The basic capability that the *2D Intake SLC Software* was initially required to handle is outlined below:

- Facilitate performance analysis in two dimensions of conical and annular intakes
- Carry out DP and OD analysis
- Handle both subsonic and transonic regimes
- Identify intake choking conditions
- Handle any intake geometry
- Calculate the properties of the viscous flow field at predefined stations throughout the intake annulus
- Calculate overall intake map
- Handle non uniform inlet flow conditions
- Handle standard and user defined models for rounded or sharp lip losses, diffuser losses, entry-diffuser interaction losses, Reynolds effects, incidence angle effects, boundary layer blockage etc.
- Link to lower fidelity cycle analysis software for high-resolution studies
- Provide a converged solution at any given operating point within minutes
- Facilitate performance analysis in two dimensions of conical and annular ducts and nozzles with little modification

The basic capability that the *2D Compressor SLC Software* was initially required to handle is outlined below:

- Facilitate compressor performance analysis in two dimensions
- Carry out DP and OD analysis

- Handle both subsonic and transonic regimes
- Identify conditions for surge and choking
- Handle multi-stage compressors
- Handle any type of blade profile such as the British C-series, NACA 65-series, DCA or user defined blade geometries
- Handle any 3D compressor geometry
- Calculate the properties of the viscous flow field at predefined stations throughout the compressor annulus
- Calculate overall compressor map
- Handle non uniform inlet flow conditions
- Handle standard and user defined models for secondary losses, shock losses, Reynolds, deviation, incidence, boundary layer blockage etc.
- Link to lower fidelity cycle analysis software for high-resolution studies
- Provide a converged solution at any given operating point within minutes

The above software was also required to provide great flexibility, in the sense that it could be used as:

- A performance prediction tool for components of a known design
- A development tool to assess the changes in performance of a known component after implementing small geometry changes
- A design tool to verify and refine the outcome of a preliminary design analysis
- A 'teaching' tool to provide the user with an insight of the two-dimensional flow field inside an engine component and how this could be effectively predicted using the streamline curvature method, combined with various algorithms and loss models
- A plug-in tool that could be integrated into a conventional 0D gas turbine engine simulation code for high-fidelity studies

### Secondary Objectives

The secondary objective of this work was the investigation of the de-coupled, iterative and fully integrated advanced simulation strategies, utilising 3D engine component models based on CFD analysis. As mentioned before, a three-dimensional CFD analysis of an entire propulsion system may remain impractical for the time being, however, in the long term it will probably become the standard in high-fidelity analysis and therefore needs to be thoroughly researched.

Similarly to the primary objectives, the three advanced simulation strategies were to be investigated in terms of their actual implementation and potential by looking into the relative changes in engine performance after integrating the CFD-generated, high-fidelity component performance back into the 0D engine analysis. For this purpose, several case studies were to be looked at, such as different types and extents of compressor inlet pressure distortion and of turbine inlet temperature distortion.

Due to the magnitude of the primary and secondary objectives, the secondary objectives were to be fulfilled through the technical leadership of the author with the assistance of visiting and Thermal Power MSc students.



**CHAPTER III****THESIS STRUCTURE**

This manuscript is divided into ten *Chapters*, each one subdivided into several *Sections* and *Subsections*. *Chapters* are referenced using Latin numerals (i.e. *Chapter I - Introduction*) while *Sections* and *Subsections* are identified by two and three numbers respectively (i.e. *Section 5.2. Continuity of Mass Flow* and *Subsection 5.11.1. Calculation of Profile Losses*).

*Chapter IV - Literature Review*, refers to the broader literature review that was performed in the context of this investigation. It is focused on three key areas of interest, which were identified to be closely linked to the objectives of this research. These three broader topics are covered in individual *Sections*, namely *Section 4.1. 0D Gas Turbine Performance Simulation Software*, *Section 4.2. High-Fidelity Gas Turbine Performance Simulation* and *Section 4.3. Turbomachine Through-Flow Analysis Methods*.

*Chapter V - 2D Compressor Flow Modelling*, refers to the modelling of the compressor flow field using Streamline Curvature (SLC). The scope of this chapter is to explain in detail the theoretical background of the streamline curvature through-flow analysis method and of the various empirical models adopted by this work for the modeling of the compressor flow field and the development of the *2D Compressor SLC Software*. More analytically, the derivation of the streamline curvature equations and the full radial equilibrium equation is discussed in *Section 5.1. Compressor Streamline Curvature Equations*. Sections 5.2 to 5.5 discuss general flow field modelling issues such as the calculation of the continuity of mass flow by integration, the calculation of velocity triangles, and the calculation of thermodynamic and streamline properties. Sections 5.6 and 5.7 discuss analytically the various models used for the calculation of blade incidence and deviation. Blade passage choking and stall are discussed in sections 5.8 and 5.9 respectively. *Section 5.10. Calculation of Compressor End-Wall Boundary Layer* discusses the calculation of the boundary layer blockage factors throughout the compressor flow passage and finally section 5.11 explains the calculation of blade losses, with different sources of blade loss being addressed in separate subsections.

*Chapter VI - 2D Intake and Duct Flow Modelling*, explains in detail the various empirical models adopted by this work for the modeling of conical and annular intakes and ducts and the subsequent development of the *2D Intake Compressor SLC Software*. *Section 6.1. Intake Streamline Curvature Equations* examines the streamline curvature equations that were used for the modelling of the flow field inside intakes and ducts. *Section 6.2. Calculation of Intake Pressure Recovery* explains the loss models adopted for the calculation of pressure recovery loss due to intake lip geometry, diffuser geometry, entry-diffuser interactions and incidence angle effects. Finally, section 6.3 describes the calculation of the intake end-wall boundary layer.

*Chapter VII - 2D SLC Component Algorithms*, focuses on the description of the individual component algorithms that were developed for the purposes of this investigation. Apart from describing in detail the design, structure and execution of each algorithm this chapter also refers to the general programming features and principles that were adopted by this work. Software programming features are discussed in section 7.1. *Section 7.2. 2D Compressor SLC Algorithm* describes the capability and general execution of the 2D compressor SLC algorithm, and similarly *Section 7.3. 2D Intake SLC Algorithm* describes the capability and general execution of the 2D intake SLC algorithm. Section 7.4 discusses some convergence stability issues and the numerical methods that were used in the development of the software.

*Chapter VIII - 2D SLC Software Validation*, refers to the validation of the streamline curvature component algorithms developed in the context of this work, against experimental and published data. This chapter describes analytically the initial validation that was first carried out for the *2D Compressor SLC Software* against experimental data, the adaptation of the loss model, and the final agreement achieved with the published data. Compressor 2D flow property profiles are also presented and compared against experimental data in this chapter. The validation of the *2D Intake SLC Software* was carried out using ESDU data as a reference.

*Chapter IX - High-Fidelity Engine Performance Simulation*, first discusses in detail the three basic advanced performance simulation strategies, described briefly in *Chapter I - Introduction*, and then focuses on their actual implementation by looking at several case studies of high-fidelity SLC and CFD components integrated into a 0D cycle analysis. This chapter also describes briefly the software tools that were used to carry out this analysis and their integration requirements. More analytically, the advantages and limitations of the three advanced performance simulation strategies are discussed in section 9.1. *Section 9.2. 2D SLC Gas Turbine Performance Simulation* discusses changes in the simulated engine performance arising from the integration of 2D SLC components into a 0D cycle analysis, and *Section 9.3. 3D CFD Gas Turbine Performance Simulation* refers to high-fidelity engine performance simulation by looking at the integration of 3D CFD component characteristics into a 0D cycle analysis.

Finally, *Chapter X – Conclusions and Future Work*, summarises the conclusions, achievements and limitations of this study and provides a list of future work and recommendations for potential software and methodology improvements.



**CHAPTER IV*****LITERATURE REVIEW***

The scope of this work is the investigation of simulation strategies to facilitate engine performance analysis performed at different levels of resolution. This involves the integration of high-fidelity engine components, capable of capturing complex flow phenomena, into a cycle analysis performed at a lower level of resolution. The broader literature review performed in the context of this investigation was focused on the following three key areas of interest, which were identified to be closely linked to the objectives of this research:

- 0D gas turbine performance simulation software
- High-fidelity gas turbine performance simulation
- Turbomachine through-flow analysis methods

The following sections in this chapter address the above three broader topics. The literature review carried out for specific loss and deviation models, which were incorporated in the *2D SLC Software*, is covered in subsequent chapters and sections explicitly.

#### **4.1. 0D Gas Turbine Performance Simulation Software**

There is a large number of in-house and commercially successful gas turbine (and related) performance modelling software which is currently used by industry and academia. The majority of this software has been available for many years now, even decades in many cases, and has been developed by several different people which makes tracing accurately the beginning of its development a rather difficult task. However, the features and capabilities of each software package can be easily identified from public resources and categorised (*Appendix A - 0D Performance Simulation Software Matrix*). In the following paragraphs, the different categories have been highlighted in *italic*. The twenty two, most popular simulation codes that were reviewed, are listed below in alphabetical order:

- |               |              |             |
|---------------|--------------|-------------|
| •GasTurb      | •GateCycle   | •GECAT      |
| •GSP          | •GT MASTER   | •GT Pro     |
| •GTS          | •NCP         | •NEPP       |
| •PEPSE-GT     | •PYTHIA      | •RRAP       |
| •STEAM Master | •STEAMOMATCH | •STEAM Pro  |
| •TESS         | •Thermoflex  | •TURBOFLEXI |
| •TURBOMATCH   | •TURBOTEST   | •TURBOTRANS |
| •VARIFLOW     |              |             |

##### Application

Most software share similar range of application and are used either as *design* tools (i.e. GT Pro, STEAM Pro) or performance *simulation* packages (i.e. GasTurb, GSP,

TURBOMATCH) or both (i.e. NCP). Approximately half of the software reviewed can only handle *aero-type* engines (i.e. GasTurb, NEPP, TESS) while the other half can handle *industrial-type* engines (i.e. Thermoflex, GT Master). A limited number of software can actually handle both engine types (i.e. TURBOMATCH, PYTHIA, PEPSE-GT). The most sophisticated ones are of the *fully flexible* configuration (i.e. TESS, NEPP, GTS) with a large number of *application specific* software (i.e. GateCycle, NCP) still being used widely.

### Configuration

In terms of configuration, software can be distinguished between *fixed* and *modular*, meaning that engine models are assembled from interconnected engine components treated as separate bricks. An example of *fixed* configuration software is GasTurb, whereas TURBOMATCH and PYTHIA adopt the fully *modular* approach.

### Performance Modelling

The vast majority of gas turbine performance simulation software handles the *design point* and *off-design* performance of engines (steady-state). The *transient* performance is only covered by a small number of software such as TURBOTRANS, RRAP, GTS, GasTurb etc.

### Cycle

Most software, such as GTS and GECAT will handle the modelling of simple *gas turbine* cycles with or without *recuperation* and *inter-cooling*. More specialised codes such as Thermoflex and GateCycle can also model *steam turbines*, *combined cycle / cogeneration*, *steam power plants*, *coal – gasification* and *waste – to – energy* cycles. *Biomass – gasifiers* can be handled by GSP while *heat recovery steam generators* can be modelled by PEPSE-GT, Thermoflex and GasTurb.

### Performance Features

Different software incorporates different performance modelling capability. Perhaps the most common features, which are encountered in more than one code, are listed below:

- |                                     |   |
|-------------------------------------|---|
| • <i>Alternative Working Fluids</i> | • <i>Alternative Working Fuels</i>        |
| • <i>Effects of Deterioration</i>   | • <i>Effects of Inlet Flow Distortion</i> |
| • <i>Small Effects</i>              | • <i>Monte Carlo</i>                      |
| • <i>Flight Envelope</i>            | • <i>Exhaust Gas Emissions</i>            |
| • <i>Installation Losses</i>        | • <i>Reynolds</i>                         |
| • <i>Chemical Dissociation</i>      | • <i>Rig Test Analysis</i>                |
| • <i>Engine Diagnostics</i>         | • <i>Optimisation</i>                     |
| • <i>Engine Limiters</i>            | • <i>Multimode VSE Simulation</i>         |
| • <i>Combustor Blow-out</i>         | • <i>Relight</i>                          |

From the above list, *alternative working fluids*, *different working fuels*, *small effects* and *engine limiters* are handled by the majority of software. NCP, NEPP, GECAT and GasTurb seem to be the most versatile codes, incorporating most of the features listed above.



### Control

All software reviewed here is of the *open loop* control type, apart from GTS that can handle both *open* and *closed loop* control types.

### Software Features

Other features that gas turbine performance simulation software tends to incorporate are listed below:

- Control Loop
- Macro
- Fix-A-Pressure
- Multiple Model Simulation
- GUI
- Parameter Matching
- Fix-A-Flow
- Dynamic Convergence Control
- OLE Automation

The objective of most of the above features is to make software more versatile, more flexible and hence, more user-friendly. The use of *macro*, *fix-a-flow*, *fix-a-pressure* and *GUI* is particularly common amongst the codes reviewed.

## **4.2. High-Fidelity Gas Turbine Performance Simulation**

This section reviews attempts towards high-fidelity analysis that were published before and during this particular research work. Because there is only a handful of known cases, and due to their relevance with this investigation, it is proper to discuss them in a bit more detail. The author's own publications during this period are also briefly reviewed in this section.

It is acknowledged that research on gas turbine high-fidelity performance simulation is being carried out worldwide, by several engine manufacturers and research establishments. It seems however that NASA in the USA and Cranfield University in Europe have been involved in a very large portion of the total publications on the subject over the last five years or so.

### **4.2.1. NASA Numerical Propulsion System Simulation (NPSS)**

In the context of the NPSS program (Lytle, 2000), Reed and Afjeh (June 1994 and January 1995) have published several papers on high-fidelity analysis and numerical zooming techniques. By utilizing Object Oriented programming (OO), NASA and industry initiated the definition and implementation of an object class structure that enables the integration of a conventional, zero-dimensional cycle simulation (NPSS Version 1), with higher fidelity analysis codes. Within NPSS, a prototype simulation of a one-dimensional model for a complete turbofan engine, with the fan component analysed to a three-dimensional level, was created to provide support for advanced performance modelling. The three-dimensional geometry of other components such as booster, core outlet guide vanes and bypass outlet guide vanes was not included in the simulation in order to reduce computing time. Moreover, a single blade passage was only analysed using a structured, multi-blocked, three-dimensional grid consisting of 16,380 grid points. To determine the averaged flow parameters at the exit boundary,

the mass-averaging process was carried out at a location approximately one and a half fan diameters downstream of the fan trailing-edge.

Initially, the non-dimensional component representation of the fan in the zero-dimensional cycle analysis provided single inlet boundary values for total pressure, total temperature and Mach number, and the exit boundary value of static pressure, for the high-fidelity fan analysis. These were then extrapolated to appropriate three-dimensional field distributions and applied as boundary conditions to the fan simulation. The results of the high-fidelity fan simulation were then integrated to determine the mass-flow rate and the mass-averaged values of total pressure and temperature ratios. The averaged total pressure ratio was then compared with the total pressure ratio computed across the non-dimensional fan representation. If the values were found to be in agreement, then the averaged values of mass flow rate and total temperature ratio were used in the zero-dimensional simulation. Typically, the averaged total pressure ratio would not initially match the low-fidelity value and boundary conditions would have to be redefined and the above process repeated again until boundary conditions converged.

The above iterative approach to boundary condition matching was found in practice to be rather time consuming. Performing multiple runs of the high-fidelity component simultaneously and in parallel, to generate a single curve performance map from which the appropriate value could be chosen by interpolation, eliminated the need to iterate and hence, reduced the overall computation time. The simulation was carried out on a high-performance parallel computing platform (Reed and Afjeh, April 1994).

In order to further reduce the overall simulation time, established component operating points (curve points) were retained and used to create an overall component performance map. Before carrying out a high-fidelity analysis, this performance map was checked to establish whether the current operating conditions were within the data range and was then interpolated accordingly. The established overall component performance map could also be stored and used in a conventional zero-dimensional analysis at a later stage. In July 1997, Reed and Afjeh published another paper on the comparative study of high and low fidelity fan models for turbofan engine system simulation.

#### **4.2.2. NASA-Pratt & Whitney 1D Compressor Simulation**

Follen and auBuchon (2000) described a collaborative effort between NASA and Pratt & Whitney on 1-D compressor zooming. In the context of the NPSS program, Pratt & Whitney demonstrated the one-dimensional, row-by-row analysis of a high-pressure compressor, integrated with the zero-dimensional NPSS Version 1 cycle simulator. The objective of the analysis was to incorporate the high fidelity results back in the zero-dimensional system simulation so that the system effects could be captured. Basically, the row-by-row analysis of the high-pressure compressor established the performance of each row of the compressor and the integrated prediction for the overall engine system.

In order to establish a baseline for the compressor high-fidelity demonstration, the zero-dimensional compressor characteristics were calibrated such that at the baseline



conditions there was no difference between the non-dimensional high pressure compressor representation and the characteristics predicted by the one-dimensional, mean-line analysis code.

The analysis followed the general iterative process described before in the case of the high-fidelity fan simulation:

- A baseline, zero-dimensional cycle analysis was first executed in the absence of the one-dimensional, high-pressure compressor representation.
- The high-fidelity component analysis was then carried out at the same boundary conditions defined by the zero-dimensional simulation. Speed was allowed to vary in the one-dimensional model, in order to adjust the speed-flow characteristic of the one-dimensional component. A different value of efficiency, at the same inlet airflow and pressure ratio, was then obtained from the one-dimensional analysis.
- The new speed and efficiency were then imposed on the non-dimensional component by utilizing scaling factors.
- With the updated high-pressure compressor performance characteristics, a zero-dimensional cycle analysis was executed again.
- Compressor speed and boundary conditions were checked and if outside of tolerance, the one-dimensional code was launched again with updated compressor boundary conditions from the converged engine system simulation.

Two case studies were explored by Pratt & Whitney in order to demonstrate the advantages of advanced performance modelling:

- A 2% increase in high-pressure compressor bleed, relative to a baseline. The bleed was assumed to be taken at the fifth stage of the six-stage high-pressure compressor.
- A linear change in high-pressure compressor rotor tip clearance. In this case, the forward tip clearances were increased and the aft decreased such that there was no change to the “average” compressor clearance.

In NPSS Version 1 the effects of inter-stage bleeds on the performance of the high-pressure compressor are only simplistically taken into account. The high-fidelity analysis in the first case demonstrated that the non-dimensional compressor model was not able to capture the effect of the change in compressor bleed on compressor efficiency and hence, on overall engine performance. On the other hand, the high-fidelity analysis provided a more accurate prediction of system and component behaviours, which could lead to a more optimum design, or perhaps optimised control implementations to accommodate the limits in high-pressure compressor stall margin.

Similarly, effects of changes in rotor tip clearances in NPSS Version 1 were simulated via adjustments to the compressor efficiency as a function of a change in the average compressor clearance from a default value. In the second case, the zero-dimensional model was incapable of predicting the effect of row-by-row changes in tip clearances since the average clearance remained unchanged. The high-fidelity analysis revealed a small change in overall engine performance, in addition to the change in stability margin of individual stages. With tighter clearances the rear stages demonstrated

higher stage loading and therefore less stability margin than the baseline case. This information could be used to determine if sufficient stability margin existed to accommodate a clearance change of this magnitude.

In both cases the analysis was carried out more rapidly and at more operating conditions than would be practical with manual execution of the one-dimensional analysis, and provided more information than could previously be obtained through the traditional zero-dimensional engine simulation.

The NPSS approach described above could be expanded to include more engine components by utilising distributed and parallel computing. Directly replacing the zero-dimensional compressor model with its one-dimensional counterpart was not attempted in order to retain a common strategy for interfacing other high-fidelity components and avoid limiting the number of high-fidelity components that could be integrated in the analysis at one time.

### 4.2.3. NASA-GE Multi-Fidelity Turbofan Engine Simulation

Although Smith (1994) first reported a collaborative research effort between NASA and GE on fan and compressor high-fidelity zooming, Reed, et al. (2003) and Turner, et al. (2004) discussed the multi-fidelity simulation of an entire turbofan engine with component characteristics zoomed into mini-maps, in the sense that they were developed only for a narrow component operating range. A 0D cycle simulation of the GE90-94B high-bypass turbofan engine was achieved utilizing partial component characteristics generated from a high-fidelity CFD simulation. The simulation integrated the NPSS thermodynamic cycle simulation system with a set of coupled 3D CFD component models representing the full engine model. 1D mean-line turbomachinery programs were used for the integration of the partial performance maps into the 0D cycle simulation.

The three-dimensional CFD simulations of the fan, booster, high-pressure compressor, high- and low- pressure turbines were performed using the APNASA turbomachinery code. The combustor flow was simulated using the National Combustor Code (NCC). The stage stacking program STGSTK was used for the generation of the partial performance maps by appropriate averaging of the three-dimensional CFD flow solutions for use in a 1D mean-line program. Turbine mini-maps were generated using an entropy-based blade-row model to take into account the turbine cooling flows.

The analysis showed that component efficiencies were overestimated in some cases and underestimated in others. This resulted in the engine operating at a 1% higher wheel speed in both the low pressure spool and core and in a 1.6 degrees C difference in exhaust gas temperature. The overall agreement however was satisfactory. The analysis identified several key areas that needed to be improved in order to achieve a better agreement between the NPSS cycle using mini-maps and the actual engine performance, such as: the loss models in the 1D blade row codes, inconsistencies between the bleed and cooling flows, thermodynamic inconsistencies between the different codes used in the analysis etc.



#### 4.2.4. Cranfield Rolls-Royce UTC 2D Fan Radial Profile Simulation

In gas turbine performance simulation, it is common practice to either represent the fan as a single, non-dimensional component or as two compressors with separate non-dimensional flow characteristics for the bypass and core flows. Cranfield collaborating with Rolls-Royce developed a method by which radial profiles can be used to make a more accurate estimation of engine performance. Yin, et al. (2001) conducted a comparative study of the effect of the following three fan models on the steady state and transient performance of a two-shaft high-bypass ratio turbofan engine:

- A 0D fan model represented by a single component map
- A 0D fan model represented by two maps
- A 2D fan model based on the radial profile approach

To make the comparison meaningful the same initial information was used in all cases. Notional profiles of fan performance were generated that were realistic but did not apply to any particular fan (Figure 4.2.4.1). The work was assumed to be directly proportional to the wheel speed and the change in absolute swirl velocity across the rotor. The majority of losses were divided into those related to Mach number (shock waves) and viscous losses related to diffusion acting on boundary layers. The pressure ratio was increased according to the shaft speed. The pressure ratio at rotor hub was much smaller than the one closer to the rotor tip. Due to the influence of tip clearance and secondary flows, the pressure ratio near the tip was reduced.

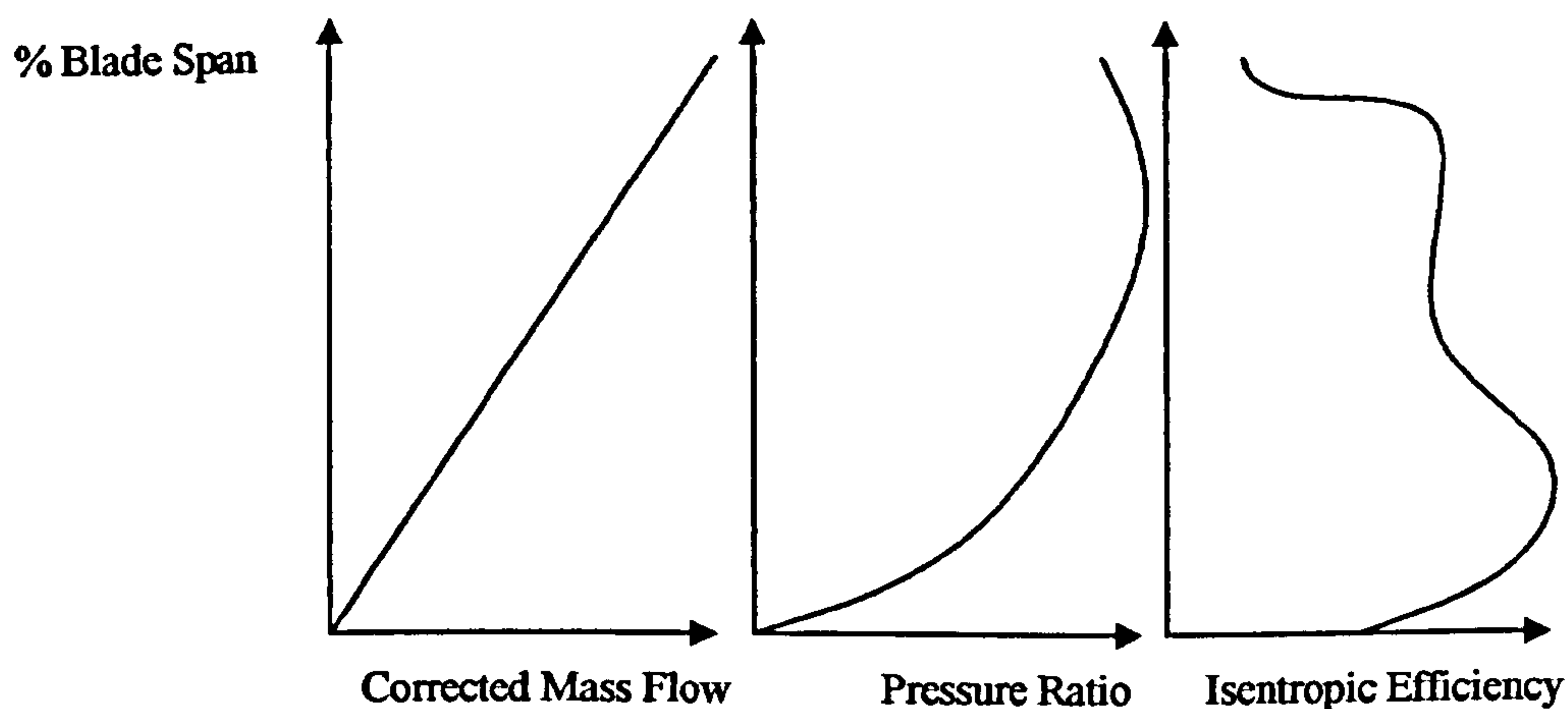


Figure 4.2.4.1: Sample fan outlet radial profiles

The different fan models were then incorporated in the model of a high-bypass turbofan engine so that a comparison could be carried out.

##### 0D Fan Model (Single Fan Map)

This model utilised a single component characteristic. The characteristic map was generated by mass flow-averaging the property profiles across the complete fan disc. The pressure ratio and isentropic efficiency were assumed constant with fan radius. So the same pressure ratio, efficiency and corrected entry mass flow were applied to both core and bypass streams.

The independent variables used were  $\beta$  and non-dimensional speed. Each  $\beta$  point corresponded to the average of a profile. The actual operating condition of the fan was therefore defined by the rotational speed of the shaft, the inlet temperature and the backpressure caused by the downstream components. The first two defined the non-dimensional speed. The back pressure caused by the downstream components in the core and bypass duct influenced the fan pressure ratio and mass flow, defining the  $\beta$  parameter, fully defining fan operation.

#### 0D Fan Model (Two Fan Maps)

In this case the fan was represented by two sets of compressor characteristics, one for the flow going into the core and the other for the flow going into the bypass duct (Figure 4.2.4.2).

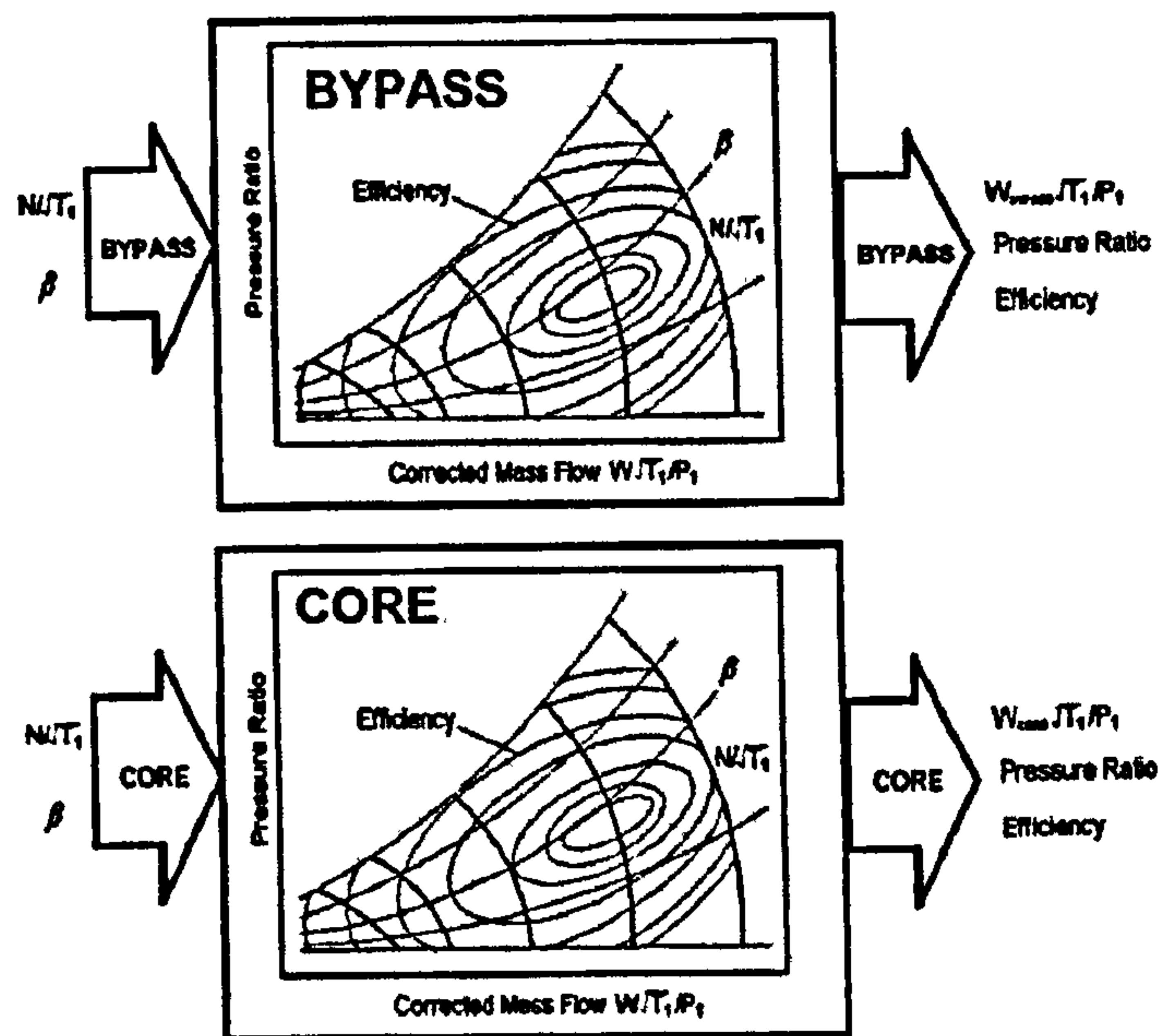


Figure 4.2.4.2: 0D fan model (Two fan maps)

A curve of Bypass Ratio (BPR) versus non-dimensional speed was determined during the fan design and then rig tests were done to obtain the fan-exit radial profiles according to this curve. For each value of bypass ratio a map was produced in the following manner. Firstly, the radial position at the fan rotor outlet of the streamline where the fan flow is split into two streams was estimated from the mass flow profile. Then the properties were integrated radially and averaged for both the bypass and core flows. This process was repeated for each  $\beta$  point on all the non-dimensional speed lines, so that a complete set of two maps was created, one for the core stream and one for the bypass stream. Each  $\beta$  point corresponded to a different profile along a constant speed line obtained from rig tests.

#### 2D Fan Model (Fan Radial Profile Map)

This model was based on direct use of the radial distribution of flow properties. It was assumed that when integrating over the radius, the averaged parameters like pressure ratio and fan work remained the same as those for the 0D models. Also, radial profiles at the fan rotor inlet were uniform.



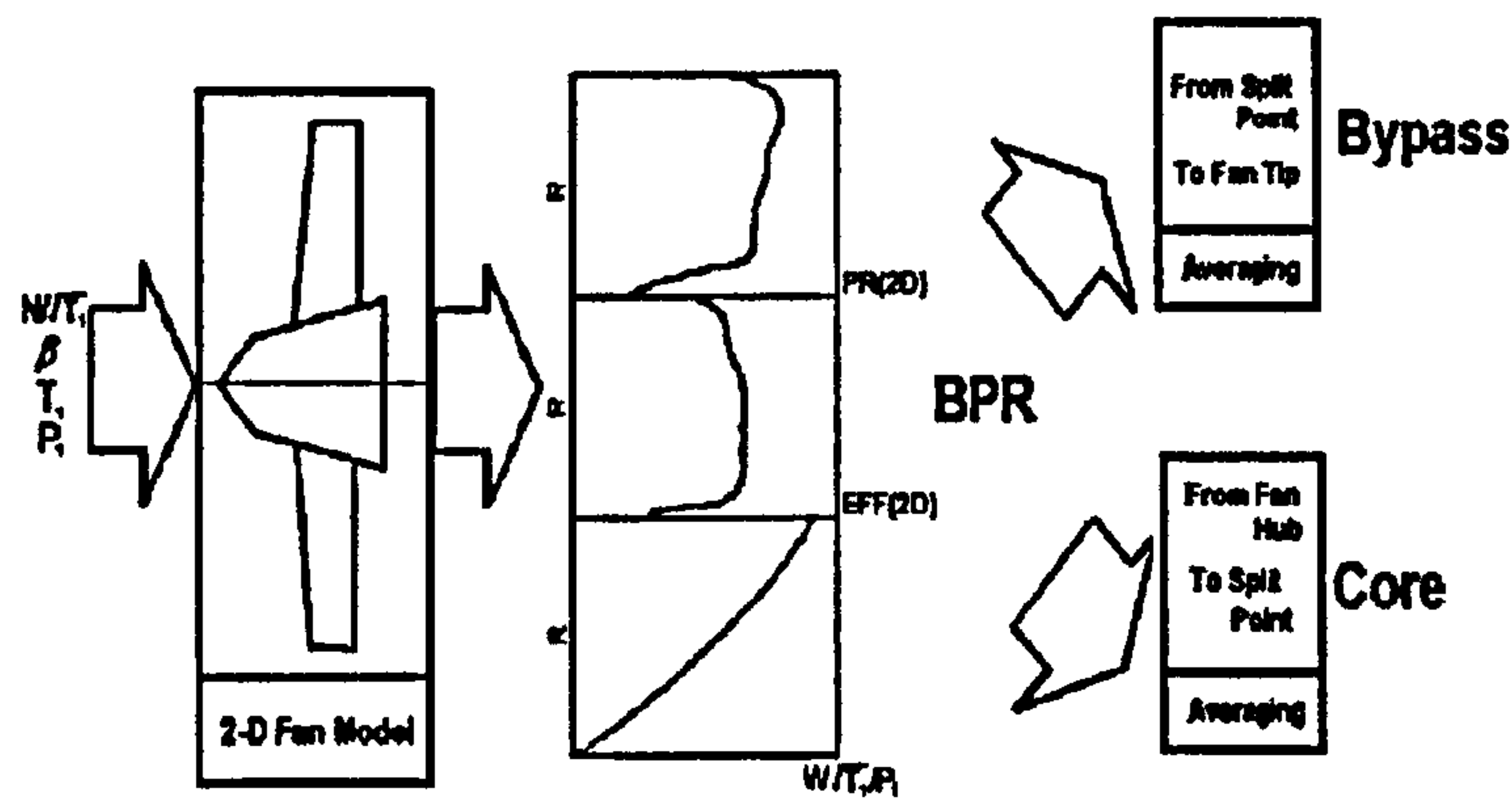


Figure 4.2.4.3: 2D fan model (Fan radial-profile map)

Using a new whole fan map, for a given non-dimensional speed and  $\beta$ , the whole exit non dimensional mass flow and pressure ratio were calculated together with the radial profiles of pressure ratio, isentropic efficiency and non-dimensional mass flow at the outlet of the fan. These profiles were subsequently re-produced by the fan model as a function of corrected shaft speed and  $\beta$ . At this point an arbitrary choice was made of the radial location of the splitting streamline at the rotor exit. This effectively determined the bypass ratio and enabled the calculation of bypass and core stream characteristics. Like in a traditional model the choice of radius was then examined relative to the mass flow capability of components downstream, in this case the bypass nozzle. The results of the calculation were compared to the choice of radial point of split. The radial point of split was moved and the calculation was repeated until it converged.

The comparative analysis showed that the first fan model produced higher SFC and thrust values than the other two models which produced the same results for a given relationship between bypass ratio and power setting. When the area of the fan nozzle was changed slightly, the relationship of bypass ratio and power setting became invalid. In this case, the prediction of the two-map fan model was different compared to that of the 2D fan model.

Generally, the 2D fan model, demonstrated that it could accommodate changes in bypass ratio arising from changes in geometry, transient conditions and other effects without the need to produce a new characteristic. It was therefore a more general model that could be used independently of a fixed relationship between bypass ratio and power setting. Because this model was capable of coping with radial profiles, it demonstrated the potential to investigate issues such as fan tip clearance effects on jet engine performance.

#### 4.2.5. MTU Low-Bypass Fan Model

This fan model for low-bypass ratio multistage fans (Riegler, et al., 2001) involves a similar method to the Cranfield 2D fan model. The MTU model is using the following variables:

- Independent variables:  $N/\sqrt{T_{in}}$ ,  $\beta_{fan}$ , BPR
- Dependent variables:  $W\sqrt{T_{in}}/P_{in}$ ,  $PR_{core}$ ,  $PR_{bypass}$ ,  $\eta_{core}$ ,  $\eta_{bypass}$

Attempts were made to avoid the cost of testing for several schedules of bypass ratio versus  $N/\sqrt{T_{in}}$ , for engine operation away from the nominal bypass ratio schedule. From rig test analysis it was found that away from the nominal bypass ratio curve the fan exit profile remained unchanged when the fan non-dimensional speed and exit corrected mass flow were constant, with varying bypass ratio. In this case the map needed to be based on nominal bypass ratio only, using corrected speed and mean exit corrected flow.

The MTU approach does not store any flow profiles obtained from rig tests, but approximates them and calculates them from the 1D mean values derived from the core and bypass streams in the standard inner and outer fan model. These values are used as coefficients to approximate a parabola as the profile. Next, the split point is found for the new bypass ratio of interest, and then the profiles are averaged for the core and bypass, based on the split point at the fan exit station. The basis for the model is that the splitter is far enough downstream of the last stator of the fan so that it does not affect the streamline split point.

#### 4.2.6. Discussion of Published Literature

The research efforts mentioned above, all follow one way or the other, the de-coupled and iterative approaches to 'Advanced Performance Simulation' identified in *Chapter I - Introduction*, but not the fully integrated approach. Each simulation strategy described above has its own advantages and limitations but generally speaking one can observe two distinctive trends. NASA is pursuing the three-dimensional CFD analysis of the entire engine utilising huge computational resources of distributed and parallel architecture which are still impractical for other research establishments particularly in Europe. Other research efforts have followed a rather conservative approach to high-fidelity analysis by implementing 1D component models at an affordable computational cost but at reduced fidelity and accuracy.

The pseudo-2D fan models proposed in the past by Cranfield and MTU may offer some flexibility but are severely limited by the number of rig tests that can be carried out to generate realistic profiles. Moreover, when 'default' profiles are used, both models may take into account the change in radial location of the splitting streamline with bypass ratio, but they can not take into account changes in the actual flow profiles caused by operating conditions other than those under which the rig tests were carried out.

Some of the above publications describe the high-fidelity simulation strategy adopted in detail, a lot of important information however, such as convergence times, technical difficulties, details on boundary condition matching etc. still remains proprietary and unpublished.

One of the main difficulties in implementing high-fidelity analysis is to accurately resolve two-dimensional or three-dimensional flow fields from the single value supplied from non-dimensional component simulations. None of the research efforts mentioned above seems to be addressing this issue satisfactorily.



Finally, although 2D through-flow methods have been routinely used since the early 50's, they have been mainly focused on the simulation of the flow field inside isolated components. There is actually little evidence in literature on the full integration of several 2D through-flow component models with zero-dimensional cycle analysis, for high-fidelity studies in the context of the whole engine performance.

#### **4.2.7. Author's Publications**

This author's research work in the area of high-fidelity analysis, supported by visiting and Thermal Power MSc students, resulted in several conference and journal publications which are briefly mentioned here. Individual cases are discussed in much more detail in the context of this thesis in subsequent chapters.

Generally speaking, these publications covered the full spectrum of high-fidelity analysis from 0D to 3D, included both CFD and through-flow analysis tools, discussed all three high-fidelity simulation strategies in detail (de-coupled, iterative, fully integrated) and looked into several different aspects of engine performance such as compressor inlet flow distortion and turbine inlet temperature distortion.

More analytically, the author with Charalambous, et al. (2004), published a paper that discussed the response of a modern military, low-pressure, axial compressor to inlet flow distortion. A three-dimensional CFD model was used utilising the de-coupled approach to high-fidelity analysis.

A year later the author published two papers (Pachidis, et al., 2005a and 2005b) that discussed in detail the partially (iterative) and fully integrated approaches to component zooming using CFD. For the purposes of this investigation three-dimensional CFD models of the intake of a high-bypass ratio turbofan engine were used. This work also resulted into two journal publications (Pachidis, et al., 2006a and 2006b). The same year the author with Zilli, et al. (2005) published a paper discussing the CFD investigation of the performance of a military HP axial turbine subjected to inlet temperature distortion utilising the de-coupled approach.

In 2006, the author published a paper that discussed the prediction of engine performance under compressor inlet flow distortion using streamline curvature (Pachidis, et al., 2006c). This study incorporated a two-dimensional SLC compressor model, fully integrated into a 0D cycle analysis. The same year the author with Melloni, et al. (2006), continuing the work initiated with Charalambous, et al. (2004), published a paper discussing the response of a modern military engine to compressor inlet stratified pressure distortion by an integrated CFD analysis.

While carrying out research at Cranfield University, this author also collaborated with the Hellenic Air Force Academy as far as high-fidelity engine performance simulation research is concerned. This successful collaboration resulted in several publications. The author with Templalexis, et al. (2005a) published a paper on the three-dimensional simulation of a convergent-divergent aero engine intake using two different CFD methods. The same year the author with Templalexis, et al. (2005b) also discussed the three-dimensional simulation of an axi-symmetric convergent-constant area intake using a panel method approach. A year later, the author with



Templalexis, et al. (2006a) published a paper discussing the development of a 2D compressor streamline curvature code, together with the quasi-three-dimensional compressor performance simulation using streamline curvature and multi-parallel compressor theory (Templalexis, et al., 2006b).

### **4.3. Turbomachine Through-Flow Analysis Methods**

The development of gas turbine performance modelling software, that integrates simulation techniques of different fidelity, demands a good understanding of the through-flow calculation methods in use today. This section reviews the development of several through-flow analysis methods, discusses the underlying principles and assumptions of each method and highlights the principal problems in their application to current axial-flow compressors and turbines. The streamline curvature method is discussed in more detail due to its relevance with this particular work.

A through-flow calculation method is defined as a computational technique for predicting fluid velocities and thermodynamic properties at designated locations in the internal flow path of a turbomachine. In the simpler through-flow analysis methods, a single computation location, at the mean flow passage radius is usually specified at the inlet and outlet of each blade row. In the more advanced methods, computation points may be specified at locations throughout the flow path, both in the axial spaces between rows and within the blade rows at arbitrary coordinate locations.

Development of turbomachine through-flow analysis methods begun in the early 50's, almost in parallel with the rapid development of the first electronic digital computers. Over the years, the accuracy and applicability of through-flow analysis methods increased enormously through the use of improved and more realistic modelling approximations in the equations describing the flow field. The addition of methods for representing features of the experimentally observed flow field that are not adequately modelled by the equations, such as clearance and corner flows, passage choking and shock wave losses, together with the development of robust and fast numerical methods for solving the approximate equations, contributed considerably to the widespread use of through-flow analysis methods by industry and academia.

#### **4.3.1. Characteristics of the Turbomachine Flow Field**

The flow field encountered in turbomachines is highly three-dimensional, viscous, compressible and unsteady. Some of the flow phenomena that can influence the performance of modern axial-flow compressor and turbine blade rows are shown in Figure 4.3.1.1. Most of the flow phenomena illustrated in this figure are usually referred to as secondary flows or secondary effects and take place in a strong primary flow, which is generally understandable in terms of the physical laws and corresponding equations of fluid dynamics. The way such flow features are taken into account in individual through-flow analysis methods, consists an important criterion for distinguishing amongst them.

Turbomachine flow-fields occur in passages characterized by some unique geometric and kinematic features. First of all, the sequence of rotating and stationary internal

flow passages demands the continuous transferring of frames of reference from inertial to non-inertial coordinates, considering relative flows in rotating rows and absolute flows in stationary blading. The effect of rotation on the flow within rotating blade rows has also to be considered. A second unique feature is the transfer of energy between the fluid and the blade elements.

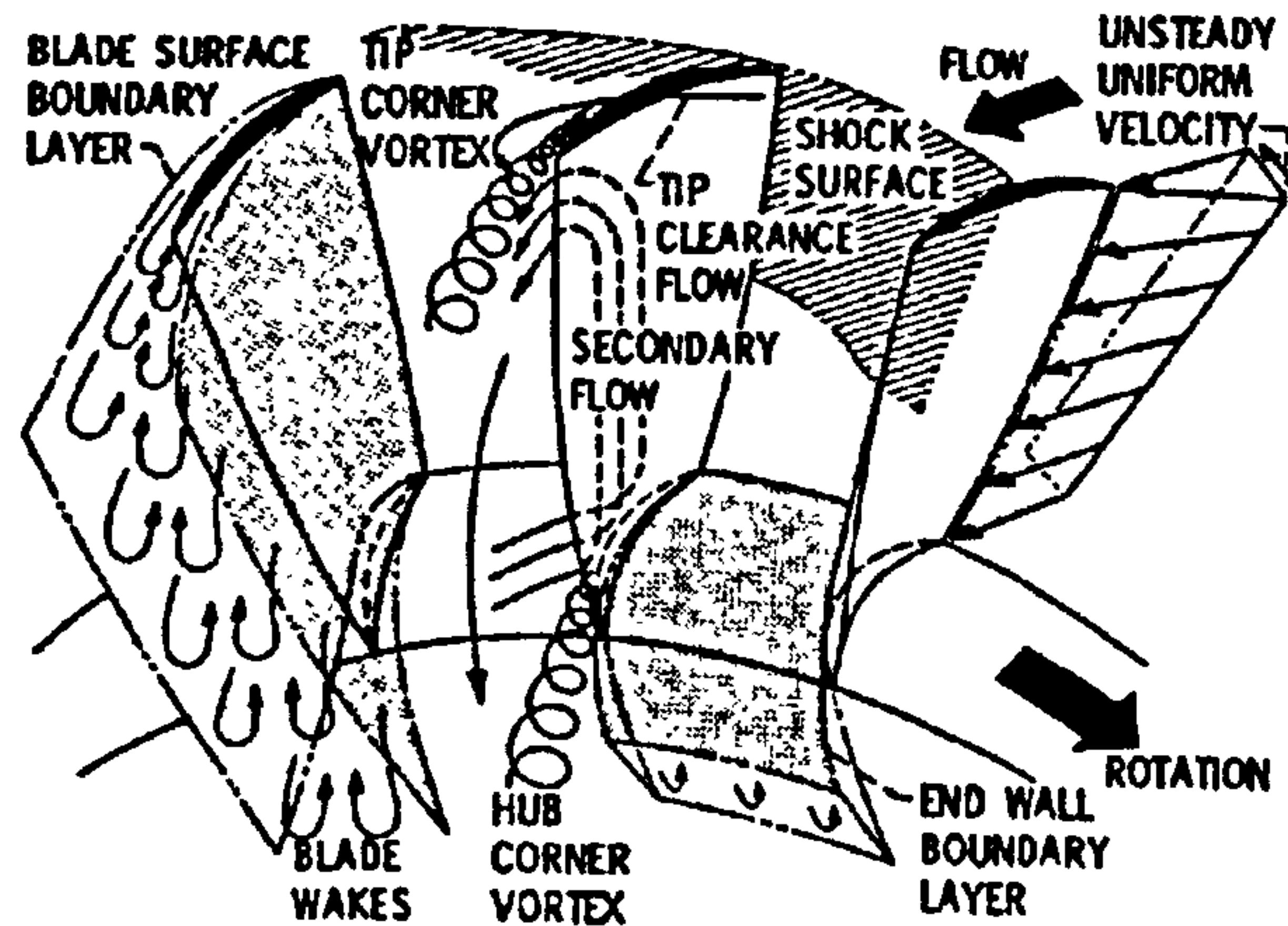


Figure 4.3.1.1: Flow phenomena in axial-flow blade rows (Hirsch and Warzee, 1979)

A third characteristic of turbomachine flows is the close proximity of moving and stationary surfaces, as indicated in Figure 4.3.1.2. This complicates any attempts to evaluate the flow field using traditional boundary layer-main flow iterative methods.

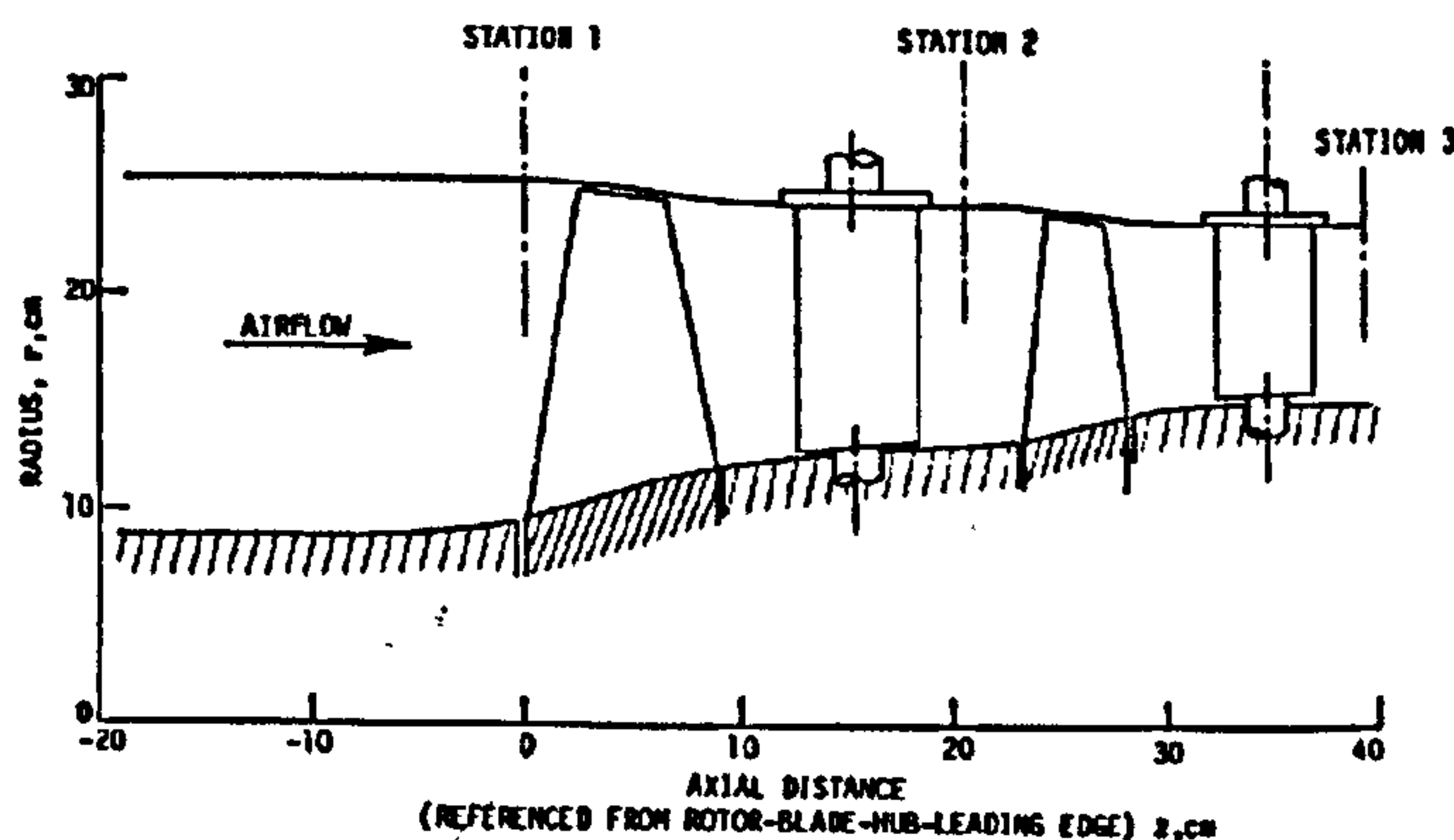


Figure 4.3.1.2: Meridional section of a 2-stage axial flow compressor (Hirsch and Warzee, 1979)

### 4.3.2. General Through-Flow Modelling Assumptions

There are several assumptions that are almost universally made in through-flow analysis. First of all, the relative flow at the inlet and outlet of each blade row is considered to be steady. The assumption of steady relative flow permits the definition of fluid particle paths by means of streamlines, stream surfaces and stream tubes. This simplifies the through-flow problem considerably by treating the three-dimensional nature of the real flow as being locally two-dimensional.



Whether a specific through-flow method is based on the use of differential equations, integral equations or both, generally control surfaces are used which subdivide the flow passage by intersecting both the hub and tip (casing) boundaries. These control surfaces may be simple-plane surfaces perpendicular to the rotational axis, or they may be conical or curved surfaces to conform to a leading or trailing edge trace in the meridional plane, or to reach into some particular region of interest. The control surfaces may be, in particular through-flow methods, called computation surfaces, calculation stations, and channel solution surfaces.

The majority of through-flow procedures utilize the concept of S1 and S2 stream surfaces introduced by Wu (1952). S1 surfaces are stream surfaces which divide the flow passage into several sections in the blade-to-blade direction. Similarly, S2 surfaces are through-flow surfaces which intersect both the hub and casing. Families of S2 surfaces might be used as a third kind of control surface to divide the blade-to-blade flow into hub-to-shroud (casing) stream tubes (Figure 4.3.2.1).

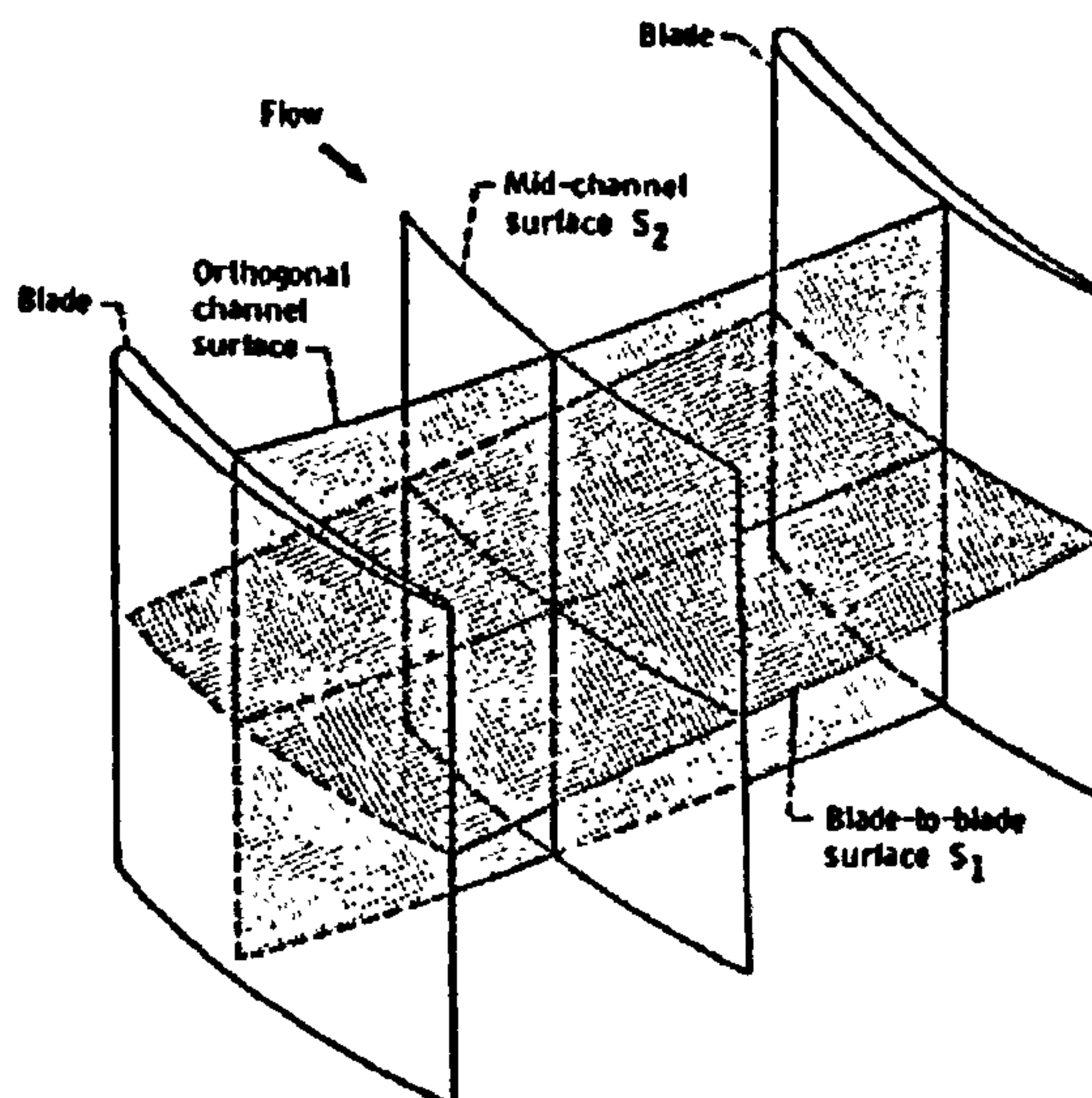


Figure 4.3.2.1: S1 and S2 control surfaces (Katsanis and McNally, 1977)

A second nearly universal assumption is that the flow can be treated as axi-symmetric and circumferentially averaged. The term axi-symmetric flow basically means that for any given set of axial and radial flow field coordinates, no fluid property varies in the circumferential direction. The term circumferentially averaged flow is usually used in reference to the flow on some designated S2 surface. It basically means that the fluid velocity and properties at all coordinate points on that surface are the circumferential averages of the values across the blade-to-blade passage at the corresponding radius and axial location.

The above two assumptions justify the subsequent modelling of S1 surfaces as surfaces of revolution, and further support the use of linear cascade data in axial-flow turbomachine design, flow passage circumferential measurements at constant radius, and the use of stream surface intersections with the meridional plane to show the nature of the hub-to-casing flow pattern. Moreover, these two assumptions allow one



hub-to-shroud surface to be considered as representative, which obviously reduces the computational complexity of the through-flow analysis even more. The significance of the above two assumptions and the distinction between them has been discussed by several researchers such as Smith (1966) and Horlock and Marsh (1971). Another very important assumption is that the flow is adiabatic, so that there is no heat transfer between fluid elements or across stream surfaces.

Finally, it should be noted that by studying the available literature, it becomes quite evident that in the development of flow models for the individual through-flow methods within the general classes described in the following sub-sections, not all of the thermodynamic laws are always used or satisfied, nor are all of the terms in the generalized equations representing each law used. In most cases it is very difficult to establish what simplifications are made in each method.

### **4.3.3. Classification of Through-Flow Methods**

Although several apparently independent efforts have led to remarkably similar approaches to the through-flow problem, this sub-section attempts to briefly describe the most common classes of through-flow analysis that can be identified in literature.

#### **Mean-Line Method**

This simple method is based on a mean line, which is defined along the flow passage under consideration. Fluid properties and velocities are estimated at specified locations on the mean line using one dimensional calculations supported by empirical correlations of experimental data. These conditions are assumed representative of the passage at that location along the mean line.

#### **Simple Radial Equilibrium Method**

The dominant effect in the radial equation of momentum, for most axial compressors, is the centripetal acceleration generated by the swirl velocity. The approximation in which only this term is considered in the radial direction is usually known as simple radial equilibrium. The meridional flow passage is subdivided by a set of plane control surfaces perpendicular to the rotational axis. In each control surface the effects of any radial component of velocity are assumed very small and therefore neglected. The governing physical laws and empirical data are used to determine the distribution of velocity and flow properties from hub to shroud. This method is limited to assumed axi-symmetric flows in axial turbomachines.

#### **Streamline Curvature Method**

This is an iterative approach based on the direct determination of the projections of streamlines on the meridional flow passage of a turbomachine. An initial set of streamlines is assumed, and by successive iterative calculations, with each iteration improving the degree of satisfaction of the physical laws and empirical data correlations used in the flow model, a final set of streamlines is determined for a given flow rate, rotational speed and inlet conditions. Velocities and fluid properties are predicted at locations on the streamlines corresponding to control surface intersections (Figure 4.3.3.1).

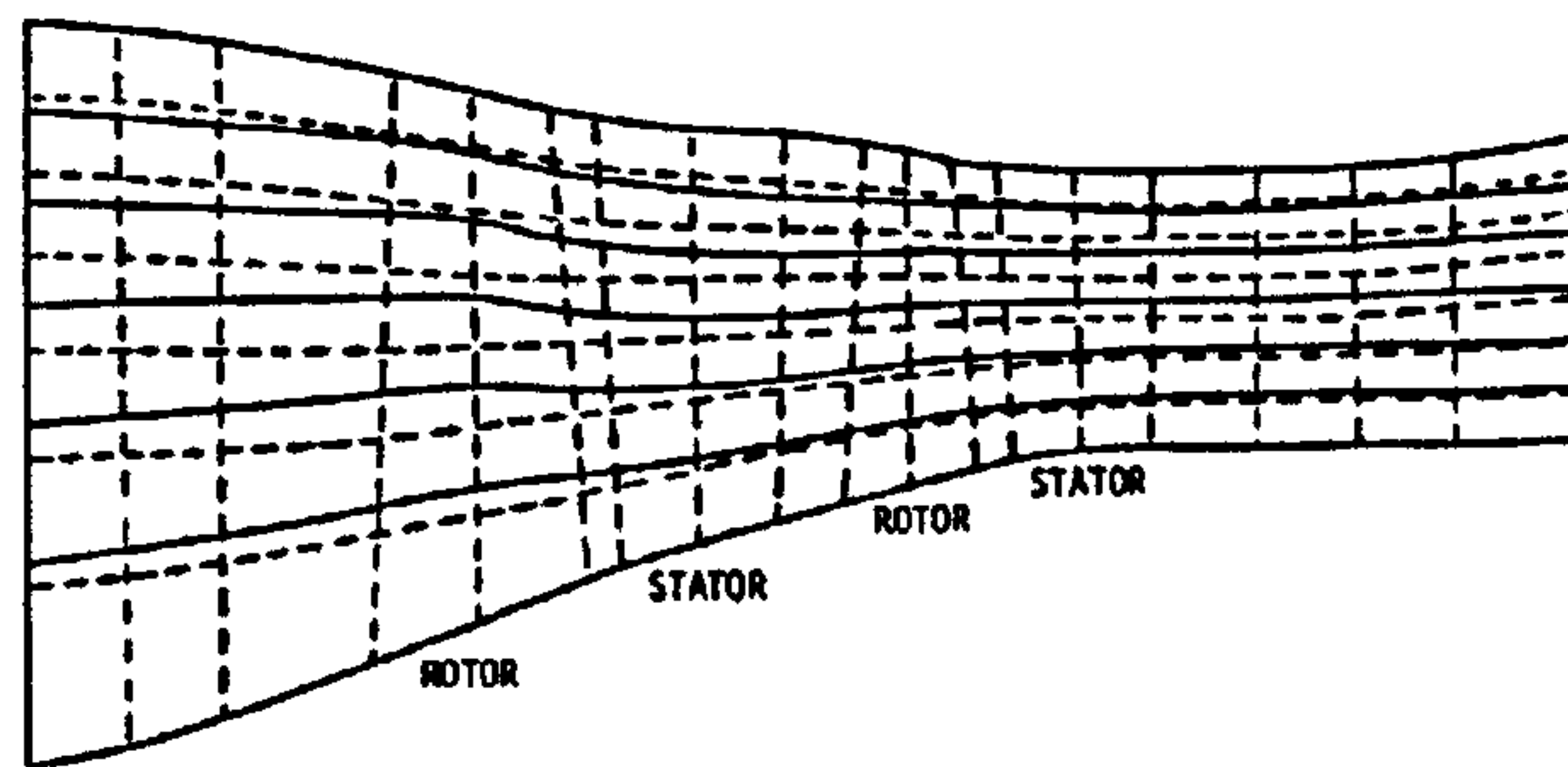


Figure 4.3.3.1: 2-stage fan geometry with calculated streamlines (Hirsch and Warzee, 1979)

### Finite Difference Method

An initial system of grid points or nodes is defined throughout the flow passage under study. In order to satisfy the combination of physical laws and empirical information used in the method, finite difference equations are written for each grid point. The equations are subsequently solved to determine the distributions of fluid properties and velocities at the nodal points. Similarly to the previous method, these distributions can be used to construct streamline patterns.

### Finite Element Method

A network of lines subdivides the flow passage to be studied into elements. Nodal points are located on the lines forming the boundary of each element. The physical laws and empirical input data are formulated so that the fluid properties and velocities can be determined at each nodal point by iteration.

### Finite Volume Method

The flow passage is subdivided into a large number of small volume elements, fitted to the passage geometry. The physical laws and empirical information governing the calculation are used to generate integral conservation equations for each small volume. The equations are solved, typically by an iterative time-marching process to reach a converged distribution of velocities and properties for the finite volume surfaces (Figure 4.3.3.2).

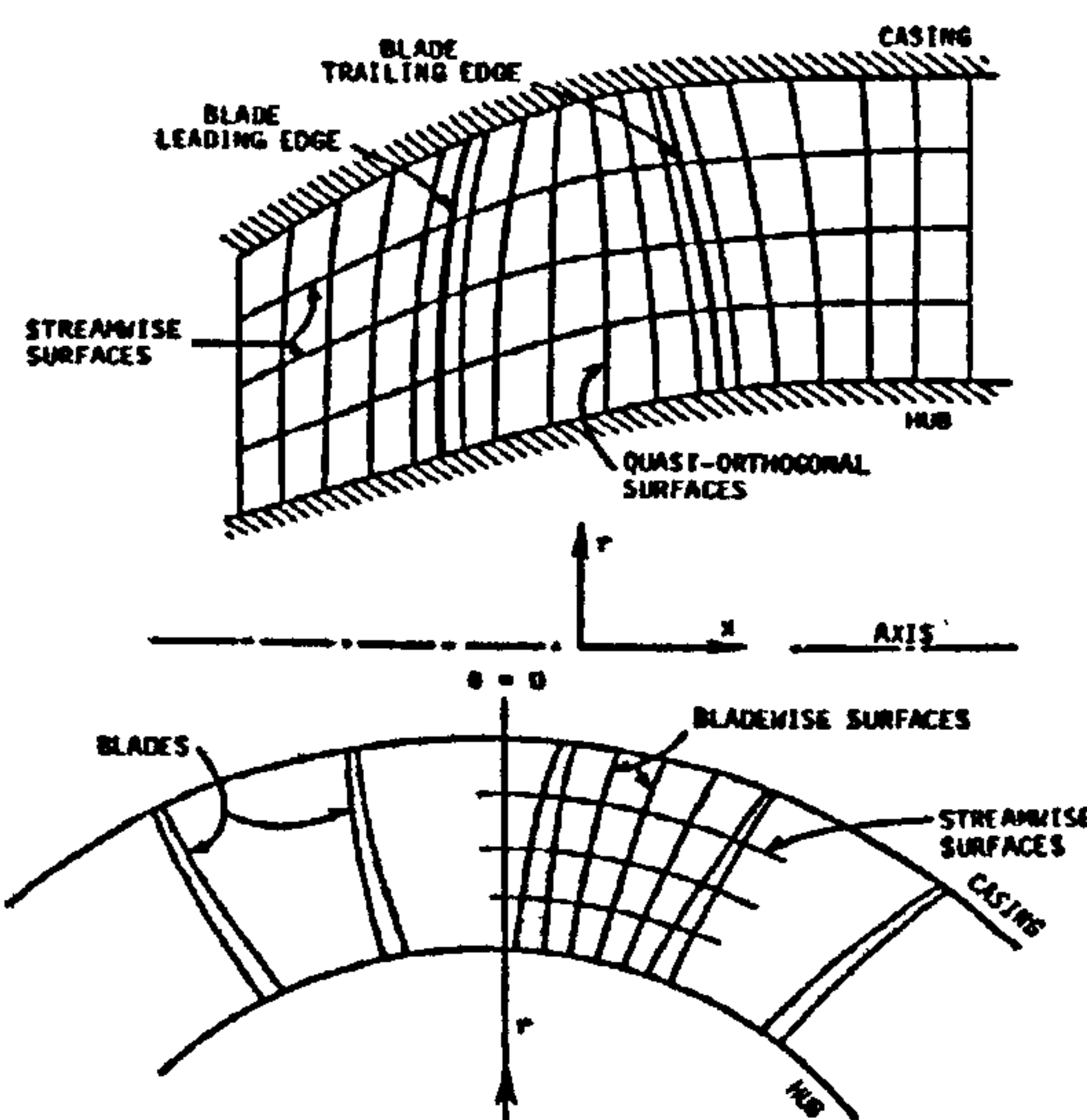


Figure 4.3.3.2: Finite volume elements for a 3D flow field computation (Denton and Singh, 1979)



The vast majority of through-flow calculation methods may be placed within these classes.

#### 4.3.4. Development of Through-Flow Analysis Methods

This sub-section reviews the development of the through-flow analysis methods described above.

##### Mean-Line Methods

The earliest through-flow calculation methods to be routinely used were mean-line analyses (Howell and Calvert, 1978). This class of methods continues to be developed and used in conceptual and preliminary design studies. Typical examples are the relatively recent publications by Casey (1987), Rolls-Royce (Wright and Miller, 1991) and Honeywell Aerospace (Cunningham, et al., 2006). The one-dimensional nature of the mean-line analysis, coupled with the necessary empirical flow turning, deviation and loss models, eliminates the possibility for a realistic flow field prediction.

##### Simple Radial Equilibrium Methods

The first attempts towards two-dimensional analysis were based on approximate, inviscid, simple radial equilibrium equations. Usually, in design point applications the radial variation in blade row loss was neglected (Voit, 1953). Hatch, et al. (1954) first discussed and evaluated the importance of the cumulative loss effect, as a measure of the radial gradient of entropy. Later on, in off-design applications, compressor performance maps were derived based on non-isentropic simple radial equilibrium equations.

##### Streamline Curvature Methods

The terms in the radial component of the equation of motion representing streamline slope and curvature, and their effect on the radial flow pattern, were first described by Wu and Wolfenstein (1949) and Hamrick, et al. (1951). Mechanisms for quantitative inclusion of the streamline shape effect in compressor and turbine design were reported by Wright and Kovach (1953). Although, in performance prediction Swan (1961) included both streamline shape and loss distributions, in design procedures used during this period there was little if any combined accounting for streamline shape and radial entropy gradient until it was discussed by Giamati and Finger (1965). However, the term 'streamline curvature method' became generally associated with this class of through-flow analysis following the work of Novak (1967) and Jansen and Moffatt (1967).

The assumption of an inviscid flow in streamline curvature calculations generally meant that only the local fluid shear stress effects were neglected by eliminating the corresponding terms in the momentum equations. However, the cumulative effect of fluid shear as measured by the entropy increase through a blade-to-blade stream tube was taken into account through the hub-to-tip entropy variation. Other researchers, such as Bosman and Marsh (1974), suggested the use of correction terms to simulate the irreversibility generated by the fluid shearing stress along a given streamline.

One of the difficulties in applying the streamline curvature method is the necessity to calculate the streamline pattern and then obtain the slope and curvature of the streamlines through an iterative process. Usually a spline fit through points of equal stream function on neighbouring calculation planes is used to approximate the shape of the streamlines. The spline curve is differentiated once to obtain the slope and twice to obtain the curvature, a procedure which can lead to a loss of accuracy. A slightly different approach was followed by Shaalan and Daneshyar (1972). They suggested fitting a second spline curve to the variation of slope and then differentiating to obtain the curvature, as a more accurate method for estimating the streamline pattern.

Between 1960 and 1990 a substantial number of computer codes for axial-flow turbomachine flow field analysis were developed using streamline curvature methods such as Creveling and Carmody (1968), Frost (1970), Wilkinson (1970), Glenny (1974), Denton (1978), Jennions and Stow (1985 and 1986) and Barbosa (1987). Most of these codes were based on the axi-symmetric, inviscid and adiabatic flow assumption and utilised experimental and empirical correlations for blade row turning and losses. Although streamline curvature methods were initially developed to handle calculation stations at the inlet and outlet of blade rows, several of the above examples utilised computation stations in-between blades for a quazi-three-dimensional analysis.

#### Finite Difference Methods

The term 'matrix through-flow method' began to be commonly used to describe one group of finite difference methods following the work of Marsh (1968). Davis and Millar (1974) have also reported results from finite difference through-flow methods.

Perhaps the versatility of finite difference methods can be found in calculations where internal blade row calculation stations are needed, and where three-dimensional effects are under study (Bosman and El-Shaarawi, 1977). However the methods have not been as effectively developed for transonic flow cases as have some of the streamline curvature methods.

The majority of the finite difference methods developed up to about the early 1970's were of the inviscid type, and included viscous effects only as an entropy distribution in the computed flow field, based on experimental loss correlations. The work of Bosman and Marsh (1974) has included a mechanism for local viscous shear stress accounting.

#### Finite Element Methods

Finite element methods were developed as usable through-flow analysis techniques almost in parallel with finite difference methods in the 1970's. Several publications on finite element methods and their application can be found in open literature such as Adler and Krimerman (1974) and Hirsch and Warzee (1976). A key feature of the finite element method is its potential to handle three-dimensional flow fields since the finite element mesh can be easily adapted to quite complex turbomachine geometries. Finite element three-dimensional analysis has been reported by Hirsch and Warzee (1979). The same forms of correlation for turning and loss used in streamline curvature methods can and have been used in finite element analyses.



### Finite Volume Methods

Along with the finite element and finite difference methods, finite volume methods have a relatively short history. Although they were first proposed for blade-to-blade flow field analysis, recent advances in computational power have led to hub-to-tip flow field analysis and effective three-dimensional analysis. Results have been reported by Denton and Singh (1979) and Ivanov and Kimasov (1978). The finite volume regions can, as in the case of the finite element mesh, be generated to conform to complex passage geometries.

### **4.3.5. Through-Flow Method Limitations**

The through-flow analysis methods discussed above have been routinely used for many years by industry and academia and the majority of them have now become quasi-three-dimensional in character. Usually iterations are carried out between two-dimensional hub-to-shroud computation surfaces and either two-dimensional blade-to-blade computation surfaces or correlations of experimental turning and loss data.

The flow field inside the passage however, is still treated as being locally two-dimensional. Although according to the two-dimensional through-flow assumption, a blade-to-blade stream tube may change radius and vary in radial thickness, variations in fluid properties do occur in the y and x directions, but the flow in each blade-to-blade stream tube is assumed to be independent of the flow in adjacent tubes. In other words mass flow is not allowed to cross stream tube boundaries.

Obviously the quasi-three-dimensional methods are not well adapted to capturing three-dimensional aerodynamic flow features such as flow separation, shock waves and end-wall clearance and corner flows. Evidence of the limitations of quasi-three-dimensional methods is available in reported work on axi-symmetric streamline curvature and finite difference analyses by Novak and Hearsey (1977).

As mentioned before, although a considerable literature now exists on the development, capability and applicability of various through-flow methods, it should be noted that flow models and equations remain controversial in many cases or proprietary. Reports on through-flow computation code development and application frequently do not provide adequate information concerning numerical methods and code organization. Because the solutions are iterative in character, the iterative strategy is important and methods used to improve stability at convergence significantly influence the cost and quality of results.

Moreover, the results obtained by any through-flow calculation method heavily depend on the quality of the blade correlation methods, and their coherence with the flow model selected for the computation. It has been the general experience that correlations found in the open literature at least, may be valid for some cases and machine geometries but may be unreliable for others.

### 4.3.6. Comparison of Through-Flow Analysis Methods

As mentioned before, the estimation of the curvature of streamlines when defined by a small, discrete number of points can be error prone, while the correct simulation of curved end-walls in the finite difference method requires complicated mathematical tricks. It seems that finite element methods do not suffer from these difficulties. Estimations of streamline curvature do not appear in the calculation, while quadrilateral curved (iso-parametric) elements can be used to simulate accurately the curvature of boundaries, at the expense of a higher computational demand and grid complexity.

As far as 2D analysis is concerned, the streamline curvature methods and the matrix inversion schemes, using either finite difference or finite elements, seem to have now reached a sufficient degree of maturity. For several years, the matrix through-flow and streamline curvature methods were regarded as two separate methods for calculating turbomachinery flows. Marsh (1971) showed that these two mathematical techniques are actually based on the same model and that they could be regarded as two different but similar methods for solving the flow field governing equations.

The most comprehensive comparison of the two methods was carried out by Davis and Millar (1974) who have compared solutions for a duct flow, transonic fan and three-stage axial flow compressor. They found little difference in the difficulty, or ease, of programming, but the matrix method required about 50% more RAM memory in the computer. The matrix method converged within a few iterations whereas the streamline curvature program required 40 to 60 iterations, probably due to difficulty in calculating the curvature of the streamlines. Their conclusion was that there was a marginal advantage for the matrix method on the grounds of greater stability.

In practice, none of these methods however, has an overwhelming advantage over the others. The streamline curvature approach might be easier to incorporate the manufacturer's practical experience, while the matrix inversion perhaps offers a greater potential for extension to three-dimensional and quasi-three-dimensional calculations. This is especially true for the finite element approach, which allows a good description of complicated geometries, and gives less convergence problems, at the expense of a larger computational cost due to the far more complex grid required.

In view of the above, streamline curvature was adopted as the through-flow method to carry out the 2D analysis in this work, on the grounds of accuracy, ease of use, realistic execution times, and established in-house experience on the subject.



CHAPTER V**2D COMPRESSOR FLOW MODELLING**

The compressor flow field is highly three-dimensional, turbulent and viscous. An inviscid through-flow analysis method, however, in which viscosity effects are taken into account by means of empirical models and correlations, can offer sufficient accuracy. The scope of this chapter is to explain in detail the theoretical background of the Streamline Curvature (SLC) through-flow analysis method and of the various empirical models adopted by this work.

The SLC method basically solves the discrete equations of continuity, motion, energy and state in a form that incorporates the full three-dimensional compressor geometry and on a computational grid which is constructed in the meridional direction. Computation nodes are defined at the intersections of the streamlines and the blade edges. After the transformation of the discrete equations, the result is a non-linear partial differential equation which is solved by a finite difference approximation following an iterative approach. At the beginning, node coordinates are unknown since the streamline positions have not been determined yet. An initial guess of the streamline positions is made and calculations are carried out until new positions for the nodes are determined. At every iteration the grid changes and an assessment of the streamline positions is made based on the previous guess. The iterative procedure is carried out so that the streamlines are repositioned until, eventually, their position remains constant and all the flow field properties are established.

**5.1. Compressor Streamline Curvature Equations**

This section presents analytically the derivation of the non-linear, partial differential equation which is used in establishing the meridional flow field taking into account full radial equilibrium and streamline curvature. This equation is often called the 'radial equilibrium equation' and consist the basis of all streamline curvature through-flow analysis methods.

The flow within the compressor is considered as axi-symmetric, compressible and inviscid. For this specific type of flow the law of conservation of angular momentum has the following form in vector quantities:

$$-\frac{1}{\rho} \vec{\nabla} P = \frac{D\vec{W}}{Dt} + \vec{\omega} \times (\vec{\omega} \times \vec{r}) + 2\vec{\omega} \times \vec{W} + \vec{F} \quad [\text{Eq. 5.1.1}]$$

Blade forces  $\vec{F}$  are neglected in this case.

Resolving each term of the above equation into cylindrical coordinates (z, r, w - axial, radial, tangential) the following four expressions are derived:

i) The pressure forces:

$$-\frac{1}{\rho} \vec{\nabla} P = \left( -\frac{1}{\rho} \frac{\partial P}{\partial r} \right) \vec{e}_r + \left( -\frac{1}{r\rho} \frac{\partial P}{\partial w} \right) \vec{e}_w + \left( -\frac{1}{\rho} \frac{\partial P}{\partial z} \right) \vec{e}_z \quad [\text{Eq. 5.1.2}]$$

ii) The material derivative of the relative velocity in steady state conditions ( $\frac{\partial \vec{W}}{\partial t} \approx 0$ ):

$$\frac{D\vec{W}}{Dt} = \left( \vec{W} \cdot \vec{\nabla} \right) \vec{W} + \frac{\partial \vec{W}}{\partial t} \Leftrightarrow \frac{D\vec{W}}{Dt} = \left[ W_r \frac{\partial}{\partial r} + \frac{W_w}{r} \frac{\partial}{\partial w} + W_z \frac{\partial}{\partial z} \right] \vec{W} \Leftrightarrow$$

$$\Leftrightarrow \begin{cases} \frac{DW_r}{Dt} = W_r \frac{\partial W_r}{\partial r} + \frac{W_w}{r} \frac{\partial W_r}{\partial w} + W_z \frac{\partial W_r}{\partial z} \\ \frac{DW_w}{Dt} = W_r \frac{\partial W_w}{\partial r} + \frac{W_w}{r} \frac{\partial W_w}{\partial w} + W_z \frac{\partial W_w}{\partial z} \\ \frac{DW_z}{Dt} = W_r \frac{\partial W_z}{\partial r} + \frac{W_w}{r} \frac{\partial W_z}{\partial w} + W_z \frac{\partial W_z}{\partial z} \end{cases} \quad [\text{Eq. 5.1.3}]$$

iii) The centripetal acceleration:

$$\vec{\omega} \times (\vec{\omega} \times \vec{r}) = \left( \vec{\omega} \cdot \vec{r} \right) \vec{\omega} - \left( \vec{\omega} \cdot \vec{\omega} \right) \vec{r} = -(\omega^2 r) \vec{e}_r + 0 \vec{e}_w + 0 \vec{e}_z \quad [\text{Eq. 5.1.4}]$$

Where the terms  $\vec{e}_w$  and  $\vec{e}_z$  are neglected ( $= 0$ ).

iv) The coriolis acceleration:

$$2\vec{\omega} \times \vec{W} = (-2\omega W_w) \vec{e}_r + (2\omega W_r) \vec{e}_w + 0 \vec{e}_z \quad [\text{Eq. 5.1.5}]$$

Where the term  $\vec{e}_z$  is neglected ( $= 0$ ).

Collecting similar terms the following system of equations is derived:

$$\begin{cases} \vec{e}_r: & -\frac{1}{\rho} \frac{\partial P}{\partial r} = W_r \frac{\partial W_r}{\partial r} + \frac{W_w}{r} \frac{\partial W_r}{\partial w} + W_z \frac{\partial W_r}{\partial z} - 2\omega W_w - \omega^2 r \\ \vec{e}_w: & -\frac{1}{r\rho} \frac{\partial P}{\partial w} = W_r \frac{\partial W_w}{\partial r} + \frac{W_w}{r} \frac{\partial W_w}{\partial w} + W_z \frac{\partial W_w}{\partial z} + 2\omega W_r \\ \vec{e}_z: & -\frac{1}{\rho} \frac{\partial P}{\partial z} = W_r \frac{\partial W_z}{\partial r} + \frac{W_w}{r} \frac{\partial W_z}{\partial w} + W_z \frac{\partial W_z}{\partial z} \end{cases} \quad [\text{Eq. 5.1.6}]$$



Considering the flow as axi-symmetric, the partial derivatives with respect to the circumferential direction equal to zero. Accordingly, the above equations reduce to:

$$\begin{cases} \rightarrow \\ e_r : & -\frac{1}{\rho} \frac{\partial P}{\partial r} = W_r \frac{\partial W_r}{\partial r} + W_z \frac{\partial W_r}{\partial z} - 2\omega W_w - \omega^2 r \\ \rightarrow \\ e_w : & 0 = W_r \frac{\partial W_w}{\partial r} + W_z \frac{\partial W_w}{\partial z} + 2\omega W_r \\ \rightarrow \\ e_z : & -\frac{1}{\rho} \frac{\partial P}{\partial z} = W_r \frac{\partial W_z}{\partial r} + W_z \frac{\partial W_z}{\partial z} \end{cases} \quad [\text{Eq. 5.1.7}]$$

Making use of the velocity triangle equations, the relative velocity in tangential direction can be substituted by the absolute velocity minus the blade speed, so that the final equations can be directly applicable for both rotor and stator:

$$\begin{cases} \rightarrow \\ e_r : & -\frac{1}{\rho} \frac{\partial P}{\partial r} = V_r \frac{\partial V_r}{\partial r} + V_z \frac{\partial V_r}{\partial z} - 2\omega(V_w - U) - \omega^2 r \\ \rightarrow \\ e_w : & 0 = V_r \frac{\partial (V_w - U)}{\partial r} + V_z \frac{\partial (V_w - U)}{\partial z} + 2\omega V_r \\ \rightarrow \\ e_z : & -\frac{1}{\rho} \frac{\partial P}{\partial z} = V_r \frac{\partial V_z}{\partial r} + V_z \frac{\partial V_z}{\partial z} \end{cases} \quad [\text{Eq. 5.1.8}]$$

Subsequently, the above equations are reformed in order to be expressed into the m (meridional) and s (tangential to the blade edge) directions. According to Figure 5.1.1 the magnitude of the meridional velocity equals:

$$V_m = \sqrt{V_r^2 + V_z^2} \quad [\text{Eq. 5.1.9}]$$

where

$$V_r = V_m \sin \varepsilon \quad [\text{Eq. 5.1.10}]$$

and

$$V_z = V_m \cos \varepsilon \quad [\text{Eq. 5.1.11}]$$

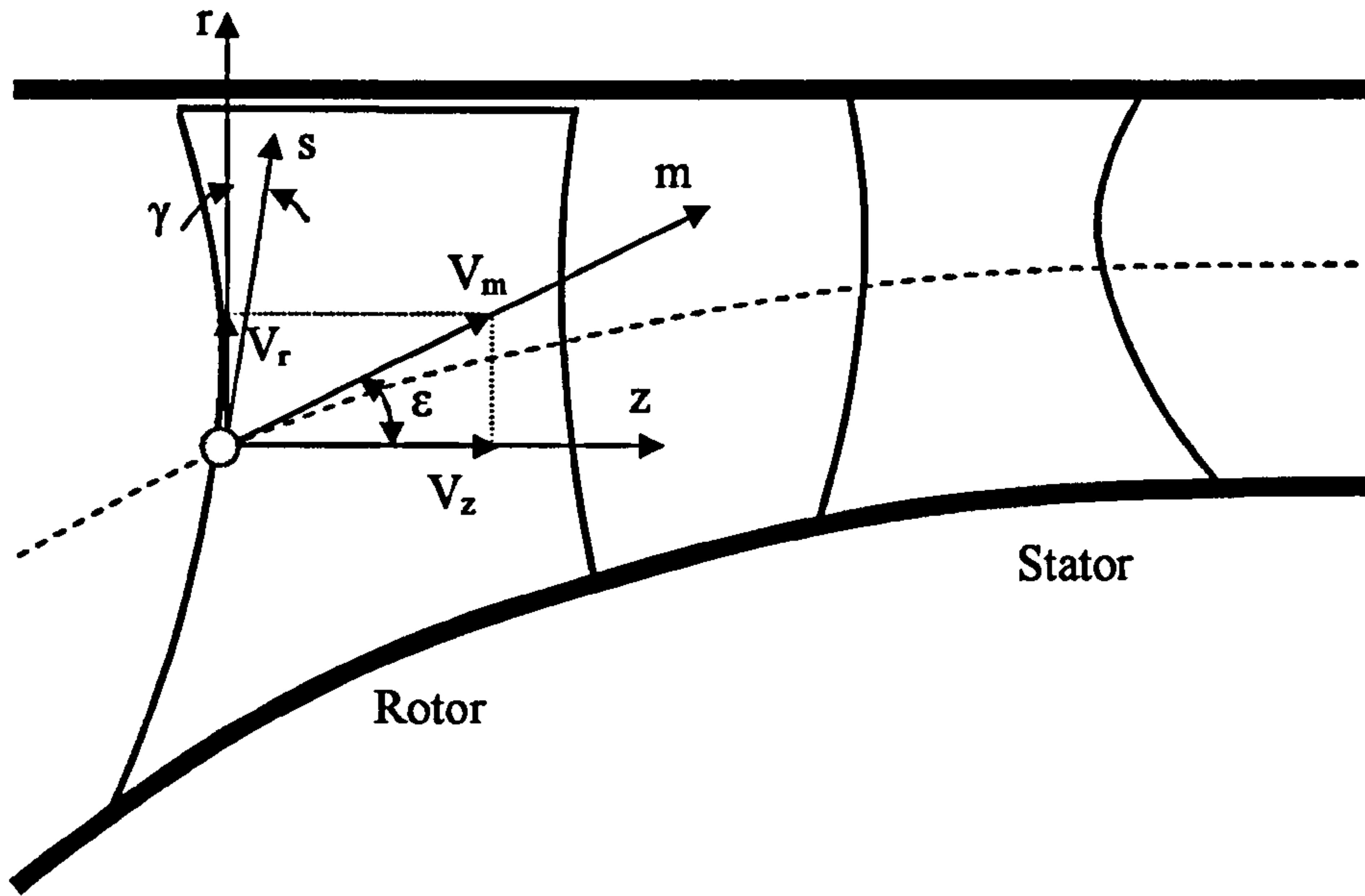


Figure 5.1.1: Coordinate system

The meridional projection of the streamline curve can be expressed as a function of the  $r$  and  $z$  coordinates:

$$m = m(r, z) \quad [\text{Eq. 5.1.12}]$$

Consequently, the partial derivative with respect to the meridional direction, equals:

$$\frac{\partial(\ )}{\partial m} = \frac{\partial r}{\partial m} \frac{\partial(\ )}{\partial r} + \frac{\partial z}{\partial m} \frac{\partial(\ )}{\partial z} \quad [\text{Eq. 5.1.13}]$$

From Figure 5.1.1 and Equations 5.1.10 and 5.1.11:

$$\frac{\partial r}{\partial m} = \sin \varepsilon = \frac{V_r}{V_m} \quad [\text{Eq. 5.1.14}]$$

$$\frac{\partial z}{\partial m} = \cos \varepsilon = \frac{V_z}{V_m} \quad [\text{Eq. 5.1.15}]$$

$$\frac{\partial r}{\partial z} = \tan \varepsilon = \frac{V_r}{V_z} \quad [\text{Eq. 5.1.16}]$$

Therefore, according to the above three equations Equation 5.1.13 equals to:

$$\frac{\partial(\ )}{\partial m} = \sin \varepsilon \frac{\partial(\ )}{\partial r} + \cos \varepsilon \frac{\partial(\ )}{\partial z} \Leftrightarrow V_m \frac{\partial(\ )}{\partial m} = V_r \frac{\partial(\ )}{\partial r} + V_z \frac{\partial(\ )}{\partial z} \quad [\text{Eq. 5.1.17}]$$



Using the above operator, Equation 5.1.8 becomes:

$$\begin{cases} \rightarrow e_r: & -\frac{1}{\rho} \frac{\partial P}{\partial r} = V_m \frac{\partial V_r}{\partial m} - 2\omega(V_w - U) - \omega^2 r \\ \rightarrow e_w: & 0 = V_m \frac{\partial(V_w - U)}{\partial m} + 2\omega V_r \\ \rightarrow e_z: & -\frac{1}{\rho} \frac{\partial P}{\partial z} = V_m \frac{\partial V_z}{\partial m} \end{cases} \quad [\text{Eq. 5.1.18}]$$

Radial and axial directions can be expressed as a function of the s direction (blade edge path).

$$r = r(s) \quad [\text{Eq. 5.1.19}]$$

$$z = z(s) \quad [\text{Eq. 5.1.20}]$$

Therefore, the variation of static pressure along the s path can be expressed as a function of the radial and axial gradients of pressure:

$$-\frac{1}{\rho} \frac{\partial P}{\partial s} = \cos \gamma \left( -\frac{1}{\rho} \frac{\partial P}{\partial r} \right) + \sin \gamma \left( -\frac{1}{\rho} \frac{\partial P}{\partial z} \right) \quad [\text{Eq. 5.1.21}]$$

Substituting Equation 5.1.18 into Equation 5.1.21:

$$-\frac{1}{\rho} \frac{\partial P}{\partial s} = \cos \gamma \left( V_m \frac{\partial V_r}{\partial m} \right) + \sin \gamma \left( V_m \frac{\partial V_z}{\partial m} \right) - 2 \cos \gamma \omega (V_w - U) - \cos \gamma \omega^2 r \quad [\text{Eq. 5.1.22}]$$

Finally, making use of Equations 5.1.14, 5.1.15 and 5.1.16, Equation 5.1.22 takes the following form:

$$\begin{aligned} -\frac{1}{\rho} \frac{\partial P}{\partial s} &= \cos \gamma V_m \frac{\partial(\sin \varepsilon V_m)}{\partial m} + \sin \gamma V_m \frac{\partial(\cos \varepsilon V_m)}{\partial m} - 2 \cos \gamma \omega (V_w - U) - \cos \gamma \omega^2 r \Rightarrow \\ -\frac{1}{\rho} \frac{\partial P}{\partial s} &= \cos \gamma V_m \left( \frac{\partial V_m}{\partial m} \sin \varepsilon + V_m \cos \varepsilon \frac{\partial \varepsilon}{\partial m} \right) + \sin \gamma V_m \left( \frac{\partial V_m}{\partial m} \cos \varepsilon - V_m \sin \varepsilon \frac{\partial \varepsilon}{\partial m} \right) - \\ &- 2 \cos \gamma \omega (V_w - U) - \cos \gamma \omega^2 r \Rightarrow \\ -\frac{1}{\rho} \frac{\partial P}{\partial s} &= \cos \gamma V_m \frac{\partial V_m}{\partial m} \sin \varepsilon + \cos \gamma V_m^2 \cos \varepsilon \frac{\partial \varepsilon}{\partial m} + \sin \gamma V_m \frac{\partial V_m}{\partial m} \cos \varepsilon - \sin \gamma V_m^2 \sin \varepsilon \frac{\partial \varepsilon}{\partial m} - \\ &- 2 \cos \gamma \omega (V_w - U) - \cos \gamma \omega^2 r \Rightarrow \\ -\frac{1}{\rho} \frac{\partial P}{\partial s} &= \cos(\varepsilon + \gamma) V_m^2 \frac{\partial \varepsilon}{\partial m} + \sin(\varepsilon + \gamma) V_m \frac{\partial V_m}{\partial m} - 2 \cos \gamma \omega (V_w - U) - \cos \gamma \omega^2 r \Rightarrow \\ -\frac{1}{\rho} \frac{\partial P}{\partial s} &= \cos(\varepsilon + \gamma) \frac{V_m^2}{R_c} + \sin(\varepsilon + \gamma) V_m \frac{\partial V_m}{\partial m} - 2 \cos \gamma \omega (V_w - U) - \cos \gamma \omega^2 r \quad [\text{Eq. 5.1.23}] \end{aligned}$$

Consequently, the above derived equation corresponds to Newton's second law of motion. The pressure gradient along the  $s$  direction can also be derived from the differential form of the equation of state of a perfect gas:

$$-\frac{1}{\rho}dP = TdS - dH \quad [\text{Eq. 5.1.24}]$$

The static enthalpy  $H$  equals:

$$H = C_p T_o - \frac{V^2}{2} \quad [\text{Eq. 5.1.25}]$$

From the velocity triangles we get the following expression for  $V^2$ :

$$W^2 = V^2 + U^2 - 2UV \cos \alpha \Rightarrow V^2 = W^2 - U^2 + 2UV_w \quad [\text{Eq. 5.1.26}]$$

Substituting Equation 5.1.26 into Equation 5.1.25, the last takes the following form:

$$\begin{aligned} H &= C_p T_o - \frac{W^2}{2} + \frac{U^2}{2} - UV_w \Rightarrow H = (C_p T_o - UV_w) - \frac{W^2}{2} + \frac{U^2}{2} \Rightarrow \\ H &= I - \frac{W^2}{2} + \frac{U^2}{2} \end{aligned} \quad [\text{Eq. 5.1.27}]$$

Where  $I$  is the 'rothalpy' (for a stationary row  $I=H_o$ ). The partial derivative of the state equation along the  $s$  path equals:

$$\begin{aligned} -\frac{1}{\rho} \frac{\partial P}{\partial s} &= T \frac{\partial S}{\partial s} - \frac{\partial \left( I - \frac{W^2}{2} + \frac{U^2}{2} \right)}{\partial s} \Rightarrow \\ -\frac{1}{\rho} \frac{\partial P}{\partial s} &= T \frac{\partial S}{\partial s} - \frac{\partial I}{\partial s} + \frac{1}{2} \frac{\partial W^2}{\partial s} - \frac{1}{2} \frac{\partial U^2}{\partial s} \Rightarrow \\ -\frac{1}{\rho} \frac{\partial P}{\partial s} &= T \frac{\partial S}{\partial s} - \frac{\partial I}{\partial s} + \frac{1}{2} \frac{\partial \left( \frac{V_m^2}{\cos^2 \alpha} \right)}{\partial s} - \frac{1}{2} \frac{\partial U^2}{\partial s} \Rightarrow \\ -\frac{1}{\rho} \frac{\partial P}{\partial s} &= T \frac{\partial S}{\partial s} - \frac{\partial I}{\partial s} + \frac{V_m}{\cos \alpha} \frac{\partial \left( \frac{V_m}{\cos \alpha} \right)}{\partial s} - U \frac{\partial U}{\partial s} \Rightarrow \\ -\frac{1}{\rho} \frac{\partial P}{\partial s} &= T \frac{\partial S}{\partial s} - \frac{\partial I}{\partial s} + \frac{V_m}{\cos \alpha} \left( \frac{\frac{\partial V_m}{\partial s} \cos \alpha + V_m \sin \alpha \frac{\partial \alpha}{\partial s}}{\cos^2 \alpha} \right) - \frac{U^2}{r} \cos \gamma \Rightarrow \\ -\frac{1}{\rho} \frac{\partial P}{\partial s} &= T \frac{\partial S}{\partial s} - \frac{\partial I}{\partial s} + \frac{V_m}{\cos \alpha} \left( \frac{\frac{\partial V_m}{\partial s} + V_m \tan \alpha \frac{\partial \alpha}{\partial s}}{\cos \alpha} \right) - \frac{U^2}{r} \cos \gamma \Rightarrow \end{aligned}$$



$$-\frac{1}{\rho} \frac{\partial P}{\partial s} = T \frac{\partial S}{\partial s} - \frac{\partial I}{\partial s} + \frac{1}{2 \cos^2 \alpha} \frac{\partial V_m^2}{\partial s} + \frac{V_m^2 \tan \alpha}{\cos^2 \alpha} \frac{\partial \alpha}{\partial s} - \frac{U^2}{r} \cos \gamma \quad [\text{Eq. 5.1.28}]$$

From Equation 5.1.28 and Equation 5.1.23:

$$T \frac{\partial S}{\partial s} - \frac{\partial I}{\partial s} + \frac{1}{2 \cos^2 \alpha} \frac{\partial V_m^2}{\partial s} + \frac{V_m^2 \tan \alpha}{\cos^2 \alpha} \frac{\partial \alpha}{\partial s} - \frac{U^2}{r} \cos \gamma = \cos(\varepsilon + \gamma) \frac{V_m^2}{R_c} + \sin(\varepsilon + \gamma) V_m \frac{\partial V_m}{\partial m} - 2 \cos \gamma \omega (V_w - U) - \cos \gamma \omega^2 r \quad [\text{Eq. 5.1.29}]$$

The above equation is a second degree, non-linear, partial differential equation with respect to the meridional velocity. In order to convert it into a linear equation, the term  $V_m \cdot \partial V_m / \partial m$  can be substituted by the law of conservation of mass, which for an axi-symmetric flow has the following differential form:

$$\frac{\partial(r\rho V_r)}{\partial r} + \frac{\partial(r\rho V_z)}{\partial r} = 0 \quad [\text{Eq. 5.1.30}]$$

Transformation into the s-m coordinate system gives:

$$\begin{aligned} & \frac{1}{\cos(\varepsilon + \gamma)} \left( \cos \varepsilon \frac{\partial(r\rho V_r)}{\partial s} - \sin \gamma \frac{\partial(r\rho V_r)}{\partial m} \right) + \frac{1}{\cos(\varepsilon + \gamma)} \left( -\sin \varepsilon \frac{\partial(r\rho V_z)}{\partial s} + \cos \gamma \frac{\partial(r\rho V_z)}{\partial m} \right) = 0 \Rightarrow \\ & \cos \varepsilon \frac{\partial(r\rho V_r)}{\partial s} - \sin \gamma \frac{\partial(r\rho V_r)}{\partial m} - \sin \varepsilon \frac{\partial(r\rho V_z)}{\partial s} + \cos \gamma \frac{\partial(r\rho V_z)}{\partial m} = 0 \Rightarrow \\ & \cos \varepsilon \frac{\partial(r\rho V_m \sin \varepsilon)}{\partial s} - \sin \gamma \frac{\partial(r\rho V_m \sin \varepsilon)}{\partial m} - \sin \varepsilon \frac{\partial(r\rho V_m \cos \varepsilon)}{\partial s} + \cos \gamma \frac{\partial(r\rho V_m \cos \varepsilon)}{\partial m} = 0 \Rightarrow \\ & \cos \varepsilon \sin \varepsilon \frac{\partial(r\rho V_m)}{\partial s} + \cos \varepsilon \cos \varepsilon \rho V_m \frac{\partial \varepsilon}{\partial s} - \sin \gamma \sin \varepsilon \frac{\partial(r\rho V_m)}{\partial m} - \sin \gamma \cos \varepsilon \rho V_m \frac{\partial \varepsilon}{\partial m} + \\ & + \sin \varepsilon \sin \varepsilon \rho V_m \frac{\partial \varepsilon}{\partial s} + \sin \varepsilon \cos \varepsilon \frac{\partial(r\rho V_m)}{\partial s} - \cos \gamma \sin \varepsilon \rho V_m \frac{\partial \varepsilon}{\partial m} + \cos \gamma \cos \varepsilon \frac{\partial(r\rho V_m)}{\partial m} = 0 \Rightarrow \\ & (\cos \varepsilon \sin \varepsilon + \sin \varepsilon \cos \varepsilon) \frac{\partial(r\rho V_m)}{\partial s} + (\cos \gamma \cos \varepsilon - \sin \gamma \sin \varepsilon) \frac{\partial(r\rho V_m)}{\partial m} + \\ & + (\cos \varepsilon \cos \varepsilon \rho V_m + \sin \varepsilon \sin \varepsilon \rho V_m) \frac{\partial \varepsilon}{\partial s} - (\sin \gamma \cos \varepsilon \rho V_m + \cos \gamma \sin \varepsilon \rho V_m) \frac{\partial \varepsilon}{\partial m} = 0 \Rightarrow \\ & 2 \cos \varepsilon \sin \varepsilon \frac{\partial(r\rho V_m)}{\partial s} + \cos(\varepsilon + \gamma) \frac{\partial(r\rho V_m)}{\partial m} + (\cos^2 \varepsilon + \sin^2 \varepsilon) \rho V_m \frac{\partial \varepsilon}{\partial s} - \sin(\varepsilon + \gamma) \rho V_m \frac{\partial \varepsilon}{\partial m} = 0 \Rightarrow \\ & \frac{\partial(r\rho V_m)}{\partial m} + \frac{1}{\cos(\varepsilon + \gamma)} \rho r V_m \frac{\partial \varepsilon}{\partial s} - \tan(\varepsilon + \gamma) \rho r V_m \frac{\partial \varepsilon}{\partial m} = 0 \Rightarrow \\ & \frac{\partial(r\rho V_m)}{\partial m} \frac{1}{\rho r V_m} + \frac{1}{\cos(\varepsilon + \gamma)} \frac{\partial \varepsilon}{\partial s} - \tan(\varepsilon + \gamma) \frac{\partial \varepsilon}{\partial m} = 0 \Rightarrow \\ & \frac{\partial r}{\partial m} \frac{\rho V_m}{\rho r V_m} + \frac{\partial \rho}{\partial m} \frac{r V_m}{\rho r V_m} + \frac{\partial V_m}{\partial m} \frac{r \rho}{r \rho V_m} + \frac{1}{\cos(\varepsilon + \gamma)} \frac{\partial \varepsilon}{\partial s} - \tan(\varepsilon + \gamma) \frac{\partial \varepsilon}{\partial m} = 0 \Rightarrow \end{aligned}$$

$$\frac{1}{r} \frac{\partial r}{\partial m} + \frac{1}{\rho} \frac{\partial \rho}{\partial m} + \frac{1}{V_m} \frac{\partial V_m}{\partial m} + \frac{1}{\cos(\varepsilon + \gamma)} \frac{\partial \varepsilon}{\partial s} - \tan(\varepsilon + \gamma) \frac{\partial \varepsilon}{\partial m} = 0 \Rightarrow$$

$$\frac{\partial(\ln(r\rho))}{\partial m} + \frac{1}{V_m} \frac{\partial V_m}{\partial m} + \frac{1}{\cos(\varepsilon + \gamma)} \frac{\partial \varepsilon}{\partial s} - \tan(\varepsilon + \gamma) \frac{\partial \varepsilon}{\partial m} = 0 \Rightarrow$$

$$V_m \frac{\partial V_m}{\partial m} = V_m^2 \left( -\frac{1}{\cos(\varepsilon + \gamma)} \frac{\partial \varepsilon}{\partial s} + \frac{\tan(\varepsilon + \gamma)}{R_c} - \frac{\partial(\ln(r\rho))}{\partial m} \right) \quad [\text{Eq. 5.1.31}]$$

The above equation can be substituted directly into Equation 5.1.29, in order to replace the partial derivative of the meridional velocity along the meridional direction.

$$T \frac{\partial S}{\partial s} - \frac{\partial I}{\partial s} + \frac{1}{2 \cos^2 \alpha} \frac{\partial V_m^2}{\partial s} + \frac{V_m^2 \tan \alpha}{\cos^2 \alpha} \frac{\partial \alpha}{\partial s} - \frac{U^2}{r} \cos \gamma = \cos(\varepsilon + \gamma) \frac{V_m^2}{R_c} +$$

$$\sin(\varepsilon + \gamma) V_m^2 \left( -\frac{1}{\cos(\varepsilon + \gamma)} \frac{\partial \varepsilon}{\partial s} + \frac{\tan(\varepsilon + \gamma)}{R_c} - \frac{\partial(\ln(r\rho))}{\partial m} \right) - 2 \cos \gamma \omega (V_w - U) - \cos \gamma \omega^2 r \Rightarrow$$

Rearranging:

$$\frac{\partial V_m^2}{\partial s} = V_m^2 2 \cos^2 \alpha \left( \frac{\cos(\varepsilon + \gamma)}{R_c} - \frac{\tan \alpha}{\cos^2 \alpha} \frac{\partial \alpha}{\partial s} + \right. \\ \left. + \sin(\varepsilon + \gamma) \left( -\frac{1}{\cos(\varepsilon + \gamma)} \frac{\partial \varepsilon}{\partial s} + \frac{\tan(\varepsilon + \gamma)}{R_c} \right) - \frac{\partial(\ln(r\rho))}{\partial m} \right) + \quad [\text{Eq. 5.1.32}]$$

$$+ 2 \cos^2 \alpha \left( \frac{\partial I}{\partial s} - 2 \cos \gamma \omega (V_w - U) - T \frac{\partial S}{\partial s} \right)$$

Assuming that the flow properties included in the above equation vary smoothly along the blade edges, the coefficients of the meridional velocity can be replaced by the corresponding average values between two neighboring streamlines and thus be considered as constants. Under the above assumption Equation 5.1.32 becomes:

$$\frac{\partial V_m^2}{\partial s} = \bar{B} V_m^2 + \bar{A} \quad [\text{Eq. 5.1.33}]$$

Where:

$$\bar{A} = 2 \cos^2 \alpha \left( \frac{\partial I}{\partial s} - 2 \cos \gamma \omega (V_w - U) - T \frac{\partial S}{\partial s} \right) \quad [\text{Eq. 5.1.34}]$$

and



$$\bar{B} = 2\cos^2\alpha \left[ \frac{\cos(\varepsilon+\gamma)}{R_c} \frac{\tan\alpha}{\cos^2\alpha} \frac{\partial\alpha}{\partial s} + \sin(\varepsilon+\gamma) \left( \frac{1}{\cos(\varepsilon+\gamma)} \frac{\partial\varepsilon}{\partial s} + \frac{\tan(\varepsilon+\gamma)}{R_c} \frac{d(\ln(r\rho))}{dm} \right) \right] \quad [\text{Eq. 5.1.35}]$$

Equation 5.1.33 is a second degree ordinary differential equation. Making the following substitution:

$$Y = V_m^2 \quad [\text{Eq. 5.1.36}]$$

Equation 5.1.33 reduces to a first order linear differential equation of the following type:

$$\frac{dY}{ds} = \bar{A} + \bar{B}Y \quad [\text{Eq. 5.1.37}]$$

The general solution of the homogeneous equation associated to Equation 5.1.37 is:

$$Y_h = Ce^{\bar{B}s} \quad [\text{Eq. 5.1.38}]$$

Where  $s$  is a characteristic distance. Whereas a particular solution when the first derivative of the function equals to zero is:

$$Y_p = k \quad [\text{Eq. 5.1.39}]$$

Therefore from Equation 5.1.37:

$$0 = \bar{A} + \bar{B}k \Leftrightarrow k = -\frac{\bar{A}}{\bar{B}} \quad [\text{Eq. 5.1.40}]$$

Substituting back to the general solution:

$$Y = Ce^{\bar{B}s} - \frac{\bar{A}}{\bar{B}} \quad [\text{Eq. 5.1.41}]$$

Assuming  $Y_1$  is the function value at a particular node, then:

$$Y_1 = C_1 e^{\bar{B}s_1} - \frac{\bar{A}}{\bar{B}} \Leftrightarrow C_1 = \left( Y_1 + \frac{\bar{A}}{\bar{B}} \right) e^{-\bar{B}s_1} \quad [\text{Eq. 5.1.42}]$$

Substituting Equation 5.1.42 back into 5.1.41:

$$Y = \left( Y_1 + \frac{\bar{A}}{\bar{B}} \right) e^{-\bar{B}s_1} e^{\bar{B}s} - \frac{\bar{A}}{\bar{B}} \Leftrightarrow Y = Y_1 e^{\bar{B}(s-s_1)} - \frac{\bar{A}}{\bar{B}} (1 - e^{\bar{B}(s-s_1)}) \quad [\text{Eq. 5.1.43}]$$

Consequently, considering two consecutive nodes  $j$  and  $j+1$ , the solution of Equation 5.1.33 is:

$$V_{m,j+1}^2 = V_{m,j}^2 e^{\bar{B}(s-s_1)} - \frac{\bar{A}}{\bar{B}} \left(1 - e^{\bar{B}(s-s_1)}\right) \quad [\text{Eq. 5.1.44}]$$

$A$  and  $B$  constants are functions of blade geometry, streamline properties, fluid properties and the solution of the equation itself,  $V_{m,j}$ . Therefore, an iterative procedure is required to solve Equation 5.1.44.

Equations 5.1.32 and 5.1.33, basically describe the gradient of meridional velocity from hub to tip but not its average magnitude. A further constraint is required to determine the level of meridional velocity which can be provided by integrating the meridional velocity profile across the compressor annulus to check for continuity of mass flow. The integral form of the continuity equation is presented in detail in Section 5.2 but generally speaking, the radial equilibrium equation and the equation of mass flow need to be solved iteratively. A first guess for the shape of streamlines and distribution of meridional velocity from hub to tip is made. After calculating velocity triangles, entropy along streamlines and enthalpy, the terms  $A$  and  $B$  in Equation 5.1.33 are calculated. Solving Equation 5.1.44 establishes the rate of change of meridional velocity from hub to tip. Integrating the meridional velocity profile establishes the compressor mass flow which is then compared to the overall (actual) mass flow. Based on the mass flow difference, the overall level of meridional velocity is re-adjusted accordingly and a new iteration takes place. During this process the streamtube mass flow is used to determine the new positions of the streamlines at the intersections with the blade edges, to be used in the new iteration.

Finally, the author would like to point out that within the current derived expression of the full radial equilibrium equation, the blade force and dissipative force terms are neglected. The blade force is related to the rate at which the flow is turned in the circumferential plane and therefore the blade force component that appears in the radial equilibrium equation is the component introduced by the blade lean angle. Consequently, the current *2D Compressor SLC Software* cannot be applied for compressor blade geometries with appreciable leaning. As far as the dissipative force is concerned, if the calculating station direction is nearly perpendicular (like in this case) to the streamline direction, it can be considered negligible.

## 5.2. Continuity of Mass Flow

As described in the previous section, the meridional velocity profile needs to be integrated across the compressor annulus to check for continuity of mass flow. The continuity equation therefore is solved together with the radial equilibrium equation iteratively to determine the constants of integration in the latter. The continuity equation is used in its integral form (Equation 5.2.1) to determine the mass flow in stream tubes and compressor annulus. In order to solve the continuity equation, the same approach is used that was also adopted by Barbosa (1987, p. 41-43). The integrand is made discrete over the nodes at the intersections of the streamlines with the blade edges and a trapezoidal rule is applied for the evaluation of the integral.



$$\dot{m} = \int_A \rho V dA \quad [\text{Eq. 5.2.1}]$$

At each stream tube the mass flow rate is generally given by:

$$\dot{m}_j = \int_A \bar{\rho}_j \bar{V}_{m,j} dA \quad [\text{Eq. 5.2.2}]$$

Equation 5.2.2 can be numerically solved as:

$$\dot{m}_j = \frac{\pi}{2} \left[ \rho_{j+1} V_{m,j+1} \cos(\varepsilon_{j+1} + \gamma_{j+1}) + \rho_j V_{m,j} \cos(\varepsilon_j + \gamma_j) \right] \left[ \frac{r_{j+1}^2 - r_j^2}{\cos\left(\frac{\gamma_{j+1} + \gamma_j}{2}\right)} \right] \quad [\text{Eq. 5.2.3}]$$

For a large number of streamlines and small values of blade sweep, the above equation can be simplified to:

$$\dot{m}_j = \pi (r_{j+1} \rho_{j+1} V_{m,j+1} \cos \varepsilon_{j+1} + r_j \rho_j V_{m,j} \cos \varepsilon_j) (r_{j+1} - r_j) \quad [\text{Eq. 5.2.4}]$$

This simple technique can give fairly accurate solutions given a reasonable number of streamlines and a small streamline spacing.

A fairly similar approach is described in Cumpsty (1989, p. 110) and could be used instead. According to Cumpsty, the meridional velocity profile can be integrated across the annulus to give the total mass flow across the quasi-orthogonals in the  $s$  direction using:

$$\frac{\dot{m}}{N} = \int_{hub}^{tip} \rho V_m \cos(\varepsilon + \gamma) \omega ds \quad [\text{Eq. 5.2.5}]$$

Where  $N$  is the number of blades and  $\omega$  the stream surface thickness given by:

$$\omega = \frac{2\pi B}{N} \quad [\text{Eq. 5.2.6}]$$

Where  $B$  is a measure of the blockage, strongly affected by the boundary layer displacement on the annulus walls and blades.

Both methods are very similar in concept and implementation. Perhaps the only difference is that in the first approach, the blockage factor due to boundary layer growth is taken into account indirectly, via the actual streamline radial positions  $r_j$ , while the second method incorporates blockage directly in the formulation.

### Implementation

The first method, as described above, has been programmed in the *2D Compressor SLC Software*. Since this is a fairly short, straight forward calculation it has not been contained into a separate dedicated subroutine. The calculation is carried out in subroutines *Compressor2D\_BladeRowInletMeridVelDistrbConverg.f90* and *Compressor2D\_BladeRowOutletMeridVelDistrbConverg.f90*, in order to establish the resultant stream tube and overall mass flows corresponding to the generated blade row inlet and outlet meridional velocity profiles respectively.

### Limitations and Potential Expansion

As it was mentioned above, this is practically a numerical integration and consequently any potential improvement in terms of accuracy or calculation time is associated to a better numerical technique. The accuracy of the numerical integration may be limited by the number of streamlines that the user selects in the input file. The number of streamlines however cannot be changed independently for this particular integration process only, as it is also associated with the more general meridional velocity profile convergence procedure.

## **5.3. Calculation of Velocity Triangles**

The sign convention and velocity triangle nomenclature adopted by this work are illustrated in *Appendix B - Sign Convention and Velocity Triangles*. Velocity triangles are calculated from hub to tip, at the intersection of streamlines with the blade edges (nodes), at every blade row inlet and outlet, for both normal and minimum loss operating conditions.

The calculation is based on the fundamental Euler turbomachinery equations and it is carried out with respect to the notional plane in the streamline direction and not in the axial one which is usually the case in compressor preliminary design.

At the blade row inlet, the calculation of velocity triangles is based on the meridional velocity, which is derived from the solution of the radial equilibrium equation, and the air absolute angle  $\alpha$ , which is a user input or a boundary condition from an upstream blade row. The axial velocity is calculated from the meridional velocity and the cosine of the streamline slope  $\varepsilon$  at the blade row inlet:

$$V_{a,1} = V_{m,1} \cos \varepsilon_1 \quad [\text{Eq. 5.3.1}]$$

The absolute whirl velocity is calculated from the meridional and the tangent of the air absolute angle:

$$V_{w,1} = V_{m,1} \tan \alpha_1 \quad [\text{Eq. 5.3.2}]$$

The absolute velocity is calculated from the meridional and the cosine of the air absolute angle:



$$V_1 = \frac{V_{m,1}}{\cos \alpha_1} \quad [\text{Eq. 5.3.3}]$$

The above equations apply for both stationary and rotating blade rows. Additionally, for rotating blade rows relative quantities are calculated as follows:

$$\omega = 2\pi N \quad [\text{Eq. 5.3.4}]$$

Where  $\omega$  is the compressor angular speed and  $N$  the compressor rotational speed. The blade velocity at the blade row inlet at any streamline position is calculated from:

$$U_1 = \omega r_1 \quad [\text{Eq. 5.3.5}]$$

The relative whirl velocity can then be calculated from absolute whirl and blade velocities:

$$W_{w,1} = V_{w,1} - U_1 \quad [\text{Eq. 5.3.6}]$$

The relative angle  $\beta$  is calculated from the inverse tangent of relative whirl and meridional velocities:

$$\beta_1 = \arctan\left(\frac{W_{w,1}}{V_{m,1}}\right) \quad [\text{Eq. 5.3.7}]$$

Finally, the relative velocity is calculated from the meridional and the cosine of the relative angle:

$$W_1 = \frac{V_{m,1}}{\cos \beta_1} \quad [\text{Eq. 5.3.8}]$$

Calculating the blade row losses requires knowledge of the minimum loss conditions. For minimum loss conditions, the meridional velocity is considered to be roughly unchanged and the air inlet minimum loss absolute angle is calculated from the blade inlet angle and the minimum loss incidence angle. The rest of the velocity triangle parameters for minimum loss conditions are derived as shown above.

Similarly, at the blade row outlet, input quantities are again the meridional velocity and the air absolute angle at the outlet. The last is calculated from the blade outlet angle and the deviation angle. The air outlet minimum loss absolute angle is calculated from the blade outlet angle and the minimum loss deviation angle. The calculation procedure for establishing all velocity triangle parameters is similar to the one presented above, for both normal and minimum loss conditions.

### Implementation

The above calculations are carried out in four subroutines. More precisely, at blade row inlet *Compressor2D\_BladeInletMinLossTriangleCalc.f90* calculates the minimum loss velocity triangles and *Compressor2D\_BladeInletTriangleCalc.f90* calculates the velocity triangles for all other operating conditions. Similarly, at blade row outlet, subroutines *Compressor2D\_BladeOutletMinLossTriangleCalc.f90* and *Compressor2D\_BladeOutletTriangleCalc.f90* calculate the velocity triangles at the corresponding operating conditions.

Velocity triangles for minimum loss conditions are only involved in the determination of losses. The subroutine for the blade row inlet minimum loss velocity triangle calculation is called outside the inlet meridional velocity convergence loop by the main subroutine *Compressor2D\_MainProgram.f90*, before the blade row outlet meridional velocity convergence procedure starts.

On the contrary, the remaining three subroutines are directly involved in the meridional velocity convergence processes at blade row inlet and outlet. *Compressor2D\_BladeInletTriangleCalc.f90* is called when calculations are performed for the blade row inlet by *Compressor2D\_BladeRowInletMeridVelDistrbGener.f90*. *Compressor2D\_BladeRowOutletMeridVelDistrbGener.f90* calls the remaining two subroutines when calculations are performed for the blade row outlet.

The input variables for all subroutines are the streamline slope, air angles and blade speed at the blade row inlet and outlet calculation nodes.

## 5.4. Calculation of Thermodynamic Properties

Thermodynamic properties are calculated from hub to tip, at the intersection of streamlines with the blade edges (nodes), at every blade row inlet and outlet. All calculations are based on fundamental compressible flow functions.

At every blade row inlet, the radial distributions of total temperature, total pressure and static entropy are considered as input boundary conditions, defined either by the user or established during the calculation of an upstream blade row. The thermodynamic parameters  $C_{p,1}$  and  $\gamma_1$  are allowed to vary with static temperature not only axially, through out the compressor, but also in the span-wise direction. The static temperature  $T_1$  at any node is calculated from Equation 5.4.1, given total temperature  $T_{o,1}$  and air inlet absolute velocity  $V_1$ .

$$T_{o,1} = T_1 + \frac{V_1^2}{2C_{p,1}} \quad [\text{Eq. 5.4.1}]$$

In order to establish the static temperature  $T_1$ , the above equation needs to be solved iteratively because initially the value of  $C_{p,1}$  is not known. To start the iteration, the total temperature value is taken as a first guess equal to the static temperature. The specific heat at constant pressure that corresponds to this static temperature is then calculated and subsequently the static temperature is reevaluated using Equation



5.4.1. The two values of static temperature are compared and a new guess is made based on the previous values through a weighting rule. Convergence is achieved when the two values of static temperature agree within a pre-established error margin.

The calculation of  $C_{p,1}$  at every iteration, is based on the model provided in Walsh and Fletcher (1998, p. 115-116) according to which:

$$C_{p,1} = A_0 + A_1TZ + A_2TZ^2 + A_3TZ^3 + A_4TZ^4 + A_5TZ^5 + A_6TZ^6 + A_7TZ^7 + A_8TZ^8 \quad [\text{Eq. 5.4.2}]$$

Where  $TZ=T/1000$  and  $A_n$  are constants for dry air as shown below:

$A_0$	0.992313
$A_1$	0.236688
$A_2$	-1.852148
$A_3$	6.083152
$A_4$	-8.893933
$A_5$	7.097112
$A_6$	-3.234725
$A_7$	0.794571
$A_8$	-0.081873
$A_9$	0.422178
$A_{10}$	0.001053

Table 5.4.1:  $C_p$  polynomial function constants for dry air

Gamma is then calculated from:

$$\gamma_1 = \frac{C_{p,1}}{C_{p,1} - R} \quad [\text{Eq. 5.4.3}]$$

Where R is the gas constant.

Having calculated the static temperature, the speed of sound is determined from:

$$C_1 = \sqrt{\gamma_1 RT_1} \quad [\text{Eq. 5.4.4}]$$

Mach numbers with respect to all different velocity vectors are then calculated as follows. The meridional Mach number:

$$M_{m,1} = \frac{V_{m,1}}{C_1} \quad [\text{Eq. 5.4.5}]$$

The absolute Mach number:

$$M_1 = \frac{V_1}{C_1} \quad [\text{Eq. 5.4.6}]$$

And the absolute whirl Mach number:

$$M_{w,1} = \frac{V_{w,1}}{C_1} \quad [\text{Eq. 5.4.7}]$$

Static pressure  $P_1$  is calculated from:

$$\frac{P_1}{P_{o,1}} = \left(1 + \frac{\gamma_1 - 1}{2} M_1^2\right)^{\frac{-\gamma_1}{\gamma_1 - 1}} \quad [\text{Eq. 5.4.8}]$$

Static density is calculated from the equation of state for a perfect gas:

$$P_1 = \rho_1 R T_1 \quad [\text{Eq. 5.4.9}]$$

Total density is calculated from:

$$\frac{\rho_1}{\rho_{o,1}} = \left(1 + \frac{\gamma_1 - 1}{2} M_1^2\right)^{\frac{-1}{\gamma_1 - 1}} \quad [\text{Eq. 5.4.10}]$$

Finally, having calculated the properties of air, based on the static temperature dependent polynomial functions for ideal gas, the total and static enthalpy are calculated as follows:

$$H_1 = C_{p,1} T_1 \quad [\text{Eq. 5.4.11}]$$

$$H_{o,1} = C_{p,1} T_{o,1} \quad [\text{Eq. 5.4.12}]$$

The above relationships apply to the absolute frame of reference and are sufficient to fully establish the thermodynamic properties at the inlet of a stationary blade row (stator). In the case of a rotor, relative thermodynamic properties need also to be derived in a similar manner.

The relative Mach number at the blade row inlet is calculated from:

$$M'_1 = \frac{W_1}{C_1} \quad [\text{Eq. 5.4.13}]$$

The relative whirl Mach number is calculated from:

$$M'_{w,1} = \frac{W_{w,1}}{C_1} \quad [\text{Eq. 5.4.14}]$$

The relative total temperature is calculated from:



$$T'_{o,1} = T_1 + \frac{W_1^2}{2C_{p,1}} \quad [\text{Eq. 5.4.15}]$$

The relative total density is calculated from:

$$\frac{\rho_1}{\rho'_{o,1}} = \left(1 + \frac{\gamma_1 - 1}{2} M_1^2\right)^{\frac{-1}{\gamma_1 - 1}} \quad [\text{Eq. 5.4.16}]$$

The relative total pressure is derived from:

$$\frac{P_1}{P'_{o,1}} = \left(1 + \frac{\gamma_1 - 1}{2} M_1^2\right)^{\frac{-\gamma_1}{\gamma_1 - 1}} \quad [\text{Eq. 5.4.17}]$$

And finally the relative total enthalpy at the inlet of the blade row is calculated from:

$$H'_{o,1} = C_{p,1} T'_{o,1} \quad [\text{Eq. 5.4.18}]$$

At the outlet of every blade row the calculation of the thermodynamic conditions commences from the determination of the absolute total temperature. Across a stator the absolute total temperature is considered to remain almost unchanged. Knowing the outlet absolute total temperature, the stator outlet static temperature  $T_2$ ,  $C_{p,2}$  and  $\gamma_2$  can be calculated through the iterative process described above.

Across a rotor, however, the absolute total temperature increases considerably due to the work done on the flow. In order to calculate the change in absolute total temperature across the rotor, the total enthalpy rise has to be calculated first. According to Euler's basic law of turbomachinery, the absolute total enthalpy rise across a rotor blade row can be calculated from velocity triangles and equals to:

$$\Delta H_o = U_2 V_{w,2} - U_1 V_{w,1} \quad [\text{Eq. 5.4.19}]$$

However, the absolute total enthalpy rise is also equal to:

$$\Delta H_o = C_{p,2} T_{o,2} - C_{p,1} T_{o,1} \quad [\text{Eq. 5.4.20}]$$

Knowing the outlet absolute velocity  $V_2$ , Equations 5.4.19, 5.4.20 and 5.4.21 are solved iteratively, as described above, to determine the correct rotor outlet absolute total temperature  $T_{o,2}$ , static temperature  $T_2$ ,  $C_{p,2}$  and  $\gamma_2$ .

$$T_{o,2} = T_2 + \frac{V_2^2}{2C_{p,2}} \quad [\text{Eq. 5.4.21}]$$

The relative total temperature is calculated from:

$$T'_{o,2} = T_2 + \frac{W_2^2}{2C_{p,2}} \quad [\text{Eq. 5.4.22}]$$

The speed of sound at the blade row outlet is then calculated from:

$$C_2 = \sqrt{\gamma_2 RT_2} \quad [\text{Eq. 5.4.23}]$$

And similarly to the blade row inlet, Mach numbers with respect to all different velocity vectors are then calculated as follows. The blade row outlet relative Mach numbers:

$$M'_2 = \frac{W_2}{C_2} \quad [\text{Eq. 5.4.24}]$$

$$M'_{w,2} = \frac{W_{w,2}}{C_2} \quad [\text{Eq. 5.4.25}]$$

The blade row outlet meridional Mach number:

$$M_{m,2} = \frac{V_{m,2}}{C_2} \quad [\text{Eq. 5.4.26}]$$

And the blade row outlet absolute Mach numbers:

$$M_2 = \frac{V_2}{C_2} \quad [\text{Eq. 5.4.27}]$$

$$M_{w,2} = \frac{V_{w,2}}{C_2} \quad [\text{Eq. 5.4.28}]$$

The total pressure across blade rows is not constant due to the presence of losses. For a rotating blade row, the relative total pressure is slightly reduced, where as for a stationary blade row this is sensed by the reduction in absolute total pressure. The reduction in total pressure is proportional to the losses generated within the blade passage and is incorporated in the calculations through the definition of the mass-averaged, total loss factor (or total pressure loss coefficient) given for the stator and rotor respectively by:

$$\bar{\omega}_{tot} = \frac{P_{o,1} - P_{o,2}}{P_{o,1} - P_1} \quad [\text{Eq. 5.4.29}]$$

$$\bar{\omega}'_{tot} = \frac{P'_{o,1} - P'_{o,2}}{P'_{o,1} - P_1} \quad [\text{Eq. 5.4.30}]$$



The above two equations can provide reasonable accuracy given that the blade row operates close to its design point and that shock losses and secondary losses are small enough compared to blade profile losses (Cumpsty, 1989, page 137). At higher Mach numbers and when secondary losses are stronger, the following definition of the total loss factor, given below for the relative frame of reference, should be used instead (Bullock and Johnsen, 1965). The following expression is considered to be more accurate since it takes into account the magnitude of the inlet relative Mach number and the change in radius, from blade row inlet to blade row outlet, of any given streamline. Blade losses are discussed in detail in Section 5.11.

$$\bar{\omega}_{tot} = \frac{(P'_{o,2})_{ideal} - P'_{o,2}}{P'_{o,1} - P_1} = \left( \frac{P'_{o,2}}{P'_{o,1}} \right)_{ideal} \left( \frac{1 - \frac{\left( \frac{P'_{o,2}}{P'_{o,1}} \right)}{\left( \frac{P'_{o,2}}{P'_{o,1}} \right)_{ideal}}}{1 - \frac{1}{1 + \frac{\bar{\gamma} - 1}{2} (M_1')^2}} \right)^{\left( \frac{\bar{\gamma}}{\bar{\gamma} - 1} \right)} \quad [\text{Eq. 5.4.31}]$$

The ideal relative pressure ratio is given by:

$$\left( \frac{P'_{o,2}}{P'_{o,1}} \right)_{ideal} = \left\{ 1 + \frac{\bar{\gamma} - 1}{2} \frac{(\omega r_2)^2}{\bar{\gamma} R T'_{o,1}} \left[ 1 - \left( \frac{r_1}{r_2} \right)^2 \right] \right\}^{\left( \frac{\bar{\gamma}}{\bar{\gamma} - 1} \right)} \quad [\text{Eq. 5.4.32}]$$

Where  $\omega$  is the spool angular speed,  $r_1/r_2$  is the streamline inlet over outlet  $r$  coordinate ratio, and  $\bar{\gamma}$  is the average ratio of specific heats between blade row inlet and outlet.

Knowing the total loss factor, which is established during the calculation of the radial equilibrium equation, and the total and static pressures at the blade row inlet, the total pressure at the outlet can easily be determined. The outlet static pressure is then calculated as previously, for known Mach number values, from Equations 5.4.31 and 5.4.32, for rotor and stator respectively.

$$\frac{P_2}{P'_{o,2}} = \left( 1 + \frac{\gamma_2 - 1}{2} M_2'^2 \right)^{\frac{-\gamma_2}{\gamma_2 - 1}} \quad [\text{Eq. 5.4.33}]$$

$$\frac{P_2}{P_{o,2}} = \left( 1 + \frac{\gamma_2 - 1}{2} M_2'^2 \right)^{\frac{-\gamma_2}{\gamma_2 - 1}} \quad [\text{Eq. 5.4.34}]$$

The entropy generation due to the non-isentropic compression is calculated through the following formula:

$$S_2 - S_1 = R \left( \frac{P_{o,2} - P_{o,1}}{P_{o,2}} \right) \quad [\text{Eq. 5.4.35}]$$

The above equation refers to the absolute frame of reference but can also be used in the relative frame of reference by substituting absolute values with relative ones. It only provides an estimate of static (or total if needed) entropy rise.

Equation 5.4.35 stems from the 1<sup>st</sup> law of thermodynamics in its differential form:

$$dq = du + dw \Rightarrow TdS = du + Pdv \quad [\text{Eq. 5.4.36}]$$

For an ideal gas we have:

$$H = u + Pv \quad [\text{Eq. 5.4.37}]$$

$$dH = C_p dT \quad [\text{Eq. 5.4.38}]$$

And the equation of state:

$$Pv = RT \quad [\text{Eq. 5.4.39}]$$

Consequently in the case of an ideal gas Equation 5.4.37 becomes:

$$\frac{dS}{R} = \frac{\gamma}{\gamma-1} \frac{dT}{T} - \frac{dP}{P} \quad [\text{Eq. 5.4.40}]$$

It can be proven that the above Equation 5.4.40 can also be written for total values of pressure and temperature:

$$\frac{dS}{R} = \frac{\gamma}{\gamma-1} \frac{dT_o}{T_o} - \frac{dP_o}{P_o} \quad [\text{Eq. 5.4.41}]$$

For adiabatic flow without work absorption  $dT_o=0$  and the above equation reduces to the following form:

$$\frac{dS}{R} = -\frac{dP_o}{P_o} \quad [\text{Eq. 5.4.42}]$$

Consequently, Equation 5.4.42 holds for a rotating blade row when referring to the relative frame of reference and a stationary blade row in the absolute frame of reference. For the exact calculation of entropy rise, Equation 5.4.42 should be integrated across the limits of the blade row. Therefore the last equation is only used in this work as an approximation.

Alternatively, if greater accuracy is required the following model can be used from Walsh and Fletcher (1998, p. 115-116).



$$S_2 - S_1 = \int \frac{C_p}{T} dT - R \ln \left( \frac{P_2}{P_1} \right) \quad [\text{Eq. 5.4.43}]$$

The integral in the last equation is calculated from:

$$\int \frac{C_p}{T} dT = FT_2 - FT_1 \quad [\text{Eq. 5.4.44}]$$

Where  $FT_2$  and  $FT_1$  can be calculated from the following polynomials and Table 5.4.1.

$$FT_2 = A_0 \ln T_2 + A_1 TZ_2 + \frac{A_2}{2} TZ_2^2 + \frac{A_3}{3} TZ_2^3 + \frac{A_4}{4} TZ_2^4 + \frac{A_5}{5} TZ_2^5 + \frac{A_6}{6} TZ_2^6 + \frac{A_7}{7} TZ_2^7 + \frac{A_8}{8} TZ_2^8 + A_{10} \quad [\text{Eq. 5.4.45}]$$

$$FT_1 = A_0 \ln T_1 + A_1 TZ_1 + \frac{A_2}{2} TZ_1^2 + \frac{A_3}{3} TZ_1^3 + \frac{A_4}{4} TZ_1^4 + \frac{A_5}{5} TZ_1^5 + \frac{A_6}{6} TZ_1^6 + \frac{A_7}{7} TZ_1^7 + \frac{A_8}{8} TZ_1^8 + A_{10} \quad [\text{Eq. 5.4.46}]$$

Where  $TZ = T/1000$ .

Static density at the outlet of the blade row is calculated from the equation of state for a perfect gas:

$$P_2 = \rho_2 RT_2 \quad [\text{Eq. 5.4.47}]$$

Relative and absolute total densities are calculated as follows:

$$\frac{\rho_2}{\rho_{o,2}} = \left( 1 + \frac{\gamma_2 - 1}{2} M_2'^2 \right)^{-\frac{1}{\gamma_2 - 1}} \quad [\text{Eq. 5.4.48}]$$

$$\frac{\rho_2}{\rho_{o,2}} = \left( 1 + \frac{\gamma_2 - 1}{2} M_2^2 \right)^{-\frac{1}{\gamma_2 - 1}} \quad [\text{Eq. 5.4.49}]$$

Finally, static and total enthalpies are calculated at the blade row outlet similarly to Equations 5.4.11, 5.4.12 and 5.4.18.

$$H_2 = C_{p,2} T_2 \quad [\text{Eq. 5.4.50}]$$

$$H'_{o,2} = C_{p,2} T'_{o,2} \quad [\text{Eq. 5.4.51}]$$

$$H_{o,2} = C_{p,2} T_{o,2} \quad [\text{Eq. 5.4.52}]$$

### Implementation

The calculation of the thermodynamic properties is carried out separately at blade row inlet and outlet by subroutines *Compressor2D\_BladeInletBoundaryCondCalc.f90* and *Compressor2D\_BladeOutletBoundaryCondCalc.f90* respectively. Blade row inlet and outlet boundary conditions need to be continuously updated as the generated meridional velocity profile changes in every iteration, until convergence is achieved. Therefore, the above two subroutines are called in an iterative fashion by *Compressor2D\_BladeRowInletMeridVelDistrbGener.f90*, for the inlet convergence, and *Compressor2D\_BladeRowOutletMeridVelDistrbGener.f90*, for the outlet convergence respectively. Input parameters for these subroutines are as explained above.

### Limitations and Potential Expansion

There are no major limitations concerning the calculation of the thermodynamic properties as far as the working medium obeys the laws of perfect gas. In a potential future expansion of the code the subroutines could be enriched with thermodynamic relations for real gases and mixture of gases. In this case, the code would be able to simulate the compressor operation working into a closed gas turbine cycle, or take into account the humidity present in the incoming flow.

## **5.5. Calculation of Streamline Properties**

This section refers to the streamline properties that need to be calculated prior to the solution of the radial equilibrium equation. Several terms in the radial equilibrium equation contain streamline geometric and flow properties that need to be established before the radial equilibrium equation is solved. As mentioned in previous sections, the radial equilibrium equation needs to be solved iteratively, therefore the calculation of the streamline properties consists actually a part of the whole iterative process. The accuracy and stability of the calculation depends strongly on the ability to predict the streamline movement accurately, as well as calculate the streamline properties correctly.

Streamline properties are calculated from hub to tip, at the intersection of streamlines with the blade edges (nodes), at every blade row inlet and outlet. In the case of a single blade row however, two streamline locations in the meridional direction are not enough to accurately establish the flow field. To overcome this problem and at the same time increase the calculation accuracy, streamline properties are also calculated at notional, inter-row points (Figure 5.5.1). These points lay in the bladeless space in-between the blade rows and their coordinates are calculated as the arithmetic average of two neighboring blade edge points.



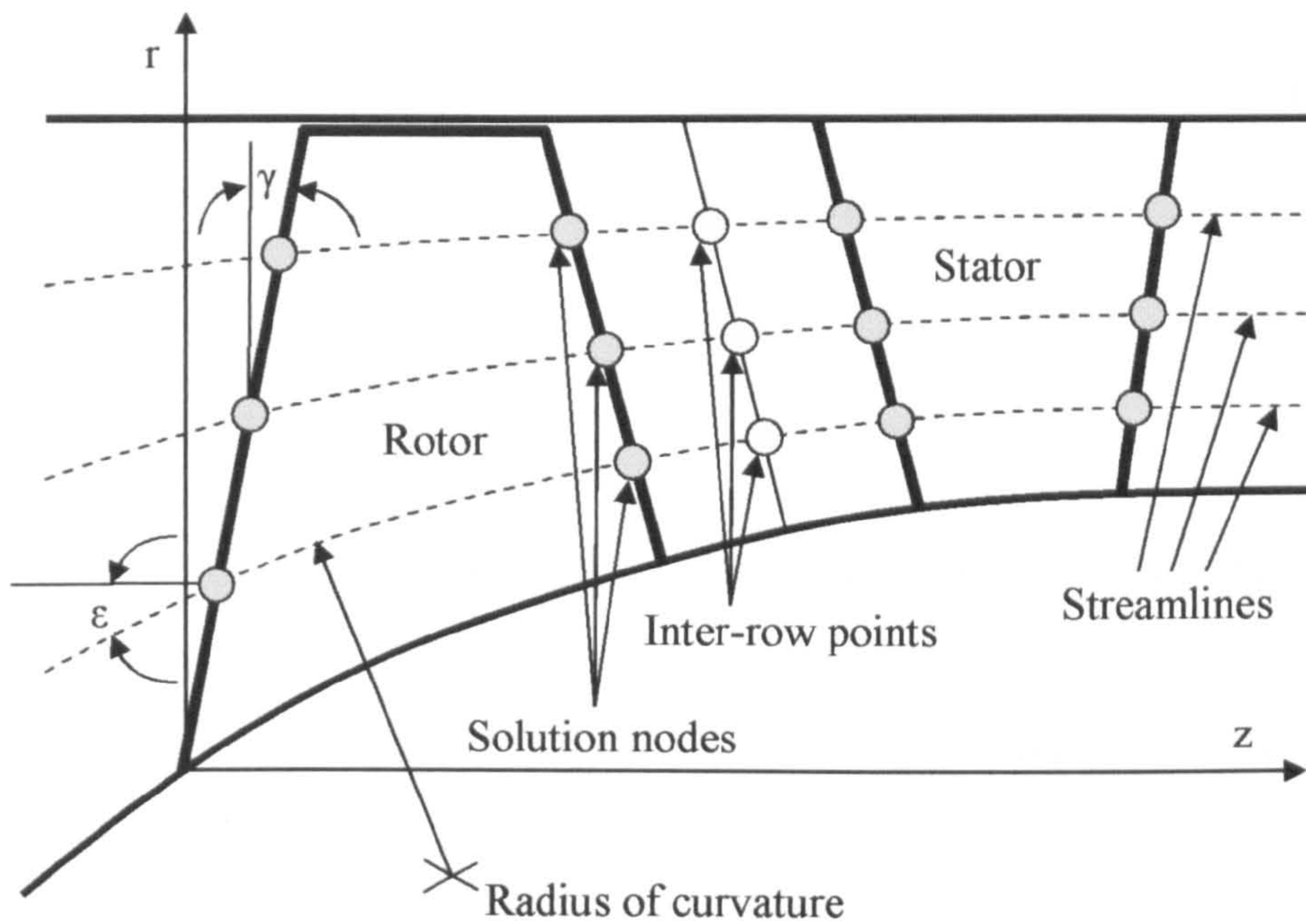


Figure 5.5.1: Streamline curvature grid

The coordinates of the nodes are initialized in the  $r$ - $z$  plane, before the calculation of the streamline properties begins. The point of intersection of the first blade row leading edge with the hub is considered to be the origin of the cylindrical coordinate system. In order to increase the chances for a converged solution, typically nodes are initialized on blade edges and inter-row points between rows, at equally spaced distances from hub to tip, taking also into account the blockage factor due to the growth of the end wall boundary layer and blade wake momentum thickness.

The calculation of the streamline properties begins with establishing the ratio  $\frac{r_{out}}{r_{in}}$  for all streamlines. Where  $r_{in}$  and  $r_{out}$  are the radial co-ordinates of a streamline at the inlet and outlet of a blade row respectively. This quantity is needed for the blade wake momentum thickness calculation, as well as for determining the equivalent diffusion factor.

The following properties are calculated at every blade row inlet and outlet:

1. The streamline sweep angle is set equal to the blade sweep angle that can vary from hub to tip:

$$\gamma_{streamline} = \gamma_{blade} \quad [\text{Eq. 5.5.1}]$$

2. The ratio  $\frac{r - r_{hub}}{r_{tip} - r_{hub}}$  is calculated and is proportional to the ratio of the total annulus area and the percentage of the area that is bounded between the hub and an arbitrary streamline.



3. The first and second derivatives of the radial co-ordinates in the meridional direction are defined and calculated as  $\left(\frac{dr}{dz}\right)_{merid}$  and  $\left(\frac{d^2r}{dz^2}\right)_{merid}$  respectively.

4. The streamline slope angle is calculated as follows:

$$\varepsilon = \arctan\left(\frac{dr}{dz}\right)_{merid} \quad [\text{Eq. 5.5.2}]$$

5. The variation of the streamline slope in the radial direction, moving along the r-axis  $\left(\frac{d\varepsilon}{dr}\right)_{radial}$ .

6. The variation of the streamline slope in the radial direction, moving along the streamline direction  $\left(\frac{d\varepsilon}{dr}\right)_{merid}$ .

7. The variation of the slope in the axial direction, moving along the streamline direction  $\left(\frac{d\varepsilon}{dz}\right)_{merid}$ .

8. The derivative  $\left(\frac{d\varepsilon}{dr}\right)_{radial}$  appears as such in the full radial equilibrium equation, whereas  $\left(\frac{d\varepsilon}{dr}\right)_{merid}$  and  $\left(\frac{d\varepsilon}{dz}\right)_{merid}$  are used to determine the streamline curvature  $\alpha$  as the meridional variation of the streamline slope as follows:

$$\alpha = \frac{d\varepsilon}{dm} = 0.5 \left[ \left(\frac{d\varepsilon}{dr}\right)_{merid} \sin \varepsilon + \left(\frac{d\varepsilon}{dz}\right)_{merid} \cos \varepsilon \right] \quad [\text{Eq. 5.5.3}]$$

9. The radius of curvature is then calculated as the inverse of the gradient of the streamline slope in the meridional direction:

$$R_c = \frac{1}{\frac{d\varepsilon}{dm}} \quad [\text{Eq. 5.5.4}]$$

The streamline curvature is also equivalent to the second derivative of the radial streamline co-ordinate with respect to the meridional direction  $\left(\frac{d^2r}{dz^2}\right)_{merid}$ .

10. Finally, the first derivative of the static entropy with respect to the meridional direction is calculated. This term also appears in the full radial equilibrium equation. As in the case of the streamline curvature, the radial and axial entropy variations, in the streamline direction have to be established first.

$$\frac{dS}{dm} = 0.5 \left[ \left(\frac{dS}{dr}\right)_{merid} \sin \varepsilon + \left(\frac{dS}{dz}\right)_{merid} \cos \varepsilon \right] \quad [\text{Eq. 5.5.5}]$$



### Implementation

As shown above, solving the non-linear, partial differential equations involves the calculation of several derivatives and therefore the solution is greatly dependent upon the density of the grid points and numerical derivation method selected. All derivations are handled by a dedicated subroutine called *Compressor2D\_Derivate.f90* that calculates the derivatives required for the solution of the radial equilibrium equation based on a central difference differentiation method. Based on this method, calculating derivatives at the compressor inlet presents a difficulty due to the lack of geometric nodes upstream the first blade row. This inconsistency (which also appears in the hub and tip points of the radial differentiation) is overcome by extrapolating a notional node upstream, in the streamline direction. This is handled by subroutine *Compressor2D\_ExtrapolatePoint.f90*. The method of differentiation could be easily changed by the user if required.

Subroutine *Compressor2D\_BladeInterRowCoordCalc.f90* calculates the co-ordinates of the inter-row points and it is called just before streamline properties are calculated. Streamline geometric and flow properties are calculated by subroutine *Compressor2D\_StreamlinePropCalc.f90*. This subroutine is called several times during the calculation of the radial equilibrium equation, at every blade row inlet and outlet, to update the streamline properties every time the position of the streamlines changes until the solution converges.

The streamline curvature method is extremely sensitive to the actual shape of the streamlines. Ideally, streamlines need to be smoothly curved in the meridional plane, even if the actual compressor geometry has significant discontinuities of radius of curvature. Calculation nodes also need to be reasonably separated one from the other to ensure smooth derivative calculation and robust code execution. In order to achieve this, stream-wise calculations take place only at inter-row points throughout the compressor. At the inlet plane of the compressor, inter-row points coincide with nodes on the first rotor leading edge and at the outlet plane of the compressor inter-row points coincide with nodes on the last stator trailing edge. Streamline properties at other nodes, on rotor and stator edges, are then established by cubic spline interpolation handled by *Compressor2D\_CubicSplineInterpolation.f90*.

### Limitations and Potential Expansion

The user is free to select any number of streamlines. The greater the number of streamlines the greater the accuracy achieved in calculating radial derivatives, at the expense of increased computational time. A sensitivity analysis to determine the optimum number of streamlines in terms of the accuracy of the results and computational efficiency is highly recommended. It should be mentioned that this optimization is not an easy process, because a great number of independent parameters are involved.

In the stream-wise direction the distance of the calculation stations is bounded by the axial chord, resulting in a quite coarse calculation grid. In the future expansion of the code it would be useful to increase the stream-wise points. However, defining new streamline points within the bladed regions of the compressor would require a major

restructuring of the code, to solve the full radial equilibrium equation at those locations as well. This would result in a considerable increase in computational time. Consequently, an optimization analysis would be absolutely necessary at this point, before concluding to the number of intermediate calculation stations.

## 5.6. Calculation of Incidence Angle

This section discusses briefly the different approaches in defining the optimum incidence angle and describes how this is handled in the *2D Compressor SLC Software*. A method for calculating the minimum-loss incidence angle is presented in this section together with the limitations of the model adopted and scope for future development.

### Introduction

The incidence angle  $i$  is defined as the difference between the flow direction angle and the angle  $k_1$  formed by the tangent to the camber line at the blade leading edge. For example, in the relative frame of reference the incidence angle is given by:

$$i = \beta_1 - k_1 \quad [\text{Eq. 5.6.1}]$$

The flow incidence for a given setting of mean inlet flow direction, leading edge thickness, blade solidity and camber angle, will position the stagnation point on the region of the leading edge. The stagnation point position will subsequently determine the pressure distribution around the airfoil and fix the blade lift to drag ratio as well as the level of generated losses.

Ideally, the incidence angle at design point operating conditions should be such as to cause the minimum possible loss and the maximum blade lift to drag ratio. Unfortunately, these two optima do not coincide and in the past there have been several contradicting attempts to define the optimum incidence angle accurately. Carter (1950), for example, oriented his research based on the later definition of optimum incidence angle, whereas Lieblein (1960) was guided by the former definition.

As reported in Cumpsty (1989, p. 159-168), Carter's approach calculates the incidence to give the highest lift to drag ratio for a cascade with a given camber, regardless the overall deflection of the flow. For this reason Carter's predictions of optimum incidence, especially at low camber values, have been regarded to be inaccurate.

On the other hand, Lieblein's method has drawn the biggest attention over the years because it takes into account blade solidity, camber, thickness to chord ratio and thickness distribution and because it is easier to determine the minimum-loss incidence from experimental data. Several variations of the same basic approach have been presented over the years. Levine (1956) suggested an alternative method for predicting the minimum-loss incidence for sonic and supersonic flows. Lieblein



(1965) took his own study a step further by using correlations based on inlet Mach number and by adjusting the minimum-loss incidence such as to include three-dimensional effects. Cetin, et al. (1989) suggested an inlet Mach number correlation, based on the blade type (DCA or MCA), since Lieblein's correlation to its original form is only valid for relatively low Mach numbers.

In any case, the two definitions for optimum incidence will not deviate substantially from each other, because as it has been reported by Lieblein (1965) and Cumpsty (1989, p. 159-168), there is a very wide range of incidence over which the loss remains low and nearly constant. This is particularly true for the low inlet Mach number flow regimes. It therefore seems that the difference between the two definitions is relatively unimportant.

### Calculation of Minimum-Loss Incidence Angle

This study adopts Lieblein's approach because it provides a versatile and convenient method for calculating the optimum incidence angle for a wide range of combinations of shape, thickness, camber and solidity. Lieblein assumed a correlation of the following form:

$$i^* = i_0 + n\theta \quad [\text{Eq. 5.6.2}]$$

Where  $\theta$  is the camber angle,  $i_0$  is the required incidence angle to place the stagnation point onto the leading edge for zero camber and  $n$  is the slope of the variation in incidence with camber. As  $i_0$  can be assumed to depend on the shape of the leading edge and the maximum thickness to chord ratio, Equation 5.6.1 can be re-written as:

$$i^* = (K_i)_{sh} (K_i)_t (i_0)_{10} + n\theta \quad [\text{Eq. 5.6.3}]$$

The thickness distribution around the leading edge is accounted for by the term  $(K_i)_{sh}$  which becomes equal to unity for NACA-65 aerofoils, 1.1 for the C4 and 0.7 for DCA blades.  $(K_i)_t$  accounts for the different magnitudes of thickness to chord ratio and  $(i_0)_{10}$  is the minimum-loss incidence for a reference NACA-65 cascade of zero camber and 10 per cent thickness to chord ratio.

The air minimum-loss angle can then be calculated from the difference of the blade angle minus the minimum-loss incidence angle. In the relative frame of reference the air minimum-loss angle would be equal to:

$$\beta_1^* = k_1 - i^* \quad [\text{Eq. 5.6.4}]$$

### Implementation

The calculation of blade incidence is handled in the *2D Compressor SLC Software* by *Compressor2D\_BladeIncidenceCalc.f90*. Similarly, the minimum-loss incidence angle is calculated by subroutine *Compressor2D\_BladeIncidenceMinLossCalc.f90*. Both subroutines are called by the main subroutine *Compressor2D\_MainProgram.f90*

in sequence and immediately after flow properties at the inlet of every blade row converge. The aim of these subroutines is to calculate the incidence and minimum-loss incidence angles at various locations from hub to tip (nodes), depending on the number of streamlines.

The input variables needed for the calculations are the air inlet angle, the blade inlet angle, the cascade solidity, the thickness to chord ratio and the blade camber angle. Moreover, several graphs, stored as array tabular data in module *Compressor2D\_BladeIncidenceMinLossVarDeclar.f90*, are fed as inputs and used in the necessary interpolations for the  $(K_i)_t$ ,  $(i_0)_{10}$  and  $n$  factors.

More analytically, the  $(K_i)_t$  factor is interpolated from graphical data illustrated in Figure 5.6.1, according to the input blade maximum thickness to chord ratio, at each streamline position, and then corrected for the case of a NACA-65 airfoil.

**Blade Maximum Thickness to Chord Ratio Correction**

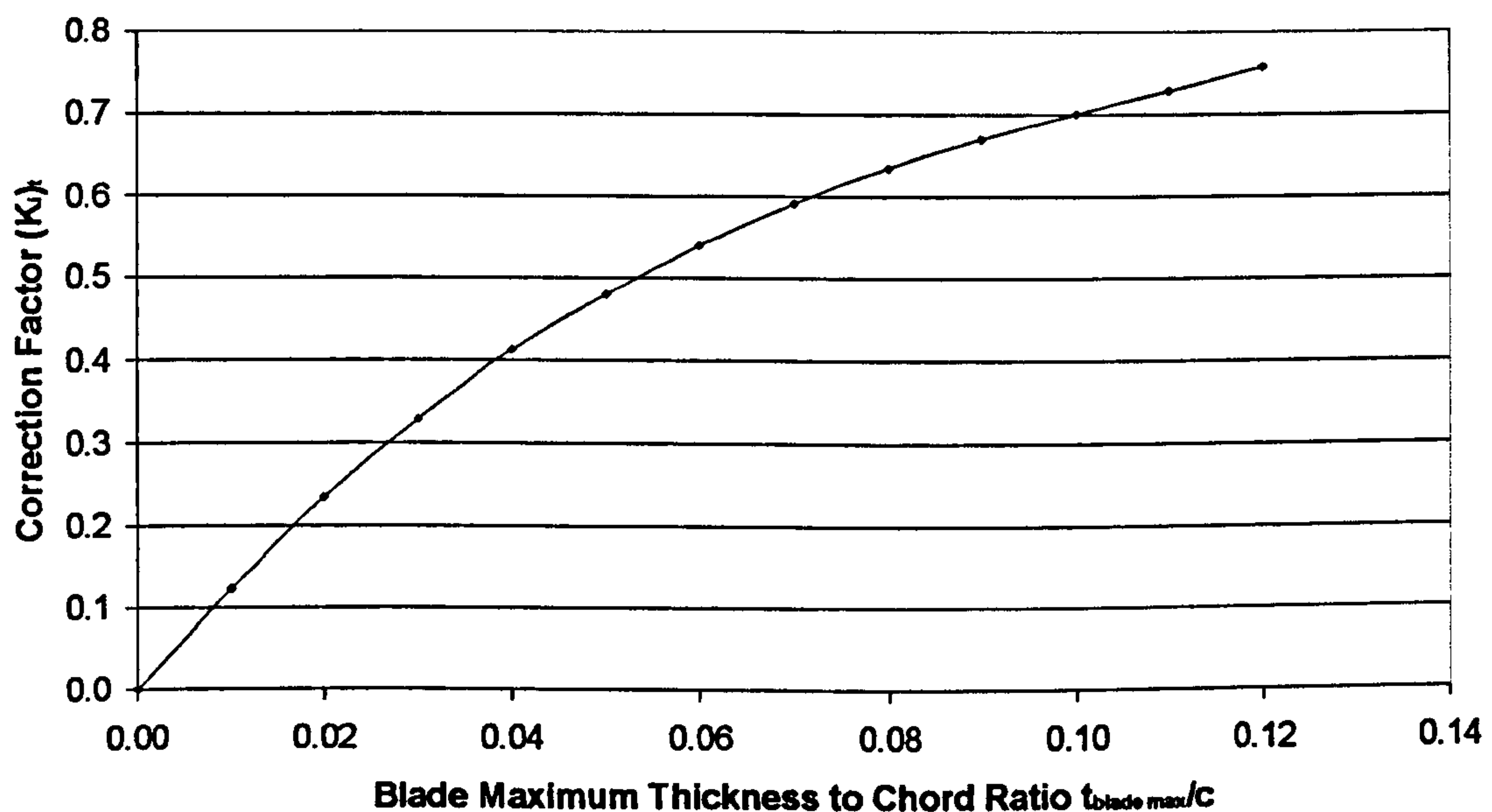


Figure 5.6.1: Blade maximum thickness to chord ratio correction for zero-camber reference minimum-loss incidence angle (Lieblein, 1965)

To determine the value of the  $(i_0)_{10}$  term, a double interpolation is carried out, firstly for the air inlet angle and then for the cascade solidity, as shown in Figure 5.6.2.



Reference Minimum-Loss Incidence Angle for Zero Camber

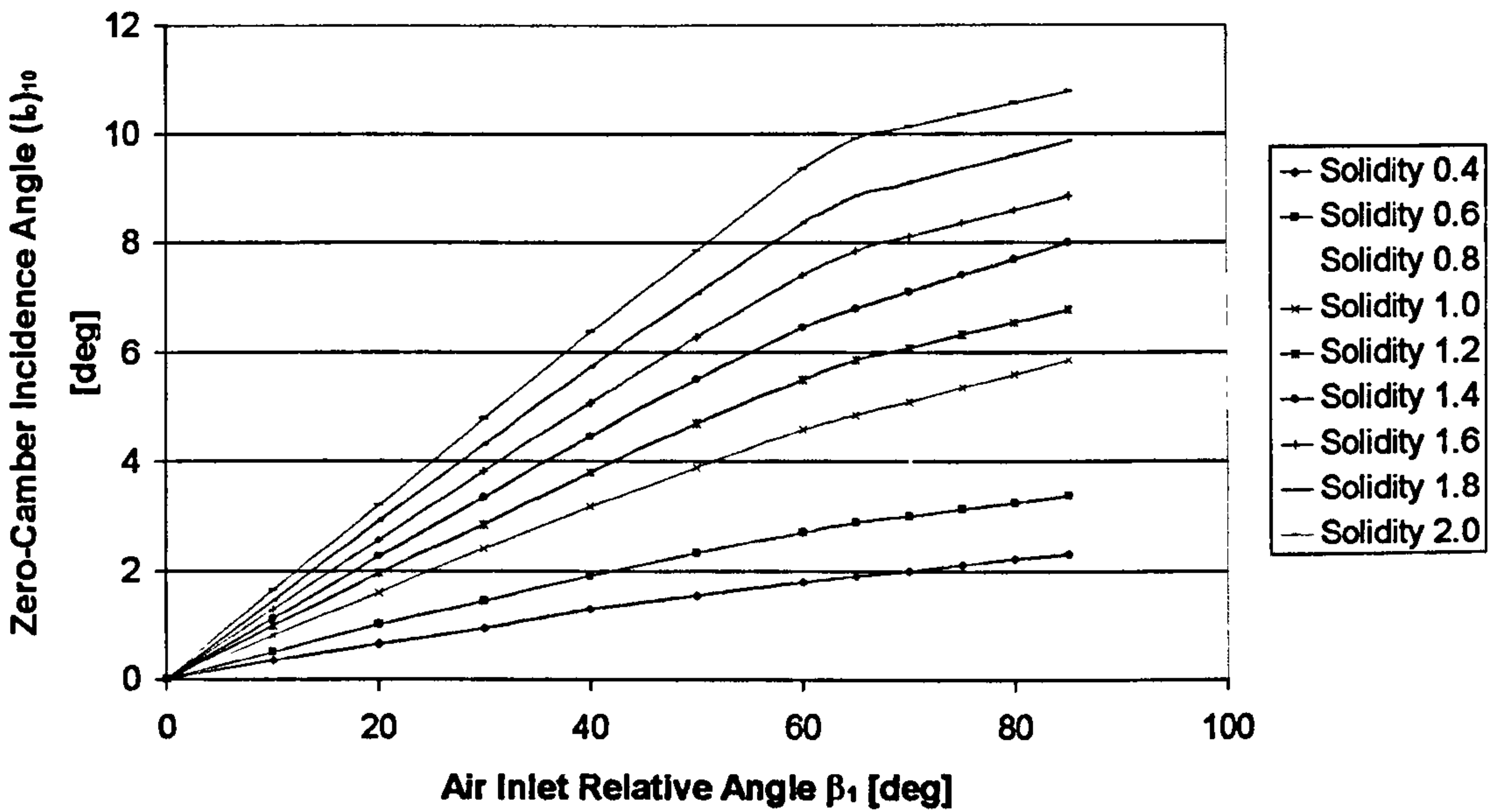


Figure 5.6.2: Reference minimum-loss incidence angle for zero camber deduced from low-speed-cascade data of 10-per-cent-thick NACA 65 series blades (Lieblein, 1965)

The value of  $n$  is again determined after a double interpolation with respect to the air inlet minimum-loss angle and then with respect to the cascade solidity, as shown in the following figure.

Reference Minimum-Loss Incidence Angle Slope Factor

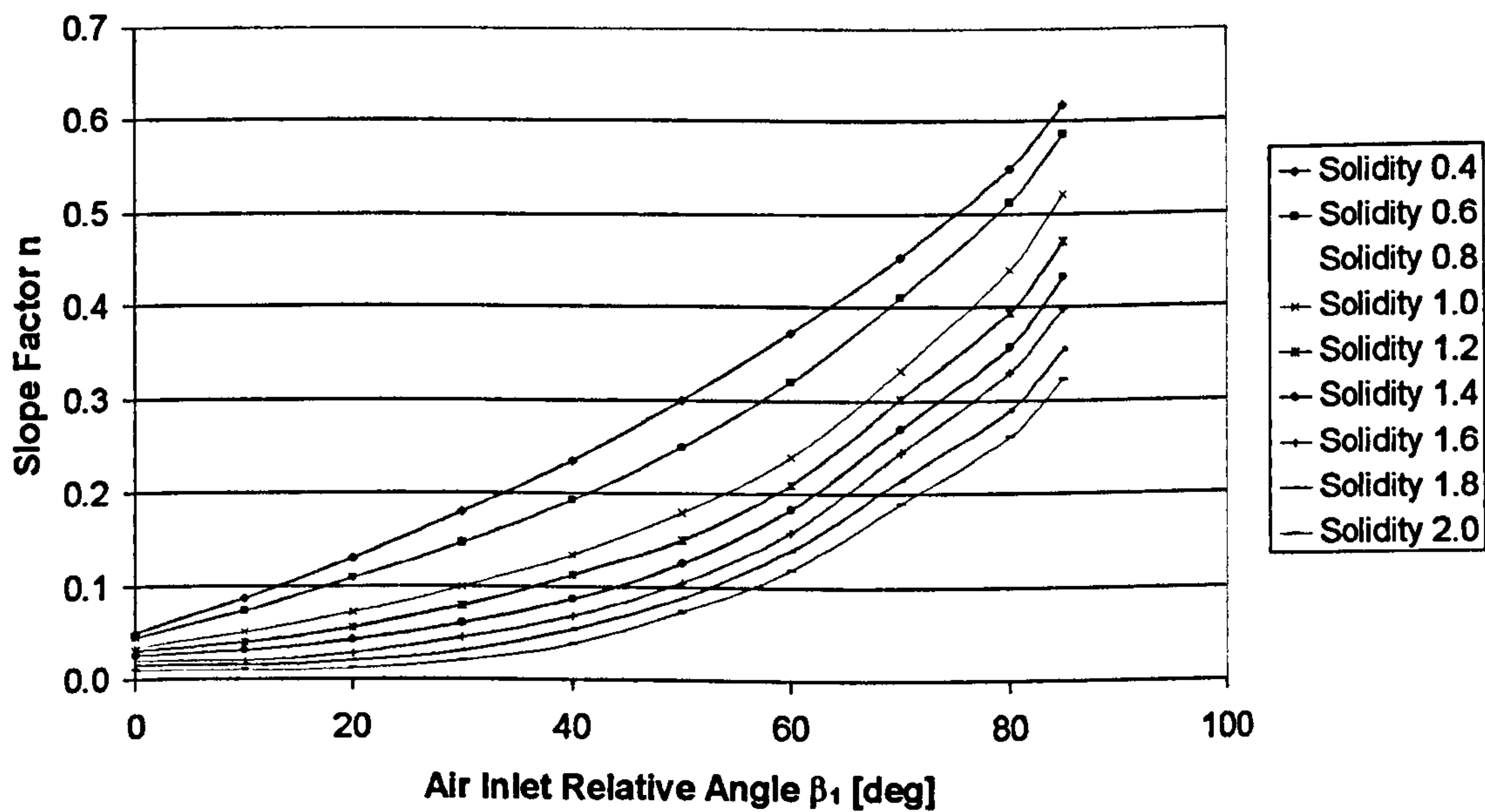


Figure 5.6.3: Reference minimum-loss incidence angle slope factor deduced from low-speed-cascade data of NACA 65 series blades (Lieblein, 1965)

In order to make the code more robust, tabular data for  $(i_0)_{10}$  and  $n$  terms were slightly extended to cover inlet air angles up to 85 degrees as shown in the last two figures.

The output values are the incidence angle, minimum-loss incidence angle and the minimum-loss air inlet angle. The later could potentially become useful in expanding the code to handle compressor design studies while the first two are used subsequently in the calculation of the deviation angle and blade losses.

Finally, the air minimum-loss angle is calculated from the difference of the blade angle minus the minimum-loss incidence angle through an iterative calculation process. The value of the air minimum-loss angle is required during the incidence calculations. Consequently, an iterative loop is established having as a starting value for the air minimum-loss angle, the actual air inlet angle. The above calculation procedure is programmed separately for rotating and stationary blade rows, using relative and absolute flow angles respectively.

### Limitations and Potential Expansion

The above correlation is limited to low inlet Mach numbers below 0.5. At sonic or supersonic flow it has been experimentally proven that when the bow oblique shock is attached onto the blade leading edge, the cascade operates at minimum-loss conditions for a unique value of air inlet angle. In other words, there is only one incidence at which minimum-losses can be achieved, the unique incidence. The subroutine for calculating the minimum-loss incidence can be expanded to include a correlation for the calculation of the unique incidence angle  $i_{unique}$  as shown in Barbosa (1987, p. 51-53):

$$i_{sc}^* = i^* + \frac{1}{2}(i_{unique} - i^*) \left[ 1 + \sin\left(\frac{\pi M_1 - M_o}{2(1 - M_o)}\right) \right] \quad [\text{Eq. 5.6.5}]$$

Where  $i_{sc}^*$  is the minimum-loss incidence angle at sonic and supersonic conditions and  $M_o$  is equal to 0.5, the point at which the basic correlation for low Mach numbers starts to become inaccurate.

Reduced accuracy is also expected on the grounds that three dimensional effects are not taken into account. The current correlation could be extended to include the flow three dimensional effects by adding an extra experimental-corrective term to Equation 5.6.3 as shown below:

$$i_{2D}^* = (K_i)_{sh}(K_i)_t(i_0)_{10} + n\theta + (i_c^* - i_{2D}^*) \quad [\text{Eq. 5.6.6}]$$

Where the difference  $(i_c^* - i_{2D}^*)$  represents the comparison between a measured reference minimum-loss incidence angle  $i_c^*$  and the predicted two-dimensional minimum-loss incidence angle  $i_{2D}^*$  (Robbins, et al., 1965).

Finally, several limiters are imposed in the case where the input values for interpolation fall outside the domain of the input data functions.



There is great potential in expanding the subroutine for the minimum-loss incidence calculation. However, for the current range of application of the code, which is the simulation of an existing compressor, the reduced accuracy of the minimum-loss incidence angle calculation, would probably not affect much the accuracy of the end results. That is because this value appears only in a correlation for the calculation of the deviation angle. The *2D Compressor SLC Software* is a performance analysis code that uses several empirical models which are all discussed in this chapter. The accuracy of the overall performance prediction depends on the complete set of models, more than on any individual model.

It would also be an advantage for the code to offer several alternative correlations, which could then be compared against experimental data (if available) to find the most adequate, given the application.

## 5.7. Calculation of Deviation Angle

This section discusses briefly the different approaches in defining and calculating the deviation and minimum-loss deviation angles and describes how this is handled in the *2D Compressor SLC Software*. The following paragraphs discuss also the limitations of the models adopted and scope for future development.

### Introduction

Blade deviation is a crucial parameter for accurate off-design compressor performance simulation. The deviation angle  $\delta$  is defined as the difference between the air outlet angle and the blade outlet angle  $k_2$ . For example, in the relative frame of reference the deviation angle is given by:

$$\delta = \beta_2 - k_2 \quad [\text{Eq. 5.7.1}]$$

Deviation arises mainly due to a potential flow effect. The air flowing through a blade passage cannot follow the blade camber direction up to the passage outlet, due to the Kutta-Joukowski boundary condition for zero loading at the blade trailing edge. The chord-wise position where the flow direction starts to deviate from the tangential to the blade camber line depends mainly on blade and cascade geometrical characteristics, such as the cascade solidity, blade camber angle and blade stagger. The boundary layer development makes only a small contribution to the deviation, provided that the blades are not operating under stalled conditions. The axial velocity ratio, between the leading and trailing edges of a blade row, has been proven to influence the amount of flow deviation and has quite a strong interaction with the boundary layer development.

In order to calculate the deviation angle, and from that the air outlet angle, the minimum-loss deviation needs to be established first. The correlation for calculating the minimum-loss deviation, which is still most often used, is known as 'Carter's rule'. Carter's (1950) correlation was based on data taken for Axial Velocity-Density Ratios (AVDR) larger than one and was intended for application at an optimum

incidence, which experiments have shown to be quite close to the minimum-loss incidence. However, over the years it has been applied widely at incidences other than the optimum with local modifications and adaptation.

Lieblein (1960 and 1965) produced a correlation for the minimum-loss deviation with a systematic approach similar to the one described in Section 5.6 for the prediction of minimum-loss incidence. Lieblein's method has been considered to be more accurate and reliable than the much simpler Carter's rule. Lieblein's correlation is known to give accurate estimates for deviation of the most common profile families but only for axial velocity-density ratios equal to unity.

Pollard and Gostelow (1967) examined the influence of axial velocity ratio by making a series of measurements. They finally concluded to an empirical correlation for the minimum-loss deviation angle for any given velocity ratio, based on the corresponding minimum-loss deviation angle value for unity velocity ratio, given by:

$$\delta^* - \delta_1^* = 10(1.0 - AVDR) \quad [\text{Eq. 5.7.2}]$$

Where  $\delta^*$  is the minimum-loss deviation and  $\delta_1^*$  is the minimum-loss deviation for AVDR equal to unity.

Basically, Carter's and Lieblein's approaches were the basis for many other subsequent models having embedded within them extra empiricism, with the intention of adapting the correlations to specific blade profiles, flow regimes and specific ranges of individual geometrical properties. Such an effort was also carried out by Cetin, et al. (1989) in order to adjust the minimum-loss deviation angle calculated by Carter's correlation from 2-D flow to 3-D flow.

Swan (1961) related the flow deviation to the passage inlet Mach number and the difference between the equivalent diffusion factor  $D_{eq}$  and the minimum-loss equivalent diffusion factor  $D_{eq}^*$ . His approach applies only for subsonic flow. It is reported to give results close to the measured ones, but it exhibits some difficulties concerning its application, since the deviation angle is needed for the calculation of the equivalent diffusion factor.

Creveling and Carmody (1968) related the deviation angle to the design flow turning angle. More precisely, they developed a relationship between two terms having as a denominator the flow turning angle and a nominator the difference between the incidence and minimum-loss incidence for the one, and the deviation and minimum-loss deviation for the other. This correlation can be applied without any recurrent calculation, since the incidence angle is usually known before the calculation of the blade deviation.

### Calculation of Minimum-Loss Deviation Angle

For extra flexibility, this work adopts the models of Carter, Lieblein and Cetin for the calculation of the minimum-loss deviation angle. As discussed above, for design point calculations, the most widely used and generally accepted empirical correlation for the determination of the minimum-loss deviation angle is Carter's rule. Carter's



empirical correlation is a straightforward simple calculation, depending only on the blade profile and cascade geometrical characteristics:

$$\delta^* = m\theta \left( \frac{s}{c_{geom}} \right)^n \quad [\text{Eq. 5.7.3}]$$

Where  $\delta^*$  is the minimum-loss deviation angle,  $m$  is an empirical relation usually a function of the exit flow angle or stagger angle,  $\theta$  is the blade camber and  $s/c_{geom}$  is the cascade solidity. The solidity exponent  $n$  takes the value of 0.5 for decelerating flow cascades and unity for accelerating flow cascades.

Lieblein assumed the minimum-loss deviation angle to be given by an expression of the following form:

$$\delta^* = \delta_o + m\theta \quad [\text{Eq. 5.7.4}]$$

Where  $\delta_o$  is a reference deviation angle for a similar cascade of un-cambered airfoils under the same inlet flow direction and  $m$  is an empirical slope which depends on cascade solidity and inlet flow direction. The term  $m$  can be expressed as:

$$m = \frac{m_{\sigma=1}}{\sigma^b} \quad [\text{Eq. 5.7.5}]$$

Where the term  $m_{\sigma=1}$  represents the value of  $m$  at a solidity of 1 and  $b$  is the solidity exponent that varies with air inlet angle. Similarly to Section 5.6 for the zero-camber reference minimum-loss incidence angle, the zero-camber deviation angle  $\delta_o$  can be expressed as a function of the blade shape and Equation 5.7.4 can be modified as follows:

$$\delta^* = (K_\delta)_{sh} (K_\delta)_t (\delta_o)_{10} + m\theta \quad [\text{Eq. 5.7.6}]$$

Where  $(\delta_o)_{10}$  represents the deviation for the reference 10 percent thickness to chord ratio NACA 65-series blade,  $(K_\delta)_{sh}$  represents the correction for blade thickness distributions other than that of the reference 65-series aerofoil and becomes equal to unity for NACA-65 aerofoils, 1.1 for the C4 and 0.7 for DCA blades and  $(K_\delta)_t$  represents the correction for blade maximum thicknesses other than 10 percent.

Cetin's equation is a second order correlation to Carter's rule. This equation was derived in order to improve the poor fit of Carter's correlation to experimental data by taking into account the transonic and three dimensional effects, which were absent from the original correlation. Cetin's equation has the following form:

$$\delta^* = -1.099379 + 3.0186(\delta_{Carter}^*) - 0.1988(\delta_{Carter}^*)^2 \quad [\text{Eq. 5.7.7}]$$

### Calculation of Deviation Angle

Creveling's method is applied for the determination of the deviation angle. The deviation angle can be expressed as:

$$\delta = \delta^* + \left( \frac{\delta - \delta^*}{\varepsilon^*} \right) \varepsilon^* \quad [\text{Eq. 5.7.8}]$$

Where  $\varepsilon^*$  is the flow deflection angle calculated as follows:

$$\varepsilon^* = \theta - \delta^* + i^* \quad [\text{Eq. 5.7.9}]$$

Where  $i^*$  is the minimum-loss incidence angle. A parameter P1, which is the ratio of the incidence angle increment to the deflection angle, is defined as shown below:

$$P1 = \left( \frac{i - i^*}{\varepsilon^*} \right) \quad [\text{Eq. 5.7.10}]$$

Similarly, a parameter P2 can be defined as:

$$P2 = \left( \frac{\delta - \delta^*}{\varepsilon^*} \right) \quad [\text{Eq. 5.7.11}]$$

From Creveling and Carmody (1968), P2 can be related to P1 through experimental data as a second order polynomial:

$$P2 = aP1^2 + bP1 + c \quad [\text{Eq. 5.7.12}]$$

The coefficients of the polynomial are determined empirically. If P1 is positive or equal to zero then  $a = -0.2928$ ,  $b = 0.5588$  and  $c = -0.0008090$ . If P1 is negative then  $a = -0.3452$ ,  $b = 0.48$  and  $c = 0.0001191$ .

Finally, the flow deviation angle is determined by the following correlation:

$$\delta = \delta^* + P2\varepsilon^* \quad [\text{Eq. 5.7.13}]$$

A distinction is made between stationary and rotating blade rows.

Having established the deviation angle, the air outlet angle can be calculated from Equation 5.7.1.

### Implementation

Blade deviation is handled in the *2D Compressor SLC Software* by subroutine *Compressor2D\_BladeDeviationCalc.f90*. Similarly, the minimum-loss deviation angle is calculated by subroutine *Compressor2D\_BladeDeviationMinLossCalc.f90*.



Both subroutines are called by the main subroutine *Compressor2D\_MainProgram.f90* in sequence and before the radial equilibrium equation is iteratively solved at the blade row outlet. The aim of these subroutines is to calculate the deviation and minimum-loss deviation angles at various locations from hub to tip (nodes), depending on the number of streamlines.

Subroutine *Compressor2D\_BladeDeviationMinLossCalc.f90* includes three models for predicting the minimum-loss deviation that the user is free to select from. Carter's, Lieblein's and Cetin's models have all been programmed to provide the user with extra flexibility. The inputs to this subroutine are blade geometrical properties such as solidity, blade camber and stagger and air properties such as the inlet Mach number and the air inlet angle. The subroutine output is a two dimensional array that contains the calculated minimum-loss deviation for each blade row and streamline position.

Moreover, several graphs, stored as array tabular data in module *Compressor2D\_BladeDeviationMinLossVarDeclar.f90*, are fed as inputs and used in the necessary interpolations for  $(K_s)_t$ ,  $(\delta_0)_{10}$  and  $m$  factors.

For example, the  $(K_s)_t$  factor is interpolated from graphical data illustrated in Figure 5.7.1, according to the input blade maximum thickness to chord ratio, at each streamline position, and then corrected for the case of a NACA-65 airfoil. To determine the value of the  $(\delta_0)_{10}$  term, a double interpolation is carried out, firstly for the air inlet angle and then for the cascade solidity, as shown in Figure 5.7.2. Factor  $m$  is determined in a similar way. In order to make the code more robust, tabular data for  $(\delta_0)_{10}$  and  $m$  terms were slightly extended to cover inlet air angles up to 85 degrees.

**Blade Maximum Thickness to Chord Ratio Correction**

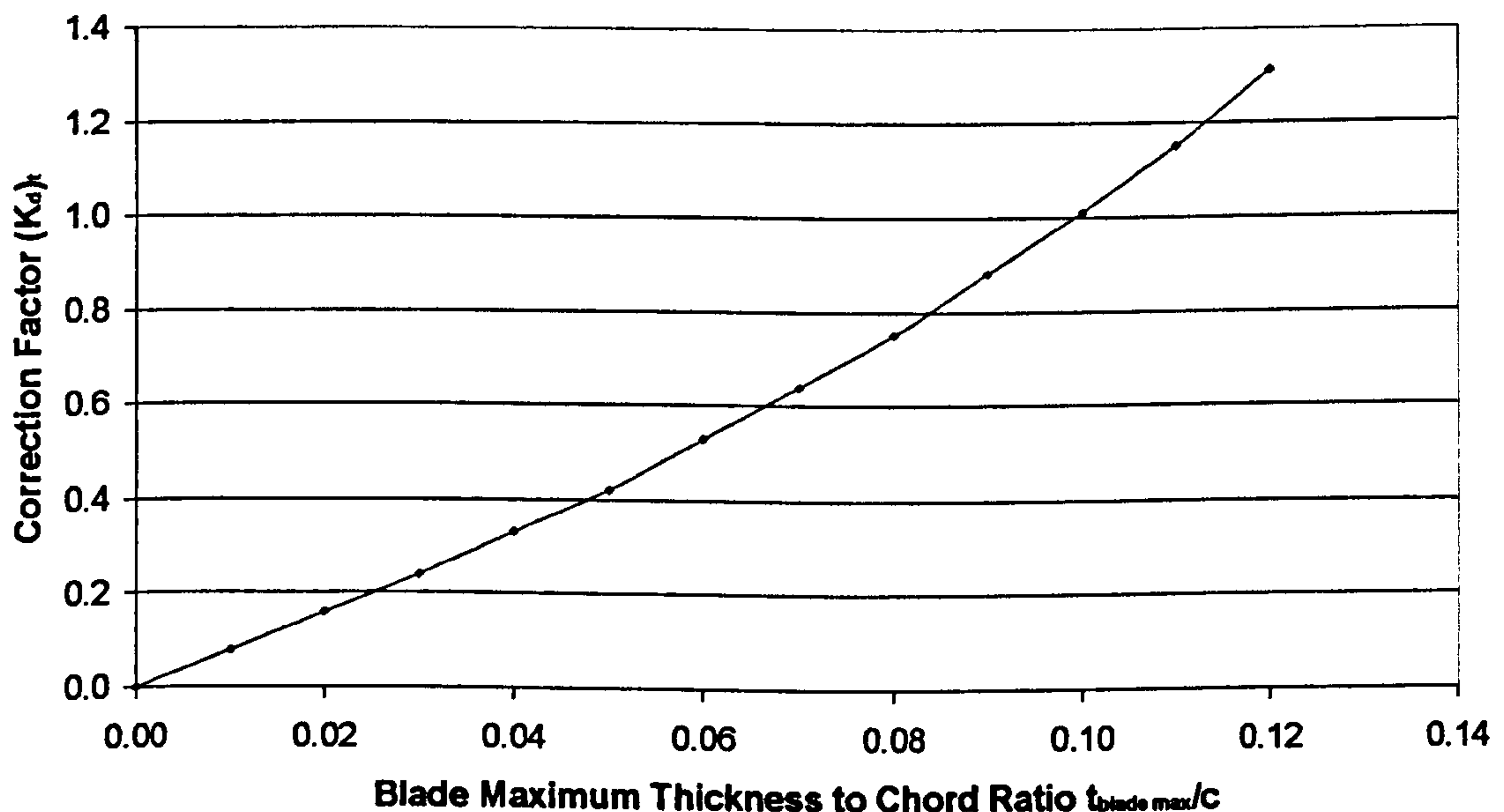


Figure 5.7.1: Blade maximum thickness to chord ratio correction for zero-camber reference minimum-loss deviation angle (Lieblein, 1965)

The input data required for subroutine *Compressor2D\_BladeDeviationCalc.f90* are the blade outlet angle, the blade minimum-loss deviation angle, the blade camber



angle, as well as the incidence and the minimum-loss incidence angle. The subroutine calculates the flow deflection angle, the deviation angle, the air outlet angle and the air minimum-loss outlet angle based on Creveling's method. The last parameter could potentially become useful in expanding the code to handle compressor design studies.

Reference Minimum-Loss Deviation Angle for Zero Camber

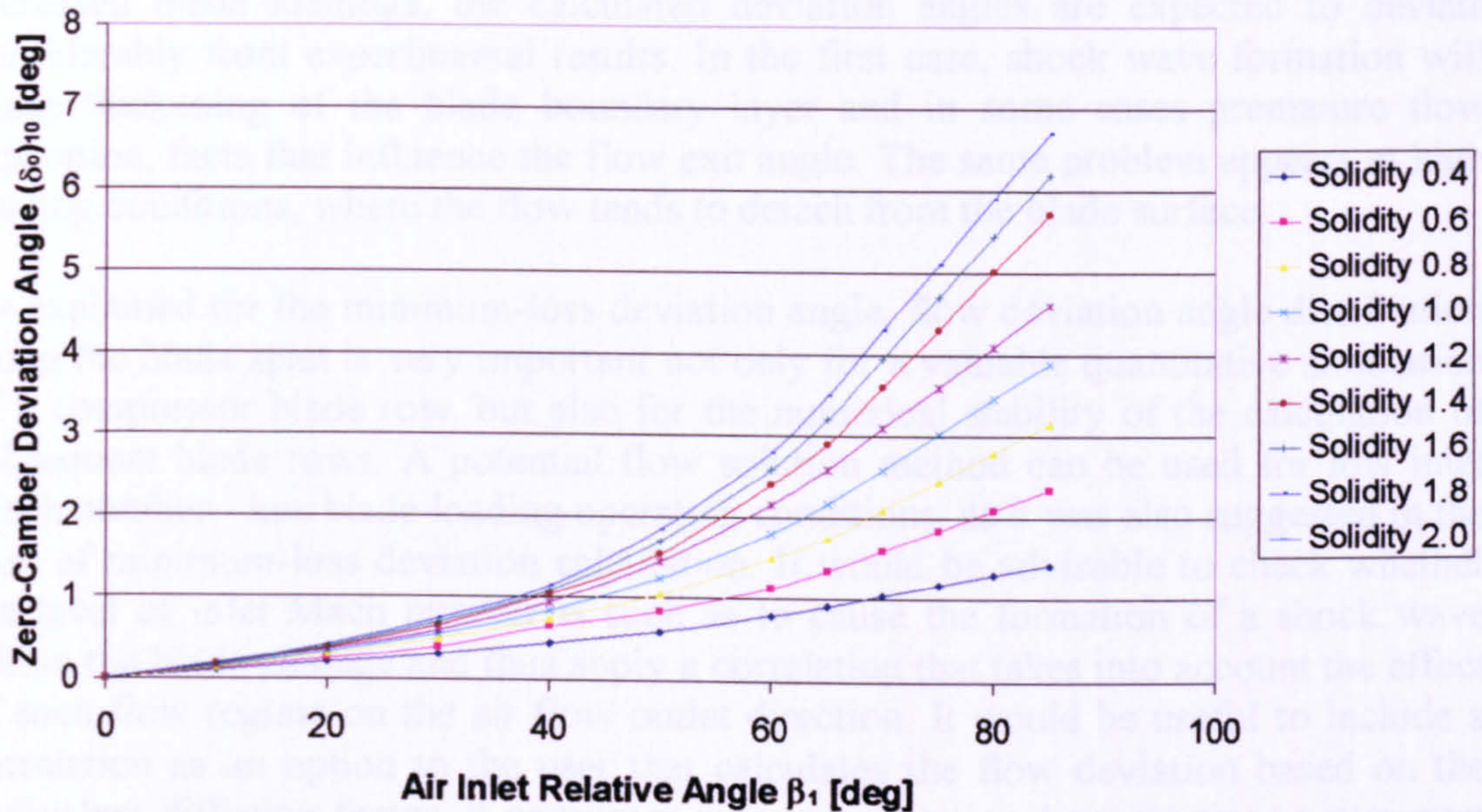


Figure 5.7.2: Reference minimum-loss deviation angle for zero camber deduced from low-speed-cascade data of 10-percent-thick NACA 65 series blades (Lieblein, 1965)

### Limitations and Potential Expansion

The minimum-loss deviation is an extremely important parameter for the preliminary design of a compressor. It is also needed for the determination of the off design deviation angle. Its accurate prediction at all conditions is very crucial, because it affects not only the work input to the row, but also the work absorption distribution along the blade span. Consequently, an inaccurate minimum-loss deviation model will probably result into wrong temperature and pressure profiles at rotor outlet, which will harden a lot, if not prohibit, the stator inlet convergence process. Therefore, a lot of attention needs to be given to the determination of the correct minimum-loss deviation angle.

A unique correlation cannot work efficiently over the entire range of inlet Mach numbers. Generally, Lieblein's and Cetin's models for the calculation of the minimum-loss deviation are expected to give more accurate results at high inlet Mach numbers. Moreover, these two correlations can not take into account the three dimensionality of the flow. At low Mach numbers and normal level of blade loading, an independent potential flow solution method can be used having as inputs the blade geometry and the inlet Mach number.



The programmer however should very carefully assess the experimental data where the correlation came from and make sure it matches the simulated compressor conditions. In all cases it would be very useful to adapt the correlation to the specific compressor application, if experimental data are available.

Moreover, Creveling's correlation does not take into account the inlet Mach number as well as the level of blade loading. Consequently, at high Mach numbers and increased blade loadings, the calculated deviation angles are expected to deviate considerably from experimental results. In the first case, shock wave formation will cause thickening of the blade boundary layer and in some cases premature flow separation, facts that influence the flow exit angle. The same problem appears at high loading conditions, where the flow tends to detach from the blade surface.

As explained for the minimum-loss deviation angle, flow deviation angle distribution along the blade span is very important not only for a valuable quantitative simulation of a compressor blade row, but also for the numerical stability of the calculation of subsequent blade rows. A potential flow solution method can be used for low inlet Mach number - low blade loading operating conditions, as it was also suggested in the case of minimum-loss deviation calculation. It would be advisable to check whether the level of inlet Mach number is such as to cause the formation of a shock wave within the blade passage and thus apply a correlation that takes into account the effect of such flow regime on the air flow outlet direction. It would be useful to include a correlation as an option to the user that calculates the flow deviation based on the equivalent diffusion factor. It consumes more computational power since a recurrent calculation procedure needs to be established between the two, but as the blade loading increases it tends to give more accurate results. Finally an attempt may be done to adapt the coefficients of the P2 parameter to the corresponding experimental curve (if available) of the compressor under simulation.

As in the case of the minimum-loss incidence, reduced accuracy is also expected on the grounds that three dimensional effects are not taken into account. Equation 5.7.6 could be extended to include the flow three dimensional effects by adding two extra experimental-corrective terms, as shown below:

$$\delta_{2D}^* = (K_{\delta})_{sh} (K_{\delta})_i (\delta_0)_{10} + m\theta + (i_C^* - i_{2D}^*) \left( \frac{d\delta^*}{di^*} \right)_{2D} + (\delta_C^* - \delta_{2D}^*) \quad [\text{Eq. 5.7.12}]$$

Where the difference  $(\delta_C^* - \delta_{2D}^*)$  represents the comparison between a measured reference minimum-loss deviation angle  $\delta_C^*$  and the predicted two-dimensional minimum-loss incidence angle  $\delta_{2D}^*$ ,  $(i_C^* - i_{2D}^*)$  represents the comparison between a measured reference minimum-loss incidence angle  $i_C^*$  and the predicted two-dimensional minimum-loss incidence angle  $i_{2D}^*$  and  $(d\delta^*/di^*)_{2D}$  is the slope of the two-dimensional variation of deviation angle with incidence angle at the reference conditions (Robbins, et al., 1965).

## 5.8. Blade Passage Choking

This section briefly introduces the phenomenon of compressor blade passage choking and describes how this is handled in the *2D Compressor SLC Software*. A method for calculating the blade throat width of blades on a circular camber line is presented in this section together with the limitations of the model adopted and scope for further improvement.

### Introduction

Blade passage choking is an important aspect of compressor aerodynamic performance. With increasing inlet Mach number, the velocity on the blade surface will eventually reach the local sonic velocity. This condition is often referred to as the critical condition and the corresponding inlet Mach number as the critical Mach number. The critical Mach number is largely affected by the angle of incidence but also depends on many other variables such as blade spacing and the distribution of blade thickness and camber along the chord, particularly near the leading edge. If the inlet Mach number is increased beyond the critical value the flow will eventually become sonic or supersonic across the entire passage. At this condition the flow is said to be choked, meaning that the corrected mass flow cannot be further increased and the conditions in the inlet region and upstream remain unaffected by changes in the downstream static pressure. Any reduction in the downstream pressure would cause the flow to accelerate even further in the diverging part of the blade passage to higher supersonic velocities which would terminate in a strong shock giving rise to shock losses and boundary layer separation.

The following diagram (Figure 5.8.1) illustrates choked flow in a blade passage (Cumpsty, 1989, p. 185).

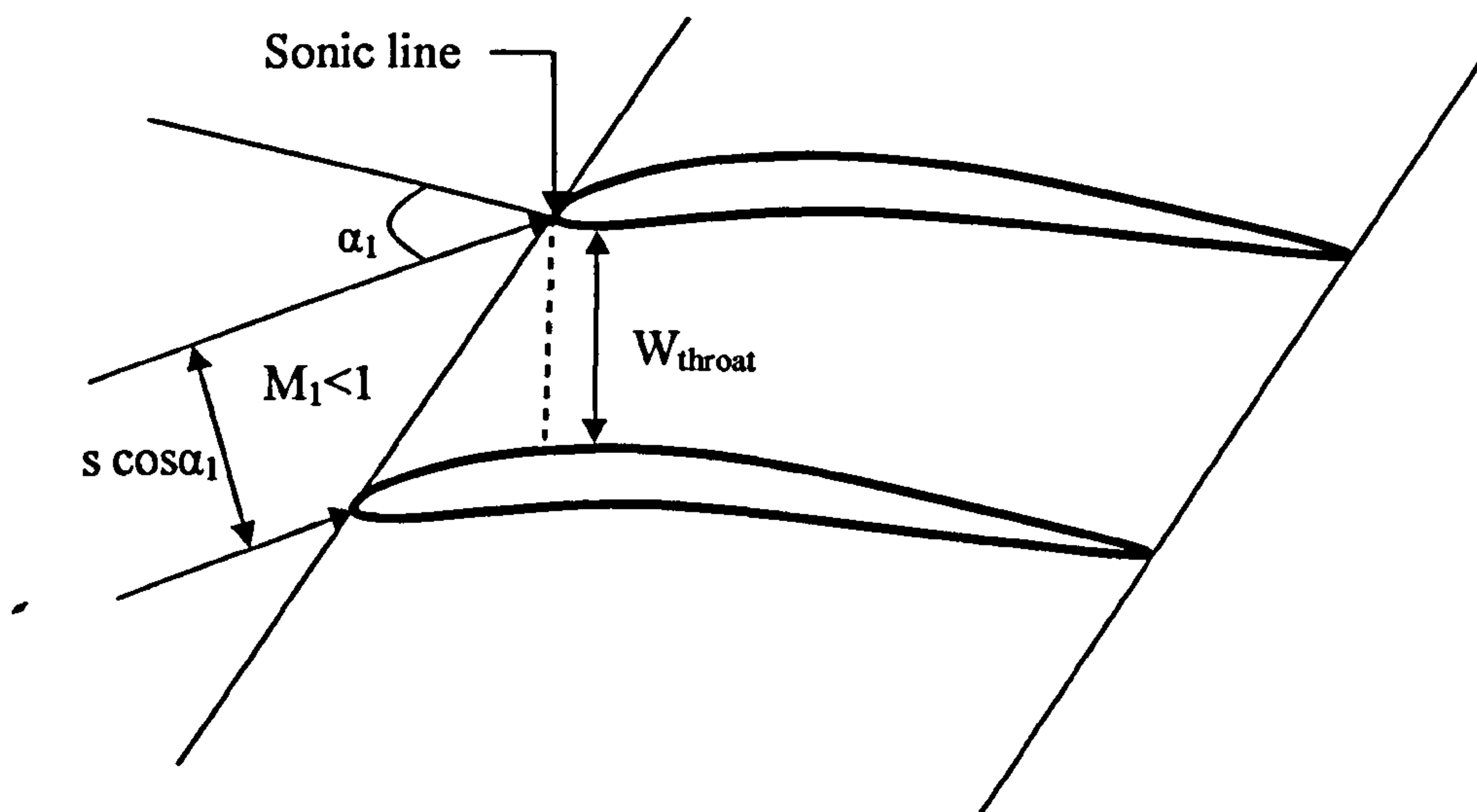


Figure 5.8.1: Typical sketch of choked flow in a blade passage

Assuming an ideal flow, the sonic line (along which the velocity is equal to the local velocity of sound) is drawn nearly straight at the blade passage throat and  $W_{throat}$  is



used to denote the throat width. Conservation of mass flow between the uniform conditions upstream and the uniform conditions across the throat can be expressed as:

$$\rho_1 V_1 s \cos \alpha_1 = \rho_{throat} V_{throat} W_{throat} \quad [\text{Eq. 5.8.1}]$$

Where 'throat' indicates sonic conditions at the throat,  $s$  is the blade spacing and  $\alpha_1$  is the inlet flow angle. Re-arranging the above equation gives:

$$\frac{W_{throat}}{s \cos \alpha_1} = \frac{\rho_1 V_1}{\rho_{throat} V_{throat}} \quad [\text{Eq. 5.8.2}]$$

It can be shown that for reversible flow up to the throat:

$$\frac{\rho_1 V_1}{\rho_{throat} V_{throat}} = M_1 \left[ \frac{1 + \frac{\gamma - 1}{2}}{1 + \frac{\gamma - 1}{2} M_1^2} \right]^{\frac{\gamma + 1}{2(\gamma - 1)}} \quad [\text{Eq. 5.8.3}]$$

Hence  $\frac{W_{throat}}{s \cos \alpha_1}$  is a unique function of the inlet Mach number  $M_1$ .

### Calculation of Blade Passage Throat Width

The throat width determines the beginning of local flow choking within the blade passage. At sufficiently high inlet Mach numbers, this will define the maximum flow capacity that the compressor can pass. The best approach to determine the throat opening is to define adjacent blades using the stagger angle, camber line and profile coordinates to locate the minimum distance between the blades. The minimum distance between adjacent blades is usually regarded as the perpendicular to the blade suction surface that passes through the leading edge of the adjacent blade as shown in Figure 5.8.1.

The most important geometric features of a Double Circular Arc (DCA) aerofoil are shown in *Appendix C - DCA Blade Geometry*. Given the aerodynamic chord  $c_{aero}$ , camber angle  $\theta$ , blade maximum thickness  $t_{blade\_max}$  and leading edge radius  $R_{LE}$ , the radii of the three circular arcs (i.e. suction surface, camber line and pressure surface) can be found from Oldham (1965, p. 3-4):

$$R_{CL} = \frac{c_{aero}}{2 \sin \frac{\theta}{2}} \quad [\text{Eq. 5.8.4}]$$

$$R_{SS} = \frac{R_{CL}(2R_{CL} + t_{blade\_max})(1 - \cos\phi) + \frac{t_{blade\_max}^2}{4} - R_{LE}^2}{2(R_{CL} - R_{CL} \cos\phi + \frac{t_{blade\_max}}{2} - R_{LE})} \quad [\text{Eq. 5.8.5}]$$

$$R_{PS} = \frac{R_{CL}(2R_{CL} - t_{blade\_max})(1 - \cos\phi) + \frac{t_{blade\_max}^2}{4} - R_{LE}^2}{2(R_{CL} - R_{CL} \cos\phi - \frac{t_{blade\_max}}{2} + R_{LE})} \quad [\text{Eq. 5.8.6}]$$

Where the angle  $\phi$  is defined by [1] as:

$$\phi = \sin^{-1} \left( \frac{c_{aero} - 2R_{LE} \sin \frac{\theta}{2}}{c_{aero}} \right) \quad [\text{Eq. 5.8.7}]$$

The above relationships can also be used for other blade profiles on a circular camber with a reasonable accuracy (Barbosa, 1987, p. 46-48). Generally, for blades on a circular camber the blade passage throat width  $W_{throat}$  can be found from the following relationship:

$$W_{throat} = \frac{Y_{chord}}{\cos\gamma} - R_{LE} - t_{blade\_throat} - \frac{Y_{throat\_PS}}{\cos\gamma} \quad [\text{Eq. 5.8.8}]$$

Where  $Y_{chord}$  is the distance between the chords of two successive blades, as measured parallel to the major principal axis YY (see *Appendix C - DCA Blade Geometry*) given by:

$$Y_{chord} = s \cos\zeta \quad [\text{Eq. 5.8.9}]$$

Where  $\gamma$  is the angle formed by the line passing through the blade mid-chord (major principal axis YY) and the notional 'throat line' AB. Angle  $\gamma$  is calculated from:

$$\gamma = \tan^{-1} \left( \frac{X_{c/2} - X_{LE}}{Y_{chord} + \sqrt{R_{SS}^2 - X_{c/2}^2}} \right) \quad [\text{Eq. 5.8.10}]$$

Where  $X_{LE}$  is the distance between the leading edges of two successive blades, as measured parallel to the minor principal axis XX, given by:

$$X_{LE} = Y_{chord} \tan\zeta + R_{LE} \quad [\text{Eq. 5.8.11}]$$

Assuming a large suction surface radius of curvature  $R_{SS}$  and a small  $\gamma$ , the distance  $X_{throat\_CL}$  between the LE and the point of intersection between the 'throat line' AB and blade camber line can be given to a good approximation by:



$$X_{throat\_CL} = X_{c/2} - \gamma \left( R_{SS} - \left( \frac{t_{blade\_max}}{2} \right) \right) \quad [\text{Eq. 5.8.12}]$$

Establishing  $X_{throat\_CL}$ , the blade thickness at the throat  $t_{blade\_throat}$  can be derived from published thickness distribution tabulations for various blade profiles (e.g. Cumpsty, 1989, p. 480). The distance  $X_{throat\_SS}$  between the LE and the point of intersection between the 'throat line' AB and blade suction surface is calculated as:

$$X_{throat\_SS} = X_{throat\_CL} - \sin \gamma \left( \frac{t_{blade\_throat}}{2} \right) \quad [\text{Eq. 5.8.13}]$$

The distance  $X_{throat\_PS}$  between the LE and the point of intersection between the 'throat line' AB and blade pressure surface is calculated as:

$$X_{throat\_PS} = X_{throat\_CL} + \sin \gamma \left( \frac{t_{blade\_throat}}{2} \right) \quad [\text{Eq. 5.8.14}]$$

Finally, the distance  $Y_{throat\_PS}$  between the blade chord and the point of intersection between the 'throat line' AB and blade pressure surface is calculated as:

$$Y_{throat\_PS} = \sqrt{R_{PS}^2 - (X_{c/2} - X_{throat\_PS})^2} - \sqrt{R_{PS}^2 - (X_{c/2})^2} \quad [\text{Eq. 5.8.15}]$$

In the case of DCA blades, the radii of curvature of the three circular arcs remain the same from leading edge to trailing edge and the above calculation for the blade passage throat width can be simplified to:

$$W_{throat} = \frac{Y_{chord}}{\cos \gamma} - R_{LE} - \frac{Y_{throat\_SS}}{\cos \gamma} \quad [\text{Eq. 5.8.16}]$$

In this case, the distance  $Y_{throat\_SS}$  between the blade chord and the point of intersection between the 'throat line' AB and blade suction surface is calculated as:

$$Y_{throat\_SS} = \sqrt{R_{SS}^2 - (X_{c/2} - X_{throat\_SS})^2} - \sqrt{R_{SS}^2 - (X_{c/2})^2} \quad [\text{Eq. 5.8.17}]$$

The above method for calculating the throat width of a blade passage was implemented in the *2D Compressor SLC Software* and derives purely from blade geometric features. It is also possible to approximate throat widths with reasonable accuracy using empirical correlations from open literature. For example, Aungier (2003, p. 73-75) developed a throat-opening correlation for NACA 65-series blades based on a modified stagger angle parameter defined as:

$$\phi = \zeta \left( 1 - 0.05 C_{lo}^{1.5} \right) + 5 C_{lo}^{1.5} - 2 \quad [\text{Eq. 5.8.18}]$$

The throat width can then be estimated from:

$$W_{throat} = s \left[ \left( 1 - t_{blade\_max} \sqrt{\sigma} / c_{aero} \right) \cos \phi \right]^{\sqrt{\sigma}} \quad [\text{Eq. 5.8.19}]$$

Where  $c_{aero}$  is the aerodynamic chord length,  $\sigma$  is the solidity and  $C_{l_0}$  is the lift coefficient of an isolated aerofoil.

Using empirical correlations such as the ones suggested by Aungier introduces the uncertainty as to the applicability of the empirical correlation to the specific blades used. Therefore, it is preferable to use throat widths, derived from actual blade geometry calculations, for performance analysis applications. This will ensure accurate treatment of special blade types for which the correlation is not likely to apply.

### Implementation

Blade passage choking is handled in the *2D Compressor SLC Software* by subroutine *Compressor2D\_BladePassageChoking.f90*. This subroutine is called by the main subroutine *Compressor2D\_MainProgram.f90* immediately after flow properties at the inlet of every blade row converge. The purpose of this subroutine is to identify choking conditions within the blade passage at various locations from hub to tip (depending on the number of stream tubes) and notify the user. *Compressor2D\_BladePassageChoking.f90* basically calculates the ratio  $W_{throat}/s \cos \alpha_1$  and calls subroutine *Compressor2D\_CriticalMachNoCalc.f90*. The calculation of the critical Mach number is based on Equation 5.8.3 and follows a 'trial and error' approach. Several inlet Mach numbers are tried until the one which will cause choking at the passage throat is identified. The subroutine uses a Newton-Raphson convergence algorithm to converge to the critical Mach number. Once the critical Mach number has been calculated, a 'Blade Passage Choke Margin' (BPCM) is established based on the actual inlet Mach number and defined as:

$$BPCM_{stator} = \frac{M_1}{M_{cr,1}} \quad [\text{Eq. 5.8.20}]$$

$$BPCM_{rotor} = \frac{M'_1}{M'_{cr,1}} \quad [\text{Eq. 5.8.21}]$$

If BPCM becomes larger than 1.0 at any stream tube then the flow in that stream tube is considered choked and a warning message is displayed to the user. A fairly similar approach was followed by Creveling and Carmody (1968) who used a BPCM of the order of 1.05 (5%).

### Limitations and Potential Expansion

The current model for the calculation of blade passage choking can identify the conditions likely to cause a choked passage throat at various stations along the span but makes no attempt to identify complete annulus choking. It is left to the user to decide when to stop program execution as soon as one or more passages become



choked. The possibility of one or more stream tubes being choked needs to be taken carefully into account in the solution of the full radial equilibrium equations and more particularly in the execution of the meridional velocity convergence algorithm. This will allow the software to produce more realistic flow profiles after the onset of passage choking and also detect complete annulus choking.

The current model for the calculation of blade passage throat width can calculate the throat width of DCA cascades fairly accurately and can also be used for other blade profiles on a circular camber line to a good approximation. Extending the model to handle a wider range of blade profiles will improve the accuracy in identifying choking conditions and also improve the versatility of the software.

## ***5.9. Prediction of Stall***

This section briefly introduces the phenomenon of compressor stall and describes how this is handled in the *2D Compressor SLC Software*. A method for predicting compressor blade row passage stall is presented in this section together with the limitations of the model adopted and scope for further improvement.

### **Introduction**

The surge line of a compressor map represents the locus of points of operation where compressor surge is likely to occur. Surge is associated with a sudden reduction in compressor delivery pressure. If the compressor is operating at some point to the left of the point of maximum isentropic efficiency, on a given constant speed line, a hypothetical decrease in mass flow could be followed by a fall of delivery pressure. If the air pressure downstream of the compressor does not fall quickly enough, the air will tend to reverse course and flow in the direction of the resulting pressure gradient (towards compressor inlet). Generally speaking, adverse pressure gradient in the flow direction sets the upper limit on compressor operating range. The precise pressure ratio and mass flow, for a non-dimensional speed line, where surge occurs, can only be determined experimentally. However, for values slightly bigger than the limiting 'stability' mass flow, several stalled cells will have already appeared within the annulus. These might extend right across the annulus or only over part of it, while rotating in the direction of the rotor at maximum 50% of its design rotational speed. What is important from a simulation point of view is to establish a criterion that predicts the minimum mass flow above which the compressor can work stably.

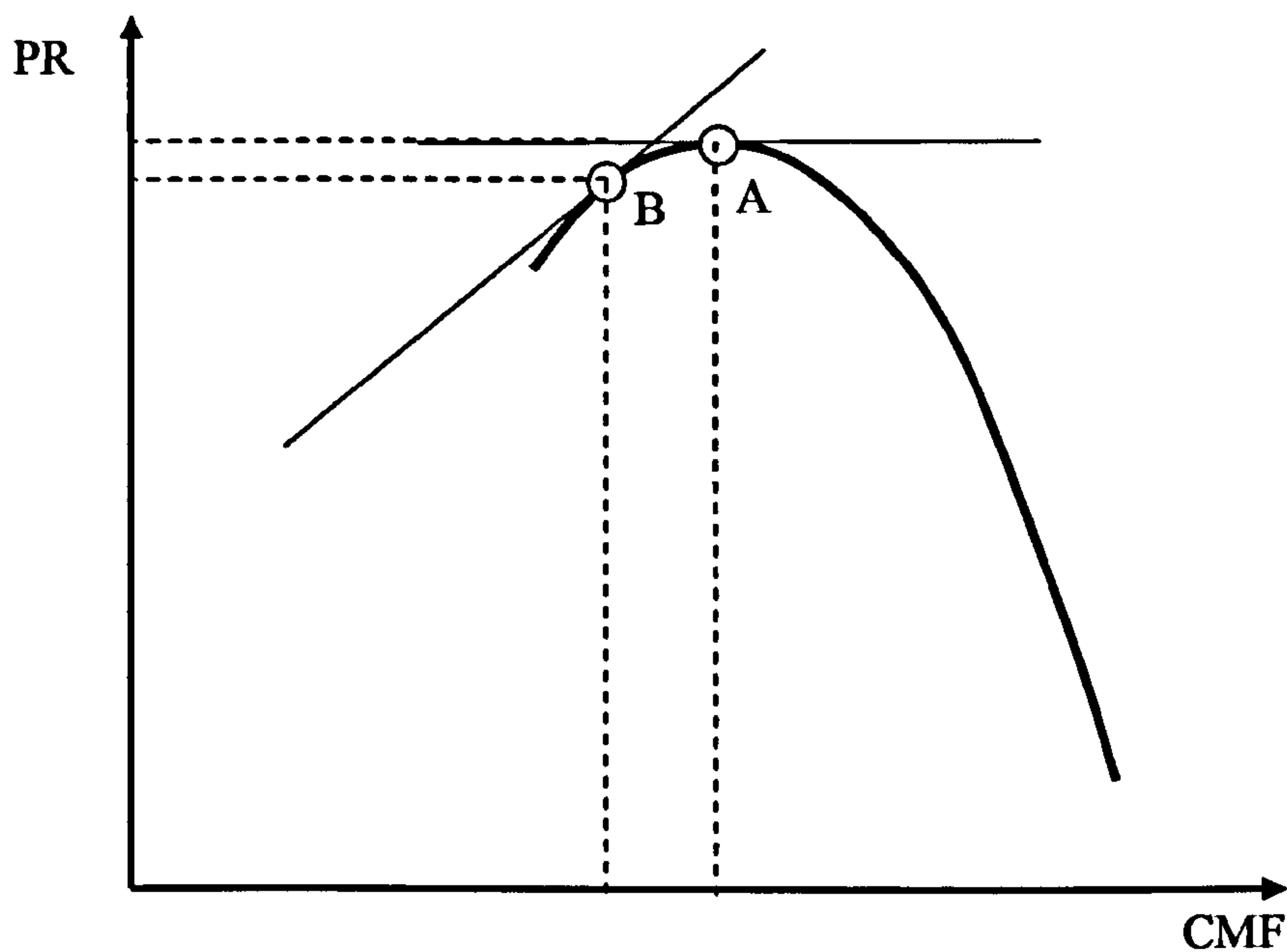


Figure 5.9.1 Compressor characteristic

Theoretically, the positive slope of a mass flow versus pressure ratio compressor characteristic, at a certain non-dimensional rotational speed, characterizes an unstable compressor operating point. Consequently, the zero slope could be considered as the surge onset (Point A, Figure 5.9.1). However, there are two problems associated with this approach. Firstly, when the compressor operates as a part of a gas turbine system, upstream of a combustion chamber and exhaust nozzle, the instability point can move further down the region of positive slopes (Point B, Figure 5.9.1), depending on the exhaust duct and combustion chamber volumes. Secondly, the computed performance characteristic, as a result of the compressor simulation, may not be accurate enough to predict the behavior of the compressor within the stall region. In other cases, it may never reach to exhibit a negative slope.

An alternative approach for predicting the starting point of the compressor unstable region is to focus on the diffusion process itself, taking place within the blade passages. It is known that blade stall occurrence, and ultimately compressor surge, is a function of some kind of limiting loading diffusion factor such as the equivalent diffusion factor  $D_{eq}$  introduced by Lieblein (1959).

A simpler stall criterion was introduced by de Haller in 1953, where the relative velocity ratio  $W_R$  should not fall below the limiting value of 0.72. Although this criterion has been found to be more effective than diffusion factors, as an indicator of the onset of surge, according to Aungier (2003, p. 204-207) and other researchers, it is a generally accepted opinion today that de Haller's criterion is associated with an end wall stall rather than a blade stall. Nevertheless, in practice both criteria mentioned above have been proven to be quite invalid and inaccurate.

The main drawbacks of the above approaches are the following: Firstly, these are actually blade stall criteria and not surge criteria. As it was mentioned before, the compressor may still operate stably even with the existence of rotating stall cells within the annulus. Moreover, both criteria do not take into account blade or



compressor annulus geometric characteristics which do affect the location of the surge point on the performance map. Consequently, these two criteria are very rarely used as surge criteria of an existing compressor under simulation. They are however used extensively in blade profile selection during preliminary compressor design.

Koch (1981) suggested an improved stall criterion which takes into consideration blade geometry parameters. More specifically, Koch approximated the blade passages, averaged over a stage, as a simple diffuser and showed reasonable agreement between observed stage pressure coefficients at stall and two-dimensional, experimental diffuser data for a specific inlet blockage level. Unfortunately, Koch's correlation applies only as a stall criterion for a compressor stage instead of a single blade row and requires a number of correction factors and adjustments before it can become applicable to a specific compressor design.

This work adopts a correlation developed by Aungier for predicting the onset of stall in a blade row which was found to be more appropriate to the needs of this simulation software. The method followed by Aungier is similar to Koch's work and is described in detail in the following paragraphs.

### Description of Stall Criterion

Aungier correlated Reneau's (1967) data for simple two dimensional diffusers, operating at their peak static pressure recovery, as follows:

$$V_R = \frac{1}{1 + 0.4 \left( \frac{L}{b} \right)^{0.65}} \quad [\text{Eq. 5.9.1}]$$

Where  $L$  is the diffuser length,  $b$  the diffuser width at the inlet and  $V_R$  the ideal diffuser velocity ratio. Assuming that the onset of stall in any diffusing passage corresponds closely to the peak pressure recovery condition, identified by the above equation, Aungier approximated the blade passage geometry to the diffuser geometry by assigning the diffuser length to the blade camber line length and the diffuser width to the blade staggered spacing (Figure 5.9.2).

Approximating the camber line as a circular arc, the non-dimensional parameter of Equation 5.9.1 takes the form:

$$\frac{L}{b} = \frac{\theta \sigma}{2 \sin\left(\frac{\theta}{2}\right) \cos \gamma} \quad [\text{Eq. 5.9.2}]$$

Based on experimental data and observed axial-flow compressor surge limits, Aungier defined an equivalent relative velocity ratio  $W_{REq,geom}$  across the blade row, established from blade geometric properties and given by:

$$W_{REq,geom} = \frac{\left[ 0.15 + 11 \left( \frac{t_{blade\_max}}{c_{geom}} \right) \right] / \left[ 0.25 + 10 \left( \frac{t_{blade\_max}}{c_{geom}} \right) \right]}{1 + 0.4 \left[ \frac{\theta \sigma}{2 \sin \left( \frac{\theta}{2} \right) \cos \gamma} \right]^{0.65}} \quad [\text{Eq. 5.9.3}]$$

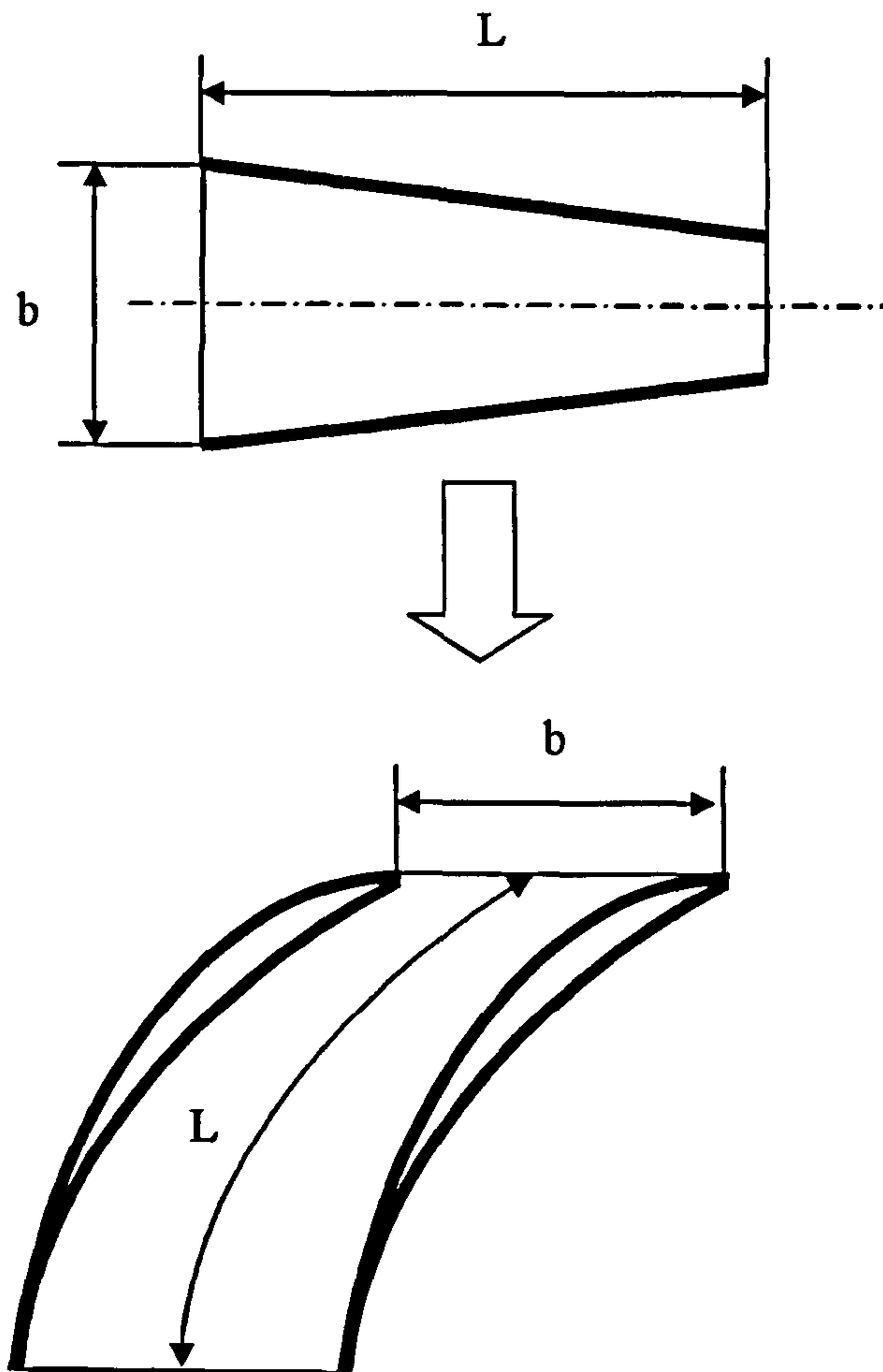


Figure 5.9.2: Blade passage – diffuser passage equivalence

Similarly to Equation 5.9.3, an ‘aerodynamic’ velocity ratio  $W_{REq,aero}$ , can be calculated based on the aerodynamic performance of the blade row flow passage, given by:

$$W_{REq,aero} = \sqrt{\frac{P'_{o,2} - P_2}{P'_{o,1} - P_1}} \quad [\text{Eq. 5.9.4}]$$

The flow passage is considered to operate unstalled, while the ‘aerodynamic’ relative velocity ratio remains below the ‘geometrical’ relative velocity ratio:



$$W_{REq,geom} > W_{REq,aero} \quad [\text{Eq. 5.9.5}]$$

It has been observed that Equation 5.9.3 tends to overestimate blade row stall when the equivalent diffusion factor exceeds the value of 2.2. In this case Aungier proposed an alternative empirical correction. He suggested multiplying Equation 5.9.3 with an equivalent diffusion factor ( $D_{eq}$ ) dependent term. Therefore, whenever  $D_{eq}$  is greater than 2.2, the following empirical correction to Equation 5.9.3 can be used instead:

$$W_{REq,geom} = \frac{\left(\frac{2.2}{D_{eq}}\right)^{0.6} \left[ 0.15 + 11 \left( \frac{t_{blade\_max}}{c_{geom}} \right) \right] / \left[ 0.25 + 10 \left( \frac{t_{blade\_max}}{c_{geom}} \right) \right]}{1 + 0.4 \left[ \frac{\theta\sigma}{2 \sin\left(\frac{\theta}{2}\right) \cos\gamma} \right]^{0.65}} \quad [\text{Eq. 5.9.6}]$$

### Implementation

Blade row passage stall is handled in the *2D Compressor SLC Software* by subroutine *Compressor2D\_StallPredictionCalc.f90*. This subroutine is called by the main subroutine *Compressor2D\_MainProgram.f90* immediately after flow properties at the outlet of every rotor blade row converge. The purpose of this subroutine is to identify stall conditions within the blade passage at various locations from hub to tip (depending on the number of stream tubes) and notify the user. Basically, *Compressor2D\_StallPredictionCalc.f90* calculates and compares the ‘aerodynamic’ and ‘geometric’ equivalent relative velocity ratios based on input air relative velocities and the necessary blade row geometrical characteristics. The output is a message on the screen about the location along the blade span where surge conditions have been identified.

### Limitations and Potential Expansion

Accurate compressor surge prediction is certainly one of the most important requirements of a compressor simulation code. However, with inviscid calculation methods it is extremely difficult to accurately detect flow separation on blades that is likely to cause blade row stall and subsequently compressor surge.

The model adopted by this work has been reported in Aungier (2003, p. 204-207) to provide reasonably accurate predictions especially for  $L/b$  ratios greater than 1.1 and compressor speeds greater than 85% of the design speed.

As mentioned before, the current model is only used to indicate stall conditions in individual stream tubes. Consequently, a limit should be defined as to how much of the blade span can be allowed to operate under stalled conditions before it is assumed that complete compressor surge has taken place. According to the author’s current

experience, this cannot be set universally for all compressor geometries. The user should decide for each case individually based on experimental data if available.

Alternative or additional surge prediction models could easily be programmed within *Compressor2D\_StallPredictionCalc.f90* such as the one proposed by Greitzer (1976). In this way, when experimental data of the compressor under simulation are available, the user will have the option to select the most appropriate stall prediction model.

## ***5.10. Calculation of Compressor End-Wall Boundary Layer***

This section deals with the phenomenon of the end-wall boundary layer and describes how the annulus flow blockage factors are calculated in the *2D Compressor SLC Software*. The following paragraphs discuss also the limitations of the model adopted and scope for future development.

### **Introduction**

It has become a custom in literature to refer to the regions of the compressor flow field where the viscous effects are largest, as boundary layers. Viscous effects can have a major influence on the performance of a compressor. They can limit the achievable pressure rise, reduce the mass flow capacity by reducing the effective flow area, reduce the work input and give rise to losses. Boundary layers developed on compressor wetted surfaces can be classified into two major categories, the end-wall or annulus boundary layer and the blade-to-blade boundary layer.

The blade-to-blade boundary layer is generally considered to be less crucial for the overall compressor performance. It is mostly important in determining more accurately the actual blade passage throat dimensions and thus predicting flow choking. Similarly, in the case when the compressor is operating close to the surge limit, a close boundary layer observation is crucial for the exact prediction of the blade stall point. On the other hand, end-wall boundary layers can cause flow blockage large enough for the compressor performance to be considerably affected over its entire operating range. Consequently, the inclusion of their effects on the compressor flow simulation is of paramount importance for the accuracy of the results.

The complete compressor flow field can only be fully described by the Reynolds-Averaged, Navier-Stokes equations. In the boundary layer regions, however, and especially close to the blade-end-wall connection points, some empiricism still needs to be implemented into the turbulence models. As discussed before, solving Navier-Stokes equations is still not a practical method, especially when it comes to simulating several blade rows. An alternative approach has been the use of inviscid flow calculation methods, such as streamline curvature, incorporating explicitly coupled boundary layer models for the prediction of the boundary layer displacement thickness.

There is a vast amount of literature concerning boundary layer theory and many empirical correlations associated to it. For example, classic boundary layer theory can



be found in Schlichting (1960), whereas an extensive account specifically devoted to the calculation of end-wall boundary layers in turbomachines can be found in Horlock and Perkins (1974). Early work on end-wall boundary layer calculation, by Sandercock, et al. (1954), for example, was simplistically based on assigning blockage factors that linearly varied throughout the compressor annulus. Jansen and Moffat (1967), based on previous industrial experience, assumed that the blockage varied linearly through the front stages and remained constant in the rear stages. First attempts to actually analyze the pitch-averaged boundary layer flow using integral boundary layer analysis techniques were reported by Stratford (1967) and Jansen (1967). Stratford employed flat-plate approximations for the boundary layer shape factor  $H$  and the wall shear stress, while Jansen used an approximate integral solution. Since then, many others have significantly contributed to the analysis of end-wall boundary layers, such as Mellor and Wood in 1971, Koch and Smith in 1976 and Hunter and Cumpsty in 1982.

Most of the empirical correlations, however, were developed for external flow regimes and when applied to the compressor internal flow, they do not exhibit the same quantitative value, as discussed by Dransfield and Calvert (1976) and later on by Cumpsty (1989, p. 331-356). They do however indicate correct qualitative trends. Cumpsty actually stresses that no boundary layer method can encompass the full range of three-dimensional flow effects, not even those that solve the Navier-Stokes equations. Therefore, the application of these methods has been traditionally treated as an approximation.

### Calculation of Boundary Layer Blockage Factors

This work adopts a simplified two-dimensional boundary layer approach for the calculation of the annulus blockage factors, similar to the one adopted by Barbosa (1987, p. 38-41). Considering the boundary layer to be turbulent throughout the compressor and the core flow dominated by the meridional velocity, the following integral can be calculated on the boundary layer edges for both hub and tip regions:

$$\int_{z_{inlet}}^{z_{outlet}} V_m^4(z) dz \quad [\text{Eq. 5.10.1}]$$

Where  $V_m$  is the meridional velocity on the assumed boundary layer edge and  $z$  is the axial distance measuring from the compressor inlet. The integral can be calculated numerically using the trapezoidal rule. From Schlichting (1960) and Jansen (1967) it can be shown that the boundary layer momentum thickness for each axial location is given by the following formula:

$$\theta(z) = \theta(z_o) + k_{units} \left( \frac{\int_{z_{inlet}}^{z_{outlet}} V_m^4(z) dz}{V_m^{3.2}(z)} \right)^{0.8} \quad [\text{Eq. 5.10.2}]$$

Where  $k_{units}$  is a units correction factor and  $\theta(z_o)$  is the boundary layer momentum thickness at the inlet of the compressor to take into account any boundary layer ingestion from the intake. If the boundary layer displacement thickness  $\delta^*(z_o)$  is known at the inlet of the compressor, then  $\theta(z_o)$  can be found from the following equation assuming a shape factor  $H(z_o)$  equal to 1.4, which is a typical value for a simple flat-plate boundary layer flow:

$$\theta(z_o) = \frac{\delta^*(z_o)}{H(z_o)} \quad [\text{Eq. 5.10.3}]$$

The next step is to evaluate the first derivative of the boundary layer momentum thickness with respect to  $z$  which is then used for the determination of the shape factor along the compressor:

$$H(z) = 1.5 + 30 \frac{d\theta}{dz} \quad [\text{Eq. 5.10.4}]$$

The boundary layer displacement thickness at any point throughout the compressor annulus can then be calculated from the definition of the shape factor:

$$\delta^*(z) = \theta(z)H(z) \quad [\text{Eq. 5.10.5}]$$

The resultant reduction in flow area is subsequently translated into a more convenient coefficient for representing area reduction, the flow blockage factor  $k_B$ . The general definition of the flow blockage factor is the following:

$$k_B = \frac{\text{Free Stream Area}}{\text{Metal Area}} \quad [\text{Eq. 5.10.6}]$$

The hub and tip blockage factors can be expressed individually in terms of the radial coordinates and displacement thickness, as follows:

$$k_{B\_hub} = \frac{(R_{hub} + \delta_{hub}^*)^2 - R_{hub}^2}{R_{tip}^2 - R_{hub}^2} \quad [\text{Eq. 5.10.7}]$$

$$k_{B\_tip} = \frac{R_{tip}^2 - (R_{tip} - \delta_{tip}^*)^2}{R_{tip}^2 - R_{hub}^2} \quad [\text{Eq. 5.10.8}]$$

Where  $R_{hub}$  and  $R_{tip}$  are the radial locations of the streamlines close to the end walls, and  $\delta_{hub}^*$ ,  $\delta_{tip}^*$  the displacement thicknesses at hub and tip respectively calculated as shown previously.

Finally, the resultant overall blockage factor at the inlet and outlet of each blade row can be established from:

$$k_B = 1 - (k_{B\_hub} + k_{B\_tip}) \quad [\text{Eq. 5.10.9}]$$



### Implementation

End-wall boundary layer calculations are carried out in the *2D Compressor SLC Software* by subroutine *Compressor2D\_BoundaryLayerCalc.f90* based on the model described above. This subroutine is called by the main subroutine *Compressor2D\_MainProgram.f90* immediately after the entire compressor flow field has been calculated. The purpose of this subroutine is to calculate the end-wall and annulus blockage factors at every blade row inlet and outlet. The input variables needed for the calculation are the co-ordinates of the solution nodes along the hub and casing and the meridional velocity distribution at these positions.

Blockage factor calculation based on the above theory requires the two-dimensional meridional velocity distribution throughout the compressor. On the other hand, the blade row inlet and outlet blockage factors are needed as input values for the determination of the flow field within the compressor. For this reason, a first flow field calculation is carried out based on guessed blockage factors that the user specifies as inputs. Once the calculation has converged at all blade rows for the first time, new values of blockage factors are calculated and a second full compressor calculation begins. This iterative calculation should be repeated until convergence is obtained between the guessed and calculated blockage factors. Before each iteration, streamline coordinates are updated setting the minimum effective blade height at the outer edge of the hub boundary layer and the maximum effective blade height at the inner edge of the tip boundary layer. The current code is set to do this iteration only once in order to save computational time.

To carry out this analysis, extra calculation stations need to be established in the bladeless areas between blade rows, where it can be assumed that there is little obstruction to the flow by the blades and where the meridional velocity can be established reasonably accurately. For this purpose, a number of auxiliary points are defined along the compressor annulus in-between standard solution nodes as shown in Figure 5.10.1. In order to only assist the mathematical derivations required, auxiliary points are also established within the bladed regions. The blockage factors calculated there, however, are highly inaccurate and for that reason they are not included in any calculation for determining the compressor flow field.

The user is free to select the exact number of auxiliary points according to the required accuracy and the available computational power. The flow meridional velocity can then be interpolated for all the annulus points, based on the meridional velocity distribution calculated along the first and last streamline.



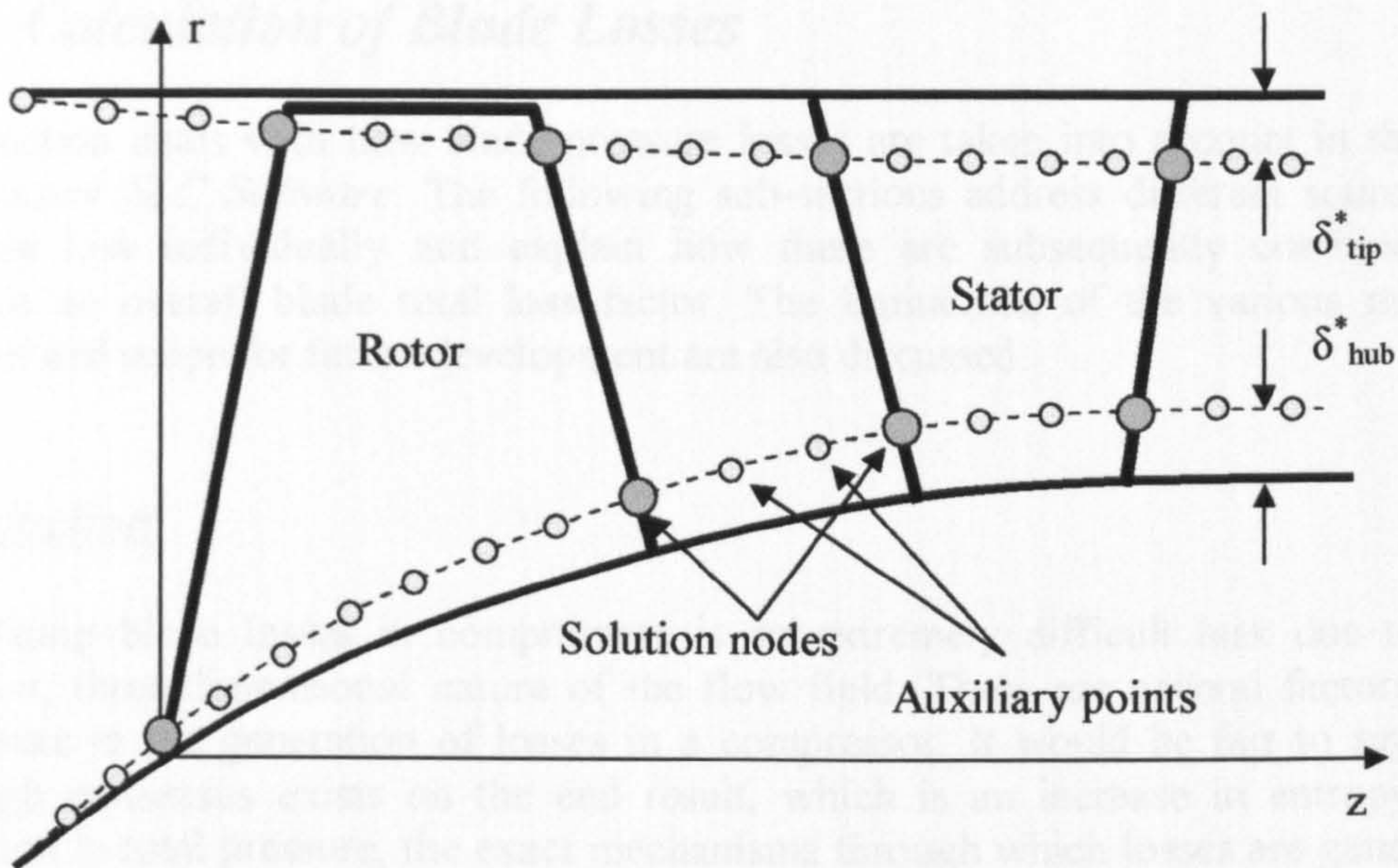


Figure 5.10.1: Solution nodes and auxiliary points along the end-wall boundary layer edges

### Limitations and Potential Expansion

The model adopted by this study is valid for shape factors  $H(z)$  below 2.2 for accelerating flows, and below 1.1 for decelerating flows. Moreover, the resultant overall blockage factor is restricted above 0.7, whereas hub and tip blockage factors are kept below 0.25 and 0.2 respectively.

A sensitivity analysis should be performed in order to determine the optimum number of auxiliary points for the best accuracy and minimum computational time. As the whole compressor calculation has to converge first, every iteration is very time consuming. A similar sensitivity analysis is also necessary to set a reasonable convergence tolerance for the blockage factors.

The current method does not take into account the boundary layer growth within the bladed regions. Subroutine *Compressor2D\_BoundaryLayerCalc.f90* could be extended to include a three dimensional boundary layer calculation, at least for the bladed regions, as the accurate prediction of the flow blockage is generally considered to be very crucial for the accurate simulation of the compressor flow field.

Finally, the subroutine could be expanded to include boundary layer models for the blade surfaces. This information, as commented before, would be valuable in the more precise calculation of the blade passage throat area, choking conditions and entropy generation across the blade row.



## 5.11. Calculation of Blade Losses

This section deals with how blade pressure losses are taken into account in the *2D Compressor SLC Software*. The following sub-sections address different sources of pressure loss individually and explain how these are subsequently combined to produce an overall blade total loss factor. The limitations of the various models adopted and scope for future development are also discussed.

### Introduction

Calculating blade losses in compressors is an extremely difficult task due to the complex, three-dimensional nature of the flow field. There are several factors that contribute to the generation of losses in a compressor. It would be fair to say that although consensus exists on the end result, which is an increase in entropy and reduction in total pressure, the exact mechanisms through which losses are generated and their complicated interactions have not been completely understood yet.

The standard approach is based on the assumption that different types of cascade loss are independently generated and can be analytically related to the resulting deficit in total pressure. To a good estimation, the total loss in a compressor blade row is typically established by properly adding together, and correcting for three-dimensional effects, different loss factors. Several researchers have incorporated their expertise into correlations of parameters which describe the flow in blade passages. Such correlations usually attempt to synthesize the results of many tests into simpler formulae or sets of curves. They are generally averages of test results or their statistical curve fits.

The main limitation of this approach is that the various empirical correlations can not be expected to represent accurately every individual compressor design. A generic model for all compressors is rather unrealistic and the success or failure of this approach really depends on in-house expertise which allows for the incorporation of suitable correction factors that can bring a particular model closer to reality.

This work adopts a similar approach to blade row total loss prediction, followed before by other researchers in the field, such as Miller, et al. (1961) and Creveling and Carmody (1968). It is assumed that the total pressure loss of the blade row is the result of the interaction of different loss components, i.e. profile losses, secondary losses and shock losses, which are considered to act through independent mechanisms.

More analytically, the blade mass flow-averaged total loss factor, defined in Section 5.4, is calculated for the rotor from:

$$\overline{\omega}_{tot} = \overline{\omega}_{prof} f_{Re} + \overline{\omega}_{sh} + \overline{\omega}_{sec} \quad [\text{Eq. 5.11.1}]$$

End for the stator from:

$$\bar{\omega}_{tot} = \bar{\omega}_{prof} f_{Re} + \bar{\omega}_{sh} \quad [\text{Eq. 5.11.2}]$$

Where  $\bar{\omega}_{prof}$  is the blade profile loss factor,  $\bar{\omega}_{sh}$  is the blade shock wave loss factor,  $\bar{\omega}_{sec}$  is the secondary loss factor and  $f_{Re}$  is a correction due to the Reynolds effects. Secondary losses in the case of a stator are ignored. The following sub-sections explain how individual loss factors and corrections are calculated.

### 5.11.1. Calculation of Profile Loss

This sub-section explains how blade profile losses are calculated in the *2D Compressor SLC Software*. The limitations of the models adopted and scope for future development are also discussed.

#### Introduction

Blades are known to operate with a separated region towards the trailing edge. Profile losses are associated with the development of the boundary layers on the blade surfaces, and the generated wake behind them, and make up only a small percentage of the total loss in a stage. Concerning the profile loss associated to the blade wetted surface, it is related to the blade-to-blade boundary layer momentum thickness and usually it's a small percentage of the overall profile loss, accounted as blade friction loss. The wake mixing process downstream the blade trailing edge is considered to be the greatest contributor to profile losses, especially under extreme incidence angles.

Lieblein and Roudebush (1956) experimenting with low-speed, two-dimensional compressor blade cascades, showed that the blade profile loss can be expressed in terms of the blade wake momentum thickness. They used a power law profile to represent the wake and were then able to correlate the profile loss in terms of the wake momentum thickness and shape factor  $H$ , defined as the ratio of the displacement to the momentum thickness. The loss in stagnation pressure is not constant downstream of the blades but increases as the wakes mix out. Lieblein and Roudebush used the definition of the shape factor  $H$  as a measure of the degree to which the wake has mixed out and to quantify the entropy generation process. They also showed that mixing was almost completed approximately within 33 percent of a chord downstream the blade trailing edge, at an average shape factor value between 1.1 and 1.2, provided that the boundary layer remained attached on the blade surfaces. Much later on, Koch and Smith (1976) verified Lieblein's and Roudebush's method by looking into several different sources of loss based on a boundary layer calculation method that could take into account compressibility effects, Reynolds effects, surface roughness and streamline movement.

Lieblein (1957 and 1959), continuing the analysis of low-speed, 10-percent-thick compressor cascade sections, tried to relate the blade wake momentum thickness to velocity diffusion and blade loading. Through experiments he concluded that blade surface velocity distributions that result in large amounts of diffusion tend to produce relatively thick boundary layers on the blade surfaces that subsequently merge



forming strong wakes. By analyzing a wide range of blade sections at various angles of attack he eventually established universal correlations between the wake momentum thickness and blade loading parameters such as the diffusion factor  $D$  and the equivalent diffusion factor  $D_{eq}$ .

Although Lieblein's approach was restricted to low-speed, two-dimensional cascade flow, his equivalent diffusion factor in particular, appeared to describe satisfactorily the relationship between blades and profile losses over a wide range of flow conditions. Based on Lieblein's work, Swan (1961) introduced a more practical method of predicting blade profile losses in transonic compressors. According to Swan's model, the equivalent diffusion factor  $D_{eq}$  and minimum loss equivalent diffusion factor  $D_{eq}^*$  can be established as per Lieblein. From the minimum loss equivalent diffusion factor the minimum loss wake momentum thickness can be established through a statistical curve fit. At off-design, the wake momentum thickness can be calculated from tabulations relating the wake momentum thickness and minimum-loss wake momentum thickness to  $D_{eq}^*$  and  $D_{eq}$ . Having established the wake momentum thickness, the blade profile loss can be calculated as per Lieblein. Monsarrat in 1969 worked on the same philosophy having though extracted more empiricism from the experimental data. However, a major drawback of his method is that his correlations were confined only to design point conditions.

Jansen and Moffatt (1967) based their research on the definition of the design (or minimum-loss) diffusion factor in order to relate the profile loss coefficient to the blade loading at design point conditions. At off-design they assumed a parabolic variation of loss with incidence such that at stall or negative stall the loss is twice the minimum-loss value.

Similarly to Jansen and Moffatt, Oldham (1965, p. 6-7) derived a simplified correlation for the calculation of profile losses for double circular arc stator blades, based on Swan's work and Lieblein's basic definition of the diffusion factor. Oldham's correlation applies to all radial locations.

### Description of Blade Profile Loss Models

The models developed by Swan and Jansen and Moffatt for the calculation of the blade profile loss, are described here in more detail, for the relative frame of reference.

In order to address the problem of the three-dimensional nature of the flow in real compressor blade rows, Swan extended Lieblein's (1957) basic correlation of the minimum-loss equivalent diffusion factor for two-dimensional cascades given by:

$$D_{eq}^* = \frac{\cos \beta_2}{\cos \beta_1} \left[ k_1 + k_4 \frac{\cos^2 \beta_1}{\sigma} (\tan \beta_1 - \tan \beta_2) \right] \quad [\text{Eq. 5.11.1.1}]$$

to

$$D_{eq}^* = \left[ k_1 + k_4 \frac{\sin^2 \beta_1}{\sigma} \left( \cot \beta_1 - \frac{r_2 V_{m2}}{r_1 V_{m1}} \cot \beta_2 - \frac{r_1}{V_{m1}} \left( 1 - \frac{r_2^2}{r_1^2} \right) \right) \right] \frac{\sin \beta_2 V_{m1}}{\sin \beta_1 V_{m2}} \quad [\text{Eq. 5.11.1.2}]$$

The minimum-loss wake momentum thickness parameter can be established from the minimum-loss equivalent diffusion factor through experimental-statistical curve fits. At off-design conditions, Swan derived the following correlation for the equivalent diffusion factor that takes into account changes in incidence.

$$D_{eq} = \left[ k_1 + k_2 (i - i^*)^{k_3} + k_4 \frac{\sin^2 \beta_1}{\sigma} \left( \cot \beta_1 - \frac{r_2 V_{m2}}{r_1 V_{m1}} \cot \beta_2 - \frac{r_1}{V_{m1}} \left( 1 - \frac{r_2^2}{r_1^2} \right) \right) \right] \frac{\sin \beta_2 V_{m1}}{\sin \beta_1 V_{m2}} \quad [\text{Eq. 5.11.1.3}]$$

The above expression is again an extension to Lieblein's more fundamental definition of equivalent diffusion factor for two-dimensional cascades given by:

$$D_{eq} = \frac{\cos \beta_2}{\cos \beta_1} \left[ k_1 + k_2 (i - i^*)^{k_3} + k_4 \frac{\cos^2 \beta_1}{\sigma} (\tan \beta_1 - \tan \beta_2) \right] \quad [\text{Eq. 5.11.1.4}]$$

Where the constants  $k_i$  are determined from tests and depend on the particular blade profile and thickness distribution selected. For example,  $k_1$  is equal to 1.12,  $k_2$  equals 0.0117 for NACA 65-series blades and 0.007 for the C4 circular-arc blades,  $k_3$  is equal to 1.43 and  $k_4$  was found to be equal to 0.61.

Having established the minimum-loss wake momentum thickness parameter, minimum-loss equivalent diffusion factor and equivalent diffusion factor, the wake momentum parameter can be established from experimental curve fits correlated by Swan as shown below.

For  $D_{eq} > D_{eq}^*$ :

$$\frac{\theta}{c_{aero}} - \left( \frac{\theta}{c_{aero}} \right)^* = \left( 0.827M_1' - 2.692M_1'^2 + 2.675M_1'^3 \right) (D_{eq} - D_{eq}^*)^2 \quad [\text{Eq. 5.11.1.5}]$$

And for  $D_{eq} < D_{eq}^*$ :

$$\frac{\theta}{c_{aero}} - \left( \frac{\theta}{c_{aero}} \right)^* = \left( 2.80M_1' - 8.71M_1'^2 + 9.36M_1'^3 \right) (D_{eq} - D_{eq}^*)^2 \quad [\text{Eq. 5.11.1.6}]$$

As mentioned before, Lieblein established a relationship between the blade profile loss and wake momentum thickness through the shape factor  $H$ . For incompressible two-dimensional cascade flow, the wake momentum thickness can be theoretically established from the following correlation:

$$\frac{\theta}{c_{aero}} = \frac{\bar{\omega}_{prof} \cos^3 \beta_2}{2\sigma \cos^2 \beta_1} \left\{ \frac{3H - 1}{2H} \left[ 1 - \left( \frac{\theta}{c_{aero}} \right) \frac{H\sigma}{\cos \beta_2} \right]^3 \right\} \quad [\text{Eq. 5.11.1.7}]$$



Experiments showed that at conventional cascade measuring stations,  $H$  actually varied very little with different blade profiles and incidence angles. In other words, the wake momentum thickness was found to vary over most of the typical diffusion range primarily with the terms before the brackets in the last equation. Therefore, the last equation can be safely reduced to the following for a more straightforward calculation of the blade profile loss factor.

$$\frac{\theta}{c_{aero}} = \frac{\overline{\omega}_{prof} \cos^3 \beta_2}{2\sigma \cos^2 \beta_1} \quad [\text{Eq. 5.11.1.8}]$$

It must be stated that Swan's model for calculating the blade profile loss factor does not include any contribution from shock losses. These are accounted for by different loss models as described in the following sub-sections.

In order to quantify the blade loading and empirically relate it to the loss coefficient, Jansen and Moffatt used the definition of the design diffusion ratio  $D^*$  as the basic parameter for the determination of losses given by:

$$D^* = \frac{W_{max}}{W_1} - \frac{W_2}{W_1} \quad [\text{Eq. 5.11.1.9}]$$

Where  $W_{max}$  is the peak velocity on the blade suction surface calculated at the throat. The design wake momentum thickness can be expressed as a function of the design diffusion factor in a polynomial form as:

$$\left(\frac{\theta}{c_{aero}}\right)^* = 0.003 + 0.02375D^* - 0.05D^{*2} + 0.125D^{*3} \quad [\text{Eq. 5.11.1.10}]$$

The design loss coefficient can be expressed as:

$$\overline{\omega}_{prof}^* = \frac{2\sigma}{\cos \beta_2^*} \left(\frac{\theta}{c_{aero}}\right)^* \quad [\text{Eq. 5.11.1.11}]$$

For relative inlet Mach numbers greater than the critical Mach number, a design-point profile loss coefficient correction factor can be calculated from:

$$f_{M'} = [2(M_1' - M_{\sigma,1}') + 1] \quad [\text{Eq. 5.11.1.12}]$$

For off-design operation the profile loss coefficient is given by the following relation:

$$\overline{\omega}_{prof} = \overline{\omega}_{prof}^* f_{M'} (0.8333\overline{S}^2 + 0.1667\overline{S} + 1.0) \quad [\text{Eq. 5.11.1.13}]$$

Where  $\overline{S}$  is given by:

$$\bar{S} = \frac{\beta_1 - \beta_1^*}{\beta_{1,c} - \beta_1^*} \quad \text{for } \beta_1 < \beta_1^* \quad [\text{Eq. 5.11.1.14}]$$

$$\bar{S} = \frac{\beta_1 - \beta_1^*}{\beta_{1,s} - \beta_1^*} \quad \text{for } \beta_1 > \beta_1^* \quad [\text{Eq. 5.11.1.15}]$$

Where  $\beta_{1,s}$  and  $\beta_{1,c}$  are the inlet relative angles for stalling and negative stalling respectively that can be calculated iteratively from empirical correlations as shown in Aungier (2003, p. 135) :

$$i_c - i^* = -9 + \left[ 1 - \left( \frac{30}{\beta_{1,c}} \right)^{0.48} \right] \frac{\theta}{4.176} \quad [\text{Eq. 5.11.1.16}]$$

$$i_s - i^* = 10.3 + \left[ 2.92 - \frac{\beta_{1,s}}{15.6} \right] \frac{\theta}{8.2} \quad [\text{Eq. 5.11.1.17}]$$

Where  $i - i^*$  is the incidence angle range to stall taken approximately equal to  $\pm 10$  degrees.

In order to calculate the blade profile losses in a stator passage, Oldham adopted a much more simplified approach based on Lieblein's experimental results and definition of the diffusion factor given by:

$$D = 1 - \frac{V_2}{V_1} + \frac{\Delta V_w}{2\sigma V_1} \quad [\text{Eq. 5.11.1.18}]$$

Below a diffusion factor of 0.244 the wake momentum thickness is assumed equal to 0.0193. For a diffusion factor larger than 0.244 the following parabolic function can be used:

$$\frac{\theta}{c_{aero}} = 0.02224 - 0.02436D + 0.05D^2 \quad [\text{Eq. 5.11.1.19}]$$

The blade profile loss is then calculated from the wake momentum thickness through the following simplified formula:

$$\frac{\theta}{c_{aero}} = \bar{\omega}_{prof} \frac{\cos \alpha_2}{2\sigma} \quad [\text{Eq. 5.11.1.20}]$$

Oldham's model applies only in the case of double circular arc blades.



### Implementation

The above mentioned models have all been programmed to provide the user with flexibility when experimenting with different loss models. The calculation of diffusion factors and wake momentum thickness for rotor and stator is carried out in subroutine *Compressor2D\_WakeMomentumThicknessCalc.f90*. The blade profile loss parameter is calculated by subroutine *Compressor2D\_BladeProfileLossCalc.f90*.

Both these subroutines need to be repeatedly called by subroutine *Compressor2D\_BladeRowOutletMeridVelDistribGener.f90* in sequence and while the radial equilibrium equation is being iteratively solved at the blade row outlet. The aim is to calculate the blade profile loss at various locations from hub to tip (nodes), depending on the number of streamlines, so that the total loss factor can be established later on.

Inputs to these subroutines are blade geometrical properties such as solidity, aerodynamic chord and streamline radius and air properties such as inlet Mach number, critical Mach number, air angles, incidence and minimum-loss incidence. Moreover, Figure 5.11.1.1 is stored as array tabular data in module *Compressor2D\_WakeMomentumThicknessVarDeclar.f90*, and is used in the necessary interpolation for the minimum-loss wake momentum thickness from  $D_{eq}^*$ .

**Variation of Wake Momentum Thickness with Minimum-Loss Equivalent Diffusion Factor**

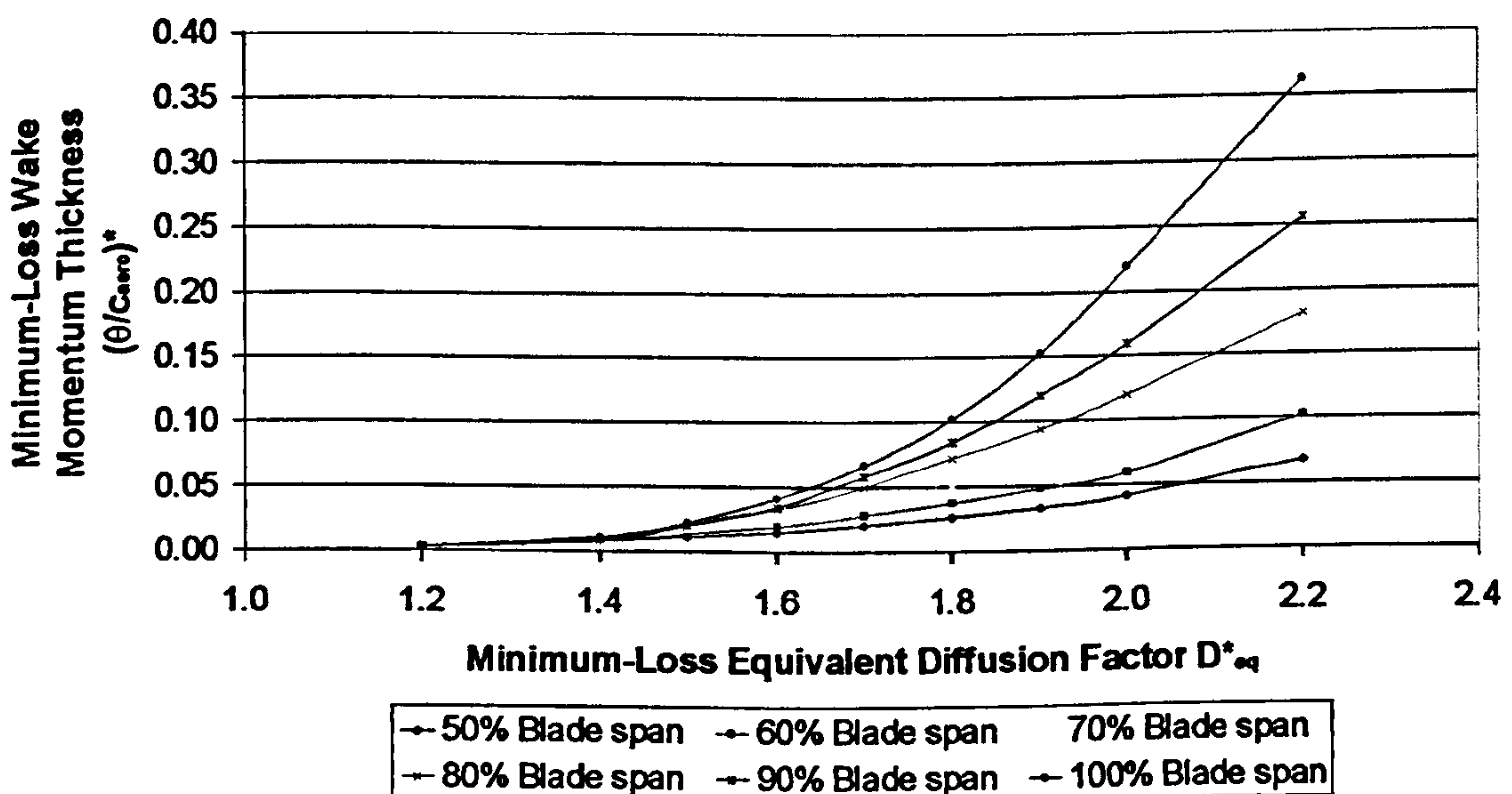


Figure 5.11.1.1: Estimated variation of wake momentum thickness with minimum-loss equivalent diffusion factor for DCA subsonic rotors (Swan, 1961)

### Limitations and Potential Expansion

There are no analytical methods other than those based on the Reynolds-Averaged Navier-Stokes equations, for the calculation of blade losses. Instead, empirical correlations are used, deduced from experimental results. As it is known, empirical correlations are very dependent on the experiment's conditions. Consequently, one should be very cautious when applying these correlations to different geometries. For example, if the wake momentum thickness correlation comes from experimental data of a single rotor, or a stationary single row cascade, when applied to a multistage compressor in order to calculate the loss coefficient, the results would be different. That would happen because the wake would be truncated by the downstream rotor and the wake mixing process would not have enough space to be completed.

It is the author's view that there is no loss model without limitations or at least without a given restricted range of applicability. For example, Lieblein's correlations were derived from low-speed, two-dimensional cascade experiments. One needs to have in mind that the losses of blades operating inside a compressor behave quite differently to that in cascades. Also the approximation of the blade profile loss coefficient being equal to twice the wake momentum thickness in Equation 5.11.1.8 is only valid in the case of a fully attached flow. Swan's correlations address the problem of the three-dimensionality of the flow field but still the flow needs to be kept subsonic for a reasonable control on data scatter to be maintained. Swan's loss model also assumes that losses increase continuously from hub to tip which is a rather crude approximation. Monsarrat's model assumes bigger losses close to the end walls, which is a more realistic approach, however a major drawback of his method is that his correlations are confined only to design point conditions. Oldham's model is a rather simplified one and assumes the same profile loss regardless blade radial position.

It would be an advantage for the code to offer the user several more alternative correlations, which could then be compared against experimental data (if available) to find the most adequate, given the application. Perhaps combining different loss models together would be sufficient to predict the flow field reasonably accurate. However, even this approach would need to be thoroughly experimentally tested before put in practical use.

#### **5.11.2. Loss due to Reynolds Effects**

Reynolds effects, or  $P_1$  effects as they are alternatively called, refer to the reduced compressor pressure ratio, efficiency and flow capacity due to reduced values of Reynolds number. This sub-section explains how Reynolds effects are taken into account in the *2D Compressor SLC Software* and briefly discusses the limitations of the model adopted and scope for future development.



## Introduction

It is well known that the Reynolds number is a non-dimensional quantity defined as the ratio of the inertial forces to the viscous forces within the flow. For compressor applications, the Reynolds number is defined as follows:

$$\text{Re} = \frac{W_1 c_{\text{aero}} \rho_1}{\mu_1} \quad [\text{Eq. 5.11.2.1}]$$

Where  $c_{\text{aero}}$  is the blade aerodynamic chord representing the characteristic length,  $W_1$  the air inlet relative velocity (absolute velocity  $V_1$  in the case of a stationary row),  $\rho_1$  is the fluid inlet static density and  $\mu_1$  the fluid inlet absolute viscosity.

The reduction in compressor performance depends basically on the development of the boundary layer over the blade surfaces, the magnitude of the effect depending on the magnitude of Reynolds number, the turbulence level and the pressure gradients in the flow. For Reynolds number values greater than  $5 \times 10^5$ , the flow is considered turbulent throughout the blade passage. Under such flow regimes, losses are calculated as described in the preceding sections and the Reynolds number variation has only a small impact on the overall blade profile loss. The above is a direct consequence of the boundary layer behavior. As long as the boundary layer remains turbulent, the flow separation on the blade suction surface and the generated losses associated to this phenomenon, can be adequately predicted by the profile loss models. On the contrary, as Reynolds number falls and the boundary layer is gradually transforming to laminar, flow separation will take place prematurely and the losses will be much higher than they would have been under turbulent conditions. The most common cause of Reynolds number reduction is associated to the reduced compressor inlet pressure, due to high altitude flight for instance, fact that explains the alternative name of the Reynolds number effects mentioned at the beginning.

Several researchers in the past have studied the effects of Reynolds number variation trying to establish empirical correlations for their quantitative determination. Carter, et al. (1957) suggested that the variation of losses generated from the change in Reynolds number can be assessed by making use of the following equation:

$$1 - \eta = k \text{Re}^n \quad [\text{Eq. 5.11.2.2}]$$

Where  $\eta$  is the compressor efficiency,  $k$  a proportionality constant and  $n$  the Reynolds number exponent, whose value varies according to the Reynolds number value. If  $\text{Re} > 0.5 \times 10^5$  then  $n = -0.2$ , otherwise  $n = -0.5$ .

Wassel (1968) based his study on Carter's work. He proposed the same equation adding some extra empiricism to the definition of the Reynolds number exponent  $n$  that he acquired from the vast amount of experimental data he produced. He expressed  $n$  as the quotient of  $p$  and  $q$ . Parameter  $p$  was determined by the level of mean Mach number through the compressor and  $q$  was calculated based on a geometrical non-dimensional quantity (effective length over annulus height). As a result of these, the exponent  $n$  varies significantly from compressor to compressor. Wassel's correlation proved to work well only for smooth blades, as he has not elaborated on the effect of surface roughness.

An alternative approach for including the effects of Reynolds number in profile losses is to correct the profile loss coefficient by multiplying it with a Reynolds-effects correction factor. Such a method was followed by Raw and Weir (1980) and is presented below in more detail.

### Calculation of Reynolds Effects Correction Factor

Raw adopts Sutherland's relation to calculate the fluid viscosity based on inlet properties:

$$\mu_1 = \frac{145.8187 \cdot 10^{-8} T_1^{1.5}}{110.35 + T_1} \quad [\text{Eq. 5.11.2.3}]$$

Subsequently, the Reynolds number is calculated as indicated by Equation 5.11.2.1. Based on the Reynolds number value, the Reynolds-effects correction coefficient is determined from the following equations, each one covering a certain Reynolds number range:

$$\text{If } 0.02 \leq \text{Re } 10^{-5} \leq 0.76 \text{ then } f_{\text{Re}} = -8.735294 \text{Re } 10^{-5} + 8.66888 \quad [\text{Eq. 5.11.2.4}]$$

$$\text{If } 0.76 < \text{Re } 10^{-5} \leq 2.00 \text{ then } f_{\text{Re}} = 0.3(\text{Re } 10^{-5})^2 - 1.5 \text{Re } 10^{-5} + 3.0 \quad [\text{Eq. 5.11.2.5}]$$

$$\text{If } 2.00 < \text{Re } 10^{-5} \leq 5.00 \text{ then } f_{\text{Re}} = -0.6666 \text{Re } 10^{-5} + 1.3333 \quad [\text{Eq. 5.11.2.6}]$$

$$\text{If } 5.00 < \text{Re } 10^{-5} \quad \text{then } f_{\text{Re}} = \frac{5.0}{(\text{Re } 10^{-5})^{-0.1}} \quad [\text{Eq. 5.11.2.7}]$$

The above calculation is repeated for each blade row and every streamline location.

### Implementation

The above calculation of the Reynolds-effects correction factor is handled in the *2D Compressor SLC Software* for the rotor and stator by subroutine *Compressor2D\_ReynoldsCorrectionCalc.f90*. Since the Reynolds number calculation is based only on the blade row inlet properties, this subroutine is called directly from the main program *Compressor2D\_MainProgram.f90*, before the iterative process for the outlet meridional velocity profile begins. The input data necessary for the calculation are the air inlet velocity, the inlet static temperature and density and the blade aerodynamic chord.

### Limitations and Potential Expansion

A major limitation and at the same time a potential expansion of the Reynolds number effects subroutine, is to include the effect of aerodynamic roughness. For example,



Schaffler (1979) proves through a series of compressor tests that Wassel's derived efficiency agrees to these results up to a critical Reynolds number value which is a function of roughness height. Above this value compressor efficiency remains constant. Consequently, a correlation to determine the value of the critical Reynolds number is strongly suggested to be implemented into the code. Such a correlation could well be the one proposed by Miller (1977).

$$\text{Re}_{\text{critical}} = \frac{16c_{\text{aero}}}{k_{\text{CLA}}} \quad [\text{Eq. 5.11.2.8}]$$

Where  $k_{\text{CLA}}$  is the surface roughness as determined by a Centre Line Average (CLA) method.

### 5.11.3. Calculation of Shock Losses

This sub-section describes how losses generated due to supersonic flow through the blade passages are calculated in the *2D Compressor SLC Software*. The limitations of the models adopted and scope for future development are also discussed.

#### Introduction

In the forties it was generally believed that for optimum compressor performance the flow should everywhere be maintained subsonic. The stage pressure rise was also limited resulting into an increased number of stages, for a given pressure rise requirement. This perception was therefore changed from the early fifties. Many compressors were started to be designed with transonic regions and even, some years later, completely supersonic. The philosophy has changed over the years and the important issue nowadays in compressor design is not for the shock waves to be avoided, but to be predicted concerning their position, strength and generated losses, at all operating conditions. Meridional and absolute velocities are still maintained subsonic throughout the compressor. The supersonic regions are usually located on the relative frame of reference at the highest radii of the front rotor blades. From the above it is evident that losses due to supersonic flow regions should definitely not be left out of the simulation, by a modern compressor performance prediction code.

In the case of a 'supersonic flow compressor' the flow on the relative frame of reference is supersonic across the entire blade span. A simplistic shock loss model is not adequate for compressor performance simulation, because the blade-to-blade and meridional flows are much strongly coupled together, than in a subsonic rotor. The current streamline simulation code is intended to handle only partially supersonically operating blades. In this case it is considered generally acceptable to include just a shock loss calculation model to account for the supersonic regions.

Several researchers in the past, and especially in the 1960s, experimented with compressors or cascades with supersonic inlet flows such as Bullock (1961) and Lieblein and Johnsen (1961). Shock loss prediction was very early addressed by Miller, et al. (1961). According to their research shock losses were originated from

two different sources, i.e. the shock waves themselves and the interaction of the shock waves with the boundary layer at the point of intersection between the two. The first case was referred as passage shock loss, while the second case as the profile loss discussed separately in *Subsection 5.11.1*. Miller et al. examined the entropy increase across shock waves as well as the thickening of the boundary layer (and in some cases detachment) due to the sudden compression across the shock wave plane.

From open literature it seems that most of the published methods for shock loss estimation, for example Swan (1961), Oldham (1965), Creveling and Carmody (1968) and Koch and Smith (1976), follow the classification indicated by Miller, et al. Various models are mostly differentiated as far as the shock wave pattern description is concerned. More precisely, according to the simpler methods, one normal shock is encountered sitting perpendicularly onto the blade's suction surface, extending to the leading edge of the neighboring blade. More complicated methods adopt a pattern that corresponds more to the actual conditions. They assume an extra oblique shock wave located at the blade leading edge, attached or detached according to the operating condition. Experimental research however has shown that these oblique shock waves which can propagate upstream of the blade row are comparatively weak and are essentially cancelled by the subsequent expansion waves. It is the passage shocks, stretching across from one blade to the next which produce the biggest losses.

### Description of Shock Loss Model

This work adopts the shock loss model according to Schwenk, et al. (1957). The flow is assumed to approach the blade at 'unique incidence' conditions, with the bow oblique shock attached to the leading edge and choking occurring where the flow is still supersonic, ahead of the enclosed part of the blade passage. As mentioned above, for the low Mach numbers encountered in compressor applications, the oblique shock waves are assumed to be very weak and the entropy rise across them negligible. Therefore, the bow oblique shock is neglected by this method, despite the fact that it is present, and only the normal shock is taken into account. The normal shock is assumed to stand perpendicularly to the mean streamline, mid-way between two consecutive blades. This is only assumed for simplicity, because in practice its exact position should be determined through an iterative procedure.

According to Figure 5.11.3.1, which refers to the absolute frame of reference, conditions at blade row inlet are denoted by 1 whereas A and B are the intersection points of the normal shock with the blade leading edge and suction surface respectively. According to Prandtl-Meyer relation, it holds that:

$$v_B(M_B) - v_A(M_A) = \tau \quad [\text{Eq. 5.11.3.1}]$$

Where  $\tau$  is the flow turning angle and  $v$  is the Prandtl-Meyer function, given in its general form by the following equation:

$$v(M) = \sqrt{\frac{\gamma+1}{\gamma-1}} \tan^{-1} \sqrt{\frac{\gamma-1}{\gamma+1} (M^2 - 1)} - \tan^{-1} \sqrt{M^2 - 1} \quad [\text{Eq. 5.11.3.2}]$$



Consequently:

$$\tau = v_B - v_A = \sqrt{\frac{\gamma+1}{\gamma-1}} \tan^{-1} \sqrt{\frac{\gamma-1}{\gamma+1} (M_B^2 - 1)} - \tan^{-1} \sqrt{M_B^2 - 1} - \sqrt{\frac{\gamma+1}{\gamma-1}} \cdot \tan^{-1} \sqrt{\frac{\gamma-1}{\gamma+1} (M_A^2 - 1)} + \tan^{-1} \sqrt{M_A^2 - 1} \quad [\text{Eq. 5.11.3.3}]$$

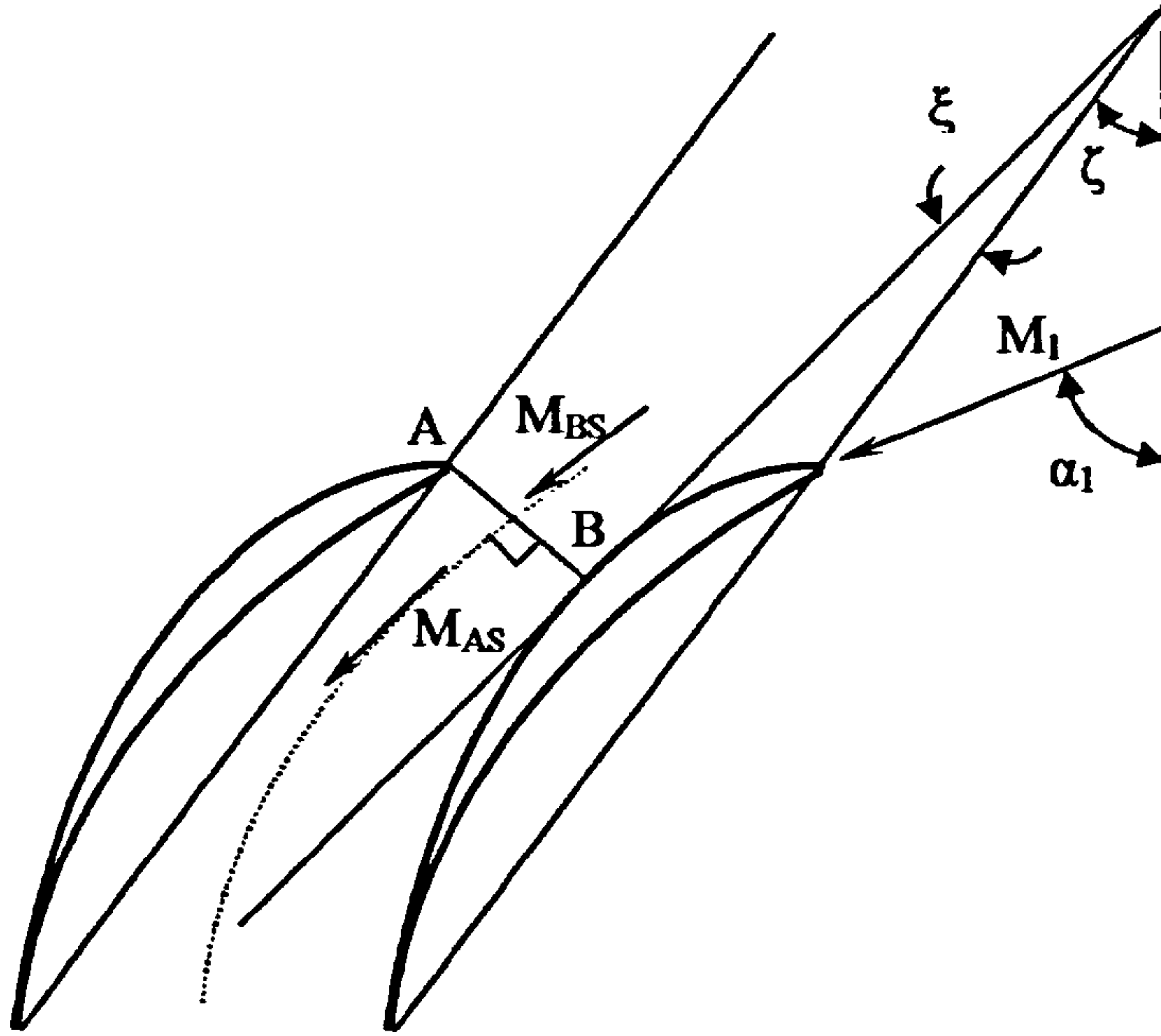


Figure 5.11.3.1: Flow turning angle calculation

$M_A = M_1$  because point A is located at the blade row inlet plane. Therefore, once the blade row inlet Mach number is fixed the  $v_A$  function is also fixed and can be easily determined. Solving Equation 5.11.3.3 with respect to  $M_B$  we get the following expression:

$$M_B = \sqrt{1 + \left[ \frac{\sqrt{\frac{\gamma+1}{\gamma-1}} \tan \frac{\tau + v_A + \tan^{-1} \sqrt{M_B^2 - 1}}{\sqrt{\frac{\gamma+1}{\gamma-1}}}}{\sqrt{\frac{\gamma+1}{\gamma-1}}} \right]^2} \quad [\text{Eq. 5.11.3.4}]$$

From the above equation  $M_B$  is calculated iteratively. The flow turning angle according to Figure 5.11.3.1 equals:

$$\tau = \alpha_1 - \zeta + \xi \quad [\text{Eq. 5.11.3.5}]$$

Where  $\zeta$  is the stagger angle and  $\xi$  is defined as follows:

$$\xi = \sin \left( \left( \frac{2x}{c'} - 1 \right) \sin \left( \frac{\phi_s}{2} \right) \right) \quad [\text{Eq. 5.11.3.6}]$$

Where:

$$c' = c_{aero} - 2r_b \quad [\text{Eq. 5.11.3.7}]$$

$$\phi_s = 4 \tan^{-1} \left( \frac{1 - \cos \frac{\theta}{2}}{\sin \frac{\theta}{2}} + \frac{t_{blade\_max} - 2r_b}{c'} \right) \quad [\text{Eq. 5.11.3.8}]$$

Where  $t_{blade\_max}$  is the maximum blade thickness and  $r_b$  is the leading edge radius.

$$\frac{2x}{c'} = 1 + \sin 2\Sigma \cot \frac{\theta}{2} - \cos 2\Sigma \quad [\text{Eq. 5.11.3.9}]$$

Where  $\Sigma$  equals:

$$\Sigma = \tan^{-1} \left( \frac{\sin k_1 \sin \frac{\theta}{2}}{\frac{c'}{s} + \cos k_1 \cdot \sin \frac{\theta}{2}} \right) \quad [\text{Eq. 5.11.3.10}]$$

Where  $k_1$  the blade inlet angle.

$M_B$  is the Mach number before the normal shock. According to the model it is assumed that the flow is decelerated across the normal shock from the average value of  $M_1$  and  $M_B$  to the Mach number indicated by the corresponding Prandtl – Meyer tables for shock waves. Therefore, the Mach number before the normal shock equals:

$$M_{BS} = \frac{M_B + M_1}{2} \quad [\text{Eq. 5.11.3.11}]$$

And the Mach number after the normal shock equals:

$$M_{AS} = \sqrt{\frac{(\gamma - 1)M_{BS}^2 + 2}{2\gamma M_{BS}^2 - (\gamma - 1)}} \quad [\text{Eq. 5.11.3.12}]$$

The loss in total pressure across the shock, according to the general definition of the loss coefficient, is non-dimensionalised by the inlet pressure dynamic head, to give the shock loss coefficient:

$$\bar{\omega}_{sh} = \frac{P_{01} - P_{0B}}{P_{01} - P_1} \quad [\text{Eq. 5.11.3.13}]$$

From the isentropic relation it is known that the ratio of the total to static pressure equals:



$$\frac{P_{01}}{P_1} = \left(1 + \frac{\gamma-1}{2} M_1^2\right)^{\frac{\gamma}{\gamma-1}} \quad [\text{Eq. 5.11.3.14}]$$

Also according to normal shock wave relations the ratio of the total pressure before the shock to the free stream static pressure equals:

$$\frac{P_{0B}}{P_1} = \frac{\left(\frac{\gamma+1}{2} M_{BS}^2\right)^{\frac{\gamma}{\gamma-1}}}{\left(\frac{2\gamma M_{BS}^2 - (\gamma-1)}{\gamma+1}\right)^{\frac{1}{\gamma-1}}} \quad [\text{Eq. 5.11.3.15}]$$

Dividing both the numerator and denominator of Equation 5.11.3.14 with  $P_{01}$  the following expression is derived:

$$\bar{\omega}_{sh} = \frac{1 - \frac{P_{0B}}{P_{01}}}{1 - \frac{1}{\frac{P_{01}}{P_1}}} \Rightarrow \bar{\omega}_{sh} = \frac{1 - \frac{P_{0B}/P_1}{P_{01}/P_1}}{1 - \frac{1}{P_{01}/P_1}} \quad [\text{Eq. 5.11.3.16}]$$

### Implementation

Shock losses are calculated by subroutine *Compressor2D\_ShockWaveCalc.f90* for rotor and stator and at several locations along the blade span based on the procedure presented above. This subroutine is called directly from the main program *Compressor2D\_MainProgram.f90*, before the iterative process for determining the outlet meridional velocity profile begins. The input data necessary for the calculation are the inlet Mach number and the critical Mach number as well as the supersonic flow turning angle and the incidence and minimum loss incidence angles. The output is the shock loss factor due to the entropy increase across the shock.

All the above calculations are triggered in the case when the inlet Mach number becomes greater than the critical Mach number. The critical Mach number is defined as the value of the inlet Mach number, which will result to supersonic conditions at the passage throat (see *Section 5.8*).

### Limitations and Potential Expansion

Shock wave patterns within and around the blade passages are three dimensional and are affected by a number of geometrical and flow parameters, meaning that their strength and positions vary according to the operating conditions. At present the magnitude of the shock losses cannot be reliably predicted, even by the methods based on the Navier-Stokes set of equations. Although good estimates of the actual flow patterns are extracted from such methods, shear stresses cannot be accurately

described by the available turbulence models. Consequently, one should not be completely relying, at least quantitatively, on the results of whichever shock model is applied.

Research has shown that the traditional, two-dimensional approach can overestimate the losses generated by shock waves that appear to be nearly normal to the blade suction surface. Therefore, a potential improvement would be the implementation of an iterative procedure with the intention to determine more accurately the position and the inclination of the normal shock, according to the cascade solidity, camber, staggering and inlet flow conditions.

Although losses attributed to bow oblique shock waves are considered to be comparatively small, they should be included in the calculations for a more accurate loss prediction at any operating condition. Generally speaking, more correlations should be programmed and be given as potential options to the user. In the case where experimental data are available, the user should be able to select the most appropriate model, for the specific compressor under simulation, or even switch between different loss models according to the operating conditions.

#### ***5.11.4. Calculation of Secondary Loss***

As discussed before, boundary layer effects are usually taken into account by introducing some approximate correlations or correction factors derived from two-dimensional cascade tests or from inviscid flow theory. Boundary layers in blade rows of actual turbomachines exhibit certain differences from two-dimensional boundary layer theory which is incapable of analysing lateral variations of the main flow and the associated boundary layers i.e. secondary flows. Secondary losses of compressor blade rows account for a large portion of the total pressure loss. This sub-section describes how blade secondary flow losses are calculated in the *2D Compressor SLC Software*. The limitations of the models adopted and scope for future development are also discussed.

##### **Introduction**

Secondary flows are basically boundary layer flows having components in other than the mainstream direction that can result in the displacement and accumulation of momentum-deficit fluid. They can be attributed to the relative motion between blade ends and casing walls, centrifugal force effects, blade tip clearance effects and blade-to-blade and radial pressure gradients. The secondary loss is a measure of the secondary flow kinetic energy. The flow that moves at right angles with respect to the direction of the primary flow is usually defined as secondary flow and is directly dependent on flow vorticity and circulation and also on the flow static pressure field. For the kinematic investigation of the secondary flow field it is enough to know either of the two.

Vorticity is conveyed by the flow and diffused within it. The first is an inviscid flow phenomenon, whereas the second comes as a result of the flow viscosity. Vorticity transport counts for a much bigger percent for vorticity overall movement and what is



generally referred to as secondary flow theory, represents only the inviscid contributor on vorticity movement. In other words, it is only applicable outside the boundary layer that is in regions where the shear stresses are small in relation to the pressure gradients.

In most of the cases it is also assumed that secondary velocities are relatively small in magnitude, when compared to the main stream velocities and therefore vorticity transport is not affected by them.

Traditionally, the theoretical research on boundary layers and secondary flows has been concerned with steady incompressible flows that can be described in their most general form by the Navier-Stokes equations. In practice however, and as far as real aerodynamic problems is concerned, the set of Navier-Stokes equations needs to be greatly simplified if a solution to the complete set of equations is to be obtained. In fact, even for relatively simple three-dimensional configurations, several analyses still require the application of numerical methods to obtain solutions.

In the case of inviscid secondary flow research, two reports have become classical references i.e. the works of Squire and Winter (1949) and Hawthorne (1953). Squire and Winter starting from the equations of motion, conservation of vorticity and continuity of mass flow, first examined the vorticity transport and derived a Poisson's type of equation for the cross-flow stream function. Hawthorne derived an equation for secondary flow field determination commencing from the alternative starting point which is the static pressure gradients within the flow passage. The above theories provided a very good insight and understanding of secondary flow although they can only be used to indicate qualitative trends rather than to provide trustful quantitative results.

Concerning the secondary loss, Howell (1945) was one of the first to refer to them, but as a part of the end-wall loss. The counterpart was what he called the annulus loss due to the flow friction on the walls. The secondary loss was taken to be related to the reduction in blade circulation at the blade trailing edge. He also assumed that it is only dependent on the amount of flow turning within the blade passage. Squire's and Winter's secondary flow theory analysis also showed clearly the stream-wise vorticity component appearing due to the flow turning.

Griepentrog offered a similar approach for the secondary loss determination focusing on the drag generated by the trailing edge vorticities.

### Description of Secondary Loss Models

Griepentrog's and Howell's models are described here for the relative frame of reference. Griepentrog's method takes advantage of correlated data between the fraction of the secondary losses to the total losses:

$$f_{\text{sec}} = \frac{\overline{\omega_{\text{sec}}}}{\overline{\omega_{\text{tot}}}} \quad [\text{Eq. 5.11.4.1}]$$

Against the following geometrical parameter:

$$\frac{c_{aero}}{h_{mean}} \quad [\text{Eq. 5.11.4.2}]$$

Where  $h_{mean}$  is the blade mean height,  $c_{aero}$  the blade cord and  $\theta$  the blade camber angle. The blade mean height is calculated as the arithmetic average of the blade row inlet and outlet height.

$$h_{mean} = \frac{h_1 + h_2}{2} \quad [\text{Eq. 5.11.4.3}]$$

At each streamline position at the blade row outlet plane, the geometrical parameter, as defined above by Equation 5.11.4.2, is determined and the corresponding  $f_{sec}$  quantity is interpolated from the given input table data. Finally, the secondary loss coefficient is calculated as follows:

$$\bar{\omega}_{sec} = \bar{\omega}_{tot} \left( \frac{f_{sec}}{1 + f_{sec}} \right) \quad [\text{Eq. 5.11.4.4}]$$

To a good approximation, the total loss coefficient can be assumed equal to the blade profile loss and shock loss coefficients.

According to Howell's method, first a relative air mean angle is defined, as the arithmetic average between the air inlet angle and the air outlet angle.

$$\beta_{mean} = \frac{1}{2}(\beta_1 + \beta_2) \quad [\text{Eq. 5.11.4.5}]$$

The blade lift coefficient is calculated as follows:

$$C_{L\_blade} = \frac{2 \cos \beta_{mean}}{\sigma} (\tan \beta_1 - \tan \beta_2) \quad [\text{Eq. 5.11.4.6}]$$

The secondary flow drag coefficient is related to the square of the blade lift coefficient multiplied by 0.18.

$$C_{D\_sec} = 0.18 C_{L\_blade}^2 \quad [\text{Eq. 5.11.4.7}]$$

Finally, the secondary loss coefficient equals:

$$\bar{\omega}_{sec} = \sigma \left( \frac{\cos \beta_1}{\cos \beta_2} \right)^2 C_{D\_sec} \quad [\text{Eq. 5.11.4.8}]$$



### Implementation

Both methods are available to the user who can select to employ either of them by means of a switch. Secondary losses are calculated for the rotor only, by subroutine *Compressor2D\_SecondaryLossCalc.f90*. This subroutine is repeatedly called by subroutine *Compressor2D\_BladeRowOutletMeridVelDistribGener.f90* in sequence after blade profile and shock losses have been established and while the radial equilibrium equation is being iteratively solved at the blade row outlet. The aim is to calculate the blade secondary loss at various locations from hub to tip (nodes), depending on the number of streamlines, so that the total loss factor can be established later on.

**Griepentrog's Secondary Loss Factor Variation**

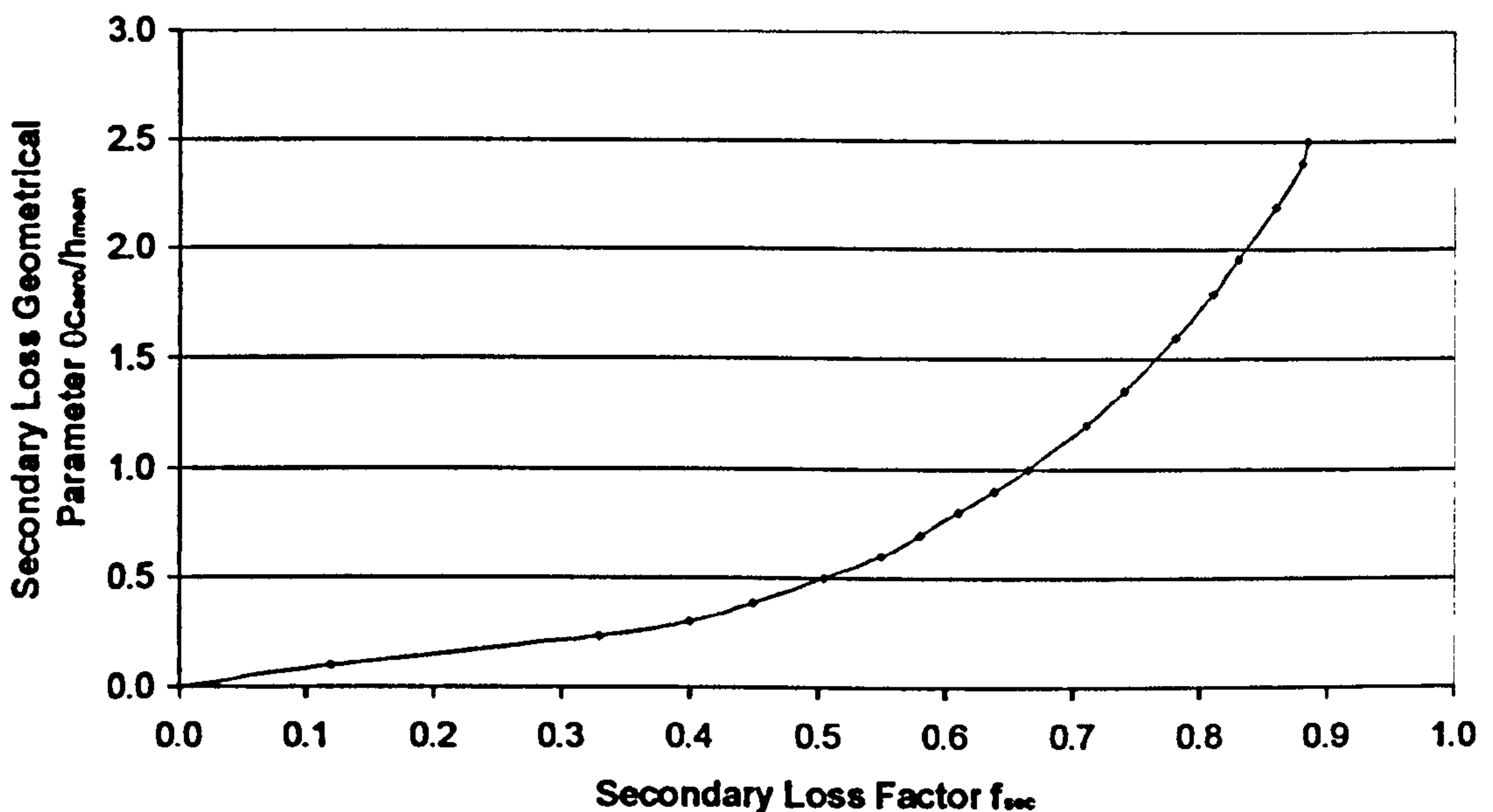


Figure 5.11.4.1: Griepentrog's secondary loss factor variation with geometric parameter

The input variables to the subroutine are the air angles and certain geometrical characteristics of the blade row cascade. The output is the secondary loss coefficient. Moreover, Figure 5.11.4.1 is stored as array tabular data in module *Compressor2D\_SecondaryLossVarDeclar.f90*, and is used in the necessary interpolation for  $f_{sec}$  according to Griepentrog's model.

### Limitations and Potential Expansion

The only known limitation inherent to the correlations presented above is perhaps the reduced accuracy in the case of highly loaded blades. However, looking at the literature available on secondary flow theory, it becomes evident that only a very basic understanding of the flow behavior has been achieved so far. Expressing secondary flows and three-dimensional boundary layer effects mathematically has been extremely difficult and empirical correlations developed over the years have been restricted to predicting 'orders of magnitude' of the various quantitative aspects

of the flow. Experimental studies and correlations, at best, can indicate how secondary flows may occur in simple compressor configurations and can be used as a basis for constructing more comprehensive loss models. When applied with caution, the results could be used in predicting blade row losses to a good approximation.

This subroutine may be expanded to include a potential flow calculation, in order to predict the vorticity transport within the blade row passage and thus determine more accurately the secondary velocities. Unfortunately even in this case, the weakness of the calculations for highly loaded blades will persist, because potential flow cannot handle flow separation.

Alternatively, secondary losses could be broken down to the various different causes of loss described in the introduction above. For example a tip clearance loss model for rotor blades could be implemented as per Aungier (2003, p. 146-147). A leakage flow is produced through the blade clearance gap due to the pressure difference on the two sides of the blades. The pressure difference across the blades must balance the blade torque  $\tau_{blade}$  expressed as:

$$\tau_{blade} = \pi \delta_c [(r \rho V_m)_1 + (r \rho V_m)_2] (r_2 V_{w,2} - r_1 V_{w,1}) \quad [\text{Eq. 5.11.4.9}]$$

Where  $\delta_c$  is the tip clearance. The average pressure difference across each blade in the blade row is given by:

$$\Delta P_o = \frac{\tau_{blade}}{N_{blade} r_{tip} \delta_c c_{geom} \cos \gamma} \quad [\text{Eq. 5.11.4.10}]$$

Where  $N_{blade}$  is the number of blades in the blade row. The velocity of the leakage flow can be found empirically from:

$$V_{leakage} = 0.816 \sqrt{\frac{2 \Delta P_o}{\rho}} \frac{1}{N_{row}^{0.2}} \quad [\text{Eq. 5.11.4.11}]$$

Where  $N_{row}$  is the number of blade rows.

The leakage mass flow rate can be determined by:

$$\dot{m}_{leakage} = \bar{\rho} V_{leakage} N_{blade} \delta_c c_{geom} \cos \gamma \quad [\text{Eq. 5.11.4.12}]$$

Finally, the clearance gap total pressure loss for the entire blade row can be calculated directly from:

$$\Delta P_{o\_leakage} = \frac{\Delta P_o \dot{m}_{leakage}}{\dot{m}} \quad [\text{Eq. 5.11.4.13}]$$



**CHAPTER VI****2D INTAKE AND DUCT FLOW MODELLING**

Although the intake flow field is less complex compared to the compressor flow field due to the absence of rotating parts, it is still three-dimensional, turbulent and viscous. An inviscid through-flow analysis method, however, in which viscosity effects are taken into account by means of empirical models and correlations, can offer sufficient accuracy. The scope of this chapter is to explain in detail the theoretical background of the streamline curvature through-flow analysis method and of the various empirical models adopted by this work for the modeling of conical and annular intakes and ducts.

**6.1. Intake Streamline Curvature Equations**

Similarly to the compressor, the flow field in the intake is considered as axisymmetric, compressible and inviscid. The analysis described in this section makes use of the streamline curvature equations, which represent a natural formulation of the equations for this type of flow field. The streamline curvature equations, as used in the present analysis, represent a form of the exact, compressible, inviscid flow equations. The method is therefore applicable from low subsonic to supersonic speeds.

The intake flow field is much less complicated compared to the compressor flow field due to the absence of stationary and rotating blade rows, blade forces and strong radial and circumferential gradients in flow properties. Potential use of the full, non-linear, partial differential, radial equilibrium equations, as in the case of the compressor, to resolve a relatively simple flow field problem has limited scope since it introduces unnecessary complexity as well as increased computational time.

This work adopts the same philosophy for calculating the meridional flow field in subsonic and transonic intakes and ducts as presented by Barger (1973). Neglecting the circumferential component of velocity, the compressible inviscid streamline curvature equations for axisymmetric flow inside ducts can be reduced to the following three basic relationships.

i) The continuity equation in integrated form:

$$\dot{m} = 2\pi \int_0^n \rho V_{o,m} r \, dn \quad [\text{Eq. 6.1.1}]$$

Where  $n$  is the normal distance between two adjacent streamlines, and  $V_{o,m}$  is the total meridional velocity given by:

$$V_{o,m} = \frac{V_m}{\sqrt{T_o}} = M_m \left[ \frac{\sqrt{\gamma R}}{\sqrt{1 + \left(\frac{\gamma-1}{2}\right) M_m^2}} \right] \quad [\text{Eq. 6.1.2}]$$

ii) The velocity equation:

$$V_{o,m} = V_{o,m_{cl}} \exp\left(\int_0^n \alpha \, dn\right) \quad [\text{Eq. 6.1.3}]$$

Where  $V_{o,m_{cl}}$  is the center-line total meridional velocity.

iii) And the streamline curvature given by:

$$\alpha = \frac{d\varepsilon}{dm} \quad [\text{Eq. 6.1.4}]$$

The streamline slope angle  $\varepsilon$  is calculated as follows:

$$\varepsilon = \arctan\left(\frac{dr}{dz}\right)_{merid} \quad [\text{Eq. 6.1.5}]$$

Consequently, considering two consecutive streamlines  $j$  and  $j-1$ , the velocity distribution on the  $j^{\text{th}}$  streamline is determined by the following approximation, which is basically a simplified form of the full radial equilibrium equation derived in Section 5.1:

$$V_{o,m_j} = V_{o,m_{j-1}} e^{\bar{\alpha} \Delta n} \quad [\text{Eq. 6.1.6}]$$

The mass flow between streamlines is estimated by:

$$\Delta \dot{m} = 2\pi r \overline{\rho V_{o,m}} \Delta n \quad [\text{Eq. 6.1.7}]$$

### Effect of Swirling Inlet Flow

The purpose of this subsection is to briefly discuss the effects of swirl, qualitatively only. Perhaps the most significant effect of swirl is that it tends to change the pressure distribution by giving rise to radial pressure gradients which interact with the axial flow. Experiments have shown that pressure recovery generally tends to increase as the inlet swirl angle increases up to a maximum value, where swirl is in the range of 7 to 15 degrees. This phenomenon of course is not so simple and seems to depend strongly on diffuser semi-angle  $\phi$  and the thickness of the inlet boundary layer which may cause the pressure recovery to initially decrease with increasing swirl. Moreover,



the magnitude of inlet swirl may affect the transitional stability of wall boundary layers and significantly alter the flow separation patterns.

The equations listed above do not account for inlet swirl. The effects of swirl on intake flow angle, pressure recovery and boundary layer stability could potentially be incorporated by means of a separate model, as in the case of intake pressure losses. Although several researchers, such as Bardina, et al. (1982), Srinath (1968) and Markowski, et al. (1978), have examined the effects of swirl in intakes and diffusers, no adequate computational models could be found in the available literature by the author.

Very simplistically, the intake outlet swirl angle can be calculated from the inlet value assuming that the intake is basically a large diffuser without any severe flow separation and with the angular momentum approximately conserved throughout. In that case the mean exit swirl angle can be related to the inlet value as shown in ESDU Item No. 76027 (1976):

$$\psi_2 = \psi_1 \frac{A_2}{A_1} \quad [\text{Eq. 6.1.8}]$$

## 6.2. Calculation of Intake Pressure Recovery

This section deals with how pressure losses in axi-symmetric intakes operating in subsonic flows are taken into account in the *2D Intake SLC Software*. The following subsections address different sources of pressure loss individually and explain how these are subsequently combined in order to calculate the overall intake pressure recovery. The limitations of the various models adopted and scope for future development are also discussed.

### Introduction

The flow field inside an intake, although highly viscous and three-dimensional is much less complex compared to the flow field inside a compressor annulus. Therefore, it is fair to say that calculating the pressure recovery of an intake is a relatively straight forward calculation compared to calculating pressure losses in compressors. The pressure recovery  $\eta_{\text{intake}}$  of an intake is generally defined as the ratio of the area-averaged total pressure at the engine face  $\overline{P_{o,eng}}$  divided by the free-stream total pressure  $P_{o,\infty}$ .

$$\eta_{\text{intake}} = \frac{\overline{P_{o,eng}}}{P_{o,\infty}} \quad [\text{Eq. 6.2.1}]$$

Usually, gas turbine performance simulation software uses simple one-dimensional equations to calculate the pressure recovery, assuming for simplicity uniform flow properties across any intake section. In many cases, the pressure recovery is even

taken as a fixed percentage of the total pressure available in the free-stream at both design-point and off-design conditions.

There are several factors that contribute to the generation of losses in an intake whose magnitudes can vary radially and circumferentially with intake geometry and according to operating conditions. For example, losses can be the result of flow separation occurring on sharp lips or in the case of well rounded lips with attached flows, losses can be associated with the boundary layer growth on the diffuser walls. Generally speaking, losses tend to increase the entropy and reduce the total pressure. The exact mechanisms through which intake losses are generated and their interactions have been thoroughly researched and understood since the late 50s.

Similarly to the compressor, the standard approach for more detailed studies considers that different types of intake loss are independently generated and can be analytically related to the resulting deficit in total pressure. To a good estimation, the total loss in an intake can be typically established by properly adding together, and correcting for three-dimensional effects, various loss factors. As stated before, the largest limitation of this approach is that the various empirical correlations can not be expected to sufficiently represent every individual intake design. A generic model for all intakes is rather unrealistic and the success or failure of this approach really depends on in-house expertise which allows for the incorporation of suitable correction factors that can bring a particular model closer to reality.

This work adopts a similar approach to intake pressure recovery calculation as the one-dimensional calculation procedure outlined in detail in ESDU Item No. 80037 (1980) for axi-symmetric intakes at subsonic speeds, converted however into a two-dimensional calculation. It is assumed that the total pressure loss of the intake is the result of the interaction of two different loss components, which are considered to act through independent mechanisms. The loss associated with flow separations, which can occur at the lip for some combinations of intake mass flow, lip geometry and incidence angle, and the loss associated with the diffuser, which results mainly from the boundary-layer growth on the diffuser walls and the effect of the pressure gradient imposed on it by the flow diffusion. The diffuser loss is significantly influenced by the state of the boundary layer at the entry to the diffuser. Therefore, the interaction effect between the entry flow and the diffuser is also taken into account together with the pressure loss in any constant section duct which may be present in the intake.

The intake pressure recovery is calculated by:

$$\eta_{\text{intake}} = 1 - \Delta\eta_{\text{lip}} - \Delta\eta_{\text{diff}} N_{\text{mag}} - \Delta\eta_{\text{csd\_upstr}} - \Delta\eta_{\text{csd\_dwstr}} \quad [\text{Eq. 6.2.2}]$$

Where  $\Delta\eta_{\text{lip}}$  is the loss in pressure due to intake lip flow separation.  $\Delta\eta_{\text{diff}}$  is the diffuser loss assuming no interaction between the entry flow and the diffuser and  $N_{\text{mag}}$  is a magnification or scaling factor that accounts for the interaction between the entry flow and the diffuser loss.  $\Delta\eta_{\text{csd\_upstr}}$  and  $\Delta\eta_{\text{csd\_dwstr}}$  are factors that account for the loss due to any lengths of constant-section duct which may be present upstream and downstream of the diffuser respectively.



### Implementation

The calculation of the final pressure recovery value is handled in the *2D Intake SLC Software* by subroutine *Intake2D\_PressureRecoveryCalc.f90*. The values of individual pressure loss factors, magnification factors and corrections are calculated separately by corresponding subroutines and then past to *Intake2D\_PressureRecoveryCalc.f90* for the calculation of the overall intake pressure recovery.

In order to establish a more realistic intake outlet pressure profile, it is assumed that the overall pressure loss in the intake is concentrated within the boundary layer regions of the lip and cone. Therefore, the overall intake pressure loss is subsequently divided into a cone pressure loss and lip pressure loss according to the boundary layer displacement thickness of the cone and lip respectively.

### Limitations and Potential Expansion

The above approach of dividing the overall intake pressure loss into two parts, based on the boundary layer displacement thicknesses of the cone and lip is a rather simple one. Ideally, an iterative loop should be employed in order to take into account the progressive drop in pressure along the length of the boundary layer and how this would in turn affect the displacement thickness of the boundary layer and overall pressure loss. Implementing this however, would involve a lot of sophisticated programming and would increase the computational complexity and time enormously, without really changing the intake's performance considerably, given that typical intake pressure recovery values change very little at off-design conditions.

The following sub-sections explain in detail how individual pressure loss factors and correction factors are calculated and implemented in the *2D Intake SLC Software*. References to specific past research work on intake pressure recovery losses are also provided in the following subsections.

#### **6.2.1. Calculation of Lip Pressure Recovery Loss**

This section discusses briefly the phenomenon of lip pressure recovery loss and describes how losses in pressure recovery due to the presence of different intake lip configurations are calculated in the *2D Intake SLC Software*. The limitations of the procedure adopted and scope for future development are also discussed.

### Introduction

Military aircraft usually employ thin, sharp lips in order to avoid the large drag penalties associated with blunt lips at supersonic speeds. On the contrary, civil aircraft employ well-rounded lips in order to minimise flow separation at low speeds and high angles of attack usually encountered during takeoff and landing. Being able to predict the performance characteristics of sharp and rounded lips in the low speed range as

well as at transonic and supersonic speeds is of paramount importance. As a result of the efforts of a number of researchers, considerable information is now available for the design and performance analysis of intake systems operating efficiently either at subsonic or supersonic speeds.

Fradenburgh and Wyatt (1954), experimenting with a sharp-lip supersonic inlet model established a method for estimating the characteristics of sharp-lip intakes applicable from zero to supersonic speeds. Based on a simple momentum balance consideration, they derived a correlation for calculating the loss in total pressure from the difference in momentum between the free-stream and inlet planes. Their work showed that sharp lip intake performance may be severely penalised at velocity ratios  $\rho_1 V_1 / \rho_\infty V_\infty$  other than 1.0. At lower velocity ratios an additive drag component is generated that is not cancelled by lip suction as in the case of rounded lips. At higher velocity ratios, losses in total pressure may increase due to flow separation in the inlet.

Blackaby and Watson (1954) investigated the effects of inlet lip bluntness and profile on diffuser performance and body drag. They carried out a series of low-speed wind tunnel tests of a sharp inlet lip profile in addition to five circular-arc and two elliptical profiles at zero incidence. Tests conducted for mass flows from zero up to choking, showed that for lips of moderate bluntness, an elliptical profile provides better pressure recovery than a circular profile. The sharp lip provided the poorest pressure recovery for mass-flow ratios  $m_1/m_\infty$  greater than 1.0 throughout the Mach number range tested. The experimental data obtained by Blackaby and Watson showed that the correlation by Fradenburgh and Wyatt tends to underestimate the loss in total pressure at high inlet Mach numbers. A correction factor is provided in ESDU Item No. 80037 (1980), derived from their measured data, to be applied to the loss in total pressure predicted by Fradenburgh's and Wyatt's relationship.

Similarly, Mossman and Anderson (1954) experimented with four lips of varying degrees of bluntness at Mach numbers of 0.0 to 1.5 and incidence angles of 0.0 to 12 degrees. Blunting the lip, generally led to an increase in pressure recovery at all speeds tested and especially at take-off conditions. On the other hand, a more blunt lip resulted in a considerable increase in drag at supersonic conditions.

Continuing the same research effort, Milillo (1954) looked into the mass flow and pressure recovery performance of a conical-shock inlet and a nose inlet with three lip shapes, a sharp lip, a round lip and a bell-type lip. He also proved that the performance of the sharp-lipped intakes was quite similar and inferior to that of the other two intake designs. Rounding the lip of the intake inlet led to increased pressure recoveries and choking mass flow ratios, especially in the case of the bell-type lip. A separation bubble was observed in the case of the sharp-lip inlets that reduced the effective flow area and increased losses.

One could safely conclude that in the case of rounded lips, two flow phenomena tend to reduce the loss in total pressure compared to that obtained with sharp lips at the same operating conditions. Firstly, separation of flow on rounded lips seems to be delayed until velocity ratios much higher than unity are reached and may be completely suppressed if the entry contraction ratio is large enough. Secondly, rounded lips with flow separation tend to recover some of the deficit in thrust as



mentioned before. Therefore, the effect of the loss in pressure recovery tends to be less pronounced compared to that for sharp lips at the same operating conditions.

### Calculation of Loss in Pressure Recovery due to Sharp Lips

This work adopts Fradenburgh's and Wyatt's model for predicting the loss in pressure recovery for sharp lips. When the inlet velocity ratio  $\rho_1 V_1 / \rho_\infty V_\infty$  is less than unity, the total pressure at the intake inlet is equal to the free-stream value, the flow will generally remain attached on the intake lip and the pressure recovery will be equal to 1.

For a sharp lip and  $\frac{A_\infty}{A_1} < 1$ :

$$\eta_{lip} = \frac{\overline{P_{o,1}}}{P_{o,\infty}} = 1.0 \quad [\text{Eq. 6.2.1.1}]$$

For velocity ratios greater than one, the flow will normally separate on the inner surface of the lip resulting in a loss in total pressure. The pressure recovery can be obtained from momentum and mass flow continuity relations, as shown below.

For a sharp lip and  $\frac{A_\infty}{A_1} > 1$ , it holds from momentum balance that:

$$\gamma P_1 M_1^2 A_1 + (P_1 - P_\infty) A_1 = \gamma P_\infty M_\infty^2 A_\infty \quad [\text{Eq. 6.2.1.2}]$$

From continuity it holds that:

$$P_1 \left( M \frac{\alpha_o}{\alpha} \right)_1 A_1 = P_\infty \left( M \frac{\alpha_o}{\alpha} \right)_\infty A_\infty \quad [\text{Eq. 6.2.1.3}]$$

Where  $\alpha_o$  is the total speed of sound and the ratio  $\alpha_o/\alpha$  is calculated from:

$$\frac{\alpha_o}{\alpha} = \left( 1 + \frac{\gamma-1}{2} M^2 \right)^{\frac{1}{2}} \quad [\text{Eq. 6.2.1.4}]$$

For a known value of free-stream Mach number, combining the last three equations yields the following expression for the pressure recovery:

$$\eta_{hp} = \frac{\left[ \frac{f(M_1)}{f(M_\infty)} \right]^{\frac{\gamma}{\gamma-1}}}{1 + \gamma M_1^2 - \gamma M_\infty M_1 \left[ \frac{f(M_1)}{f(M_\infty)} \right]^{\frac{1}{2}}} \quad [\text{Eq. 6.2.1.5}]$$

$$\text{Where } f(M) = \left(1 + \frac{\gamma-1}{2} M^2\right) \quad [\text{Eq. 6.2.1.6}]$$

The Mach number at the intake entry plane  $M_1$ , can be calculated from the entry contraction ratio and mass flow parameter at the throat. From geometry, the entry contraction ratio is given by:

$$\lambda_{\text{contr}} = \frac{A_1}{A_{\text{intake\_throat}}} \quad [\text{Eq. 6.2.1.7}]$$

For a given value of Mach number at the intake throat  $M_{\text{intake\_throat}}$ , the non-dimensional mass flow function at the intake throat  $Q_{\text{intake\_throat}}$  can be calculated as shown below:

$$Q_{\text{intake\_throat}} = \frac{M_{\text{intake\_throat}} \sqrt{\gamma}}{\left(1 + \frac{\gamma-1}{2} M_{\text{intake\_throat}}^2\right)^{\frac{\gamma+1}{2(\gamma-1)}}} \quad [\text{Eq. 6.2.1.8}]$$

The non-dimensional mass flow function at the intake inlet  $Q_1$  is given from continuity by:

$$Q_1 = \frac{Q_{\text{intake\_throat}}}{\lambda_{\text{contr}}} \quad [\text{Eq. 6.2.1.9}]$$

Then,  $M_1$  can be obtained iteratively with this value of  $Q_1$  from:

$$Q_1 = \frac{M_1 \sqrt{\gamma}}{\left(1 + \frac{\gamma-1}{2} M_1^2\right)^{\frac{\gamma+1}{2(\gamma-1)}}} \quad [\text{Eq. 6.2.1.10}]$$

According to ESDU Item No. 80037 and from experimental data obtained by Blackaby and Watson, a correction factor can be applied to the loss in total pressure predicted by Equation 6.2.1.5 as shown below:

$$\Delta \eta_{\text{sharp\_lip}} = (1 - \eta_{\text{lip}}) \left( \frac{2}{(1 - M_1^2)^{1/2}} - 1 \right) \quad [\text{Eq. 6.2.1.11}]$$

Blackaby's and Watson's experimental data included some interaction effects between the entry flow and the diffuser. Therefore, a correction factor needs to be applied to the last relationship such as the loss due to lip flow separation is given by:

$$\Delta \eta_{\text{lip}} = \Delta \eta_{\text{sharp\_lip}} (1 - F) \quad [\text{Eq. 6.2.1.12}]$$



Where  $F$  is the interaction loss factor which is established graphically from published data as a function of  $\frac{\Delta\eta_{sharp\_lip}}{M_{intake\_throat}^2}$ .

### Calculation of Loss in Pressure Recovery due to Rounded Lips

The method adopted and presented here for evaluating the total pressure loss of rounded lips reflects their special characteristics, as described in *Introduction*, and is based on measured data obtained by Blackaby and Watson, Mossman and Anderson and Milillo.

From the entry contraction ratio  $\lambda_{contr}$ , the critical area ratio  $(A_1/A_\infty)_{cr}$ , above which the lip loss is zero, can be graphically obtained from experimental data derived by Blackaby and Watson for circular and elliptical lips. For a given free stream Mach number, the non-dimensional mass flow function  $Q_\infty$  is obtained as follows:

$$Q_\infty = \frac{M_\infty \sqrt{\gamma}}{\left(1 + \frac{\gamma-1}{2} M_\infty^2\right)^{\frac{\gamma+1}{2(\gamma-1)}}} \quad [\text{Eq. 6.2.1.13}]$$

From continuity of mass flow:

$$Q_{1\_cr} = \frac{Q_\infty}{\left(\frac{A_1}{A_\infty}\right)_{cr}} \quad [\text{Eq. 6.2.1.14}]$$

The critical Mach number  $M_{1\_cr}$  at the intake inlet can then be derived iteratively from the following relationship:

$$Q_{1\_cr} = \frac{M_{1\_cr} \sqrt{\gamma}}{\left(1 + \frac{\gamma-1}{2} M_{1\_cr}^2\right)^{\frac{\gamma+1}{2(\gamma-1)}}} \quad [\text{Eq. 6.2.1.15}]$$

Similarly, for a given value of Mach number at the intake throat  $M_{intake\_throat}$ , the non-dimensional mass flow function at the intake throat  $Q_{intake\_throat}$  can be calculated as shown below:

$$Q_{intake\_throat} = \frac{M_{intake\_throat} \sqrt{\gamma}}{\left(1 + \frac{\gamma-1}{2} M_{intake\_throat}^2\right)^{\frac{\gamma+1}{2(\gamma-1)}}} \quad [\text{Eq. 6.2.1.16}]$$

The non-dimensional mass flow function at the intake inlet  $Q_1$  is given by:

$$Q_1 = \frac{Q_{\text{intake\_throat}}}{\lambda_{\text{contr}}} \quad [\text{Eq. 6.2.1.17}]$$

As in the case for sharp lips,  $M_1$  is obtained with this value of  $Q_1$  from:

$$Q_1 = \frac{M_1 \sqrt{\gamma}}{\left(1 + \frac{\gamma-1}{2} M_1^2\right)^{\frac{\gamma+1}{2(\gamma-1)}}} \quad [\text{Eq. 6.2.1.18}]$$

Finally, the loss in pressure recovery for rounded lips associated with lip flow separation is evaluated from  $M_{1\_cr}$  and  $M_1$  as follows:

$$\begin{aligned} \text{For } M_1 \leq M_{1\_cr}, \Delta\eta_{\text{round\_lip}} &= 0 \\ \text{and} & \\ \text{For } M_1 > M_{1\_cr}, \Delta\eta_{\text{round\_lip}} &= k_{\text{zero\_inc}} (\Delta\eta_{\text{sharp\_lip}} - \Delta\eta_{\text{sharp\_lip\_cr}}) \end{aligned} \quad [\text{Eq. 6.2.1.19}]$$

Where  $\Delta\eta_{\text{sharp\_lip}}$  and  $\Delta\eta_{\text{sharp\_lip\_cr}}$  are calculated as shown above for  $M_1$  and  $M_{1\_cr}$  respectively. Where  $k_{\text{zero\_inc}}$  is a constant that relates the loss for a rounded lip to that for a sharp lip. It is determined graphically from measurements as a function of entry contraction ratio at zero incidence angle.

Similarly to the sharp lip case, lip loss data used by this model have been obtained from measured data including some interaction effects between the entry flow and the diffuser. Therefore, a correction factor needs to be applied to the last relationship such as the loss due to lip flow separation is given by:

$$\Delta\eta_{\text{lip}} = \Delta\eta_{\text{round\_lip}} (1 - F) \quad [\text{Eq. 6.2.1.20}]$$

Where  $F$  is the interaction loss factor and is established graphically from published data as a function of  $\frac{\Delta\eta_{\text{round\_lip}}}{M_{\text{intake\_throat}}^2}$ .

### Implementation

The calculation of the pressure recovery loss for sharp and rounded lips is handled in the *2D Intake SLC Software* by subroutines *Intake2D\_SharpLipLossCalc.f90* and *Intake2D\_RoundedLipLossCalc.f90* respectively. Subroutine *Intake2D\_RoundedLipLossCalc.f90* includes two models for predicting lip loss on rounded lips that the user is free to select from, one for elliptical lips and another for lips of circular type. Each subroutine can be alternatively called by the main subroutine *Intake2D\_MainProgram.f90* to calculate the pressure loss of the lip according to the user's selection of lip configuration. The calculation is carried out iteratively until the entire intake flow field is established, including the boundary layer calculation.



The inputs to these subroutines are intake geometrical properties such as intake inlet and throat areas and air properties such as the inlet and throat Mach numbers. The pre-entry stream tube area and Mach number are also required as inputs to these subroutines. Moreover, several graphs, stored as array tabular data in module *LipLossVarDeclar.f90*, are fed as inputs and used in the necessary interpolations for the critical area ratio  $(A_1/A_\infty)_{cr}$ ,  $k_{zero\_inc}$  and F factors.

For example, the constant that relates the loss for a rounded lip to that for a sharp lip,  $k_{zero\_inc}$ , is determined graphically from Figure 6.2.1.1 as a function of entry contraction ratio at zero incidence angle.

**Lip Loss Factor For Rounded Lips at Zero Incidence**

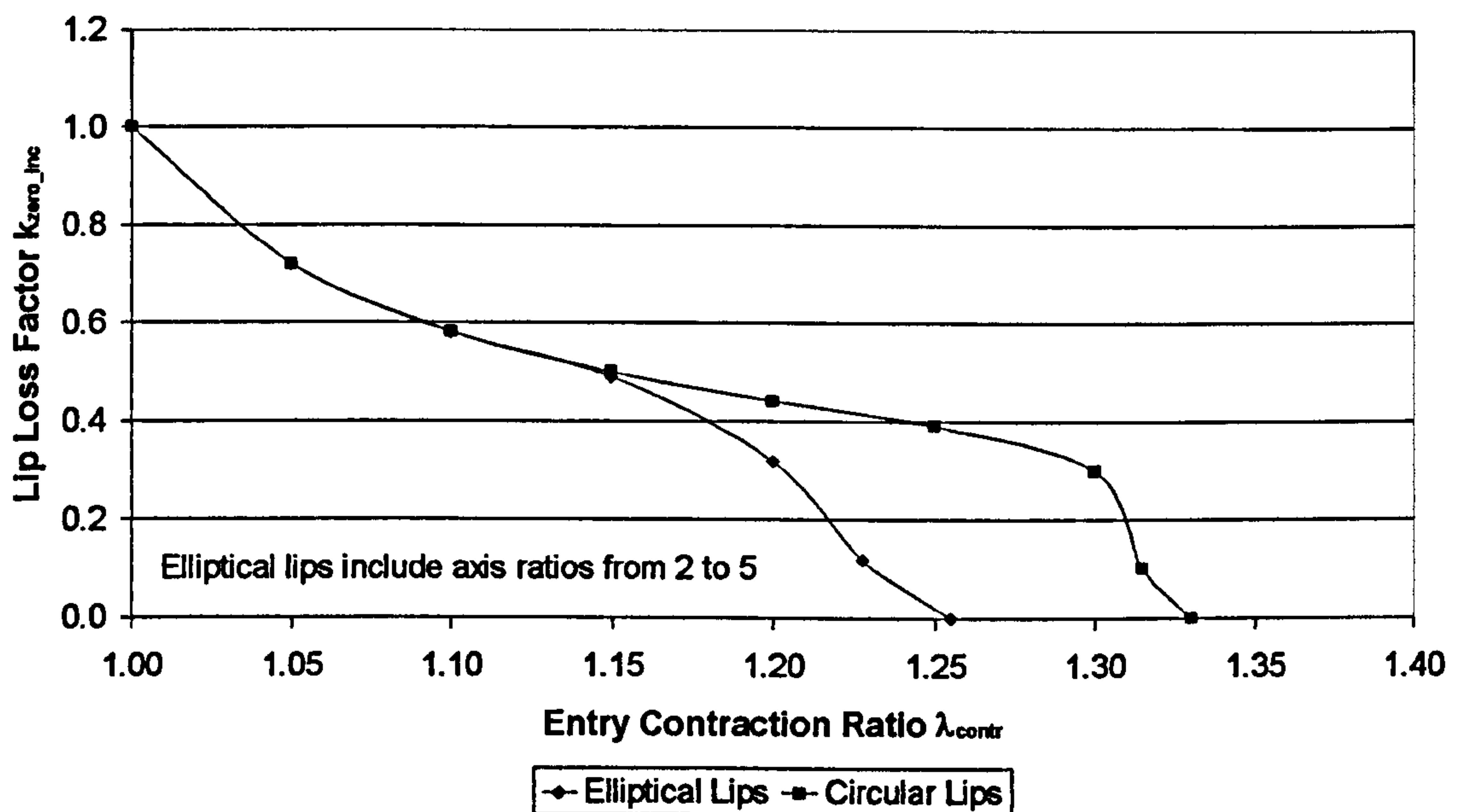


Figure 6.2.1.1: Lip loss factor for rounded lips at zero incidence

Similarly, the critical area ratio  $(A_1/A_\infty)_{cr}$ , above which the lip loss is zero, is graphically obtained from Figure 6.2.1.2, as a function of the entry contraction ratio  $\lambda_{contr}$ , for circular and elliptical lips.

Lip Loss Boundary at Zero Incidence

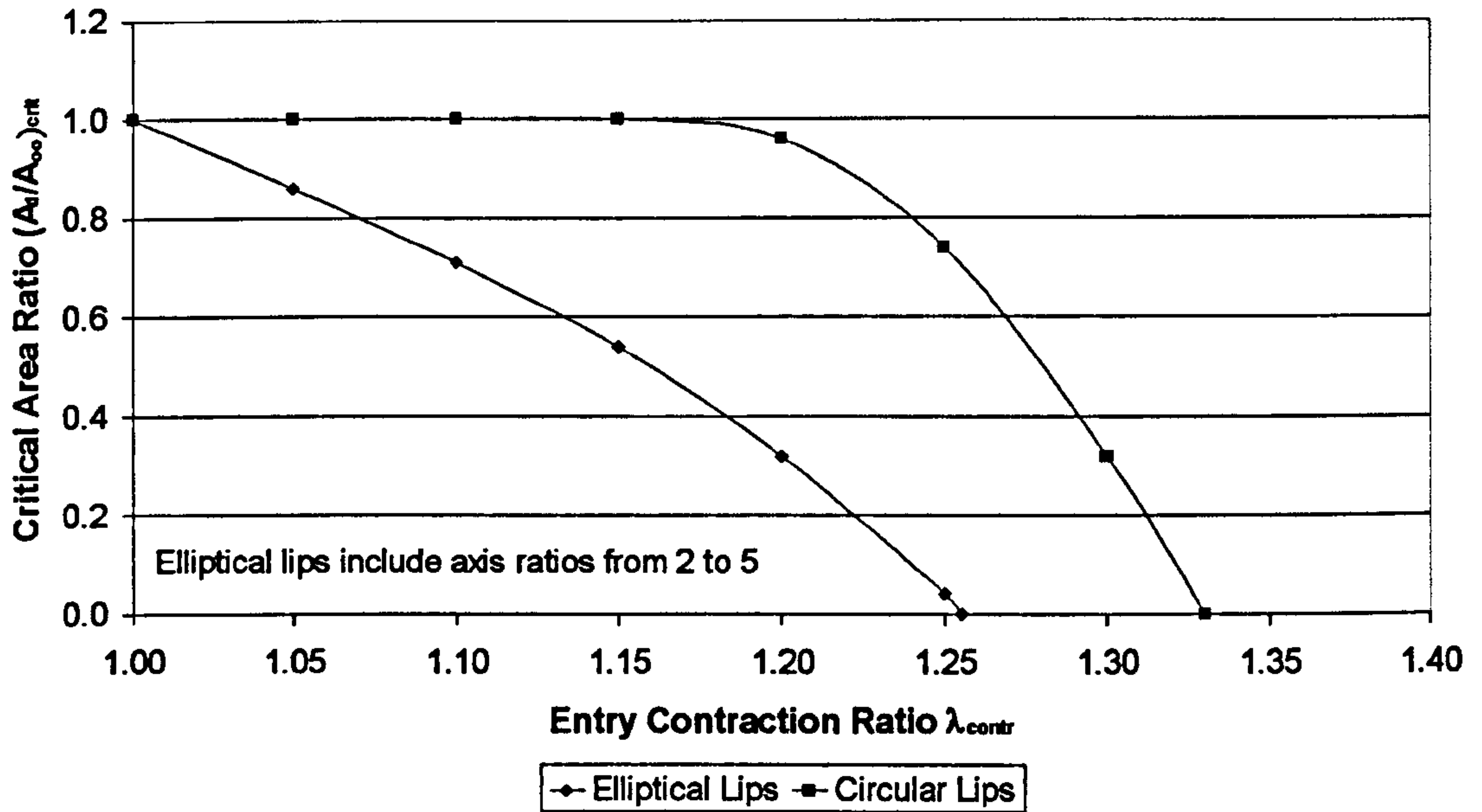


Figure 6.2.1.2: Lip loss boundary at zero incidence

Finally, the loss factor F, which accounts for interaction effects between the entry flow and the diffuser, is established graphically from Figure 6.2.1.3 for both rounded and sharp lips.

Factor Allowing for Datum Interaction Effects between Entry and Diffuser

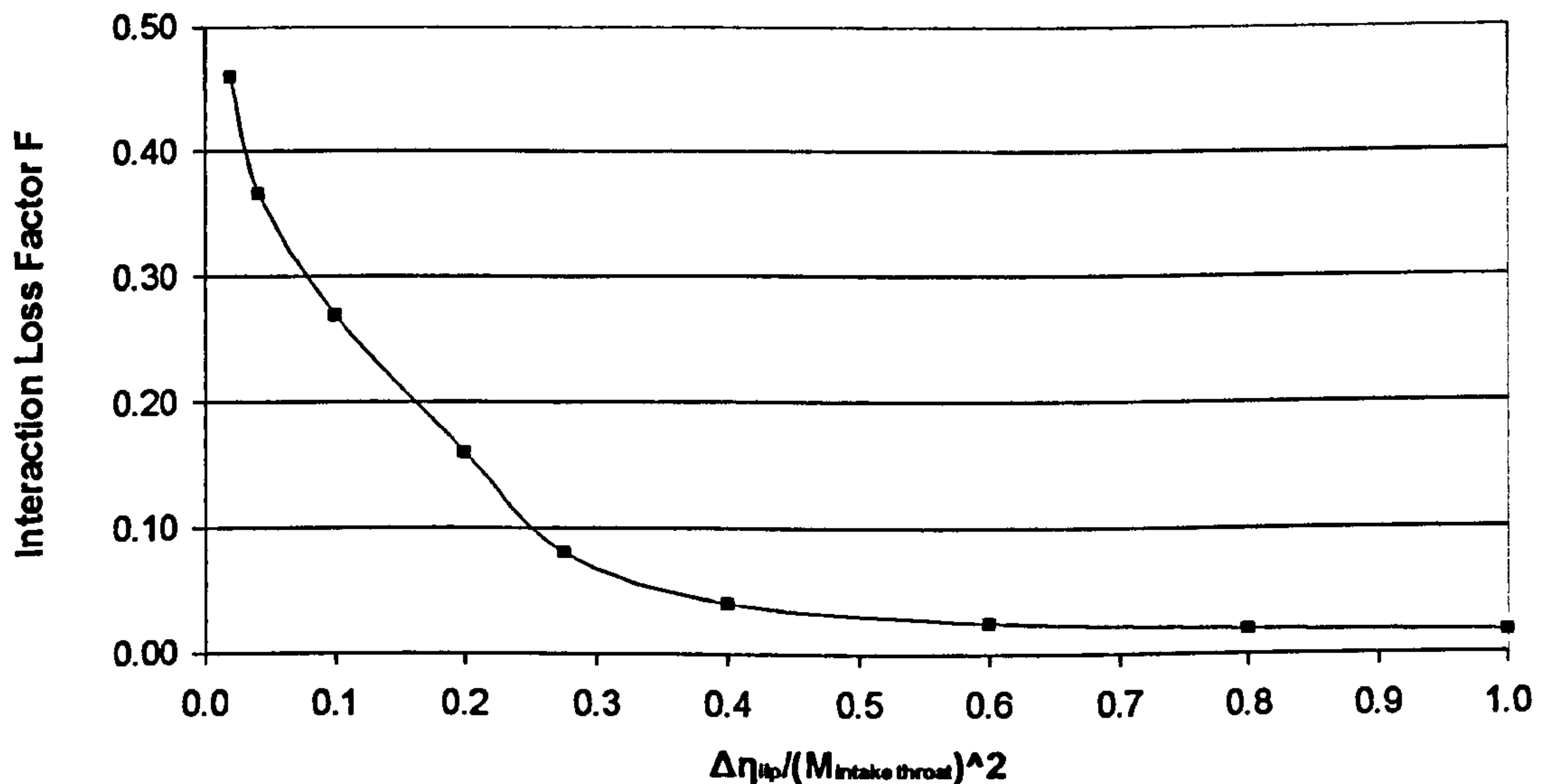


Figure 6.2.1.3: Factor allowing for datum interaction effects between entry and diffuser



### Limitations and Potential Expansion

Obviously, the applicability of the loss models described above is limited to the boundaries of the tabulations and charts adopted. For example the available data for elliptical lips include axis ratios between 2 and 5 only, and the entry contraction ratio, required for the determination of the critical area ratio and  $k_{\text{zero\_inc}}$  factor, can not exceed the value of 1.33 approximately. As mentioned before the objective here is to establish the methodology and create a software tool that has the potential to incorporate any type of loss model for a more accurate analysis. It is really up to the end user to assess the adequacy of these loss models, according to the application, and adopt additional or alternative ones.

### **6.2.2. Calculation of Diffuser Pressure Recovery Loss**

Intake systems usually consist of a large diffusing section with smaller sections of constant-area duct between the diffuser and the inlet lip, and between the diffuser and the engine plane. This section describes how losses in intake pressure recovery due to the presence of the conical diffuser and constant-area ducts are calculated in the *2D Intake SLC Software*. The limitations of the method adopted and scope for future development are also discussed.

#### Introduction

Several researchers have looked into the additional losses that can occur in the diffusing section behind the inlet and which must be taken into account in an overall intake pressure recovery calculation. Fradenburgh and Wyatt (1954), for example, based on the theoretical definition of diffuser pressure loss, established an approximate correlation between the reduction in total pressure in the diffuser and the inlet dynamic head given by:

$$P_{o,1} - P_{o,2} = kq_1 = k \frac{\gamma}{2} P_1 M_1^2 \quad [\text{Eq. 6.2.2.1}]$$

For a well-designed diffuser,  $k$  was taken to be equal to 0.135 which corresponded to a five percent reduction in total pressure associated with an inlet Mach number of 1.0.

On the other hand, Scherrer and Anderson (1956) conducted a much more analytical study by carrying out a number of tests with different diffuser geometries, surface conditions and a variety of attached and separated boundary layers. Amongst others, they investigated the effects on pressure recovery of entry flow non-uniformities, extended diffuser entry lengths, diffuser divergence angle, diffuser entry and exit slopes and entry boundary layer thickness.

Based on the experimental data derived by Scherrer and Anderson (1956) and Blackaby and Watson (1954), ESDU Item No. 80037 (1980) discusses a more detailed model for the estimation of intake diffuser pressure recovery. For uniform entry flow, the diffuser loss in total pressure can be estimated as a function of the

diffuser semi-angle  $\phi$ , the diffuser area ratio  $\lambda_{diff}$  and the intake throat Mach number  $M_{intake\_throat}$ . The data that the ESDU model is based on were obtained from model tests with smaller Reynolds numbers than those normally encountered in full-scale intakes operating at the same sea-level conditions. Therefore, the diffuser loss, as predicted by the ESDU model, refers to a datum Reynolds number and needs to be subsequently corrected to the required Reynolds number at the intake throat.

The loss in intake pressure recovery associated with any lengths of duct with constant cross-sectional area, results mainly due to the flow friction on the walls and therefore can be calculated by the skin friction expression for pipe flows. The loss in energy due to the friction loss on the duct wall is equal to a loss in total pressure averaged over the duct area.

### Calculation of Loss in Pressure Recovery due to Conical Diffusers

This work adopts the more generic diffuser loss model as described in ESDU Item No. 80037 (1980). At the datum Reynolds number the diffuser loss is given by:

$$\Delta\eta_{diff\_datum} = k_1 k_2 M_{intake\_throat}^2 \quad [\text{Eq.6.2.2.2}]$$

Factor  $k_1$  is obtained from tabulated experimental data as a direct function of the diffuser semi-angle  $\phi$  and  $k_2$  is similarly obtained from experimental data as a function of  $\phi$  and the diffuser area ratio  $\lambda_{diff}$ .

Factors  $k_1$  and  $k_2$  are derived from experimental data corrected to a constant Reynolds number of  $7.5 \times 10^5$ . The value of  $\Delta\eta_{diff\_datum}$  should be scaled for Reynolds number changes according to the method used in correcting the measured data as follows:

$$\Delta\eta_{diff} = \Delta\eta_{diff\_datum} \frac{C_{F_{diff}}}{C_{F_{diff\_datum}}} \quad [\text{Eq.6.2.2.3}]$$

Where  $C_{F_{diff}}$  is the mean skin-friction coefficient so that  $C_{F_{diff\_datum}}$  is equal to 0.00305 given by:

$$C_{F_{diff}} = \left[ 3.6 \log_{10} \left( \frac{Re_{intake\_throat}}{7} \right) \right]^{-2} \quad [\text{Eq.6.2.2.4}]$$

The above equation is based on friction factors for pipe flow, assumes fully turbulent flow, and is used to evaluate the mean skin friction coefficient for the diffuser with Reynolds number based on throat conditions.



### Calculation of Loss in Pressure Recovery due to Constant-Area Ducts

Based on ESDU Items No. 76027 (1976) and No. 73024 (1973), the loss in pressure recovery due to any constant-area ducts, upstream and downstream of the diffuser, can be similarly expressed in terms of conditions at the throat as shown below:

$$\frac{\Delta P_o}{q_{intake\_throat}} = 4 \frac{L_{csd}}{D_{csd}} C_{F_{diff}} \left( \frac{D_{intake\_throat}}{D_{csd}} \right)^4 \quad [\text{Eq.6.2.2.5}]$$

Where  $D_{csd}$  and  $D_{intake\_throat}$  are the diameters of the constant section duct and intake throat respectively. Where  $L_{csd}$  is the length of the constant section duct.  $C_{F_{diff}}$  is calculated as shown previously.

The loss in pressure recovery due to the duct is then given by:

$$\Delta \eta_{csd} = \frac{\Delta P_o}{q_{intake\_throat}} \left[ 1 - \left( 1 + 0.2 M_{intake\_throat}^2 \right)^{\frac{-\gamma}{\gamma-1}} \right] \quad [\text{Eq.6.2.2.6}]$$

### Implementation

The calculation of the diffuser pressure recovery loss is handled in the *2D Intake SLC Software* by subroutine *Intake2D\_DiffuserLossCalc.f90*. The loss in pressure recovery due to any constant-area ducts, upstream and downstream of the diffuser is calculated by subroutine *Intake2D\_ConstantAreaDuctLossCalc.f90*. Both subroutines are called in sequence by the main subroutine *Intake2D\_MainProgram.f90* iteratively until the entire intake flow field is established, including the boundary layer calculation.

Inputs to these subroutines are the geometrical properties of the diffuser, such as diffuser inlet and outlet areas, diffuser length and diffuser semi-angle, and air properties at the diffuser inlet, such as Mach number (taken as equal to the intake throat Mach number). Moreover, several graphs, stored as array tabular data in module *DiffuserLossVarDeclar.f90*, are fed as inputs and used in the necessary interpolations for the  $k_1$  and  $k_2$  factors.

More analytically,  $k_1$  is determined graphically from Figure 6.2.2.1 as a function of the diffuser semi-angle  $\phi$ , and  $k_2$  is similarly obtained from Figure 6.2.2.2 as a function of diffuser semi-angle  $\phi$  and diffuser area ratio  $\lambda_{diff}$ .



Diffuser Loss Factor Variation with Semi-Angle

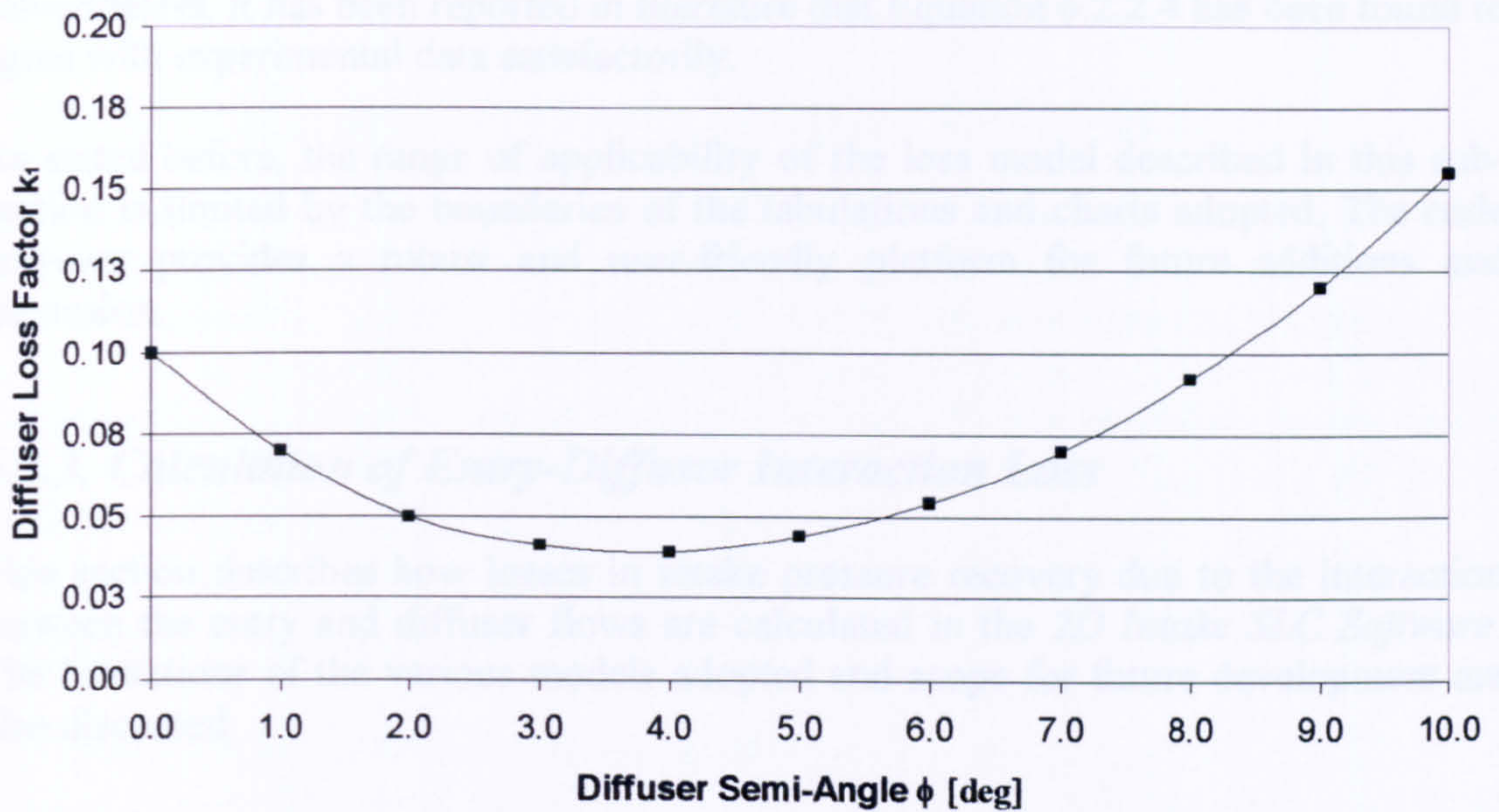


Figure 6.2.2.1: Diffuser loss factor  $k_1$  variation with semi-angle

Diffuser Loss Factor  $k_2$  Variation with Area Ratio

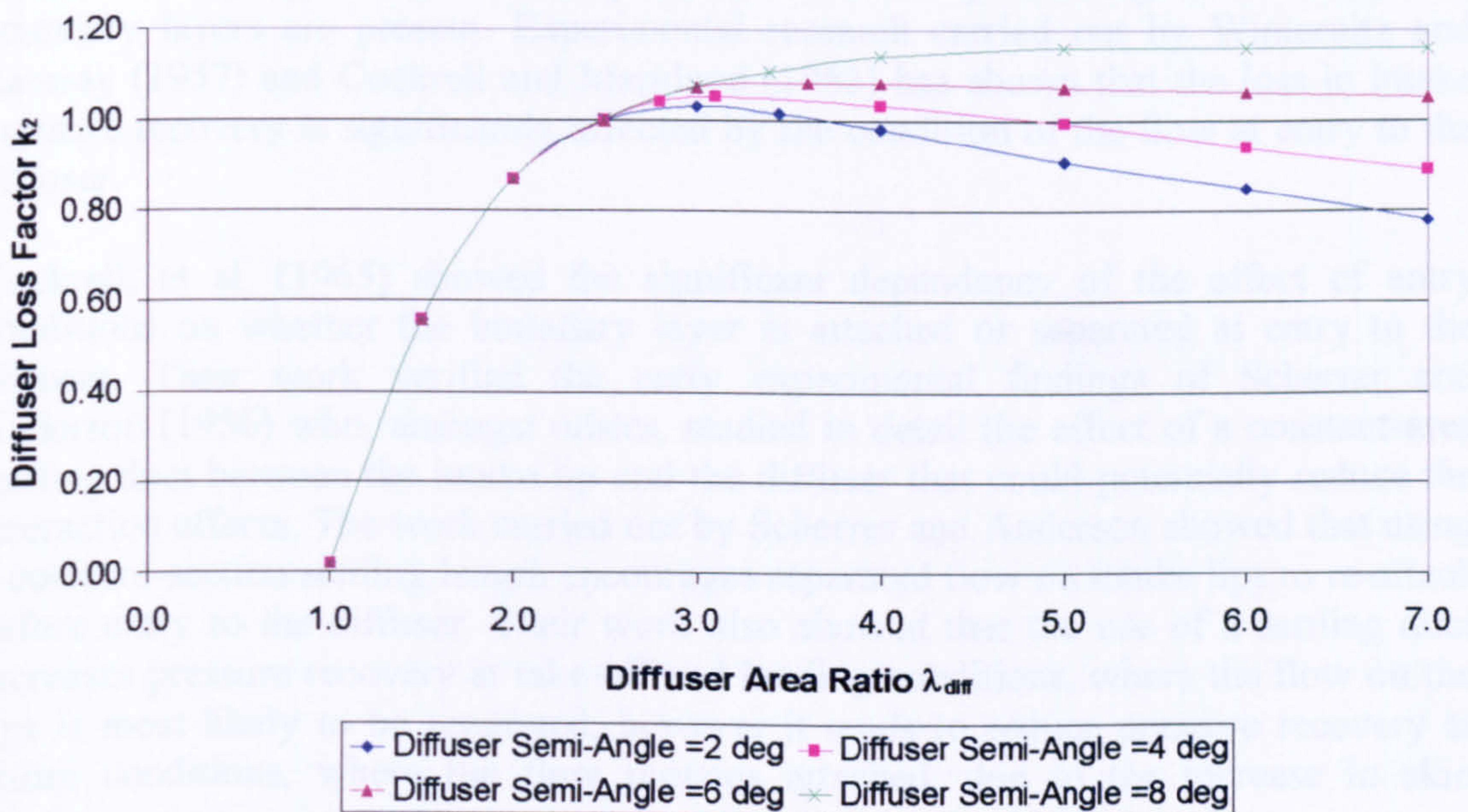


Figure 6.2.2.2: Diffuser loss factor  $k_2$

Limitations and Potential Expansion

Equation 6.2.2.3 can be used with small errors and to a good approximation for all throat Mach numbers although it is strictly only valid for incompressible flow. Boundary layer development and pressure gradient effects will tend to change the



value of  $C_F$  throughout the diffuser. Equation 6.2.2.4, however, assumes that the skin friction coefficients, based on throat conditions, remain unchanged through the intake. Nevertheless, it has been reported in literature that Equation 6.2.2.4 has been found to agree with experimental data satisfactorily.

As stated before, the range of applicability of the loss model described in this subsection is limited by the boundaries of the tabulations and charts adopted. The code however provides a robust and user-friendly platform for future additions and expansion.

### ***6.2.3. Calculation of Entry-Diffuser Interaction Loss***

This section describes how losses in intake pressure recovery due to the interaction between the entry and diffuser flows are calculated in the *2D Intake SLC Software*. The limitations of the various models adopted and scope for future development are also discussed.

#### **Introduction**

In order to estimate the loss in pressure recovery more accurately, one should make some short of allowance for the complicated interactions between the entry and diffuser flows, especially when separated flows and pressure gradient effects on boundary layers are present. Experimental research carried out by Winternitz and Ramsay (1957) and Cockrell and Markland (1963) has shown that the loss in intake pressure recovery is significantly affected by the condition of the flow at entry to the diffuser.

Cockrell, et al. (1965) showed the significant dependency of the effect of entry conditions on whether the boundary layer is attached or separated at entry to the diffuser. Their work verified the early experimental findings of Scherrer and Anderson (1956) who, amongst others, studied in detail the effect of a constant-area settling duct between the intake lip and the diffuser that could potentially reduce the interaction effects. The work carried out by Scherrer and Anderson showed that using a constant-section settling length encourages separated flow on intake lips to re-attach before entry to the diffuser. Their work also showed that the use of a settling duct increases pressure recovery at take-off and landing conditions, where the flow on the lips is most likely to be separated, however it tends to reduce pressure recovery at cruise conditions, where the flow remains attached, due to the increase in skin friction.

Intake lip geometry and the magnitude of the lip loss involved usually determine the minimum settling length required for attached flow. Scherrer and Anderson established a settling length equivalent to half an intake throat diameter as sufficient for most flow conditions up to an incidence of 15 degrees. They also suggested the use of a diffuser entry of shallow angle ( $\approx 0.5$  degrees) instead of a constant section duct, to compensate for the effect of boundary layer growth.

Dolan and Runstadler (1973) also carried out parametric investigations of the performance of conical diffusers.

### Calculation of Loss due to Attached Flow at Diffuser Entry

This work adopts the method described in ESDU Item No. 80037 (1980) for estimating the loss in pressure recovery due to entry-diffuser interactions. The method is based on experimental data published by the above mentioned researchers as well as on the extensive parametric analysis on conical diffuser performance published by Dolan and Runstadler (1973). It basically assumes that the interaction loss can be sufficiently represented by a magnification factor  $N_{mag\_attached}$  applied to the basic diffuser loss  $\Delta\eta_{diff}$ , as shown bellow:

$$\Delta\eta_{diff\_inter} = \Delta\eta_{diff} N_{mag\_attached} \quad [\text{Eq. 6.2.3.1}]$$

The magnification factor  $N_{mag\_attached}$  is given by:

$$N_{mag\_attached} = 1 + N_1 N_2 \quad [\text{Eq. 6.2.3.2}]$$

Where  $N_1$  is graphically obtained from published experimental data as a function of the loss in pressure recovery before entry to the diffuser and the intake throat Mach number  $\frac{\Delta\eta_{diff\_entry}}{M_{intake\_throat}^2}$ . The loss in pressure recovery before entry to the diffuser is

obtained from the sum of the loss in total pressure due to the lip and the loss due to any constant-section duct upstream of the diffuser:

$$\Delta\eta_{diff\_entry} = \Delta\eta_{lip} + \Delta\eta_{csd\_upstream} \quad [\text{Eq. 6.2.3.3}]$$

Similarly,  $N_2$  is graphically obtained from published experimental data as a function of the diffuser semi-angle  $\varphi$ .

### Calculation of Loss due to Detached Flow at Diffuser Entry

The method adopted here is very similar to the one for attached flow and is based on experimental data derived by Winternitz and Ramsay and Cockrell, et al. The interaction loss due to separated flow is represented by a magnification factor  $N_{mag\_detached}$  applied to the basic diffuser loss  $\Delta\eta_{diff}$ , as shown bellow:

$$\Delta\eta_{diff\_inter} = \Delta\eta_{diff} N_{mag\_detached} \quad [\text{Eq. 6.2.3.4}]$$

The magnification factor  $N_{mag\_detached}$  is given by:

$$N_{mag\_detached} = 1 + N_3 N_4 \quad [\text{Eq. 6.2.3.5}]$$



As before,  $N_3$  is graphically obtained from published experimental data as a function of the loss in pressure recovery before entry to the diffuser and the intake throat Mach number  $\frac{\Delta\eta_{diff\_entry}}{M_{intake\_throat}^2}$ , and  $N_4$  is graphically obtained from published experimental data as a function of the diffuser semi-angle  $\phi$ .

### Implementation

The calculation of the entry-diffuser interaction loss, for both attached and separated lip flows, is handled by subroutine *Intake2D\_InteractionLossCalc.f90*. This subroutine is called by the main subroutine *Intake2D\_MainProgram.f90* in sequence after the basic diffuser and constant-area duct losses have been established. This involves an iterative calculation until the entire intake flow field is established, including the boundary layer calculation.

Inputs to this subroutine are the geometrical properties of the diffuser, such as diffuser inlet and outlet areas and diffuser semi-angle, the diffuser inlet Mach number (taken as equal to the intake throat Mach number) and the losses associated with the diffuser, intake lip and any upstream constant-section duct. Moreover, several graphs, stored as array tabular data in module *InteractionLossVarDeclar.f90*, are fed as inputs and used in the necessary interpolations for the  $N_1$ ,  $N_2$ ,  $N_3$  and  $N_4$  factors.

More analytically, for attached flow,  $N_1$  is graphically obtained from Figure 6.2.3.1 as a function of the loss in pressure recovery before entry to the diffuser and the intake throat Mach number  $\frac{\Delta\eta_{diff\_entry}}{M_{intake\_throat}^2}$ .

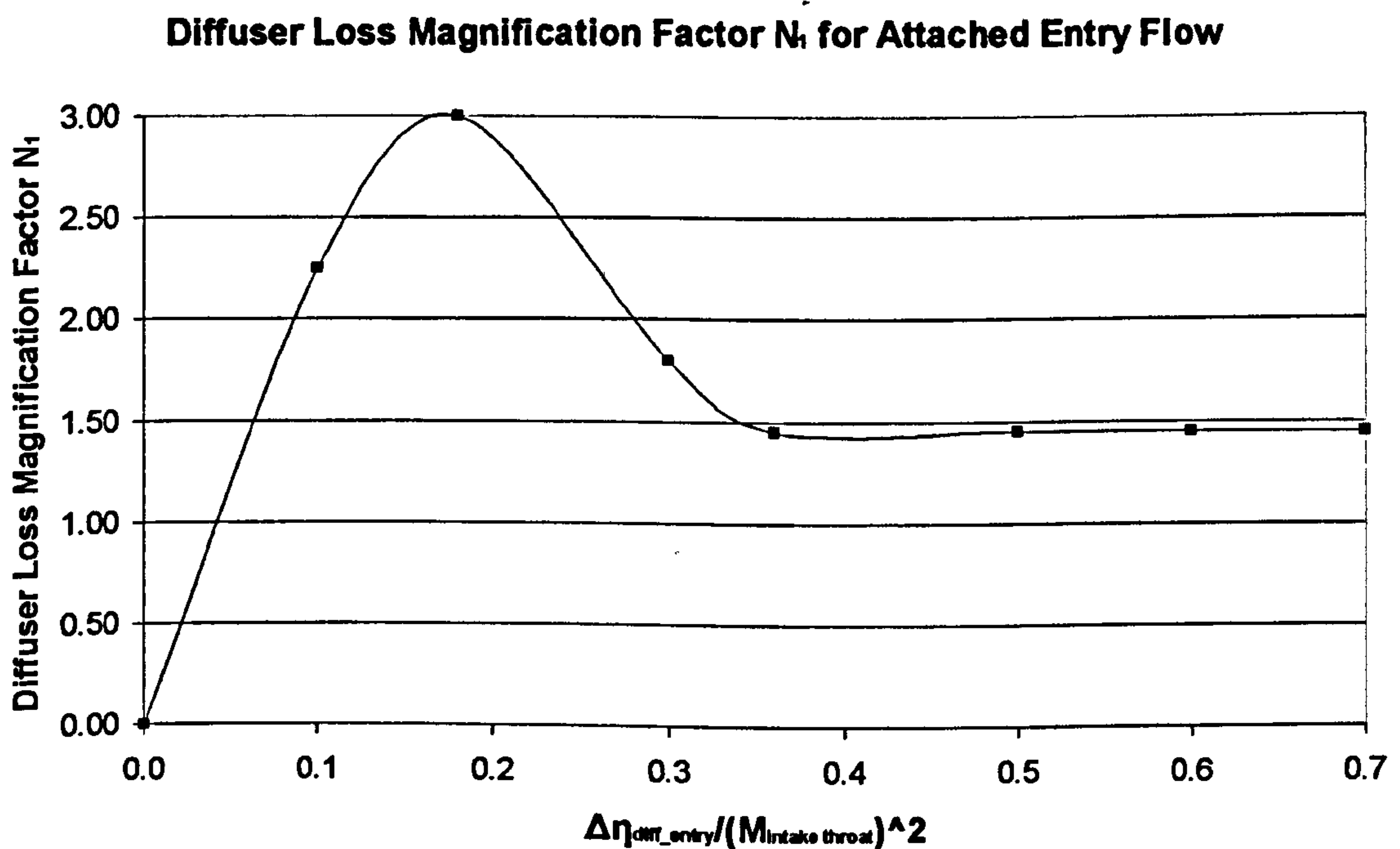


Figure 6.2.3.1: Diffuser loss magnification factor  $N_1$  for attached entry flow

$N_2$  is graphically obtained from Figure 6.2.3.2 as a function of the diffuser semi-angle  $\phi$ .

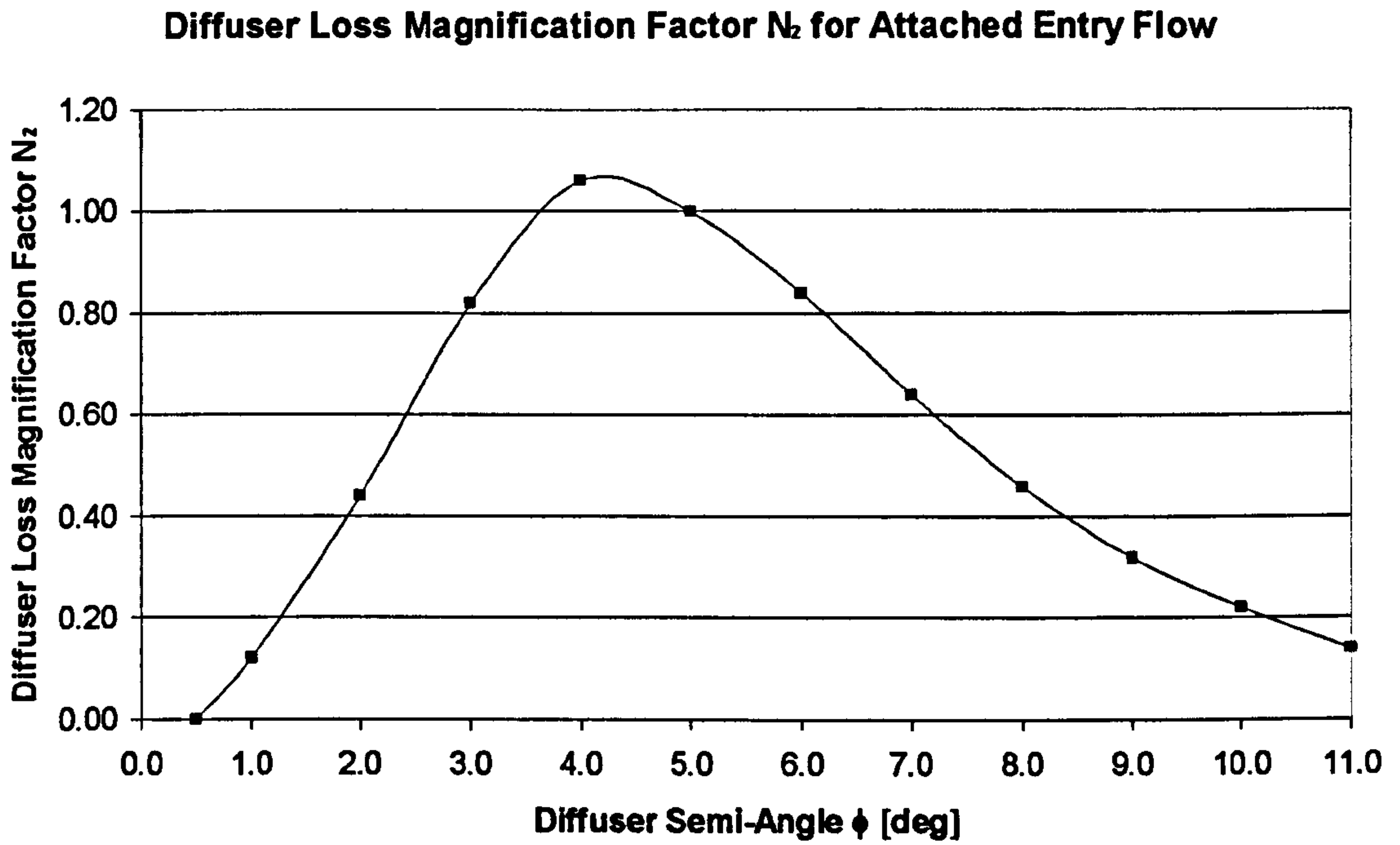


Figure 6.2.3.2: Diffuser loss magnification factor  $N_2$  for attached entry flow

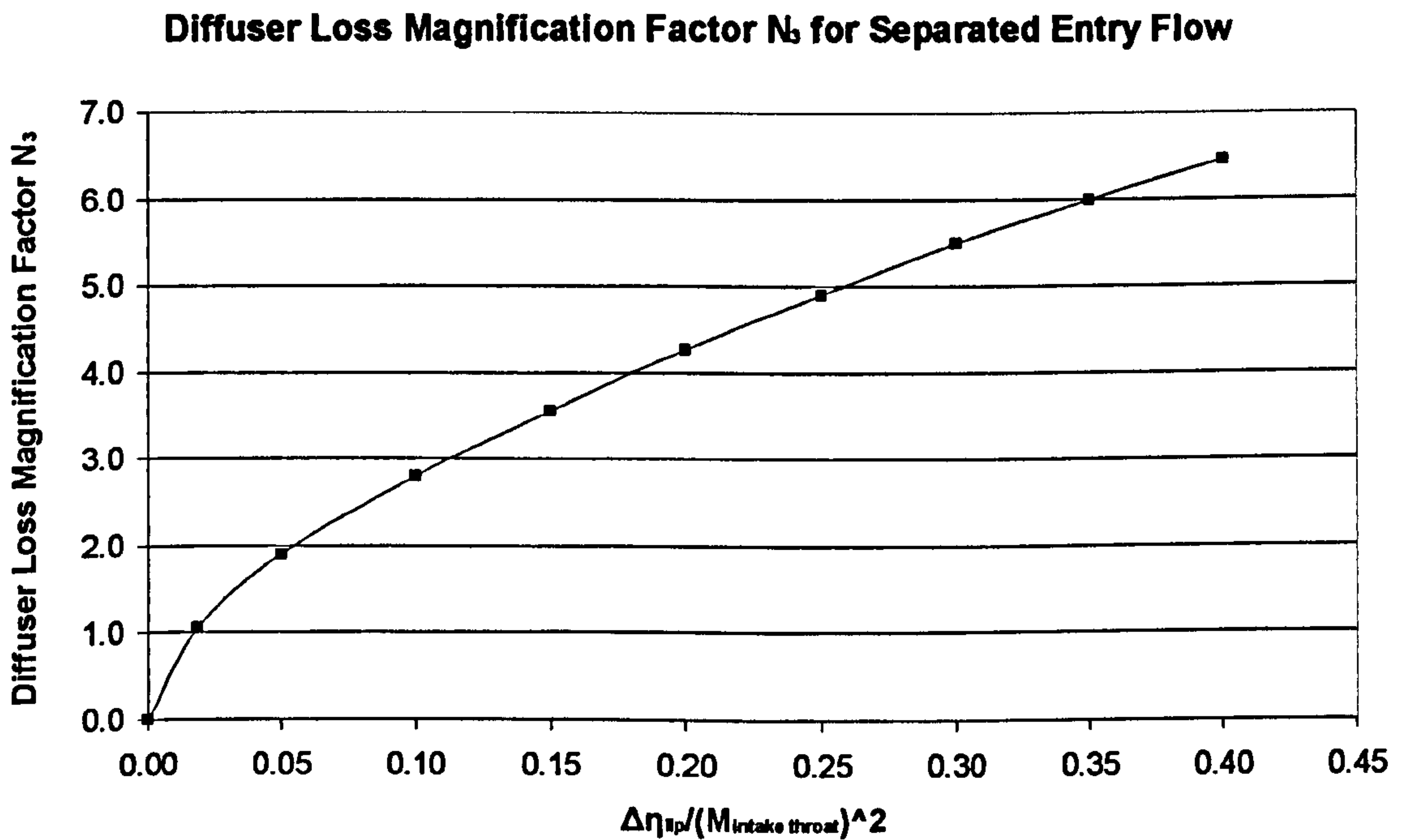


Figure 6.2.3.3: Diffuser loss magnification factor  $N_3$  for separated entry flow

Similarly, for separated flow,  $N_3$  is graphically obtained from Figure 6.2.3.3 as a function of the loss in pressure recovery before entry to the diffuser and the intake throat Mach number  $\frac{\Delta\eta_{diff\_entry}}{M_{intake\_throat}^2}$ . And  $N_4$ , for separated flow is graphically obtained

from Figure 6.2.3.4 as a function of the diffuser semi-angle  $\phi$ .



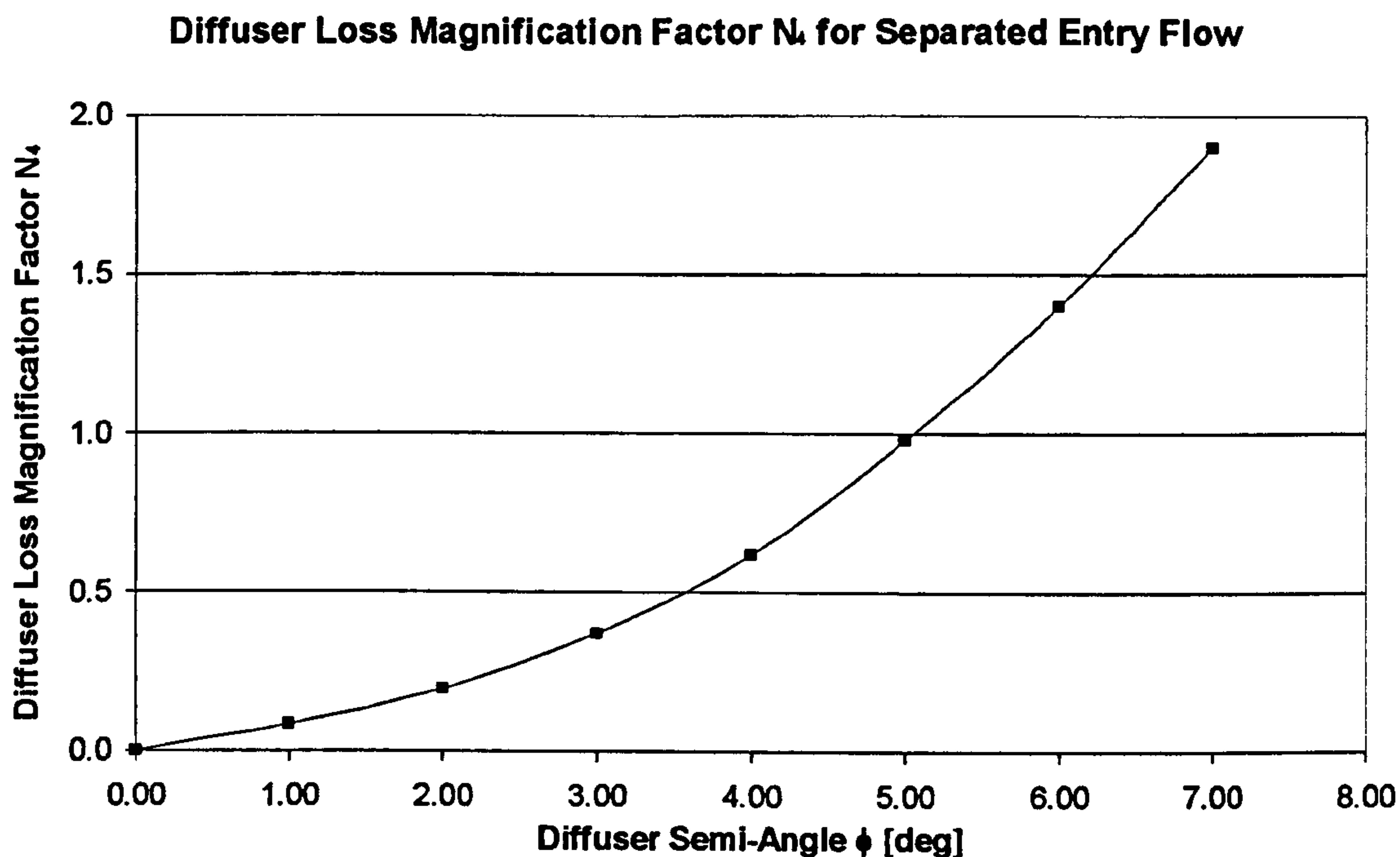


Figure 6.2.3.4: Diffuser loss magnification factor  $N_4$  for separated entry flow

### Limitations and Potential Expansion

For the method adopted here the same limitations apply as before. Entry-diffuser interaction is a fairly complex issue which is treated by the above analysis empirically only. Although the model discussed above is applicable to a large range of flow conditions and diffuser geometries, for a quantitative type of analysis the user needs to compare the results against experimental data and calibrate the model accordingly.

### **6.2.4. Effect of Incidence Angle on Pressure Recovery**

This section describes how losses in pressure recovery due to the intake incidence at low speeds are taken into account in the *2D Intake SLC Software*. The limitations of the various models adopted and scope for future development are also discussed.

#### Introduction

The loss in total pressure associated with changes in incidence angle can be related to the loss due to the presence of the intake lip, and particularly to the nature of the flow on the lip at zero incidence. If the lip flow is separated at zero incidence, any increase in incidence angle will tend to increase the magnitude of lip separation and hence, the loss in total pressure. On the other hand, if the flow on the lip is attached at zero incidence, the effect of incidence will be to increase the tendency of the lip flow to separate. The incidence angle  $\alpha$  at which the lip flow separates can be established as a function of the lip shape, the entry contraction ratio  $\lambda_{\text{contr}}$  and intake area ratio  $A_1/A_\infty$ .

Blackaby (1955) conducted a number of wind tunnel tests of a sharp inlet lip, two circular-arc profiles and two elliptical profiles at a free stream Mach number of 0.237, with inlet flows ranging from low values up to choking, and incidence angles from 0 to 25 degrees. As in the case of the zero-incidence tests, the elliptical-profile lips proved to have superior pressure recovery characteristics compared to the others. Similarly, Tyler and Williamson (1964) studied intake pressure recovery characteristics in detail by conducting a series of wind tunnel tests of full-scale circular intakes under cross-flow conditions with a range of cowl lip profiles. They tested five cowl shapes, over a range of velocity ratios from 0.0 to 0.7 and at cross-flow angles from 0.0 to 165 degrees.

Based on the experimental results obtained by Blackaby (1955) and Tyler and Williamson (1964) a method for estimating the pressure recovery loss at low speeds for intakes at incidence has been established, similar to the one for intakes at zero incidence, but with the effect of incidence included within the lip loss  $\Delta\eta_{lip}$ . This approach assumes that the change in flow angle on to the lip due to incidence can be related to changes in flow angle due to the variation in intake flow area ratio  $A_1/A_\infty$ . Actually, the only difference in this method, compared to the zero-incidence case, is the calculation and use in the equations of an effective free-stream Mach number  $M_{\infty\_eff}$ , as a function of incidence  $\alpha$  and area ratio  $A_1/A_\infty$ , instead of the conventional free-stream Mach number  $M_\infty$ .

The value of the lip loss for the intake at incidence, obtained by this method, can then be used in the calculation of the magnification factors in estimating the diffuser loss, as well as in deriving the total intake pressure loss, as shown before in previous sections.

### Calculation of Loss for Sharp Lips at Incidence

This work adopts the method as described above for predicting the loss in pressure recovery due to incidence effects for sharp lips. For known values of free-stream Mach number and intake throat Mach number, the corresponding mass flow functions can be established as follows:

$$Q_\infty = \frac{M_\infty \sqrt{\gamma}}{\left(1 + \frac{\gamma-1}{2} M_\infty^2\right)^{\frac{\gamma+1}{2(\gamma-1)}}} \quad [\text{Eq. 6.2.4.1}]$$

and

$$Q_{intake\_throat} = \frac{M_{intake\_throat} \sqrt{\gamma}}{\left(1 + \frac{\gamma-1}{2} M_{intake\_throat}^2\right)^{\frac{\gamma+1}{2(\gamma-1)}}} \quad [\text{Eq. 6.2.4.2}]$$

From geometry, the intake contraction ratio is given by:

$$\lambda_{contr} = \frac{A_1}{A_{intake\_throat}} \quad [\text{Eq. 6.2.4.3}]$$



The value of  $A_1/A_\infty$  is established from the intake contraction ratio as shown below:

$$\frac{A_1}{A_\infty} = \frac{Q_\infty}{Q_{\text{intake\_throat}}} \lambda_{\text{contr}} \quad [\text{Eq. 6.2.4.4}]$$

The effective free-stream Mach number is calculated from:

$$M_{\infty\_eff} = M_\infty \cos \left[ 15 \left( a \frac{A_1}{A_\infty} \right)^{0.5} \right] \quad \text{for } 15 \left( a \frac{A_1}{A_\infty} \right)^{0.5} < 90^\circ$$

and [Eq. 6.2.4.5]

$$M_{\infty\_eff} = 0.0 \quad \text{for } 15 \left( a \frac{A_1}{A_\infty} \right)^{0.5} \geq 90^\circ$$

Although the above relationships are valid only for  $A_1/A_\infty \leq 1.0$ , for conditions where  $A_1/A_\infty > 1.0$  a reasonable estimate can be obtained by using  $A_1/A_\infty = 1.0$ .

The pressure recovery for sharp lips can then be calculated from:

$$\eta_{lip} = \frac{\left[ \frac{f(M_1)}{f(M_{\infty\_eff})} \right]^{\frac{\gamma}{\gamma-1}}}{1 + \gamma M_1^2 - \gamma M_{\infty\_eff} M_1 \left[ \frac{f(M_1)}{f(M_{\infty\_eff})} \right]^{\frac{1}{2}}} \quad [\text{Eq. 6.2.4.6}]$$

$$\text{Where } f(M) = \left( 1 + \frac{\gamma-1}{2} M^2 \right) \quad [\text{Eq. 6.2.4.7}]$$

The Mach number at the intake entry plane  $M_1$  can be calculated using the entry non-dimensional mass flow parameter  $Q_1$  which is given from continuity by:

$$Q_1 = \frac{Q_{\text{intake\_throat}}}{\lambda_{\text{contr}}} \quad [\text{Eq. 6.2.4.8}]$$

Then  $M_1$  can be obtained iteratively with this value of  $Q_1$  from:

$$Q_1 = \frac{M_1 \sqrt{\gamma}}{\left( 1 + \frac{\gamma-1}{2} M_1^2 \right)^{\frac{\gamma+1}{2(\gamma-1)}}} \quad [\text{Eq. 6.2.4.9}]$$

As discussed before for the case of zero incidence, a correction factor can be applied to the loss in total pressure predicted by Equation 6.2.4.6 as shown below:

$$\Delta\eta_{sharp\_lip} = (1 - \eta_{lip}) \left( \frac{2}{(1 - M_1^2)^{1/2}} - 1 \right) \quad [\text{Eq. 6.2.4.10}]$$

Blackaby's and Watson's experimental data included some interaction effects between the entry flow and the diffuser. Therefore, a correction factor needs to be applied to the last relationship such as the loss due to lip flow separation is given by:

$$\Delta\eta_{lip} = \Delta\eta_{sharp\_lip} (1 - F) \quad [\text{Eq. 6.2.4.11}]$$

Where F is the interaction loss factor and is established graphically from published data as a function of  $\frac{\Delta\eta_{sharp\_lip}}{M_{intake\_throat}^2}$ .

### Calculation of Loss for Rounded Lips at Incidence

For rounded lips at incidence the procedure for calculating  $M_{\infty\_eff}$  is the same as for sharp lips. An effective critical area ratio  $\left( \frac{A_1}{A_{\infty\_eff}} \right)_{cr}$ , which varies with incidence, is graphically obtained from experimental data derived by Blackaby for circular and elliptical lips as a function of entry contraction ratio and incidence angle.

From the effective free stream Mach number, the effective non-dimensional mass flow function  $Q_{\infty\_eff}$  is obtained as follows:

$$Q_{\infty\_eff} = \frac{M_{\infty\_eff} \sqrt{\gamma}}{\left( 1 + \frac{\gamma-1}{2} M_{\infty\_eff}^2 \right)^{\frac{\gamma+1}{2(\gamma-1)}}} \quad [\text{Eq. 6.2.4.12}]$$

From continuity of mass flow:

$$Q_{1\_cr} = \frac{Q_{\infty\_eff}}{\left( \frac{A_1}{A_{\infty\_eff}} \right)_{cr}} \quad [\text{Eq. 6.2.4.13}]$$

The critical Mach number  $M_{1\_cr}$  at the intake inlet can then be derived iteratively from the following relationship:

$$Q_{1\_cr} = \frac{M_{1\_cr} \sqrt{\gamma}}{\left( 1 + \frac{\gamma-1}{2} M_{1\_cr}^2 \right)^{\frac{\gamma+1}{2(\gamma-1)}}} \quad [\text{Eq. 6.2.4.14}]$$



Having established  $Q_{\text{intake\_throat}}$ , the non-dimensional mass flow function at the intake inlet  $Q_1$  is given by:

$$Q_1 = \frac{Q_{\text{intake\_throat}}}{\lambda_{\text{contr}}} \quad [\text{Eq. 6.2.4.15}]$$

$M_1$  is obtained with this value of  $Q_1$  from:

$$Q_1 = \frac{M_1 \sqrt{\gamma}}{\left(1 + \frac{\gamma-1}{2} M_1^2\right)^{\frac{\gamma+1}{2(\gamma-1)}}} \quad [\text{Eq. 6.2.4.16}]$$

Finally, the loss in pressure recovery for rounded lips associated with lip flow separation at incidence is evaluated from  $M_{1\_cr}$  and  $M_1$  as follows:

$$\begin{aligned} \text{For } M_1 \leq M_{1\_cr}, \Delta\eta_{\text{round\_lip}} &= 0 \\ \text{and} & \\ \text{For } M_1 > M_{1\_cr}, \Delta\eta_{\text{round\_lip}} &= k_{\text{inc}} (\Delta\eta_{\text{sharp\_lip}} - \Delta\eta_{\text{sharp\_lip\_cr}}) \end{aligned} \quad [\text{Eq. 6.2.4.17}]$$

Where  $\Delta\eta_{\text{sharp\_lip}}$  and  $\Delta\eta_{\text{sharp\_lip\_cr}}$  are calculated as shown above for  $M_1$  and  $M_{1\_cr}$  respectively. Where  $k_{\text{inc}}$  is a constant that relates the loss for a rounded lip to that for a sharp lip. It is determined graphically from measurements as a function of entry contraction ratio and incidence angle.

Similarly to the sharp lip case, lip loss data used by this model have been obtained from measured data including some interaction effects between the entry flow and the diffuser. Therefore, a correction factor needs to be applied to the last relationship such as the loss due to lip flow separation is given by:

$$\Delta\eta_{\text{lip}} = \Delta\eta_{\text{round\_lip}} (1 - F) \quad [\text{Eq. 6.2.4.18}]$$

Where  $F$  is the interaction loss factor and is established graphically from published data as a function of  $\frac{\Delta\eta_{\text{round\_lip}}}{M_{\text{intake\_throat}}^2}$ .

### Implementation

The calculation of the pressure recovery loss for sharp and rounded lips at incidence is handled by subroutines *Intake2D\_IncidenceSharpLipLossCalc.f90* and *Intake2D\_IncidenceRoundedLipLossCalc.f90* respectively. As in the case of lips at zero incidence, the latter subroutine includes two further models for predicting lip loss on rounded lips that the user is free to select from, one for elliptical lips and another for lips of circular type. Each subroutine can be alternatively called by the main subroutine *Intake2D\_MainProgram.f90* to calculate the pressure loss of the lip at incidence according to the user's selection of lip configuration. The calculation is



carried out iteratively until the entire intake flow field is established, including the boundary layer calculation.

The inputs to these subroutines are intake incidence angle, intake geometrical properties such as intake inlet and throat areas and air properties such as the inlet and throat Mach numbers. The pre-entry stream tube area and Mach number are also required as inputs to these subroutines. Moreover, several graphs, stored as array tabular data in module *IncidenceLossVarDeclar.f90*, are fed as inputs and used in the

necessary interpolations for the effective critical area ratio  $\left(\frac{A_1}{A_{\infty\_eff}}\right)_{cr}$  and  $k_{inc}$  factor.

More analytically, the critical effective area ratio for circular and elliptical lips at incidence is obtained from Figures 6.2.4.1 and 6.2.4.2 respectively, as a function of incidence angle and entry contraction ratio.

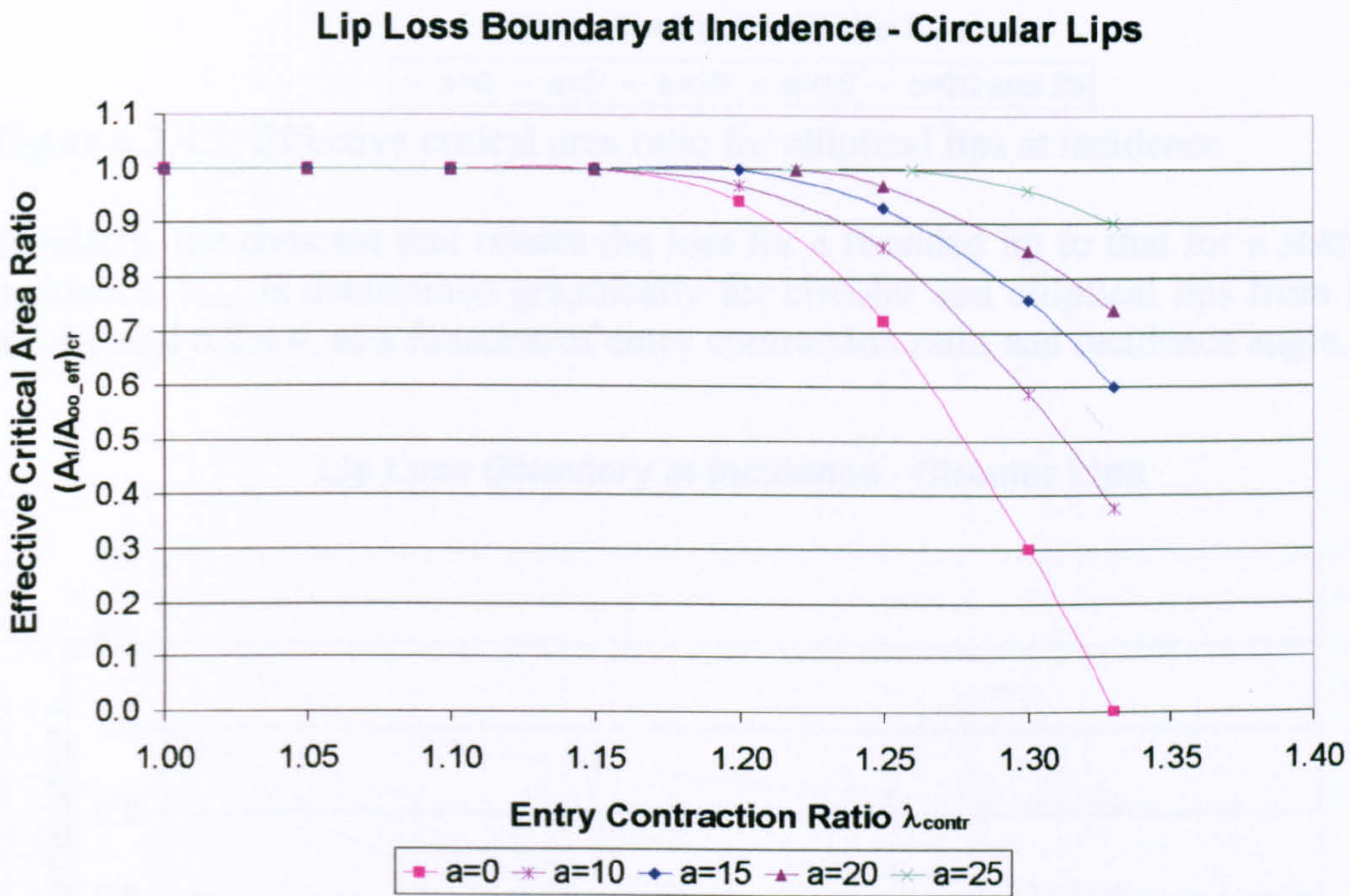


Figure 6.2.4.1: Effective critical area ratio for circular lips at incidence



Lip Loss Boundary at Incidence - Elliptical Lips

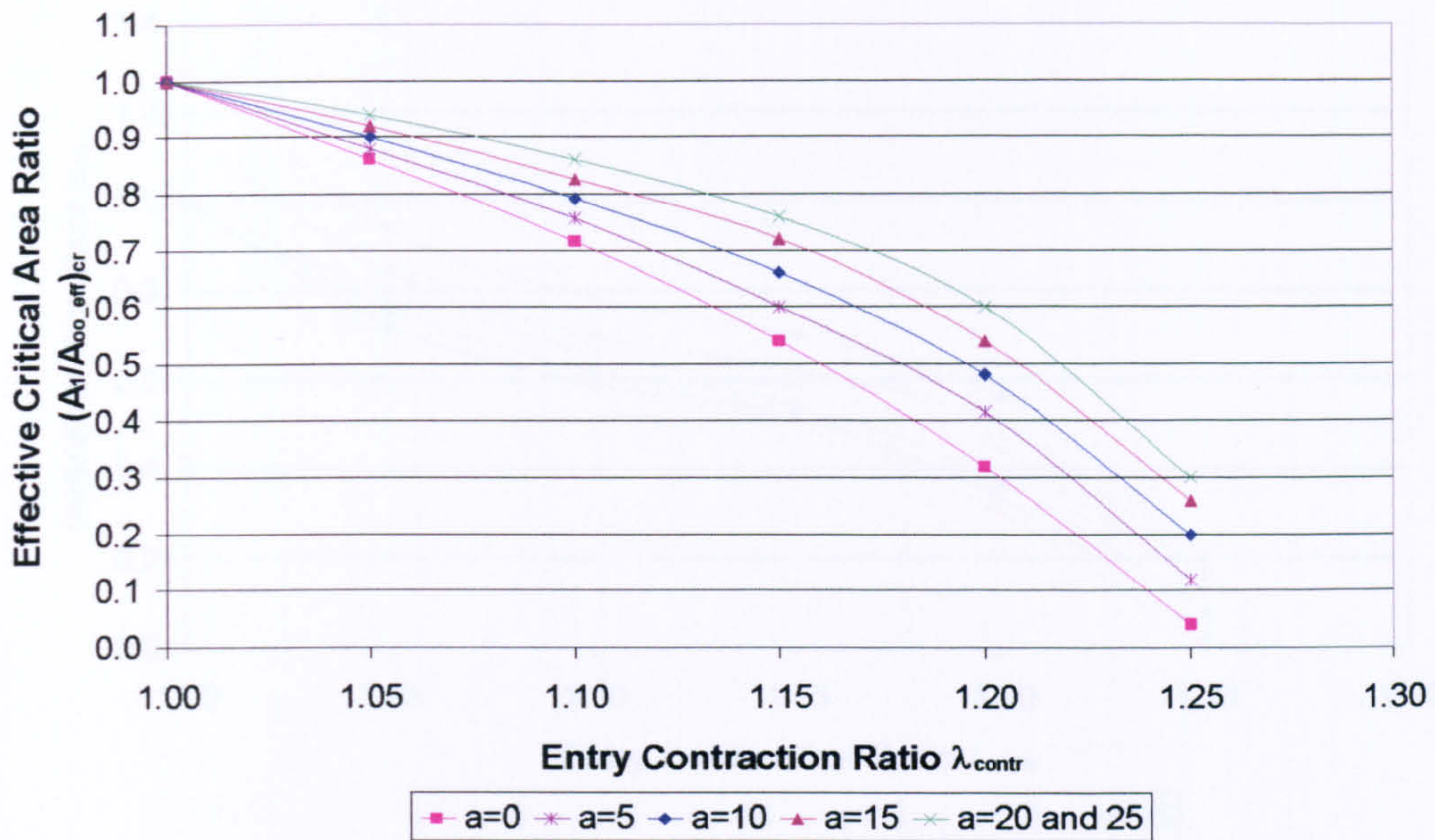


Figure 6.2.4.2: Effective critical area ratio for elliptical lips at incidence

Similarly, the constant that relates the loss for a rounded lip to that for a sharp lip at incidence,  $k_{inc}$ , is determined graphically for circular and elliptical lips from Figures 6.2.4.3 and 6.2.4.4, as a function of entry contraction ratio and incidence angle.

Lip Loss Boundary at Incidence - Circular Lips

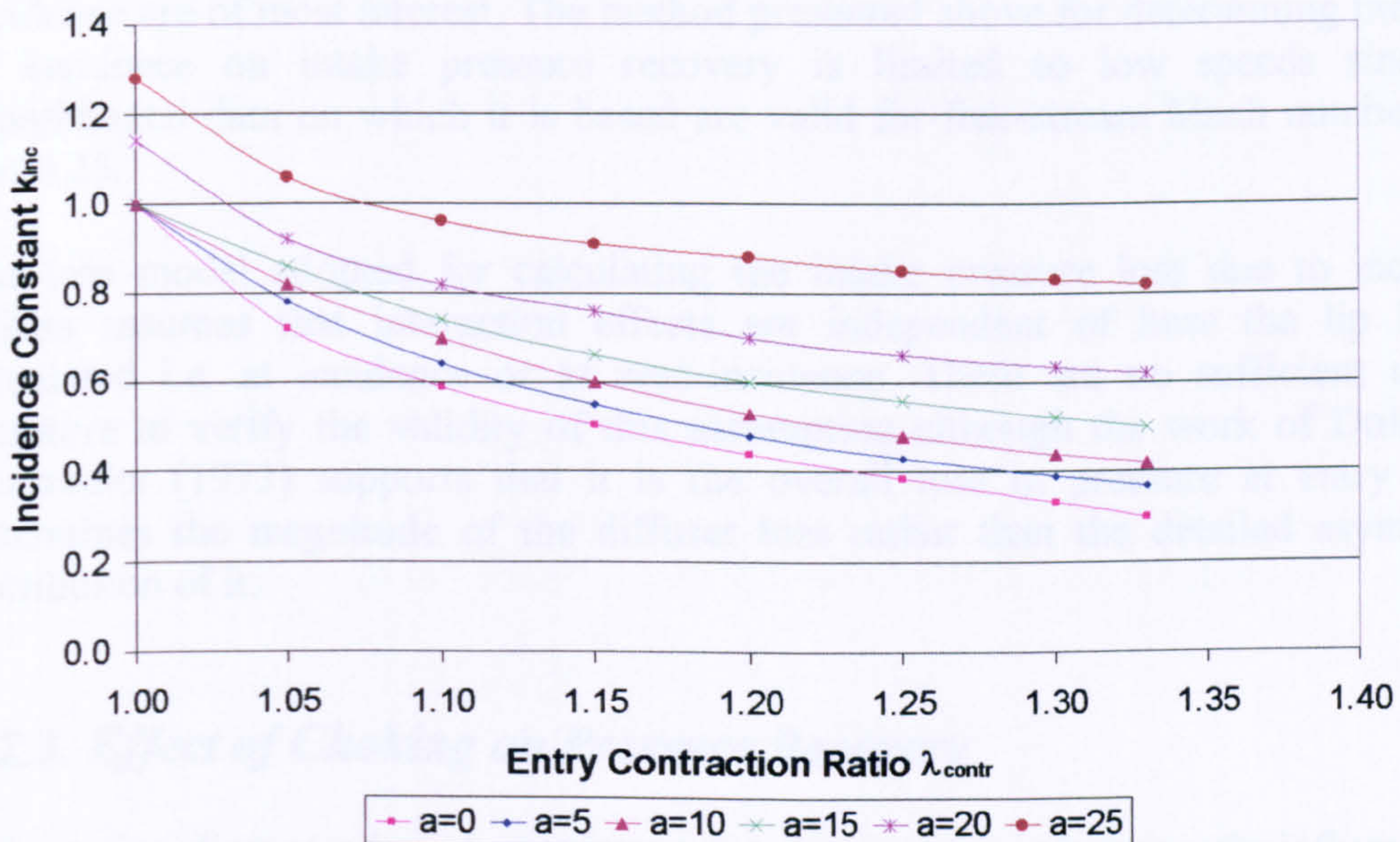
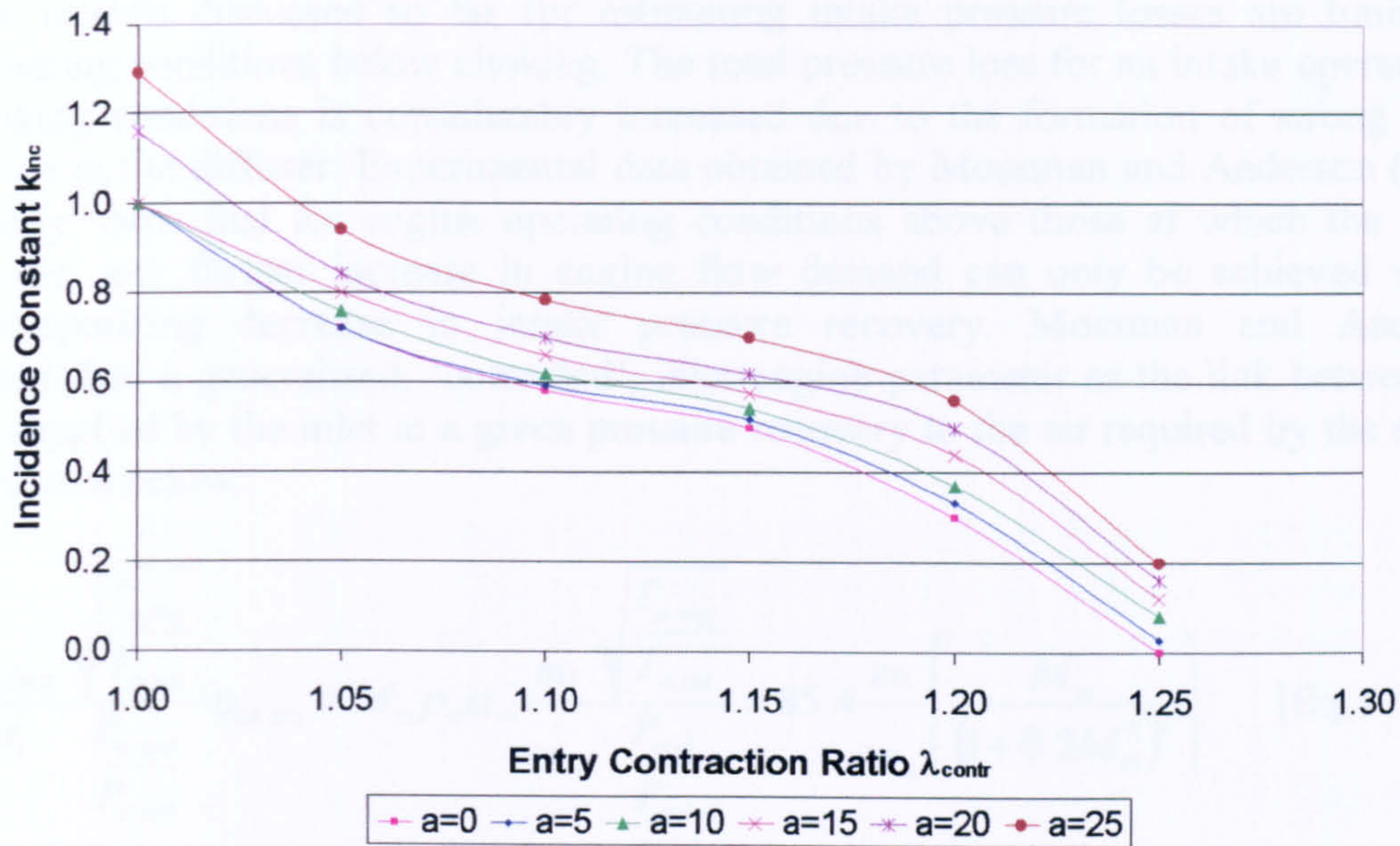


Figure 6.2.4.3:  $k_{inc}$  factor for circular lips at incidence



## Lip Loss Boundary at Incidence - Elliptical Lips

Figure 6.2.4.4:  $k_{\text{inc}}$  factor for elliptical lips at incidenceLimitations and Potential Expansion

Larger values of aircraft incidences are encountered at low speeds and therefore, especially for civil aircraft, it is at relatively low Mach numbers that the effects of incidence are of most interest. The method presented above for determining the effect of incidence on intake pressure recovery is limited to low speeds since the experimental data on which it is based are valid for free-stream Mach numbers less than 0.25.

The loss model adopted for calculating the intake pressure loss due to incidence effects assumes that interaction effects are independent of how the lip loss is calculated i.e. at incidence or at zero-incidence. There are no sufficient data in literature to verify the validity of this assumption although the work of Dolan and Runstadler (1973) supports that it is the overall loss in pressure at entry which determines the magnitude of the diffuser loss rather than the detailed asymmetric distribution of it.

**6.2.5. Effect of Choking on Pressure Recovery**

This section discusses how losses in pressure recovery may be severely influenced by engine operating conditions above those at which the intake chokes, and describes how pressure recovery estimates can be related to engine swallowing capacity in the *2D Intake SLC Software*. Limitations of the procedure adopted and scope for future development are also discussed.



### Introduction

The models discussed so far for estimating intake pressure losses are limited to operating conditions below choking. The total pressure loss for an intake operating at choking conditions is considerably increased due to the formation of strong shock waves in the diffuser. Experimental data obtained by Mossman and Anderson (1954) clearly show that for engine operating conditions above those at which the intake chokes, any further increase in engine flow demand can only be achieved with a corresponding decrease in intake pressure recovery. Mossman and Anderson established a generalised, 'corrected', inlet-engine parameter as the link between the air supplied by the inlet at a given pressure recovery to the air required by the engine as shown below:

$$\frac{\dot{m}_{gener}}{A_1} \frac{\sqrt{\frac{T_{o,eng}}{T_{o,std}}}}{\frac{P_{o,eng}}{P_{o,std}}} \eta_{intake} = M_\infty \rho_\infty \alpha_\infty \frac{\dot{m}_1}{\dot{m}_\infty} \frac{\sqrt{\frac{T_{o,eng}}{T_{o,std}}}}{\frac{P_{o,\infty}}{P_{std}}} = 85.4 \frac{\dot{m}_1}{\dot{m}_\infty} \left[ \frac{M_\infty}{(1+0.2M_\infty^2)^3} \right] \quad [\text{Eq. 6.2.5.1}]$$

The inlet-engine parameter, given by the right side of the above equation, is basically established as a function of the free-stream Mach number and mass flow ratio. The solution of the above equation is graphical. The 'correction' of temperature and pressure terms in Equation 6.2.5.1 with respect to standard conditions, enables estimation of the intake-engine performance at various conditions.

### Pressure Recovery Calculation for Conditions below Choking

In order to determine whether the intake operates un-choked or choked and before the final intake pressure recovery is established the intake entry Mach number  $M_1$  should be compared to the choking value  $M_{1ch}$ . For un-choked flow, the value of the intake entry flow Mach number  $M_1$ , at which the lip loss is calculated, should be below the choking value  $M_{1ch}$ . The choking Mach number is given by:

$$M_{1ch} = M_{1cho} - \Delta M_{1ch} \quad [\text{Eq. 6.2.5.2}]$$

Where  $M_{1cho}$  is obtained from experimental data published in ESDU Item No. 80037 (1980) as a function of the entry contraction ratio.  $\Delta M_{1ch}$  is similarly obtained from

$$\text{experimental data as a function of } k \left[ \left( \frac{A_1}{A_\infty} \right)_{cr} - \frac{A_1}{A_\infty} \right].$$

Both terms  $k$  and  $(A_1/A_\infty)_{cr}$  are parameters used in the calculation of the intake lip loss. The term  $A_1/A_\infty$  is calculated from continuity of mass flow from:

$$\frac{A_1}{A_\infty} = \frac{Q_\infty}{Q_1} \quad [\text{Eq. 6.2.5.3}]$$

Both mass flow functions in Equation 6.2.5.3 can be established from the corresponding Mach numbers as follows:

$$Q = \frac{M\sqrt{\gamma}}{\left(1 + \frac{\gamma-1}{2}M^2\right)^{\frac{\gamma+1}{2(\gamma-1)}}} \quad [\text{Eq. 6.2.5.4}]$$

If  $\left(\frac{A_1}{A_\infty}\right)_{cr} < \frac{A_1}{A_\infty}$  then  $\Delta M_{1ch}$  is taken to be equal to 0.

In calculating the lip loss for un-choked flow conditions, it is only required to make sure that  $M_1$  is less than  $M_{1ch}$  as predicted by Equation 6.2.5.2. The rest of the calculations remain the same, as described in previous sections, and the final pressure recovery is calculated as before by:

$$\eta_{intake} = 1 - \Delta\eta_{lip} - \Delta\eta_{diff}N_{mag} - \Delta\eta_{csd\_upstr} - \Delta\eta_{csd\_dwstr} \quad [\text{Eq. 6.2.5.5}]$$

### Pressure Recovery Calculation for Conditions above Choking

In order to calculate the pressure recovery at conditions above choking, the pressure recovery at the choking limit  $\eta_{intake\_ch}$  needs to be established first. This is done based on the choking values of  $M_1$  and  $M_{intake\_throat}$ , following exactly the same procedure as described in previous sections for un-choked flow.

$$\eta_{intake\_ch} = 1 - \Delta\eta_{lip\_ch} - \Delta\eta_{diff\_ch}N_{mag\_ch} - \Delta\eta_{csd\_upstr\_ch} - \Delta\eta_{csd\_dwstr\_ch} \quad [\text{Eq. 6.2.5.6}]$$

Establishing the actual choking values of  $M_1$  and  $M_{intake\_throat}$  involves an iterative procedure due to the interdependence of  $M_\infty$  and  $A_1/A_\infty$ .

From ESDU Item No. 80037 (1980) and based on the generalised intake-engine parameter established by Mossman and Anderson (1954) (Equation 6.2.5.1), the engine demand at the choking limit can be similarly related to the pressure recovery at the choking limit based on conditions at the intake throat as follows:

$$\left(\frac{m\sqrt{T_{o,eng}}}{P_{o,eng}}\right)_{ch} = \left(\frac{Q_{intake\_throat}A_{intake\_throat}}{\eta_{intake}\sqrt{R}}\right)_{ch} \quad [\text{Eq. 6.2.5.7}]$$

The value of  $Q_{intake\_throat}$  at the choking limit is obtained from  $M_{intake\_throat\_ch}$  by:

$$Q_{intake\_throat\_ch} = \frac{M_{intake\_throat\_ch}\sqrt{\gamma}}{\left(1 + \frac{\gamma-1}{2}M_{intake\_throat\_ch}^2\right)^{\frac{\gamma+1}{2(\gamma-1)}}} \quad [\text{Eq. 6.2.5.8}]$$



The recovery at engine flow conditions above choking is then given by:

$$\eta_{intake} = \frac{\left( \frac{\dot{m} \sqrt{T_{o,eng}}}{P_{o,eng}} \right)_{ch}}{\frac{\dot{m} \sqrt{T_{o,eng}}}{P_{o,eng}}} \eta_{intake\_ch} \quad [\text{Eq. 6.2.5.9}]$$

**Implementation**

The effect of choking on intake pressure recovery is handled by subroutine *Intake2D\_PressureRecoveryCalc.f90* once choking conditions are detected during the calculation of the intake flow field. The inlet choking Mach number for attached lip flow is established from Figure 6.2.5.1 as a function of the entry contraction ratio. The increment in inlet choking Mach number due to lip flow separation is established from Figure 6.2.5.2.

**Inlet Choking Mach Number for Attached Lip Flow**

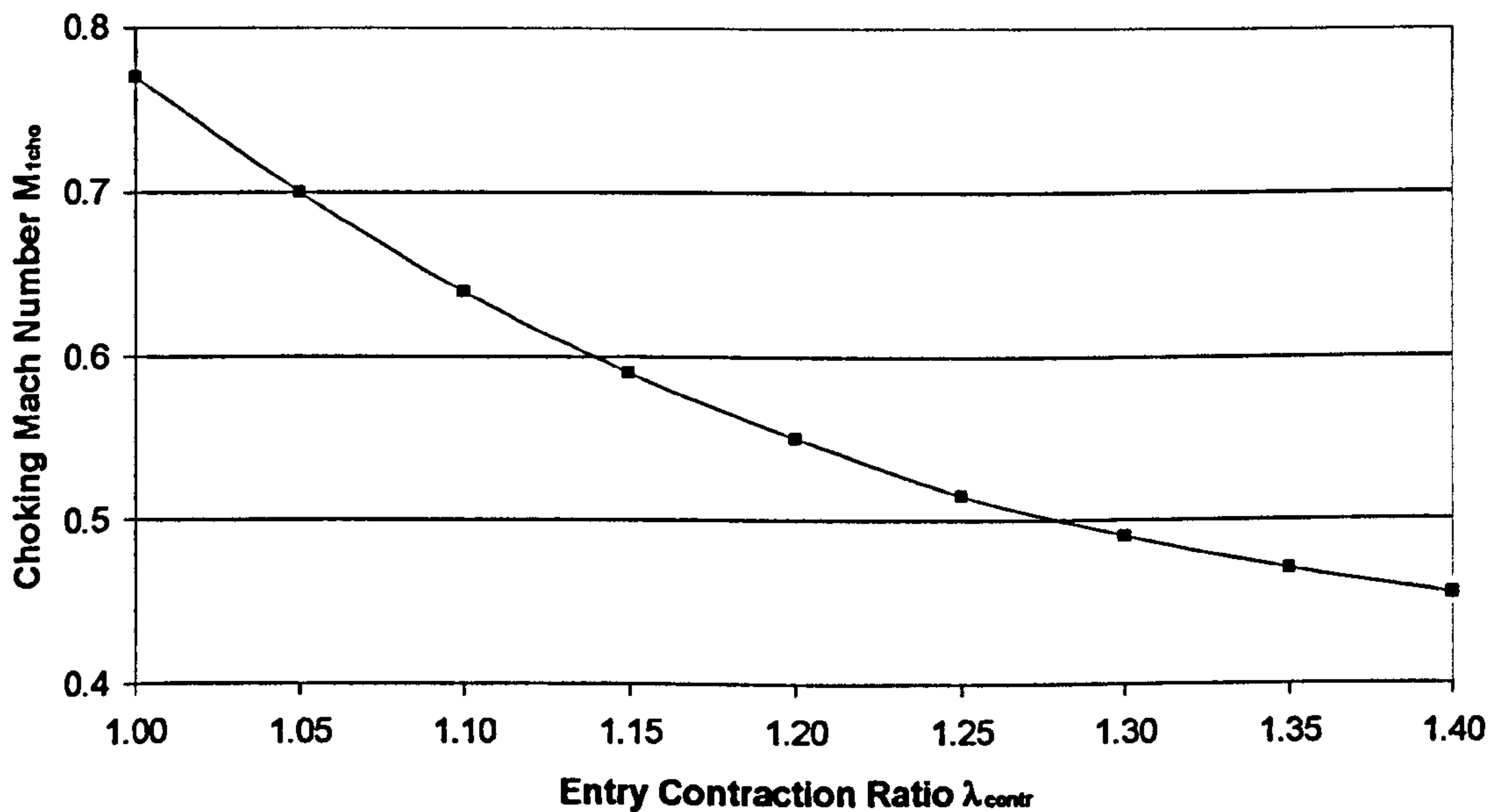


Figure 6.2.5.1: Inlet choking Mach number for attached lip flow

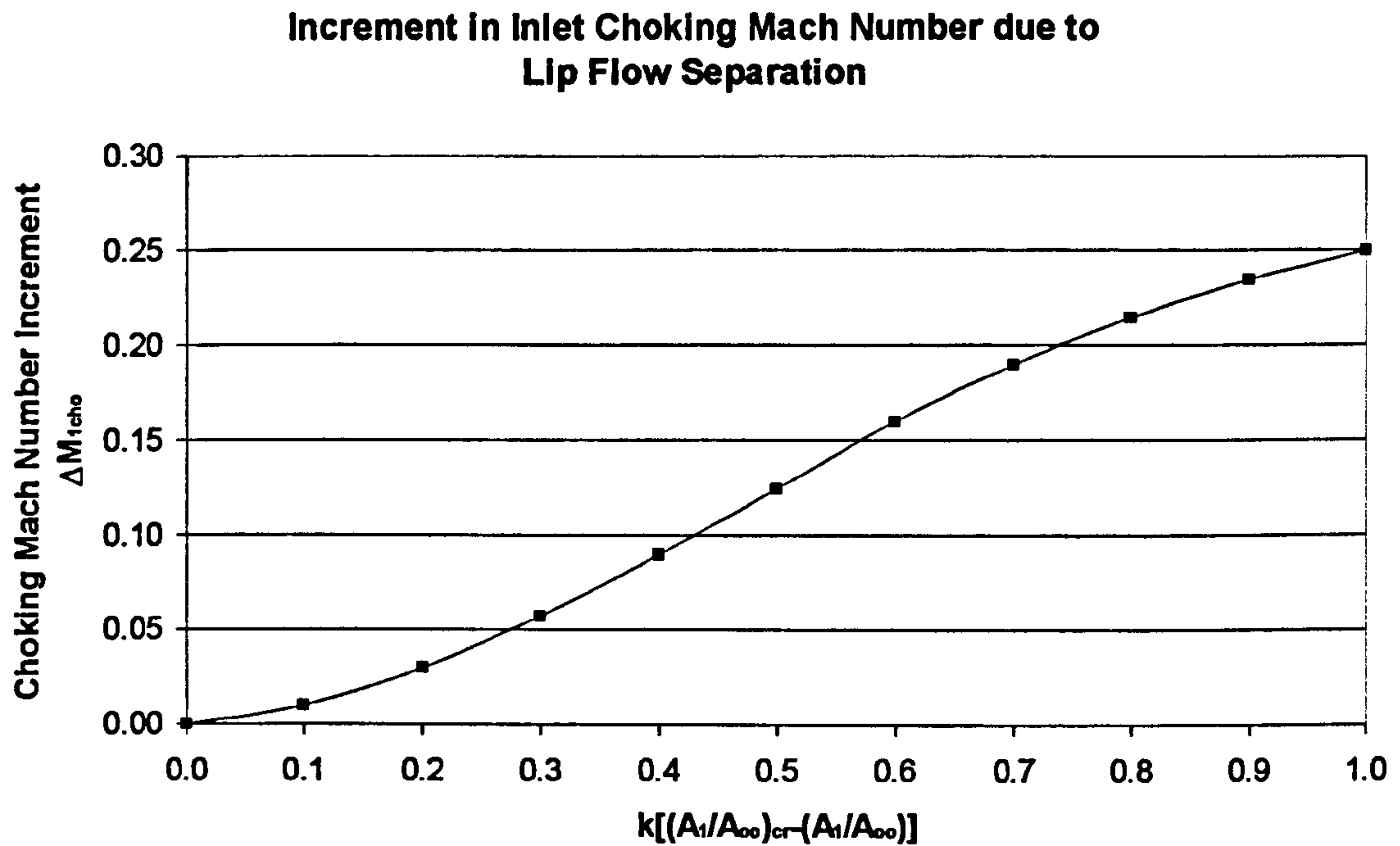


Figure 6.2.5.2: Increment in choking Mach number due to lip flow separation

### Limitations and Potential Expansion

Equation 6.2.5.9 actually implies that the effective area of the throat remains unchanged and therefore, it can only be used as an approximate estimate of the intake pressure recovery for conditions above intake choking. Moreover the estimation of the choking limit obtained from the models described in previous sections is only approximate since the flow conditions at choking are in reality very sensitive to small changes in flow parameters and geometry.

## **6.3. Calculation of Intake End-Wall Boundary Layer**

This section deals with the phenomenon of the intake end-wall boundary layer and describes how the annulus flow blockage factors are calculated in the *2D Intake Streamline Curvature Code*. The following paragraphs discuss also the limitations of the model adopted and scope for future development.

### Introduction

As previously discussed in Section 5.10, viscous effects can have a major influence on the performance of engine components, including intakes, ducts and nozzles. They can limit the achievable pressure rise by increasing losses and reduce the mass flow capacity by reducing the effective flow area. Intake end-wall boundary layers can have a significant effect on the overall engine pressure rise and cause flow blockage large enough for the fan or compressor performance to be considerably affected over



its entire operating range. Consequently, the inclusion of their effects on the intake flow simulation is of significant importance for the accuracy of the results. In an intake, boundary layers develop on the wetted surfaces i.e. the inside walls of the intake lips and the intake cone.

For purposes of consistency with the compressor flow field calculations, this work adopts exactly the same procedure for calculating intake end-wall boundary layers as in the case of the compressor (Section 5.10). Basically, the method adopted incorporates the same model for the prediction of the boundary layer displacement thickness which is explicitly coupled to the inviscid, streamline-curvature core flow calculation of the intake. Although the boundary layer literature review is not repeated again in this section, the following paragraphs repeat the basic equations of the model adopted, as described previously in Section 5.10, but with small differences.

### Calculation of Boundary Layer Blockage Factors

According to the simplified two-dimensional boundary layer approach, as in Barbosa<sup>9</sup>, the boundary layer is considered to be turbulent throughout the intake and the core flow dominated by the meridional velocity. The following integral can be calculated on the boundary layer edges for both intake lip and cone regions:

$$\int_{z_{inlet}}^{z_{outlet}} V_m^4(z) dz \quad [\text{Eq. 6.3.1}]$$

Where  $V_m$  is the meridional velocity on the assumed boundary layer edge and  $z$  is the axial distance measuring from the beginning of the intake lip and cone. The integral can be calculated numerically using the trapezoidal rule. From Schlichting<sup>1</sup> and Jansen<sup>6</sup> it can be shown that the boundary layer momentum thickness for each axial location is given by the following formula:

$$\theta(z) = k_{units} \left( \frac{\int_{z_{inlet}}^{z_{outlet}} V_m^4(z) dz}{V_m^{3.2}(z)} \right)^{0.8} \quad [\text{Eq. 6.3.2}]$$

Where  $k_{units}$  is a units correction factor. The next step is to evaluate the first derivative of the boundary layer momentum thickness with respect to  $z$  which is then used for the determination of the shape factor along the intake wetted surfaces:

$$H(z) = 1.5 + 30 \frac{d\theta}{dz} \quad [\text{Eq. 6.3.3}]$$

The boundary layer displacement thickness at any point throughout the intake annulus can then be calculated from the definition of the shape factor:

$$\delta^*(z) = \theta(z)H(z) \quad [\text{Eq. 6.3.4}]$$

The resultant reduction in flow area is subsequently translated into a more convenient coefficient for representing area reduction, the flow blockage factor  $k_B$ . The general definition of the flow blockage factor is the following:

$$k_B = \frac{\text{Free Stream Area}}{\text{Metal Area}} \quad [\text{Eq. 6.3.5}]$$

The intake lip and cone blockage factors can be expressed individually in terms of the radial coordinates and displacement thickness, as follows:

$$k_{B\_cone} = \frac{(R_{cone} + \delta_{cone}^*)^2 - R_{cone}^2}{R_{lip}^2 - R_{cone}^2} \quad [\text{Eq. 6.3.6}]$$

$$k_{B\_lip} = \frac{R_{lip}^2 - (R_{lip} - \delta_{lip}^*)^2}{R_{lip}^2 - R_{cone}^2} \quad [\text{Eq. 6.3.7}]$$

Where  $R_{cone}$  and  $R_{lip}$  are the radial locations of the streamlines close to the end walls, and  $\delta_{cone}^*$ ,  $\delta_{lip}^*$  the displacement thicknesses at hub and tip respectively calculated as shown previously.

Finally, the resultant overall blockage factor at the inlet and outlet of each blade row can be established from:

$$k_B = 1 - (k_{B\_cone} + k_{B\_lip}) \quad [\text{Eq. 6.3.8}]$$

### Implementation

End-wall boundary layer calculations are carried out in the *2D Intake Streamline Curvature Code* by subroutine *Intake2D\_BoundaryLayerCalc.f90* based on the model described above. This subroutine is called by the main subroutine *Intake2D\_MainProgram.f90* immediately after the entire intake flow field has been calculated. The purpose of this subroutine is to calculate the end-wall blockage factors and annulus blockage factor at the intake outlet. The input variables needed for the calculation are the co-ordinates of the solution nodes along the intake lip and cone and the meridional velocity distribution at these positions.

Blockage factor calculation based on the above theory requires the two-dimensional meridional velocity distribution throughout the intake. On the other hand, the boundary layer displacement thickness is required for the determination of the flow field within the intake. For this reason, a first flow field calculation is carried out based on guessed blockage factors that the user specifies as inputs. Once the calculation has converged for the first time, new values of blockage factors are calculated and a second full intake calculation begins. This iterative calculation should be repeated until convergence is obtained between the guessed and calculated blockage factors. Before each iteration, streamline coordinates are updated setting the minimum effective annulus height at the outer edge of the cone boundary layer and



the maximum effective annulus height at the inner edge of the lip boundary layer. The current code is set to do this iteration only once in order to save computational time.

To carry out this analysis, no extra calculation stations are required, in contrast to the compressor case where extra auxiliary points need to be established within the bladed regions in order to assist the mathematical derivations required.

### Limitations and Potential Expansion

The same general limitations apply as in the case of the compressor. The model adopted by this study is valid for shape factors  $H(z)$  below 2.2 for accelerating flows, and below 1.1 for decelerating flows. Moreover, the resultant overall blockage factor is restricted above 0.7, whereas cone and lip blockage factors are kept below 0.25 and 0.2 respectively.

As mentioned before, the calculated overall intake pressure loss is sub-divided into two parts, based on the boundary layer displacement thicknesses of the cone and lip. An extra iterative loop could be employed in order to take into account the progressive drop in pressure along the length of the boundary layer and how this would in turn affect the displacement thickness of the boundary layer and overall pressure loss. This would however complicate programming and would increase the computational time enormously for a small improvement in accuracy.

## CHAPTER VII

# **2D SLC ALGORITHM IMPLEMENTATION**

The main focus of this chapter is the description of the individual component algorithms that were developed for the purposes of this investigation. Apart from describing in detail the design, structure and execution of each algorithm this chapter also refers to the general programming features and principles that were adopted by this work.

## ***7.1. Software Programming Features***

The aim of this particular section is to stress the importance of developing robust, well-thought out software, and to highlight the main areas a potential programmer should focus on in order to achieve this. The following subsections highlight briefly the programming features incorporated into the development of this software before continuing to explain the internal workings of individual algorithms. Hopefully, this will provide the inexperienced in programming reader with a better understanding of the structure and execution of the algorithms described in following sections.

### ***7.1.1. Programming Requirements***

The development of the *2D SLC Software* was based on the following programming principles:

#### Clear Program Scope

The objectives and overall capability of the software were very carefully thought out before any coding begun. Having a clear objective from the onset, kept changes to the code architecture during coding to a minimum.

#### Well-Defined Program Structure

Perhaps the most important aspect of any program is its design and overall architecture. The actual coding of the program and sub-programs, although being also important, is relatively straightforward by comparison. A program with poor architecture is synonymous with coding that almost certainly begun before the program was well thought out. Experience has shown that such a program can only be made to work correctly by the author himself while others may still use it but with considerable difficulty. Usually such a program will soon become obsolete and abandoned by users on the grounds of poor reliability and user unfriendliness.

Given the size of this software, a lot of time was spent by the author in careful initial design, before writing any code, which was more than regained during the process of software testing and debugging. Actually, both the structure and execution of the software fully reflect the way the streamline curvature method was implemented.



### Maintainability and Portability

The *2D SLC Software* was developed taking the above two principles strongly into account. This becomes more evident in subsequent chapters but, generally speaking, software that aims to a real contribution and is likely to be used extensively by the wider research community needs to be easily maintainable and portable. Large programs such as this one can have an unexpectedly long life and will almost certainly, at some point during their lifetime, be found to have errors in special circumstances that were not foreseen, or were incorrectly handled, during the initial design phase. Almost inevitably, most programs will, therefore, be subsequently extended to deal with new problems not in the original specification. More time and effort is probably going to be spent in extending and maintaining this program than was spent in originally developing it.

Writing portable programs is equally important. The compilation and execution of the software was successfully tested on several machines having different specifications. The use of non-standard or obsolescent programming features was also avoided throughout the code.

### Clear Inputs and Outputs

Program input and output were made clear to understand even for the inexperienced end user. All input files have a well-defined, commented structure so that changes to the input conditions can be made easily. The form of the output was made as clear and useful as possible.

### Modular Design

The code was developed to be fully modular in the sense that the mission of every program unit (subroutine or function) is clearly defined, performing a specific task only. Individual program units can be easily identified by their name and role and updated or replaced accordingly.

### Extendable Functionality

The current *2D SLC Software* incorporates the capability mentioned before. Because of the code being of modular design this capability can be quite effortlessly improved and extended in the future by other programmers. Adding more functionality to the existing one, would make the code even more versatile.

### User Friendliness

Apart from the above principles, in order to enhance the user friendliness of the code even more, fully descriptive names for variables and program units together with comments have been used throughout. All program units (subroutines and functions) are identified by the attributes "*Compressor2D\_*" or "*Intake2D\_*", followed by a name that is indicative of the scope of that particular program unit. For example, *Compressor2D\_BladeIncidenceCalc.f90* calculates the air incidence angle at the blade leading edge whereas *Compressor2D\_BladeDeviationCalc.f90* calculates the air deviation angle at the blade trailing edge. The extension "Calc" denotes that a particular subroutine executes a set of calculations. The simple system adopted in naming program units is explained in more detail in sub-Section 7.1.3. *Program Unit Notation*. Similarly, variables have fully descriptive names to distinguish one from the other and avoid confusion, such as: *AirInletAbsVel* (air absolute velocity at inlet) and *AirMinLossEqDiffusionFactor* (minimum loss equivalent diffusion factor).

Finally, all program units begin with a brief statement about their objective and the particular method they are using to tackle a problem and comments precede almost every line of coding explaining briefly the nature of the calculation taking place.

### Error Handling

Error handling routines were added to the software where appropriate. For example, in *2D Compressor SLC Software*, during the calculation of a compressor speed line, program execution will not stop if the software fails to converge at a particular operating point, unless a fatal error occurs, indicating unreasonable input data. However, experience has shown that given reasonable speed line pressure ratio and mass flow limits, it is highly unlikely that the software fails to converge at a particular point while converging at other higher and lower points.

### Code Testing

Sufficient testing was done to ensure robust code execution not only within individual program units but of the code as a whole. Every subroutine and function was tested under a wide range of reasonable input conditions, initially individually, and later on as a part of the whole program. The output of the software was tested successfully against published experimental results.

## **7.1.2. Software Design**

Developing a robust streamline curvature program is a highly complex task due to the sophistication of the particular method. To carry out this task a fully 'modular' program development approach was followed. The aim of this section is to briefly describe how the design of the software was carried out and highlight the advantages of the method adopted.

Initially, a well-thought out structure plan was developed that gave a great assistance in the modular development as it identified in a natural way, the major components of the program. Rather than expanding these components within a single structure plan, all major components were treated as separate sub-problems whose solution was developed independently.

Extensive use of subprograms, with a well-defined interface, enabled the design of the streamline curvature program to be subdivided into several smaller, more manageable sections that could be coded and tested independently of the rest of the program. Once developed and fully tested, they were integrated back together to form the complete program according to the top-level structure plan.

Individual program units in the *2D SLC Software* are generally not aware of the internal details of any other program unit. The only link between one program unit and a subsidiary program unit is through the interface of the subsidiary program unit, which consists of the name and certain other public entities of that program unit.

The design of the *2D SLC Software* was based on FORTRAN's two basic types of procedure, subroutines and functions which were used as the primary building blocks. A further encapsulation facility, known as a 'module', was also used extensively, to



provide an extremely powerful functionality. Generally modules were used in two ways:

- To allow a defined set of variables and constants to be made available to more than one program unit through the USE association. This increased the code's flexibility and avoided the use of extremely long program unit interfaces. Examples are:
  - *Compressor2D\_AirPropVarDeclar.f90*
  - *Compressor2D\_BladeGeomVarDeclar.f90*
  - *Compressor2D\_StreamlineVarDeclar.f90*
  - *Intake2D\_LipLossVarDeclar.f90*
- To create a clearly defined program data structure. Modules enabled the grouping of data in such a way that all those 'specialised' procedures that required access to a particular group of data could do so by simply using the appropriate module. For example the subroutine which calculates the blade wake momentum thickness according to Swan's model *Compressor2D\_WakeMomentumThicknessSwanCalc.f90* has access to module *Compressor2D\_WakeMomentumThicknessSwanVarDeclar.f90* where data required by the model is stored in a table format. Similarly, subroutine *Compressor2D\_SecondaryLossCalc.f90* which calculates secondary losses accesses module *Compressor2D\_SecondaryLossVarDeclar.f90* where data for the secondary loss model is stored.

### 7.1.3. Program Unit Notation

To enhance user friendliness, the *2D SLC Software* utilises fully descriptive names for program units (modules, subroutines, functions etc.) and variables. Software architecture and execution are described in detail in subsequent chapters. The scope of this particular chapter, however, is to help the reader understand better the structure and flow of the software by describing first of all the simple system adopted in the naming of the vast majority of program units and variables.

Program units are named using a maximum of seven codewords as illustrated in the following table.

Codeword 1	Codeword 2 e.g.	Codeword 3	Codeword 4	Codeword 5 e.g.	Codeword 6	Codeword 7 e.g.
Compressor2D_ Intake2D_	Air	Inlet Or Outlet	Mean	Data	MinLoss	Calc
	Blade			Deviation		DistrbConverg
	BladePassage			GeomProp		DistrbGener
	BladeRow			Incidence		Interpolate
	BoundaryConditions			Performance		Output
	BoundaryLayer			Prop		Read
	Streamline			Triangle		VarDeclar
	...			...		...
etc.	etc.	etc.				

Table 7.1.3.1: Codeword structure for program unit notation

All names start with the codewords “*Compressor2D\_*” or “*Intake2D\_*”, followed by a series of other codewords that are indicative of the scope of that particular program unit. For example:

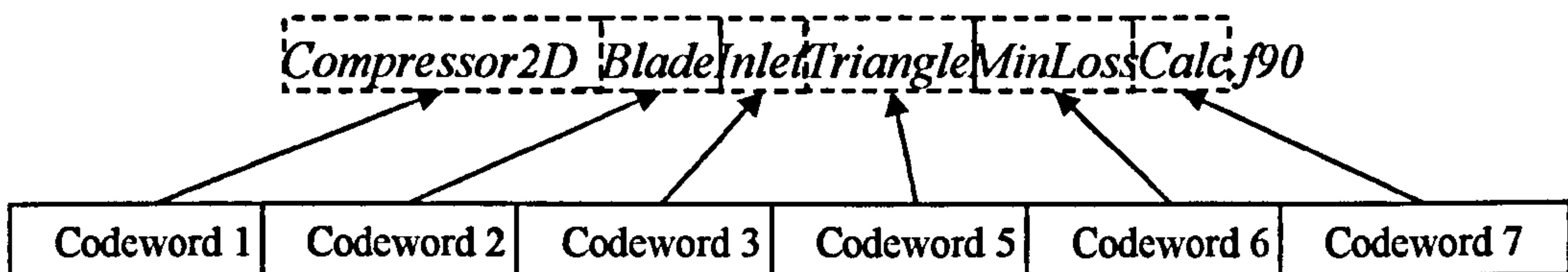


Figure 7.1.3.1: Example of program unit notation

The first codeword basically serves as an ‘identifier’. Both *2D Compressor SLC Software* and *2D Intake SLC Software* can be easily linked to other software either as external ‘black boxes’ or by compiling all program units together, under a unique program. Some users may wish to follow the second option, despite this being a bad programming practise. In this case it would be important to be able to distinguish between program units sharing similar features but coming from different sources.

The second codeword indicates whether a particular program unit deals generally with air, blade, streamline or other properties, for example:

- *Compressor2D\_AirPropVarDeclar.f90*
- *Compressor2D\_BladeGeomVarDeclar.f90*
- *Compressor2D\_StreamlineVarDeclar.f90*
- *Intake2D\_AirPropVarDeclar.f90*

The third codeword is not compulsory and it is used only in those cases where a program unit deals only with inlet or outlet conditions, for example:

- *Compressor2D\_BladeInletTriangleCalc.f90*
- *Compressor2D\_BladeOutletTriangleCalc.f90*

Similarly, the fourth codeword is only used to denote ‘mean’ conditions between two adjacent nodes. For example, *Compressor2D\_AirInletMeanPropCalc.f90* calculates the mean properties of the air flow at the leading edge of a blade between two adjacent nodes whereas *Compressor2D\_StrlineOutletMeanPropCalc.f90* calculates the mean properties of streamlines at the trailing edge of a blade between two adjacent nodes.

The fifth codeword is used to describe the particular content of a program unit and is compulsory. For example, the attribute ‘Prop’ would indicate the processing of properties (air, blade, streamline, etc.), the attribute ‘Data’ would indicate the processing of input data, ‘Triangle’ would indicate the calculation of velocity triangles and ‘Deviation’ would indicate the calculation of the deviation angle at the blade trailing edge, for example:

- *Compressor2D\_StreamlinePropCalc.f90*
- *Compressor2D\_BladeGeomInputDataRead.f90*
- *Compressor2D\_BladeInletTriangleCalc.f90*
- *Compressor2D\_BladeDeviationCalc.f90*
- *Intake2D\_StreamlinePropCalc.f90*



The sixth codeword is only used where applicable to indicate the calculation of minimum loss conditions as in *Compressor2D\_BladeDeviationMinLossCalc.f90* and in *Compressor2D\_BladeOutletTriangleMinLossCalc.f90*.

Finally, the seventh codeword provides an extension which is indicative of the program action taking place, for example 'Calc' denotes some sort of calculation as in *Compressor2D\_BladeInletMeanPropCalc.f90*, 'Read' denotes reading input data from an external file as in *Compressor2D\_BladeGeomInputDataRead.f90* and *Compressor2D\_BoundaryConditionsDataRead.f90*, 'Output' denotes printing data to an external file as in *Compressor2D\_StagePerformanceOutput.f90*, 'VarDeclar' indicates variable declaration in modules as in *Compressor2D\_AirPropVarDeclar.f90* and *Compressor2D\_BladeGeomVarDeclar.f90*.

Variables are similarly named using the same system and a maximum of seven codewords as illustrated in the following table.

Codeword 1 e.g.	Codeword 2 e.g.	Codeword 3 e.g.	Codeword 4 e.g.	Codeword 5 e.g.	Codeword 6 e.g.	Codeword 7 e.g.
Air	Input	Inlet Or Outlet	Abs	Stat	AeroChord	Mean
Blade			Rel	Tot	Ang	
BladeRow				Hub	Curvature	
Strmline			Axial	Tip	MachNo	
StrmlineInterRow			Merid		Pressure	
Strtube			Radial		RCoord	
Boundary			...	...	Slope	
...			etc.	etc.	...	
etc.					etc.	

Table 7.1.3.2: Codeword structure for variable nomenclature

## 7.2. 2D Compressor SLC Algorithm

This section describes first of all the capability of the software and then its exact structure and execution.

### 7.2.1. 2D Compressor SLC Software Capability

There is always scope for further development and expansion, almost at any stage during the lifetime of software. Although it was discussed before in *Chapter II - Project Objectives*, the basic capability that the *2D Compressor SLC Software* was initially developed to handle, is also outlined below for consistency:

- Facilitate compressor performance analysis in two dimensions
- Carry out DP and OD analysis
- Handle both subsonic and transonic regimes
- Identify conditions for surge and choking
- Handle multi-stage compressors
- Handle any type of blade profile such as the British C-series, NACA 65-series, DCA or user defined blade geometries
- Handle any compressor geometry

- Calculate the properties of the viscous flow field at predefined stations throughout the compressor annulus
- Calculate overall compressor map
- Handle non uniform inlet flow conditions
- Handle standard and user defined models for secondary losses, shock losses, Reynolds, deviation, incidence, boundary layer blockage etc.
- Link to lower fidelity cycle analysis software for high-resolution studies
- Provide a converged solution at any given operating point within minutes

This software was developed to provide great flexibility, in the sense that it can be used as:

- A performance prediction tool for compressors of a known design
- A development tool to assess the changes in performance of a known compressor after implementing small geometry changes
- A design tool to verify and refine the outcome of a preliminary compressor design analysis
- A teaching tool to provide the user with an insight of the two-dimensional flow field inside a compressor and how this could be effectively predicted using the streamline curvature method, combined with various algorithms and loss models
- A 2D compressor model that can be integrated into a conventional 0D gas turbine engine cycle simulation code, or linked to other 2D components, for the investigation of the influence of radially non-uniform flow profiles on whole engine performance

### 7.2.2. 2D Compressor SLC Algorithm Execution

This subsection discusses the structure and execution of the *2D Compressor SLC Software* and should be read alongside the algorithm flow chart provided as an appendix (*Appendix D - 2D Compressor SLC Software Flow Chart*).

The structure of the compressor streamline curvature algorithm is fairly straightforward. Basically, it consists of an outer major loop, called *Speed line Loop*, and two nested, iterative loops, called *Entropy and Boundary Layer Loop* and *Blade Row Loop*. *Blade Row Loop* is further subdivided into two, nested and iterative radial equilibrium loops, one for each blade row inlet and one for each blade row outlet, called *Inlet Rad Equilb Loop* and *Outlet Rad Equilb Loop* respectively. Each radial equilibrium loop is also subdivided into two iterative and nested loops, one for the convergence of mass flow and another for the convergence of the meridional velocity profile, called *Mass Flow Loop* and *Merid Vel Loop* respectively.

The execution of the compressor streamline curvature algorithm is controlled by the main program unit called *Compressor2D\_MainProgram.f90*. The main program unit, apart from controlling the flow of the program is also responsible for inputting data, printing results and handling errors.

Program execution begins with a call to *Compressor2D\_FileHandler.f90* subroutine. The purpose for this subroutine is to 'open' all input and output files about to be used.



There are two input files containing all the data necessary to run the software. *Compressor2D\_CompressorGeometry.txt* contains the following information:

- Number of blade rows
- Number of streamlines
- Number of blade chord locations
- Number of boundary layer auxiliary points
- Blade row type (rotor, stator or IGV )
- Number of blades in each row
- Blockage factors at the blade row inlet and outlet
- Blade profile type
- Blade profile thickness distribution from leading to trailing edge

And finally, for each blade row and at several stations from hub to tip, according to the number of streamlines:

- Inlet radial coordinate
- Outlet radial coordinate
- Inlet axial coordinate
- Outlet axial coordinate
- Pitch to chord ratio
- Stagger angle
- Inlet blade angle
- Outlet blade angle
- Maximum thickness to chord ratio
- Tip radius to maximum thickness ratio

The user can specify here a value for the blockage factor at each blade row inlet and outlet to be used later as a first guess in the calculation of the boundary layer blockage factors.

*Compressor2D\_InletBoundaryConditions.txt* contains information about the properties of the air at compressor inlet and for several locations from hub to tip:

- Total pressure
- Total temperature
- Static entropy
- Air absolute angle

The reading and initial processing of input data is handled by two particular subroutines that are called in sequence after *Compressor2D\_FileHandler.f90*. *Compressor2D\_BladeGeomInputDataRead.f90* reads geometric input data and performs unit conversions while *Compressor2D\_BoundaryConditionsDataRead.f90* reads compressor inlet boundary conditions.

Due to the two-dimensionality of the compressor input geometry, the vast majority of variables used by the program is stored as two-dimensional, 'allocatable' arrays. Allocatable arrays provide more programming flexibility, and hence user friendliness, than other array types since the allocation and de-allocation of space for their elements is complete under user control. For example, the size of most variables in the *2D Compressor SLC Software* is determined by the number of blade rows and streamlines which are both input data, specified externally of the main program in

*Compressor2D\_CompressorGeometry.txt*. Space is dynamically allocated for array elements in separate allocation statements inside the code, after which the arrays may be used in the normal way. This gives the user the flexibility to change those parameters without having to make changes to the source code.

Array allocation and initialization is handled by subroutines *Compressor2D\_ArrayAllocation.f90* and *Compressor2D\_ArrayInitialisation.f90* respectively which are in turn called after geometric data are read. All variables are initialized to 0.0 (zero) as a precaution and in order to avoid any mathematical operations taking place with NaN (Not-a-Number).

After all input data are read and processed the *Speed Line Loop* begins. This is the outer major loop and is repeated only once for every compressor operating point. The first subroutine to be called inside the *Speed Line Loop* is *Compressor2D\_CompressorOperatingPointCalc.f90*. The code can be configured to produce results for several operating points along the same speed line uninterrupted. This subroutine is responsible for defining a new compressor operating point, by changing the compressor mass flow at a given compressor speed, once the previous operating point converges. The compressor operating speed, with respect to design point, as well as the step size for the mass flow change can be specified by the user in this subroutine. Repeating the same for several speed lines eventually produces a complete compressor map.

The code can also be configured to produce the whole compressor map without any user intervention. However, this runs the risk of the code crashing unexpectedly close to surge or choking, unless some very robust rules for predicting complete compressor surge and choking are in place. In order to control program execution better, it is highly recommended to handle one constant speed line at a time.

Once the compressor operating point is established, in terms of mass flow, operating speed and inlet boundary conditions, the *Entropy and Boundary Layer Loop* begins. This is an iterative loop and should be repeated many times, together with all other nested loops inside it, until the calculations for a) entropy rise across the compressor annulus and b) boundary layer blockage factor converge to a fixed value. However, software testing revealed that even two iterations would be sufficient to produce reasonably accurate estimates for the total entropy rise and blockage factors. Using only two iterations is also justified on the grounds of minimizing total program running times, especially in the case of a complete map calculation that may take as long as 5-6 hours depending on the number of speed lines and the number of points on every speed line. Users aiming at a quantitative analysis may use a larger number of iterative loops for entropy and boundary layer convergence.

At the beginning of the *Entropy and Boundary Layer Loop* the location of streamlines has not been established yet and a first guess has to be made. This is handled in subroutine *Compressor2D\_StreamlineCoordInitialise.f90* where streamlines are positioned equally spaced from hub to tip, at the blade leading and trailing edges, taking also into account the initial guess for the blockage factors specified by the user in *Compressor2D\_CompressorGeometry.txt*.



Stream tube mass flow is calculated next in subroutine *Compressor2D\_StreamtubeMassFlowCalc.f90*, based on the initial streamline positioning and assuming a proportional increase in mass flow from hub to tip in accordance to the increase in stream tube area.

At this stage, boundary conditions at the inlet of the compressor and hence, inlet of every stream tube, are fully established and the calculation of the performance of all blade rows begins with the *Blade Row Loop*. This loop is repeated as many times as the number of blade rows and is subdivided into two iterative, nested loops (*Inlet Rad Equilib Loop* and *Outlet Rad Equilib Loop*) that basically solve the radial equilibrium, non-linear, partial differential equation at every blade row inlet and outlet, taking into account streamline curvature.

The *Inlet Rad Equilib Loop* begins by calling two subroutines which are named *Compressor2D\_BladeGeomInputDataInterpolate.f90* and *Compressor2D\_BoundaryConditionsDataInterpolate.f90* respectively. These two subroutines interpolate between the input boundary conditions and input geometric data, from hub to tip, for the corresponding properties at the streamline locations (nodes) just established. Input data are normally given at fixed blade heights along the blade span, coinciding with the initial positions of the streamlines. During execution, however, streamlines are shifted and therefore geometric and boundary condition data should be interpolated from the initial distribution given at the input file.

As the calculation proceeds, subsequent blade rows interpolate between the outlet boundary conditions and geometric data of the previous blade row to establish inlet boundary conditions and streamline locations. In reality, the flow profiles within the bladeless space between to adjacent blade rows do not remain constant. The flow is slightly redistributed and that should be taken into account. The current version of the software treats this phenomenon rather simplistically but future versions should incorporate this in the calculations for greater accuracy.

The set of the necessary input geometrical data is completed with the calculation of the blade sweep angle, the blade camber angle, the solidity, the blade pitch, the blade chord (both geometric and aerodynamic) and the blade maximum thickness. All these extra blade geometric properties, in the streamline direction, are calculated in *Compressor2D\_BladeGeomPropDataCalc.f90*, based on the available input data. Additionally, a considerably large amount of geometrical data is calculated for the accurate determination of the dimensions of the blade throat, at various locations from hub to tip, which is then used by subsequent subroutines to identify blade passage choking conditions.

*Compressor2D\_BladeInterRowCoordCalc.f90* calculates the coordinates of the quazi-orthogonal system used to define the location of the nodes. Coordinates are basically established at the first blade row leading edge, mid-way in-between blade rows and at the last blade row trailing edge.

Having established the coordinates at the nodes, subroutine *Compressor2D\_StreamlinePropCalc.f90* is called to calculate streamline properties such as streamline inlet sweep angle, slope, curvature, meridional entropy gradient etc. Similarly, *Compressor2D\_StreamlineInletMeanPropCalc.f90* is subsequently

called to calculate the average streamline properties between two adjacent nodes at the blade leading edge.

Subroutine *Compressor2D\_BladeRowInletMeridVelDistrbConverg.f90* initiates the iterative *Inlet Mass Flow Loop* by guessing the inlet meridional velocity at the hub and calling *Compressor2D\_BladeRowInletMeridVelDistrbGener.f90*. The value of the meridional velocity at the hub is not known beforehand. It is selected such as to minimize, as much as possible, the convergence time. The latter subroutine basically integrates the radial equilibrium, non-linear, partial differential equation iteratively in *Inlet Merid Vel Loop* to calculate the meridional velocity at the next streamline and eventually to calculate the entire distribution of the meridional velocity profile from hub to tip at the blade row inlet. During this process, sequential calls are made to four other subroutines for the calculation of all air and geometric properties at the nodes of the blade leading edge. *Compressor2D\_BladeInletTriangleCalc.f90* calculates velocity triangles from hub to tip, given inlet meridional velocity and absolute angle. Subroutine *Compressor2D\_BladeInletBoundaryCondCalc.f90* calculates total and static air properties at the nodes of the blade leading edge. Finally, subroutine *Compressor2D\_BladeInletMeanPropCalc.f90* calculates mean blade geometric properties between nodes and *Compressor2D\_AirInletMeanPropCalc.f90* calculates mean air properties between nodes. Once *Inlet Merid Vel Loop* converges and a first estimate for the meridional velocity distribution at blade inlet is established, execution is returned to *Compressor2D\_BladeRowInletMeridVelDistrbConverg.f90* and the continuity equation is integrated at the blade leading edge, from hub to tip, to check whether the compressor total mass flow just established corresponds to the input mass flow. If not, a new value for the meridional velocity at the blade hub is guessed and *Inlet Merid Vel Loop* is repeated again by calling *Compressor2D\_BladeRowInletMeridVelDistrbGener.f90*. If the mass flows match, *Compressor2D\_BladeRowInletMeridVelDistrbConverg.f90* checks for agreement on stream tube mass flow. If the initial stream tube mass flows are different than the ones just calculated, streamlines are repositioned along the blade leading edge and execution is returned to the beginning of the *Inlet Rad Equilib Loop* which is then repeated until *Inlet Mass Flow Loop* converges.

Once the entire *Inlet Rad Equilib Loop* converges and conditions for radial equilibrium are satisfied at the blade row inlet, code execution continues to calculate a number of other parameters related to blade row inlet conditions which do not affect radial equilibrium and hence, are not calculated within the *Inlet Rad Equilib Loop*. More specifically, choking conditions at the blade throat are established by calling subroutine *Compressor2D\_BladePassage Choking.f90*. Incidence and minimum loss incidence are also calculated in *Compressor2D\_BladeIncidenceCalc.f90* and *Compressor2D\_BladeIncidenceMinLossCalc.f90* respectively. Shock wave losses due to transonic and supersonic inlet mach numbers are calculated in *Compressor2D\_ShockWaveCalc.f90* based on the calculation of the blade passage flow turning angle in *Compressor2D\_BladePassageFlowTurningAngCalc.f90*. Finally, losses due to high Reynolds numbers are calculated in *Compressor2D\_ReynoldsCorrectionCalc.f90*.

The *Outlet Rad Equilib Loop* begins by calling subroutine *Compressor2D\_BladeGeomInputDataInterpolate.f90* to establish input geometric data, from hub to tip, at blade trailing edge nodes by interpolation. Other blade



geometric properties, in the streamline direction, are then calculated in *Compressor2D\_BladeGeomPropDataCalc.f90*, based on the interpolated input data.

Two subroutines are then called in sequence to calculate the deviation angle at the blade trailing edge namely *Compressor2D\_BladeDeviationMinLossCalc.f90* and *Compressor2D\_BladeDeviationCalc.f90*.

*Compressor2D\_BladeInterRowCoordCalc.f90* calculates the coordinates of the quasi-orthogonal system used to define the location of the nodes at the blade trailing edge. Having established the coordinates at the trailing edge nodes, subroutine *Compressor2D\_StreamlinePropCalc.f90* is called to calculate streamline properties such as streamline outlet sweep angle, slope, curvature etc. Similarly, *Compressor2D\_StreamlineOutletMeanPropCalc.f90* is subsequently called to calculate the average streamline properties between two adjacent nodes at the blade trailing edge.

*Compressor2D\_BladeRowOutletMeridVelDistribConverg.f90* initiates the iterative *Outlet Mass Flow Loop* by guessing the outlet meridional velocity at the hub and calling *Compressor2D\_BladeRowOutletMeridVelDistribGener.f90*. The latter subroutine integrates the radial equilibrium, non-linear, partial differential equation iteratively in *Outlet Merid Vel Loop* to calculate the distribution of the meridional velocity profile from hub to tip at the blade row outlet. During this process, sequential calls are made to seven other subroutines for the calculation of all air and geometric properties at the nodes of the blade trailing edge and the inclusion of losses. *Compressor2D\_BladeOutletTriangleMinLossCalc.f90* calculates velocity triangles for minimum losses conditions, from hub to tip, given outlet meridional velocity. Subroutine *Compressor2D\_WakeMomentumThicknessSwanCalc.f90* is then called to calculate the blade wake momentum thickness based on Swan's model. The blade total loss factor, based on Swan, is calculated in *Compressor2D\_BladeProfileLossSwanCalc.f90*, taking into account Reynolds losses, shock wave losses, wake losses and secondary losses calculated in *Compressor2D\_SecondaryLossCalc.f90*.

*Compressor2D\_BladeOutletTriangleCalc.f90* calculates velocity triangles from hub to tip given outlet meridional velocity and absolute angle. Subroutine *Compressor2D\_BladeOutletBoundaryCondCalc.f90* calculates all total and static air properties at the nodes of the blade trailing edge. Finally, subroutine *Compressor2D\_BladeOutletMeanPropCalc.f90* calculates mean blade geometric properties between nodes and *Compressor2D\_AirOutletMeanPropCalc.f90* calculates mean air properties between nodes.

Once *Outlet Merid Vel Loop* converges and a first estimate for the meridional velocity distribution at blade outlet is established, execution is returned to *Compressor2D\_BladeRowOutletMeridVelDistribConverg.f90* to check whether the compressor total mass flow just established from the solution of the partial differential equation corresponds to the inlet mass flow. If not, a new value for the meridional velocity at the blade hub is guessed and *Outlet Merid Vel Loop* is repeated again by calling *Compressor2D\_BladeRowOutletMeridVelDistribGener.f90*. If the mass flows match, *Compressor2D\_BladeRowOutletMeridVelDistribConverg.f90* then checks for agreement on stream tube mass flow. If the outlet stream tube mass flow is different

than the inlet stream tube mass flow calculated earlier, streamlines are repositioned along the blade trailing edge and execution is returned to the beginning of the *Outlet Rad Equilib Loop* which is then repeated until *Outlet Mass Flow Loop* converges.

When the *Outlet Rad Equilib Loop* converges, all conditions for satisfying full radial equilibrium at blade row inlet and blade row outlet are established, together with air and geometric properties at the nodes. Execution is passed back to the *Blade Row Loop* which repeats the same calculations, in exactly the same order for any subsequent blade rows. Once all blade row inlet and outlet meridional velocity profiles are established, subroutine *Compressor2D\_BoundaryLayerCalc.f90* is called to calculate the growth of the boundary layer throughout the entire compressor.

Up to this point, although the entropy rise across the compressor is calculated, it does not play a part in the solution of the radial equilibrium equation. Therefore, the entire *Entropy and Boundary Layer Loop* has to be repeated at least one more time to provide a more accurate flow field calculation, taking into account entropy as well. The second execution of this iterative loop completes the set of calculations for the selected compressor operating point.

Subroutines *Compressor2D\_BladeRowInletPerformanceOutput.f90* and *Compressor2D\_BladeRowOutletPerformanceOutput.f90* are subsequently called to print results in a tabular form to an external file called *Compressor2D\_Plot.txt*. Actually these two subroutines can be called from anywhere within the entire code to provide a snap shot of the compressor performance calculations taking place, even before the entire iterative process converges to a solution.

*Compressor2D\_StagePerformanceCalc.f90* calculates the performance of every stage in terms of pressure ratio, isentropic and polytropic efficiencies and temperature rise and *Compressor2D\_StagePerformanceOutput.f90* is finally called to print these results to an external file called *Compressor2D\_Plot.txt*. These results can be used in the construction of a compressor map.

The last four subroutine calls complete the *Speed Line Loop*. Execution is then returned to the beginning of the *Speed Line Loop* for the calculation of the next compressor operating point. When all operating points along a speed line are established subroutine *Compressor2D\_FileHandler.f90* is called again to 'save' and 'close' all input and output files that were used by the code.

The software also utilizes three purely mathematical subroutines where numerical interpolation, numerical derivation and numerical extrapolation are conducted namely *Compressor2D\_CubicSplineInterpolation.f90*, *Compressor2D\_Derivate.f90* and *Compressor2D\_ExtrapolatePoint.f90*. These subroutines are used extensively throughout the code as appropriate.

Finally, there is a large number of supporting modules used in the code either for global variable declaration or for storing data such as:

- *Compressor2D\_AirPropVarDeclar.f90*
- *Compressor2D\_BladeGeomVarDeclar.f90*
- *Compressor2D\_BoundaryLayerVarDeclar.f90*
- *Compressor2D\_LossFactorVarDeclar.f90*



### 7.2.3. Display Messages

During normal software execution, informative messages are displayed on the screen when:

- Full radial equilibrium is satisfied at blade row inlet
- Full radial equilibrium is satisfied at blade row outlet
- *Entropy and Boundary Layer Loop* is successfully executed for the first time
- The whole compressor performance is calculated successfully
- The calculation proceeds to a new operating point

Error messages are displayed when:

- Any iterative loop fails to converge, providing the user with information about the blade row and streamline number at which the problem occurred
- A mathematical error occurs during derivation, interpolation or extrapolation
- Flow conditions become highly supersonic

## 7.3. 2D Intake SLC Algorithm

This section describes the capability of this particular software, its exact structure and execution. The simulation of two-dimensional annular and conical ducts is also handled by this software.

### 7.3.1. 2D Intake SLC Software Capability

Similarly to the compressor, the basic capability that the *2D Intake SLC Software* was initially developed to handle, is also outlined below for consistency:

- Facilitate performance analysis in two dimensions of conical and annular intakes
- Carry out DP and OD analysis
- Handle both subsonic and transonic regimes
- Identify intake choking conditions
- Handle any intake geometry
- Calculate the properties of the viscous flow field at predefined stations throughout the intake annulus
- Calculate overall intake map
- Handle non uniform inlet flow conditions
- Handle standard and user defined models for rounded or sharp lip losses, diffuser losses, entry-diffuser interaction losses, Reynolds effects, incidence angle effects, boundary layer blockage etc.
- Link to lower fidelity cycle analysis software for high-resolution studies
- Provide a converged solution at any given operating point within minutes
- Facilitate performance analysis in two dimensions of conical and annular ducts and nozzles with little modification

This software can also be used as:

- A performance prediction tool for intakes of a known design

- A development tool to assess the changes in performance of a known intake after implementing small geometry changes
- A design tool to verify and refine the outcome of a preliminary intake design analysis
- A teaching tool to provide the user with an insight of the two-dimensional flow field inside an intake and how this could be effectively predicted using the streamline curvature method, combined with various algorithms and loss models
- A 2D intake model that can be integrated into a conventional 0D gas turbine engine cycle simulation code, or linked to other 2D components, for the investigation of the influence of radially non-uniform flow profiles on whole engine performance

### 7.3.2. 2D Intake SLC Algorithm Execution

This subsection discusses the structure and execution of the *2D Intake SLC Software* and should be read alongside the algorithm flow chart provided as an appendix (*Appendix E - 2D Intake SLC Software Flow Chart*).

The structure of the intake streamline curvature algorithm is much simpler than the compressor algorithm. It consists of an outer major loop, called *Boundary Layer Loop*, and two nested, iterative loops, called *Streamline Loop* and *Flow Field Loop*. The execution of the intake streamline curvature algorithm is controlled by the main program unit called *Intake2D\_MainProgram.f90*. The main program unit, apart from controlling the flow of the program is also responsible for inputting data, printing results and handling errors.

Program execution begins with a call to *Intake2D\_FileHandler.f90* subroutine. The purpose for this subroutine is to ‘open’ all input and output files about to be used. There are two input files containing all the data necessary to run the software. *Intake2D\_WallGeometry.txt* contains the following information:

- Number of streamlines
- Number of streamline points on casing (lip) wall
- Number of streamline points on engine cone wall
- Radial coordinates of casing (lip) wall
- Axial coordinates of casing (lip) wall
- Radial coordinates of engine cone wall
- Axial coordinates of engine cone wall

The input file *Intake2D\_InletBoundaryConditions.txt* contains information about the properties of the air in the radial direction, at the inlet of the intake pre-entry stream tube:

- Static pressure
- Static temperature
- Static entropy
- Air absolute angle

Reading and initial processing of input data, i.e. unit conversions, are handled by two particular subroutines that are called in sequence after *Intake2D\_FileHandler.f90*.



*Intake2D\_WallGeomDataRead.f90* reads geometric input data while *Intake2D\_BoundaryCondDataRead.f90* reads intake inlet boundary conditions.

Similarly to the compressor, space is dynamically allocated for array elements in separate allocation statements inside the code. Array allocation and initialization is handled by subroutines *Intake2D\_ArrayAllocation.f90* and *Intake2D\_ArrayInitialisation.f90* respectively which are in turn called after geometric data are read. All variables are initialized to 0.0 (zero) as a precaution and in order to avoid any mathematical operations taking place with NaN (Not-a-Number).

After all input data are read and processed, subroutine *Intake2D\_PreEntryStreamtubePropCalc.f90* is called in order to calculate conditions at the pre-entry stream tube inlet and mainly the pre-entry stream tube radius and area based on the inlet 'Q' function (non-dimensional mass flow parameter). *Boundary Layer Loop* begins next. This is an iterative loop and should be repeated many times, together with all other nested loops inside it, until the calculations for a) intake pressure recovery and b) boundary layer blockage factor converge to a fixed value. Software testing revealed that even two iterations would be sufficient to produce reasonably accurate estimates for the total pressure loss in the intake and blockage factors. Using only two iterations is also justified on the grounds of minimizing total program running times. Users aiming at a quantitative analysis may use a larger number of iterative loops.

The first subroutine to be called inside the *Boundary Layer Loop* is *Intake2D\_WallGeomPropCalc.f90*. This subroutine calculates the slope and curvature of the lip and engine cone walls based on input coordinates. The calculated wall slopes and curvatures are subsequently used by *Intake2D\_SmoothWallGeomCalc.f90* to establish new wall geometries, of smoother slope and curvature distributions, which are used instead. This reduces the chances of the streamline curvature code crashing because of inconsistent input wall coordinates. This software feature is optional and can be switched off by the user. The subroutine *Intake2D\_SmoothWallGeomOutput.f90* prints the adjusted wall geometry to the external file *Intake2D\_AdjustedWallGeometry.txt*.

At the beginning of the *Boundary Layer Loop* the location of streamlines has not been established yet and a first guess has to be made. This is handled in subroutine *Intake2D\_StreamtubeInletPropCalc.f90* where stream tube inlet properties, and especially mass flow, are calculated so that streamlines are positioned equally spaced from the centre-line to the pre-entry stream tube maximum radius. Subroutines *Intake2D\_InletBoundaryCondCalc.f90* and *Intake2D\_InletBoundaryCondOutput.f90* are responsible for calculating and printing respectively, the area-averaged flow properties at the intake inlet.

Subroutine *Intake2D\_CentrelineMeridVelDistribGener.f90* is then called to calculate the velocity distribution throughout the intake duct and along the central streamline from the 'Q' function variation. This is an iterative process that uses 1D flow assumptions in order to establish an initial estimate of the 1D velocity distribution through the intake. The velocity distribution is calculated at discrete z-locations on the central axis. The calculated velocity distribution needs to be reasonably smooth in order to obtain streamline shapes without extreme curvature, as well as to insure



stable convergence of the calculation. Next, the shape of a stream tube having a small maximum diameter is estimated from the one dimensional flow relations using the calculated center-line velocity distribution. From the shape of the estimated stream tube the first streamline is initialized. This is handled in *Intake2D\_StreamlineInitialise.f90*. At this stage the iterative process for calculating all streamlines from the center-line to the outer wall begins with the *Streamline and Flow Field Loops*.

Normals between the first and the central streamline are calculated by subroutine *Intake2D\_StreamlineNormalCalc.f90*, as well as slope and curvature distributions by subroutine *Intake2D\_NextStreamlinePropCalc.f90*. These functions permit the velocity and density distributions to be computed on the first streamline. Next, the mass flow through each normal is computed and compared with the required mass flow for this stream tube in *Intake2D\_NextStreamlineCalc.f90*. The streamline coordinates are then adjusted slightly in the direction that will reduce the error in mass flow, the error is computed, and the coordinates are readjusted, and so until the desired mass flow is obtained within a reasonable tolerance. This procedure is carried out at each point on the streamline. Then the curvature of this streamline is computed and used to obtain a new estimate for a smoother curvature distribution. With this new estimate the entire procedure is repeated to obtain a better estimate for the streamline. The velocity along this streamline is then taken as input data to compute the next streamline, which is first estimated from the one-dimensional equations, in the same manner as for the previous streamline. This is handled in *Intake2D\_NextStreamlineInitialise.f90*. As soon as the calculation of a given streamline is completed, flow properties of velocity, Mach number, static pressure, density and temperature are stored by *Intake2D\_FlowFieldCalc.f90* for every point along this streamline for later use.

Successive streamlines are computed similarly until all streamlines and two-dimensional flow field properties are estimated for the first time. This completes the *Streamline Loop*. Subroutine *Intake2D\_ConvergCheck.f90* is subsequently called to check whether the radial and axial coordinates of the last calculated streamline coincide with the outer wall. If not, a new meridional velocity distribution on the central streamline is calculated, based on the previous guess, and the whole process is repeated until convergence is achieved. This completes the *Flow Field Loop*.

Once the *Flow Field Loop* converges, execution continues within the *Boundary Layer Loop* for the calculation of the boundary layer blockage factors and total pressure loss throughout the intake. Subroutine *Intake2D\_BoundaryLayerCalc.f90* is called to calculate the boundary layer growth on the intake walls based on the established meridional velocity distributions on the intake lip and engine cone. Subsequently several other subroutines are called to calculate the pressure loss in various parts of the intake.

More analytically, subroutines *Intake2D\_IncidenceRoundedLipLossCalc.f90* or *Intake2D\_IncidenceSharpLipLossCalc.f90* can be alternatively called by the user in order to calculate the pressure recovery of the intake at incidence for rounded or sharp lips respectively. *Intake2D\_DiffuserLossCalc.f90* calculates the loss in total pressure due to the diffuser and *Intake2D\_Constant Area DuctLossCalc.f90* calculates losses associated with the presence of any constant-area ducts in the intake.



*Intake2D\_InteractionLossCalc.f90* calculates the loss in pressure recovery due to interaction effects between intake entry and diffuser, for attached and separated flows. Finally, the overall intake pressure recovery is calculated by *Intake2D\_PressureRecoveryCalc.f90* and the whole *Boundary Layer Loop* is executed once again with updated flow field properties and wall coordinates to account for the boundary layer growth.

When the *Boundary Layer Loop* is completed, subroutine *Intake2D\_FlowFieldPropOutput.f90* prints all air and geometric streamline properties to the external file *Intake2D\_FlowFieldProperties.txt*. Apart from local flow properties along streamlines, outlet radial profiles are also stored and printed to files for subsequent manipulation, along with area-averaged flow properties. This is handled by subroutines *Intake2D\_OutletBoundaryCondCalc.f90* and *Intake2D\_OutletBoundaryCondOutput.f90*. Subroutine *Intake2D\_FileHandler.f90* is called at the end to 'save' and 'close' all input and output files that were used by the code.

The software also utilizes three purely mathematical subroutines where numerical interpolation, numerical derivation and numerical extrapolation are conducted, namely *Intake2D\_CubicSplineInterpolation.f90*, *Intake2D\_Derivate.f90* and *Intake2D\_ExtrapolatePoint.f90*. These subroutines are used extensively throughout the code as appropriate.

Finally, there is a large number of supporting modules used in the code either for global variable declaration or for storing data such as:

- *Intake2D\_AirPropVarDeclar.f90*
- *Intake2D\_DiffuserLossVarDeclar.f90*
- *Intake2D\_BoundaryLayerVarDeclar.f90*
- *Intake2D\_InteractionLossVarDeclar.f90*
- *Intake2D\_PressureRecoveryVarDeclar.f90* etc.

### 7.3.3. Display Messages

During normal software execution, informative messages are displayed on the screen when:

- Input wall geometry is re-calculated successfully for smooth slope and curvature distributions
- Conditions at intake inlet are calculated
- Conditions at intake throat are calculated
- Conditions at intake outlet are calculated
- *Boundary Layer Loop* is successfully executed for the first time
- Radial equilibrium is satisfied throughout the intake
- The whole intake performance is calculated successfully

Error messages are displayed when:

- Any iterative loop fails to converge, providing the user with information about the streamline number at which the problem occurred
- A mathematical error occurs during derivation, interpolation or extrapolation



- Flow conditions become highly supersonic

## 7.4. Numerical Methods and Convergence Stability

This section addresses software convergence stability issues and briefly discusses the numerical methods employed in the software, as well as their limitations and potential expansion.

In contrast to the compressor streamline curvature algorithm, where calculations are carried out only at blade row inlet and outlet, in the *2D Intake SLC Software* several streamline points are used to define a given streamline. This results in a tendency of the solution to become unstable relatively easily. This tendency is a direct outcome of the use of the streamline curvature equations. A small relative change in radial coordinates can result in a relatively large change in curvature. Since the curvature is in the exponent in *Equation 6.1.6*, the velocity is sensitive to the curvature and thus to small changes in radial coordinates. This sensitivity was counteracted to a considerable extent by employing the following three techniques:

- In some cases, component geometry coordinates can come from old or blare drawings or are derived by hand calculations. For this reason, input wall geometry coordinates are 'assessed' by the software and an improved, smooth wall geometry with a systematic coordinate distribution is calculated and eventually used by the code, as described before. That minimizes the chances of the software crashing due to poor or inconsistent geometry coordinate selection.
- Another technique which is used to minimize the chances of the software crashing is the scaling of the z-axis coordinates during inviscid flow calculations. All z-axis geometry coordinates are scaled so that the last z coordinate (length of intake) becomes many times greater than the last y-axis coordinate (intake inlet radius). This reduces the effect of small changes in radial coordinates resulting in large changes in curvature. The results are scaled back to normal coordinates before pressure losses are calculated and the final solution is presented to the user.
- Finally, in the present method, a smooth distribution of curvature is used in the initial estimate for each streamline. Then when the actual curvature is computed, it is not used directly but is averaged with the curvature of the previous streamline. This process tends to stabilize the convergence and has been used in the calculations.

In the *2D Compressor SLC Software* the direction of integration is always from hub to tip. The software can be upgraded to provide the user the ability to select the starting point and direction of the integration. This would be a useful option since in some cases and especially at the blade row outlet plane, if the integration is set to start from the blade span extreme points, the losses can increase disproportionately to the meridional velocity. As a result of this, the whole calculation process can become



destabilized. Starting the integration from the blade mid-span towards the blade edges could potentially alleviate this problem.

Cubic spline interpolation is the only method programmed up to this point. It is a general method by which every type of function could potentially be handled. It would be advisable however, to have readily available alternative interpolation methods, because despite being a powerful method, cubic spline interpolation will not be the most accurate and efficient one in all cases.

Actually in practice, the cubic spline interpolation suffers from a serious handicap. It can only handle monotonically increasing or decreasing data. In the case when data are not monotonically increasing or decreasing, cubic spline interpolation could still be carried out if the function of the interpolated curve is known before hand and local minima and maxima can be readily identified. In the case of streamlines however, whose position, slope and curvature change in every iteration, local minima and maxima are very difficult to establish. This can introduce numerical instabilities and may result in the software crashing when streamline curvature, for example, changes from negative to positive and back to negative. This may be the case of the central streamline in a constant-mid-radius compressor. Within the time given and despite several efforts the author could not find a quick mathematical solution around this problem.

Concerning the numerical derivation, the method of central differences is used for the calculation of the first and the second derivatives. The subroutine is programmed with the option of interpolating a number of points between two given ones, with the aim of increasing the accuracy of the calculation. This however should be used with caution because it would not always lead to better results. At least the methods of backwards and forwards differences should be programmed in the future and tested against the other methods.

The third arithmetic method, numerical extrapolation, is performed as follows: Depending on which end of the function the extrapolated point is needed, the three last points are used. A second order polynomial is fitted on them and the extrapolated point is calculated using its coefficients. If the point to be extrapolated falls far from the function's last point, then depending also on the function type, some intermediate points should be interpolated before reaching the given point.

Finally, numerical integration which is needed in several cases in the *2D SLC Software*, i.e. for the radial equilibrium calculation, the boundary layer calculation and the compressor total mass flow calculation, is not programmed into a separate subroutine. Programming a separate numerical integration subroutine would certainly help isolating potential errors generated by the integration process more easily.



**CHAPTER VIII****2D SLC SOFTWARE VALIDATION**

The *2D SLC Software* developed in the context of this work is of great size and programming complexity. It was necessary to test the validity of both *2D Intake SLC Software* and *2D Compressor SLC Software* before actually using them in any subsequent high-fidelity engine performance simulation. This chapter describes the software validation that was carried out for both streamline curvature component algorithms.

**8.1. 2D Compressor SLC Software Validation**

This section discusses the initial validation that was carried out for the streamline curvature compressor algorithm, explains how the loss model was ‘adapted’ in order to match the SLC calculated results with the experimental ones, and finally presents the adapted compressor characteristics together with various two-dimensional flow property profiles.

The *2D Compressor SLC Software* was validated against published experimental data for both clean-inlet and distorted conditions. A two-dimensional model of a two-stage compressor was created according to the detailed geometric data published in NASA Technical Paper 1493 (Urasek, et al., 1979). The overall design performance of the two-stage compressor is given in Table 8.1.1.

Pressure Ratio	2.399
Temperature Ratio	1.334
Isentropic Efficiency	0.849
Corrected Mass Flow [kg/s]	33.248
rpm	16042.800
Inlet Hub to Tip Ratio	0.375
1 <sup>st</sup> Rotor Tip Speed [m/s]	428.896
2 <sup>nd</sup> Rotor Tip Speed [m/s]	405.341

Table 8.1.1: Two-stage compressor design overall parameters

The geometry of the experimental two-stage compressor is of a nearly constant-outer-diameter. As discussed before in *Section 7.4. Numerical Methods and Convergence Stability*, when the interpolated function is not known before hand, as in the case of streamline slopes and curvatures, the cubic-spline interpolation can only handle monotonically increasing or decreasing data. In order to avoid numerical instabilities arising from the use of the cubic-spline interpolation, blade geometric data were extrapolated to the maximum radius of the first-stage rotor, for a true constant-outer-diameter compressor geometry (Figure 8.1.1). The detailed geometry of the two-stage compressor has been included in this thesis as *Appendix F - Two-Stage Compressor Geometry*.



## Two-Stage Compressor Geometry Comparison

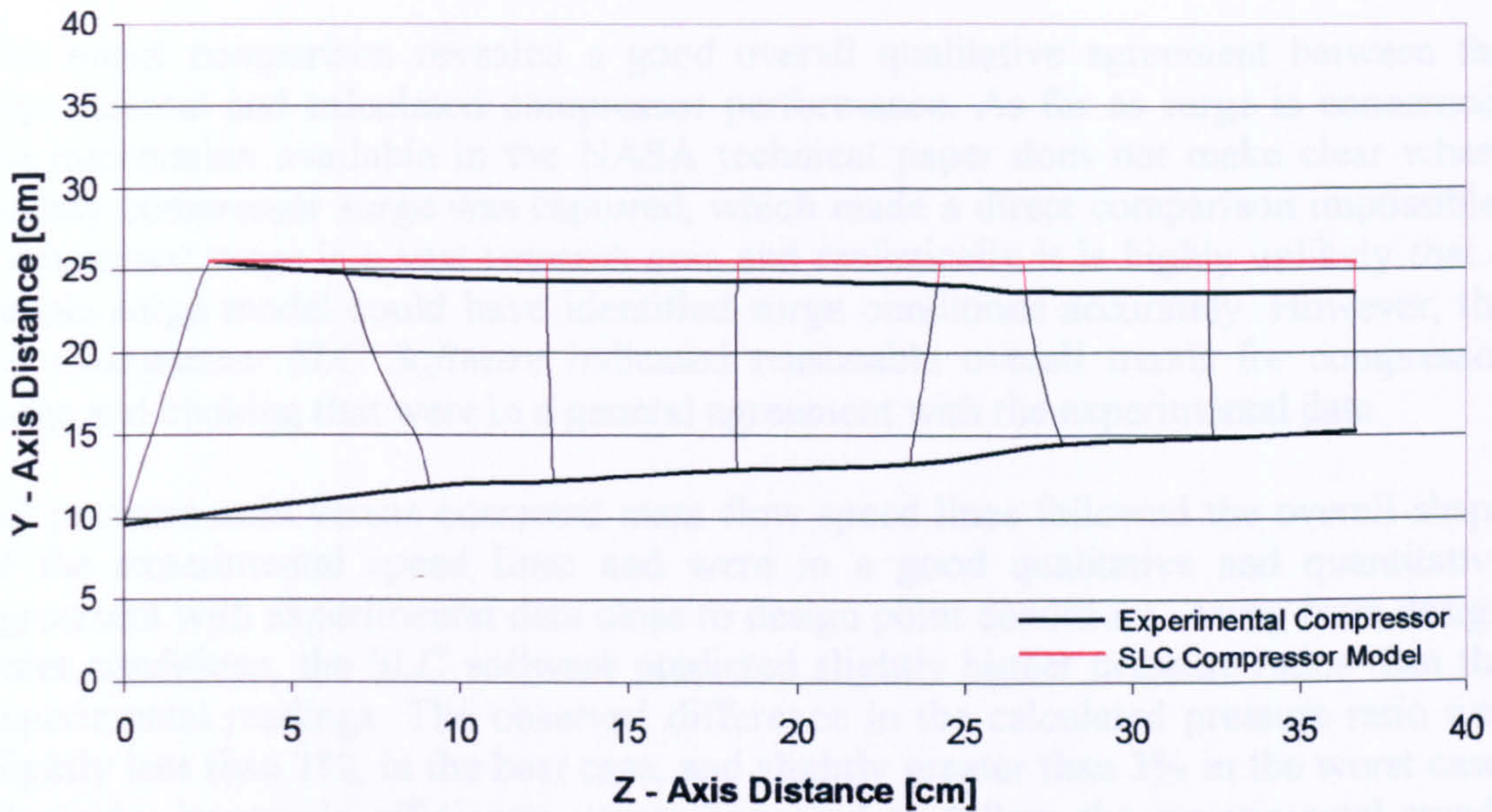


Figure 8.1.1: Geometry comparison between the NASA experimental compressor and the SLC compressor model used in the analysis

### 8.1.1. Initial Comparison against Experimental Data

The performance of the two-dimensional, streamline curvature, two-stage compressor model was compared under uniform inlet conditions against the measured performance data published in NASA Technical Paper 1493. In order to allow the comparison to take place, two-dimensional profiles of flow properties at the outlet of the compressor were averaged along the blade span, from hub to casing, back into non-dimensional values using a standard area-weighting rule. Examples of area-weighted flow properties are given below:

Area-weighted average total pressure:

$$\bar{P} = \frac{\int P dA}{A} \quad [\text{Eq. 8.1.1.1}]$$

Area-weighted average total temperature:

$$\bar{T} = \frac{\int T dA}{A} \quad [\text{Eq. 8.1.1.2}]$$

Figures 8.1.1.1 and 8.1.1.2 present the initial comparison between the measured and simulated compressor performance for the first stage. Due to the bad illustration of the



experimental data in the NASA technical paper, and due to the slightly different compressor geometry adopted, results were compared only qualitatively.

The initial comparison revealed a good overall qualitative agreement between the experimental and calculated compressor performance. As far as surge is concerned, the information available in the NASA technical paper does not make clear where exactly compressor surge was captured, which made a direct comparison impossible. Compressor surge is a vast research area and realistically it is highly unlikely that a simple surge model could have identified surge conditions accurately. However, the *2D Compressor SLC Software* indicated reasonable overall trends for compressor surge and choking that were in a general agreement with the experimental data.

All pressure ratio versus corrected mass flow speed lines followed the overall shape of the experimental speed lines and were in a good qualitative and quantitative agreement with experimental data close to design point conditions. Away from design point conditions, the SLC software predicted slightly higher pressure ratios than the experimental readings. The observed difference in the calculated pressure ratio was slightly less than 1%, in the best case, and slightly greater than 3% in the worst case. Similarly, isentropic efficiency curves appeared to follow the experimental trends close to design point conditions, however, away from the design point, the SLC prediction of isentropic efficiency appeared overestimated, resulting in the higher pressure ratio observed at almost all relative non-dimensional rotational speeds.

**First Stage Compressor Map  
Uniform Inlet Conditions**

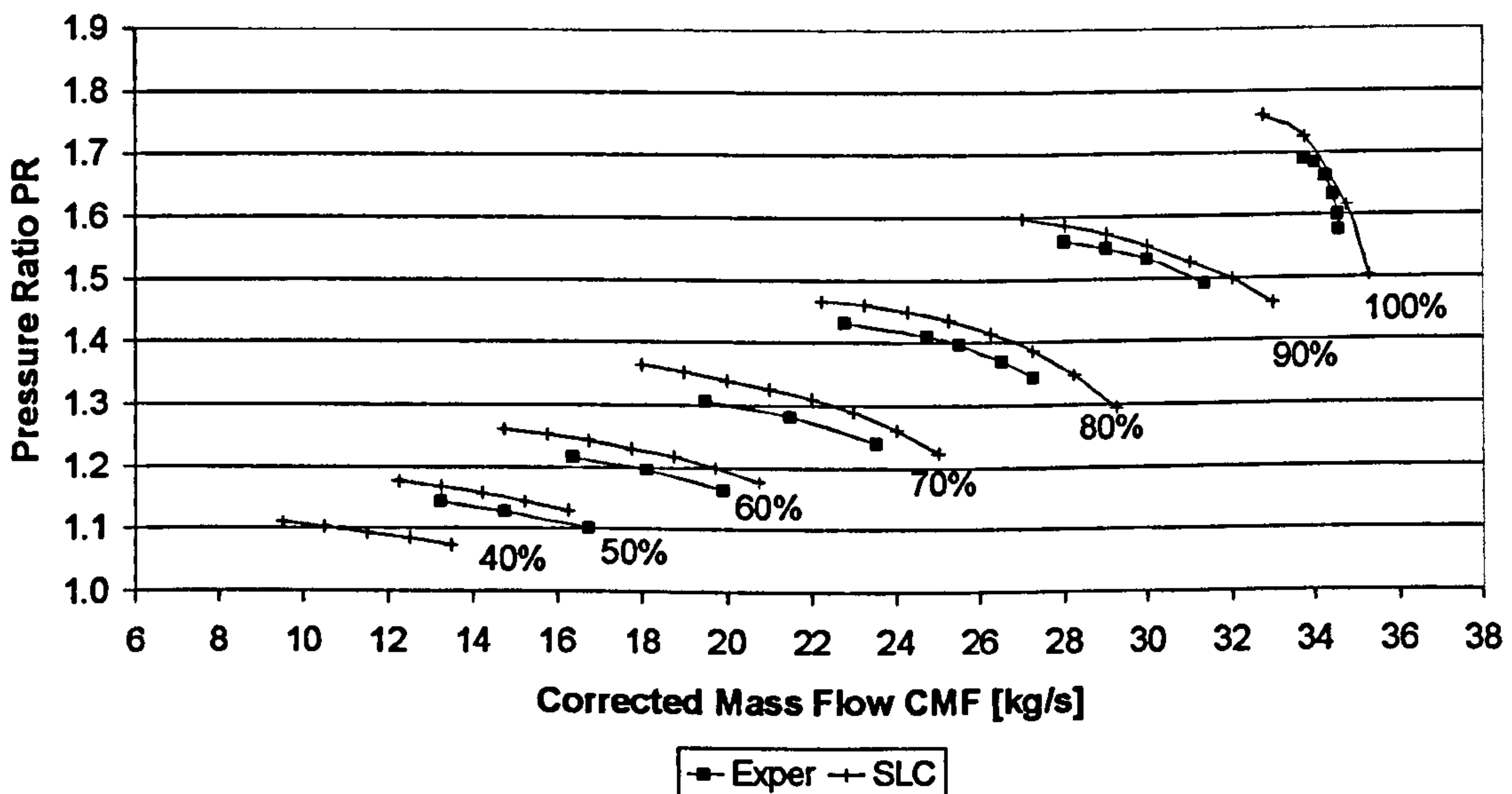


Figure 8.1.1.1: Initial comparison with experimental results for the first stage – Pressure Ratio vs Corrected Mass Flow



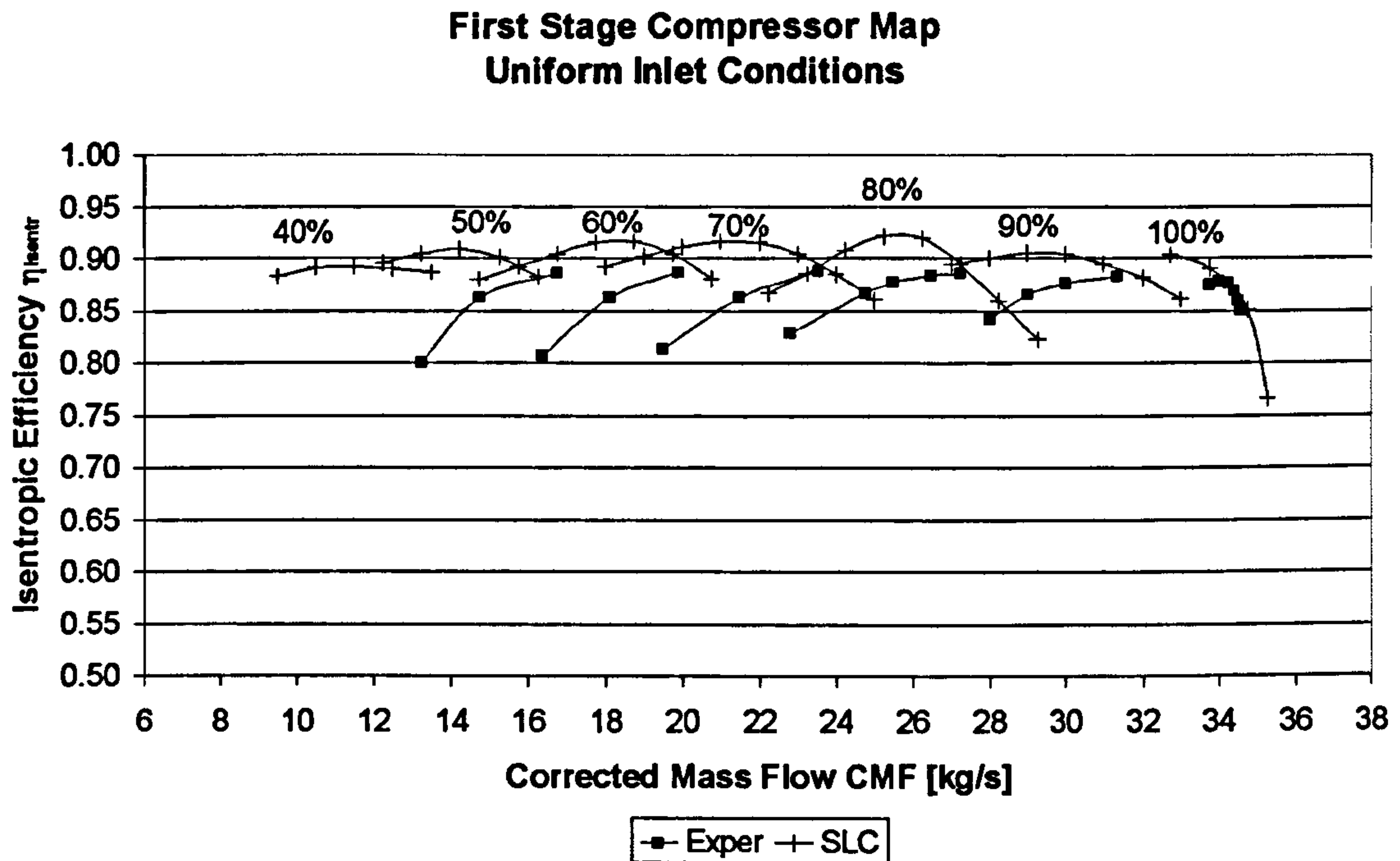


Figure 8.1.1.2: Initial comparison with experimental results for the first stage – Isentropic Efficiency vs Corrected Mass Flow

The results presented above were the direct outcome of the particular combination of loss models selected to carry out the simulation (see *Chapter V - 2D Compressor Flow Modelling*). Obviously, using a different combination of loss models would have resulted in different results, either better or worse. Given that experimental data were available in this case, and that trying to find the best combination of loss models would have taken quite a lot of time, a different approach was followed in order to improve the agreement between the SLC software predictions and the experimental results. This is explained in the following subsection.

### 8.1.2. Loss Model Adaptation

It quickly becomes evident from theory (see *Section 5.11. Calculation of Blade Losses*) that when the flow in the compressor is subsonic or transonic as in this case, and when severe shock wave losses are absent, the factor that contributes the most to the blade row total pressure loss, and hence efficiency loss, is the blade profile loss factor  $\bar{\omega}_{prof}$ . The above analysis adopted Swan's (19691) model for calculating the blade profile loss factor which strongly depends on the accurate prediction of the blade wake momentum thickness as explained in sub *Section 5.11.1 Calculation of Profile Losses*. The part of the theoretical background which is of interest here is briefly repeated and discussed below for consistency.

Lieblein (1957 and 1959), related the blade wake momentum thickness to velocity diffusion and blade loading (Figure 8.1.2.1). By analyzing a wide range of blade sections at various angles of attack (Figure 8.1.2.2) he established universal correlations between the wake momentum thickness and blade loading parameters such as the diffusion factor  $D$  and the equivalent diffusion factor  $D_{eq}$ .

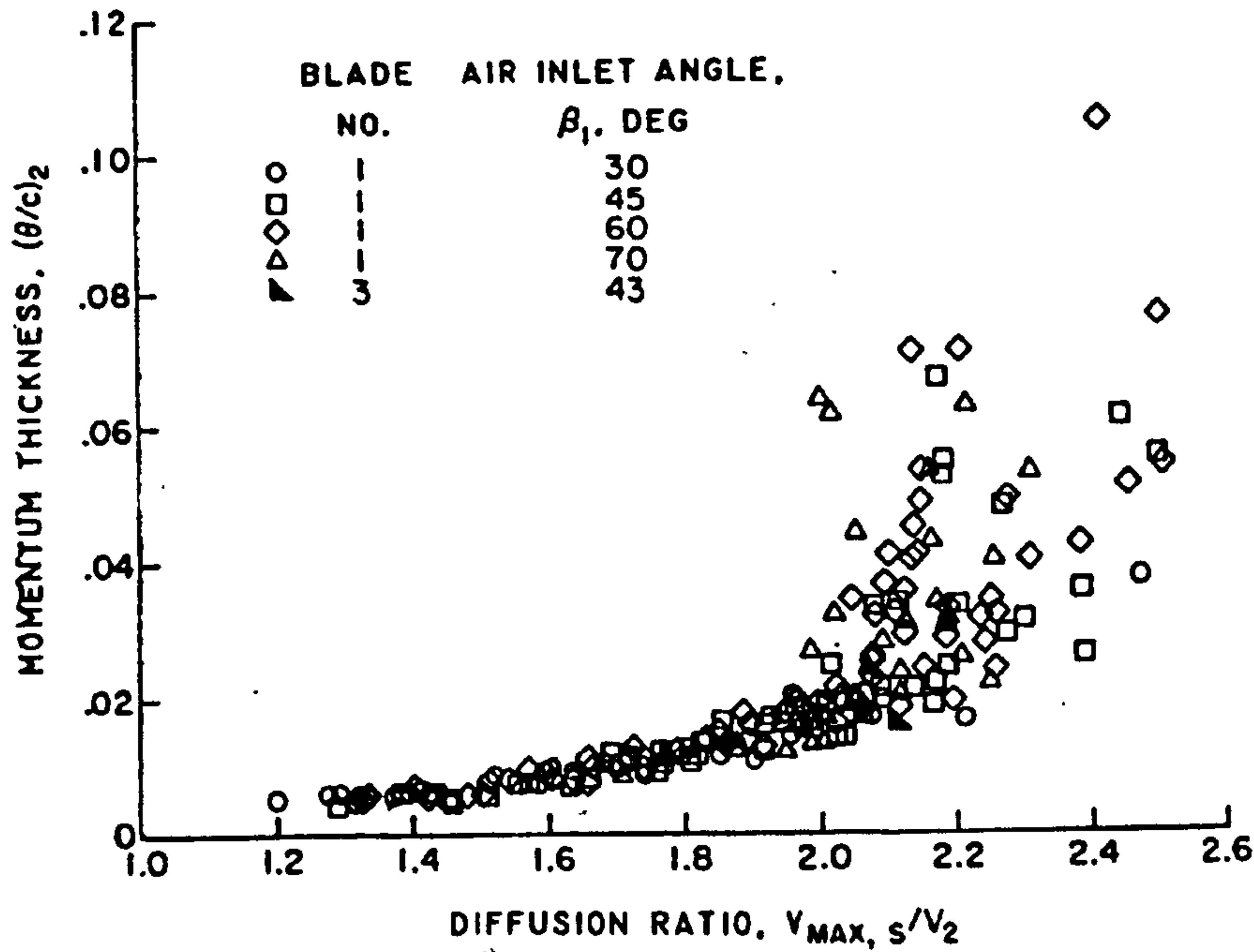


Figure 8.1.2.1: Experimental variation of wake momentum thickness with suction-surface diffusion ratio (Lieblein, 1959)

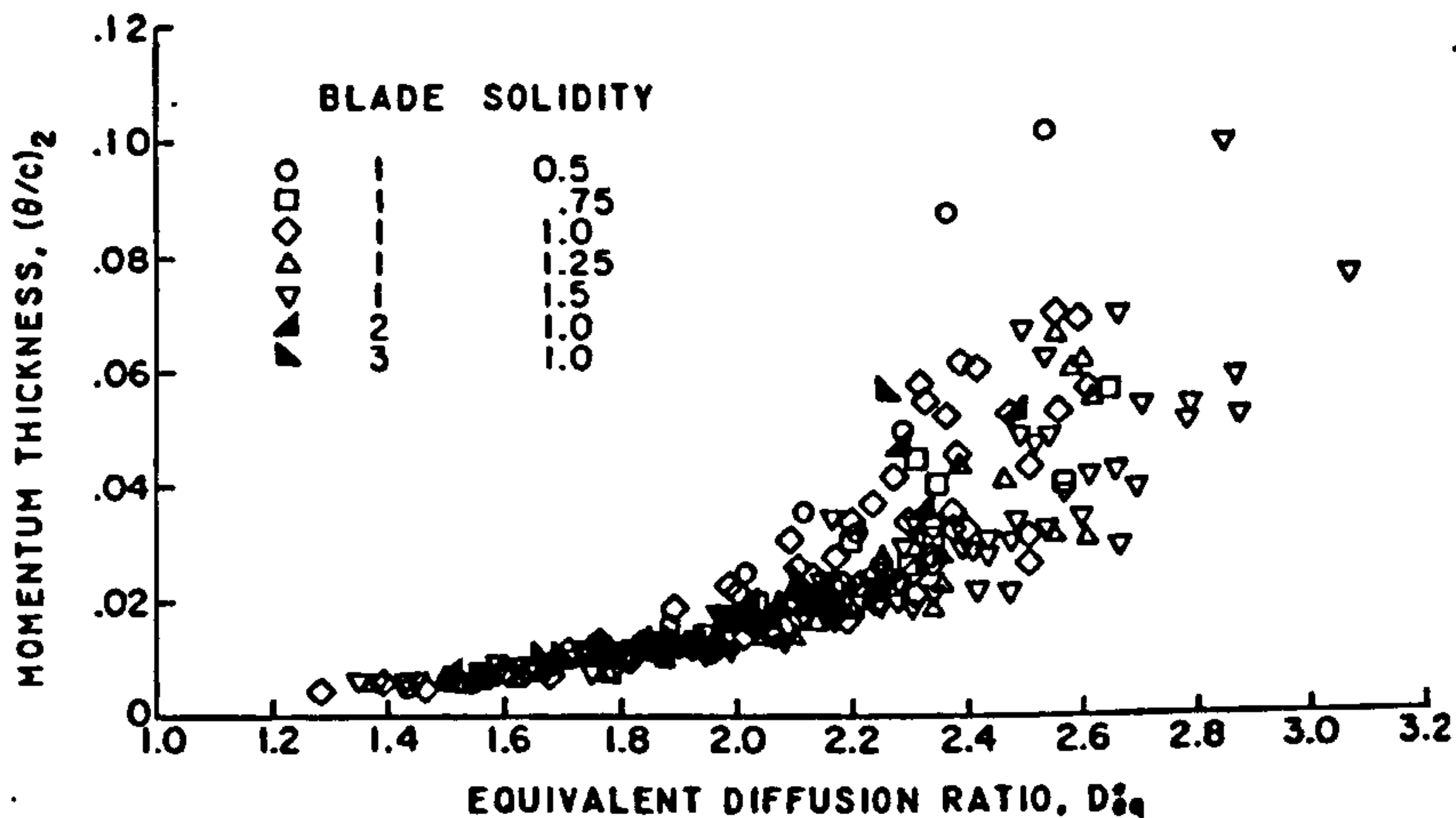


Figure 8.1.2.2: Wake momentum thickness variation with equivalent diffusion ratio for data points at angles of attack greater than minimum loss (Lieblein, 1959)

Swan (1961) introduced a more practical method of predicting blade profile losses in transonic compressors, based on Lieblein's work. According to Swan's model, the equivalent diffusion factor  $D_{eq}$  and minimum loss equivalent diffusion factor  $D_{eq}^*$  can be established as per Lieblein. From the minimum loss equivalent diffusion factor the minimum loss wake momentum thickness can be established through a statistical curve fit. At off-design, the wake momentum thickness can be calculated from tabulations relating the wake momentum thickness and minimum-loss wake momentum thickness to  $D_{eq}^*$  and  $D_{eq}$ . Having established the wake momentum thickness, the blade profile loss can be calculated as per Lieblein.



More analytically, the blade profile loss factor is found from the blade wake momentum thickness according to:

$$\frac{\theta}{c_{aero}} = \frac{\overline{\omega}_{prof} \cos^3 \beta_2}{2\sigma \cos^2 \beta_1} \quad [\text{Eq. 5.11.1.8}]$$

Swan's extension to Lieblein's basic correlation of the minimum-loss equivalent diffusion factor for two-dimensional cascades is given by:

$$D_{eq}^* = \left[ k_1 + k_4 \frac{\sin^2 \beta_1}{\sigma} \left( \cot \beta_1 - \frac{r_2 V_{m,2}}{r_1 V_{m,1}} \cot \beta_2 - \frac{r_1}{V_{m,1}} \left( 1 - \frac{r_2^2}{r_1^2} \right) \right) \right] \frac{\sin \beta_2 V_{m,1}}{\sin \beta_1 V_{m,2}} \quad [\text{Eq. 5.11.1.2}]$$

The minimum-loss wake momentum thickness parameter is established from the minimum-loss equivalent diffusion factor through experimental-statistical curve fits. At off-design conditions, the following correlation for the equivalent diffusion factor is used instead.

$$D_{eq} = \left[ k_1 + k_2 (i - i^*)^3 + k_4 \frac{\sin^2 \beta_1}{\sigma} \left( \cot \beta_1 - \frac{r_2 V_{m,2}}{r_1 V_{m,1}} \cot \beta_2 - \frac{r_1}{V_{m,1}} \left( 1 - \frac{r_2^2}{r_1^2} \right) \right) \right] \frac{\sin \beta_2 V_{m,1}}{\sin \beta_1 V_{m,2}} \quad [\text{Eq. 5.11.1.3}]$$

From the minimum-loss wake momentum thickness parameter, minimum-loss equivalent diffusion factor and equivalent diffusion factor, the wake momentum parameter is established from experimental curve fits correlated by Swan as shown below.

For  $D_{eq} > D_{eq}^*$ :

$$\frac{\theta}{c_{aero}} - \left( \frac{\theta}{c_{aero}} \right)^* = \left( 0.827M_1' - 2.692M_1'^2 + 2.675M_1'^3 \right) \left( D_{eq} - D_{eq}^* \right)^2 \quad [\text{Eq. 5.11.1.5}]$$

And for  $D_{eq} < D_{eq}^*$ :

$$\frac{\theta}{c_{aero}} - \left( \frac{\theta}{c_{aero}} \right)^* = \left( 2.80M_1' - 8.71M_1'^2 + 9.36M_1'^3 \right) \left( D_{eq} - D_{eq}^* \right)^2 \quad [\text{Eq. 5.11.1.6}]$$

From the above description it becomes obvious that Swan's loss model, as any other loss model as a matter of fact, depends strongly on experimental-statistical curve fits such as the ones illustrated in Figures 8.1.2.3 and 8.1.2.4.

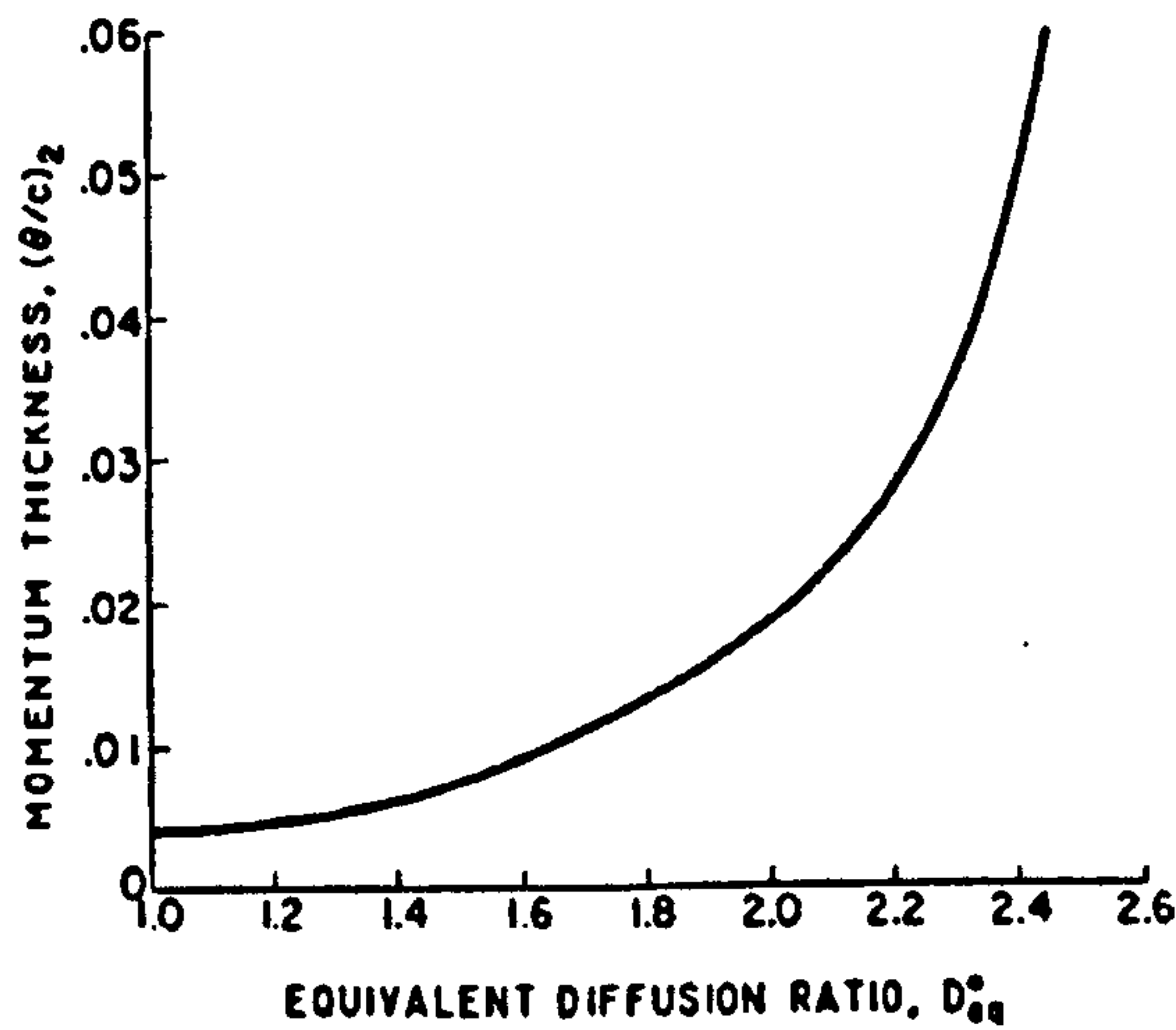


Figure 8.1.2.3: Representative variation of wake momentum thickness with equivalent diffusion ratio at minimum-loss angle of attack used in calculations of cascade loss variations (Lieblein, 1959)

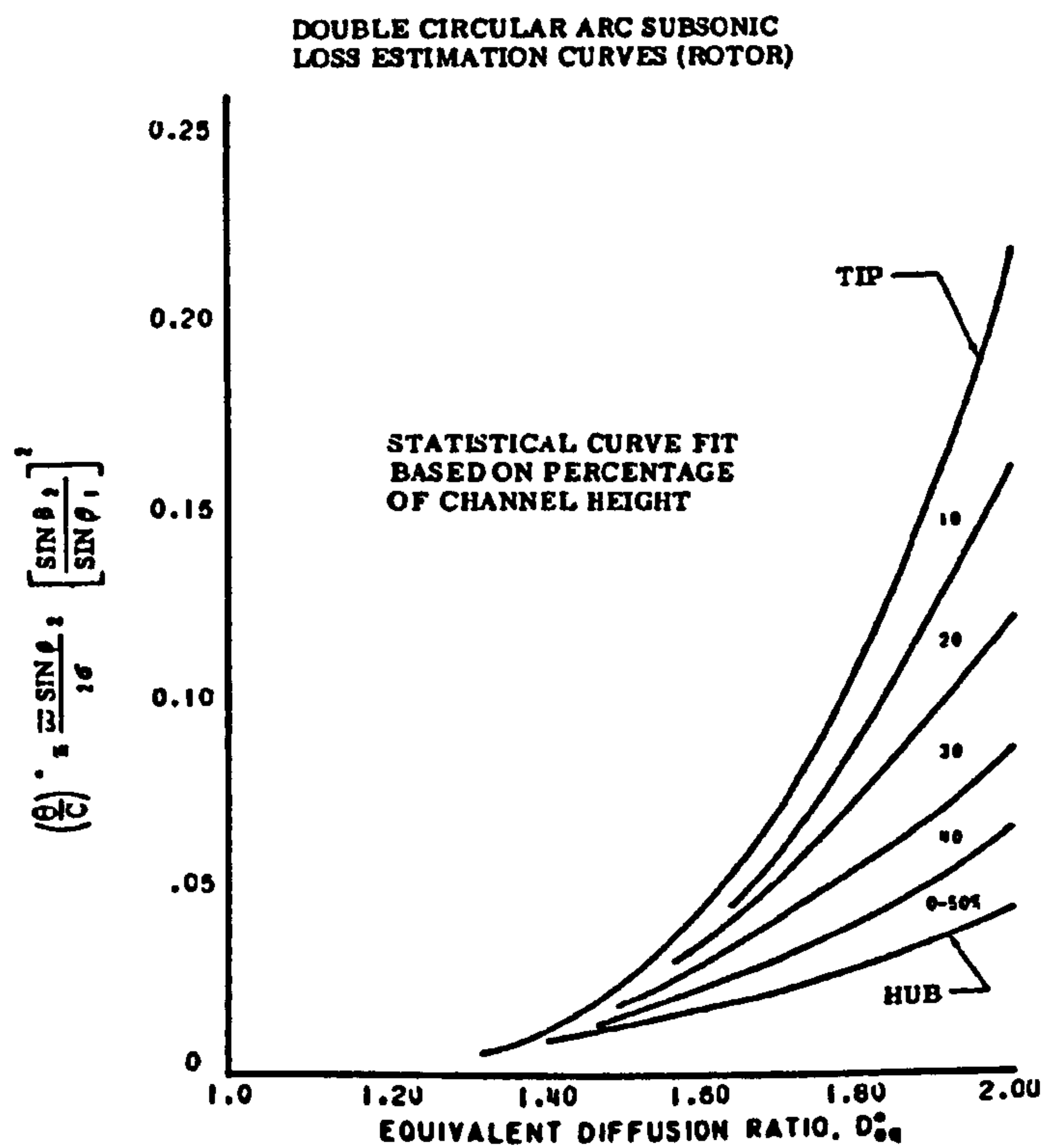


Figure 8.1.2.4: Estimated variation of wake momentum thickness with minimum loss equivalent diffusion ratio (Swan, 1961)

A closer look at the published information available, reveals that the above correlations are actually based on experimental cascade data that display a fairly large scatter, resulting in a relatively high degree of uncertainty. In other words, the differences between the SLC calculated compressor characteristics and the experimental ones may be arising not only from the slightly different compressor



geometry adopted, but also from the inability of the selected loss model to calculate the blade wake momentum thickness accurately. This assumption justifies the further ‘manual’ adjustment of the predicted wake momentum thickness, as explained in the following paragraph.

Through an iterative process, a database of scalars was created and was subsequently applied to the loss model’s prediction of blade wake momentum thickness until the SLC results matched the experimental. The shape of the characteristic non-dimensional speed lines in this case allowed the data base of scalars to be established as a function of corrected mass flow and speed, at the extreme points of every speed line including an intermediate station, as shown in Figure 8.1.2.5. Alternatively, the data base of scalars could have been established as a function of pressure ratio and relative non-dimensional rotational speed or even as a function of beta-line and non-dimensional speed. During program execution, intermediate scalars were established through interpolation between the various speed lines and corrected mass flows according to the calculated compressor operating point.

The above approach to loss model adaptation provided a simple and quick way to ‘calibrate’ the SLC model against the available experimental data. The method was attempted with the focus on matching the exact shape of pressure ratio versus corrected mass flow speed lines rather than the shape of efficiency lines, although the opposite could have been achieved as well.

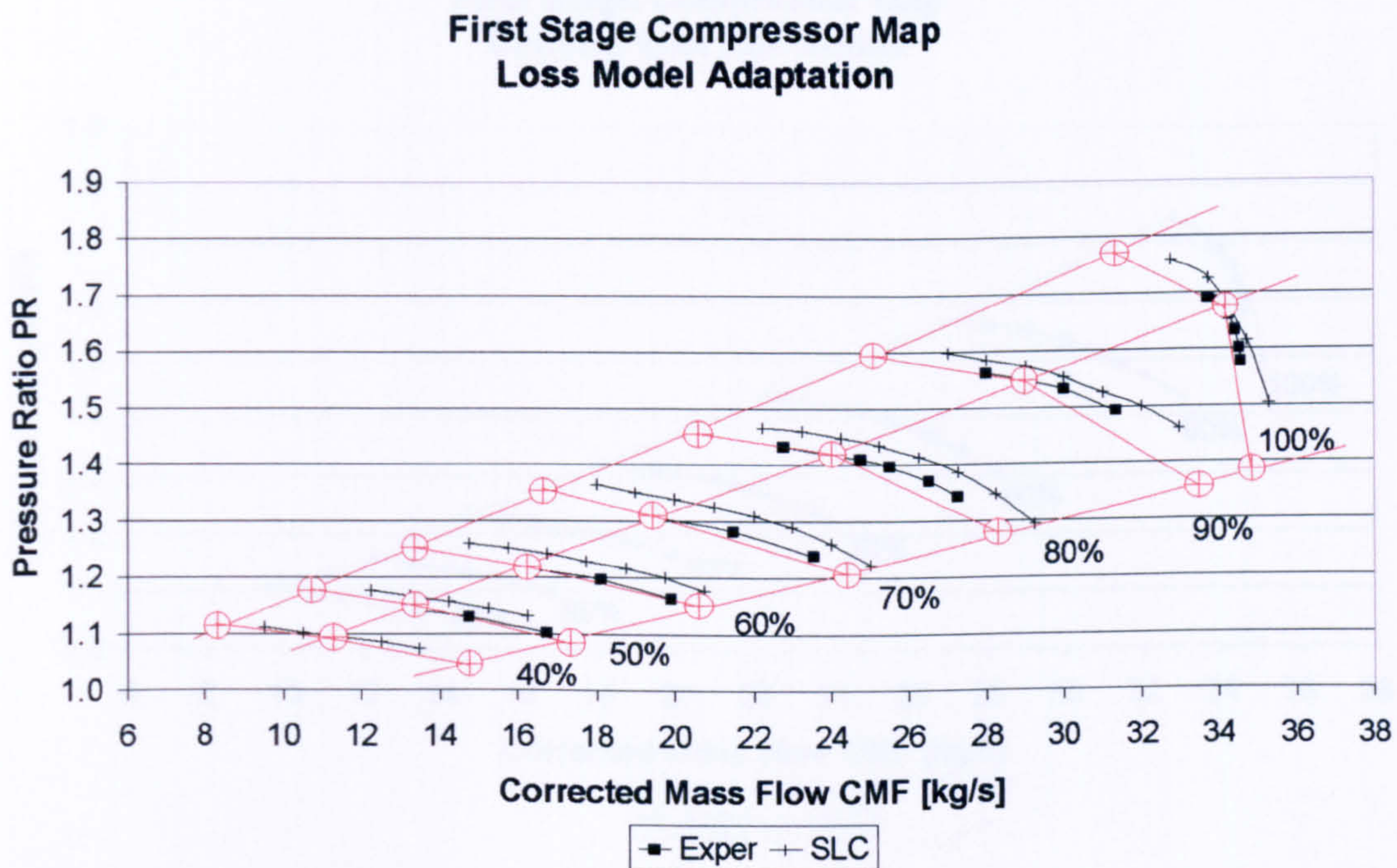


Figure 8.1.2.5: Adaptation with experimental results – Blade wake momentum thickness scaling factor matrix



### 8.1.3. Final Comparison against Experimental Data

This subsection presents the final validation of the *2D Compressor SLC Software* against experimental data for both clean and distorted inlet conditions.

#### Uniform Inlet Conditions

The loss model adaptation resulted in a very good qualitative and quantitative agreement between the simulated and experimental data for uniform inlet conditions, especially in the case of the pressure ratio versus corrected mass flow speed lines for obvious reasons. Isentropic efficiency versus corrected mass flow speed lines were in a good qualitative and quantitative agreement as well, although the overall shape of the lines did not exactly match the experimental readings of the first compressor stage.

It must be stated that no other effort was made to achieve an even better agreement between simulated and experimental data by trying different combinations of the loss models available in the *2D Compressor SLC Software*. It was decided that the agreement presented in Figures 8.1.3.1 to 8.1.3.4 was more than sufficient in order to allow any subsequent qualitative/trend analysis to take place.

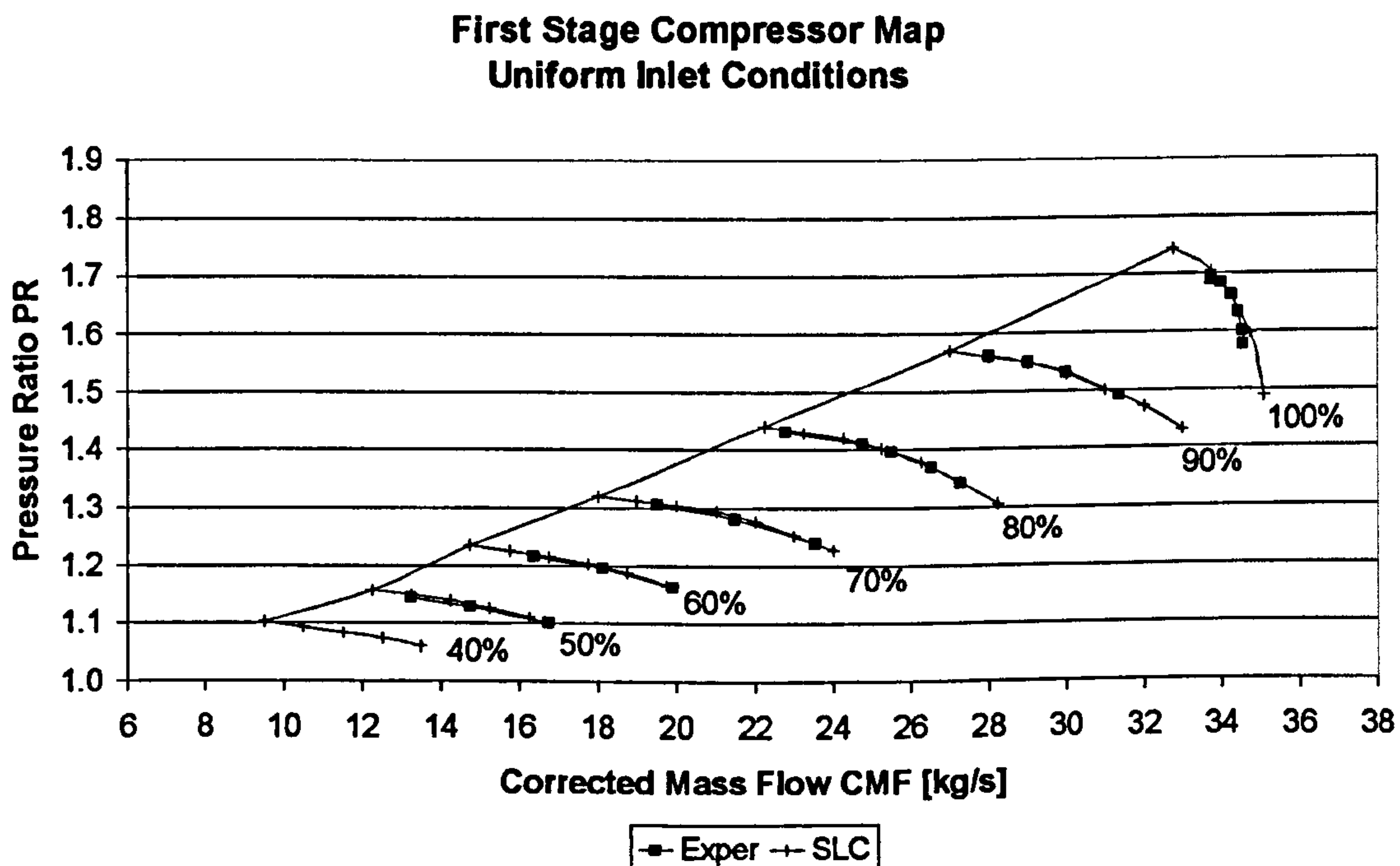


Figure 8.1.3.1: Final comparison with experimental results for the first stage – Pressure Ratio vs Corrected Mass Flow



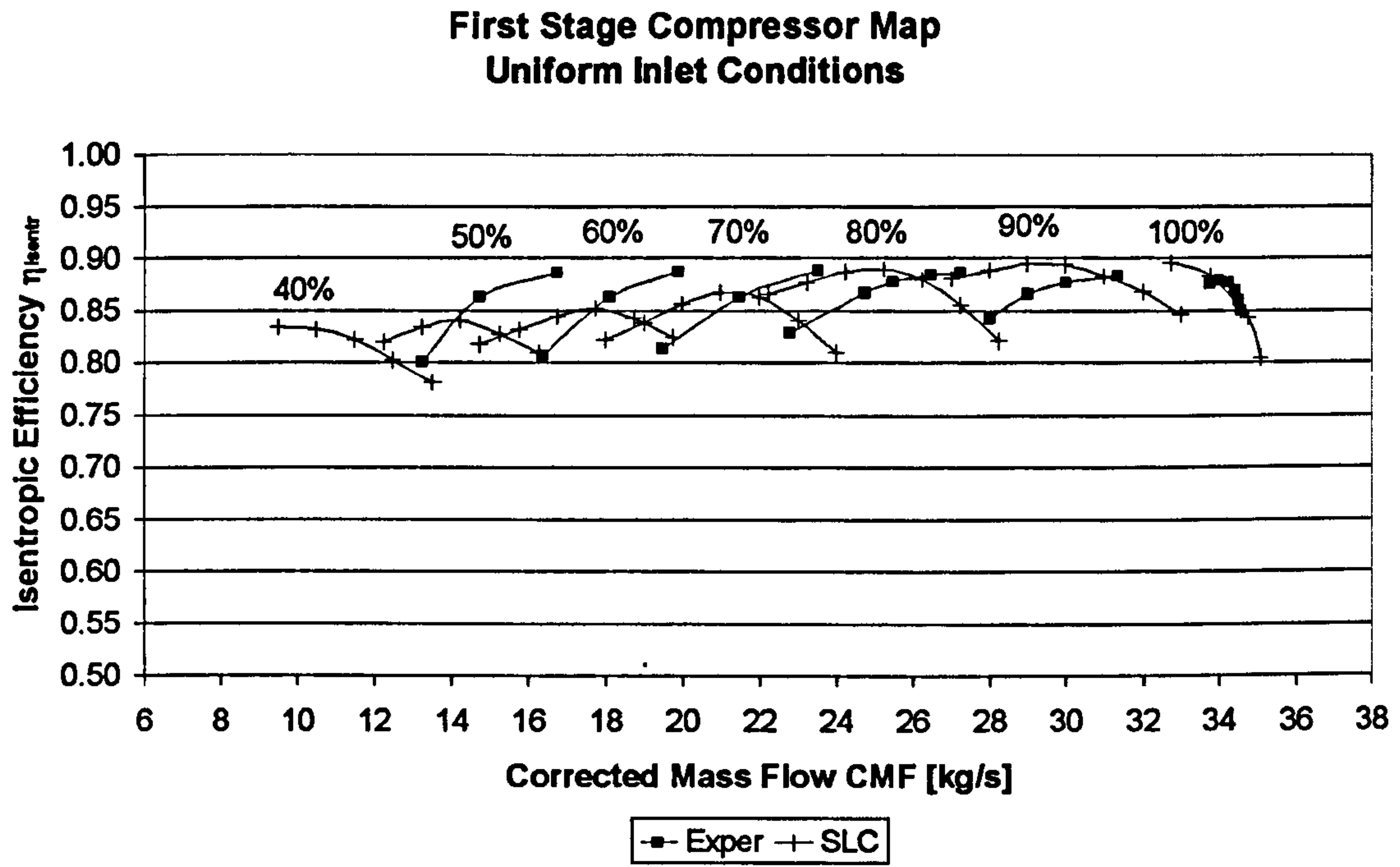


Figure 8.1.3.2: Final comparison with experimental results for the first stage – Isentropic Efficiency vs Corrected Mass Flow

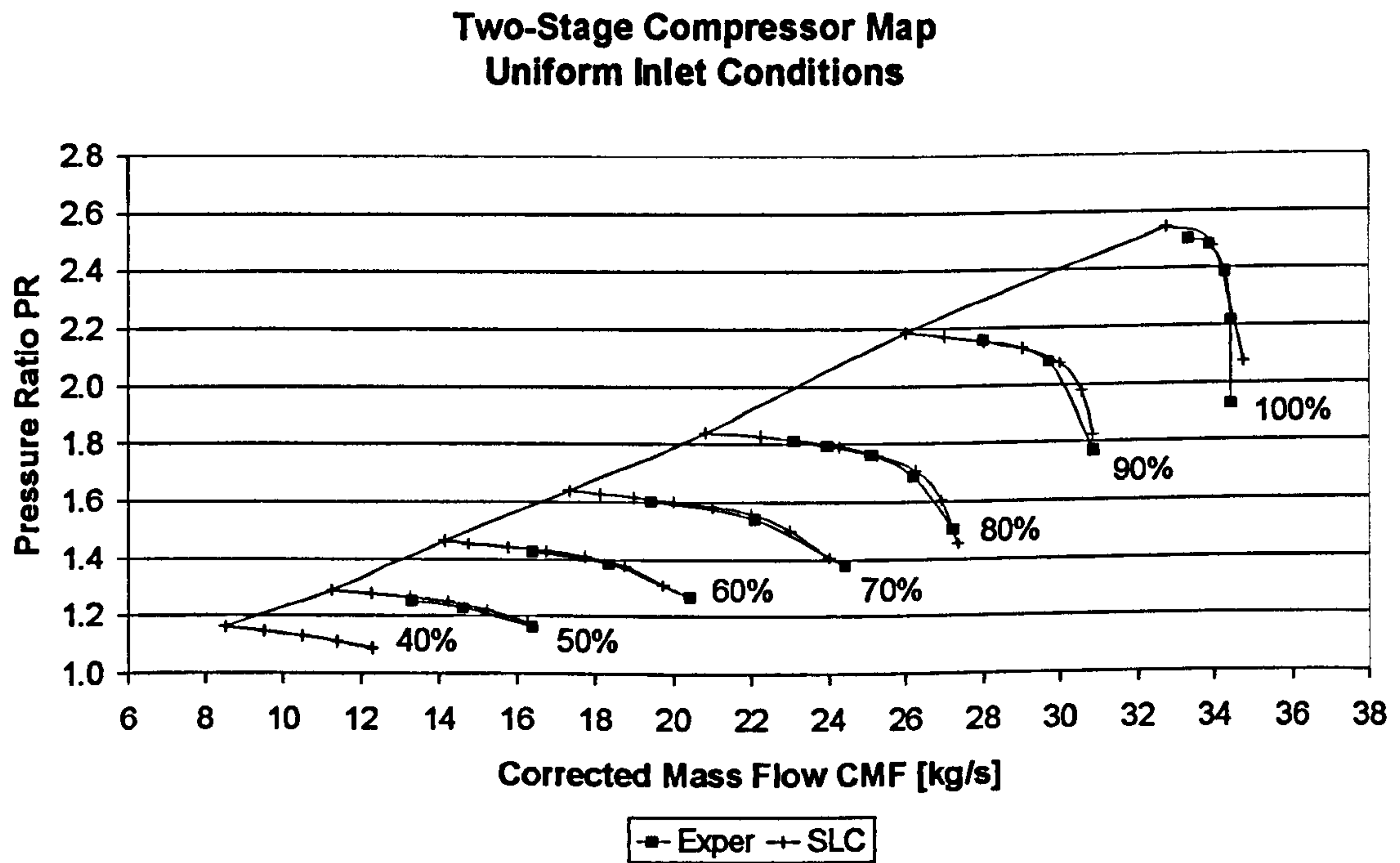


Figure 8.1.3.3: Final comparison with experimental results for both stages – Pressure Ratio vs Corrected Mass Flow

### Two-Stage Compressor Map Uniform Inlet Conditions

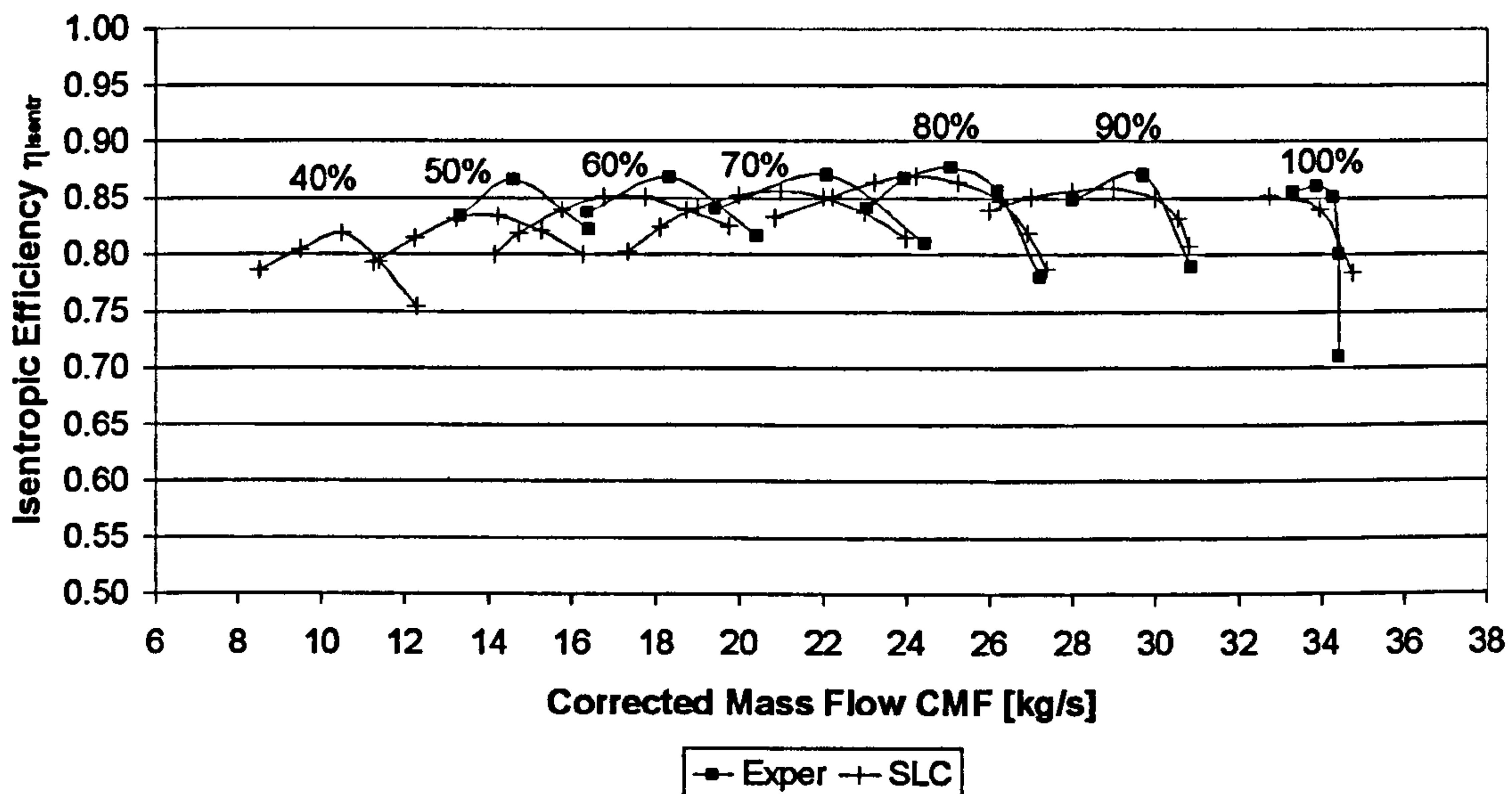


Figure 8.1.3.4: Final comparison with experimental results for both stages – Isentropic Efficiency vs Corrected Mass Flow

### Distorted Inlet Conditions

For the software validation under distorted conditions, NASA Technical Paper 1294 (Schmidt and Ruggeri, 1978) was used as a reference. This paper discusses in detail the performance of a single-stage fan with and without inlet radial distortion. The design overall parameters of the single-stage fan discussed in NASA TP 1294 are very similar to the first stage of the NASA TP 1493 two-stage compressor. The following table lists the overall design parameters of the two stages.

Stage Parameter	NASA TP 1493	NASA TP 1294
Pressure Ratio	1.590	1.574
Temperature Ratio	1.167	1.170
Isentropic Efficiency	0.848	0.816
Mass Flow [kg/s]	33.248	29.484
rpm	16042.800	16100.000
Tip Speed [m/s]	428.896	424.601

Table 8.1.3.1: Stage comparison between NASA TP 1493 and NASA TP 1294 fans

The performance of the SLC compressor model, and especially the performance of the first stage, was qualitatively compared against the measured data in NASA TP 1294 for hub and tip radial pressure distortions. The analysis showed similar trends for the same kind of radial pressure distortion and extend, defined in NASA TP 1294 as Pressure Distortion Index (PDI) given by:



$$PDI_{radial} = \frac{P_{o,max} - P_{o,min}}{P_{o,max}} \quad [Eq. 8.1.3.1]$$

Figures 8.1.3.6 and 8.1.3.7 illustrate the effect on stage performance of an inlet total pressure deficit at the tip of 20% (Figure 8.1.3.5), as predicted by the two-dimensional SLC compressor model. The trends on the map are in a very good agreement with experimental data for a  $PDI_{radial}$  of 0.189 approximately.

Profile of Inlet Tip Total Pressure Distortion

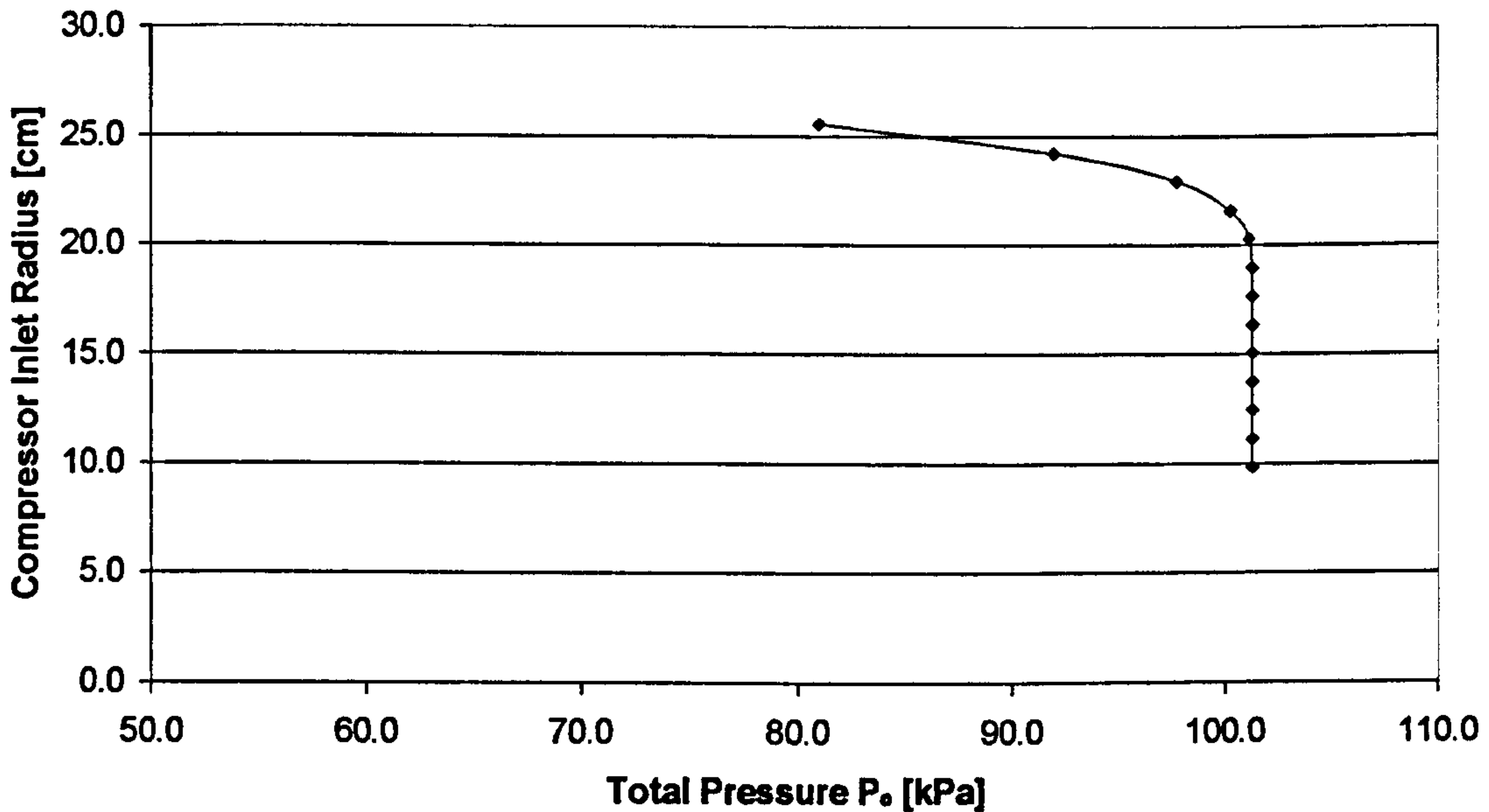


Figure 8.1.3.5: Profile of compressor inlet tip total pressure distortion

First Stage Compressor Map  
Tip Pressure Distortion

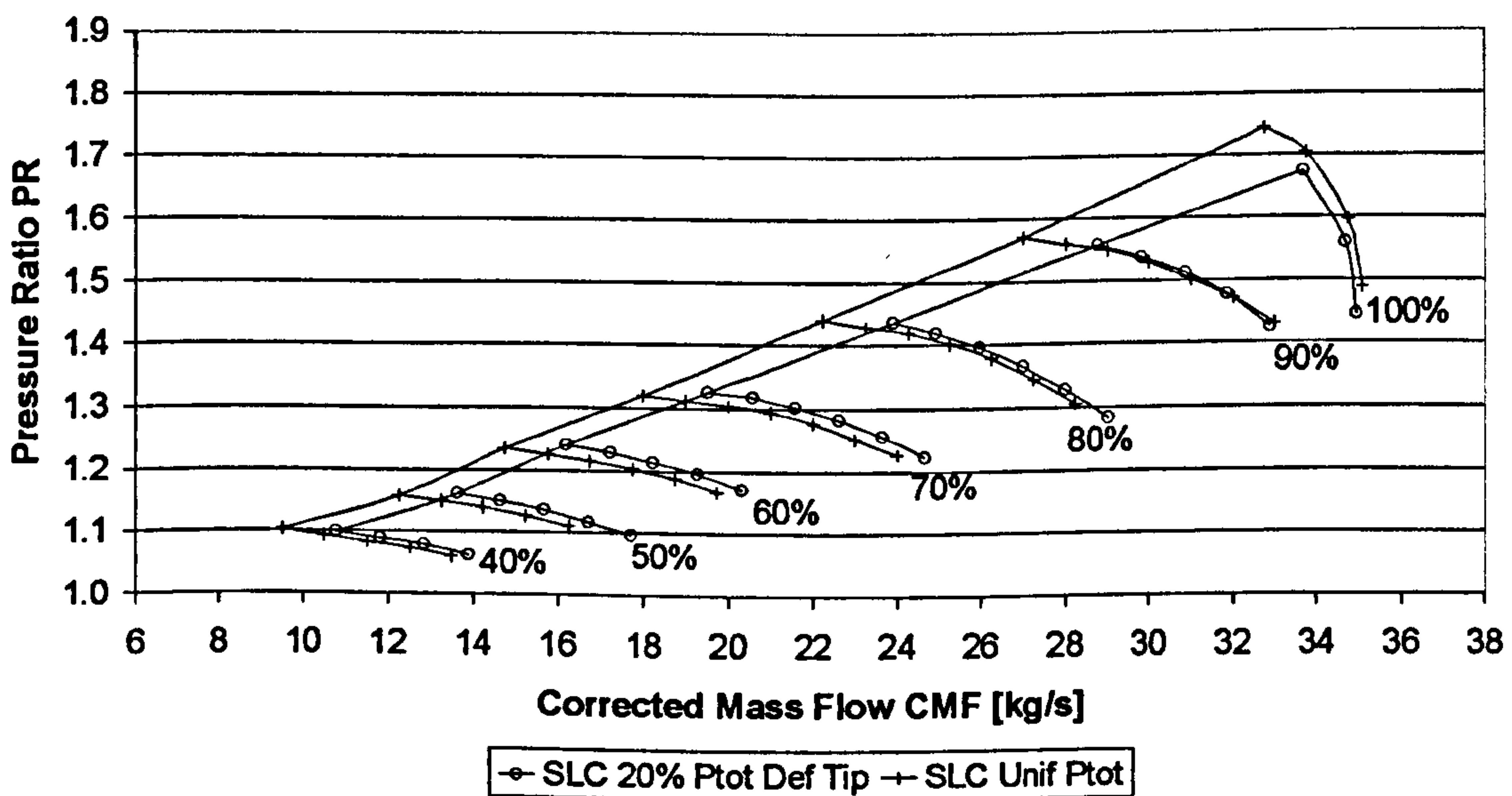


Figure 8.1.3.6: Tip pressure distortion effect – Pressure Ratio vs Corrected Mass Flow

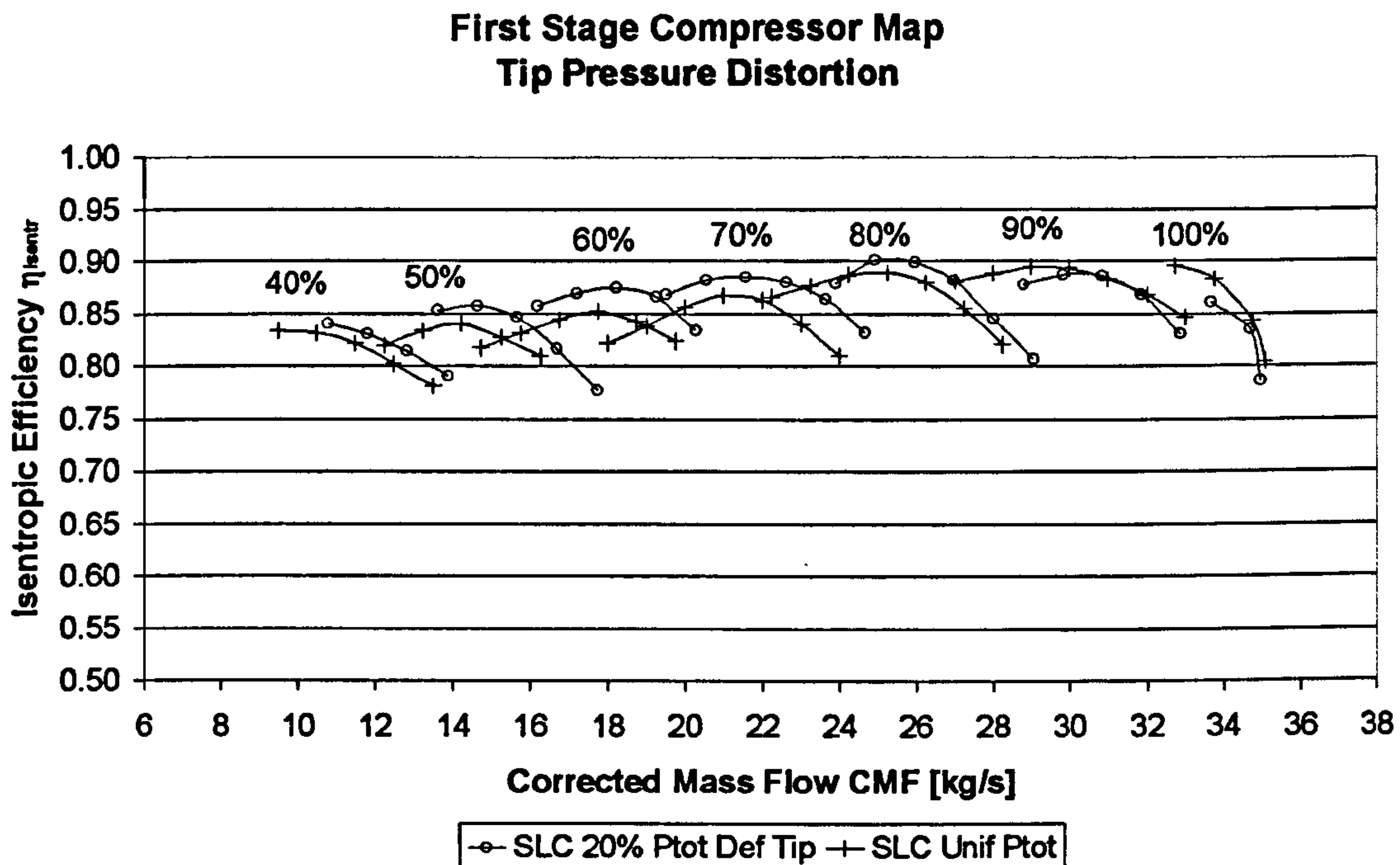


Figure 8.1.3.7: Tip pressure distortion effect – Isentropic Efficiency vs Corrected Mass Flow

More analytically, the SLC analysis predicted accurately the reduction in surge margin associated with radial pressure distortion at the tip, and the slight shift of the speed lines to the right, especially at intermediate speeds. The speed line movement to the right reduced towards higher speeds and actually reversed close to 100% design speed. Generally, the radial pressure distortion reduced the mass flow in the distorted region and caused a redistribution of flow parameters at the inlet with the total pressure and axial velocity being lower than in the case of a clean inlet. Incidence angle increased in the affected regions and reduced in the unaffected ones, increasing and reducing blade loading respectively.

The higher blade loading in the distorted region produced a total pressure and temperature ratio greater than the clean-inlet value which justifies the slight increase in efficiency throughout the operating range as shown above. However, in the distorted region the inlet total pressure was lower than the clean value and the higher pressure ratio only resulted in exit total pressures more or less equal to the clean-inlet value. In the undistorted flow region the exit total pressure was less than the average due to the blade operating unloaded, at a lower work input and total pressure ratio. Therefore, over the entire blade span the average total pressure level was lower than the corresponding clean case and the overall pressure ratio lower as well. Despite the reduction in pressure ratio, a small increase in the corrected mass flow is responsible for the speed lines appearing slightly sifted to the right at low and medium speeds.

#### 8.1.4. 2D Profile Comparison against Experimental Data

As stated before, all numerical methods depend strongly on the use of published loss correlations which may work satisfactorily for a given compressor geometry and less



so for others. Unless the loss models and correlations that are used in the performance simulation of a compressor were derived through experimental measurements for that particular compressor geometry and incorporate some in-house experience and expertise, the chances are that they will deviate from the measured flow field data, sometimes considerably.

The two-dimensional flow property profiles generated by the *2D Compressor SLC Software* were compared against the two-dimensional profile information published in NASA Technical Paper 1493 (Urasek, et al., 1979) for uniform inlet conditions and for the same two-stage compressor geometry discussed in the previous subsections. A selection of these profiles for the first rotor and stator outlets has been plotted against experimental readings for three different relative non-dimensional rotational speeds, i.e. 0.7, 0.8 and 0.9, and has been included in *Appendix H - 2D Profile Comparison*.

### First Stage Rotor Outlet

More analytically, the meridional velocity distribution from hub to tip at the first rotor outlet follows closely the corresponding experimental distribution at all relative rotational speeds examined. The experimental measurements have demonstrated clearly the presence of the boundary layer. On the other hand, the displayed calculated meridional velocity profiles do not include the boundary layer region. It is reminded that in the *2D Compressor SLC Software* flow calculations inside boundary layers do not take place. After the execution of each boundary layer loop, the compressor solid boundaries are virtually displaced towards the centreline by the previously calculated boundary layer thickness. The meridional velocity reduction at the hub area is due to the blade geometry.

The meridional Mach number distribution follows closely the corresponding velocity distribution, therefore the above mentioned comments apply also for the meridional Mach number profile comparison. This happens because any change in static temperature will have by definition a much smaller impact on Mach number than any change in velocity.

The rotor outlet absolute velocity and absolute Mach number distributions present a very good overall qualitative agreement with experimental data, apart from the hub and tip regions. The best agreement is observed at 0.9 relative rotational speed over most of the blade span. The difference appears to increase as relative rotational speed reduces. Calculated results seem to be slightly underestimated in all cases especially close to the hub region.

The rotor outlet relative velocity and relative Mach number distributions are in a good overall qualitative agreement with experimental readings, with the relative velocity and Mach number increasing from hub to tip. Better overall agreement can be observed at low speeds over most of the blade span. At high speeds relative velocities are considerably overestimated at the hub and underestimated along the rest of the blade span.

Although the meridional velocity distribution is the main outcome of the iterative solution of the full radial equilibrium equation, involving the outlet air relative angle,



the air outlet relative angle is a direct result of the blade deviation angle calculation, which strongly depends on the deviation model selected. The deviation angle is predicted more accurately at mid span and less accurately towards the hub and tip regions. The same can be observed for the meridional velocity profile. Probably the errors generated by the meridional velocity and deviation angle distributions at the hub and tip regions cancel each other out, resulting into a very close qualitative and quantitative match for the air outlet relative angle distributions.

Finally, the streamline curvature prediction of rotor outlet absolute angle is in line with the experimental data, with the best agreement achieved from the hub up to the blade mid-radius. The same trends are observed at all speeds. The interrelation between the air outlet absolute angle, air outlet relative angle and the meridional velocity can be observed through the velocity triangles at the same plane.

### First Stage Stator Outlet

As illustrated by the profiles plotted in *Appendix H - 2D Profile Comparison*, in the stator the geometry deviates substantially from the reference geometry. Consequently, the potential of the results for a quantitative analysis is further reduced. Meridional velocity and Mach number distributions follow the experimental data qualitatively as an order of magnitude, but appear underestimated over the larger portion of the blade span. Larger deviations appear in the tip region at all speeds.

The absolute velocity and the absolute Mach number distributions along the span follow similar trends to the meridional velocity and Mach number due to the small magnitude of the air outlet absolute angle. The air outlet absolute angle distribution from hub to tip seems to be in a good agreement with the experimental results over most of the blade span but deviates slightly at the tip region.

Generally, the SLC calculated results for all relative speeds examined, follow closely the experimental trends, especially close to the hub and mid-span regions. The deviation from the experimental data increases from mid-span towards the tip at all relative speeds for several reasons. First of all due to the slightly different compressor geometry adopted in this case (slightly elongated blades for a true constant-outer-diameter design). Secondly, due to the inability of the streamline curvature method to calculate flow properties inside boundary layers. Thirdly, due to the inability of the streamline curvature method to accurately predict the three-dimensionality of the flow field, particularly close to the tip regions where secondary flow phenomena are dominant.

The reader should also be reminded that the adaptation process that was carried out in this case referred only to the blade profile loss model and it was based on overall performance characteristics. Therefore, radial distribution of airflow properties could still deviate from experimental values, partly because the existing boundary layer model was not fine tuned to the reference experimental results, and partly because the profile loss adaptation was based on average values.

Moreover, dissipative and blade forces were neglected in this version of the *2D Compressor SLC Software*. Consequently, blade forces introduced by blade leaning



do not appear in the radial equilibrium equation. Although the direction along which the radial equilibrium equation is defined is considered perpendicular to the streamline direction, in reality it is not. Another limitation is that the flow conditions at the rotor outlet plane are transferred unimpaired to the stator inlet plane ignoring any flow redistribution within the bladeless space.

Finally, it must be stated that since the *2D Compressor SLC Software* was only to be used as a tool by this work and since the area-averaged, non-dimensional flow solutions matched the experimental compressor characteristics satisfactorily (Figures 8.1.3.1 to 8.1.3.4), no particular effort was made to identify and use a more appropriate combination of loss models that would give the best matching of two-dimensional flow field properties.

## ***8.2. 2D Intake SLC Software Validation***

This section discusses the validation of the *2D Intake SLC Software* developed in the context of this work for the modelling of the flow field inside conical and annular intakes and ducts. The initial validation carried out, tested the software's basic capability to model the flow field inside simple, two-dimensional, conical ducts, neglecting pressure losses and boundary layer growth. Subsequently, the full potential of the software was examined with the validation of the pressure recovery calculation in conical and annular intakes.

### ***8.2.1. Validation of Inviscid Flow in Conical Ducts***

As mentioned above, the basic capability of the software to model simple conical duct configurations in an inviscid flow was tested by modelling three different duct geometries at subsonic and supersonic speeds, and by comparing the results against PYTHIA's OD analysis (a brief description of the PYTHIA software is given in sub *Section 9.2.1. Simulation Tools and Software Integration*). Figures 8.2.1.1 to 8.2.1.3 illustrate the conical convergent, convergent-divergent and divergent duct models that were built for this purpose.



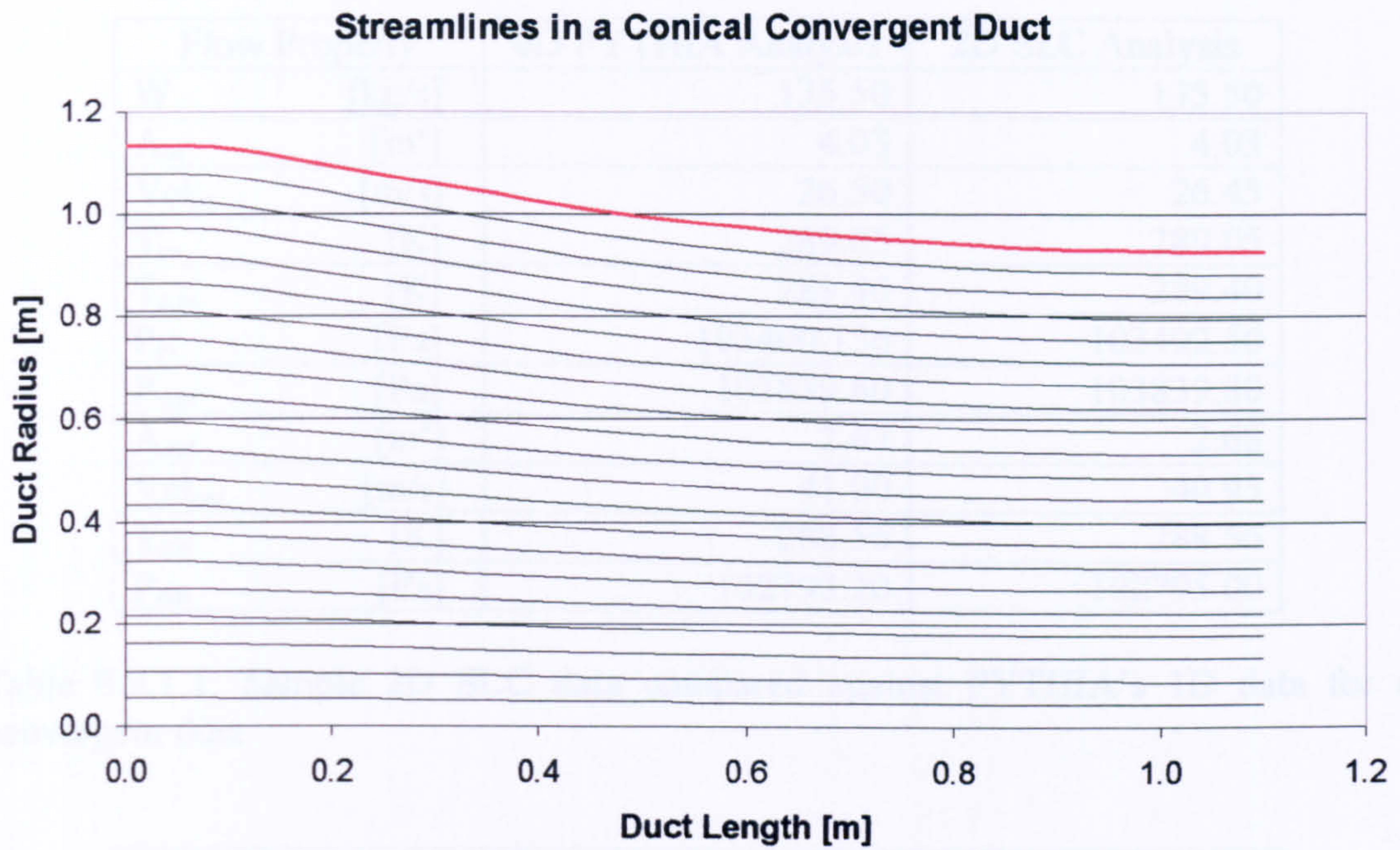


Figure 8.2.1.1: Calculated streamlines in a conical convergent duct

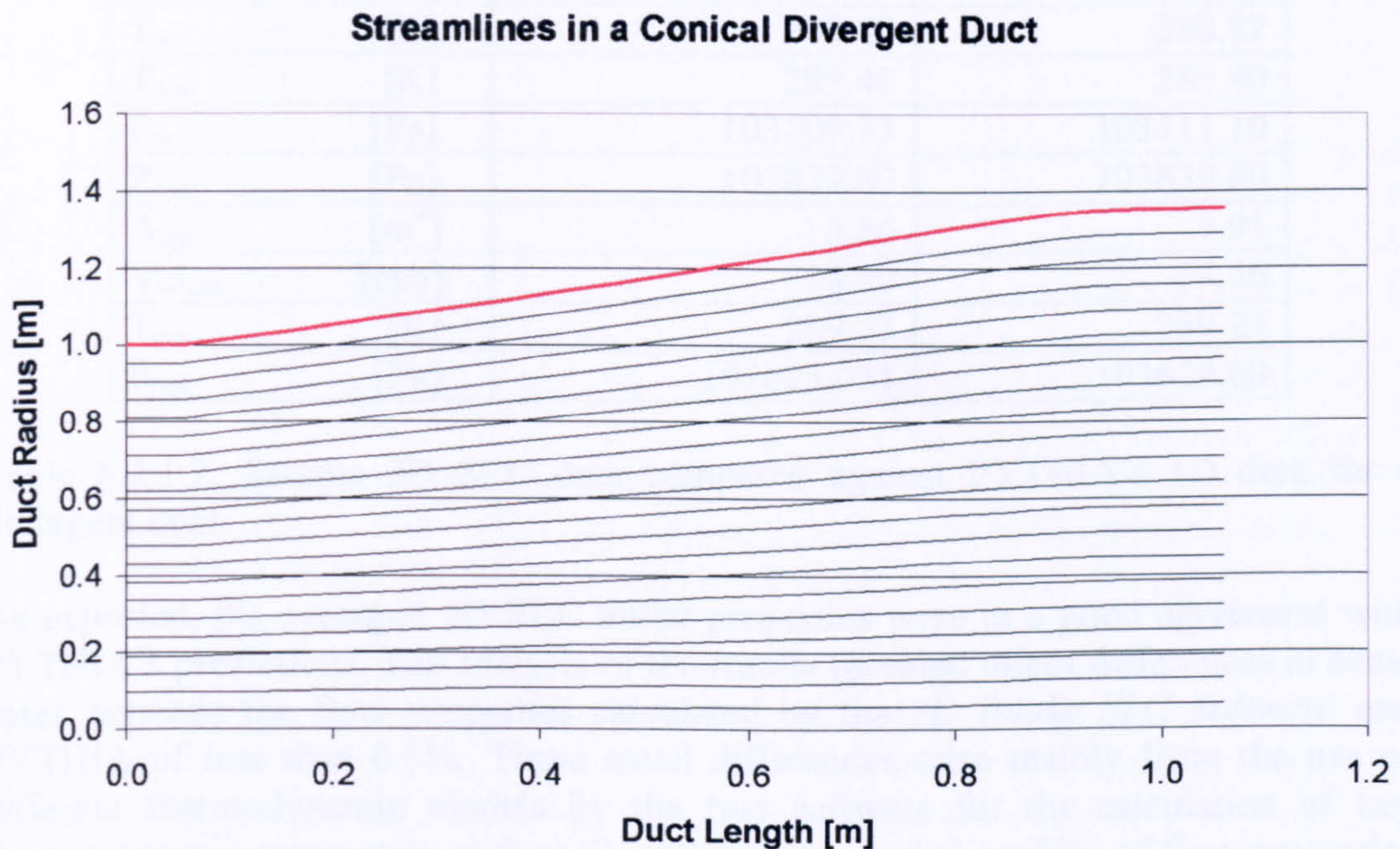


Figure 8.2.1.2: Calculated streamlines in a conical divergent duct

Outlet profile properties were averaged to 1D values using the same ‘area-weighting’ rule as in sub *Section 8.1.1. Initial Comparison against Experimental Data*. Tables 8.2.1.1 and 8.2.1.2 compare sample results calculated by the *2D Intake SLC Software* against those predicted by PYTHIA’s 0D analysis for a convergent and a divergent duct.



Flow Property	0D PYTHIA Analysis	2D SLC Analysis
W [kg/s]	135.50	135.50
A <sub>in</sub> [m <sup>2</sup> ]	4.03	4.03
Vel <sub>in</sub> [m/s]	26.50	26.45
T <sub>in</sub> [K]	289.05	289.05
T <sub>o,in</sub> [K]	289.40	289.40
P <sub>in</sub> [Pa]	103400.136	103402.50
P <sub>o,in</sub> [Pa]	103839.80	103839.80
A <sub>out</sub> [m <sup>2</sup> ]	2.67	2.68
Vel <sub>out</sub> [m/s]	41.00	40.95
T <sub>out</sub> [K]	288.56	288.56
P <sub>out</sub> [Pa]	102793.20	102795.00

Table 8.2.1.1: Sample 2D SLC data compared against PYTHIA's 1D data for a convergent duct

Flow Property	0D PYTHIA Analysis	2D SLC Analysis
W [kg/s]	135.50	135.50
A <sub>in</sub> [m <sup>2</sup> ]	3.14	3.14
Vel <sub>in</sub> [m/s]	34.20	34.19
T <sub>in</sub> [K]	288.82	288.82
T <sub>o,in</sub> [K]	289.40	289.40
P <sub>in</sub> [Pa]	103109.33	103111.10
P <sub>o,in</sub> [Pa]	103839.80	103839.80
A <sub>out</sub> [m <sup>2</sup> ]	5.86	5.91
Vel <sub>out</sub> [m/s]	18.60	18.56
T <sub>out</sub> [K]	289.23	289.23
P <sub>out</sub> [Pa]	103623.051	103624.60

Table 8.2.1.2: Sample 2D SLC data compared against PYTHIA's 1D data for a divergent duct

As expected, the averaged 2D SLC outlet properties were in a good agreement with PYTHIA's predictions. The analysis of the results revealed minor differences in some cases between the flow properties calculated by the *2D Intake SLC Software* and PYTHIA of less than 0.5%. These small differences arise mainly from the use of different thermodynamic models by the two software for the calculation of key thermodynamic parameters such as  $C_p$  and  $\gamma$ . Radial profiles of flow properties at various stations throughout the three ducts demonstrated reasonable trends in all cases.



### Streamlines in a Conical Convergent-Divergent Duct

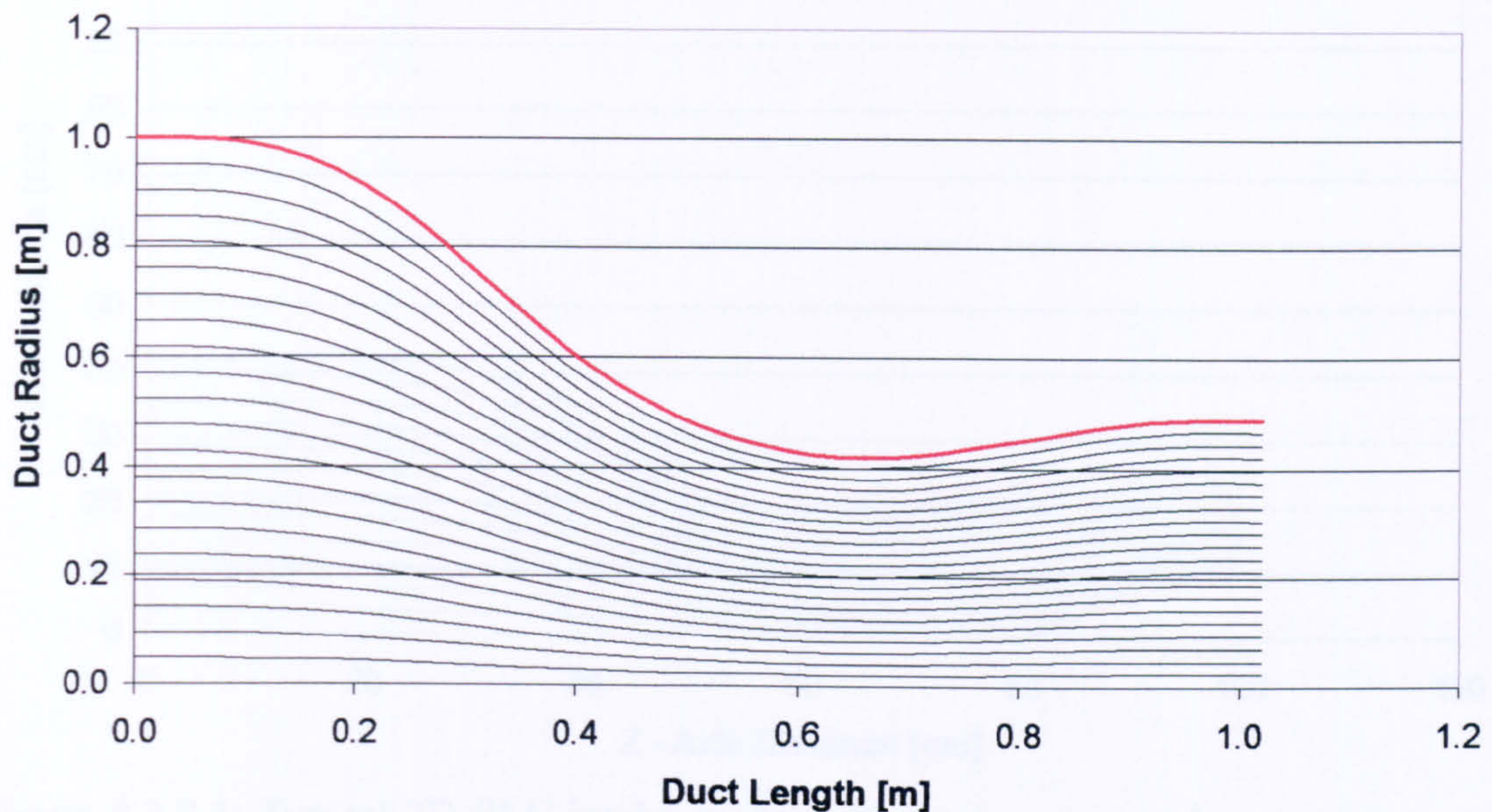


Figure 8.2.1.3: Calculated streamlines in a conical convergent-divergent duct

### 8.2.2. Validation of Viscous Flow in Annular Intakes

As mentioned before, this work adopted a similar approach to intake pressure recovery calculation as the one-dimensional analysis described in ESDU Item No. 80037 (1980) which is based on the experimental findings of several researchers (see *Chapter VI - 2D Intake and Duct Flow Modelling*). The software's capability to calculate the pressure loss in conical and annular intake configurations was tested against worked examples provided in the ESDU report. In the absence of other experimental data, the objective of this exercise was to validate the inner workings of the various loss models programmed in the *2D Intake SLC Software* and their successful conversion from 1D to 2D, rather than to assess the agreement of the loss models published in the ESDU report with other experimental results.

For the purposes of this validation, two notional 2D intake geometries were built in order to investigate the performance of two similar intake models, with and without an engine cone (Figure 8.2.2.1). Other geometric properties, such as intake lip geometry, entry contraction ratio and diffuser area ratio were kept the same for both models. More analytically, an elliptical lip configuration was assumed in both cases with a contraction ratio  $\lambda_{\text{contr}}$  of 1.1. The diffuser area ratio  $\lambda_{\text{diff}}$  was set to 1.75 and a constant section duct, between the lip and diffuser, of length  $L_{\text{csd}}$  equal to half the throat diameter was used in both cases. Attached flow was also assumed throughout both intake models at all conditions.



Streamlines in an Intake with Engine Cone

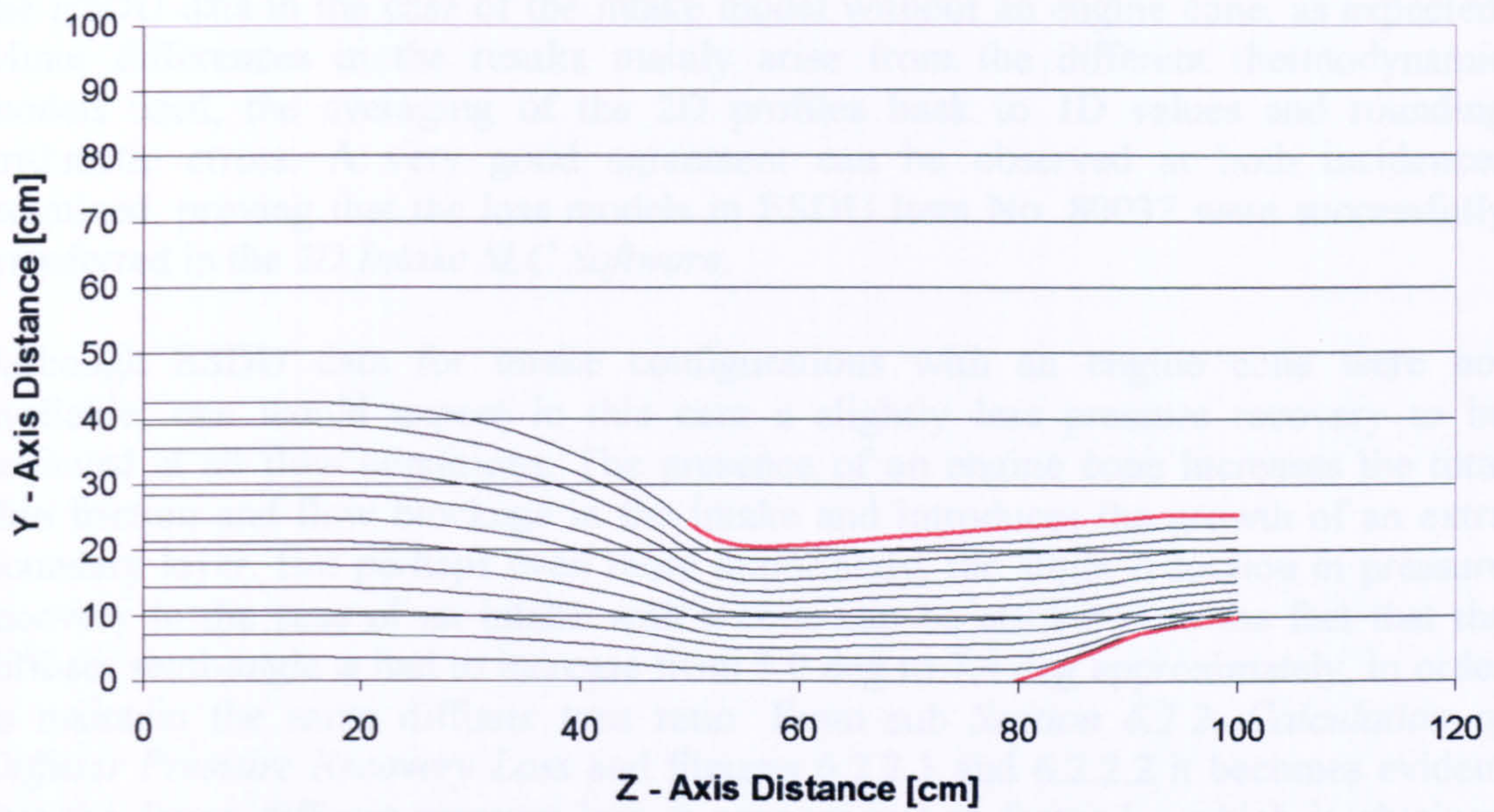


Figure 8.2.2.1: Typical 2D SLC intake model with engine cone and pre-entry stream tube

The performance of both models was established at a constant free-stream Mach number of 0.2, at 0 and 15 degrees of incidence and a range of throat Mach numbers from 0.3 to 0.7. The area-averaged, 2D SLC results are shown plotted against the 1D ESDU data in Figure 8.2.2.2.

Intake Performance Comparison

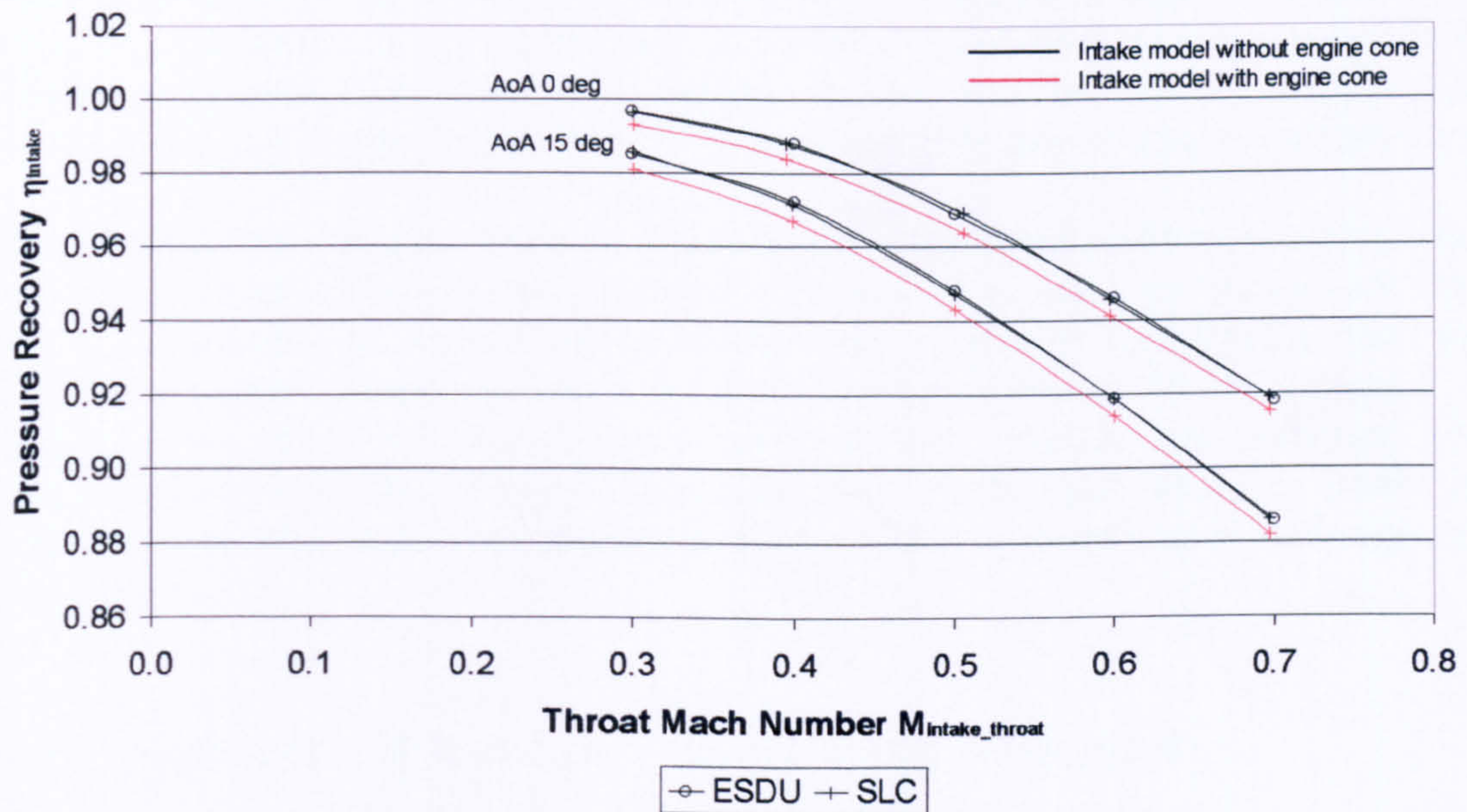


Figure 8.2.2.2: Comparison between 1D ESDU data and averaged 2D SLC results – Intake Pressure Recovery vs Intake Throat Mach Number



Since the 1D ESDU analysis does not take into account the presence of the engine cone, the averaged 2D SLC flow solutions seem to be in an excellent agreement with the ESDU data in the case of the intake model without an engine cone, as expected. Minor differences in the results mainly arise from the different thermodynamic models used, the averaging of the 2D profiles back to 1D values and rounding arithmetic errors. A very good agreement can be observed at both incidences examined, proving that the loss models in ESDU Item No. 80037 were successfully transferred in the *2D Intake SLC Software*.

Although ESDU data for intake configurations with an engine cone were not available, one would expect in this case a slightly less pressure recovery to be achieved at all flow conditions. The presence of an engine cone increases the total skin friction and flow blockage in the intake and introduces the growth of an extra boundary layer. But perhaps even more importantly, the slight reduction in pressure recovery in the case of an intake with a cone can be attributed to the fact that the diffuser semi-angle  $\varphi$  had to increase from 5.0 deg to 7.4 deg approximately, in order to maintain the same diffuser area ratio. From sub *Section 6.2.2. Calculation of Diffuser Pressure Recovery Loss* and Figures 6.2.2.1 and 6.2.2.2 it becomes evident that the datum diffuser pressure loss is proportional to factor  $k_1$ , which is obtained from tabulated experimental data as a direct function of the diffuser semi-angle  $\varphi$ , and  $k_2$  which is similarly obtained from experimental data as a function of  $\varphi$  and the diffuser area ratio  $\lambda_{\text{diff}}$ .

The intake model with an engine cone demonstrated an almost constant reduction in pressure recovery of 0.4%, with respect to the intake model without a cone, throughout the range of incidence angles and throat Mach numbers tested.



**CHAPTER IX*****HIGH-FIDELITY ENGINE PERFORMANCE  
SIMULATION***

Commercial gas turbine performance simulation software is usually 0D because there is no axial, radial or circumferential resolution within components. In these cycle simulations, individual engine components are typically represented with non-dimensional maps of experimental or default data, which sometimes also incorporate empirical adjustments for various off-design effects.

In those cases where actual component characteristics are not available and default characteristics are used instead, conventional 0D simulation tools can offer a good prediction of the performance of the whole engine close to design point, but can deviate substantially at off-design and transient conditions. Similarly, when real component characteristics are available, conventional engine cycle simulation tools can not predict the performance of the engine at other than nominal conditions satisfactorily, since individual component characteristics are usually established during component rig tests under nominal conditions. In other words, low-fidelity simulation tools are unable to capture complex physical phenomena, such as inlet flow distortion, and their effects on engine performance.

This project focuses on the investigation of the appropriate simulation strategies that will allow the performance characteristics of a gas turbine engine component, resolved from a detailed, high-fidelity analysis, to be integrated into an engine system analysis performed at a lower level of detail, at an affordable computational cost and time. By integrating a higher fidelity component simulation within a low-fidelity system simulation, it is possible to capture and analyse the relevant flow physics taking place in any given component in the context of the overall engine performance.

This chapter first discusses in detail the three basic advanced performance simulation strategies, described briefly in *Chapter I - Introduction*, and then focuses on their actual implementation by looking at several case studies of high-fidelity SLC and CFD components, integrated into a 0D cycle analysis. Due to the large number of examples presented in this chapter, different case studies are discussed and commented individually in every subsection. This chapter also describes briefly the software tools that were used to carry out the various analyses and their integration requirements.

***9.1. Advanced Performance Simulation Strategies***

From the beginning of this work, three basic methods were identified for carrying out 'Advanced Performance Simulation'. All these methods have the potential to i) 'match' the fidelity of the simulation according to the needs of the analysis for each component individually, ii) investigate relevant physical processes occurring in an

engine component in more detail, and iii) assess the effects of various isolated flow phenomena on overall engine performance in a timely and affordable manner.

These methods can be applied to all engine components and involve different levels of complexity and applicability. In the context of this study, these three methods identified in *Chapter I - Introduction* as de-coupled, iterative and fully integrated, were thoroughly investigated in terms of their actual implementation and potential. They are described in detail in the next three subsections using a high-fidelity compressor model as an example.

### 9.1.1. The De-Coupled Approach

This manual approach to high-fidelity analysis requires the initial execution of the 0D engine cycle simulation for a range of flight conditions and engine power settings (Figures 9.1.1.1 and 9.1.1.2).

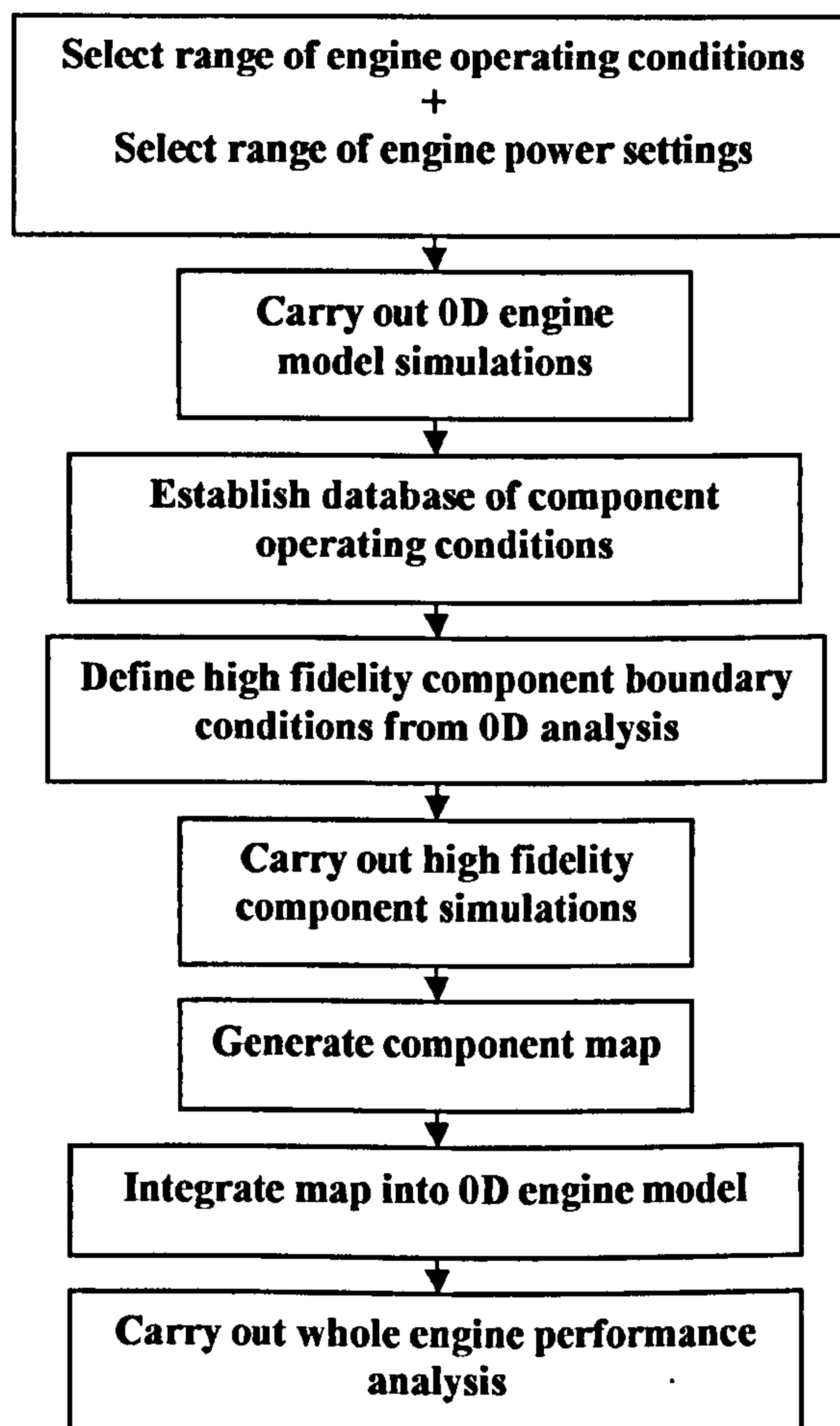


Figure 9.1.1.1: De-coupled high-fidelity analysis flow chart

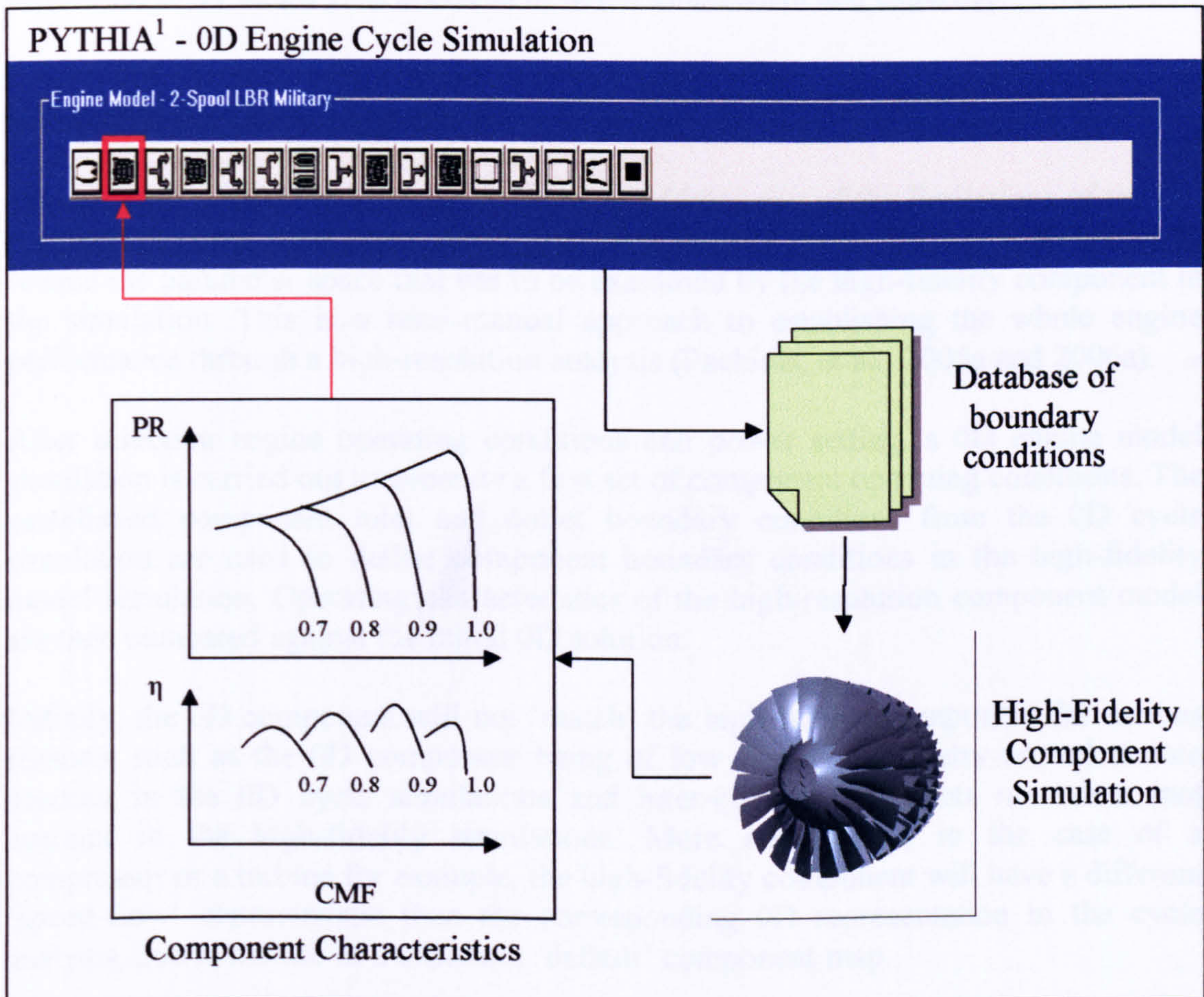
The 0D engine cycle simulations are basically carried out in order to generate a database of approximate component operating conditions which are then used as boundary conditions in the high-resolution analysis. More specifically, the high-



fidelity component model takes information generated by the corresponding baseline 0D representation of the same component, and uses that data as boundary conditions. After several high-resolution runs, the high-fidelity flow solutions are averaged back to non-dimensional values and a new component map is generated. The performance characteristics of the high-fidelity model are integrated back into the cycle model via the component characteristic map.

The generated performance map fully defines the characteristics of the component at the selected operating conditions and power settings and can be used to provide a more accurate, physics-based estimate of the component performance and hence, engine performance, replacing the default maps within the 0D cycle model.

This technique does not require the parallel or iterative execution of the 0D cycle and the high-fidelity model for the generation of the component map. This can be generated prior to the simulation by a single or even several PC platforms and used during the simulation by implementing appropriate map scaling and interpolation techniques.



<sup>1</sup>The PYTHIA Scheme is described in sub Section 9.2.1. Simulation Tools and Software Integration.

Figure 9.1.1.2: De-coupled high-fidelity analysis schematic diagram



### Concluding Remarks

The technique can be applied to all engine components which can be modeled in 2D or 3D. Since the component map can be generated before the whole engine simulation, this strategy is particularly suitable for high-fidelity studies incorporating the analysis of one or more components with CFD, where the simulation times involved can be extremely long.

An obvious limitation of this technique is that the generated component map is only applicable to the component geometry and operating conditions for which the simulations were carried out. If the component geometry changes or a particular flow phenomenon needs to be investigated, this would demand the repetition of the whole process.

Another important issue is the limitation of this simulation strategy to accurately resolve 2D or 3D boundary profiles from the 1D values supplied by the 0D cycle analysis. This could be overcome by looking into particular cases of component inlet conditions (i.e. uniform inlet conditions or a particular type and extent of inlet distortion) or by employing previous in-house empiricism and expertise.

#### **9.1.2. The Iterative Approach**

The iterative simulation strategy attempts to address one of the limitations of the decoupled approach mentioned above, by using the 0D cycle simulation primarily to reduce the parameter space that has to be examined by the high-fidelity component in the simulation. This is a semi-manual approach to establishing the whole engine performance through a high-resolution analysis (Pachidis, et al., 2005a and 2006a).

After selecting engine operating conditions and power setting, a 0D engine model simulation is carried out to generate a first set of component operating conditions. The established component inlet and outlet boundary conditions from the 0D cycle simulation are used to define component boundary conditions in the high-fidelity model simulation. Operating characteristics of the high-resolution component model are then compared against the initial 0D solution.

Initially, the 0D component will not 'match' the high-fidelity component for various reasons, such as the 0D component being of low fidelity, geometry not taken into account in the 0D cycle simulations and inter-component effects not taken into account in the high-fidelity simulations. More importantly, in the case of a compressor or a turbine for example, the high-fidelity component will have a different 'speed-flow' characteristic than the corresponding 0D representation in the cycle analysis, due to the use of a different, 'default' component map.

For the above reasons, boundary conditions need to be 'updated and exchanged' between the two component representations, in an iterative process, until a converged component performance is achieved at the selected engine operating conditions and power setting. The iterative process is carried out by changing in every iteration the default component map using scalars, until the 0D component performance matches



the performance calculated by the high-resolution component simulation. Figure 9.1.2.1 illustrates this process.

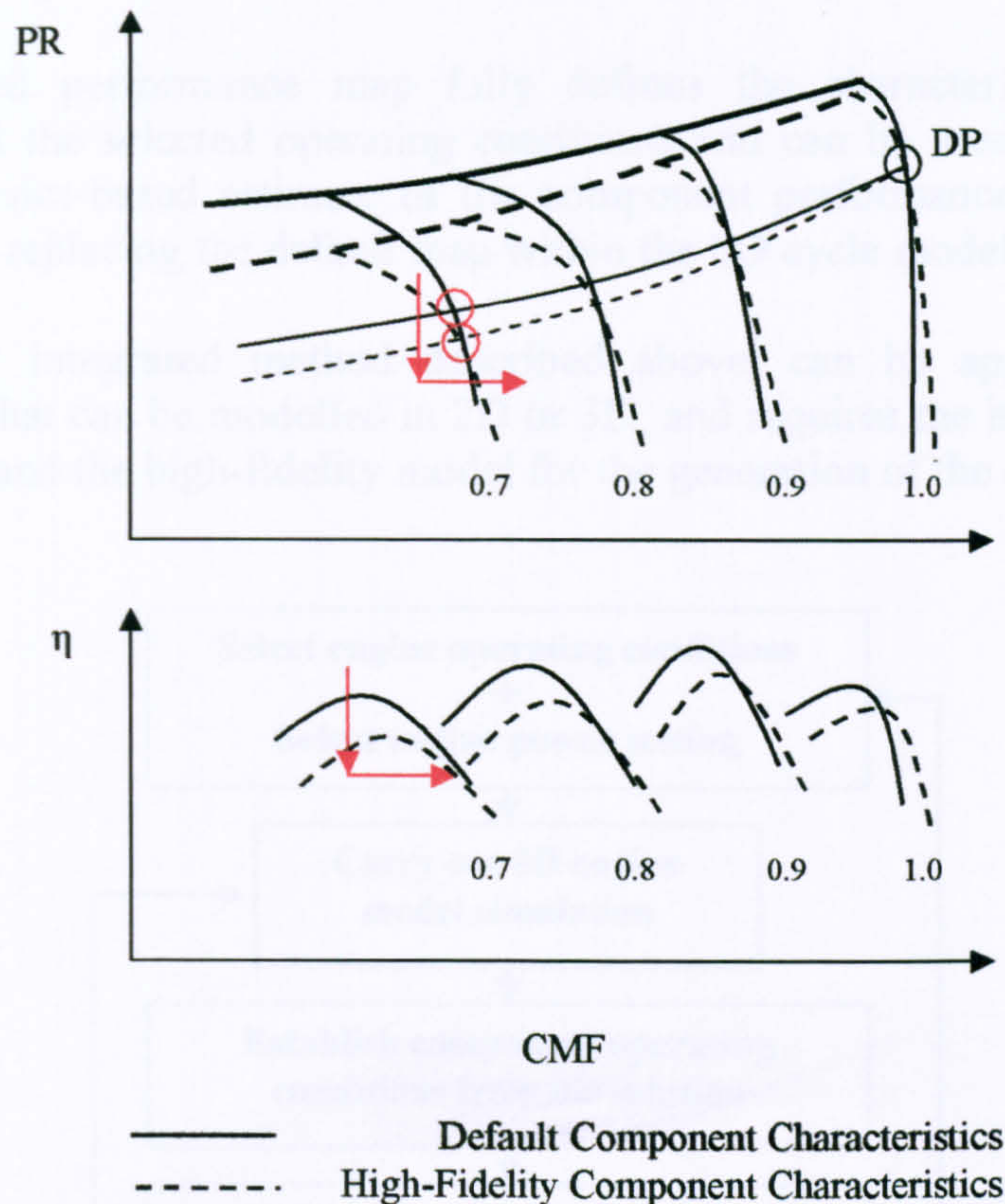


Figure 9.1.2.1: Iterative scaling of default component characteristics in order to establish the actual component operating point

At design point conditions, no iterative process is necessary to establish the correct component operating point since the initial scaling of the default map, carried out by the 0D cycle program, is usually based on the design point performance of the component and the corresponding design point on the default map. At off-design conditions, the shape of individual speed lines may still differ from the actual characteristics, despite the initial scaling carried out by the 0D cycle program. This may result in a completely different component off-design performance, different operating point locations on the equilibrium running line and hence, different overall engine performance. The red arrows in Figure 9.1.2.1 indicate the direction of the map scaling that is required in that notional case to establish every component operating point.

If the 0D and high-fidelity flow solutions are in agreement, within a pre-established error tolerance, the averaged high-fidelity flow solution establishes the correct component operating point and a point on the actual component performance map. If the flow solutions are not in agreement, the high-fidelity boundary conditions are communicated back to the 0D engine model as a second 'guess'. The 0D engine model simulation is carried out again to provide new, updated boundary conditions for the high-fidelity simulation. The process is repeated many times, until the two solutions agree within the pre-established error margin. A new point on the actual



component performance map is then generated (Figures 9.1.2.2 and 9.1.2.3). Repeating the process for different engine operating conditions and power settings establishes a 'partial' component performance map that can be used at a later stage for a whole engine performance simulation without requiring iterations.

The generated performance map fully defines the characteristic of the engine component at the selected operating conditions and can be used to provide a more accurate, physics-based estimate of the component performance and hence, engine performance, replacing the default map within the 0D cycle model.

The partially integrated method described above, can be applied to all engine components that can be modelled in 2D or 3D, and requires the iterative execution of the 0D cycle and the high-fidelity model for the generation of the component map.

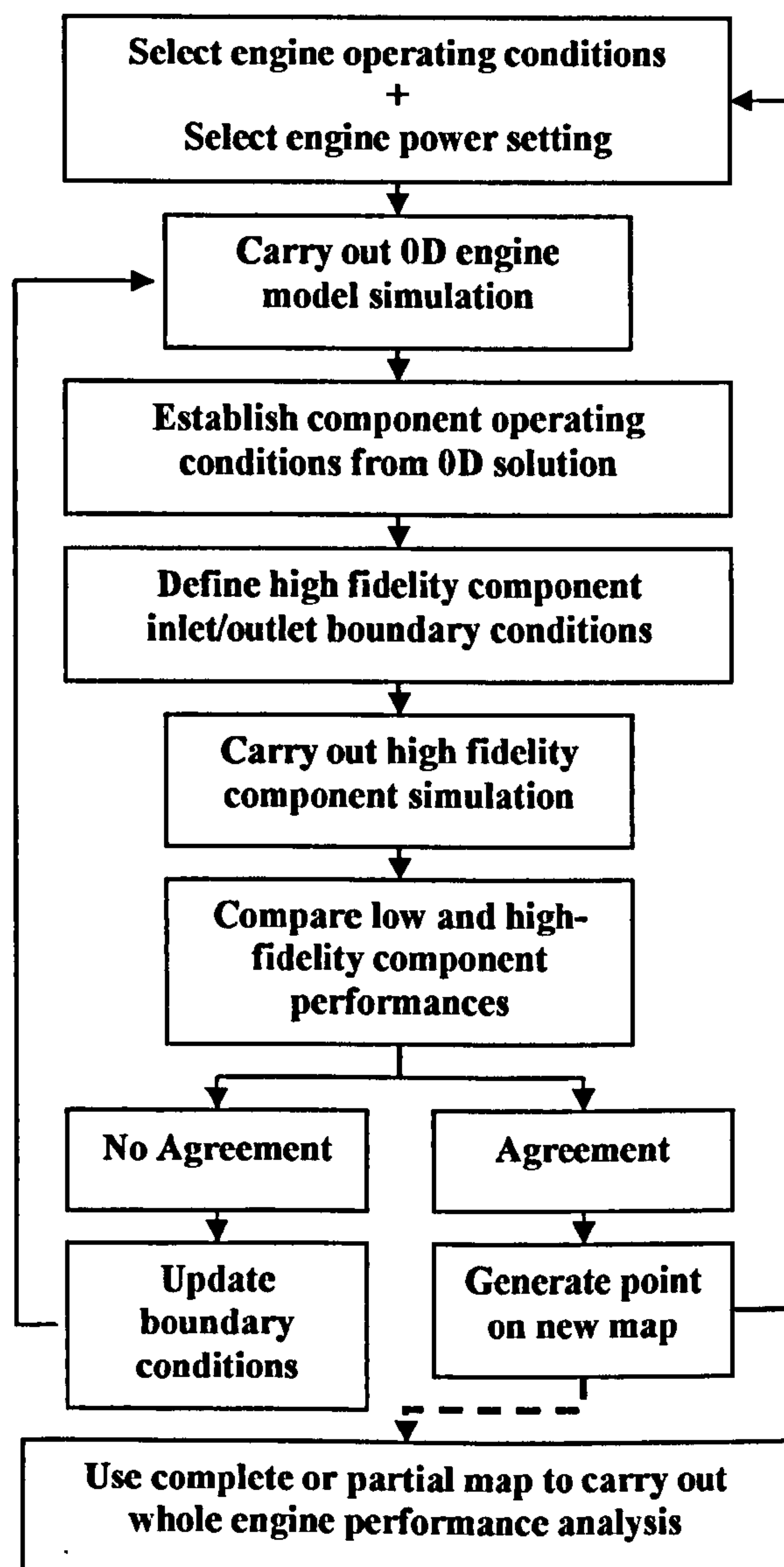
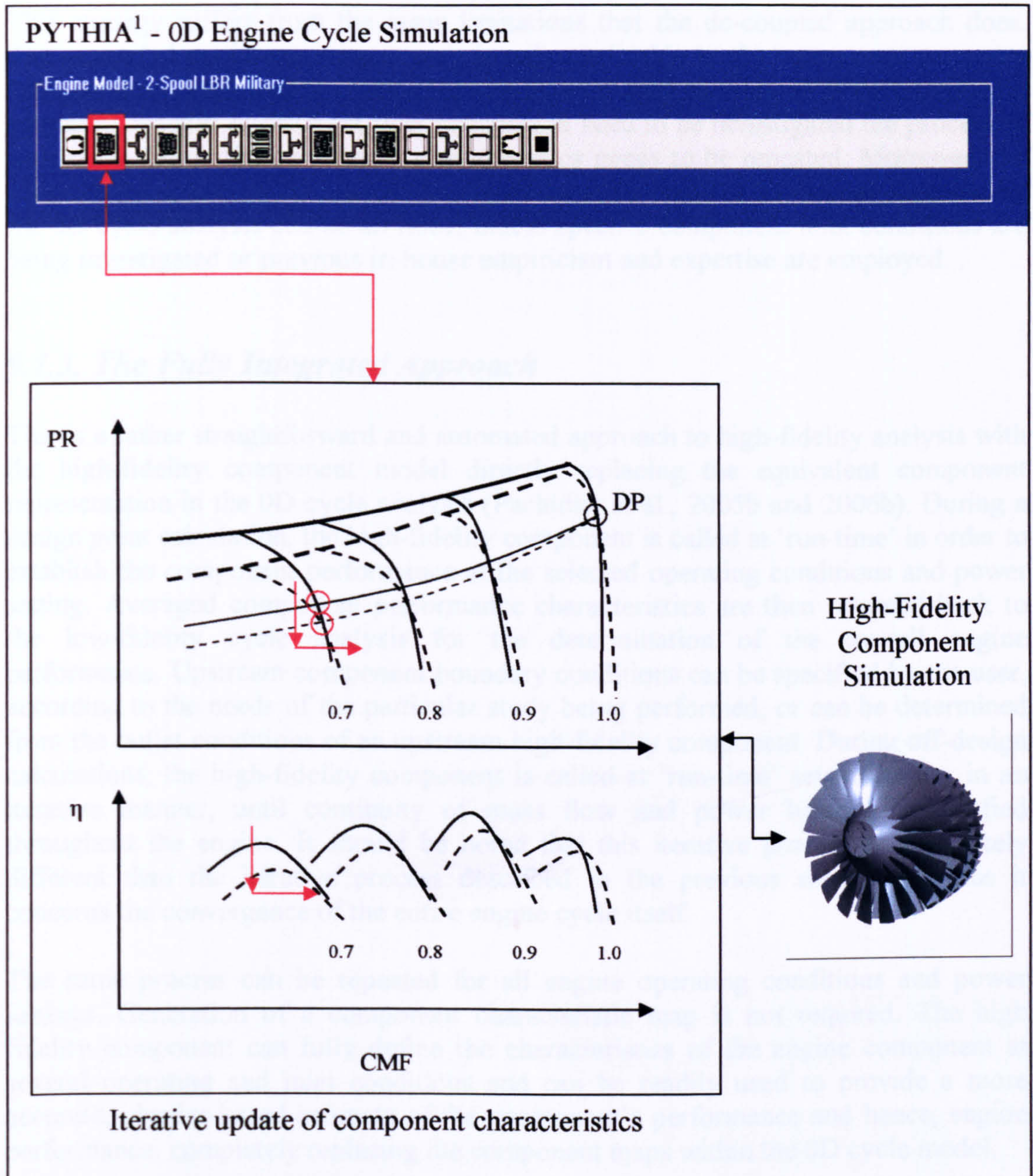


Figure 9.1.2.2: Iterative high-fidelity analysis flow chart





<sup>1</sup> The PYTHIA Scheme is described in sub Section 9.2.1. Simulation Tools and Software Integration.

Figure 9.1.2.3: Iterative high-fidelity analysis schematic diagram

Concluding Remarks

Similarly to the de-coupled approach, perhaps this simulation strategy is more suited for high-fidelity studies involving one or more 3D CFD components, where simulation times can get extremely long. Although it looks very tedious at the beginning, theoretically it could save a lot of simulation time since the generation of the whole component map is not required and only a narrow region of component performance of interest needs to be established.



This strategy suffers from the same limitations that the de-coupled approach does. The generated partial component map is only applicable to the component geometry and operating conditions for which the simulations were carried out. If the component geometry changes or different flow phenomena need to be investigated the process of generating the partial component characteristics needs to be repeated. Moreover, the accurate resolution of 2D and 3D boundary profiles from the 1D values supplied by the 0D cycle analysis can be an issue, unless specific component inlet conditions are being investigated or previous in-house empiricism and expertise are employed.

### ***9.1.3. The Fully Integrated Approach***

This is a rather straightforward and automated approach to high-fidelity analysis with the high-fidelity component model directly replacing the equivalent component representation in the 0D cycle analysis (Pachidis, et al., 2005b and 2006b). During a design point calculation, the high-fidelity component is called at 'run-time' in order to establish the component performance at the selected operating conditions and power setting. Averaged component performance characteristics are then returned back to the low-fidelity cycle analysis for the determination of the overall engine performance. Upstream component boundary conditions can be specified by the user, according to the needs of the particular study being performed, or can be determined from the outlet conditions of an upstream high-fidelity component. During off-design calculations, the high-fidelity component is called at 'run-time' several times, in an iterative manner, until continuity of mass flow and power balance is satisfied throughout the engine. It should be noted that this iterative process is completely different than the iterative process described in the previous subsection since it concerns the convergence of the entire engine cycle itself.

The same process can be repeated for all engine operating conditions and power settings. Generation of a component characteristic map is not required. The high fidelity component can fully define the characteristics of the engine component at several operating and inlet conditions and can be readily used to provide a more accurate, physics-based estimate of the component's performance and hence, engine performance, completely replacing the component maps within the 0D cycle model.

### **Concluding Remarks**

The high-fidelity model, being directly embedded in the 0D cycle analysis can be readily used regardless any design changes or particular flow phenomena under study. This technique can be applied to all engine components and is obviously more suitable for high-resolution analysis involving several high-fidelity components which do not require long execution times (Pachidis, et al., 2006c).

Finally, it should be pointed out that the fully integrated analysis, by employing several high-fidelity components, has the potential to effectively address the limitation of the other two strategies to accurately generate 2D or 3D boundary profiles from the 1D values supplied by the 0D cycle during execution.



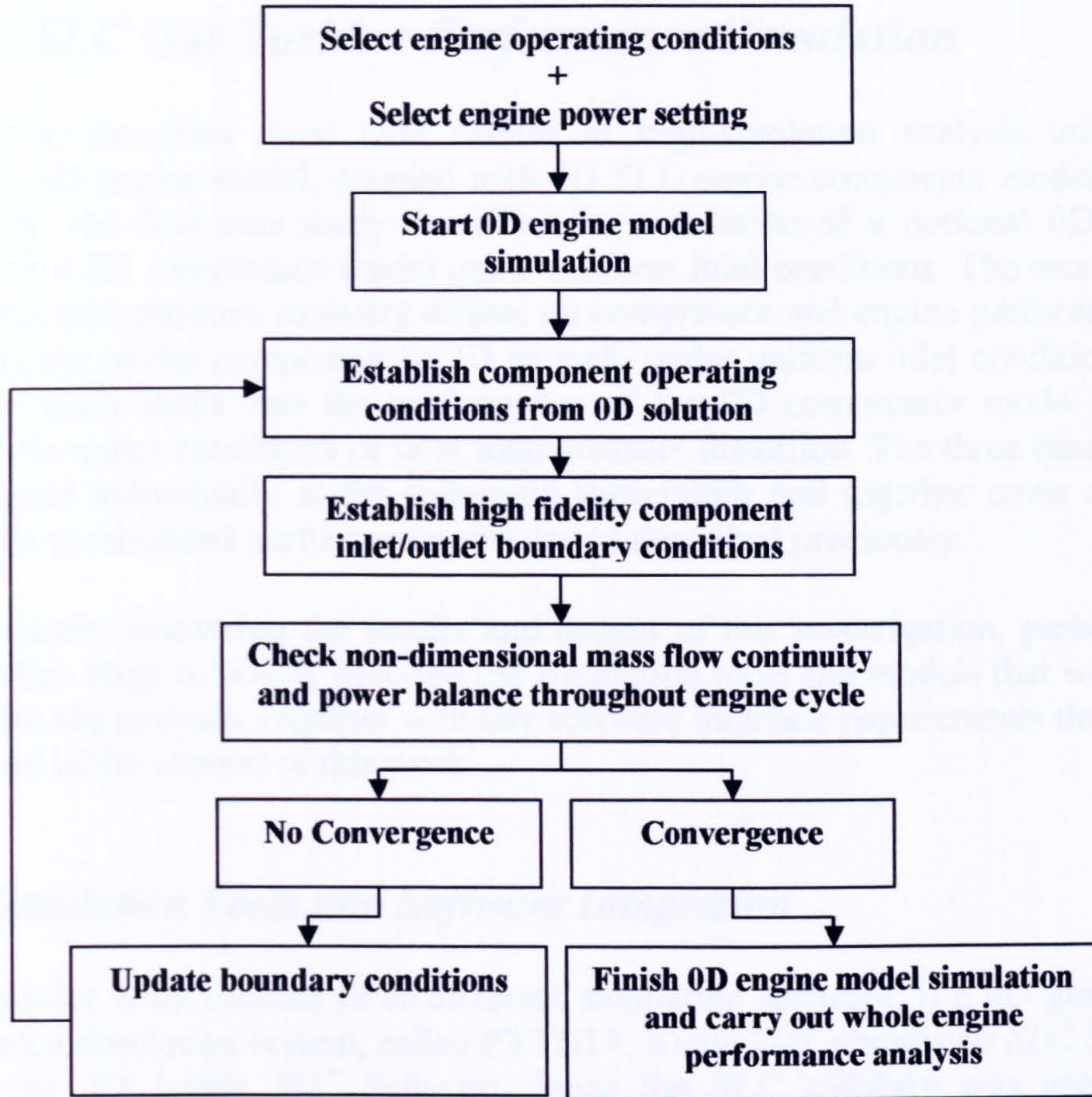
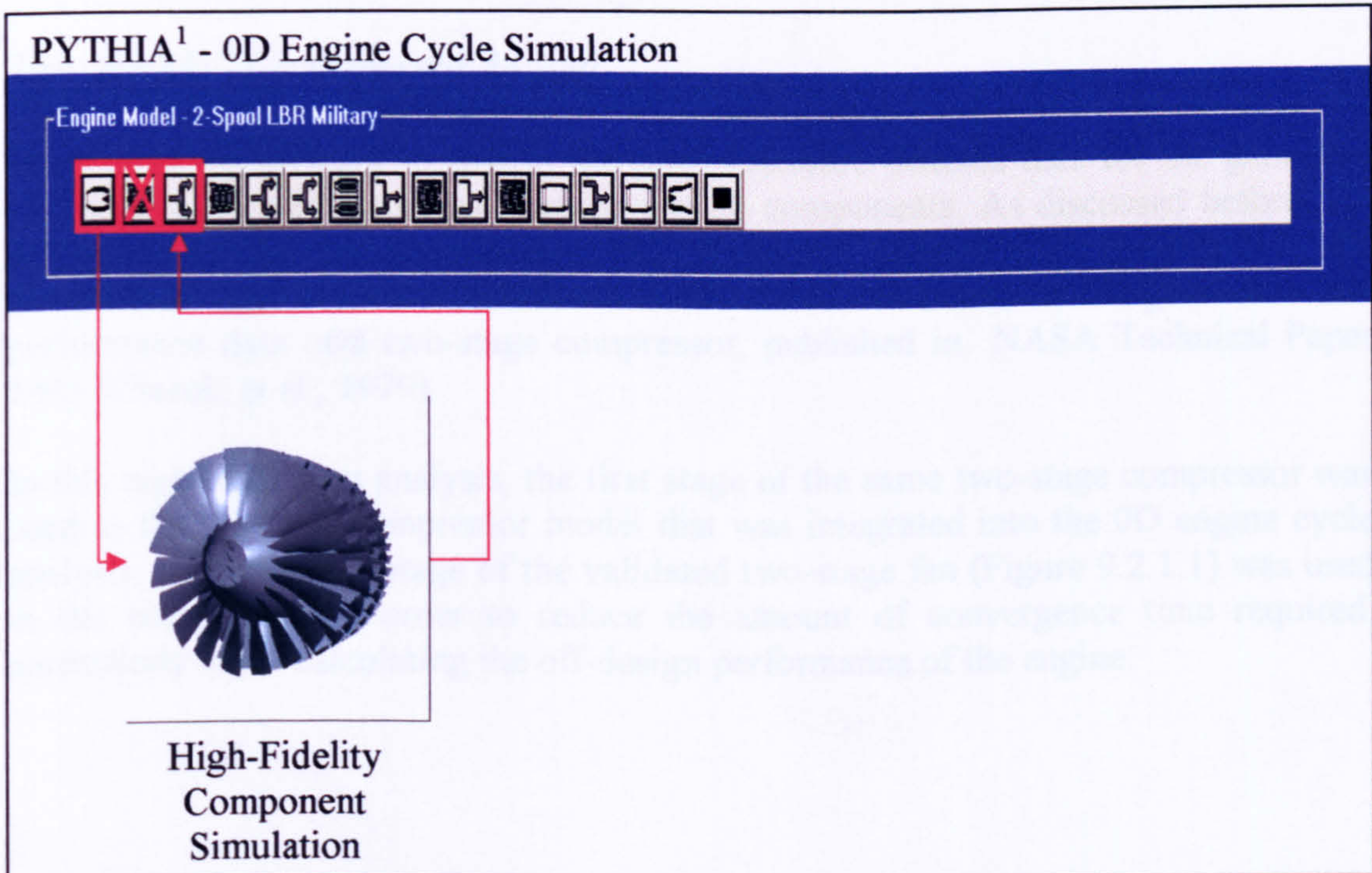


Figure 9.1.3.1: Fully integrated high-fidelity analysis flow chart



<sup>1</sup> The PYTHIA Scheme is described in sub Section 9.2.1. Simulation Tools and Software Integration.

Figure 9.1.3.2: Fully integrated high-fidelity analysis schematic diagram



## 9.2. 2D SLC Gas Turbine Performance Simulation

This section describes three case studies of high-resolution analysis utilising a traditional 0D engine model, coupled with 2D SLC engine component models. More specifically, the first case study describes the simulation of a notional 0D engine model with a 2D compressor model under uniform inlet conditions. The second case study looks into pressure recovery effects on compressor and engine performance by simulating the intake component in 2D as well, under uniform inlet conditions. The third case study looks into the performance of the 2D compressor model and 0D engine cycle under conditions of inlet total pressure distortion. The three case studies are discussed individually in the following subsections and together cover all three approaches to advanced performance simulation described previously.

Before actually discussing the results and details of this investigation, perhaps it is proper at this stage to briefly describe the simulation tools and models that were used to carry out the analysis, together with any software interface requirements that had to be resolved in the context of this work.

### 9.2.1. Simulation Tools and Software Integration

This particular work utilized three different simulation software: i) a 0D gas turbine performance simulation system, called PYTHIA, ii) the *2D Compressor SLC Software* and iii) the *2D Intake SLC Software*. Since the SLC software was specifically developed for the purposes of this investigation, its development was extensively described and discussed in previous chapters.

#### The 2D SLC Compressor Model

It is extremely difficult to find in the open literature detailed data for the geometry and performance of actual gas turbine engine components. As discussed before, the validation of the *2D Compressor SLC Software*, presented in *Section 8.1. 2D Compressor SLC Software Validation*, was carried out based on the geometric and performance data of a two-stage compressor, published in NASA Technical Paper 1493 (Urasek, et al., 1979).

In this high-resolution analysis, the first stage of the same two-stage compressor was used as the 2D SLC compressor model that was integrated into the 0D engine cycle analysis. Only the first stage of the validated two-stage fan (Figure 9.2.1.1) was used in the simulations in order to reduce the amount of convergence time required, particularly when calculating the off-design performance of the engine.



## Single-Stage 2D SLC Compressor Model

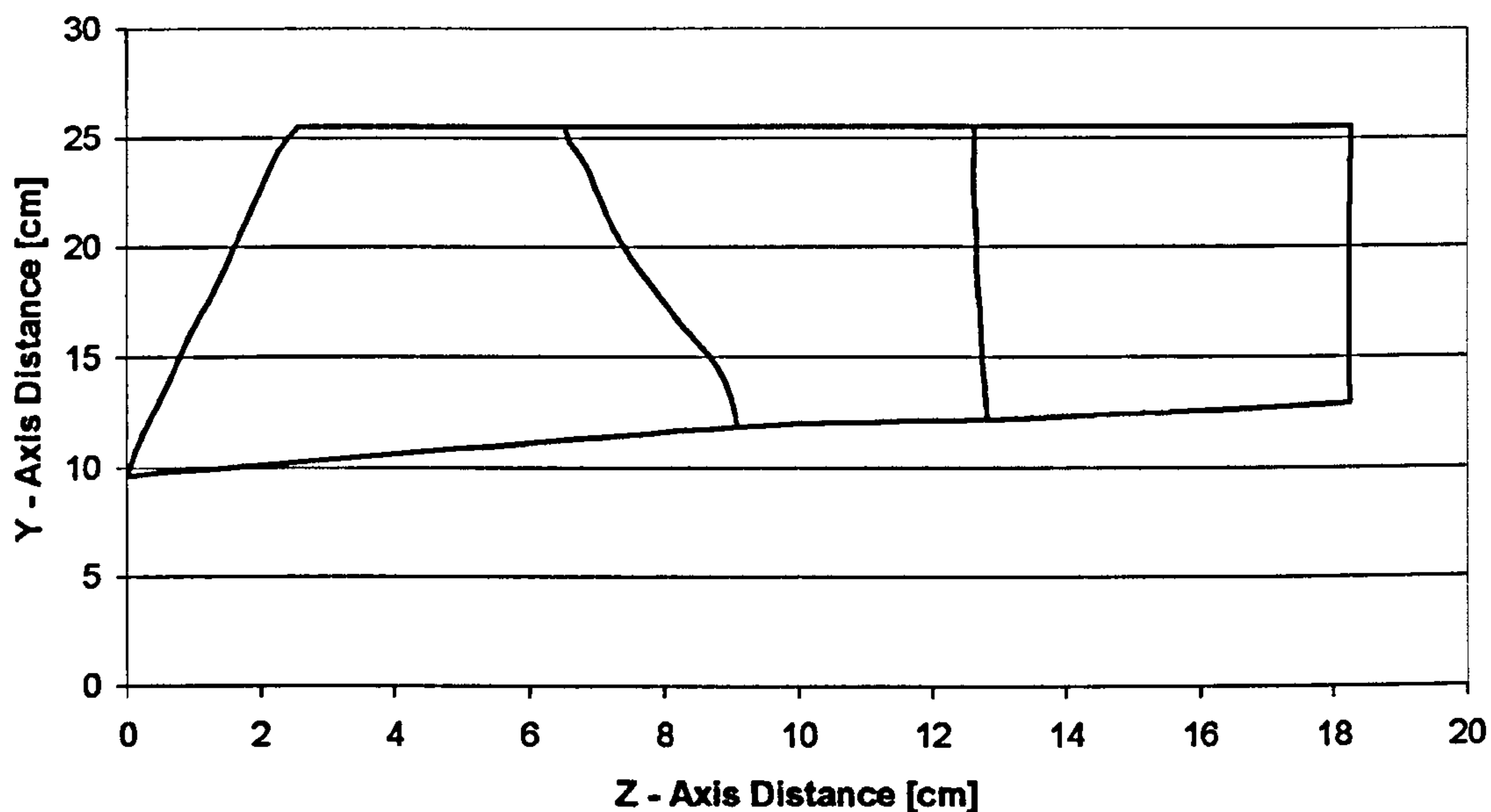


Figure 9.2.1.1: Single-stage 2D SLC compressor model

The detailed geometry of the first stage can be found in *Appendix F - Two-Stage Compressor Geometry*. The design performance of the first stage, according to the experimental data, is given in Table 9.2.1.1 and is also illustrated in Figures 9.2.1.2 and 9.2.1.3, together with the calculated overall performance of the first stage under clean inlet conditions.

Pressure Ratio	1.590
Temperature Ratio	1.167
Isentropic Efficiency	0.848
Corrected Mass Flow [kg/s]	33.248
RPM	16042.800
PCN	0.967
Inlet Hub -Tip Ratio	0.375
Rotor Tip Speed [m/s]	428.896

Table 9.2.1.1: First stage design compressor performance



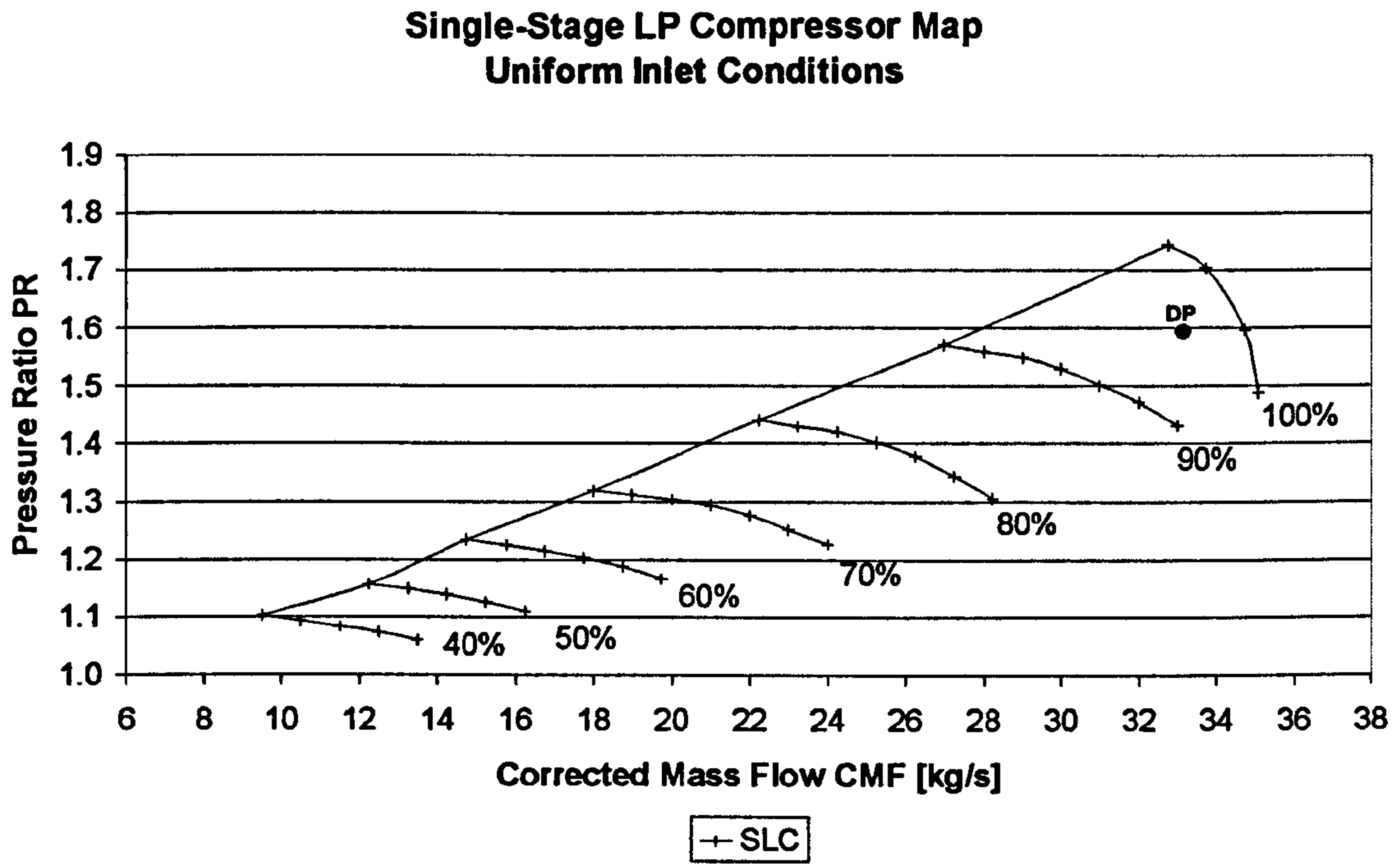


Figure 9.2.1.2: Single-stage LP compressor design point and overall performance – Pressure Ratio vs Corrected Mass Flow

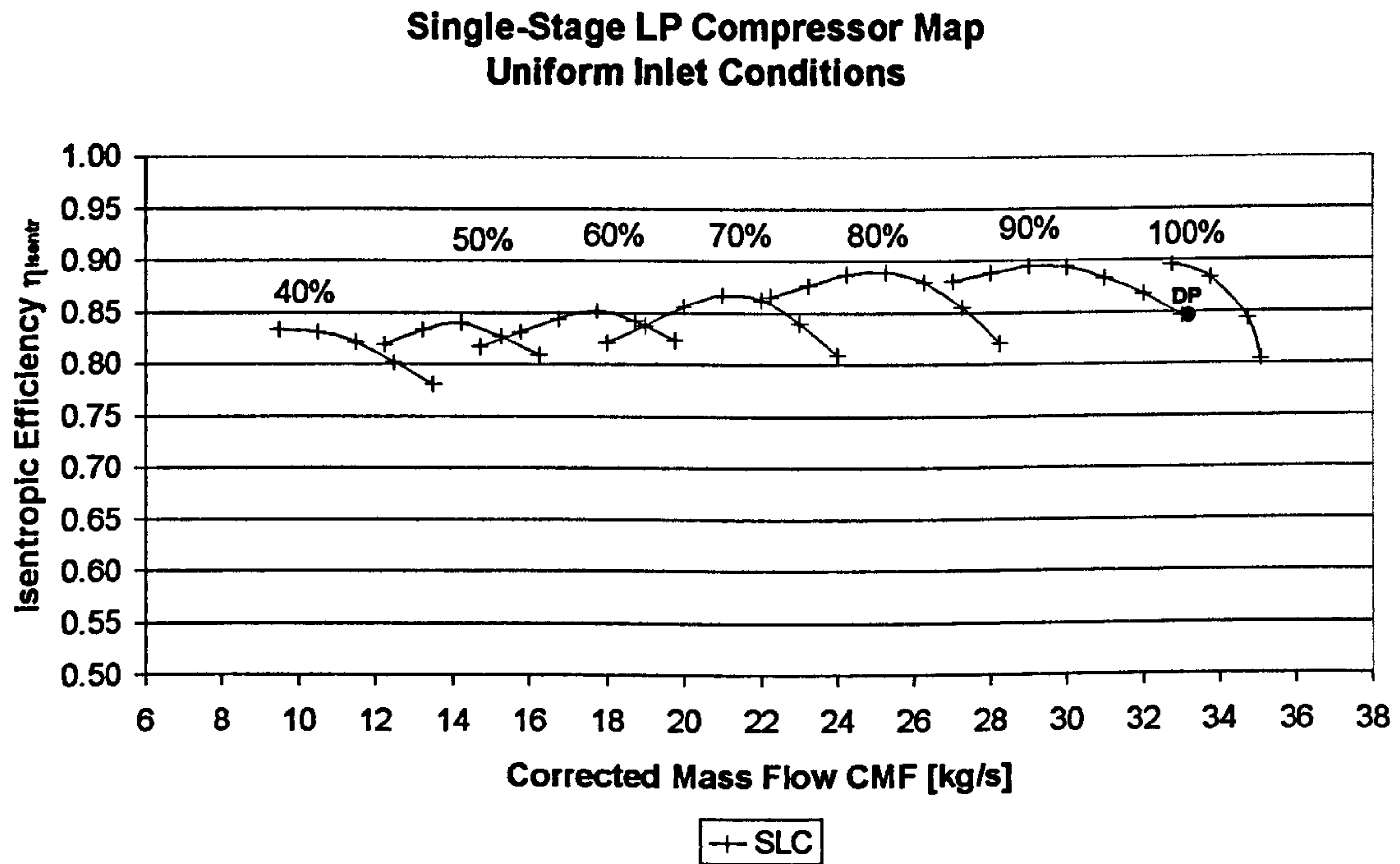


Figure 9.2.1.3: Single-stage LP compressor design point and overall performance – Isentropic Efficiency vs Corrected Mass Flow

With the 2D SLC compressor being the most critical part of the entire analysis, due to the complexity involved in modelling the compressor geometry and simulating its performance, the 0D engine model and 2D SLC intake model had to be ‘tailored’ around the available compressor geometry and performance.



### The 2D SLC Intake Model

For the purposes of this investigation a simple, notional 2D SLC intake model with an engine cone was created (Figure 9.2.1.4). The intake's outlet lip inner radius and cone's outer radius matched the compressor's casing and hub radii respectively. The 2D intake model was designed to match the mass flow requirements of the 2D compressor, throughout its operating range without choking, and featured an entry contraction ratio  $\lambda_{\text{contr}}$  of 1.38 and a diffuser area ratio  $\lambda_{\text{diff}}$  of 1.32. A constant section duct was also included between the lip and diffuser entry and between the diffuser outlet and compressor inlet as Figure 9.2.1.4 illustrates. The detailed geometry of the 2D SLC intake model has been included in this thesis as *Appendix G - Intake Geometry*.

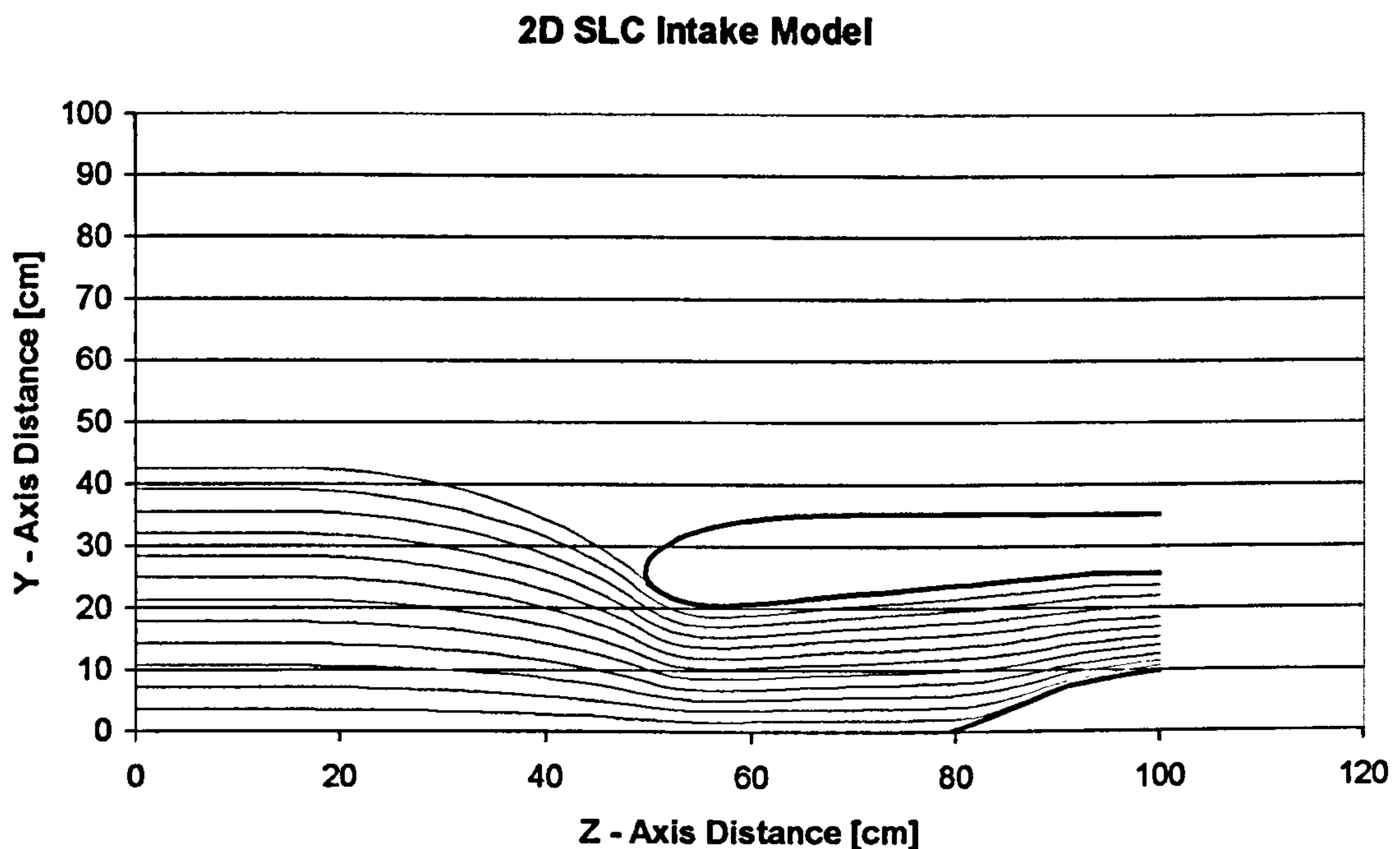


Figure 9.2.1.4: 2D SLC intake model and pre-entry stream tube

The performance of this basic intake geometry was thoroughly investigated for various lip configurations and flow conditions, at several Angles of Attack (AoA), and throughout the mass flow range of interest. The detailed performance of the 2D SLC intake model has been included in this thesis as *Appendix I - 2D SLC Intake Performance* and is discussed in sub *Section 9.2.3. Effect of 2D SLC Intake Characteristic on Engine Performance*.

### The 0D Engine Model

For the purposes of this investigation a notional 0D engine model was built in PYTHIA. The PYTHIA scheme was developed by the Gas Turbine Engineering Group at Cranfield University in the UK. Based on Cranfield's previous 'generation' engine simulation software, called TURBOMATCH (Palmer, 1990), PYTHIA was specifically developed to be a fully modular, object-oriented (OO), engine cycle



simulator that can perform steady state design, off-design and degraded performance analysis of civil aero, industrial and military engines. PYTHIA was also developed to be a versatile engine diagnostics tool (Figure 9.2.1.5).



Figure 9.2.1.5: Cranfield's gas turbine performance simulation and diagnostics software

PYTHIA's windows environment is actually subdivided into two parts, one for carrying out engine diagnosis, and another, for building engine models and simulating their performance under clean and degraded conditions. The simulation environment in PYTHIA was developed by this author while working in the Gas Turbine Engineering Group at Cranfield University as a member of research staff (Pachidis, 2004). PYTHIA's environment apart from providing a Graphical User Interface (GUI) to the legacy TURBOMATCH software, also incorporates several programming improvements and capability expansions such as:

#### Programming Improvements

- Entire legacy source code re-written in FORTRAN 95 standard
- Well written code - easy to maintain
- No "spaghetti"
- Portability
- Extensibility
- Exception handling
- Data encapsulation
- Isolated engine routine



- Introduction of MODULES
- Fundamental data structures
- Language support for (OO) concepts

### Capability Improvements

- High-density, smooth compressor and turbine maps
- Notional default and user defined maps
- Easy access to scaled maps
- Easy access to user defined maps
- Input and Output using API/ARP4868 standard
- Dynamic convergence control
- Alternative fuels
- New engine components
- Parametric analysis

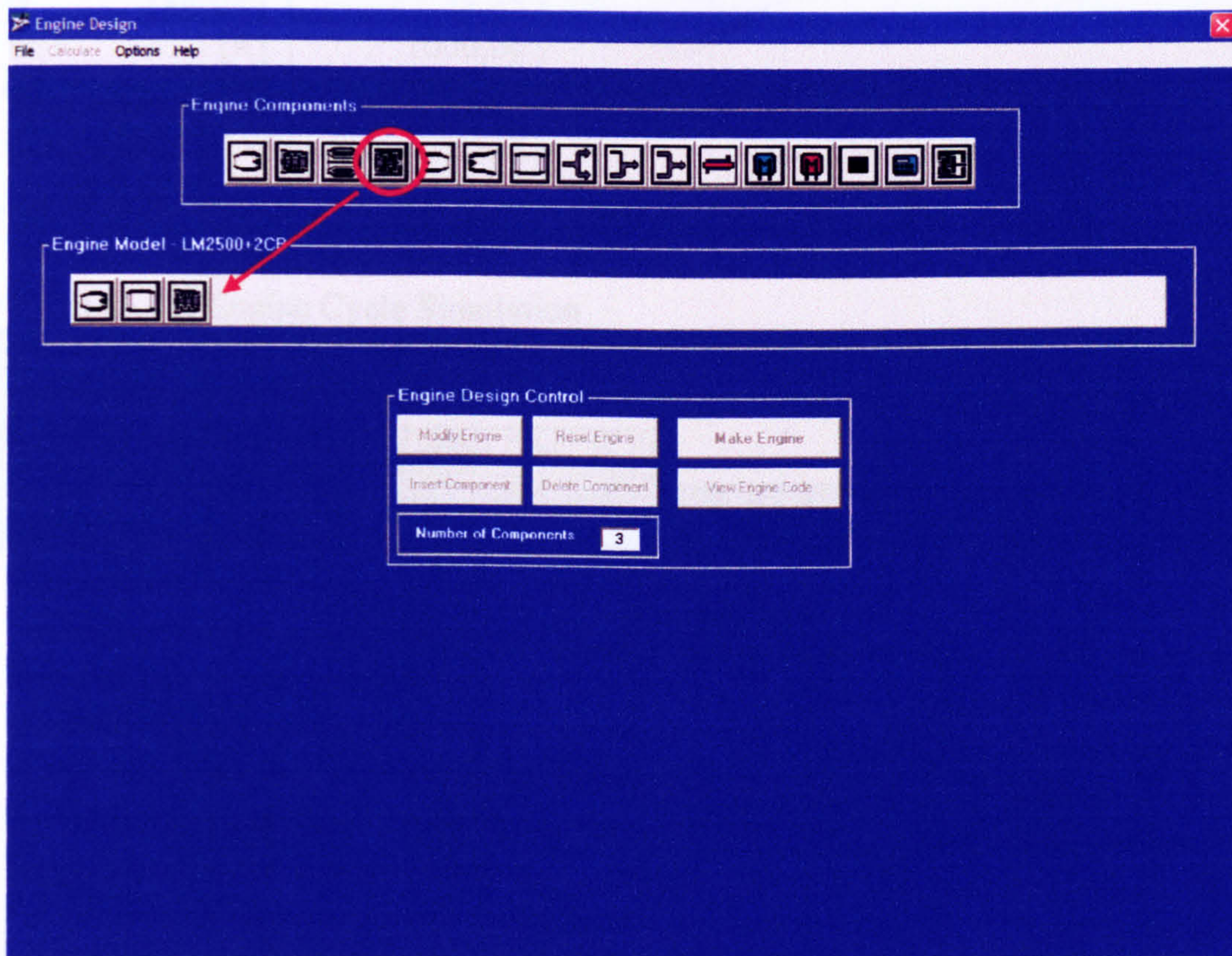


Figure 9.2.1.6: PYTHIA's engine modelling and simulation environment

In the simulation environment of PYTHIA, an engine model is assembled from a collection of interconnected elements, and is controlled by an appropriate numerical solver. By means of engine component icons (Figure 9.2.1.6) and via an engine component toolbar, various pre-programmed routines, called 'Bricks', can be called up to simulate the action of different engine components. The 0D engine analysis finally results in output of engine thrust or power, fuel consumption, specific fuel consumption, etc., together with details of individual component performance and of the gas properties at various stations within the engine. Typically, a PYTHIA engine



model uses non-dimensional performance maps for turbines and compressors to obtain a balanced, steady-state engine condition.

As mentioned before, for the purposes of this investigation a notional engine model was built in PYTHIA based on the configuration of an existing two-shaft, LBR, mixed-exhaust, military turbofan, but scaled down in terms of OPR, mass flow and TET in order to match the performance and geometry of the available 2D SLC LP compressor model (Figure 9.2.1.7). The overall design performance of the notional engine is illustrated in Table 9.2.1.2. A low value of TET was selected in order to address nozzle area matching problems arising due to the extremely low engine mass flow, fan and overall pressure ratios. Other engine performance parameters can be found in PYTHIA’s engine input data files which have been included in this thesis as *Appendix J - PYTHIA Engine Input Data Files*.

OPR		3.63
BPR		0.4:1.0
W	[kg/sec]	33.25
TET	[K]	1000.00
GT	[N]	11041.30
SFC	[mg/N sec]	26.18

Table 9.2.1.2: Notional engine design performance parameters

PYTHIA - 0D Engine Cycle Simulation

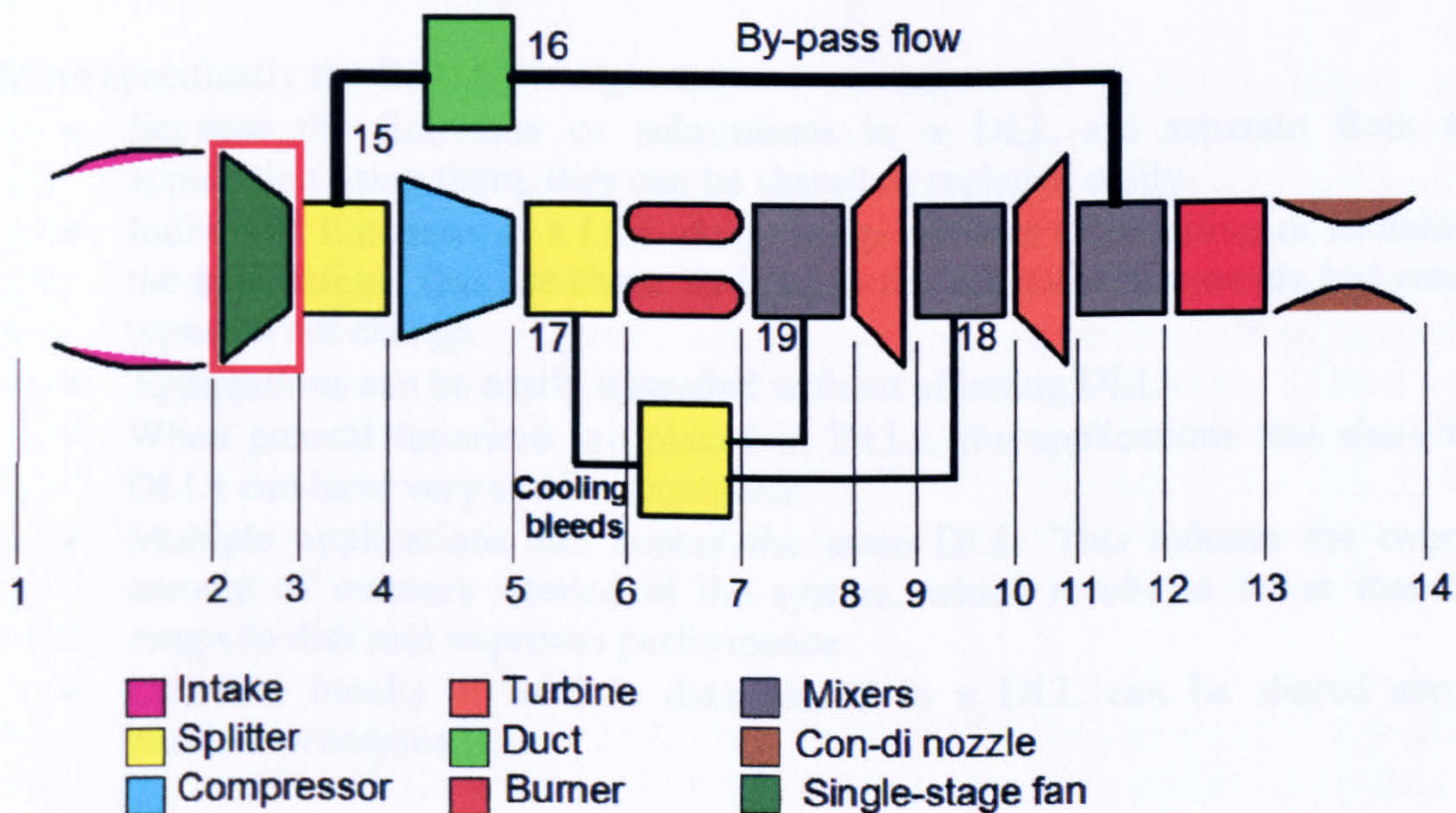
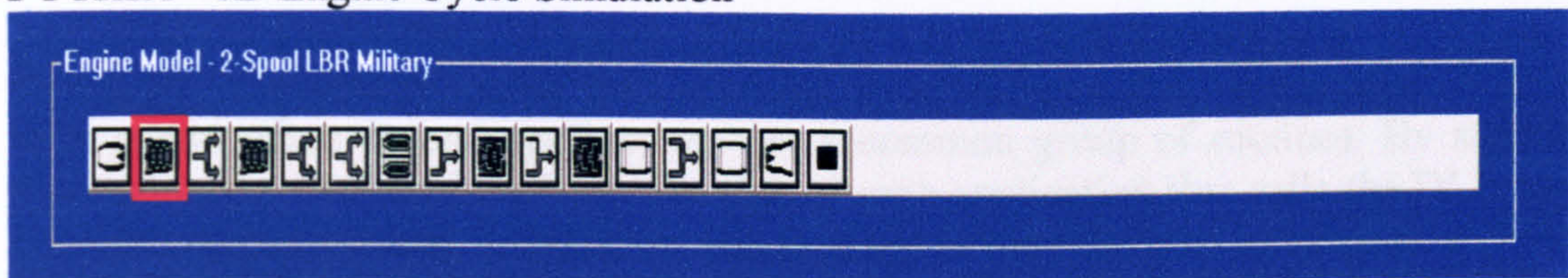


Figure 9.2.1.7: Schematic representation of PYTHIA’s model of the notional, two-shaft, LBR, mixed-exhaust, military turbofan engine



## Software Interface Requirements

According to the de-coupled and iterative simulation strategies, the high-fidelity component model can communicate with the low-fidelity engine cycle through component characteristic maps which can be manually programmed into the 0D cycle program for the determination of the whole engine performance. The fully integrated approach however, requires an explicit interface between the high-fidelity component and the low-fidelity cycle simulation. This can be facilitated through the use of Dynamic Link Libraries (DLLs).

Generally speaking, a DLL is a library of functions that uses dynamic linking. A dynamic-link library is a source code library that contains one or more subprogram procedures (functions or subroutines) that are compiled, linked, and stored separately from the application using them. A DLL contains only subprograms and not main programs and shares its code and data address space with the calling application.

Basically a DLL is an executable file which offers the organizational advantages of a static library, but with the advantage of a smaller executable file at the expense of a slightly more complex interface. Unlike a static library where routines are included in the base executable image during linking, the routines in a DLL are loaded when an application that references that DLL is loaded during run time. In other words, object code from a DLL is not included in the program's executable file, but is associated as needed in a dynamic manner while the program is executing.

More than one program can access a DLL at a time. When routines in a DLL are called, the routines are loaded into memory at run-time, as they are needed. This is most useful when several applications use a common group of routines. By storing these common routines in a DLL, the size of each application that calls the DLL can be considerably reduced. In addition, the routines in the DLL can be updated without having to rebuild any of the applications that call the DLL.

More specifically the DLL advantages are:

- Because the functions or subroutines in a DLL are separate from the application using them, they can be shared or replaced easily
- Individual functions in a DLL may change without recompiling or re-linking the applications that use them, as long as the functions arguments and return types do not change
- Applications can be easily upgraded without affecting DLLs
- When general functions are placed in DLLs, the applications that share the DLLs can have very small executables
- Multiple applications can access the same DLL. This reduces the overall amount of memory needed in the system, which results in fewer memory swaps to disk and improves performance
- Common blocks or module data placed in a DLL can be shared across multiple processes

In order to carry out a fully integrated type of high-fidelity engine performance analysis utilising 2D SLC components, both the *2D Compressor SLC Software* and *2D Intake SLC Software* had to be fully integrated within PYTHIA's 0D analysis. Traditionally, in PYTHIA (as in TURBOMATCH) the performance of compressors



and intakes has been handled by the 0D component 'Bricks' COMPRE and INTAKE respectively. For the purposes of this investigation, both *2D Compressor SLC Software* and *2D Intake SLC Software* were separately compiled as dynamic link library files (COMP2D.dll and INTAKE2D.dll respectively). They were then integrated into the 0D code by using the generated COMP2D.dll and INTAKE2D.dll files, which contain the library's executable code, and the import library files COMP2D.lib and INTAKE2D.lib, which the linker requires to associate the main program (PYTHIA in this case) with the DLL files.

Moreover, two new bricks were added in PYTHIA, namely COMP2D and INTA2D (*Appendix J – PYTHIA Engine Input Data Files*). These new bricks were programmed in order to allow the user to call the 2D bricks via the traditional input engine data file, as needed, and in order to provide the explicit interface required between the low-fidelity cycle and the high-fidelity components. The 2D bricks were also used to manipulate the data passed from one software to the other. Obviously, keeping the original 0D component representations in the code provided the extra flexibility to carry out engine performance simulation with any intake or compressor component in the engine being simulated in 0D or 2D.

### ***9.2.2. Effect of 2D SLC Fan Characteristic***

This particular case study looked into relative differences in the performance of the notional LBR military turbofan engine, arising from substituting the 0D LP compressor (single-stage fan) component with the 2D SLC compressor model described above. This case study investigated all three methods for integrating a high-fidelity component into a 0D cycle analysis. The findings are discussed below.

#### ***De-Coupled High-Fidelity Simulation***

A PYTHIA 0D engine cycle analysis was first carried out at ISA SLS conditions and for a range of power settings from a Turbine Entry Temperature (TET) of 1000.0 K (DP value), down to a TET of 775.0 K. Uniform compressor inlet conditions were assumed at all power settings. This initial 0D cycle simulation established the reference engine performance and a database of approximate boundary conditions for the subsequent high-fidelity analysis. More specifically, a database of LP fan pressure ratios, corrected mass flows, power settings and relative rotational speeds was established for operating points along the LP compressor equilibrium running line. Figure 9.2.2.1 illustrates the equilibrium running line established on the default LP compressor characteristic using TET as the handle. The default compressor map was automatically scaled by PYTHIA at design point in order to conform to the design performance of the LP compressor.

In this particular case, the 2D SLC compressor characteristic could be readily integrated into the 0D cycle program, since it was previously established during the validation of the *2D Compressor SLC Software*. Normally however, if the high-fidelity map is not readily available, it needs to be calculated based on the approximate database boundary conditions established during the calculation of the reference engine performance.



PYTHIA 0D Default LP Compressor Characteristic  
Uniform Inlet Conditions

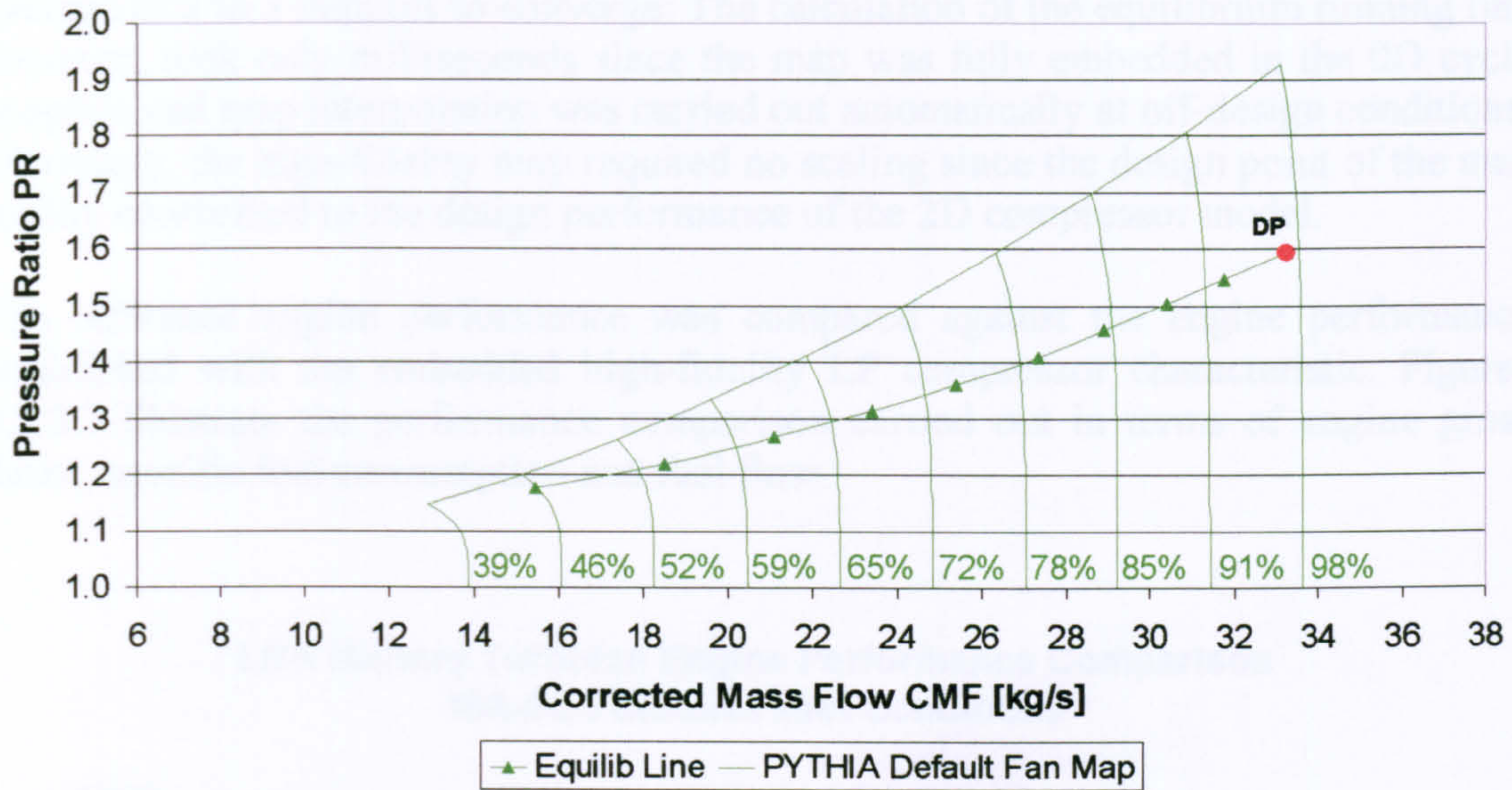


Figure 9.2.2.1: PYTHIA’s scaled default map for LP compressor and equilibrium running line

By manually programming the high-fidelity LP compressor map into the 0D cycle program, according to the de-coupled simulation strategy described before, it was possible to establish the performance of the engine, but this time taking into account the actual LP compressor geometry and performance. Figure 9.2.2.2 illustrates the new LP compressor equilibrium running line established after the manual integration of the high-fidelity map.

2D SLC LP Compressor Characteristic  
Uniform Inlet Conditions

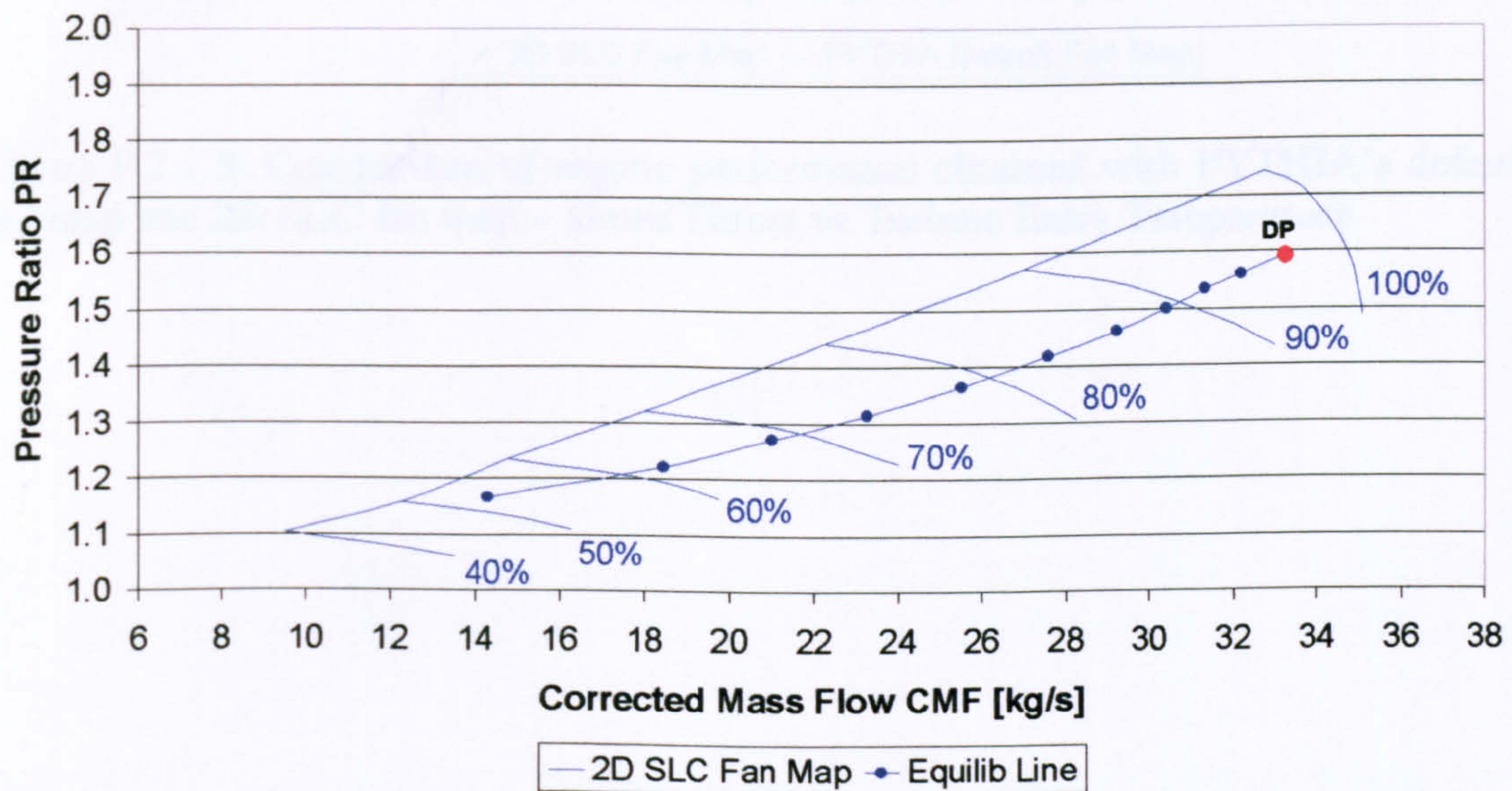


Figure 9.2.2.2: SLC derived map for LP compressor and equilibrium running line



During the software validation process it took approximately 80 minutes for the *2D Compressor SLC Software* to produce the compressor characteristic shown in Figure 9.2.2.2. This particular map consists of 41 converged points, each point requiring an average of 2 to 3 minutes to converge. The calculation of the equilibrium running line however, took only milliseconds since the map was fully embedded in the 0D cycle program and map interpolation was carried out automatically at off-design conditions. Obviously, the high-fidelity map required no scaling since the design point of the map readily conformed to the design performance of the 2D compressor model.

The reference engine performance was compared against the engine performance established with the embedded high-fidelity LP compressor characteristic. Figures 9.2.2.3 illustrate the performance comparison carried out in terms of engine gross thrust, specific fuel consumption and fuel flow.

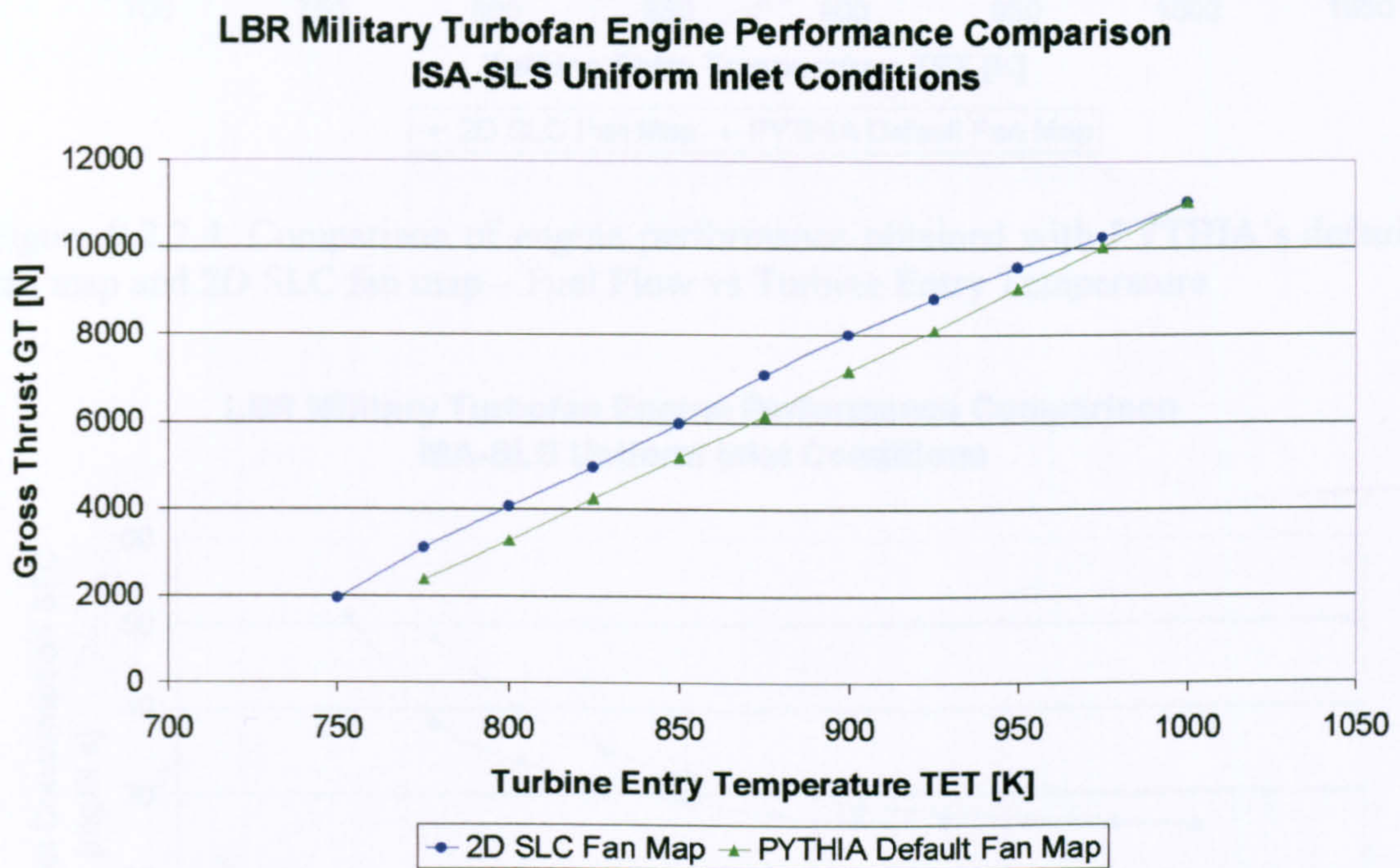


Figure 9.2.2.3: Comparison of engine performance obtained with PYTHIA’s default fan map and 2D SLC fan map – Gross Thrust vs Turbine Entry Temperature



**LBR Military Turbofan Engine Performance Comparison  
ISA-SLS Uniform Inlet Conditions**

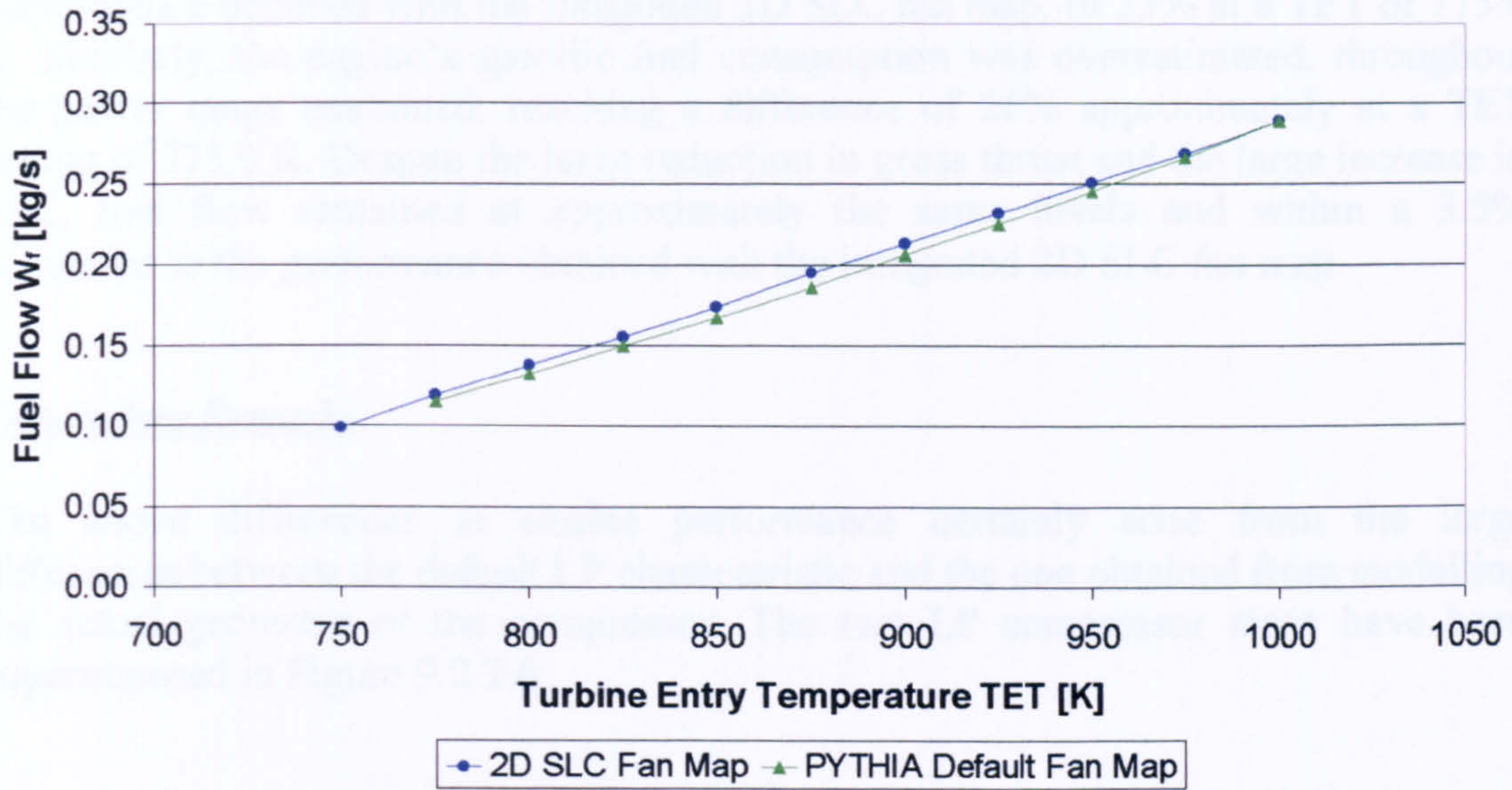


Figure 9.2.2.4: Comparison of engine performance obtained with PYTHIA’s default fan map and 2D SLC fan map – Fuel Flow vs Turbine Entry Temperature

**LBR Military Turbofan Engine Performance Comparison  
ISA-SLS Uniform Inlet Conditions**

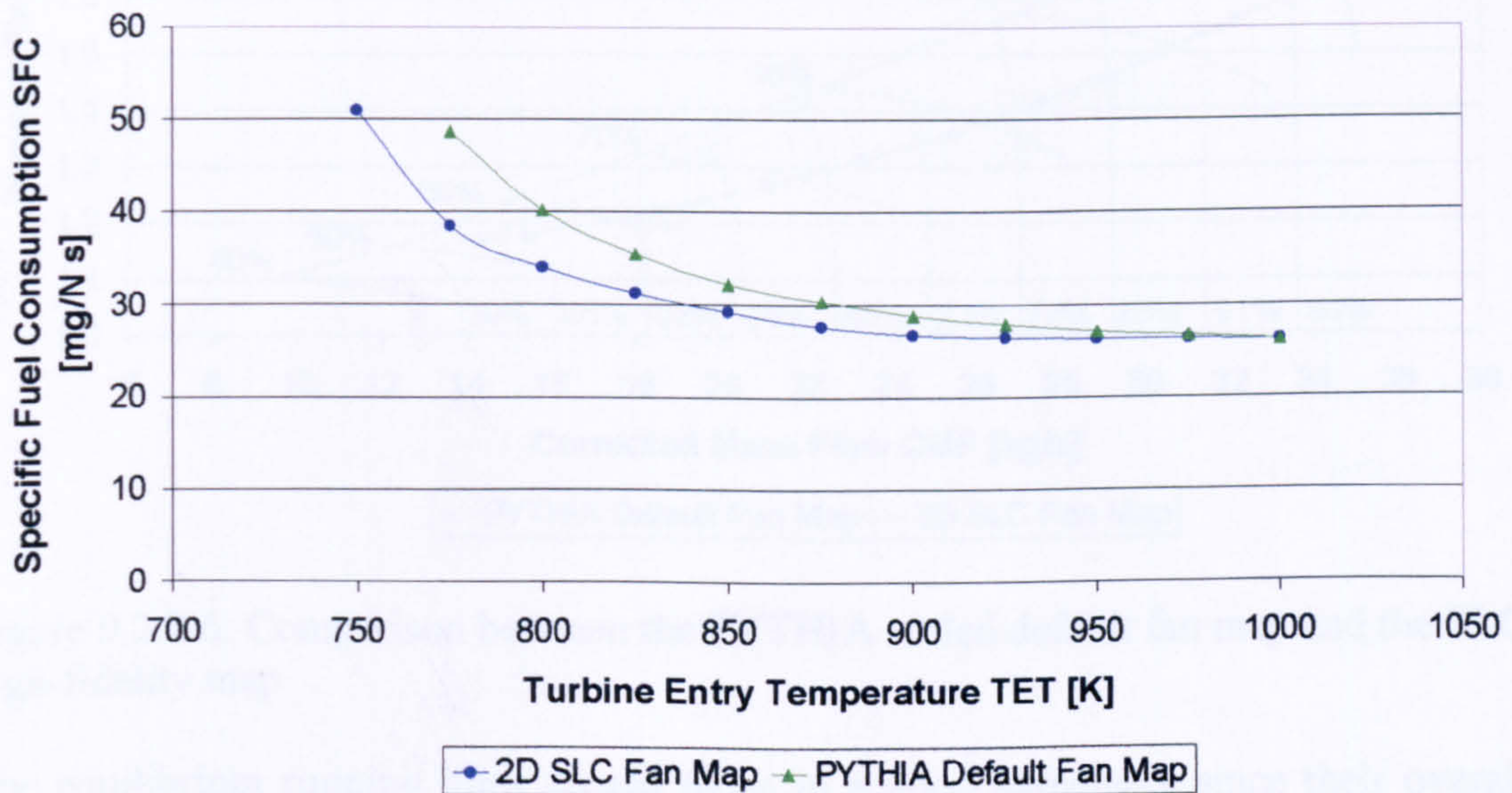


Figure 9.2.2.5: Comparison of engine performance obtained with PYTHIA’s default fan map and 2D SLC fan map – Specific Fuel Consumption vs Turbine Entry Temperature

As expected, although no difference in performance was observed at design point conditions, due to the scaling of the default map in order to match the design point performance of the LP compressor, large changes in engine performance were



observed at conditions away from the design point. More analytically, the use of PYTHIA's default map resulted in the engine's gross thrust being underestimated at almost all power settings, reaching a maximum deviation with respect to the performance obtained with the integrated 2D SLC fan map, of 23% at a TET of 775.0 K. Similarly, the engine's specific fuel consumption was overestimated, throughout the power range examined, reaching a difference of 26% approximately at a TET setting of 775.0 K. Despite the large reduction in gross thrust and the large increase in SFC, fuel flow remained at approximately the same levels and within a 3.5% compared to the performance obtained with the integrated 2D SLC fan map.

### Concluding Remarks

The above differences in engine performance certainly arise from the large differences between the default LP characteristic and the one obtained from modelling the actual geometry of the compressor. The two LP compressor maps have been superimposed in Figure 9.2.2.6.

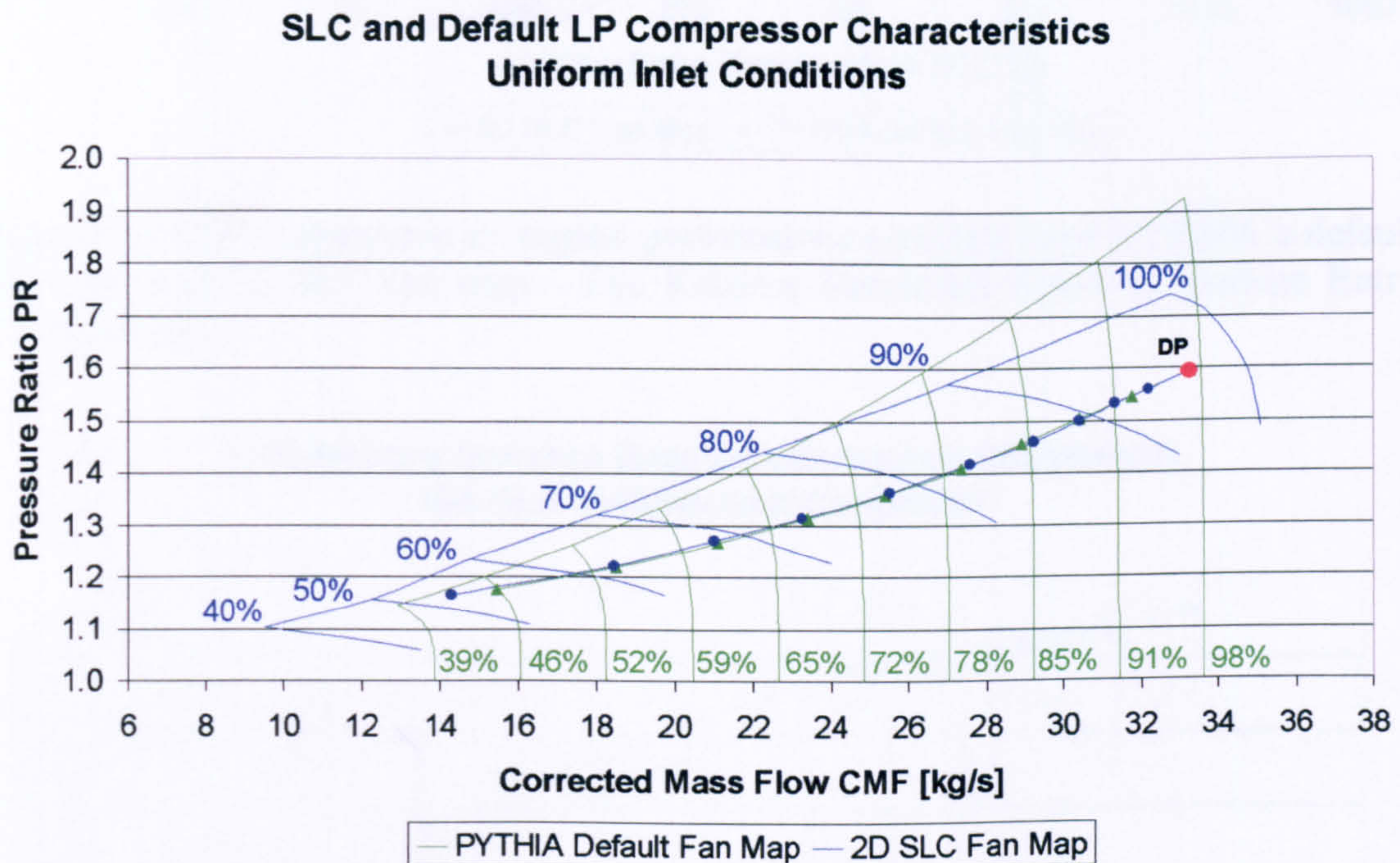


Figure 9.2.2.6: Comparison between the PYTHIA scaled default fan map and the SLC high-fidelity map

The equilibrium running lines appear to be in a good agreement since their overall position on the compressor map largely depends on turbine performance, nozzle areas and free stream Mach number, which are the same in both cases. However, operating points along these lines actually correspond to different thermodynamic balances in the engine and hence, different engine power settings, for the same relative rotational speed and corrected mass flow, as Figures 9.2.2.7 and 9.2.2.8 show.

As power setting reduces, relative rotational speed and isentropic efficiency reduce faster for the default OD compressor model than do for the high-fidelity component.



Moreover, the faster reduction in engine mass flow contributes to the faster reduction in engine's gross thrust compared to the performance obtained with the 2D SLC fan map.

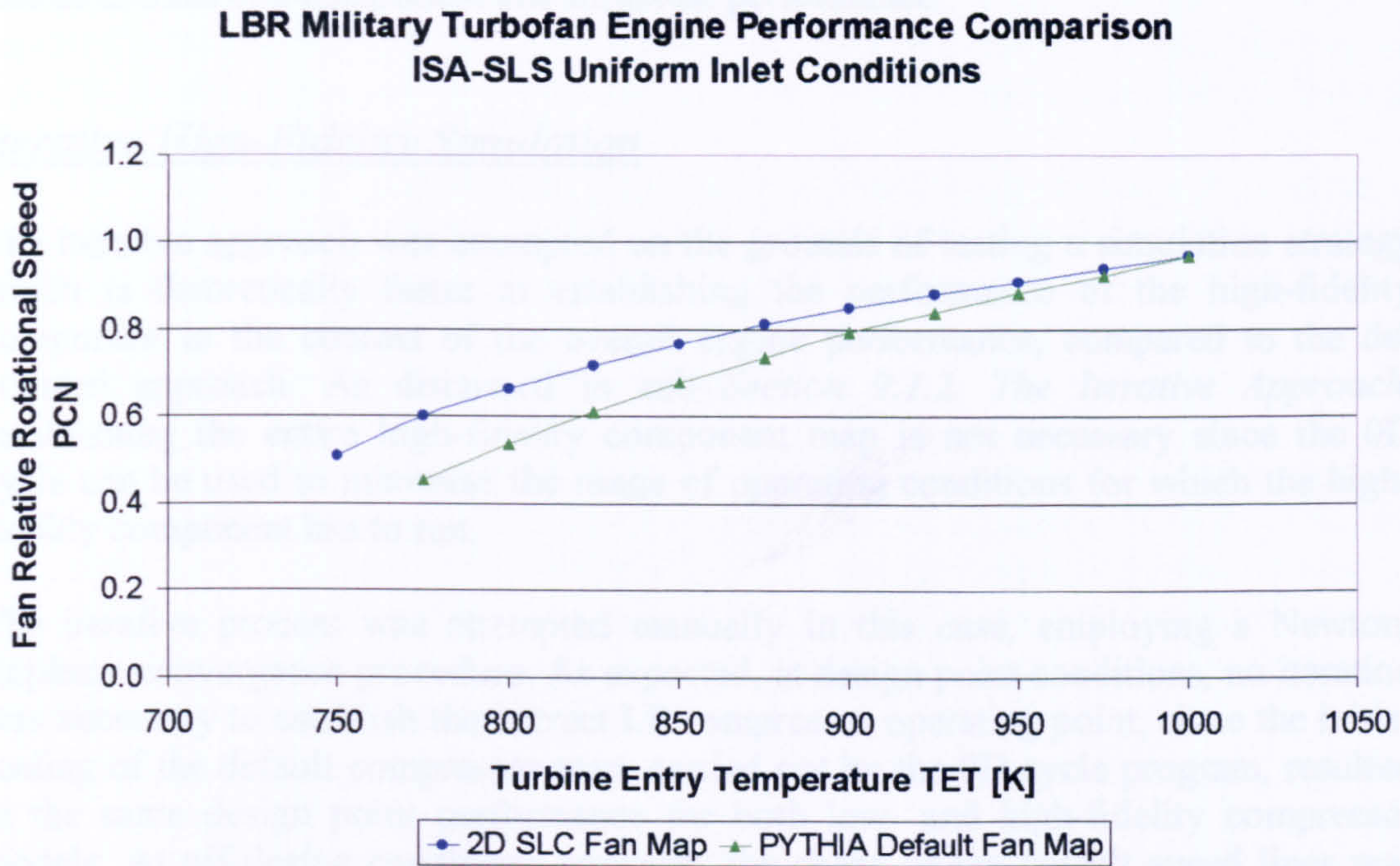


Figure 9.2.2.7: Comparison of engine performance obtained with PYTHIA's default fan map and 2D SLC fan map – Fan Relative Rotational Speed vs Turbine Entry Temperature

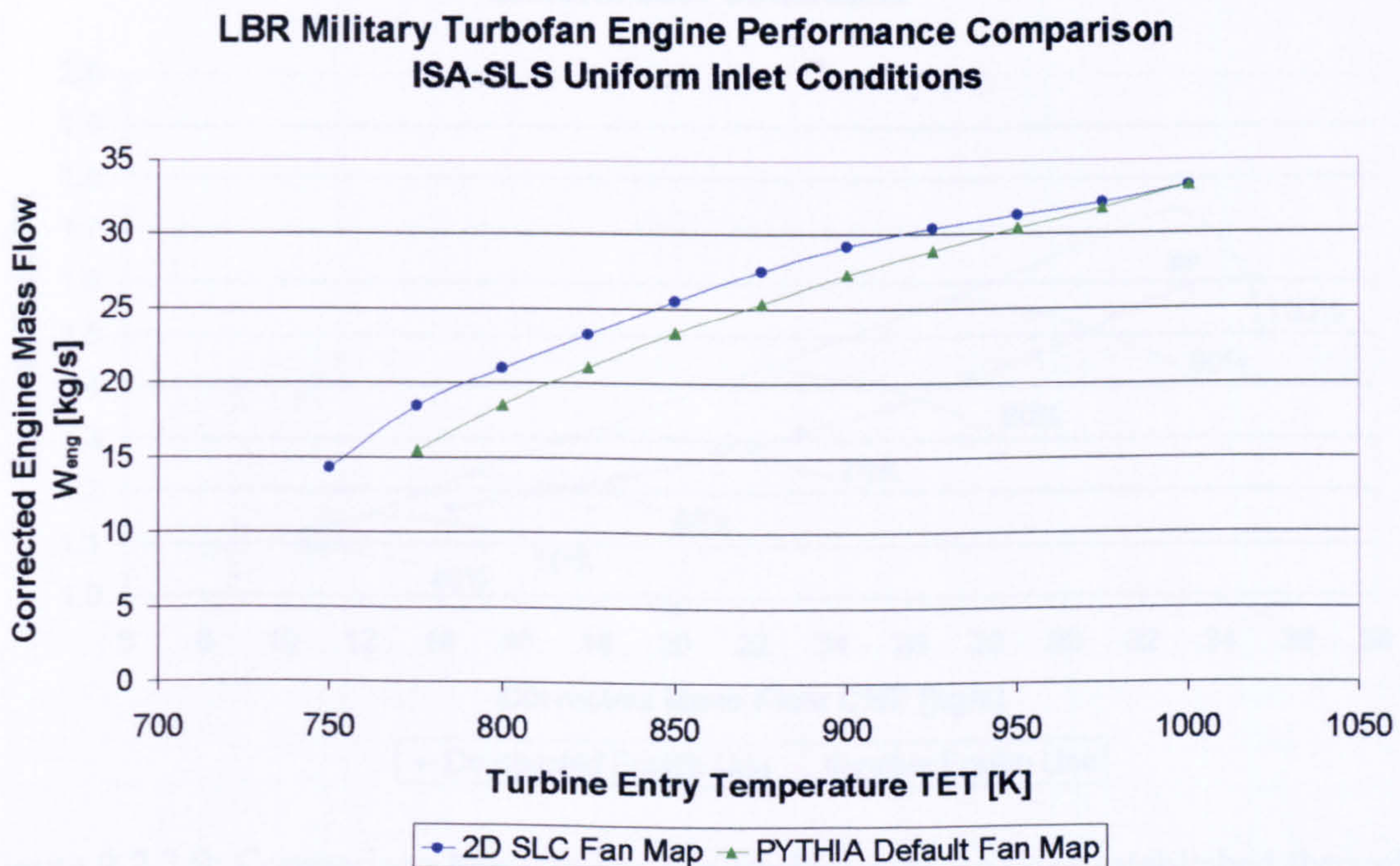


Figure 9.2.2.8: Comparison of engine performance obtained with PYTHIA's default fan map and 2D SLC fan map – Corrected Engine Mass Flow vs Turbine Entry Temperature



Finally, the de-coupled approach to high-fidelity analysis utilising a 2D SLC component model proved to be a fast and inexpensive method, in terms of computational resource, for integrating into a 0D cycle analysis the full geometric characteristics of a component and its actual performance.

### Iterative High-Fidelity Simulation

The iterative approach was attempted on the grounds of testing a simulation strategy which is theoretically faster at establishing the performance of the high-fidelity component in the context of the overall engine performance, compared to the de-coupled approach. As discussed in sub *Section 9.1.2. The Iterative Approach*, establishing the entire high-fidelity component map is not necessary since the 0D cycle can be used to minimise the range of operating conditions for which the high-fidelity component has to run.

The iterative process was attempted manually in this case, employing a Newton-Raphson convergence procedure. As expected, at design point conditions, no iteration was necessary to establish the correct LP compressor operating point, since the initial scaling of the default compressor map, carried out by the 0D cycle program, resulted in the same design point performance for both low- and high-fidelity compressor models. At off-design conditions however, the shape of the default speed lines was very different from the actual characteristics, despite the initial scaling carried out by the 0D cycle program, as shown in Figures 9.2.2.6 to 9.2.2.8.

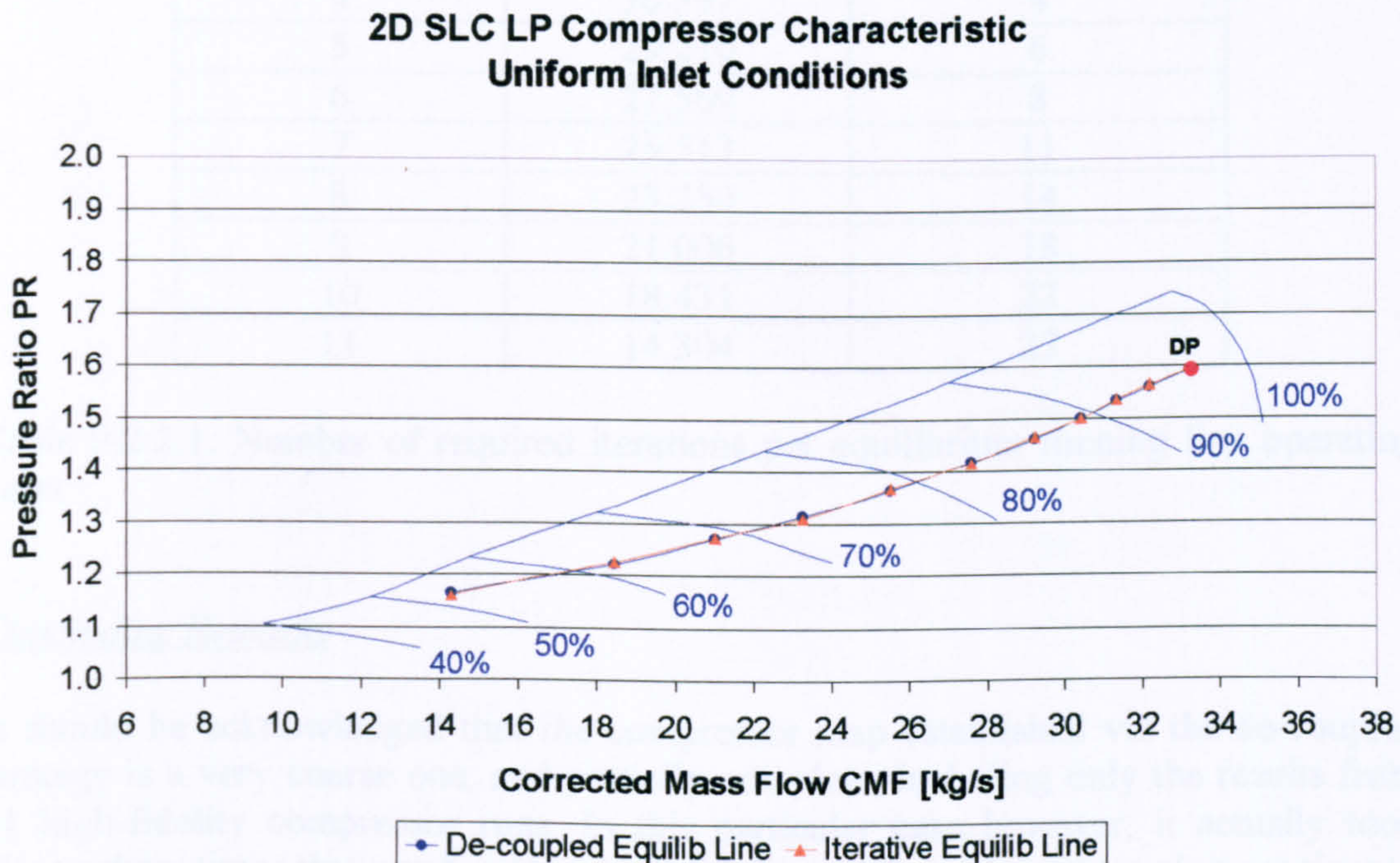


Figure 9.2.2.9: Comparison between the equilibrium running lines established through the de-coupled and iterative high-fidelity simulation strategies

Operating points along the equilibrium running line, established via the 0D cycle simulations, actually corresponded to increasingly different engine power settings, as



relative rotational speed and corrected mass flow reduced. This resulted in converged operating points being established relatively quickly close to design point conditions, and points further down the equilibrium running line requiring more and more iterations to converge. In every iteration, the default map was manually scaled in terms of pressure ratio, corrected mass flow and isentropic efficiency, according to the calculated differences with respect to the previously converged high-fidelity solutions.

The LP compressor and engine performances established through the iterative approach agreed very well with the ones calculated by the de-coupled analysis, (Figure 9.2.2.9) within less than 0.25% at all power settings examined. Small differences arose mainly due to numerical rounding errors and the inherent differences between the two simulation strategies.

It should be noted, however, that carrying out the iterations manually was an extremely tedious process, as the number of iterations required at low PCN values increased almost exponentially. Table 9.2.2.1 shows the increase in the number of required iterations per equilibrium running line operating point. The iteration numbers shown below do not include the automatic cycle convergence loops to establish a thermodynamic balance throughout the engine.

Point on Running Line	Corrected Mass Flow [kg/s]	Number of Iterations (approx.)
1	33.248	1
2	32.176	2
3	31.311	3
4	30.397	4
5	29.210	6
6	27.569	8
7	25.513	11
8	23.250	14
9	21.006	18
10	18.431	22
11	14.304	27

Table 9.2.2.1: Number of required iterations per equilibrium running line operating point

### Concluding Remarks

It should be acknowledged that the compressor map established via the de-coupled strategy is a very coarse one, and partially complete, including only the results from 41 high-fidelity compressor runs. In this particular case however, it actually took almost three times that number (116 high-fidelity runs) and hence, much more time to establish the equilibrium running line and engine performance via the iterative process. It is the author's view that the iterative simulation approach, although it offers a faster solution close to design point conditions, it can not have a real benefit off-design unless it is programmed in a PC and the iterative scaling of the default map is carried out completely automatically. This was not attempted by the current study. In those cases where the default and actual characteristics are too far apart, it is



perhaps more time effective to actually establish the high-fidelity component map through the de-coupled simulation strategy rather than carrying out the iterative process.

### Fully Integrated High-Fidelity Simulation

For the purposes of this investigation, the *2D SLC Compressor Software* was compiled as a dynamic link library file and was subsequently integrated into PYTHIA by using the generated COMPRE2D.dll and COMPRE2D.lib files. A new brick was also programmed in PYTHIA under the name COMP2D, in order to provide the explicit interface required between the low-fidelity cycle and the high-fidelity component and manipulate data passed from one software to the other. Moreover, the codeword COMP2D replaced the default 0D COMPRE in the engine input data file for the first compressor only.

During the design point calculation, the 2D SLC compressor model was called at 'run-time' in order to establish the component performance at the selected operating conditions and power setting. Averaged compressor performance characteristics were then returned back to the low-fidelity cycle analysis for the determination of the overall engine performance. Upstream compressor inlet boundary conditions were determined from the 1D values supplied by the 0D analysis for uniform inlet conditions. During off-design calculations, the 2D SLC compressor model was called at 'run-time' several times, in an iterative manner, until continuity of mass flow and power balance was satisfied throughout the engine.

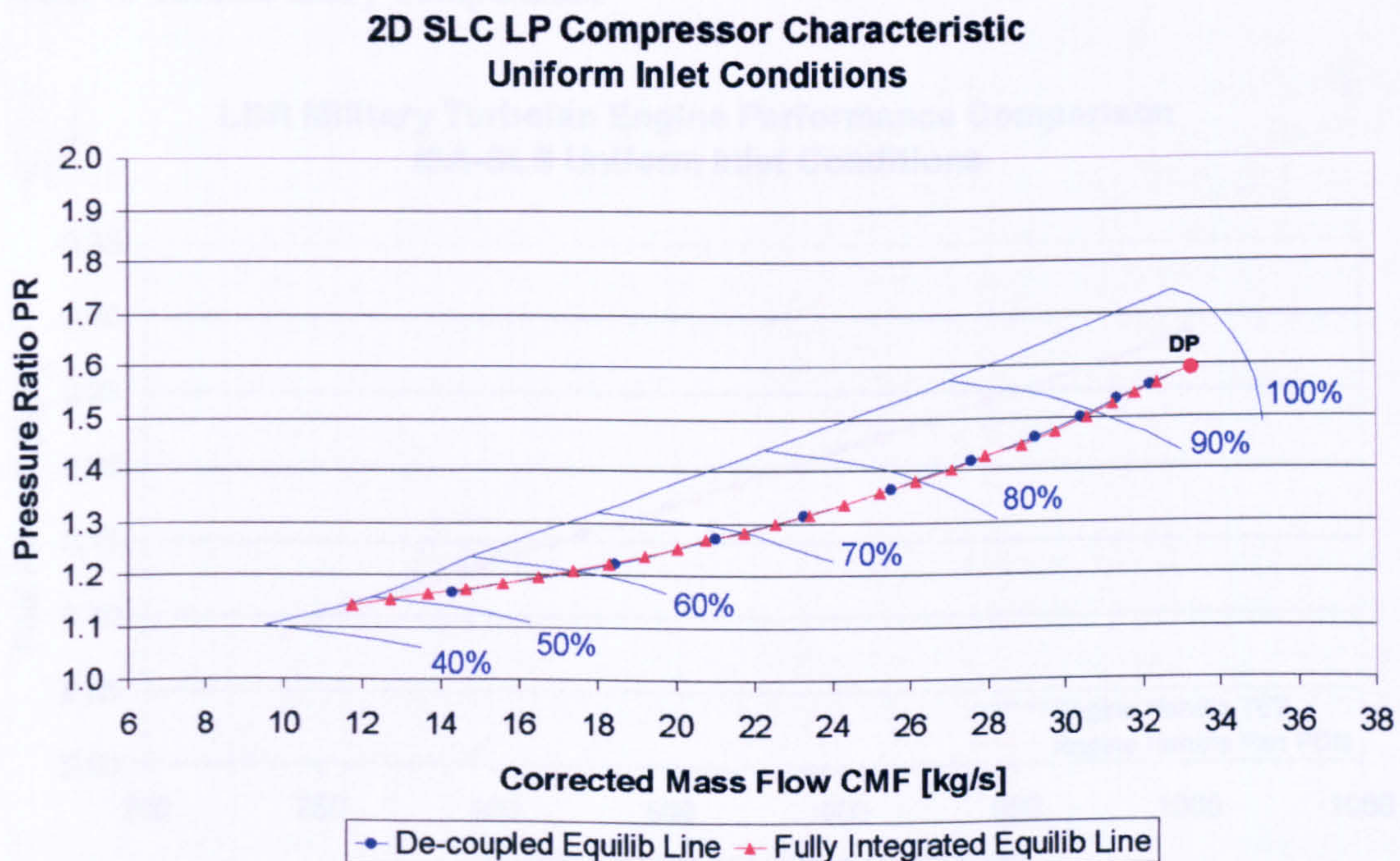


Figure 9.2.2.10: Comparison between the equilibrium running lines established through the de-coupled and fully integrated high-fidelity simulation strategies



The full integration of the 2D SLC compressor model into the 0D cycle analysis gave the same results as the two other simulation strategies described above. In this case and for comparative purposes only, the engine performance simulation was carried out using the fan relative rotational speed (PCN) as the engine handle (Figures 9.2.2.10 to 9.2.2.13).

**LBR Military Turbofan Engine Performance Comparison  
ISA-SLS Uniform Inlet Conditions**

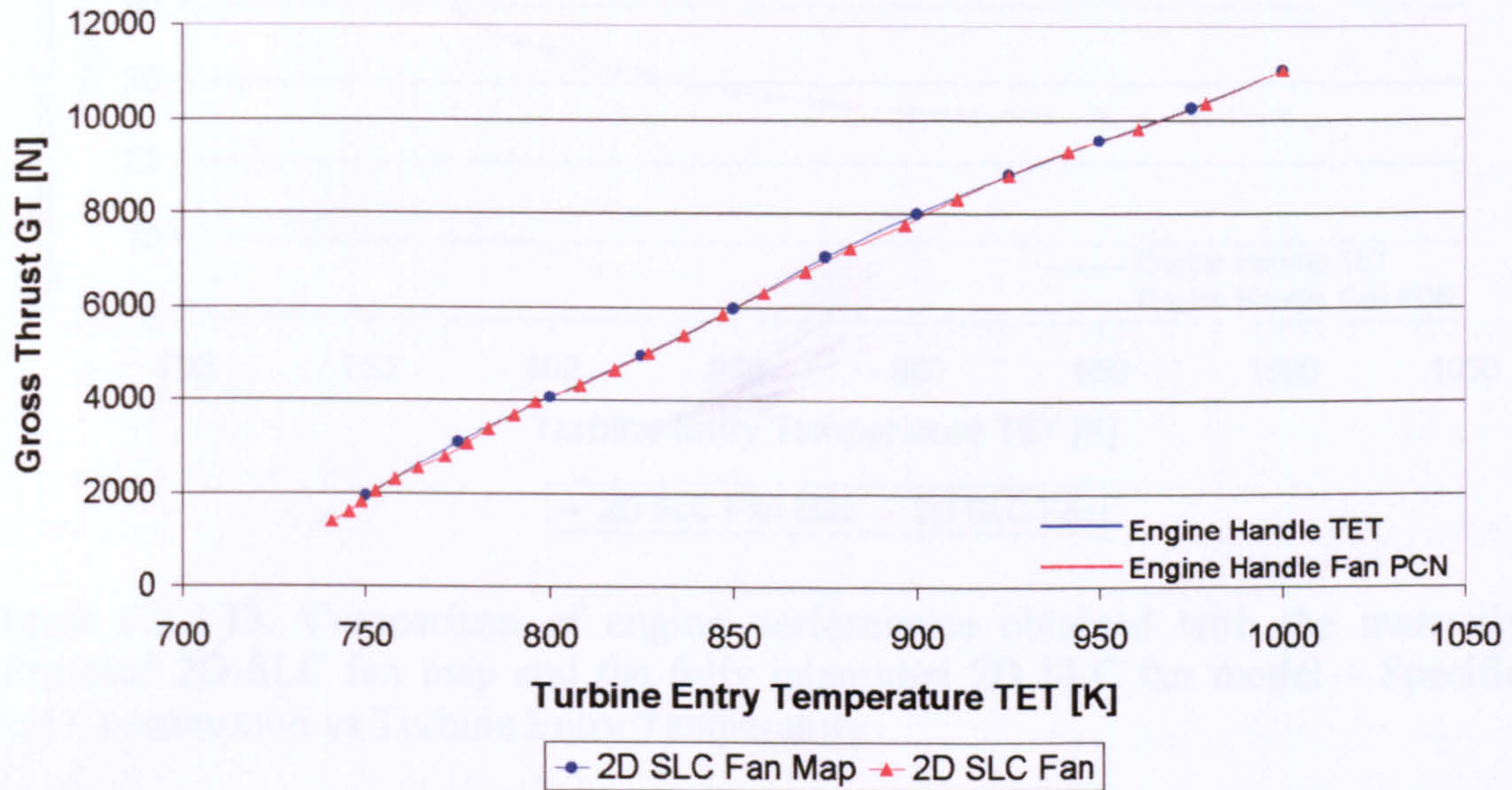


Figure 9.2.2.11: Comparison of engine performance obtained with the manually integrated 2D SLC fan map and the fully integrated 2D SLC fan model – Gross Thrust vs Turbine Entry Temperature

**LBR Military Turbofan Engine Performance Comparison  
ISA-SLS Uniform Inlet Conditions**

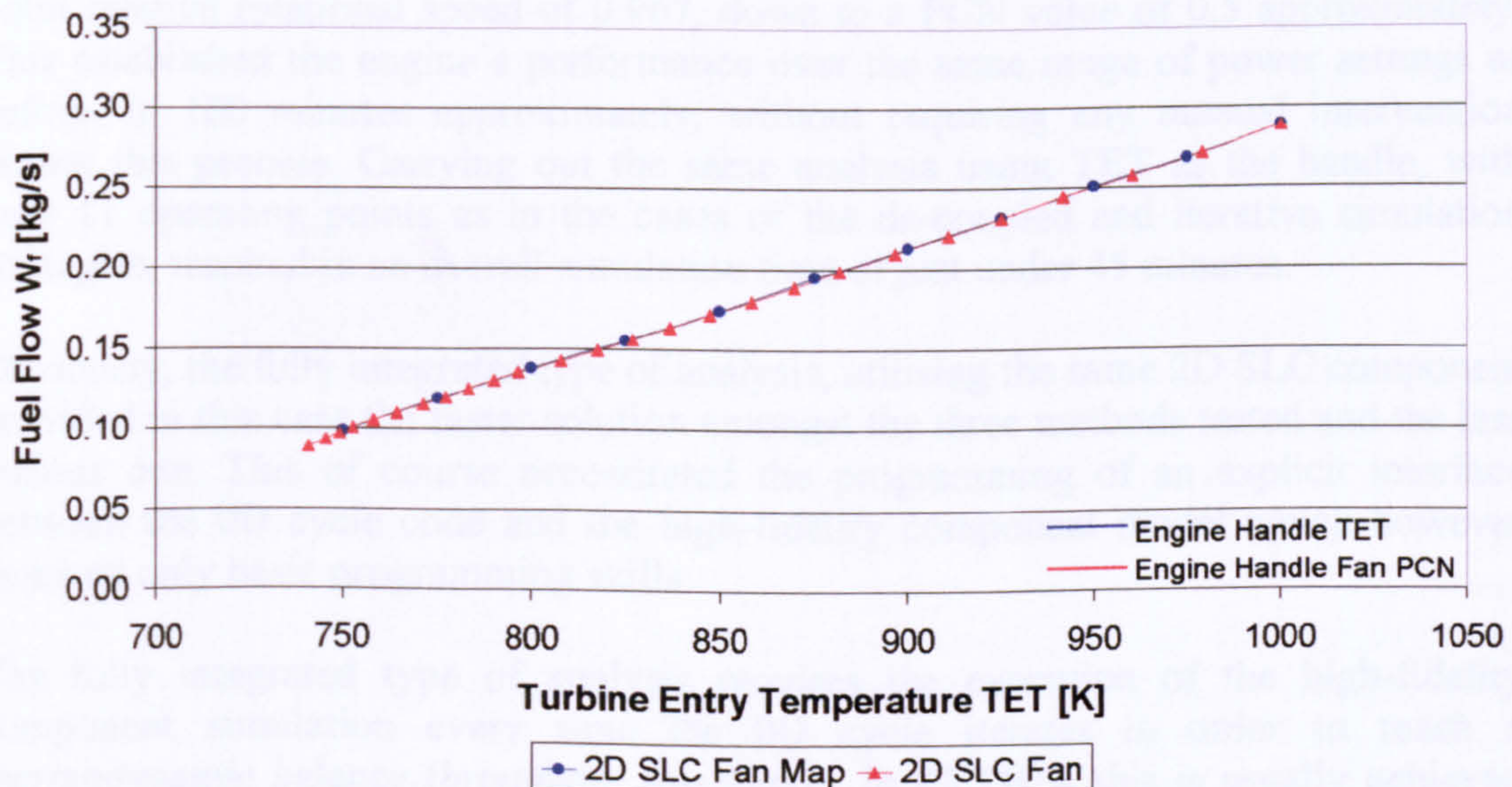


Figure 9.2.2.12: Comparison of engine performance obtained with the manually integrated 2D SLC fan map and the fully integrated 2D SLC fan model – Fuel Flow vs Turbine Entry Temperature



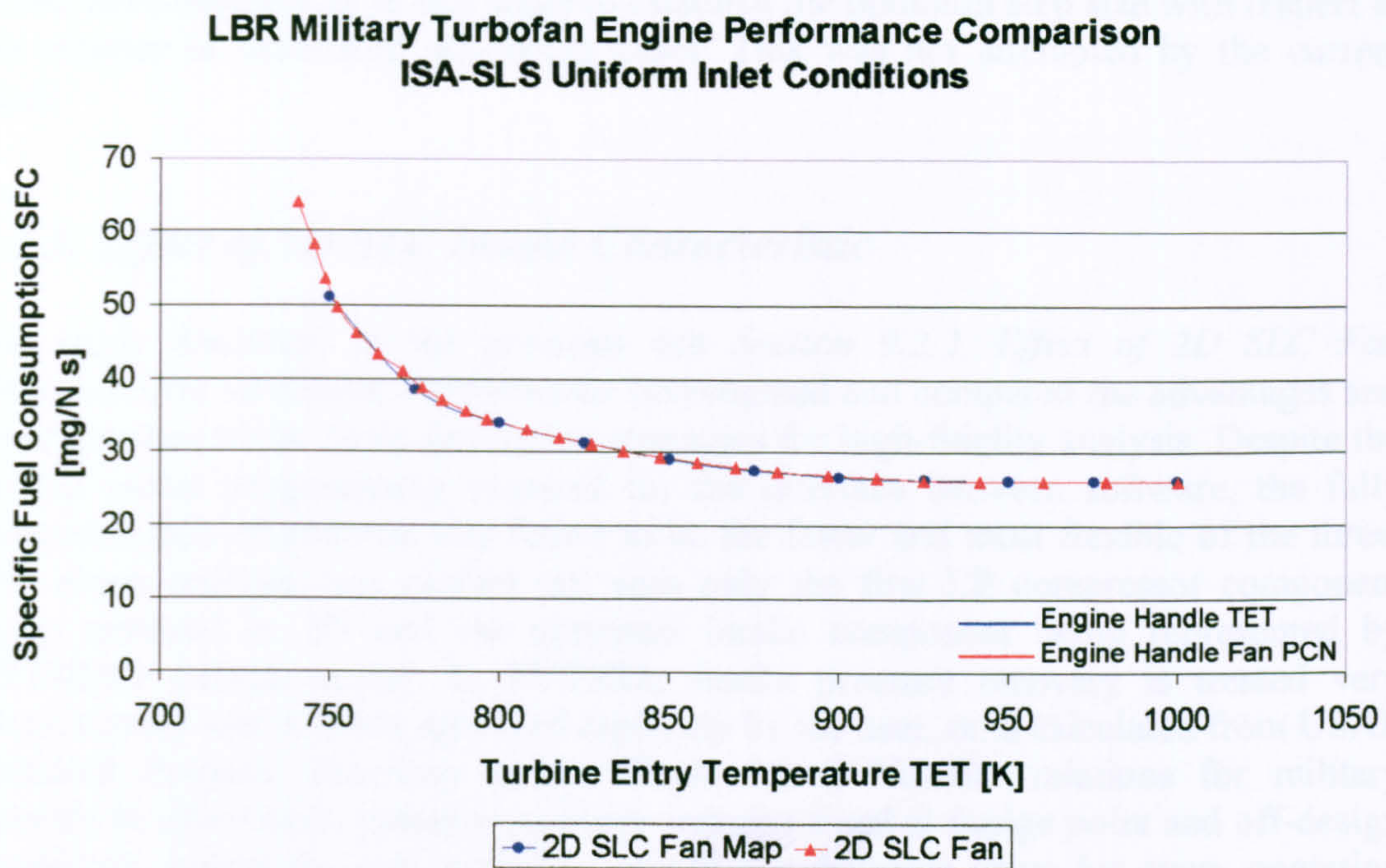


Figure 9.2.2.13: Comparison of engine performance obtained with the manually integrated 2D SLC fan map and the fully integrated 2D SLC fan model – Specific Fuel Consumption vs Turbine Entry Temperature

### Concluding Remarks

Small differences in the results presented above arose mainly due to numerical rounding errors and the inherent differences between the two convergence procedures compared in this case. The above analysis was carried out using PCN as the engine's handle for 26 operating points along the equilibrium running line, from the design point relative rotational speed of 0.967, down to a PCN value of 0.5 approximately. This established the engine's performance over the same range of power settings as before, in 100 minutes approximately, without requiring any manual intervention during this process. Carrying out the same analysis using TET as the handle, with only 11 operating points as in the cases of the de-coupled and iterative simulation strategies, resulted in an overall simulation time of just under 45 minutes.

Obviously, the fully integrated type of analysis, utilising the same 2D SLC component provided in this case the faster solution amongst the three methods tested and the less tedious one. This of course necessitated the programming of an explicit interface between the 0D cycle code and the high-fidelity component model which however required only basic programming skills.

The fully integrated type of analysis requires the execution of the high-fidelity component simulation every time the 0D cycle iterates in order to reach a thermodynamic balance throughout the engine. In PYTHIA this is usually achieved within 2 to 4 engine cycle loops, provided a small step size is selected, at the expense of more off-design cases to calculate and converge on. Obviously there is a trade-off between step size and number of calculated operating points and a sensitivity analysis



would have been useful at this stage to establish the optimum step size with respect to the number of calculated off-design cases. This was not attempted by the current study.

### 9.2.3. Effect of 2D SLC Intake Characteristic

The study discussed in the previous sub *Section 9.2.2. Effect of 2D SLC Fan Characteristic on Engine Performance* investigated and compared the advantages and disadvantages of the three simulation strategies for high-fidelity analysis. Despite the limited initial programming required for the interface between software, the fully integrated type of analysis was found to be the faster and most flexible of the three. The above analysis was carried out with only the first LP compressor component being resolved in 2D and the upstream intake component being represented by PYTHIA's default model. In PYTHIA, intake pressure recovery is treated very simplistically and is either specified explicitly by the user, or is calculated from USAF Standard Pressure Recovery versus Flight Mach Number relations for military aircraft. In either case, pressure recovery remains fixed at design point and off-design conditions, unless the user explicitly specifies a different value for every operating point or the flight Mach number becomes larger than unity (only in the case of military aircraft where the USAF pressure recovery model is employed).

By modelling the intake in 2D it was possible to investigate the effects of various intake lip geometries and flow conditions on intake performance, at several Angles of Attack (AoAs) and flight Mach numbers. The detailed performance of the 2D SLC intake model described previously has been included in this thesis as *Appendix I - 2D SLC Intake Performance*.

More analytically, three lip geometries were examined in total, namely a rounded-circular, a rounded-elliptical and a sharp lip geometry, with attached and separated diffuser entry flows, at AoAs between 0 and 25 degrees, and flight Mach numbers between 0.0 and 0.2. It should be stated that as the flight Mach number increased, this limited the range of mass flows that the 2D SLC intake model could handle, due to the pre-entry stream tube radius becoming less or equal to the intake's inlet radius at low mass flows, resulting in a sudden change in streamline curvature at the intake inlet. This is a software limitation that should be addressed in future versions.

Generally speaking, for all lip geometries and at any given Mach number and AoA setting, as inlet mass flow increased the intake pressure recovery reduced, due to the increase in intake throat Mach number and reduction in  $A_1/A_\infty$ . This seemed to be in a good agreement with the 1D calculations in ESDU Item No. 80037 (1980), as discussed before.

At high corrected mass flows, and low flight Mach numbers and AoA settings, the best performance was achieved with the rounded-circular lip configuration producing a pressure recovery in the order of 0.98 to 0.99. The rounded-elliptical lip geometry produced similar performance at the same conditions with pressure recovery values in the order of 0.98 to 0.985. The worst performance was achieved with sharp lips with the pressure recovery ranging between 0.87 and 0.89. At higher Mach numbers and same AoA the performance of the rounded-elliptical and rounded circular lips did not



change much, however sharp lip performance increased to pressure recovery values in the range of 0.93 to 0.95.

At high corrected mass flows, low flight Mach numbers and high AoA settings, the performance of the rounded-circular lip configuration dropped to pressure recovery values in the order of 0.91 to 0.92. The rounded-elliptical lip geometry produced a much better performance at high AoAs, with pressure recovery values in the order of 0.97 to 0.975. The performance of the sharp lips remained more or less the same as before, with the pressure recovery ranging between 0.87 and 0.89. At higher Mach numbers and same AoA, the performance of the rounded-circular lip increased slightly to higher pressure recovery values between 0.94 to 0.95 and the performance of the rounded-elliptical lip remained the same as before for these conditions. Sharp lip performance dropped to pressure recovery values in the range of 0.91 to 0.93.

The above description applies for the case of attached diffuser entry flow. With the flow at the diffuser inlet being separated, a slightly worse intake performance was observed for all lip geometries examined and especially at high angles of attack. This small reduction in intake pressure recovery was of the order of 0.05% only.

For the purposes of this investigation, the *2D SLC Intake Software* was compiled as a dynamic link library file and was subsequently integrated into PYTHIA by using the generated *INTAKE2D.dll* and *INTAKE2D.lib* files. A new brick was also programmed in PYTHIA under the name *INTA2D*, in order to provide the explicit interface required between the low-fidelity cycle and the high-fidelity component and manipulate data passed from one software to the other. Moreover, the codeword *INTA2D* replaced the default *0D INTAKE* in the engine input data file.

During the design point calculation, the 2D SLC intake model was called at 'run-time' in order to establish the component performance at the selected operating conditions and power setting. Intake boundary layer blockage factors, together with 2D profiles of the intake's outlet total pressure, temperature, static entropy and absolute angle were then passed as input parameters to the downstream 2D SLC compressor model via an automatically generated input file. Intake inlet boundary conditions were determined from the 1D values supplied by the 0D analysis for uniform inlet conditions. During off-design calculations, both 2D SLC intake and compressor models were called by the 0D cycle program at 'run-time' several times, in an iterative manner, until continuity of mass flow and power balance was satisfied throughout the engine.

The performance of the LBR military turbofan engine was calculated for the three intake lip configurations described before, at a flight Mach number of 0.05, angle of attack of 20 degrees and a range of engine power settings from a TET value of 1000.0 K (DP value) down to a TET value of 750.0 K approximately. Figures 9.2.3.1 to 9.2.3.4 illustrate the engine performance obtained under those conditions. A direct comparison against a reference engine performance was not possible since PYTHIA, or any other traditional low-fidelity simulation code, does not have the capability to model intake geometries or the effect of angle of attack.

As expected from the intake characteristics established previously, the worse intake pressure recovery at the design point power setting was achieved by the sharp lip



configuration (0.8945), followed by the rounded-circular lip configuration (0.9452), with the rounded-elliptical lip geometry providing the higher intake pressure recovery (0.98), and also engine performance (Figure 9.2.3.1). Engine gross thrust was found to reduce by 15.0% with a sharp-lip inlet, compared to the performance calculated with an elliptical lip at the design power setting. Similarly, the circular lip delivered 5.6% less gross thrust than the elliptical lip. Fuel flow variation remained more or less the same throughout the power range examined, for all three lip designs. The SFC however, rose by 28.8% and 32.8% for the sharp and circular lips respectively, with respect to the SFC calculated for the elliptical lip. Although this relative difference in engine performances actually increased at lower power settings due to the reduction in engine thermal efficiency and the shape of the SFC curve, the difference in engine gross thrust reduced as pressure recovery rose for all intake geometries to values close to 1.0.

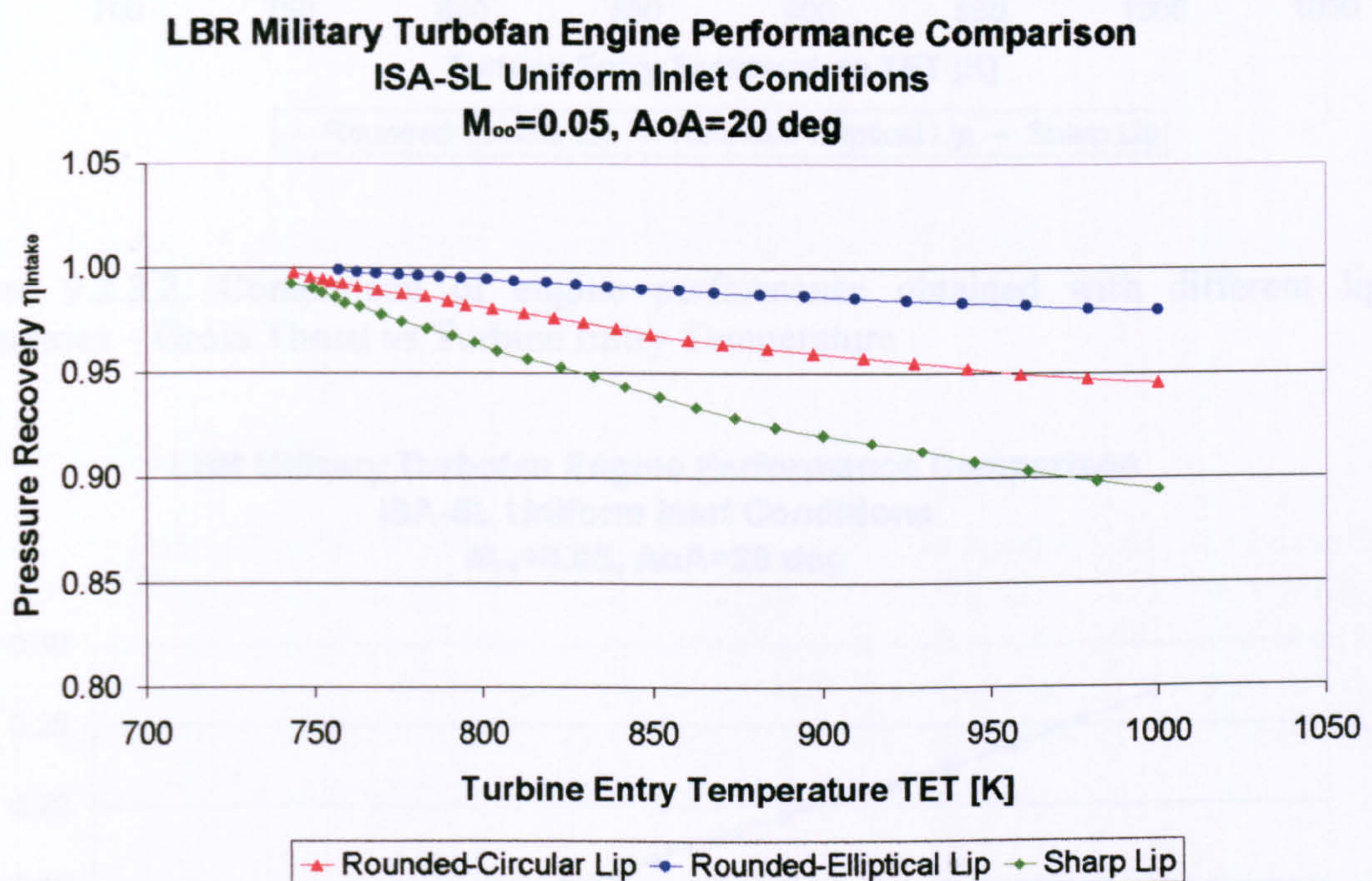


Figure 9.2.3.1: Comparison of engine performance obtained with different lip geometries – Intake Pressure Recovery vs Turbine Entry Temperature



**LBR Military Turbofan Engine Performance Comparison**  
**ISA-SL Uniform Inlet Conditions**  
 $M_{\infty}=0.05, AoA=20 \text{ deg}$

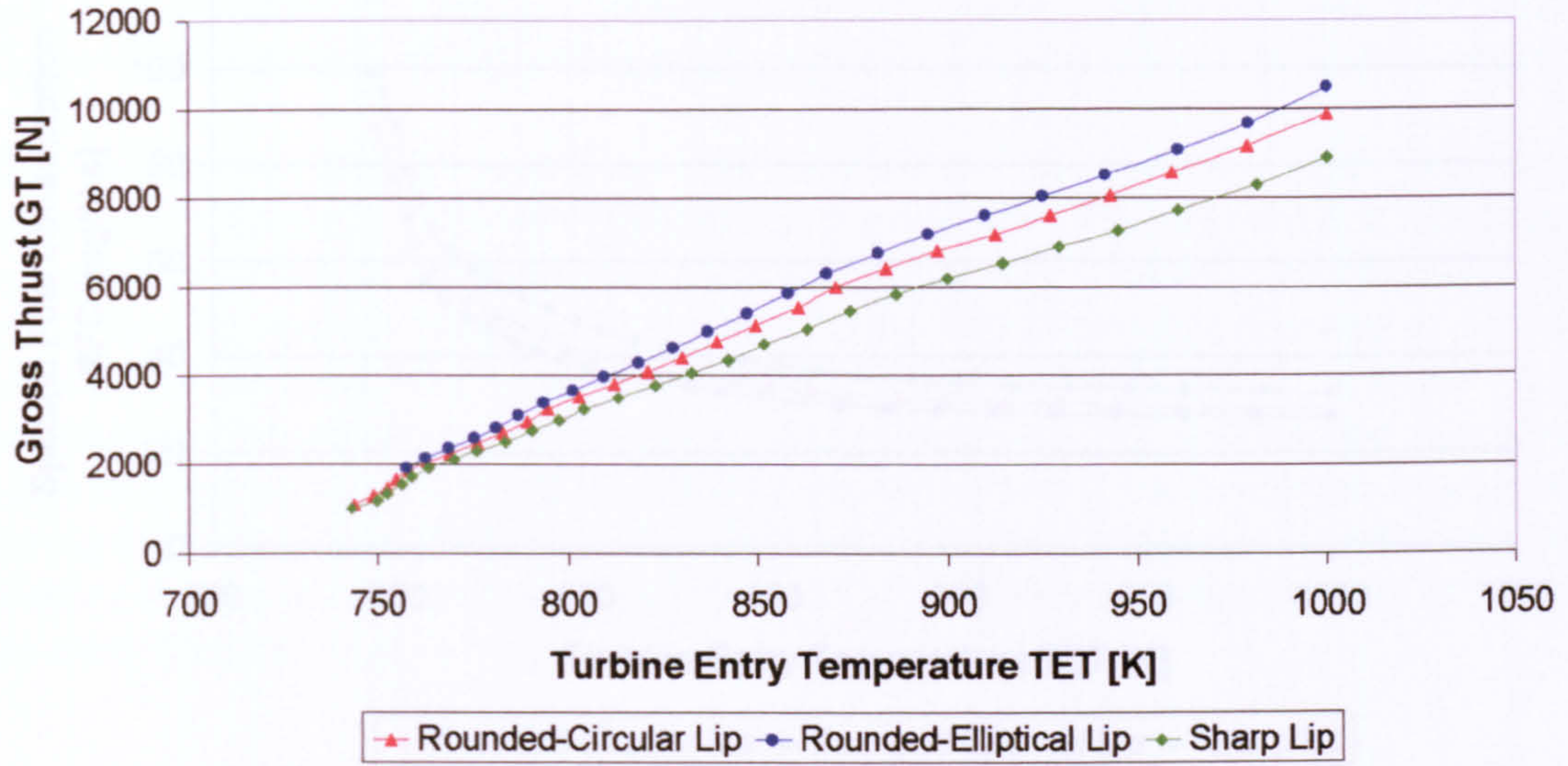


Figure 9.2.3.2: Comparison of engine performance obtained with different lip geometries – Gross Thrust vs Turbine Entry Temperature

**LBR Military Turbofan Engine Performance Comparison**  
**ISA-SL Uniform Inlet Conditions**  
 $M_{\infty}=0.05, AoA=20 \text{ deg}$

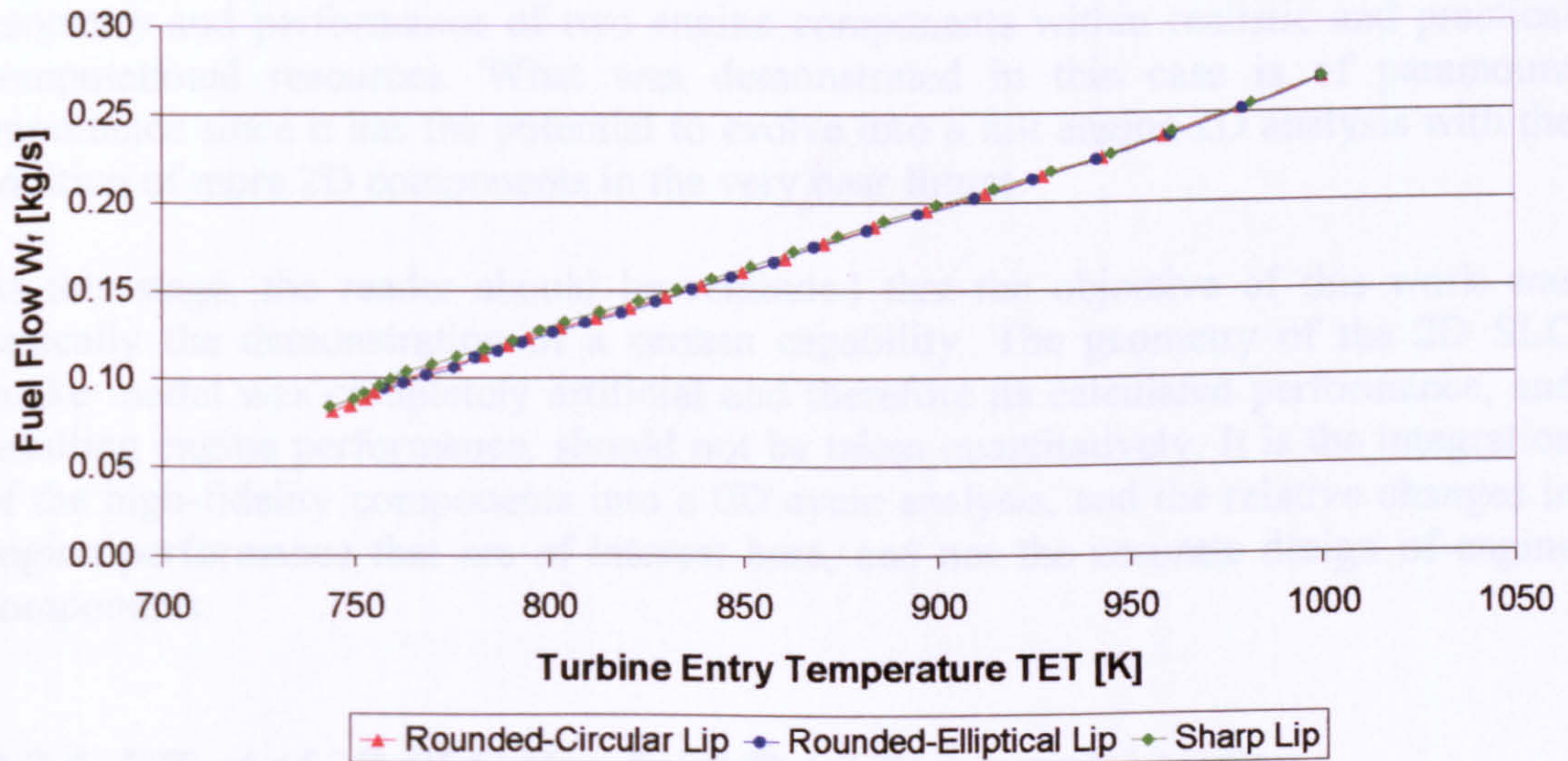


Figure 9.2.3.3: Comparison of engine performance obtained with different lip geometries – Fuel Flow vs Turbine Entry Temperature



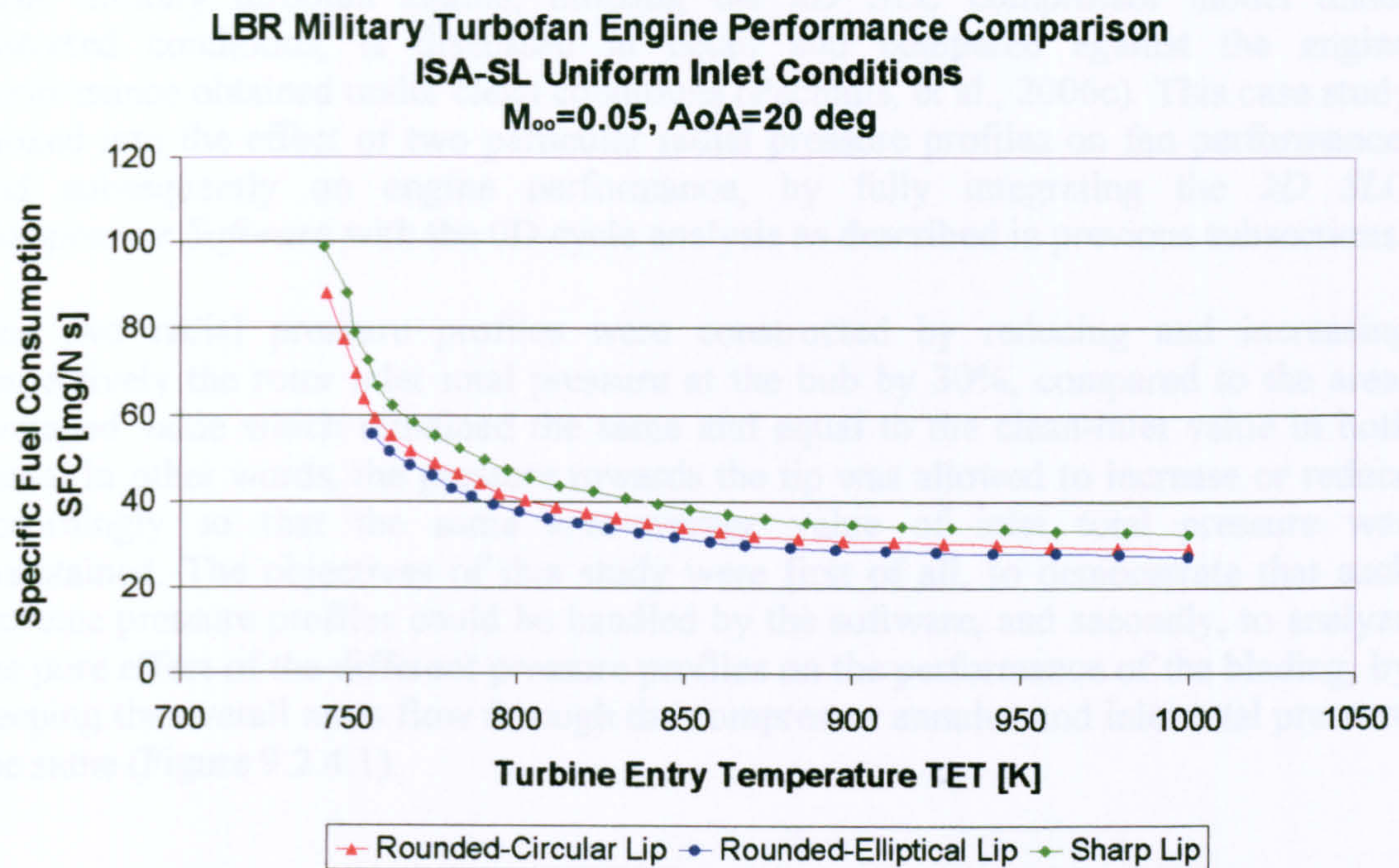


Figure 9.2.3.4: Comparison of engine performance obtained with different lip geometries – Specific Fuel Consumption vs Turbine Entry Temperature

### Concluding Remarks

In this case, the integration of two high-fidelity SLC components into a 0D cycle analysis facilitated engine performance calculations taking into account the full geometry and performance of two engine components within realistic and practical computational resources. What was demonstrated in this case is of paramount importance since it has the potential to evolve into a full engine 2D analysis with the addition of more 2D components in the very near future.

At this stage, the reader should be reminded that the objective of this work was basically the demonstration of a certain capability. The geometry of the 2D SLC intake model was completely artificial and therefore its calculated performance, and resulting engine performance, should not be taken quantitatively. It is the integration of the high-fidelity components into a 0D cycle analysis, and the relative changes in engine performance that are of interest here, and not the accurate design of engine components.

### **9.2.4. Effect of 2D SLC Fan Inlet Total Pressure Distortion**

The usual approach to compressor design considers uniform inlet flow characteristics. Especially in aircraft applications, the inlet flow is quite often non uniform, and this can result in large changes in compressor and engine performance. The third case study first discusses relative changes in the performance of the 2D SLC compressor model, with different types of radial pressure distortion, obtained by running the *2D Compressor SLC Software* independently. Moreover, the performance of the notional



LBR military turbofan engine, utilizing the 2D SLC compressor model under distorted conditions, is discussed in detail and compared against the engine performance obtained under clean conditions (Pachidis, et al., 2006c). This case study looked into the effect of two particular radial pressure profiles on fan performance, and subsequently on engine performance, by fully integrating the *2D SLC Compressor Software* with the 0D cycle analysis as described in previous subsections.

The two radial pressure profiles were constructed by reducing and increasing respectively the rotor inlet total pressure at the hub by 30%, compared to the area-averaged value which remained the same and equal to the clean-inlet value in both cases. In other words, the pressure towards the tip was allowed to increase or reduce accordingly so that the same area-average value of inlet total pressure was maintained. The objectives of this study were first of all, to demonstrate that such extreme pressure profiles could be handled by the software, and secondly, to analyze the pure effect of the different pressure profiles on the performance of the blading, by keeping the overall mass flow through the compressor annulus and inlet total pressure the same (Figure 9.2.4.1).

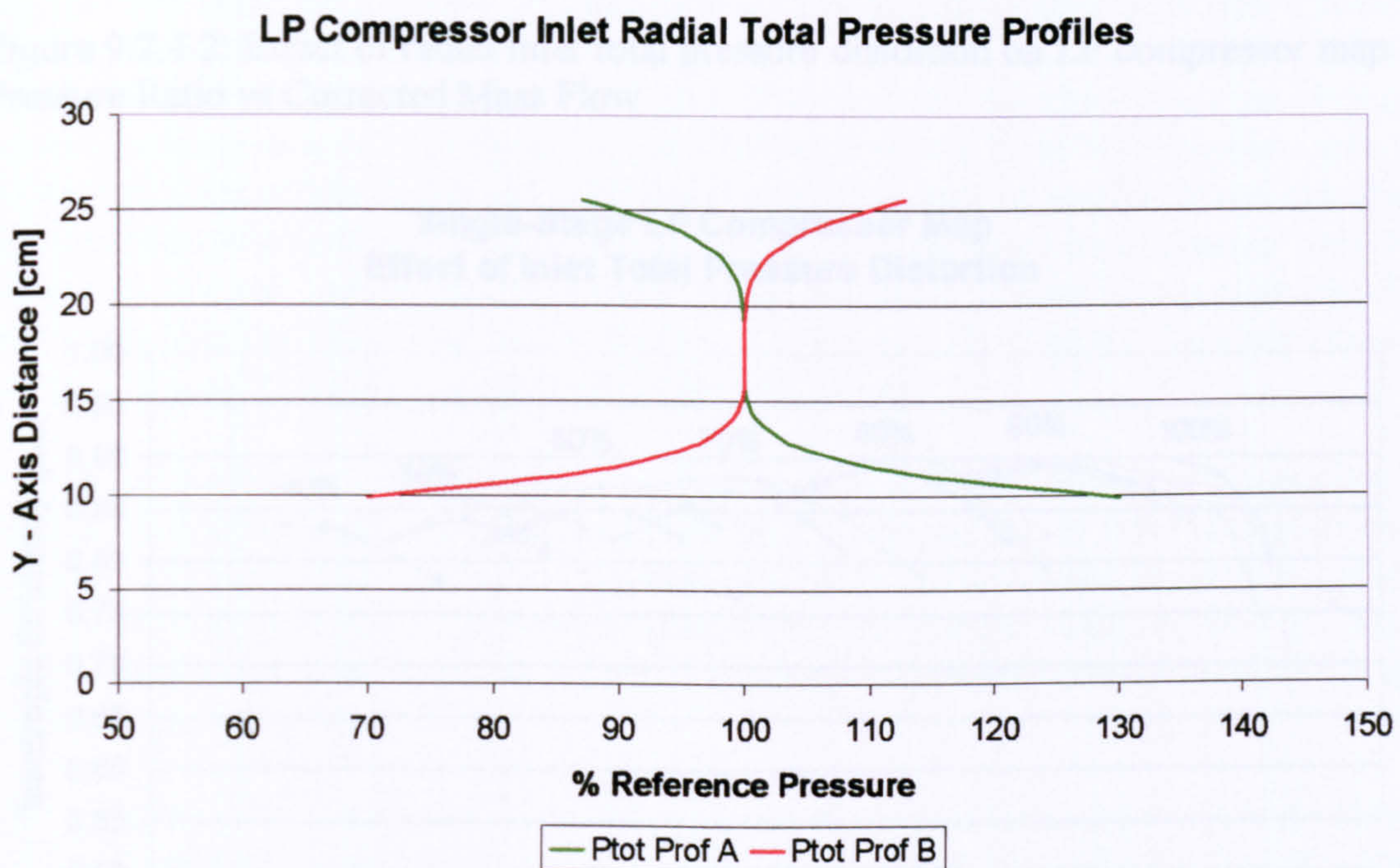


Figure 9.2.4.1: LP compressor inlet radial total pressure profiles



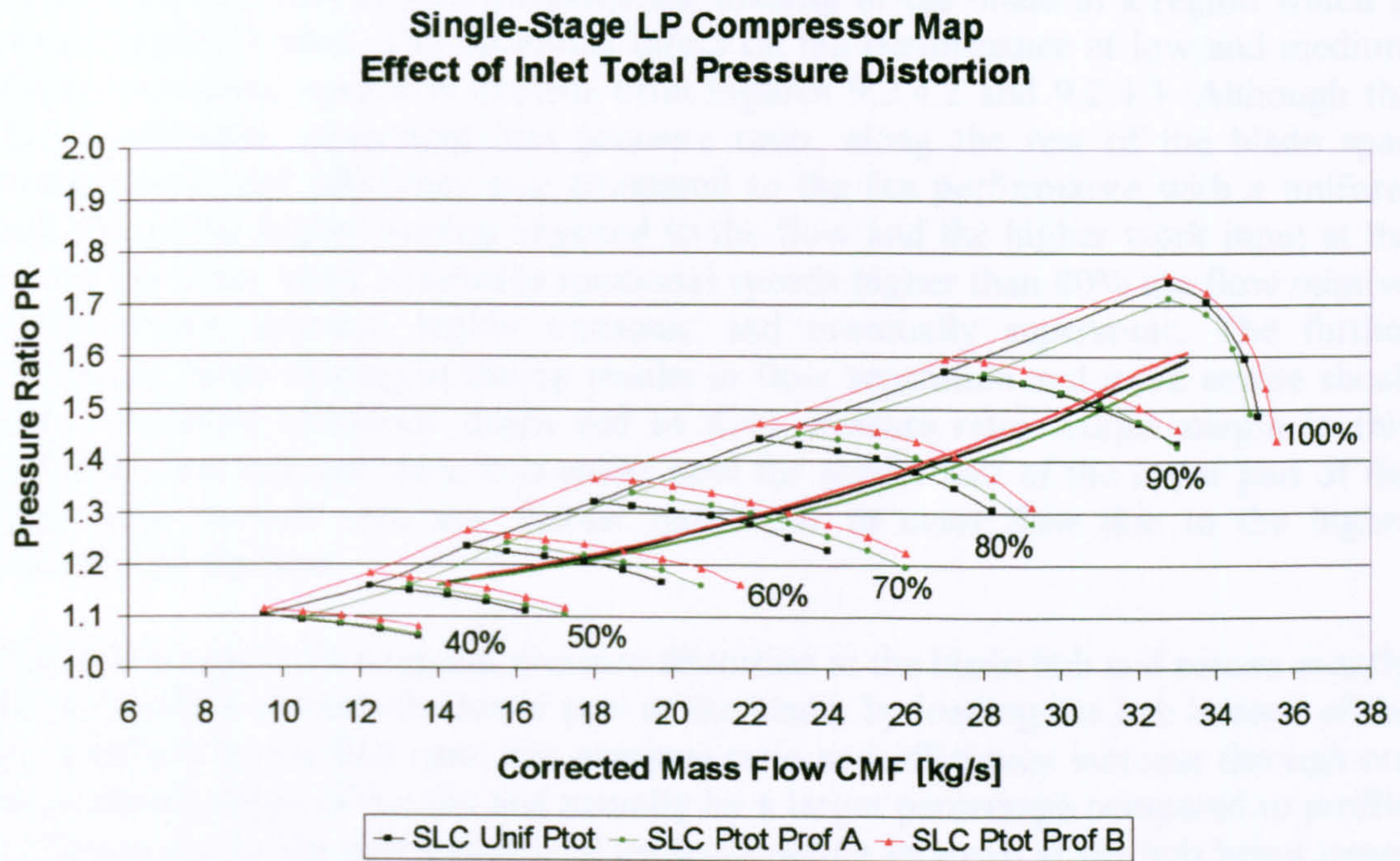


Figure 9.2.4.2: Effect of radial inlet total pressure distortion on LP compressor map – Pressure Ratio vs Corrected Mass Flow

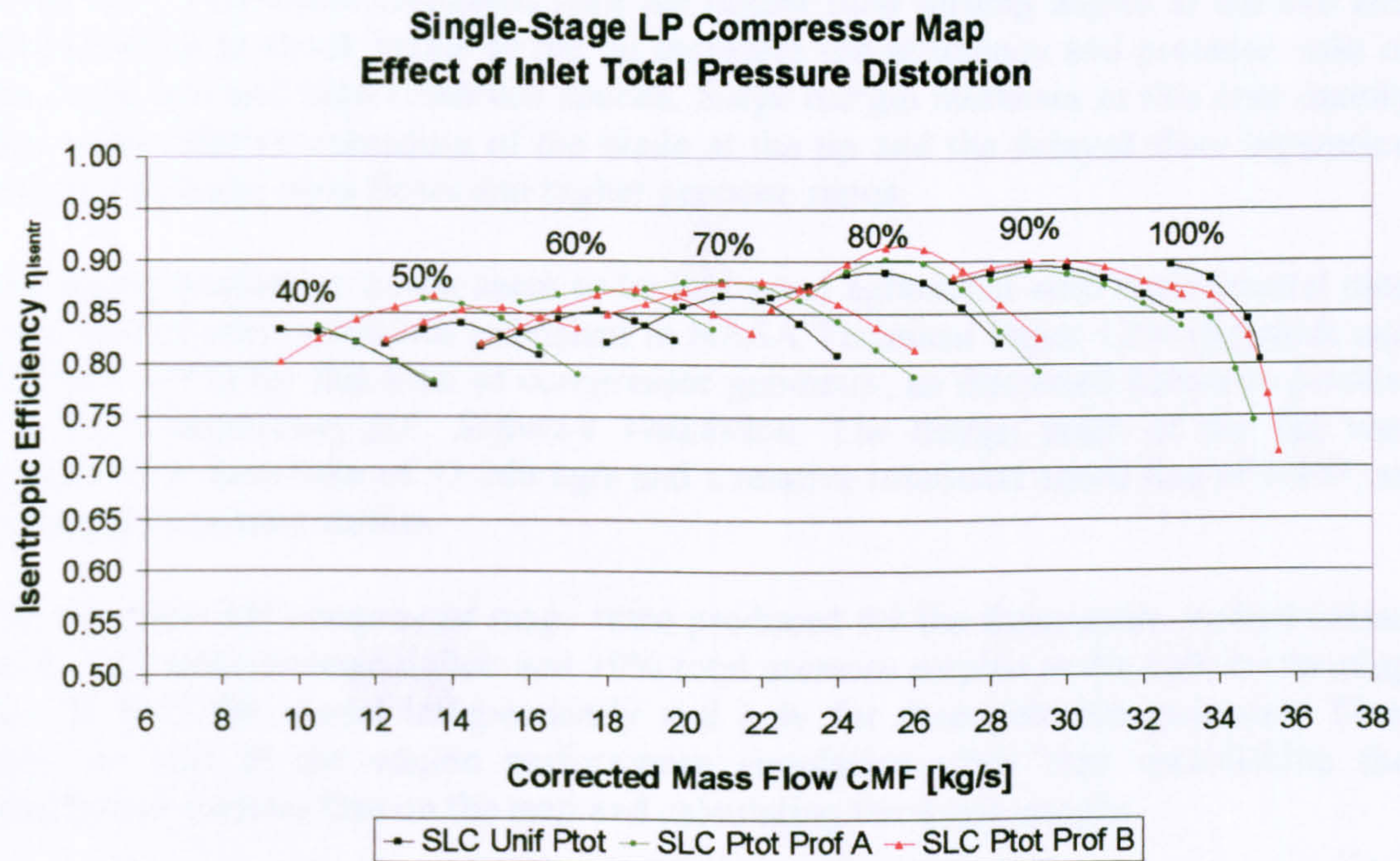


Figure 9.2.4.3: Effect of radial inlet total pressure distortion on LP compressor map – Isentropic Efficiency vs Corrected Mass Flow

Figures 9.2.4.2 and 9.2.4.3 illustrate the effect of the two radial pressure profiles on fan performance. The imposed total pressure profile A, which is similar to a typical pressure distortion at the blade tip, causes a radial redistribution of the flow which reduces the meridional velocity and increases the incidence of the flow on the blade



towards the tip. This in turn increases the loading of the blade in a region which is already highly loaded. The beneficial effect on fan performance at low and medium relative rotational speeds is evident from Figures 9.2.4.2 and 9.2.4.3. Although the hub is unloaded, generating less pressure ratio, along the rest of the blade span pressure ratio and efficiency rise compared to the fan performance with a uniform inlet due to the higher turning imposed to the flow and the higher work input at the tip. On the other hand, at relative rotational speeds higher than 80% the flow relative to the blades becomes highly transonic and eventually supersonic. The further increase in blade loading at the tip results in flow separation and more severe shock losses, therefore efficiency drops and so does pressure ratio. Surge margin in this particular case reduces since it is easier now for almost half of the upper part of the blade span to stall with any further reductions in mass flow due to the higher incidence of the flow.

Profile B is similar to a typical pressure distortion at the blade hub and causes exactly the same effect towards the lower part of the blade, by loading the hub instead of the tip. Similarly to the first case, fan pressure ratio and efficiency increase through out the operating range of the fan and actually by a larger percentage compared to profile A. This is due to the percentage total pressure deficit imposed at the hub being larger than the one imposed at the tip (Figure 9.2.4.1). The only difference in this case is that the beneficial effect in fan performance continues through out the transonic regime due to the unloading of the tip of the blades. Moreover in this case, blade incidences become more similar to the minimum-loss incidence values from high negative values at the hub. This effect combined with the higher flow turning angles at the hub and the reduction in shock losses at the tip increases the efficiency and pressure ratio of the fan at low and high rotational speeds. Surge margin increases in this case mainly due to the relative unloading of the blade at the tip and the delayed flow separation and stall at lower mass flows and higher pressure ratios.

The above qualitative trends seem to be in a good agreement with experimental data for distorted inlet conditions published in NASA Technical Paper 1294 (Schmidt and Ruggeri, 1978) for this kind of compressor geometry, as discussed before in *Section 8.1. 2D Compressor SLC Software Validation*. The design point of the fan was selected at a mass flow of 33.248 kg/s and a relative rotational speed line of 0.967, as in the previous case studies.

The complete LP compressor maps were produced for the three cases studied (clean inlet, 30% total pressure deficit and 30% total pressure surplus at the hub) by running the 2D SLC fan model independently and only for demonstration purposes. They played no part in the engine performance simulation other than establishing the equilibrium running line on the map and calculating the surge margin.

The shift of the engine running line under the different fan inlet pressure profiles is also illustrated in Figure 9.2.4.2. The 30% total pressure deficit at the hub causes the fan to run at higher pressure ratios and efficiencies which causes the equilibrium running line to appear above the one for the clean case. The 30% total pressure surplus at the hub seems to be causing the opposite effect, since the LP compressor is forced to run at lower pressure ratios and reduced efficiencies close to design point. The effect of the two different distortion profiles on the movement of the running line



appears more pronounced close to design point and seems to reduce towards lower relative rotational speeds were the displacement of the map is relatively smaller.

**LBR Military Turbofan Engine Performance Comparison  
Effect of LP Compressor Inlet Total Pressure Distortion**

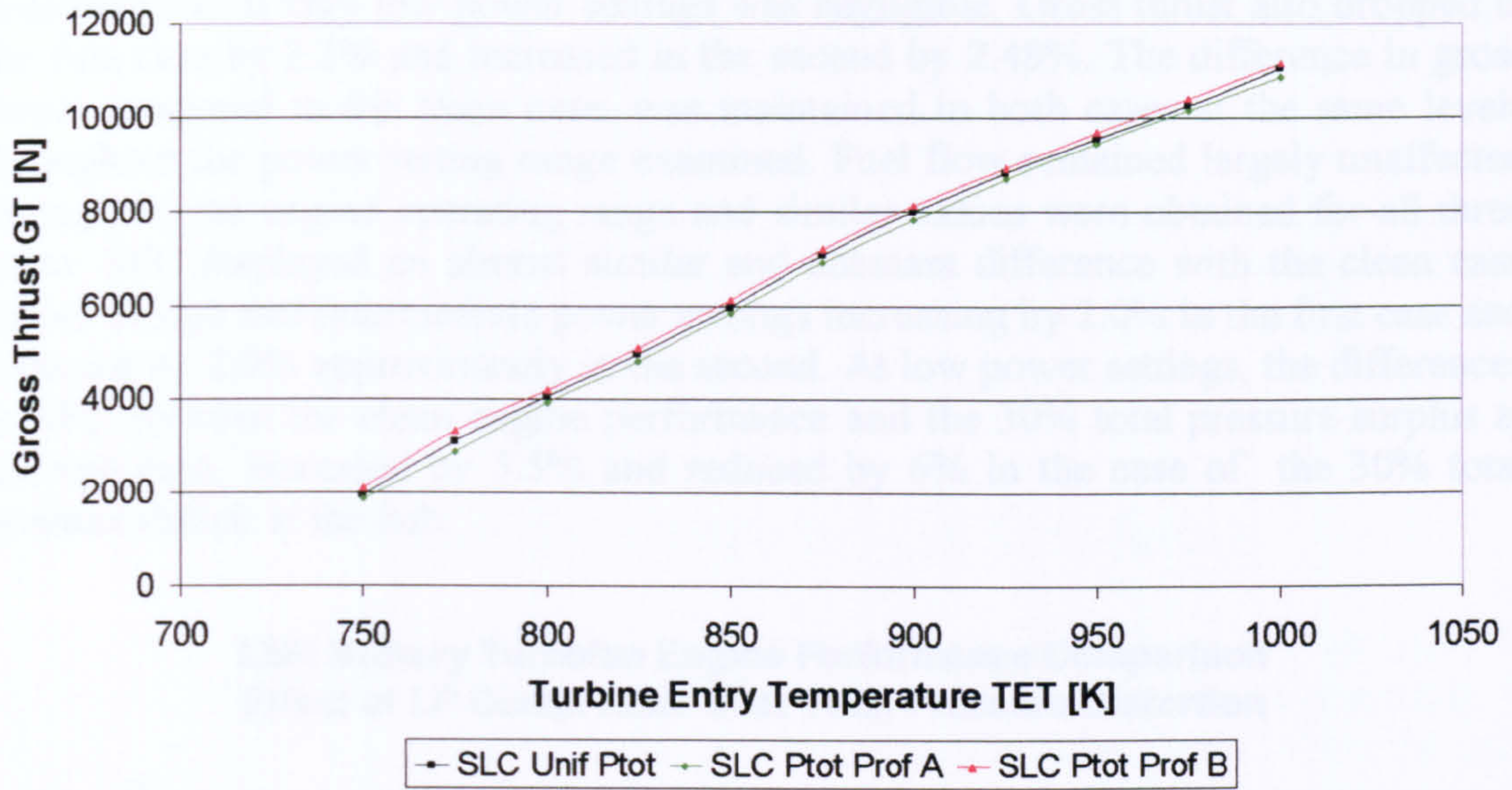


Figure 9.2.4.4: Effect of LP compressor radial inlet total pressure distortion on engine performance – Gross Thrust vs Turbine Entry Temperature

**LBR Military Turbofan Engine Performance Comparison  
Effect of LP Compressor Inlet Total Pressure Distortion**

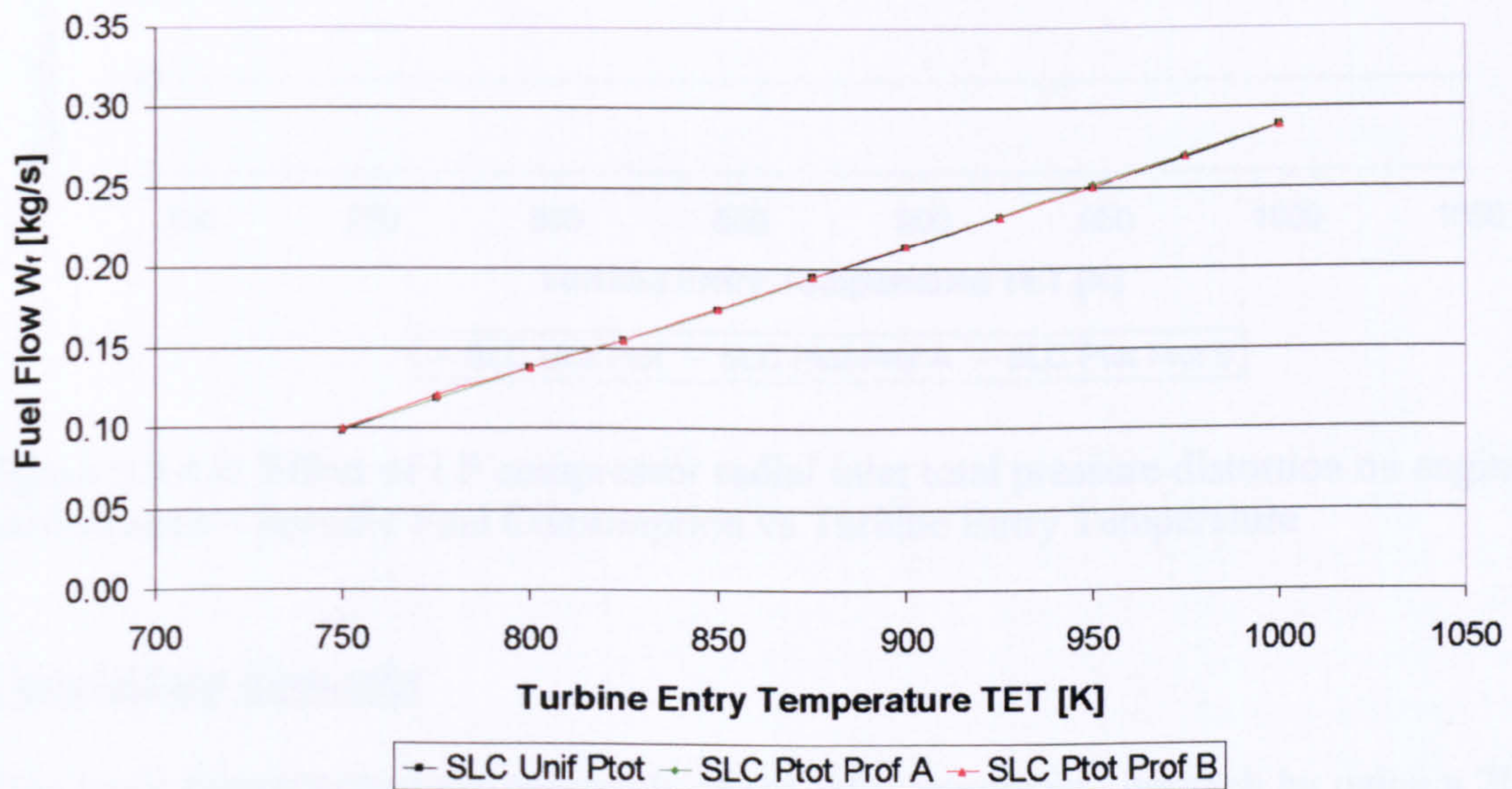


Figure 9.2.4.5: Effect of LP compressor radial inlet total pressure distortion on engine performance – Fuel Flow vs Turbine Entry Temperature



Figures 9.2.4.4 to 9.2.4.6 illustrate the effect of distortion on overall engine performance. The effect on engine performance parameters is consistent with the displacement of the equilibrium running lines. As a direct consequence of the fan pressure ratio change close to design point, the engine overall pressure ratio dropped by 1.6%, in the case of a 30% total pressure surplus at the hub, and increases by 0.94% in the case of the total pressure deficit at the hub. The difference in overall pressure ratio at very low power settings was negligible. Gross thrust also dropped in the first case by 2.3% and increased in the second by 2.48%. The difference in gross thrust compared to the clean case, was maintained in both cases at the same levels throughout the power setting range examined. Fuel flow remained largely unaffected throughout the engine operating range and similar values were obtained for all three cases. SFC displayed an almost similar and constant difference with the clean case values at high and intermediate power settings increasing by 2.0% in the first case and reducing by 2.0% approximately in the second. At low power settings, the differences in SFC between the clean engine performance and the 30% total pressure surplus at the hub case, increased by 5.5% and reduced by 6% in the case of the 30% total pressure deficit at the hub.

#### LBR Military Turbofan Engine Performance Comparison Effect of LP Compressor Inlet Total Pressure Distortion

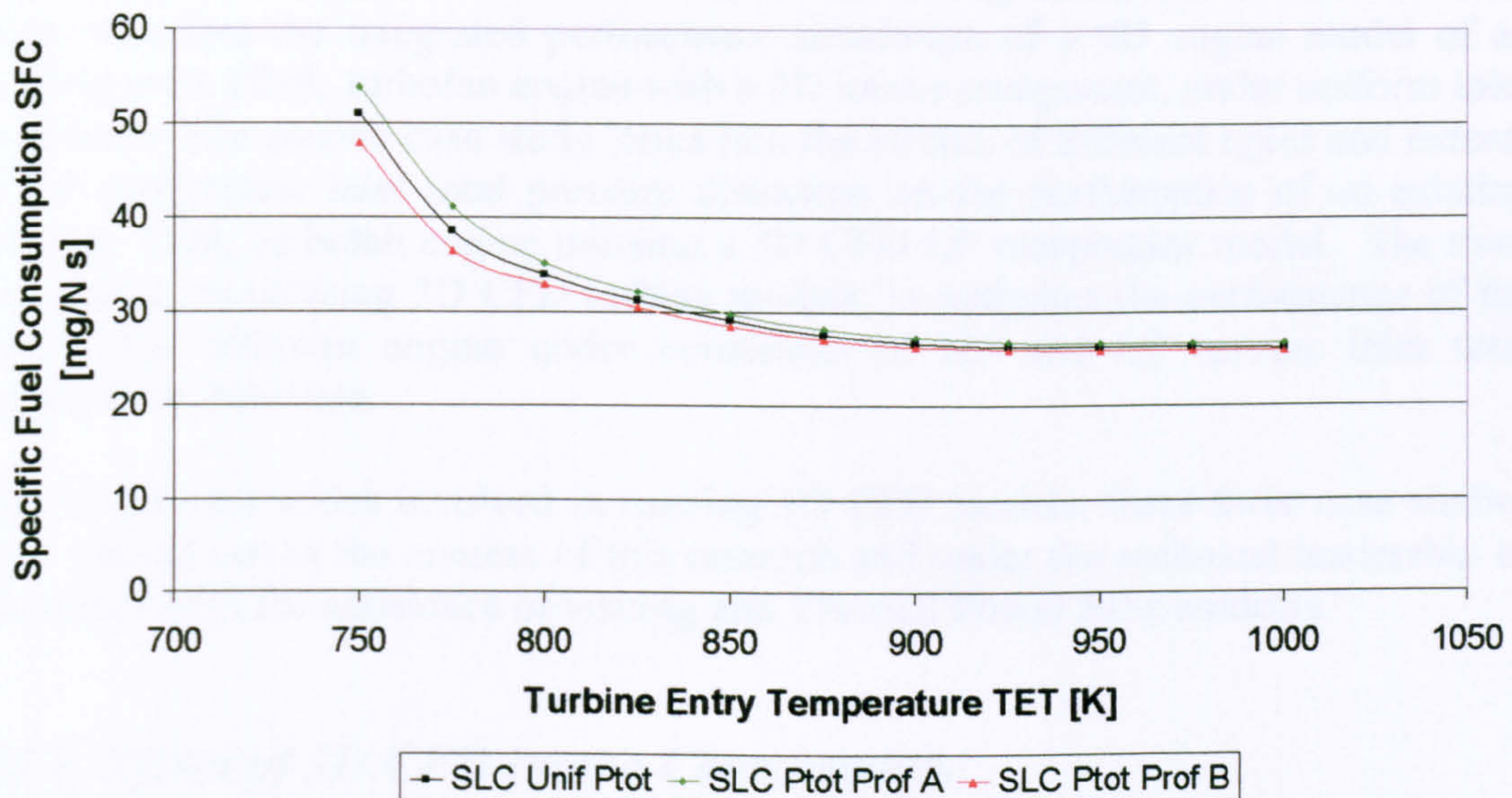


Figure 9.2.4.6: Effect of LP compressor radial inlet total pressure distortion on engine performance – Specific Fuel Consumption vs Turbine Entry Temperature

#### Concluding Remarks

This work demonstrated the potentials of the fully integrated approach by using a 2D SLC compressor model, directly coupled to a 0D engine performance simulation software. In this particular case, the high-fidelity LP compressor model fully defined the performance characteristics of that particular fan geometry, at the simulated operating conditions, and was then used to provide a more accurate, physics-based



estimate of fan performance and hence, engine performance, under clean and distorted inlet conditions.

As mentioned before, presented engine performance results, are to be taken only qualitatively, because of the notional nature of the engine model used in this case. At this stage it was outside the scope and requirements of the investigation to repeat the same methodology for a larger number of different cases. However, in the cases examined, the analysis carried out by this study, demonstrated relative changes in the simulated engine performance larger than 1%.

The above analysis proves the potential of the simulation strategy presented here to investigate relevant physical processes occurring in an engine component in a direct and more detailed way, and to assess the effects of various isolated flow phenomena on overall engine performance in a timely and affordable manner.

### ***9.3. 3D CFD Gas Turbine Performance Simulation***

This section includes the high-resolution performance analysis of conventional 0D engine models build in PYTHIA, coupled with 3D CFD engine component models. In total, three case studies are discussed in the following subsections. The first case study describes the integrated performance simulation of a 0D engine model of an existing civil, HBR, turbofan engine with a 3D intake component, under uniform inlet conditions. The second case study looks into the effects of different types and extents of LP compressor inlet total pressure distortion on the performance of an existing military, LBR, turbofan engine utilising a 3D CFD LP compressor model. The third case study, by utilising 3D CFD turbine models, investigates the performance of the same LBR turbofan engine under conditions of HP and LP turbine inlet total temperature distortion.

Due to the time scales involved in running 3D CFD models, these three case studies were carried out in the context of this research and under the technical leadership of the author with the assistance of visiting and Thermal Power MSc students.

#### ***9.3.1. Effect of 3D CFD Intake Characteristic***

The first case study looked into intake pressure recovery effects on whole engine performance using a 0D model of the CFM56-5B2 HBR turbofan engine and a 3D CFD model of the engine's intake. All three approaches to high-fidelity analysis were attempted in this case. As before, the objective of this particular work was the investigation of simulation strategies that allow the performance characteristics of an isolated engine component, resolved from a high-fidelity analysis, to be transferred to a low-resolution engine system analysis, at an affordable computing resource and time.



Simulation Tools

This study utilized two simulation software: i) PYTHIA - the 0D gas turbine modelling and performance simulation system available at Cranfield, and ii) the commercial CFD package GAMBIT/FLUENT.

For the purposes of this investigation, an engine model was built in PYTHIA that resembled the CFM56-5B2 HBR turbofan engine in both configuration and performance (Figure 9.3.1.1). The modelling was based on engine performance data available in the public domain. Some overall performance data of the CFM56-5B2 turbofan engine are shown in Table 9.3.1.1. Other engine performance parameters can be found in PYTHIA’s engine input data files which have been included in this thesis as *Appendix J - PYTHIA Engine Input Data Files*.

Max Takeoff Thrust @ SL	[kg]	14061.0
Takeoff Mass Flow @ SL	[kg/s]	433.6
Takeoff BPR @ SL		5.5
Max Climb Thrust @ 10670.0 m, 0.8 M <sub>∞</sub>	[kg]	2912.0
Max Climb OPR @ 10670.0 m, 0.8 M <sub>∞</sub>		35.4
Max Cruise Thrust @ 10670.0 m, 0.8 M <sub>∞</sub>	[kg]	2648.9

Table 9.3.1.1: CFM56-5B2 turbofan engine performance data

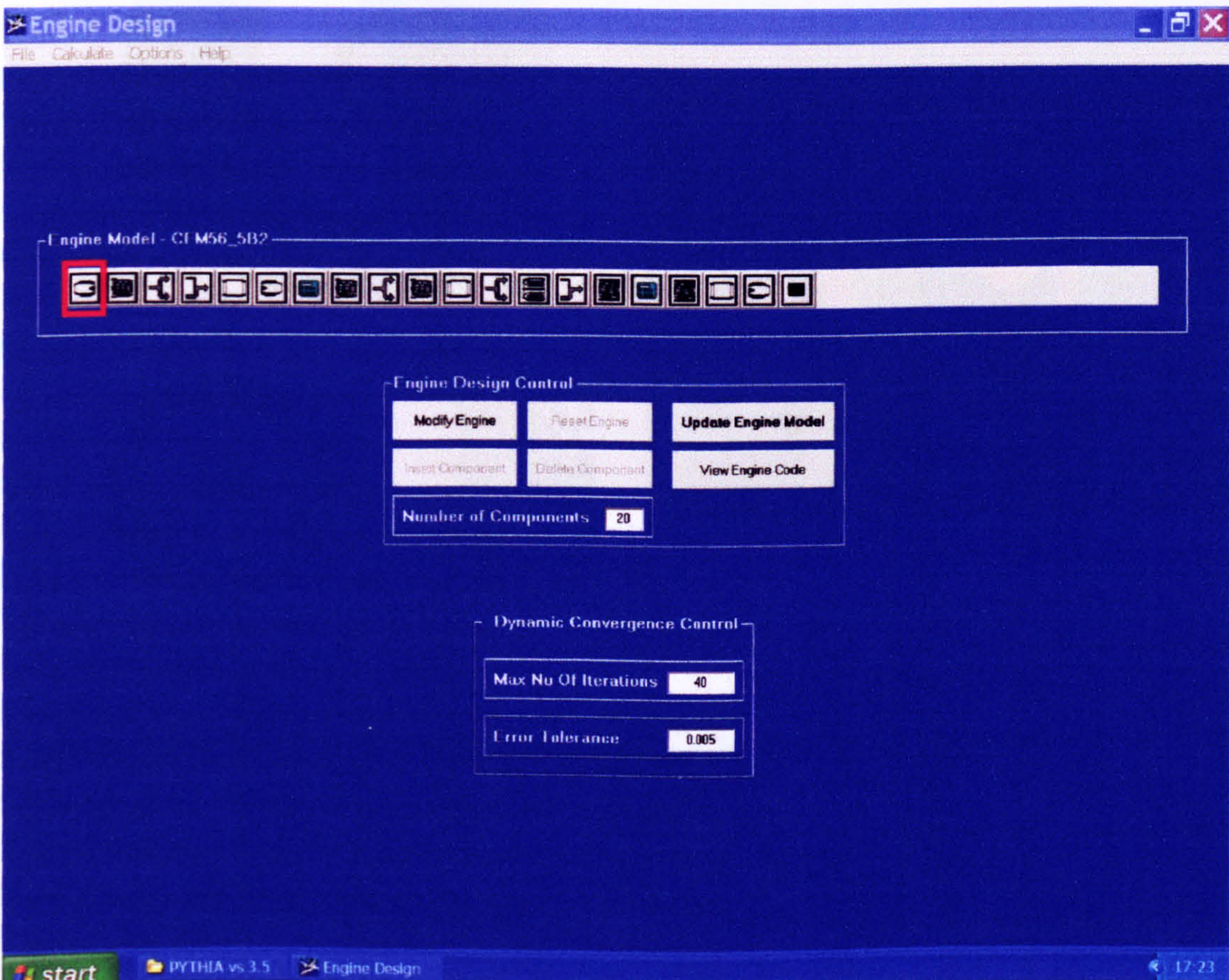


Figure 9.3.1.1: PYTHIA HBR turbofan engine 0D model (CFM56-5B2)



Moreover, a 3D CFD intake model, based on the geometry of the intake of the CFM56-5B2 HBR turbofan engine (Figure 9.3.1.2), was created and meshed in the commercial package GAMBIT using 300,000 cells approximately. The optimum number of cells was established by a ‘grid-independence’ study. The commercial CFD solver, FLUENT, was used to carry out the CFD analysis. The geometry of the intake was similarly obtained from the public domain.

As discussed before, a PYTHIA engine model uses performance maps for turbines and compressors to obtain a balanced, steady-state engine condition. Intake pressure recovery is simplistically simulated by means of an empirical total pressure drop that needs to be explicitly specified by the user for every operating condition.

In order to establish the baseline intake and engine performances for the high-fidelity analysis, the 0D intake characteristics were calibrated such that at the baseline conditions (design point) there was no difference between the 0D intake performance (i.e. pressure recovery, mass flow etc.) and the performance predicted by the full, 3D CFD intake model.

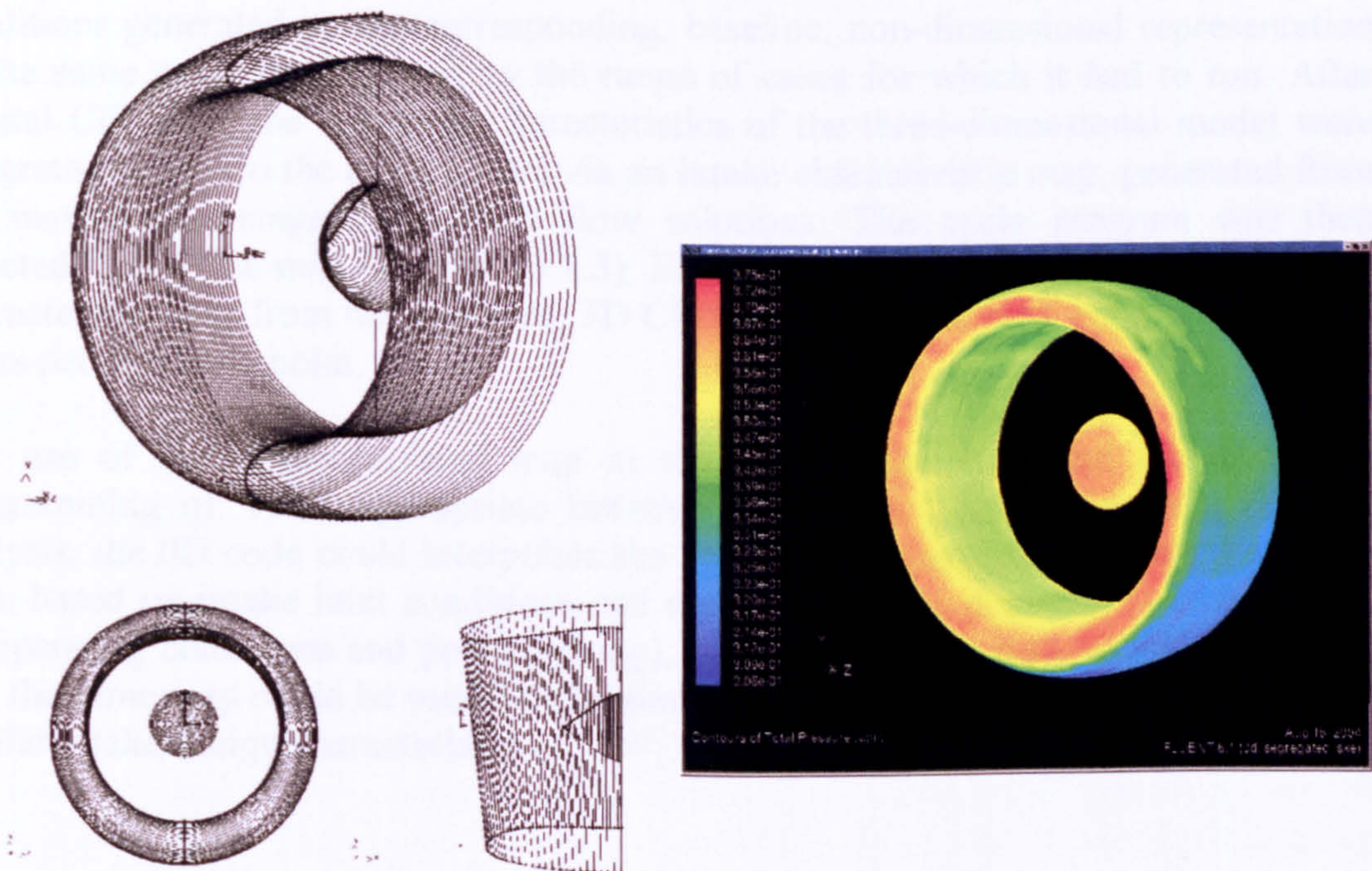


Figure 9.3.1.2: 3D CFD model based on the CFM56-5B2 intake geometry



### De-Coupled High-Fidelity Simulation

The simulation technique adopted in this case involved the generation of a component characteristic map according to the de-coupled simulation strategy discussed previously. This particular work, investigated relative changes in the simulated engine performance after integrating the CFD-generated component map into the 0D engine analysis system.

The 0D engine model of the HBR turbofan engine was run off-design several times, at different flight conditions and different power settings to generate an approximate database of different intake operating conditions. More analytically, intake operating conditions such as mass flow, inlet and outlet total and static pressure and temperature were collected for a range of altitudes between 0.0 and 10670.0 m (design point value), a range of flight Mach numbers at each altitude, from 0.2 to 0.8 (design point value) and a range of TET settings at each altitude, between 1458.15 K (design point value) down to 1000 K (30% reduction in power setting approximately).

Having generated all this data from the 0D simulations, inlet boundary values for total pressure, total temperature, and static pressure (or Mach number), and the exit boundary value of static pressure were applied as boundary conditions to the 3D CFD intake model. Basically, the 3D CFD intake model used the approximate boundary conditions generated by the corresponding, baseline, non-dimensional representation of the same component to narrow the range of cases for which it had to run. After several CFD runs the operating characteristics of the three-dimensional model were integrated back into the cycle model via an intake characteristic map, generated from the mass-flow-averaged, 3D CFD flow solutions. The cycle program was then directed to the new map (Figure 9.3.1.3). Establishing operating points on the intake characteristic map from the averaged, 3D CFD flow solutions took approximately 2-3 hours per operating point.

The use of the CFD-generated map in the 0D analysis, required the additional programming of: i) an appropriate iterative routine so that, during an off-design analysis, the 0D code could interpolate the appropriate operating point on the intake map, based on intake inlet conditions and compressor flow demands (i.e. dependent on operating conditions and power setting), ii) an appropriate map-scaling routine so that the same map could be used for the simulation of other engines of same type and similar intake design characteristics.



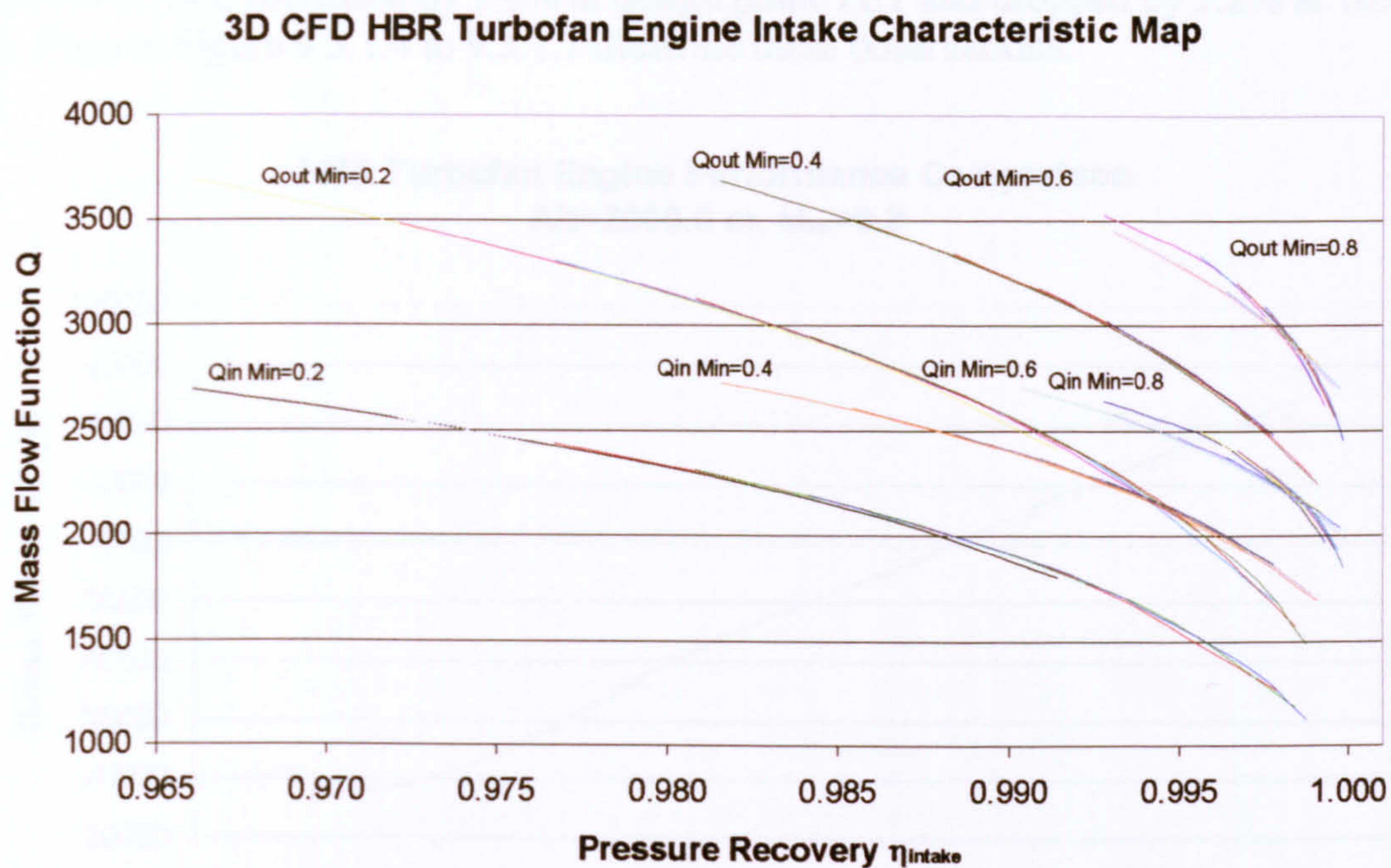


Figure 9.3.1.3: CFD-generated HBR turbofan engine full intake characteristic map

The CFD-generated map fully defined the performance characteristics of that particular intake geometry, at the simulated operating conditions, and was subsequently used to provide a more accurate, physics-based estimate of the intake's performance (i.e. pressure recovery) and hence, engine performance, replacing the empirical pressure recovery values within the PYTHIA cycle model.

### Engine Performance Simulation

Subsequent engine performance analysis demonstrated differences in the simulated engine performance between using the standard, baseline intake pressure recovery values and using the complete intake characteristic map. At cruise conditions and design point power setting the simulation results, using the CFD-generated map, matched the baseline engine performance very well, due to the initial calibration of the 0D and 3D intake models. As expected, only third-decimal-place differences were observed at design point operating conditions. The largest differences in engine performance were observed at operating conditions and engine power settings other than those at cruise (off-design conditions) due to the different pressure recovery values calculated by the 3D CFD intake model and the effect of the intake's pressure ratio on overall engine pressure ratio and hence, overall engine performance. The following paragraphs attempt to demonstrate this point by discussing the trends observed in some of the engine performance simulation results, as examples.

At an altitude of 2000.0 m and a flight Mach number of 0.2, changing the power setting from the design point value of 1458.15 K down to 1050.0 K, gave a reduction in engine gross thrust of 2.4% at design point and an increase of 3.1% at 1050.0 K. Momentum drag followed the same pattern displaying an initial reduction of 1.33%, compared to the baseline performance, but increasing by 1.5% at 1050.0 K TET.



Similarly net thrust was down by 2.7% at 1458.15 K TET, only to increase by 5% at 1050.0 K. SFC increased by 1.6% at design point TET and dropped by 5.2% at 1050.0 K. Figures Figure 9.3.1.4 to 9.3.1.7 illustrate these observations.

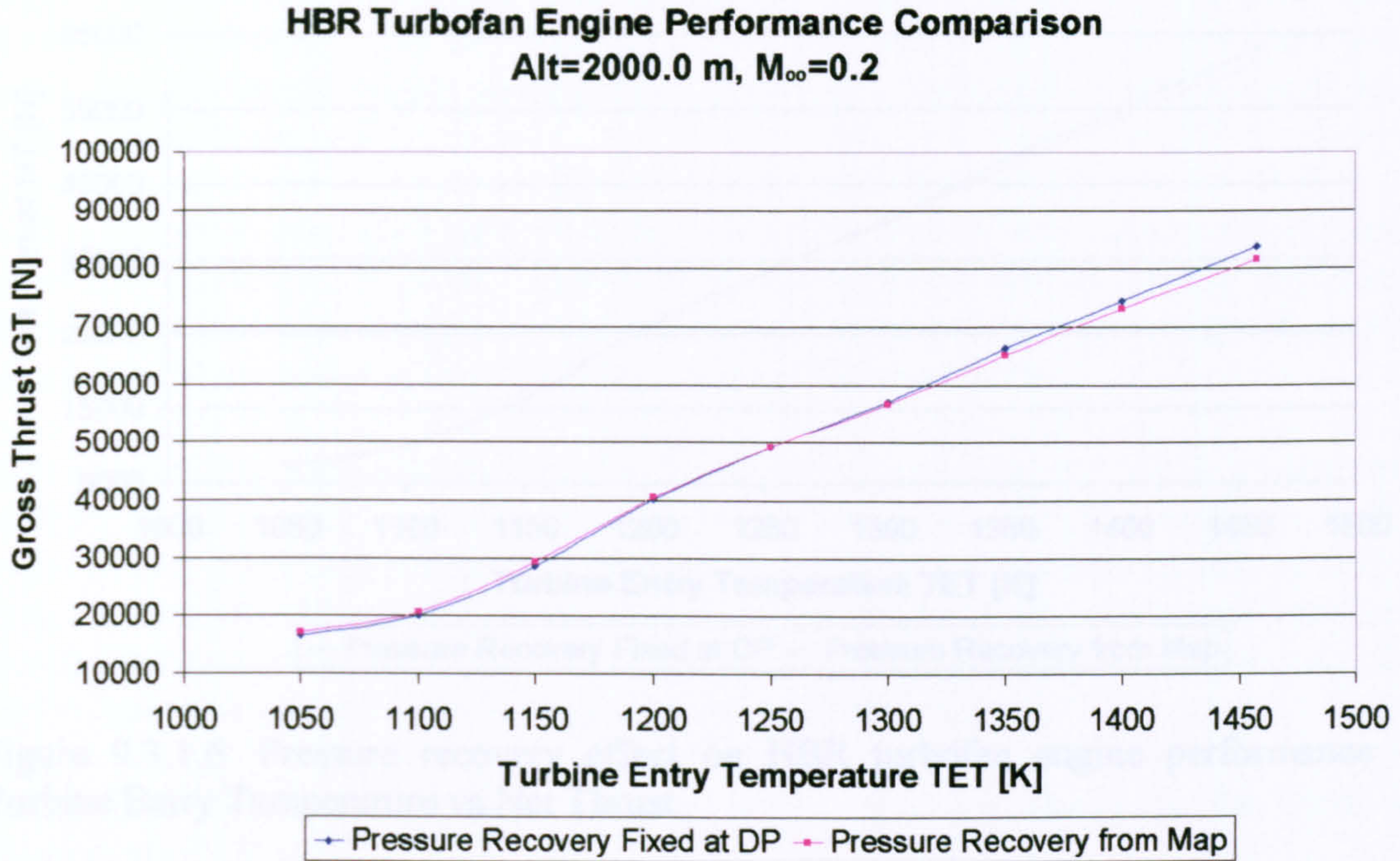


Figure 9.3.1.4: Pressure recovery effect on HBR turbofan engine performance – Turbine Entry Temperature vs Gross Thrust

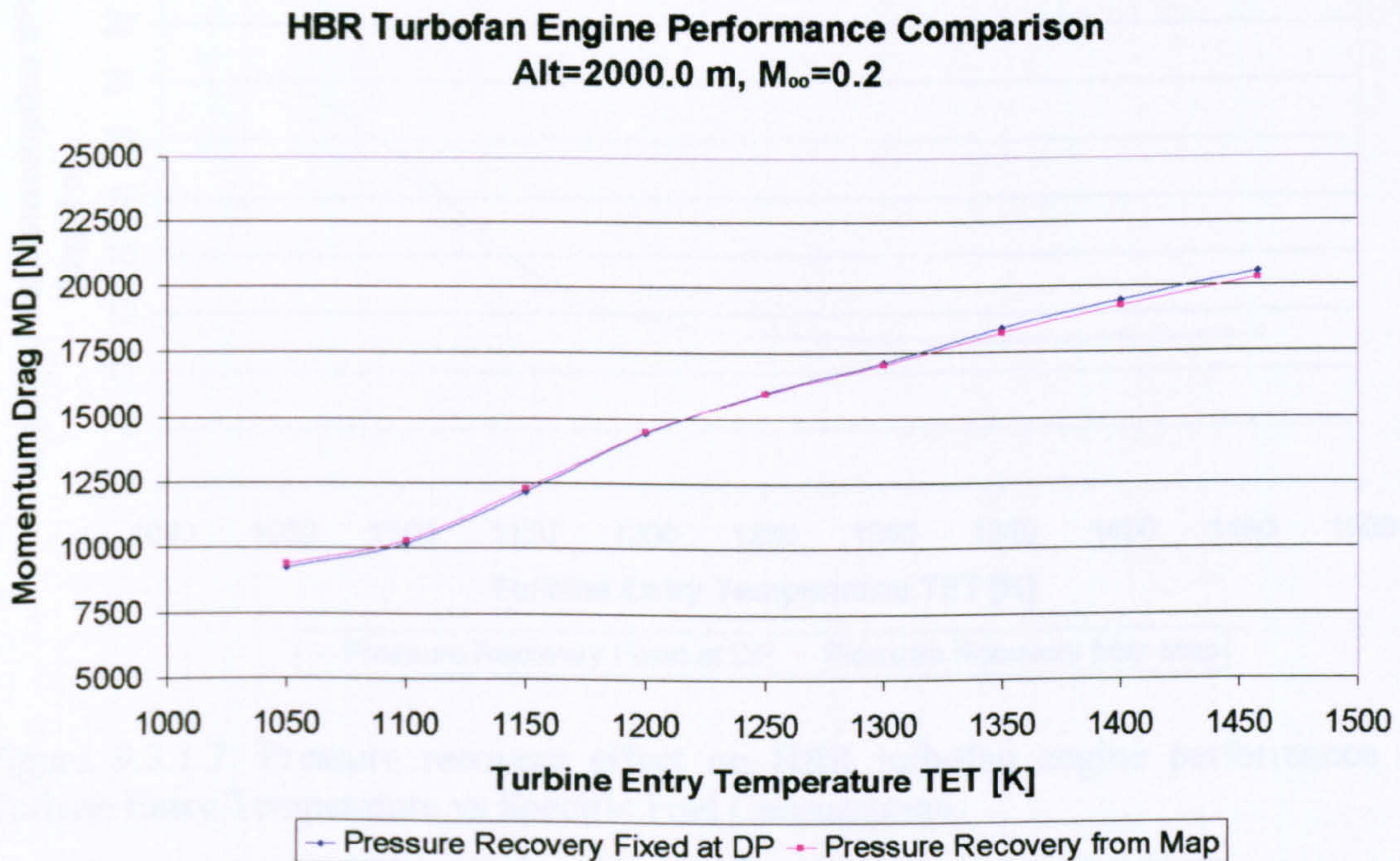


Figure 9.3.1.5: Pressure recovery effect on HBR turbofan engine performance – Turbine Entry Temperature vs Momentum Drag



**HBR Turbofan Engine Performance Comparison**  
**Alt=2000.0 m,  $M_{\infty}=0.2$**

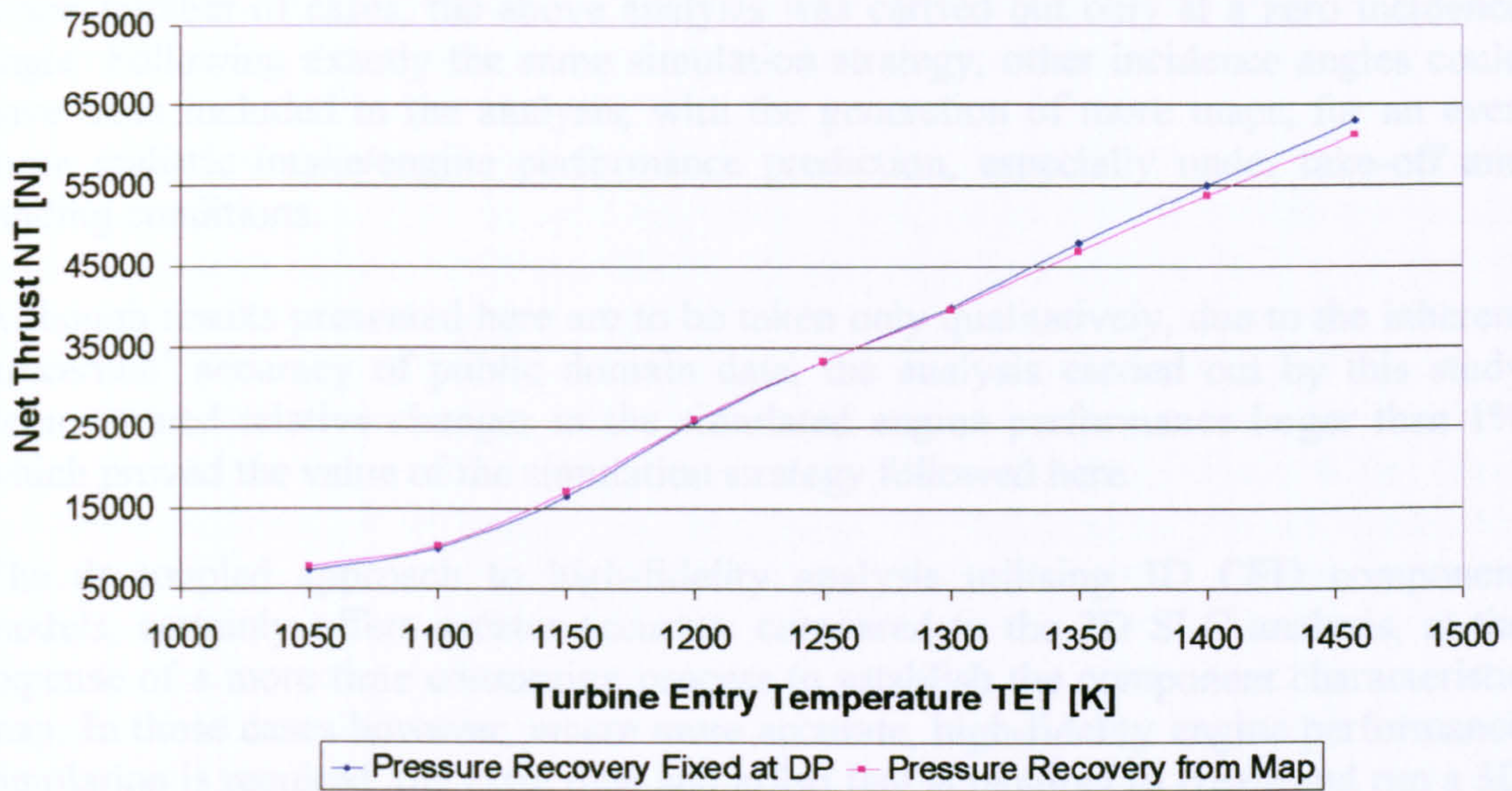


Figure 9.3.1.6: Pressure recovery effect on HBR turbofan engine performance – Turbine Entry Temperature vs Net Thrust

**HBR Turbofan Engine Performance Comparison**  
**Alt=2000.0 m,  $M_{\infty}=0.2$**

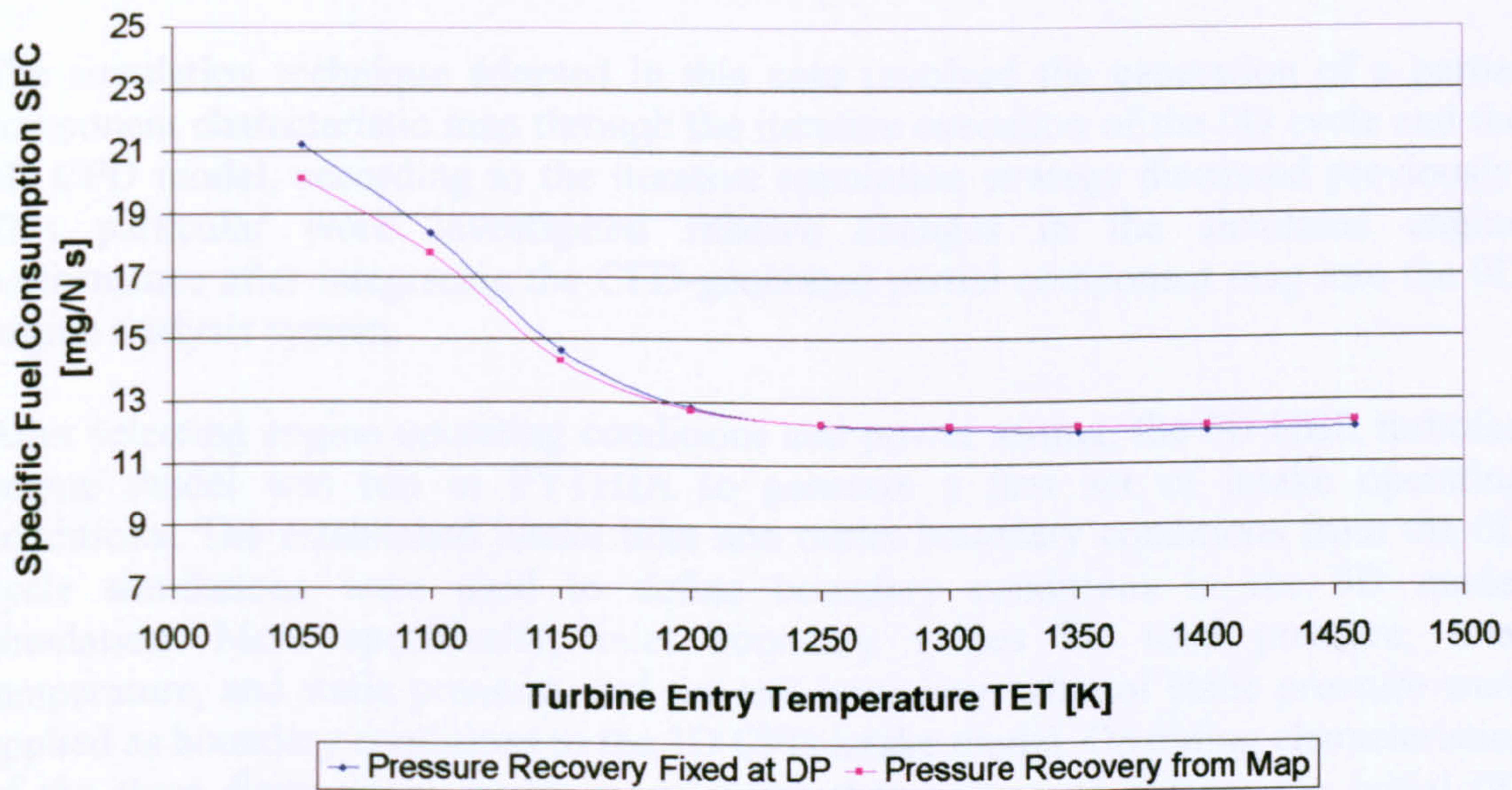


Figure 9.3.1.7: Pressure recovery effect on HBR turbofan engine performance – Turbine Entry Temperature vs Specific Fuel Consumption



### Concluding Remarks

As it was outside the scope of this investigation to repeat the same methodology for a larger number of cases, the above analysis was carried out only at a zero incidence angle. Following exactly the same simulation strategy, other incidence angles could have been included in the analysis, with the generation of more maps, for an even more realistic intake/engine performance prediction, especially under take-off and landing conditions.

Although results presented here are to be taken only qualitatively, due to the inherent 'uncertain' accuracy of public domain data, the analysis carried out by this study demonstrated relative changes in the simulated engine performance larger than 1% which proved the value of the simulation strategy followed here.

The de-coupled approach to high-fidelity analysis utilising 3D CFD component models, certainly offers greater accuracy compared to the 2D SLC analysis, at the expense of a more time consuming process to establish the component characteristic map. In those cases however, where more accurate, high-fidelity engine performance simulation is required, the extra time and effort that is required to create and run a 3D CFD engine component is perhaps justifiable if not necessary.

A complete account of the work that was briefly described above can be found in Nantua, et al. (2004).

### Iterative High-Fidelity Simulation

The simulation technique adopted in this case involved the generation of a partial component characteristic map through the iterative execution of the 0D cycle and the 3D CFD model, according to the iterative simulation strategy discussed previously. This particular work investigated relative changes in the simulated engine performance after integrating the CFD-generated partial component map into the 0D engine analysis system.

After selecting engine operating conditions and power setting, the 0D HBR turbofan engine model was run in PYTHIA to generate a first set of intake operating conditions. The established intake inlet and outlet boundary conditions from the 0D cycle simulations were used to define boundary conditions in the 3D model simulation. More specifically, inlet boundary values for total pressure, total temperature, and static pressure, and the exit boundary value of static pressure were applied as boundary conditions to the 3D CFD intake model. Operating characteristics of the three-dimensional intake model were then compared against the initial 0D solution. Initially the 3D component did not 'match' the low-fidelity component and boundary conditions had to be 'exchanged' between the two component representations, in an iterative process, until a converged component and engine performance could be achieved at the given engine operating conditions and power setting.

The above iterative process was slightly different than the one described before in the case of the 2D SLC compressor model, where a default compressor map was used in



order to reduce the range of search for possible equilibrium operating points, and where mass flow could be specified directly as a boundary condition. In PYTHIA, the intake pressure recovery is not interpolated from a default intake map nor is it calculated as a function of flight Mach number and mass flow for civil engines, as explained before. Pressure recovery is manually specified by the user.

In the high-fidelity analysis, the specified ‘boundary’  $P_{o,in}/p_{out}$  ratio, which essentially determines the mass flow through the intake, resulted in a slightly different intake mass flow, pressure recovery and exit velocity compared to the 0D flow solutions. In those cases where the 0D and averaged 3D flow solutions were in agreement, within a 0.5% difference approximately, the averaged, 3D flow solution established a point on a ‘partial’ intake characteristic map, for the given power setting, to be used at a later stage for the whole engine performance simulation. In those cases where flow solutions were not in agreement, the averaged 3D boundary conditions were ‘fed’ back to the 0D engine model as a second ‘guess’, including a new pressure recovery value which was manually imposed. The 0D engine model simulation was carried out again to provide new, updated boundary conditions for the 3D CFD simulation. The process was repeated many times until the two solutions agreed within the pre-established ‘error tolerance’, and a new point on the partial intake performance map could be generated. The error tolerance, mentioned above (0.5%), was accepted on the grounds of a qualitative analysis.

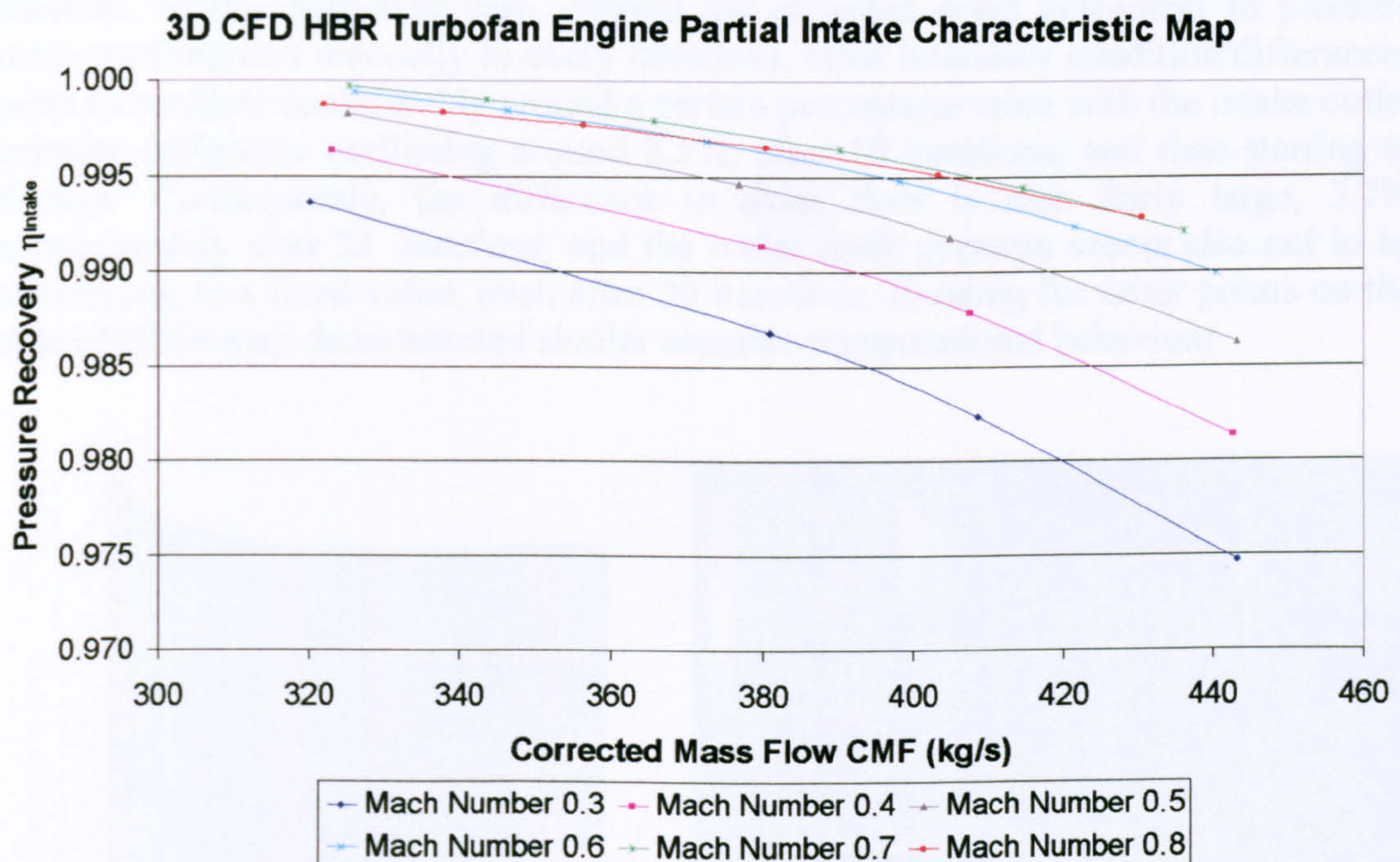


Figure 9.3.1.8: CFD-generated HBR turbofan engine partial intake characteristic map

The high-fidelity analysis reported here looked into different flight Mach numbers and operating altitudes for a fixed engine power setting and incidence angle. Varying altitude and flight Mach number gave a satisfactory range of different intake inlet operating conditions and a realistic, partial intake characteristic map for the selected power setting. More analytically, the engine’s power setting was kept at the design point value of 1458.15 K TET and incidence angle was kept at 0 degrees. Points on



the intake characteristic map were obtained for flight Mach numbers between 0.8 (design point value) and 0.3, and for a range of altitudes between 10670.0 m (design point value) and 2000.0 m (Figure 9.3.1.8).

The CFD-generated map fully defined the performance characteristics of that particular intake geometry, at the simulated operating conditions, and was then used to provide a more accurate, physics-based estimate of the intake's performance (i.e. pressure recovery) and hence, engine performance, replacing the empirical pressure recovery values within the PYTHIA cycle model.

### Convergence

As mentioned before, to generate a point on the map, 'matching' the boundary conditions of the 3D CFD intake model to those of the 0D intake component required an iterative execution of PYTHIA and FLUENT. Initial 0D cycle and 3D CFD test runs, using a 'small', localized domain (Figure 9.3.1.9), which only encompassed the flow inside the intake, revealed a very poor convergence probability (Figure 9.3.1.10). In several occasions and particularly in those cases where the intake model was tested at operating conditions further away from the design point mass flow and inlet pressure, the percentage difference between boundary conditions seemed to oscillate or even diverge. Figure 9.3.1.10 is representative of this sort of unstable iterative solution. In this particular case, despite the expected good agreement in pressure recovery (imposed manually in every iteration), other boundary condition differences seem to oscillate considerably around a certain percentage value with the intake outlet velocity difference oscillating around 2.5%, after 10 iterations, and then starting to diverge. Consequently, the difference in mass flow is also fairly large, 3.7% approximately after 21 iterations, and the outlet static pressure seems also not to be converging to a fixed value, even after 20 iterations. Iterating for other points on the characteristic map demonstrated similar unstable computational behaviour.

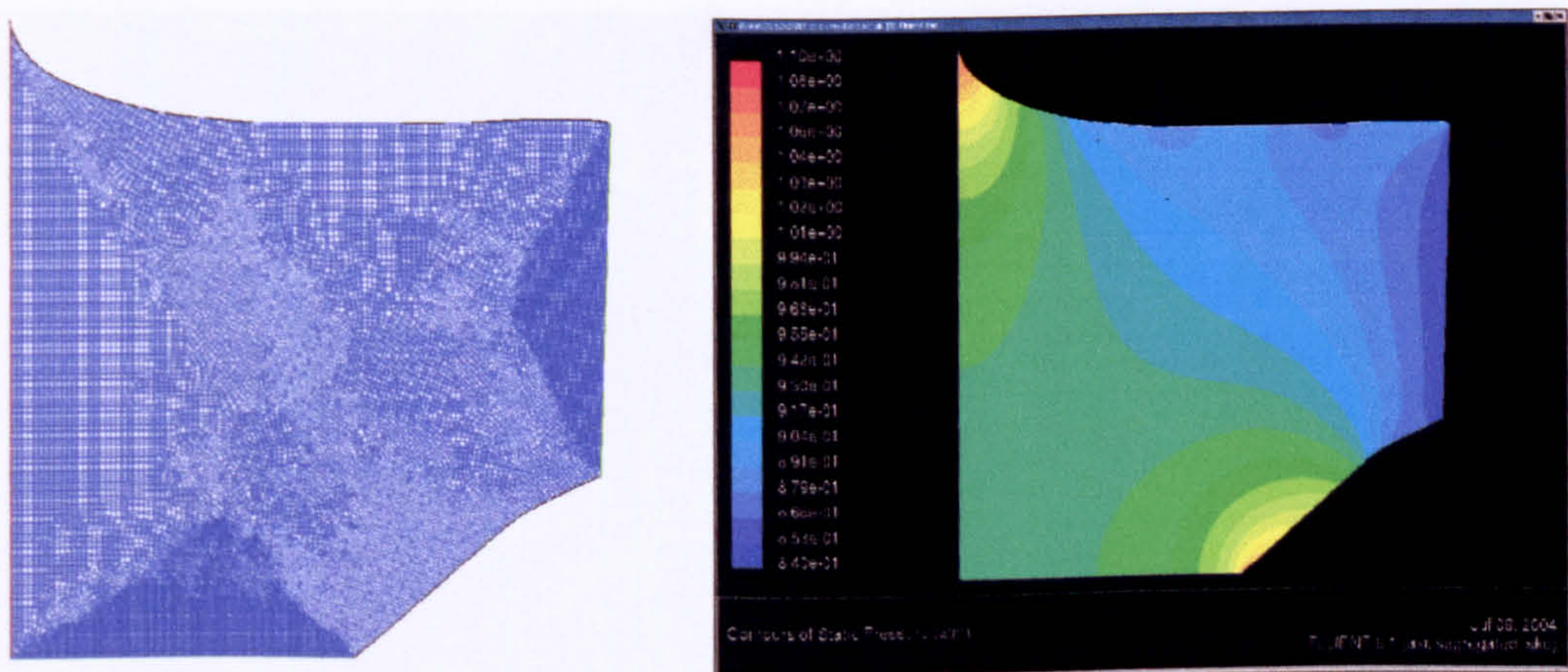


Figure 9.3.1.9: CFD model of the CFM56-5B2 intake in a 'small' flow domain



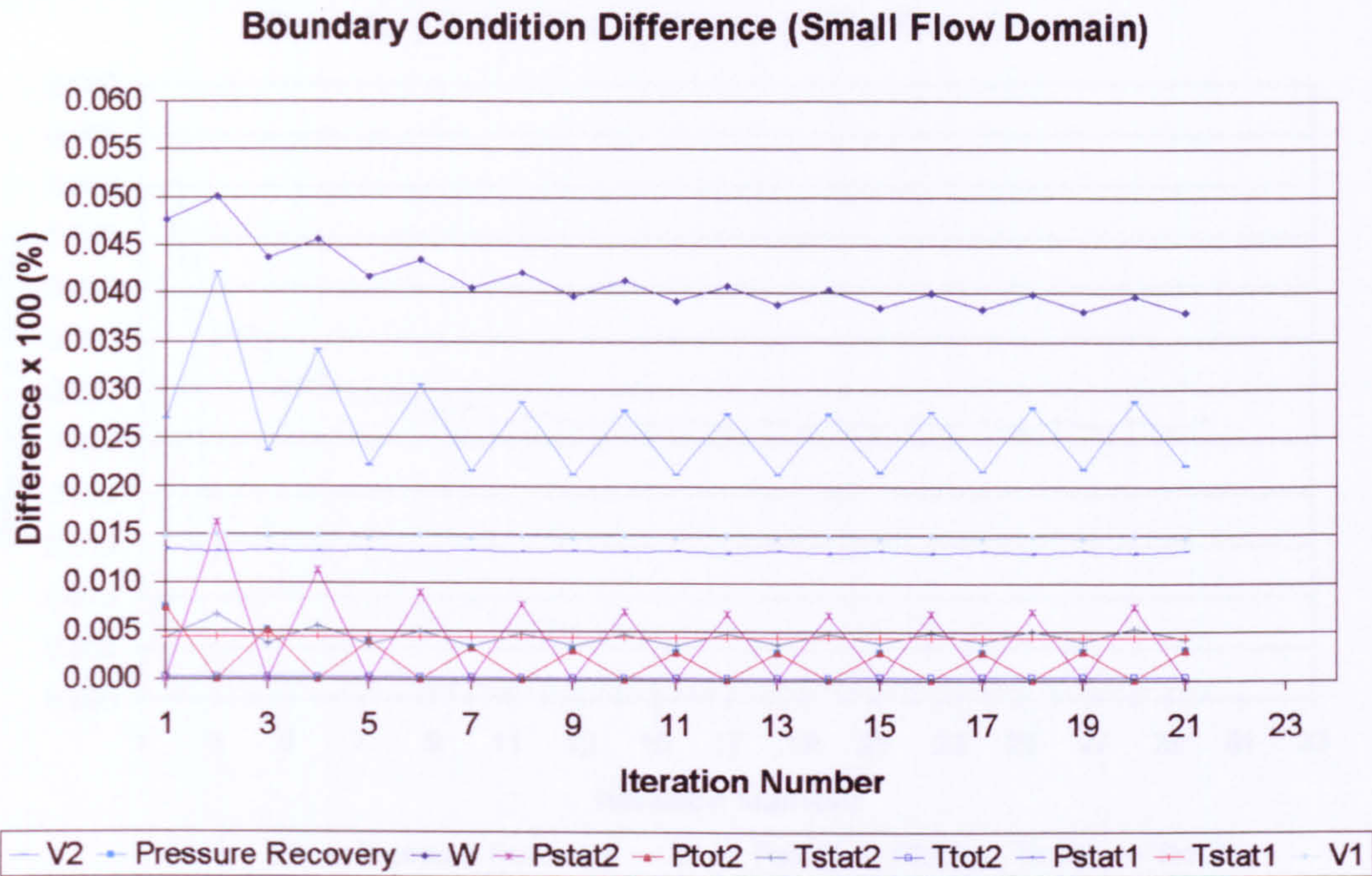


Figure 9.3.1.10: Convergence history using a ‘small’ flow domain

Improving the CFD intake model (denser grid), and using a bigger flow domain (Figure 9.3.1.11), which also accounted for the flow outside the engine’s nacelle, seemed to improve the computational stability of the solution and the chances for convergence. Figure 9.3.1.12 is representative of this group of iterative runs between PYTHIA and FLUENT. The difference in mass flow reduced to a 2.7% approximately after 15 iterations and the difference in outlet velocity converged to a satisfactory 0.6%. All other boundary conditions, such as the outlet static pressure, converged to a less than a 0.25% difference.

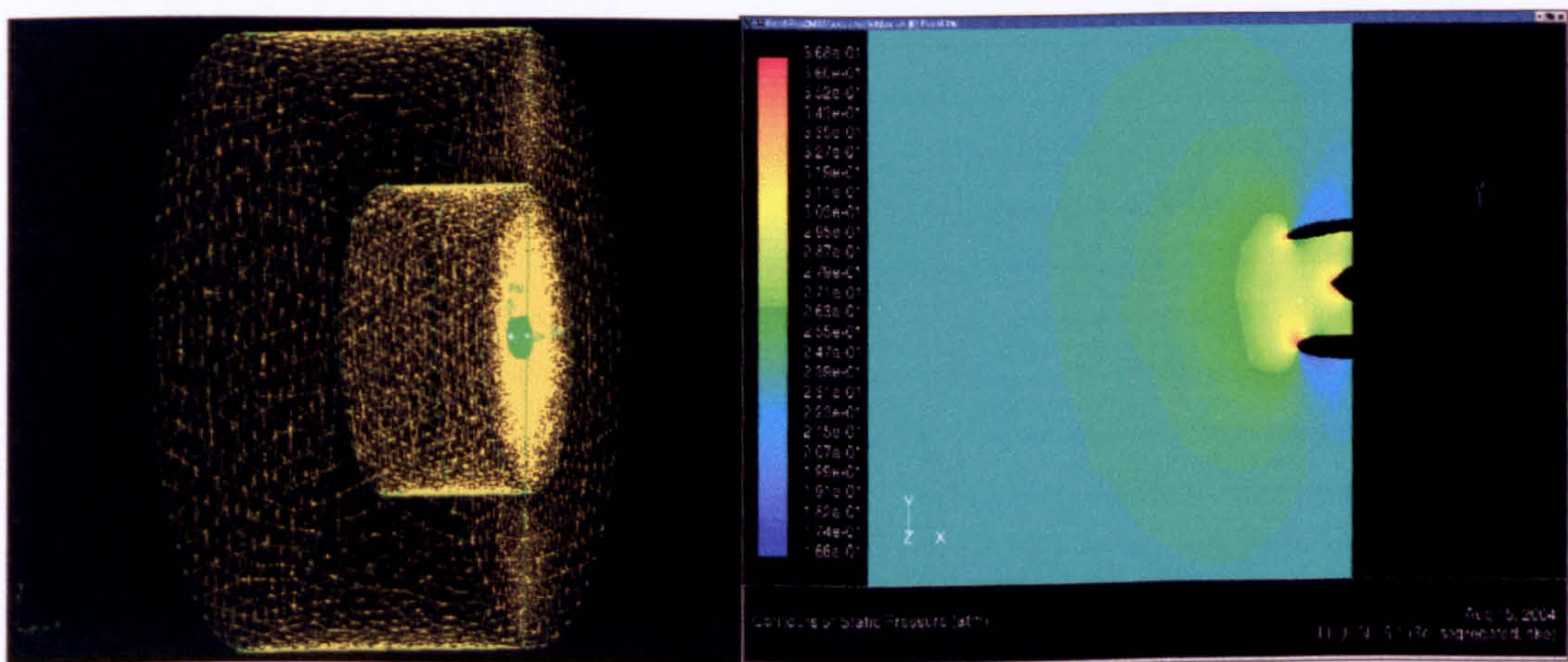


Figure 9.3.1.11: CFD model of the CFM56-5B2 intake in a ‘big’ flow domain



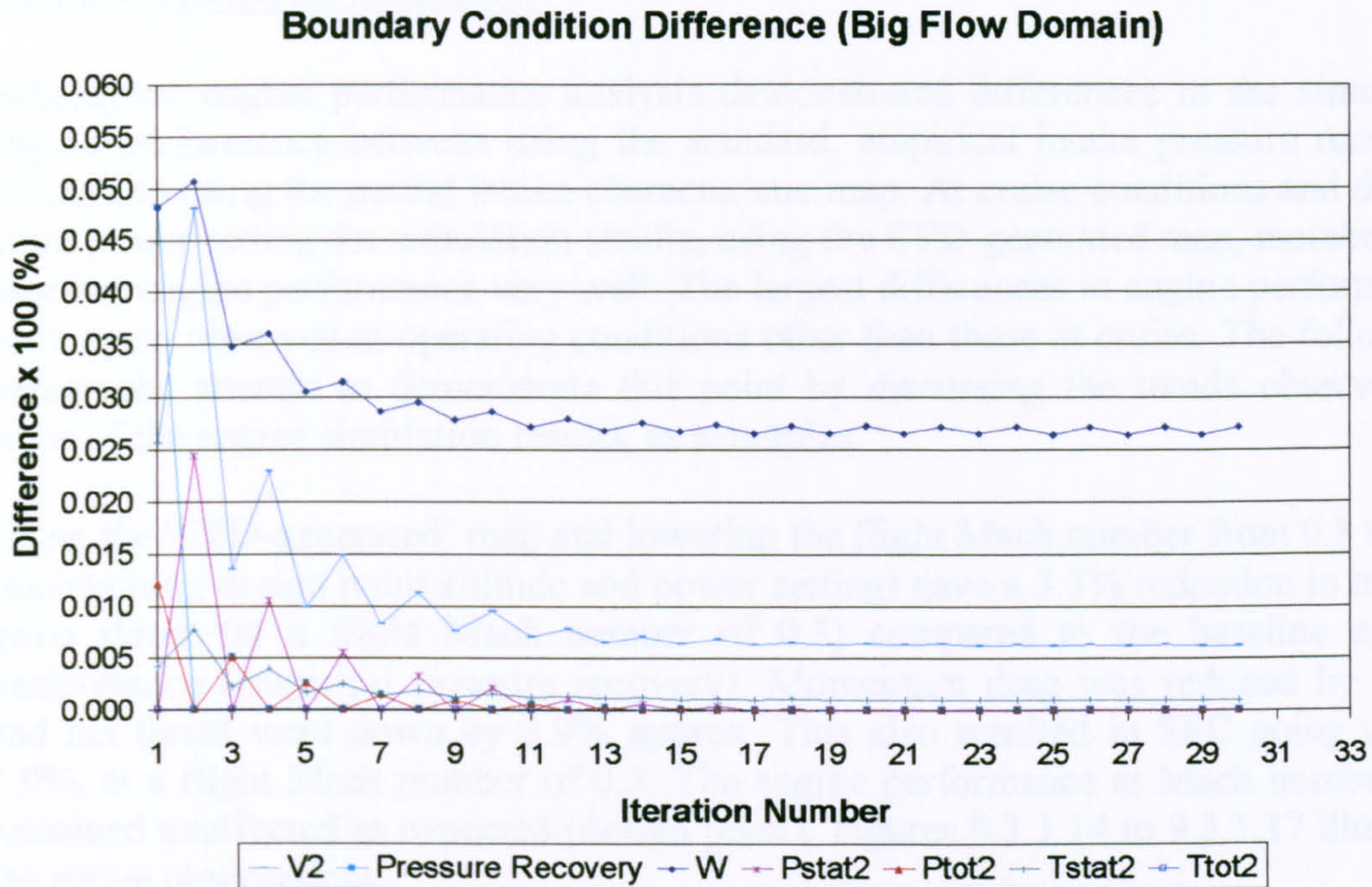


Figure 9.3.1.12: Convergence history using a ‘big’ flow domain

Adjusting in every iteration the outlet static pressure prediction of the OD intake component, to take into account the presence of the fan and its effects on the upstream flow field, improved the relatively large difference in mass flow even further and led to a much faster convergence. For this type of iterative runs all boundary conditions converged after three or four iterations within an acceptable 0.5%. Figure 9.3.1.13 demonstrates the above observation and is representative of the final group of iterative runs for the generation of the map.

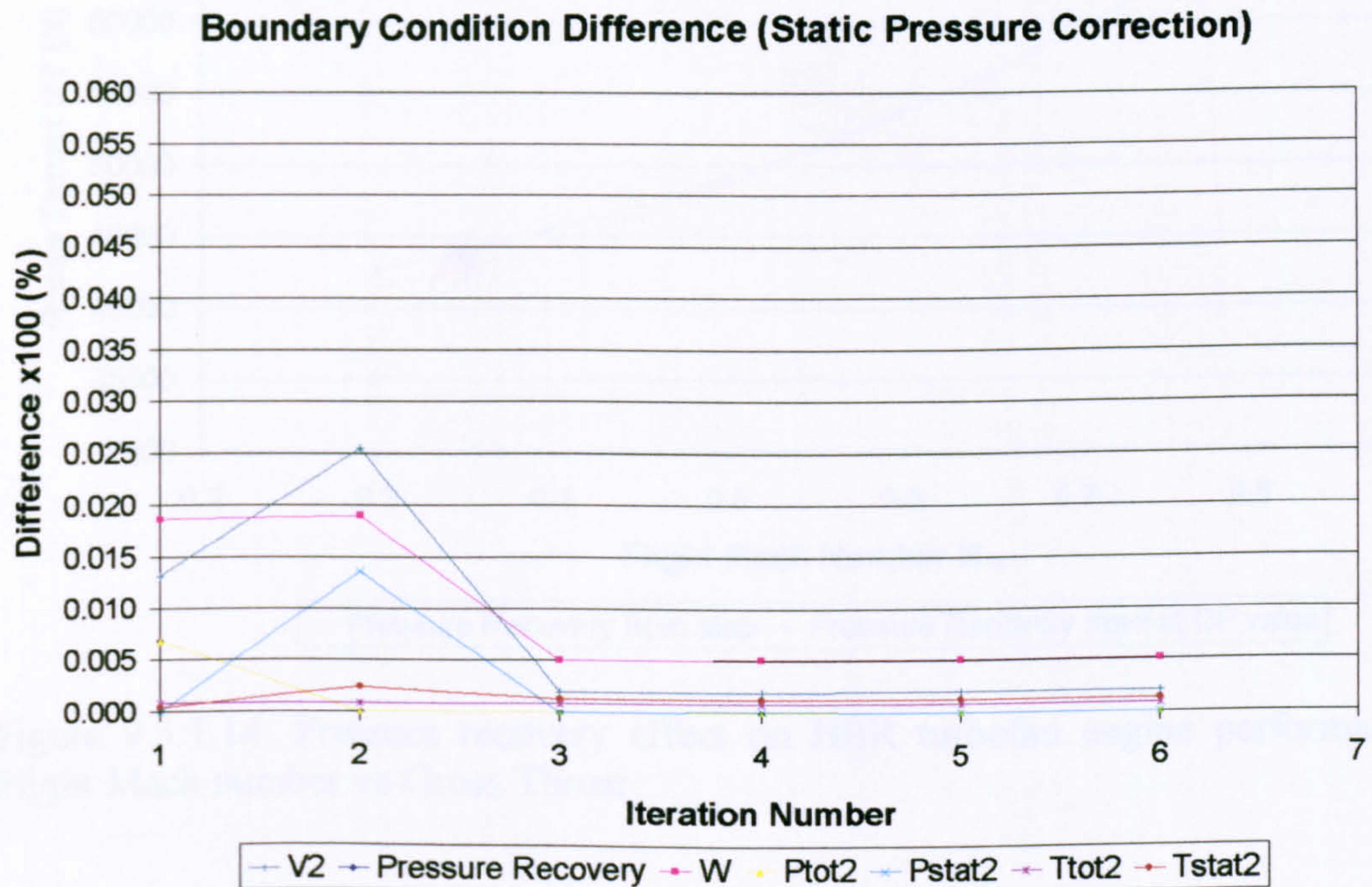


Figure 9.3.1.13: Convergence history using a ‘big’ flow domain and intake outlet static pressure correction



Engine Performance Simulation

Subsequent engine performance analysis demonstrated differences in the simulated engine performance between using the standard, empirical intake pressure recovery values and using the partial intake characteristic map. At cruise conditions and design point power setting the simulation results, using the CFD-generated map, matched the baseline engine performance very well. The largest differences in engine performance were again observed at operating conditions other than those at cruise. The following paragraphs attempt to demonstrate this point by discussing the trends observed in some of the engine simulation results, as examples.

Using the ‘CFD-generated’ map and lowering the flight Mach number from 0.8 to 0.3 (maintaining design point altitude and power setting) gave a 3.3% reduction in engine gross thrust (at a flight Mach number of 0.3) compared to the baseline engine performance (empirical pressure recovery). Momentum drag was reduced by 1.9% and net thrust went down by 3.9% approx. This also resulted in SFC going up by 1.9%, at a flight Mach number of 0.3. The engine performance at Mach number 0.8 remained unaffected as expected (design point). Figures 9.3.1.14 to 9.3.1.17 illustrate the above observations.

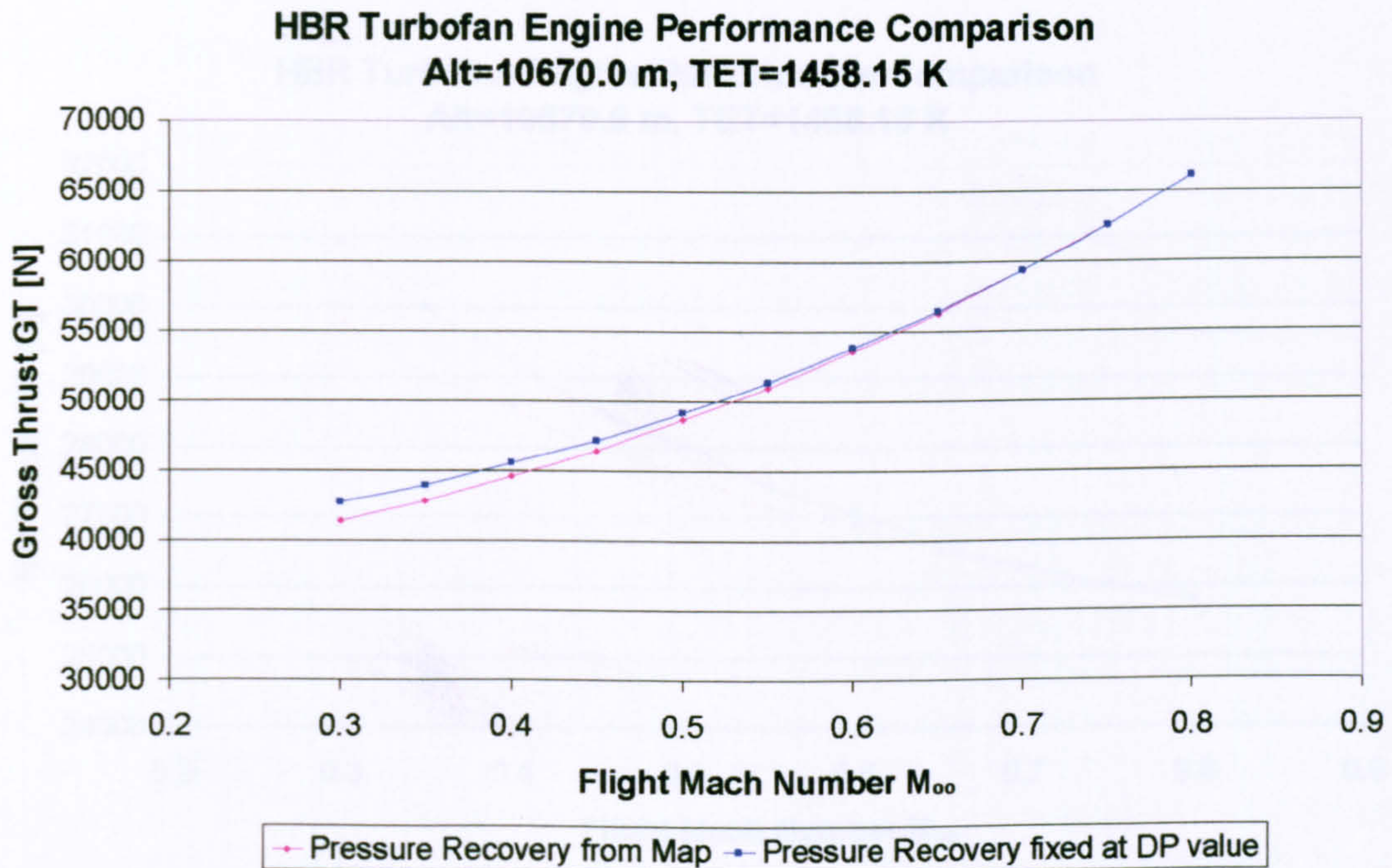


Figure 9.3.1.14: Pressure recovery effect on HBR turbofan engine performance – Flight Mach number vs Gross Thrust



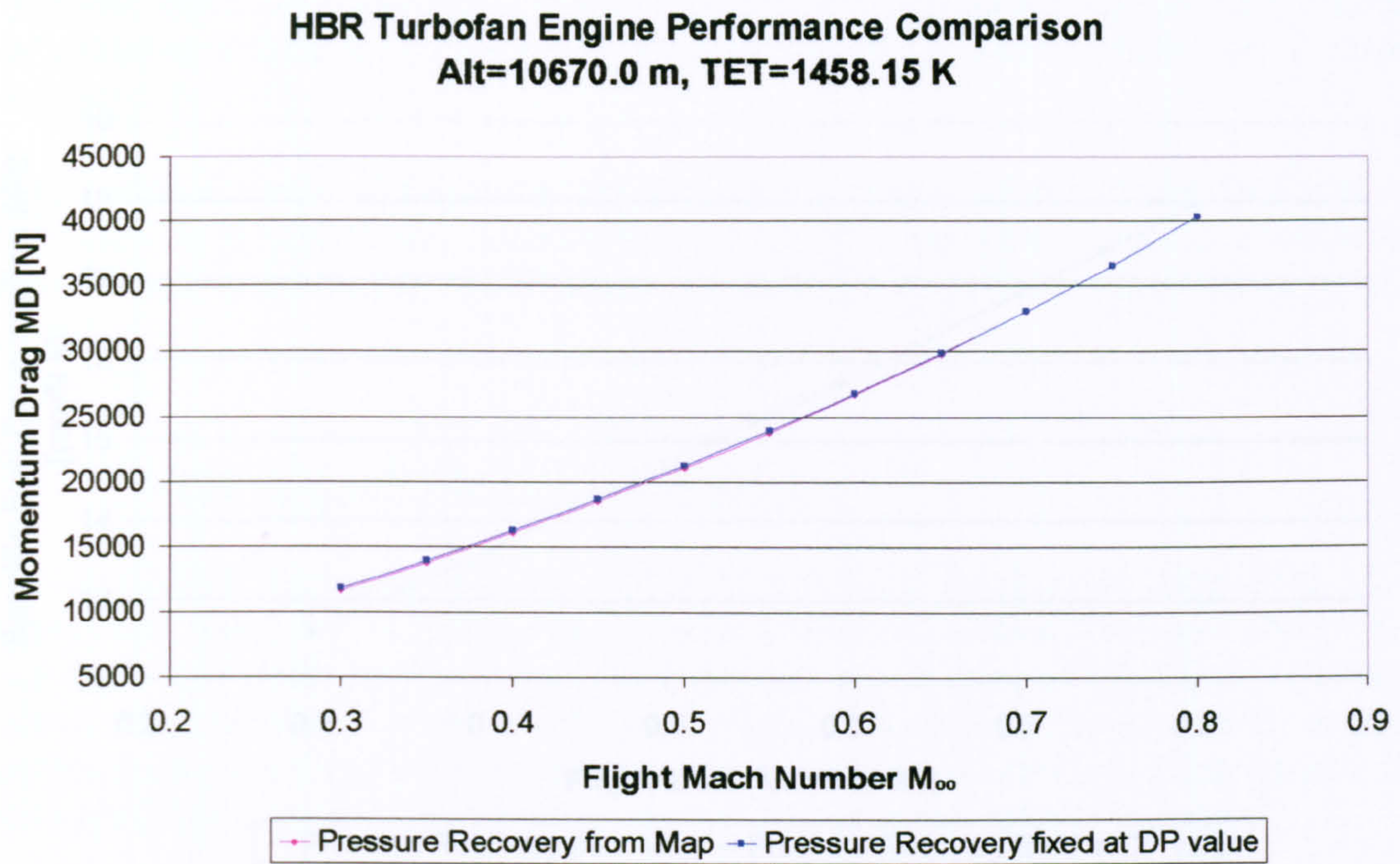


Figure 9.3.1.15: Pressure recovery effect on HBR turbofan engine performance – Flight Mach number vs Momentum Drag

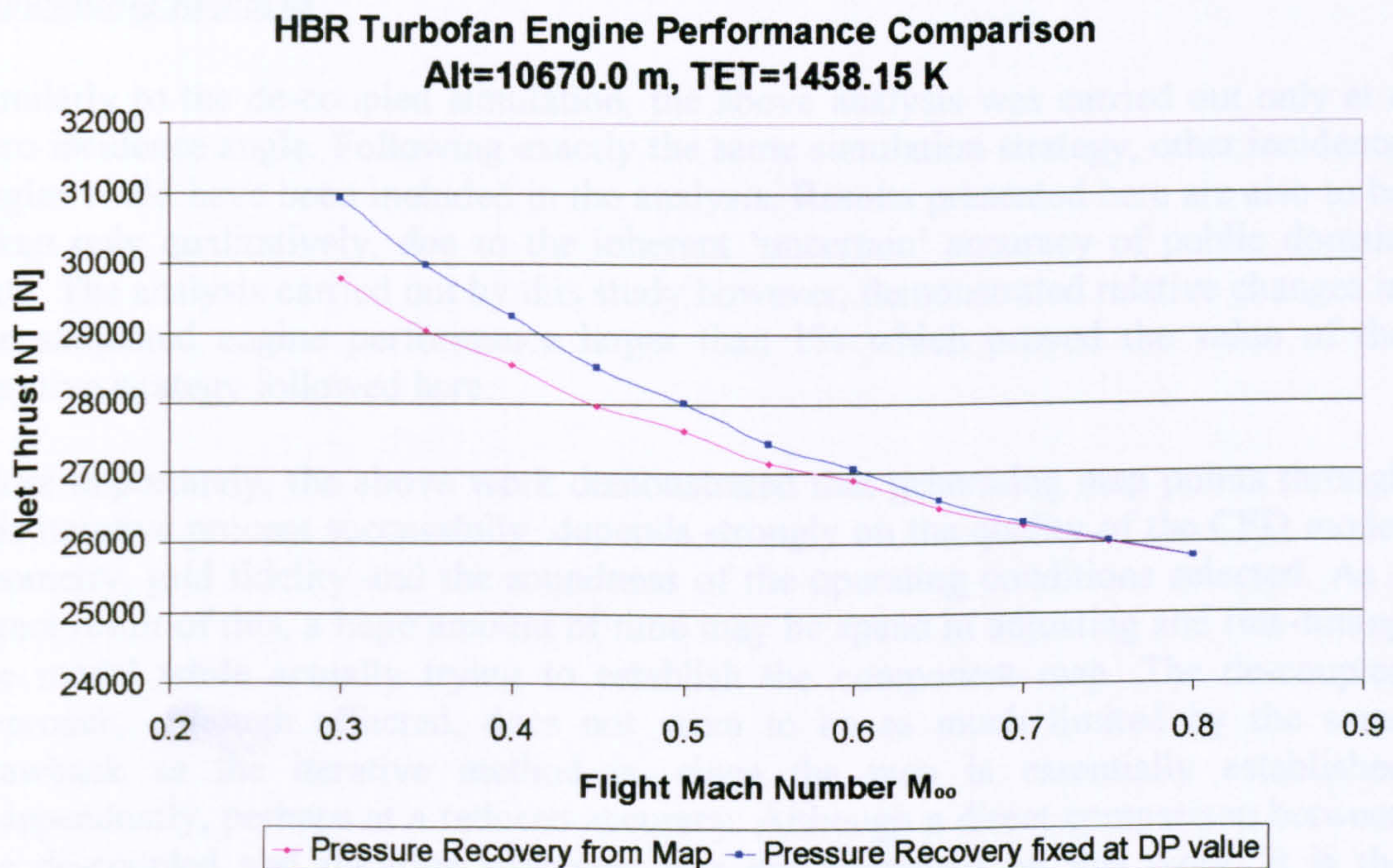


Figure 9.3.1.16: Pressure recovery effect on HBR turbofan engine performance – Flight Mach number vs Net Thrust



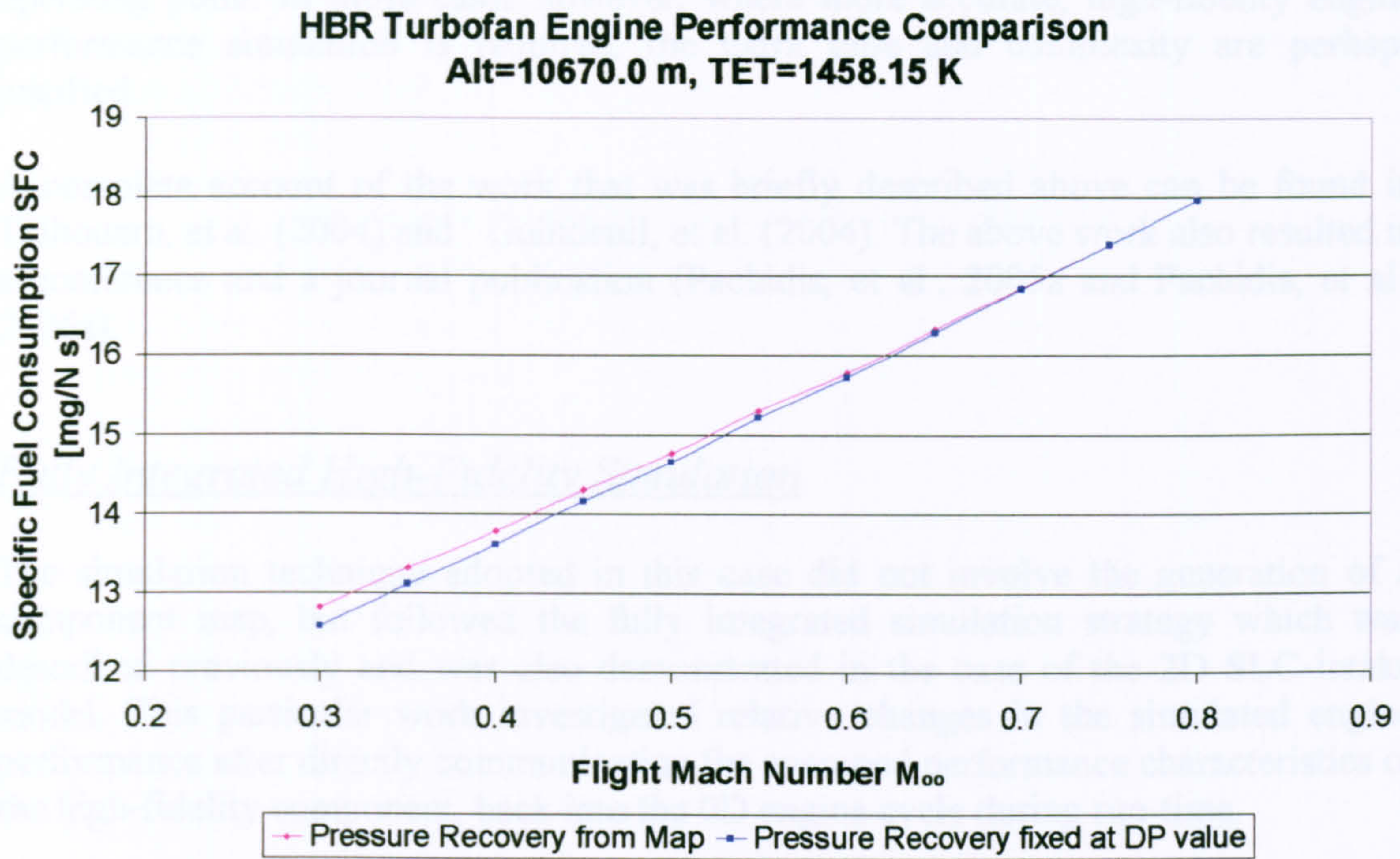


Figure 9.3.1.17: Pressure recovery effect on HBR turbofan engine performance – Flight Mach number vs Specific Fuel Consumption

### Concluding Remarks

Similarly to the de-coupled simulation, the above analysis was carried out only at a zero incidence angle. Following exactly the same simulation strategy, other incidence angles could have been included in the analysis. Results presented here are also to be taken only qualitatively, due to the inherent ‘uncertain’ accuracy of public domain data. The analysis carried out by this study however, demonstrated relative changes in the simulated engine performance larger than 1% which proved the value of the iterative strategy followed here.

More importantly, the above work demonstrated that generating map points through this iterative process successfully, depends strongly on the quality of the CFD model geometry, grid fidelity and the soundness of the operating conditions selected. As a direct result of this, a huge amount of time may be spent in adjusting and fine-tuning the model while actually trying to establish the component map. The de-coupled approach, although affected, does not seem to be as much limited by the same drawback as the iterative method is, since the map is essentially established independently, perhaps at a reduced accuracy. Although a direct comparison between the de-coupled and iterative strategies was not attempted by this work, it is the author’s view that errors arising from the independent generation of the map via the de-coupled approach could in fact be easily treated by appropriate scaling of the map. This needs to be further investigated and demonstrated in the future.

The iterative approach to high-fidelity analysis utilising 3D CFD component models, offers greater accuracy compared to the 2D SLC analysis, at the expense of a much more complex and time consuming process to establish the correct component



operating point. In those cases however, where more accurate, high-fidelity engine performance simulation is required, the extra time and complexity are perhaps justified.

A complete account of the work that was briefly described above can be found in Talhouarn, et al. (2004) and Guindeuil, et al. (2004). The above work also resulted in a conference and a journal publication (Pachidis, et al., 2005a and Pachidis, et al., 2006a).

### **Fully Integrated High-Fidelity Simulation**

The simulation technique adopted in this case did not involve the generation of a component map, but followed the fully integrated simulation strategy which was described previously and was also demonstrated in the case of the 2D SLC intake model. This particular work investigated relative changes in the simulated engine performance after directly communicating the averaged performance characteristics of the high-fidelity component, back into the 0D engine cycle during run-time.

According to the fully integrated approach, the high-fidelity component replaces completely the corresponding 0D representation in the cycle program and communicates directly with the 0D engine model. The high-fidelity component and the 0D cycle communicate with each other by means of inlet and outlet boundary conditions. In this case however, lacking an automatic and explicit interface between the commercial CFD software FLUENT and the in-house PYTHIA software, boundary conditions were exchanged between the two software manually.

During off-design analysis, establishing a converged intake and engine performance involved a much simpler iterative process than before. After selecting engine operating conditions and power setting, the 0D model of the HBR turbofan engine was run in PYTHIA to generate a first set of intake inlet operating conditions which were then used to define inlet boundary conditions in the 3D intake simulation at run-time. More specifically, inlet boundary values for total pressure, total temperature, and static pressure were applied as boundary conditions to the 3D CFD intake model. The 3D CFD intake model was then run several times independently, following a 'trial and error' approach, with different boundary values of outlet static pressure until the calculated mass flow matched the mass flow established by the 0D cycle simulation. Averaged 3D flow solutions, at the outlet of the intake, and especially the pressure recovery, were then communicated back to the cycle analysis for the calculation of the overall engine performance. Obviously, this process had to be repeated several times for every off-design case until the 0D engine cycle reached a thermodynamic balance at the selected engine operating conditions and power setting. This normally took 2 to 4 cycle convergence loops for a reasonably small off-design step size.

### **Convergence**

As mentioned before, the matching of the averaged boundary conditions between the 3D CFD intake model and the 0D flow solutions required for every cycle convergence



loop, the execution of the high-fidelity simulation, several times, following a ‘trial and error’ process. The iterative process was attempted manually in this case, employing a Newton-Raphson convergence procedure.

**Successive Iterations for Mass Flow Agreement**

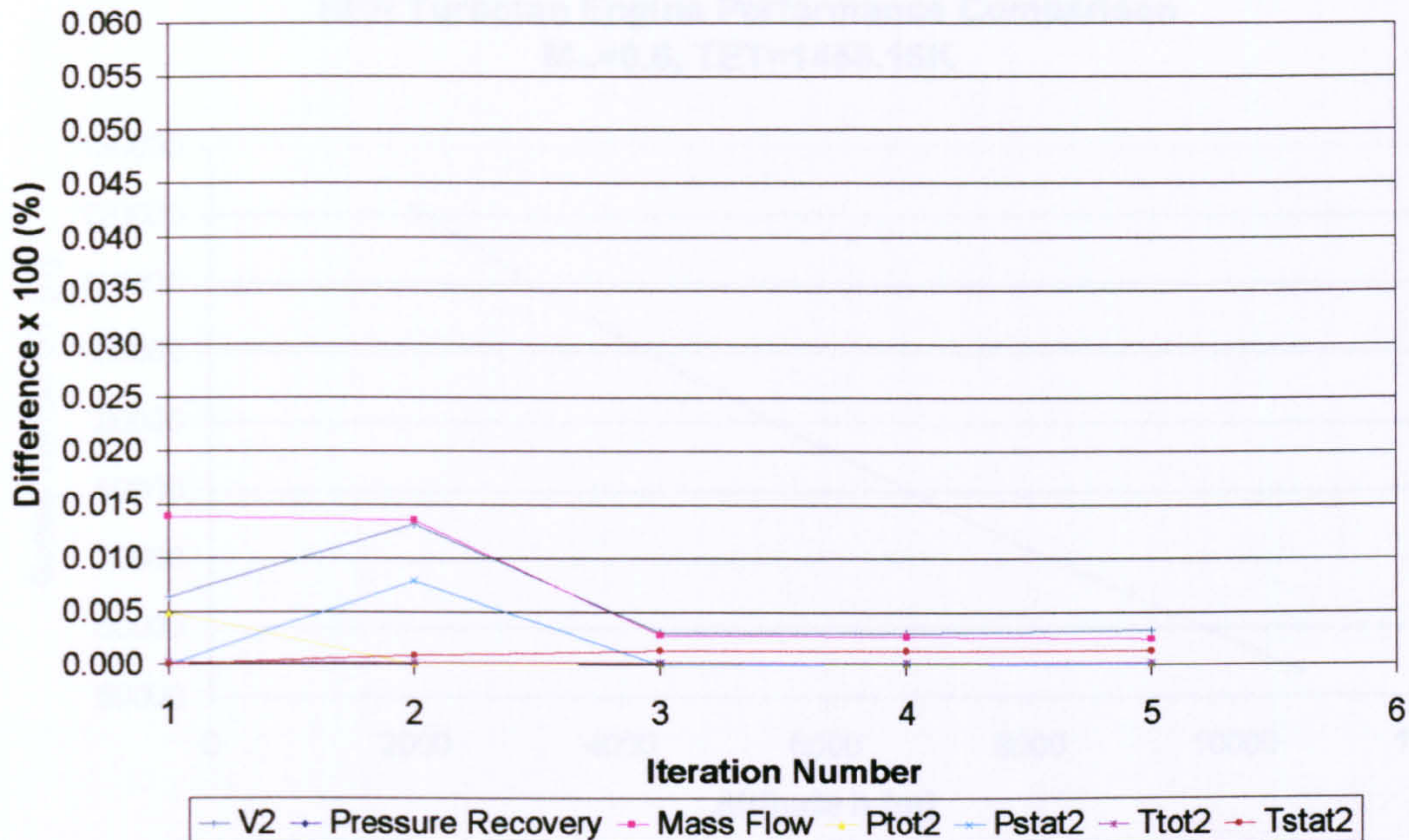


Figure 9.3.1.18: Convergence history using a ‘big’ flow domain for mass flow matching

The simplicity of this particular approach to establishing the intake operating point, together with the fine-tuning of the 3D CFD model and the previous experience gained during the implementation of the iterative simulation strategy, led to faster convergence times in this case. For this kind of simulation, using again a ‘big’ flow domain, boundary conditions reached a reasonable agreement within an acceptable 0.4% after three or four trials. Figure 9.3.1.18 demonstrates the above observation and is representative of this group of high-fidelity simulations during a given cycle convergence loop.

### Engine Performance Simulation

The analysis reported here looked into different operating altitudes for a fixed engine power setting and incidence angle. Varying altitude gave a satisfactory range of different intake inlet operating conditions and allowed for a thorough engine performance comparison. More analytically, the engine’s power setting was kept at the design point value of 1458.15 K TET and incidence angle was kept at 0 degrees. Intake operating points were obtained for a range of altitudes between 10670.0 m (design point value) and 2000.0 m.

Lowering the altitude from 10670.0 m to 2000.0 m, at a constant flight Mach number of 0.6 and TET of 1458.15 K gave a 0.5% reduction in engine gross thrust at 10670.0 m and a 1.2% increase at 2000.0 m compared to the baseline engine performance (empirical pressure recovery). Similarly, momentum drag was reduced by 0.3% at



10670.0 m and increased by 0.7% at 2000.0 m. Net thrust went down by 0.6% at 10670.0 m and up by 2.0% at 2000.0 m approximately. This also resulted in SFC going up by 0.3% at 10670.0 m and down by 1.3% at 2000.0 m. Figures 9.3.1.19 to 9.3.1.22 illustrate the above observations.

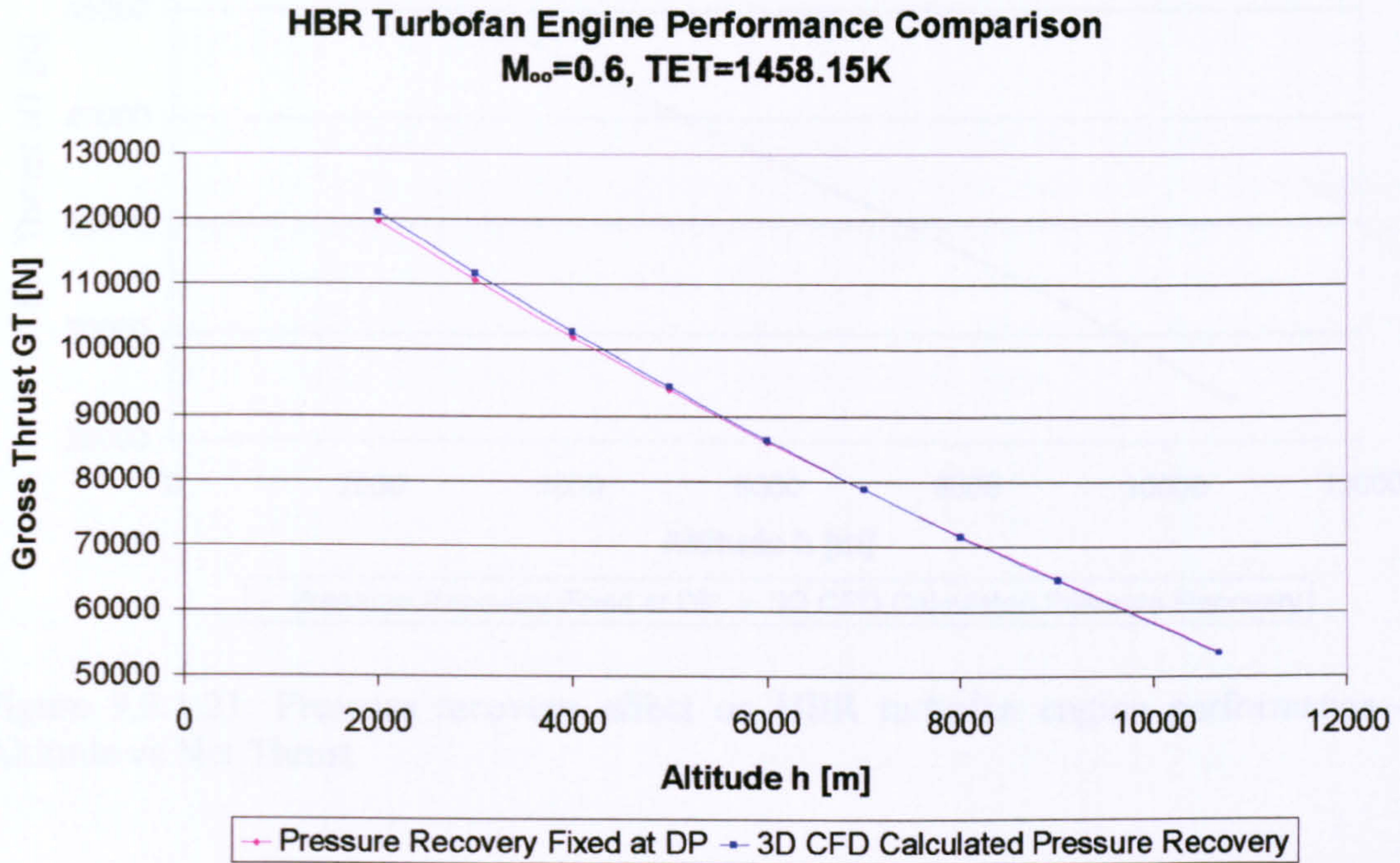


Figure 9.3.1.19: Pressure recovery effect on HBR turbofan engine performance – Altitude vs Gross Thrust

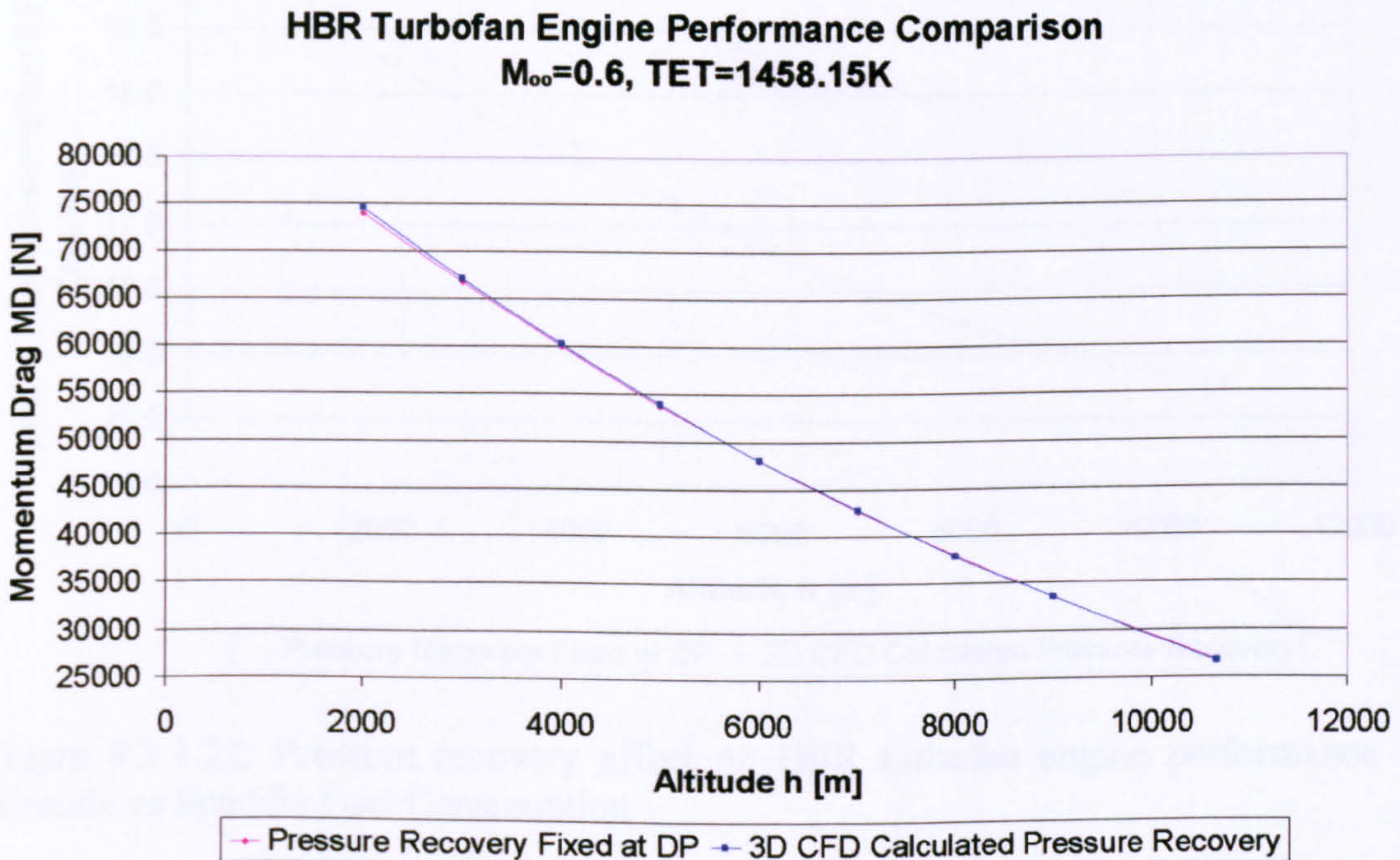


Figure 9.3.1.20: Pressure recovery effect on HBR turbofan engine performance – Altitude vs Momentum Drag



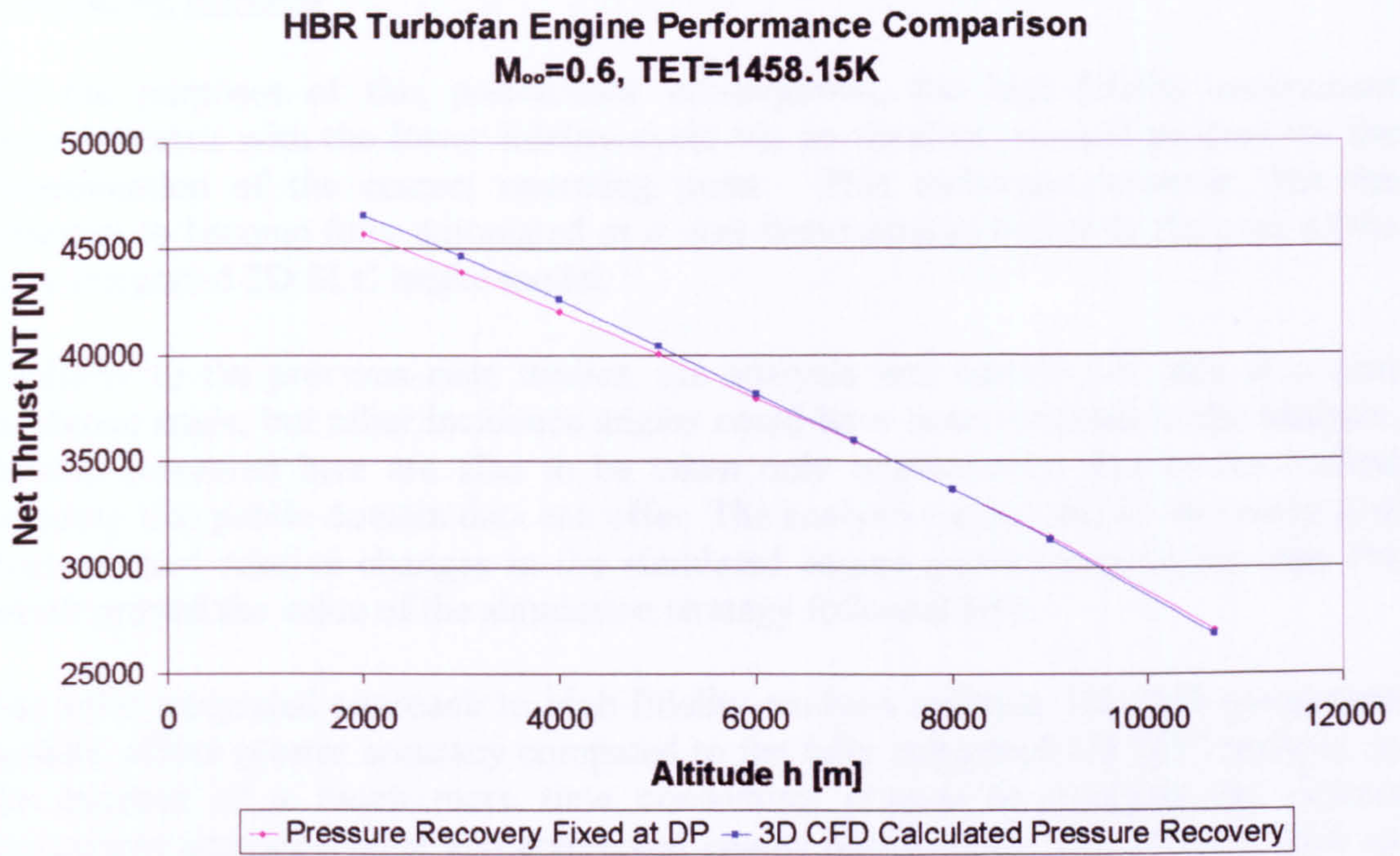


Figure 9.3.1.21: Pressure recovery effect on HBR turbofan engine performance – Altitude vs Net Thrust

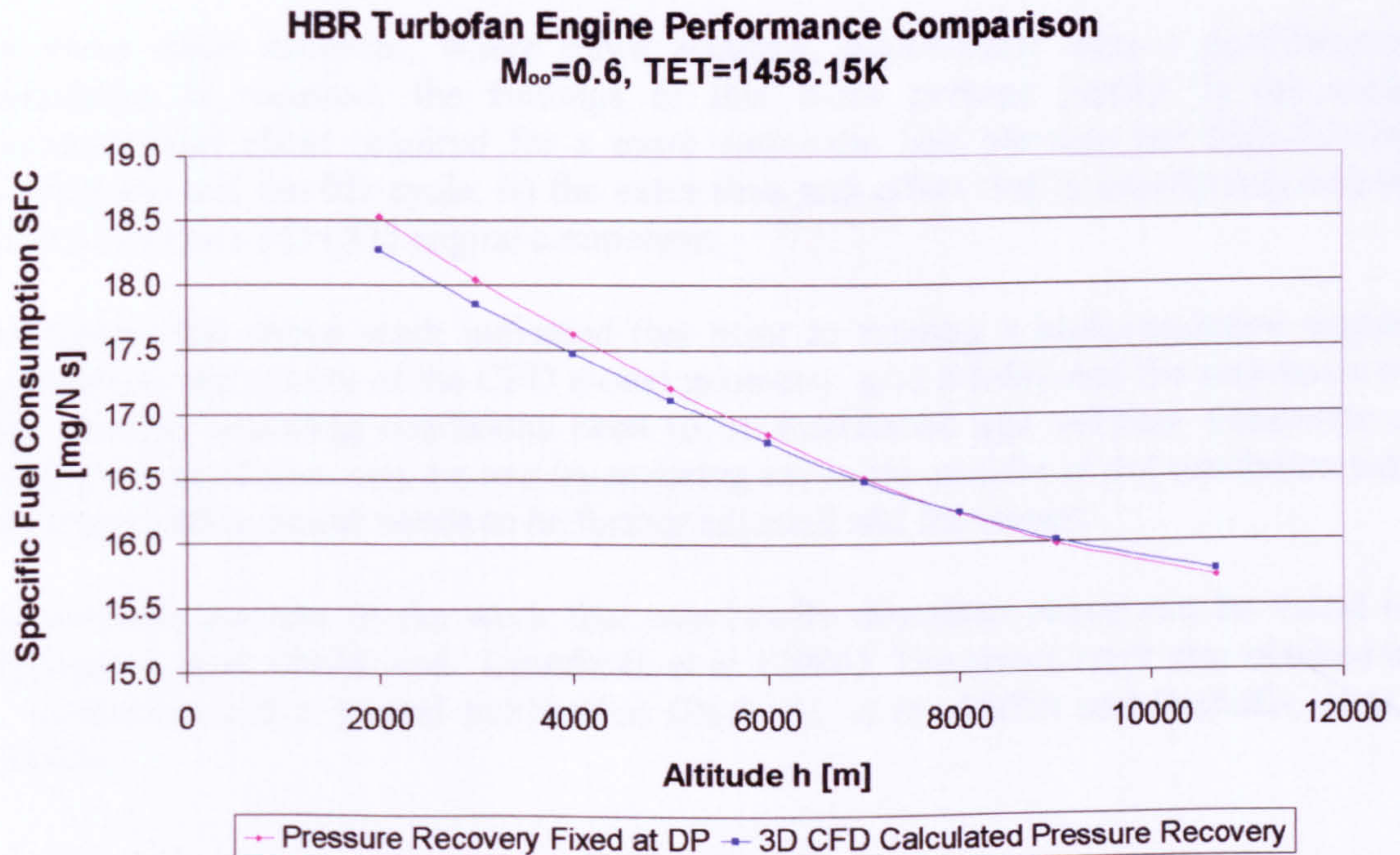


Figure 9.3.1.22: Pressure recovery effect on HBR turbofan engine performance – Altitude vs Specific Fuel Consumption



### Concluding Remarks

For the purposes of this preliminary investigation, the high-fidelity component communicated with the lower fidelity cycle via an iterative, manual process for the determination of the correct operating point. This technique however, has the potential to become fully automated as it was demonstrated before in the case of the fully integrated 2D SLC intake model.

Similarly to the previous case studies, the analysis was carried out only at a zero incidence angle, but other incidence angles could have been included in the analysis. Results presented here are also to be taken only qualitatively, due to the limited accuracy that public domain data can offer. The analysis carried out by this study also demonstrated relative changes in the simulated engine performance larger than 1% which proved the value of the simulation strategy followed here.

The fully integrated approach to high-fidelity analysis utilising 3D CFD component models, offers greater accuracy compared to the fully integrated 2D SLC analysis, at the expense of a much more time consuming process to establish the correct component operating point and converged engine performance. Given that it took an average of 2 to 3 hours to run a steady 3D CFD simulation in this case and that 2 to 4 cycle convergence loops are normally required to establish a thermodynamic balance at a given off-design condition, the fully integrated simulation strategy certainly involved in this case very long execution times.

In those cases however, where more accurate, high-fidelity engine performance simulation is required, the findings of this work perhaps justify: i) the extra computational effort required for a more automatic link between the high-fidelity component and the 0D cycle, ii) the extra time and effort that is usually required to create and run a 3D CFD engine component.

Moreover, the above work indicated that prior to running a high-resolution engine simulation, the quality of the CFD model geometry, grid fidelity and the soundness of the selected operating conditions need to be established and verified. Otherwise a huge amount of time may be lost by realising say in the middle of the simulation that the high-fidelity model needs to be further adjusted and fine-tuned.

A complete account of the work that was briefly described above can be found in Talhouarn, et al. (2004) and Guindeuil, et al. (2004). The above work also resulted in a conference and a journal publication (Pachidis, et al., 2005b and Pachidis, et al., 2006b).

### ***9.3.2. Effect of 3D CFD Fan Inlet Total Pressure Distortion***

As discussed previously in the case of the 2D SLC compressor simulation, the usual approach to compressor design considers uniform inlet flow characteristics. Especially in aircraft applications, the inlet flow is quite often non uniform, and this can result in large changes in compressor and engine performance. Complex inlet duct configurations and extreme flight conditions can amplify this phenomenon particularly in military engines.



The second case study looked into the effects of inlet total pressure distortion on compressor and engine performance by using a 0D model of an existing two-spool, LBR, military turbofan engine and a 3D CFD model of the engine's LP compressor. The main objective of this work was the definition of a simulation strategy utilizing a 3D CFD tool that could carry out compressor performance analysis at high-fidelity, and could subsequently be used in whole-engine performance simulations, at an affordable computational cost. Under the technical leadership of the author and with the assistance of MSc students, four different investigations were conducted within the time frame of two years, in order to examine extensively the effects of different types, extents and frequencies of inlet total pressure distortion on compressor and engine performance.

### Introduction

As mentioned above, one of the principal assumptions made in the design of a compressor or a fan is the uniformity of the inlet flow. Although engine intakes are usually designed to deliver reasonably uniform conditions at the fan inlet, in real engine operations the inlet flow is quite often distorted, and the extent of flow non-uniformities can be related to the particular application of the engine and its geometry. Bigger flow distortions are usually expected in military applications and in supersonic flight.

The most common type of distortion is the total pressure distortion which mainly affects the compressor and particularly the low-pressure compressor or fan of the engine. A lot of effort has been dedicated over the years to the study of its causes and effects. Nowadays it is believed that CFD can give important savings in research and development costs and time, by bringing the study of inlet distortion into the very early phases of the design process. Since the first 3D simulation of an isolated rotor (NASA rotor 67) the use of CFD for studying complex turbomachinery flows has increased exponentially and examples of successful simulations of complex geometries, such as transonic fans, under uniform inlet conditions have become quite common (Walker, 1993 and Jennions and Turner, 1993). Another example is that of Hirai, et al. (1997) who managed to perform the complete simulation of a whole compressor rotor under distorted conditions by linking together 162 processors for a total main memory of 41 GB. A further example is given by Davis, et al. (2002) who studied the effects of steady and unsteady inlet flow distortion with CFD obtaining a good match with experimental data.

This particular study attempted to tackle the problem of inlet flow distortion modelling by utilising practical computational resources. One of the aims of this study was to perform a CFD simulation of a transonic fan under clean and distorted conditions, by using a personal computer with a common RAM memory of 1 GB, and within a reasonable amount of time. For the purposes of this investigation, a transonic, three-stage fan was especially designed and modelled in three-dimensions using CFD. In order to minimise the computational demand, the performance of the first stage only was analyzed for a single rotor-stator blade passage. Simulations were carried out for operating conditions along several constant speed lines and for several different magnitudes and types of inlet total pressure distortion (namely radial, circumferential and stratified). The main objective here was to fully explore the



potentials of the high-fidelity simulation strategies discussed before, by looking into the effects of different levels, extents and frequencies of distortion on compressor and engine performance.

More specifically, the work of Charalambous (2003) was focused on the effects of different frequencies of distortion on compressor performance, Iurisci (2003) investigated the effects of different types and extents of distortion and Ghisu (2003) studied the effects of different magnitudes of distortion. Finally, Melloni (2004) investigated the effects of radial and stratified compressor inlet total pressure distortion in the context of the whole engine performance.

Simulation Tools

This study utilized two simulation software: i) a 0D gas turbine modelling and performance simulation code – PYTHIA, and ii) the commercial CFD package CFX-TASCflow/TurboGrid, developed by AEA Technology.

For the purposes of this investigation an engine model was built in PYTHIA based on the overall configuration and performance of the EJ200. This is an existing two-shaft, LBR, mixed-exhaust, military turbofan engine (Figure 9.3.2.1).

PYTHIA - 0D Engine Cycle Simulation

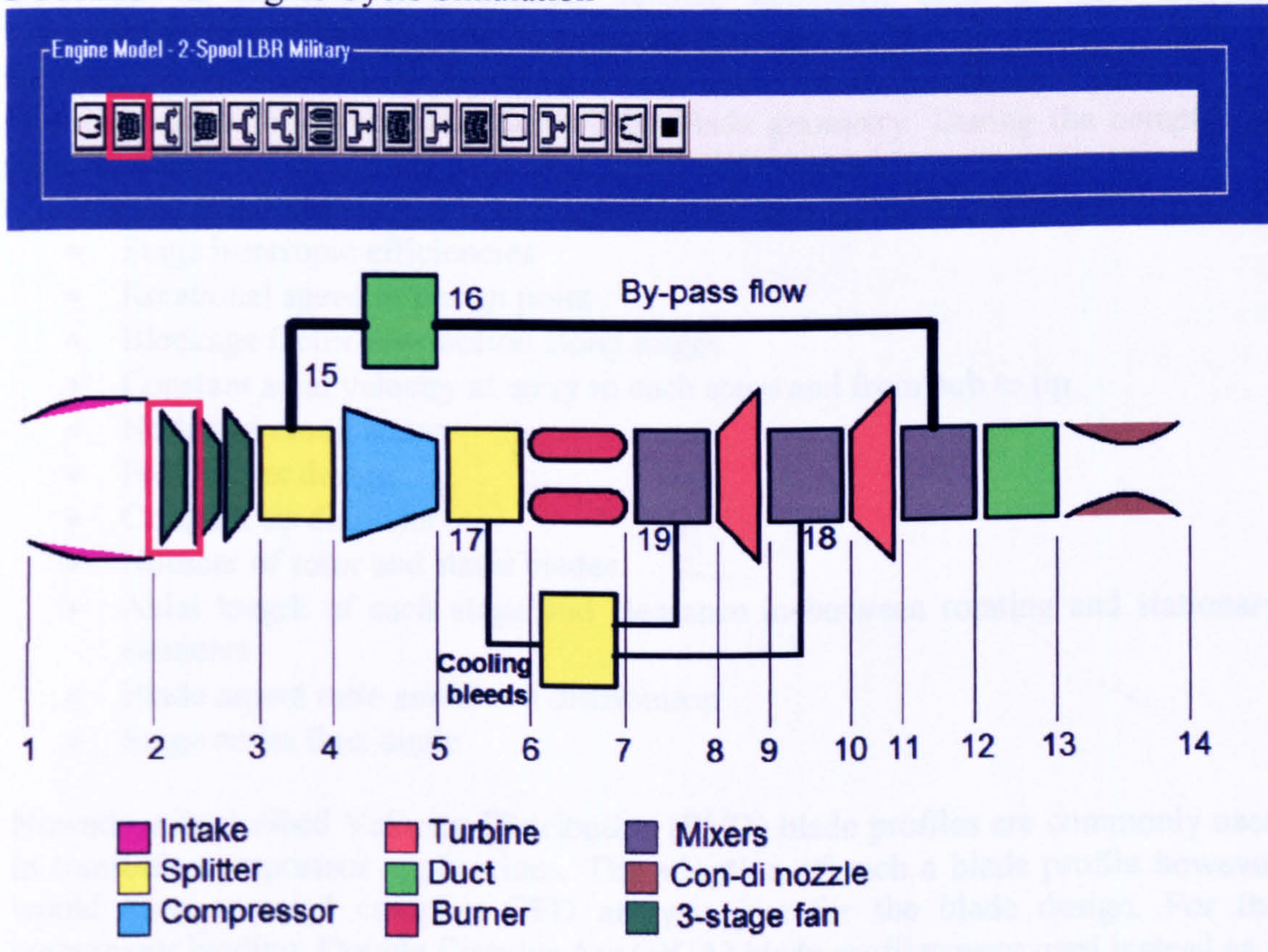


Figure 9.3.2.1: Schematic representation of PYTHIA’s model of a two-spool, LBR, mixed-exhaust, military turbofan engine



The modelling of the engine was based on limited public domain data and the author's best judgement. The overall design performance of the engine is illustrated in Table 9.3.2.1. Other engine performance parameters can be found in PYTHIA's engine input data files which have been included in this thesis as *Appendix J - PYTHIA Engine Input Data Files*.

OPR		25.0:1.0
BPR		0.4:1.0
W	[kg/sec]	70.0 - 75.0
TET	[K]	1800.0
GT with AB	[kN]	90.0
GT w/o AB	[kN]	60.0
SFC	[mg/N sec]	23.0

Table 9.3.2.1: Two-shaft, LBR, military turbofan engine design performance parameters

The three-stage LP compressor of the engine was modelled in PYTHIA using three COMPRE BRICKS, linked together in terms of rotational speed and work requirement, in order to simulate the performance of each stage separately. This is illustrated in Figure 9.3.2.1. The geometry and 3D CFD model of the investigated three-stage LP compressor (Figure 9.3.2.2), had to be specifically developed for this study due to the lack of published, detailed geometric data for this particular compressor. The design of the compressor was accomplished by using physical relations, such as the continuity equation and Euler's turbomachinery equations, and empirical rules for the optimisation of the blade geometry. During the compressor design process the following parameters had to be assumed:

- Stage isentropic efficiencies
- Rotational speed at design point
- Blockage factor distribution along stages
- Constant axial velocity at entry to each stage and from hub to tip
- No losses along stator
- Free vortex design
- Constant tip diameter
- Number of rotor and stator blades
- Axial length of each stage and clearance in between rotating and stationary elements
- Blade aspect ratio and chord distribution
- Stage outlet flow angle

Nowadays Prescribed Velocity Distribution (PVD) blade profiles are commonly used in transonic compressor applications. The adoption of such a blade profile however would have required complex CFD analysis just for the blade design. For the compressor blading, Double Circular Arc (DCA) blade profiles were used instead as a compromise between a simplified design process and a realistic compressor performance in the transonic flow regime between 0.8 and 1.2 Mach.



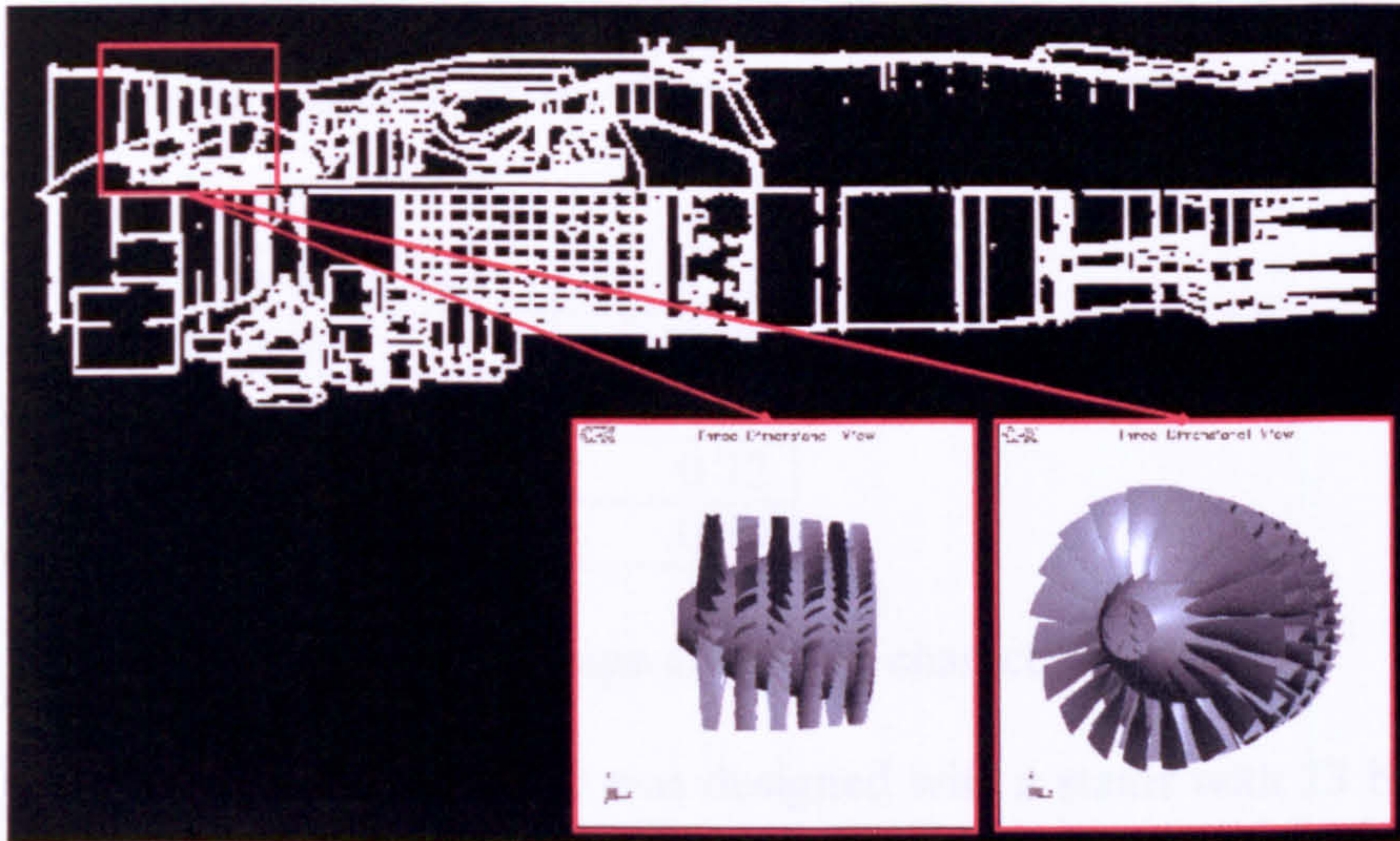


Figure 9.3.2.2: EJ200 2D schematic diagram (courtesy of MTU) and 3D CFD LP compressor model

The compressor performance requirements were obtained by carrying out PYTHIA 0D simulations of the performance of the engine at seal level – take off conditions and cruise conditions where the design point of the engine was (taken at 11000.0 m of altitude and at a flight Mach number of 1.2). More analytically, designing the three-stage LP compressor geometry involved an iterative process. After establishing the overall engine performance from PYTHIA's 0D solutions, and also the operating conditions of the LP compressor at design point and take-off, a compressor preliminary design exercise took place using Cranfield's CASSANDRA software for turbomachinery. Based on the outcome of the preliminary design a 3D CFD compressor geometry was created to meet the same performance requirements. Fine tuning the model at design point involved an iterative process where small changes and adjustments had to be done to the original design until the averaged, 3D CFD compressor performance matched the 0D cycle predictions. The 0D analysis carried out alongside the 3D CFD simulations resulted in a LP compressor design with a sea level mass flow of 72 kg/s, at a pressure ratio of 4.2 and rotational speed of 12000.0 rpm.

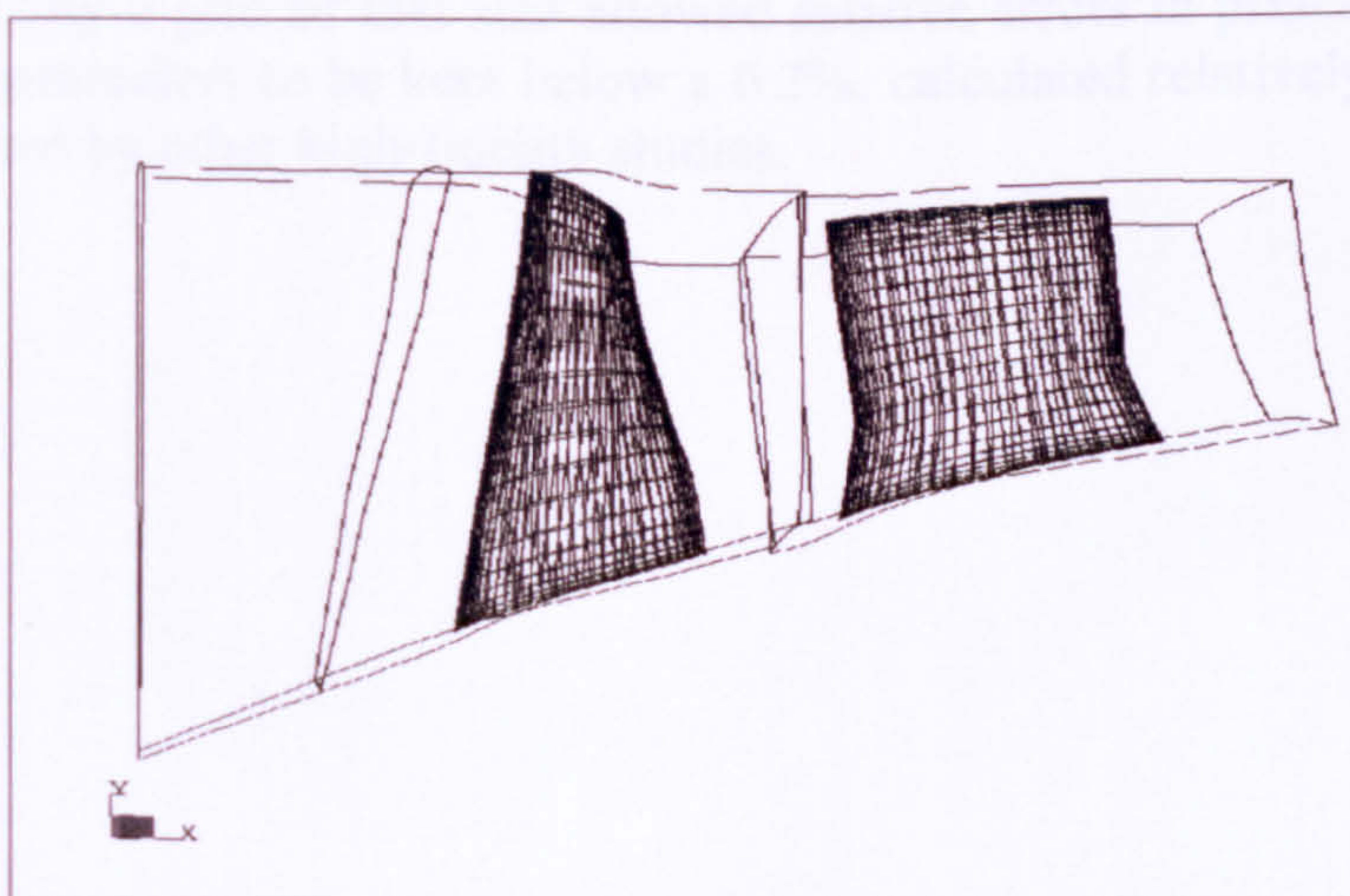


Figure 9.3.2.3: Meridional view of the first stage of the LP compressor



At design point, the first stage pressure ratio was 1.72 and the isentropic efficiency 0.88. The geometric features of the first stage (Figure 9.3.2.3) are shown in the following table:

Rotor tip relative Mach number	1.63
Rotor blade aspect ratio	2.00
Stator blade aspect ratio	1.80
Rotor space to chord ratio	0.72
Stator space to chord ratio	0.80

Table 9.3.2.2: LP compressor first stage geometric characteristics

The first stage of the LP compressor was designed with a stator with 23 blades and a rotor with 19 blades. Further details on the design process and on the final compressor characteristics are reported in Ghisu (2003), Iurisci (2003) and Charalambous (2003).

In this study the computational mesh was created using the commercial software CFX-TurboGrid. This software tool allows the creation of only one blade row (either rotor or stator) at a time. The creation of multi-row grids is done directly within the flow solver by attaching together different single-row grids. TurboGrid is particularly suitable for the generation of structured, hexahedral meshes for turbomachinery applications. A structured grid topology, by comparison with an unstructured one, allows a better alignment of the nodes which then decreases the memory requirement. However, a structured grid needs careful handling when applied to complex geometries, because of the proper alignment of grid points that is required. This apparent inadequacy for complex geometries can be overcome by the adoption of a multi-block topology. In the context of this work, a structured mesh in a multi-block topology was created due to the complexity of the flow domain involved in this study.

A grid independence study was conducted at design point conditions in order to establish the optimum number of grid points for a reasonable accuracy within a realistic simulation time. This led to the adoption of a grid consisting of 89 points in the meridional direction, 32 in the tangential one and 24 in the span wise direction (in total 68000.0 points approximately per passage for each blade row, Figures 9.3.2.4 to 9.3.2.6). Adopting a grid of that size allowed relative errors in principal compressor performance parameters to be kept below a 0.2%, calculated relatively to a 200000.0 grid size adopted by other high-fidelity studies.



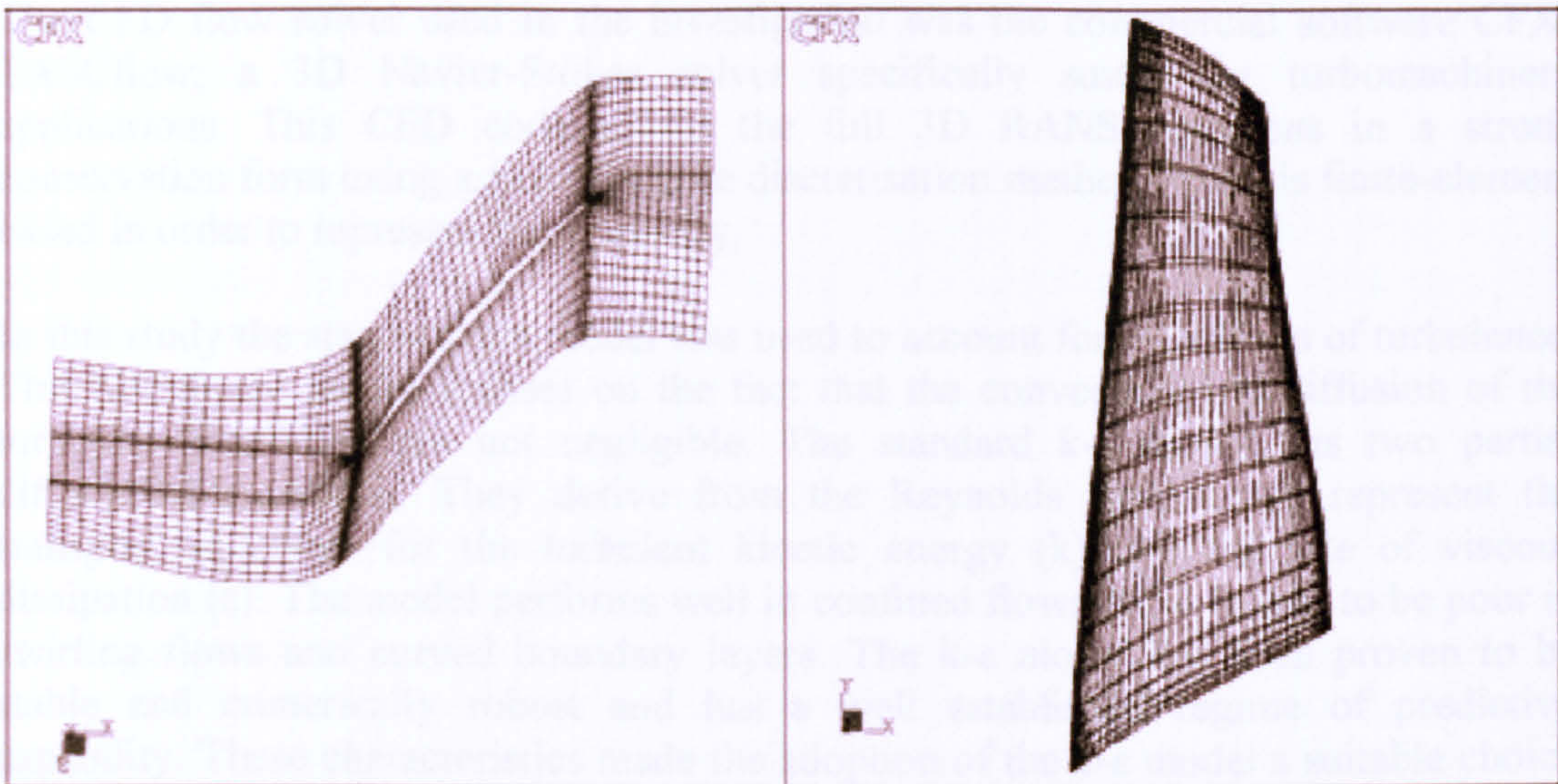


Figure 9.3.2.4: LP compressor first stage rotor computational mesh

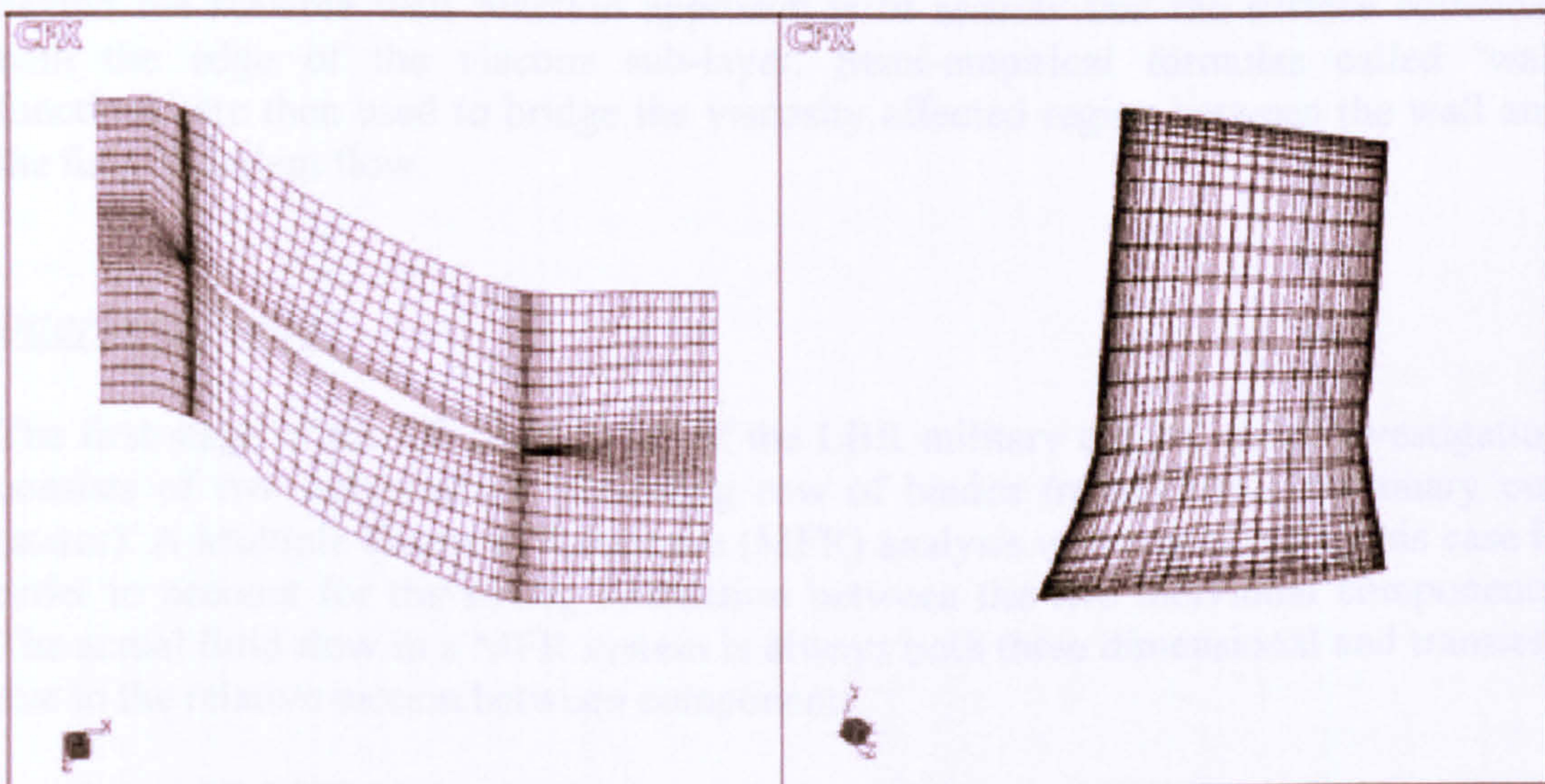


Figure 9.3.2.5: LP compressor first stage stator computational mesh

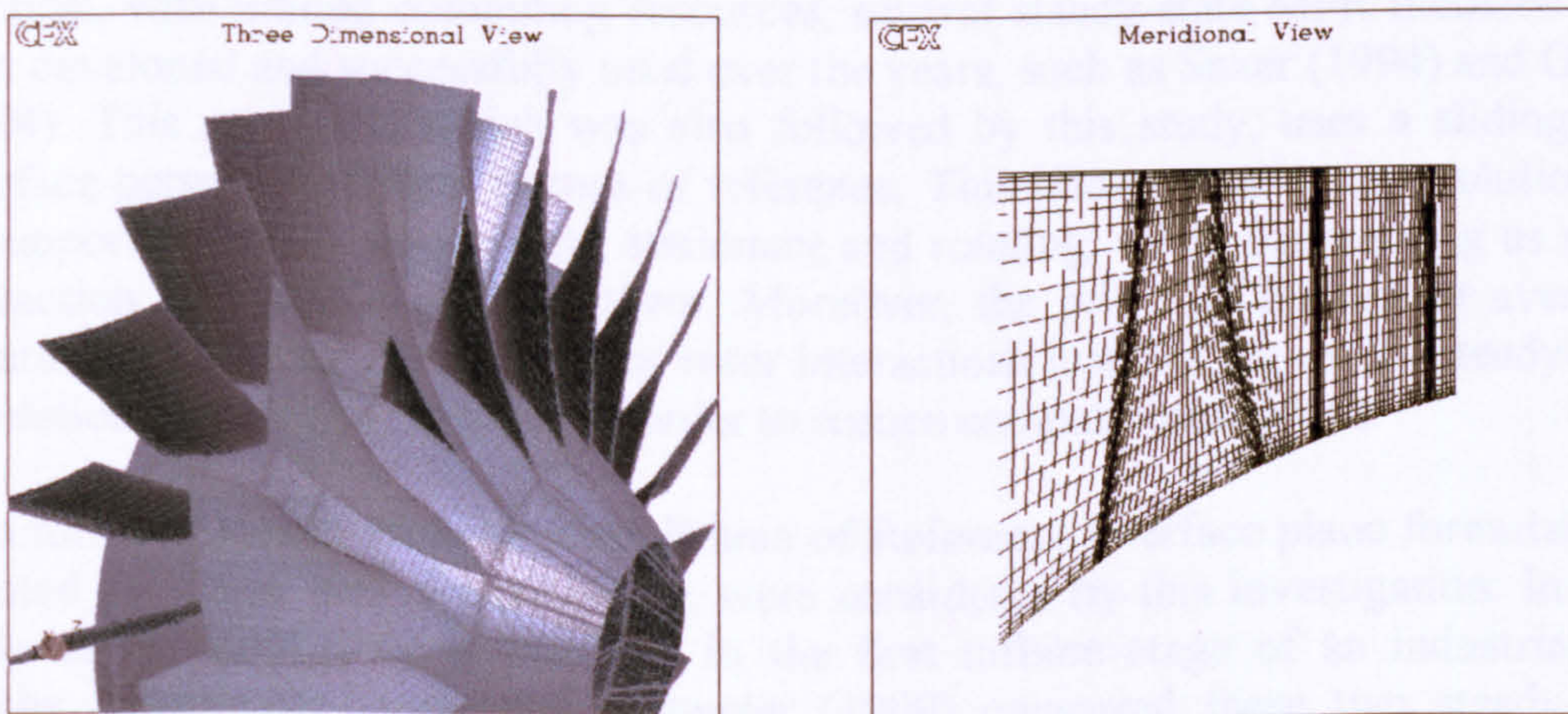


Figure 9.3.2.6: LP compressor first stage geometry and computational mesh



The CFD flow solver used in the investigation was the commercial software CFX-TASCflow, a 3D Navier-Stokes solver specifically suited for turbomachinery applications. This CFD code solves the full 3D RANS equations in a strong conservation form using a finite volume discretisation method which is finite-element based in order to represent the geometry.

In this study the standard  $k$ - $\epsilon$  model was used to account for the effects of turbulence. This turbulence model focuses on the fact that the convection and diffusion of the turbulent properties are not negligible. The standard  $k$ - $\epsilon$  model has two partial differential equations. They derive from the Reynolds system and represent the transport equations for the turbulent kinetic energy ( $k$ ) and the rate of viscous dissipation ( $\epsilon$ ). The model performs well in confined flows but it is said to be poor in swirling flows and curved boundary layers. The  $k$ - $\epsilon$  model has been proven to be stable and numerically robust and has a well established regime of predictive capability. These characteristics made the adoption of the  $k$ - $\epsilon$  model a suitable choice for the qualitative CFD simulation carried out in this study. Within CFX-TASCflow, the  $k$ - $\epsilon$  model uses the so called 'scalable wall function' approach. The basic idea behind the scalable wall function approach is to assume that the surface coincides with the edge of the viscous sub-layer. Semi-empirical formulas called 'wall functions' are then used to bridge the viscosity affected region between the wall and the fully turbulent flow.

### Interface Plane

The first stage of the LP compressor of the LBR military engine under investigation consists of two components, a rotating row of blades (rotor) and a stationary one (stator). A Multiple Frame of Reference (MFR) analysis was conducted in this case in order to account for the strong interaction between the two individual components. The actual fluid flow in a MFR system is always both three dimensional and transient due to the relative motion between components.

An unsteady MFR analysis presents a large increase in computational demand compared to a single component steady-state analysis. In order to make MFR analysis practical, with limited computing resources, several steady-state MFR methods have been developed and successfully used over the years, such as Saxer (1994) and Gallus (1994). This approach, which was also followed by this study, uses a sliding grid interface between different frames of reference. This allows steady state solutions to be supported in each component, stationary and rotating, while maintaining as much interaction as possible between them. Moreover, the principal interest in averaged quantities and not in unsteady stator-rotor interactions justifies the use of steady-state simulations with a mixing plane in order to reduce computational effort.

Two forms of steady-state Multiple Frame of Reference interface plane formulations, denoted as 'stage' and 'frozen rotor', were considered by this investigation. In their study about stator-rotor interactions in the first turbine stage of an industrial gas turbine, Hoyningen-Huene and Hermeler (1999) compared these two steady-state approaches against an unsteady calculation performed using the transient sliding interface option of the CFX-TASCflow solver. They found that the pressure



distributions around the rotor and in the downstream section of the stator could be predicted very well by the steady types of calculation.

In a stage interface, circumferential averaging occurs as the flow crosses the interface. This approach, also called 'mixing plane' interface, averages the flow in the circumferential direction while maintaining the meridional plane variation. This enables single passages to be analyzed independently of the pitch change across the interface, contributing therefore to the reduction in computational cost.

In a frozen rotor interface, the frame change occurs as the flow crosses the interface without imposing any circumferential averaging. This formulation of the MFR interface plane is consequently commonly described as corresponding to a numerically transparent interface. In frozen rotor interfaces, the relative pitch-wise position of the two components remains fixed for the entire simulation (a quasi-steady approximation where the wake/core profile is preserved across the interface). This means that the flow can freely re-circulate across the interface, thus enabling local flow features to be transported across the sliding interface. The flow field obtained from such a simulation corresponds to a snapshot of the dynamic interaction process and is hence, nearly equivalent to the situation where the rotor angular motion is frozen.

In TASCflow, the frozen rotor method is often employed as the starting point for a transient simulation or as a method of investigation of a particular flow condition regarding the relative pitch-wise positioning of two adjacent blade rows. The ability to examine the effects of the pitch-wise positioning of rotors and stators enables the investigation of aspects of unsteady interaction, such as the impingement of upstream wakes onto downstream components, while incurring steady-state simulation costs.

Despite introducing an approximation to the simulation, this preliminary investigation adopted the mixing plane type of interface between rotor and stator in order to keep simulation times to a minimum. Although it was acknowledged from the beginning that the effects of stratified and circumferential distortions could be underestimated in the stator, this was accepted as a reasonable compromise and in view of a qualitative type of analysis (relative trends would still be captured due to the rotor determining a large percentage of the stage's overall performance).

### Boundary Conditions

Solid walls for all 3D CFD simulations, i.e. blade surfaces and annulus walls, were assumed to be adiabatic and perfectly smooth. For the clean inlet simulations, rotational speed, direction of flow, total pressure and total temperature were used as boundary conditions at the inflow. To ensure stable conditions at the rotor face, all boundary conditions were set one blade cord length upstream of the inlet of the stage (Figure 9.3.2.7). Flow properties were checked at the stage inlet to confirm that between the imposed boundary conditions and the inlet of the stage, average values of total pressure and total temperature did not change considerably.



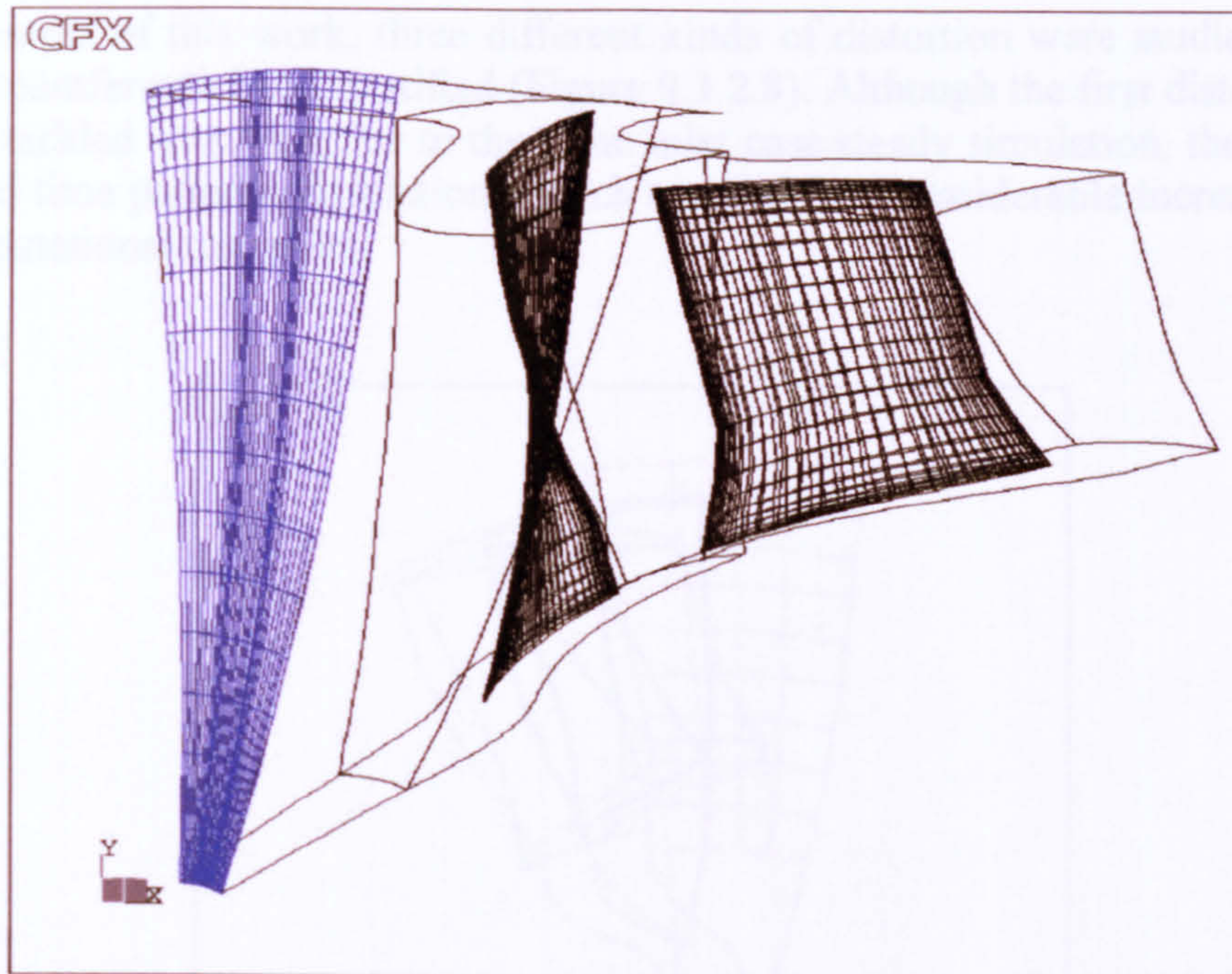


Figure 9.3.2.7: Stage passage inlet boundary conditions plane

At the outflow boundary the grid face averaged value of static pressure was imposed. Rotational speed and inlet stagnation properties were set at the constant values given by PYTHIA’s design point simulation results for the first LP compressor stage. The various points on the map were obtained by changing the stage outlet static pressure using approximate data obtained from PYTHIA’s 0D simulations. This was equivalent to allowing more or less mass flow to pass through the stage, thus changing the operating point of the fan.

In the distorted inlet simulations, both the grid and the numerical methods used for the analysis of the distorted performance of the compressor were the same as in the clean inlet simulations. The stage performance was simulated once again by using one blade passage. The main difference in this case was the definition of the boundary conditions at the inlet of the stage, where the value of total pressure was no more uniform.

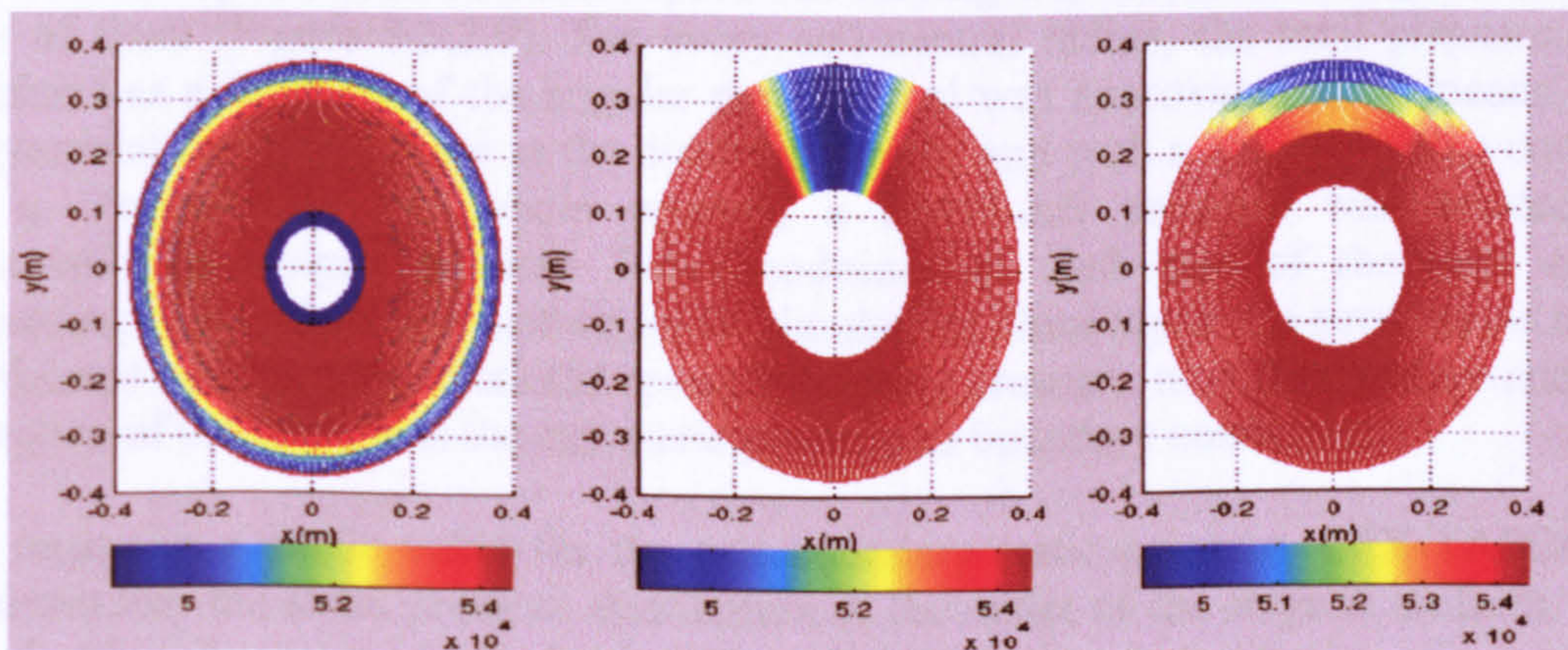


Figure 9.3.2.8: Typical contours of radial, circumferential and stratified inlet total pressure distortions



In the context of this work, three different kinds of distortion were studied, namely radial, circumferential and stratified (Figure 9.3.2.8). Although the first distortion type could be tackled with a similar to the clean inlet case steady simulation, the other two demanded time periodic simulations which resulted in a considerable increase in time and computational resources.

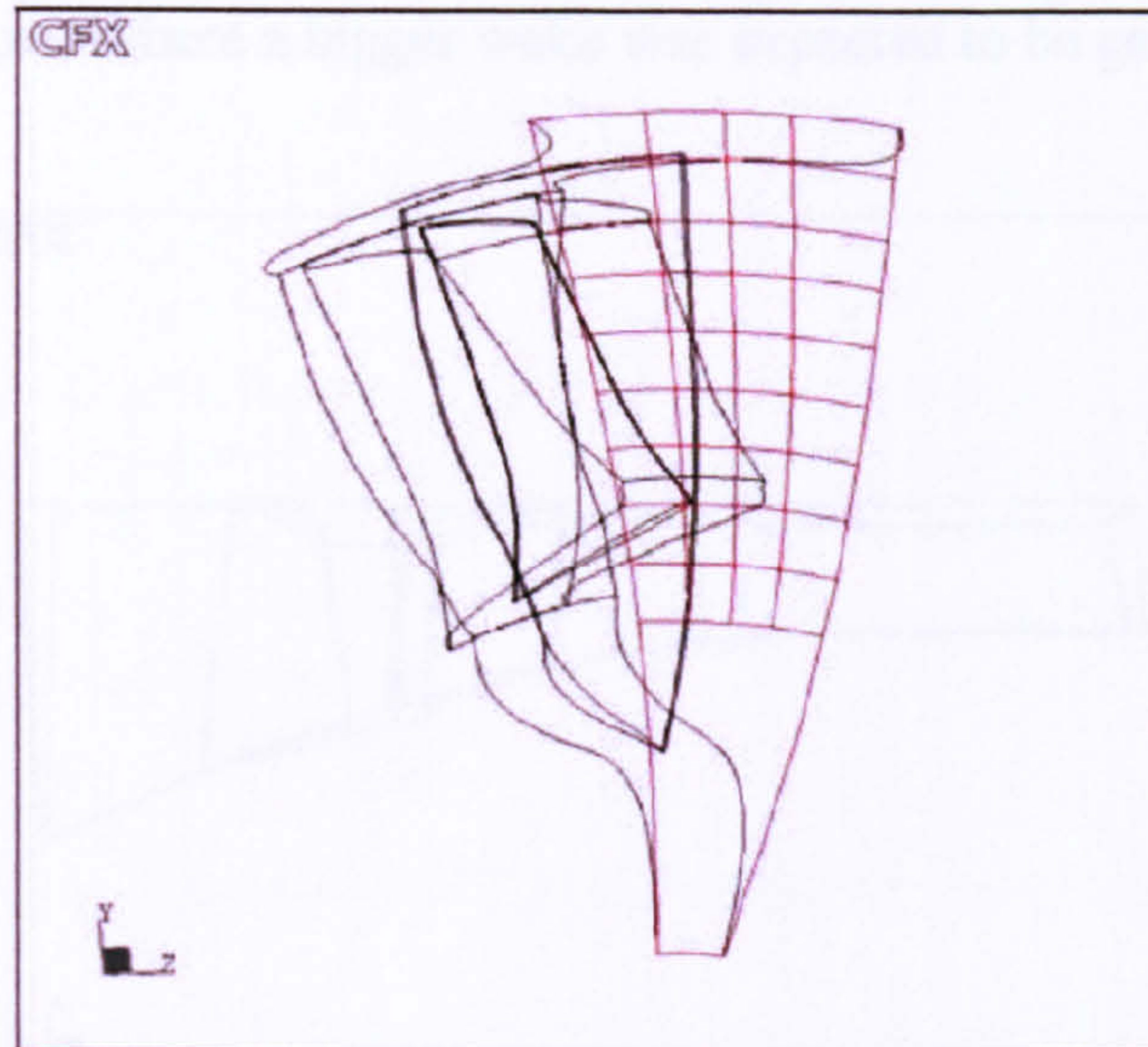


Figure 9.3.2.9: Passage inlet subdivision into several regions for the modelling of non-uniform total pressure profiles

In the case of circumferential and stratified distortions, the inlet total pressure is no longer constant but varies in both time and space. CFX-TASCflow allows time periodic boundary conditions to be imposed as a function of time only. The problem of the dependence of inlet flow characteristics on the position along the blade span was therefore solved by subdividing the inlet of the flow passage into several ‘inflows’. More analytically, in order to give a realistic approximation of the inlet total pressure distribution under stratified and circumferential total pressure distortion, the inlet was divided in several regions (4 in the span wise direction and 9 in the radial direction, in the region of the blade that was affected by the distortion) and a value of total pressure, constant in space but varying with time, was assigned to each one of them (Figure 9.3.2.9). For every cell central radius, the total pressure was obtained as a function of the angular position and was approximated by means of a polynomial of second order in the distorted region, and with a constant value outside of it. To simplify the whole process, a MATLAB program was created to automatically assign boundary flow conditions to each one of the inlet cells, according to the distortion pattern under simulation. Once again the simulations were performed by imposing rotational speed, inlet total pressure, total temperature and the direction of the flow, plus the exit static pressure as boundary conditions.

By imposing a single value for the exit boundary static pressure, CFX-TASCflow assumes that the static pressure distribution at the outlet of the stage is uniform. For low levels and extents of inlet total pressure distortion the approximation of a constant outlet static pressure could be considered acceptable. This however introduces a fairly large approximation especially when only one stage is studied in isolation. This work



adopted another solution, which was an adaptation of the ‘parallel diffuser’ technique used in other studies. By putting a long enough duct at the exit of the stator, the problem of having to specify a constant static pressure at the stator outlet was avoided (Figure 9.3.2.10). Basically, the presence of the duct enabled fixing the constant static pressure boundary condition far enough from the exit of the stage, where the static pressure was allowed to change according to the distortion imposed. Furthermore, this technique facilitated an easier flow solver convergence during simulations, especially in the near stall region where a bigger wake was expected to be generated.

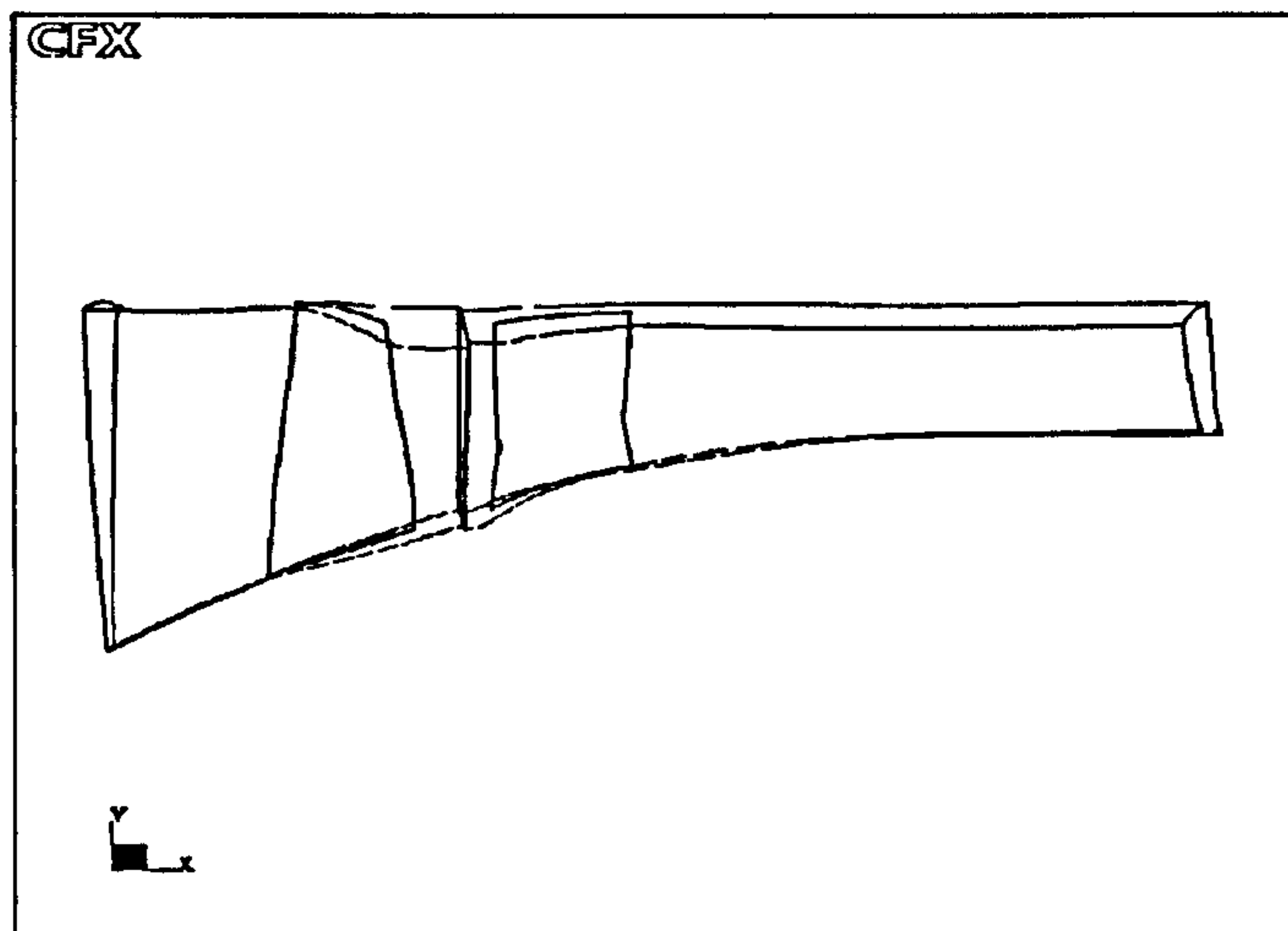


Figure 9.3.2.10: Longer passage downstream of first stage and outlet boundary conditions plane

### Preliminary Analysis

Before integrating the performance of the high-fidelity compressor stage into PYTHIA’s engine cycle analysis, a preliminary investigation took place looking at the displacement of a single constant speed line with various types and extents of distortion. 3D CFD simulations of the compressor stage were conducted at design rotational speed (12000.0 rpm) under clean and distorted inlet conditions in order to validate the performance of the stage and examine the applicability of the three high-fidelity simulation strategies discussed previously. The design non-dimensional speed line was established on the compressor map for uniform inlet conditions and was used as a reference for evaluating the effects of different types of distortion on stage performance.

Initial 3D CFD runs revealed steady-state simulation times with a uniform inlet and a radially distorted inlet of the order of 8 to 15 hours approximately. On the other hand, convergence times for the unsteady type of simulations (required in the case of stratified and circumferential distortion) were of the order of 2 to 3 days approximately. This excluded following an iterative or fully integrated type of high-fidelity analysis for establishing the engine’s performance later on and demanded the adoption of the de-coupled method.



### General Observations - Uniform Inlet Conditions

Under uniform inlet conditions the design speed line exhibited typical stage characteristics. At low pressure ratios choking was observed with the mass flow being almost constant and independent of pressure ratio. At lower mass flows the incidence of the flow on the blade increased and therefore the overall turning angle of the air also increased. The change in momentum of the flow resulted in higher temperature and pressure ratios. This occurred until a point where the blade row was not capable of increasing the deflection given to the air any more. With excessive incidence and blade loading the flow separated, the blade stalled and the pressure ratio and efficiency suddenly dropped.

As far as surge goes, the performance of the compressor stage was captured along the constant speed line until the very last point where the flow solver converged. It was assumed that stall was located close to where convergence stopped due to the presence of unsteady flow phenomena which could not be captured by the solver due to the steady state simulation carried out.

### General Observations – Radial Distortion (Steady State Simulation)

The principal effect of the presence of a lower total pressure region was the change in the span wise distribution of the flow and in related parameters. The simulations with a radially uneven pressure distribution showed a lower meridional flow velocity in the distorted region and a bigger one in the undistorted region, compared to the clean inlet results. This difference in the meridional flow distribution, together with an associated reduction in mass flow, was expected as it is one of the most recognised effects of radial distortion (Figure 9.3.2.11).

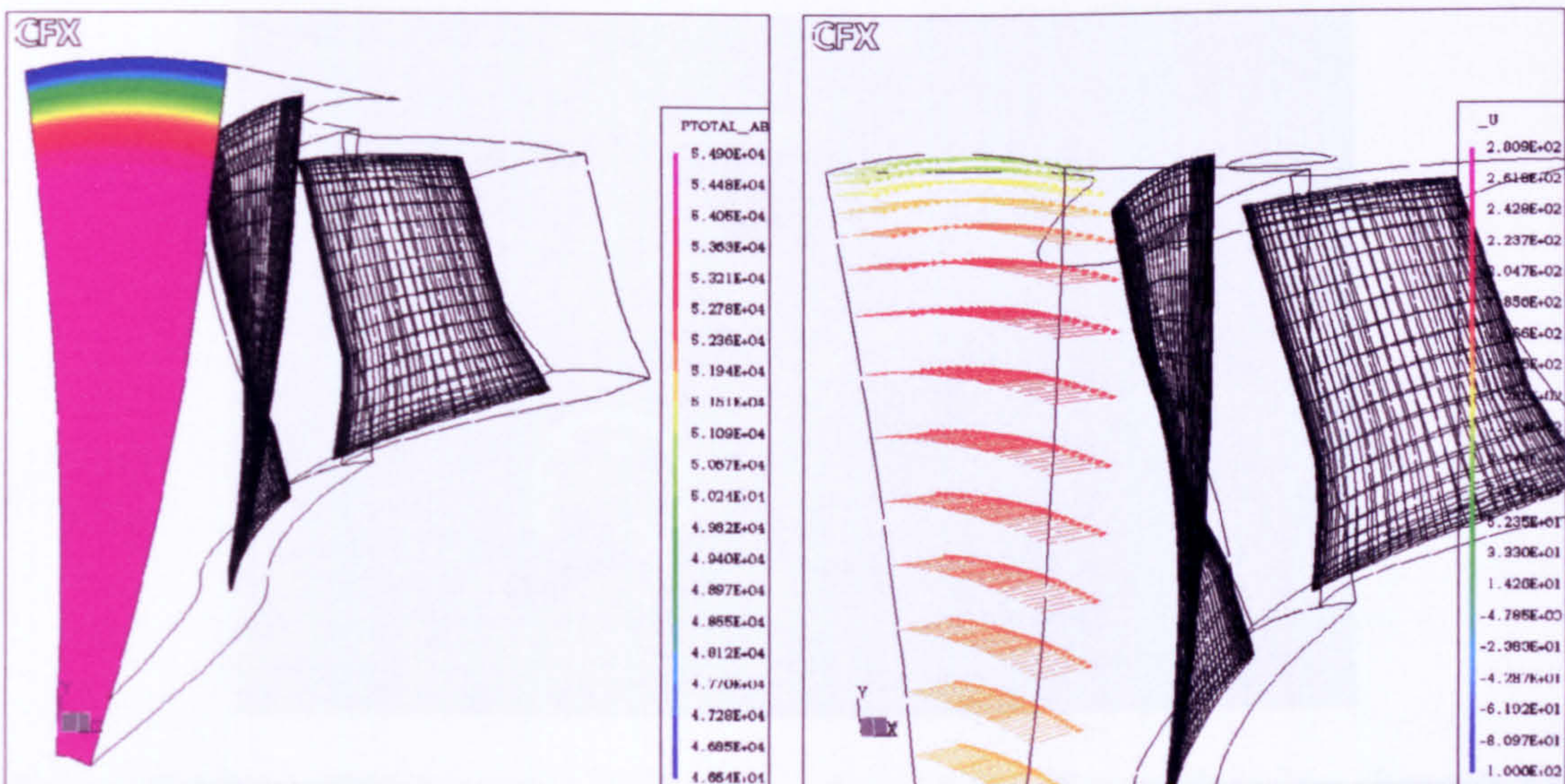


Figure 9.3.2.11: Effect of a lower total pressure region at the tip on meridional velocity distribution

The presence of a different meridional velocity clearly affected the distribution of the flow around the blade and particularly the incidence of the flow on the blade. A



bigger incidence caused the load on the blade to rise, because of the bigger turning that the blade row was trying to impose to the flow. Imposing larger magnitudes of radial distortion, especially in regions where the blade was already highly loaded, such as the hub and the tip, sometimes presented problems as far as compressor stability is concerned.

Every blade profile section along the blade span has an incidence of maximum efficiency (minimum loss incidence). Relative to this incidence, the efficiency decreases either if the angle of the flow relative to the blade is increased or is reduced. Therefore, if distortion takes place close to design point conditions or even near choke, where the incidence of the flow on the blade is low, the reduced axial velocity could actually result in an improvement in compressor efficiency. On the other hand, if the distortion takes place at conditions near stall it would surely worsen the performance, or even completely stall that portion of the already highly loaded blade. Moreover, the radial distortion had the effect of reducing the stall margin of the compressor in most cases.

#### General Observations – Circumferential and Stratified Distortions (Unsteady Simulations)

As mentioned before, the principal difference between steady and unsteady simulations is the fact that in the latter case a time periodic simulation is required to model the different inlet conditions in front of the blade passage as this rotates. The number of time steps required for a converged solution is strictly related to the particular distortion under examination. The results from this type of simulations were analyzed in terms of space- and time-averaged parameters, which basically express the mean of the flow properties across the whole annulus.

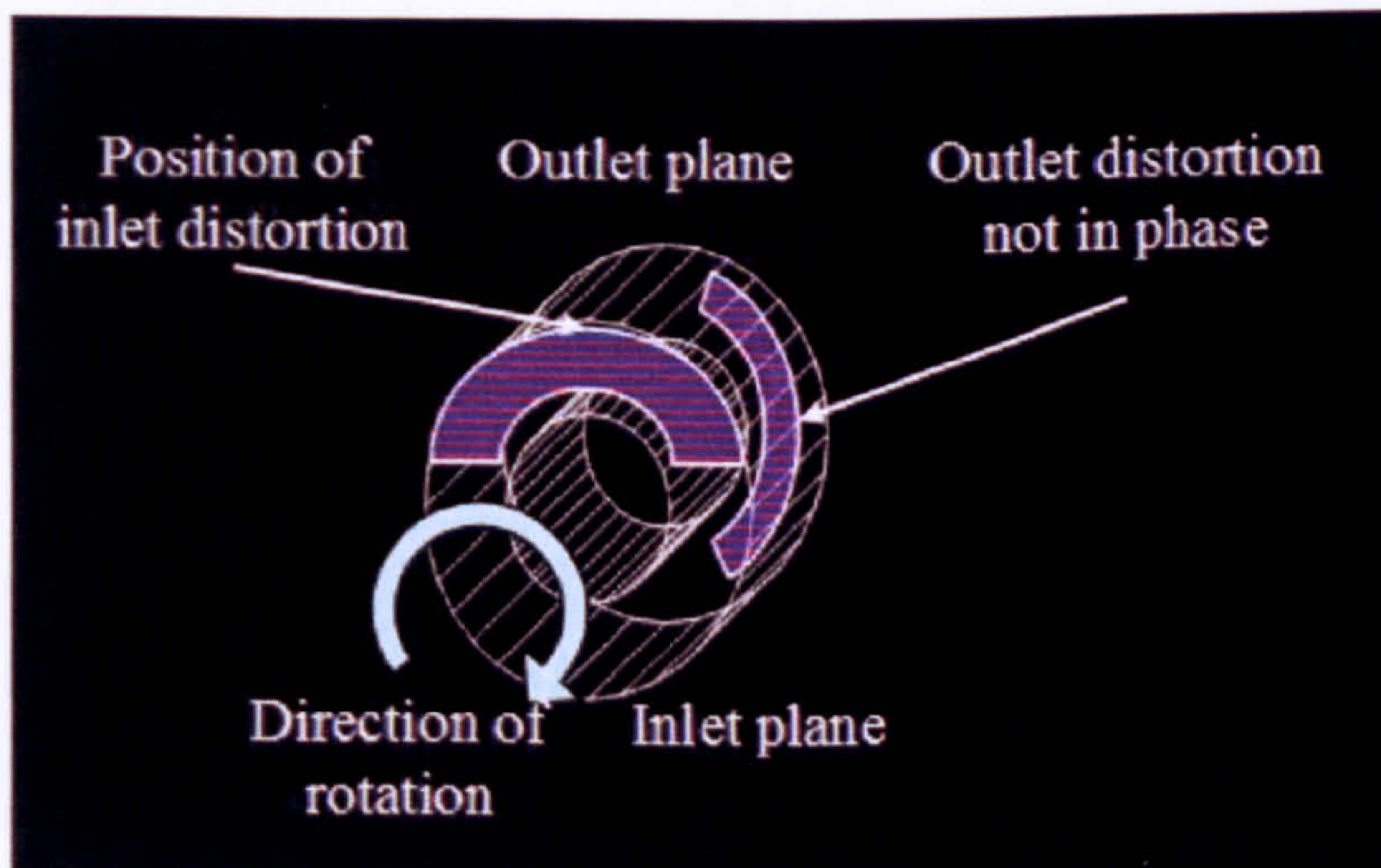


Figure 9.3.2.12: Displacement and attenuation of the distorted region through the compressor stage

Circumferential and stratified distortions caused similar flow phenomena as in the case of radial distortion discussed above. The presence of the low pressure region introduced a lower meridional velocity in the portion of the flow affected. This caused a reduction in mass flow while the flow incidence on the blade increased with an



associated rise in blade loading and a reduction in stall margin. Since the simulations were transient in this case, there was a delay in the transfer of information between the inlet and the outlet of the stage, evident from the displacement of the distorted region in the same direction of the rotation of the spool, and its attenuation through the compressor stage. This is illustrated graphically in the following figure.

In the context of the preliminary analysis, apart from the undistorted stage performance, several comparative studies were conducted. For example, one study compared the effects of different levels of the same type of distortion (stratified), while other studies compared the effects of different types, extents and frequencies of distortion on stage performance. The findings of some of these studies are discussed briefly in the following paragraphs. A more complete account is given in the conference publication Charalambous, et al. (2004) and the MSc Theses Charalambous (2003), Ghisu (2003) and Iurisci (2003).

### Different Magnitudes of Stratified Distortion with Same Distorted Area

Different parameters have been adopted over the years to describe the distortion intensity or magnitude. Among those, two seem to have the bigger completeness as shown below:

- The Distortion Parameter (DP), defined as the ratio between the maximum deviation from the undistorted (or maximum) total pressure and the maximum total pressure itself.

$$DP = \frac{P_{\max} - P_{\min}}{P_{\max}} \quad [\text{Eq. 9.3.2.1}]$$

- The level of distortion  $DC_{60}$ , defined as the difference between the total average pressure and the minimum total average pressure in a 60 degrees sector divided by the mean dynamic head.

$$DC_{60} = \frac{\bar{P} - \bar{P}_{\min, 60^\circ}}{q} \quad [\text{Eq. 9.3.2.2}]$$

The use of the second parameter to describe inlet total pressure distortion is principally due to historical reasons resulting by the studies conducted throughout the years. 60 degrees has usually been found to be the critical distortion extent (in terms of deviation from undistorted performance) for the majority of the compressors.

This case study looked into different magnitudes of inlet stratified distortion with the same distorted area. Since the application of the  $DC_{60}$  is not possible in the case of purely radial distortions, the magnitude of the distortion was defined in this case similarly to Equation 9.3.2.1, as the minimum total pressure imposed at the inlet with respect to the undistorted inlet total pressure. Three different magnitudes of inlet stratified total pressure distortion, namely 5, 10 and 15 percent were simulated at design point conditions of altitude (11000.0 m), flight Mach number (1.2), rotational speed (12000.0 rpm), undistorted inlet total pressure (55.0 kPa) and total temperature



(279.3 K). Moreover, for a more complete evaluation of the shift of the design non-dimensional speed line under distorted conditions, three different operating points along the design speed line were examined, one near the stage design point, one closer to choke and one closer to stall. The area of the distorted region was kept the same for all simulations (stratified distortion affecting 20% of the annulus area). The general findings of this investigation are shown in Table 9.3.2.3.

Distortion Level	Near choke % change wrt to clean inlet performance			Near design point % change wrt to clean inlet performance			Near surge % change wrt to clean inlet performance		
	5	10	15	5	10	15	5	10	15
Mass flow	-0.34	-0.73	-1.10	-0.34	-0.75	-1.13	-0.40	-0.84	-1.04
Pressure Ratio	0.31	0.56	0.78	0.22	0.44	0.63	0.13	0.24	0.33
Temperature Ratio	0.13	0.22	0.28	0.09	0.16	0.22	0.04	0.11	0.16
Isentropic Efficiency	-0.03	-0.01	-0.01	-0.06	-0.05	-0.14	-0.13	-0.20	-0.16

Table 9.3.2.3: Results for different magnitudes of inlet stratified total pressure distortion

For the three different levels of distortion studied in this case, the principal effect of a bigger distortion level was found to be associated with a bigger reduction in meridional velocity which was directly linked to a reduction in mass flow and an increase in pressure ratio and temperature ratio due to incidence change, as discussed before.

Changes in most flow parameters appeared to vary almost proportionally to the level of distortion imposed, either increasing or decreasing with distortion. The stage efficiency remained largely unaffected for the three levels of distortion especially near choke, started to fall however close to stall conditions and for the higher magnitudes of distortion. This was due to the fact that at these operating conditions the incidence of the flow on the blade was already high and the presence of a lower pressure region had the effect of raising it even further, causing flow separation and a subsequent drop in efficiency.

At very low pressure ratios the principal effect of the presence of the distorted region was the reduction in mass flow, while pressure ratio increased and efficiency remained largely unaffected due to the incidence angle becoming progressively similar to the minimum-loss incidence angle from high negative values. At high pressure ratios the mass flow was still reduced, the pressure ratio increased slightly and efficiency dropped considerably due to the already high blade loading. The maximum stage pressure ratio reached with distortion was roughly the same as in the undistorted case, while a reduction in peak efficiency was present due to the flow separating as it was described previously.

#### Different Types of Distortion with Same Distorted Area

In the context of the preliminary investigation, this case study looked into the effects of different types of distortion on compressor stage design performance, with the same extent and the same distortion magnitude. The following three distortion



patterns were simulated for a minimum inlet total pressure of 10% compared to the undistorted total pressure:

- Radial distortion at the tip affecting 25% of the inlet radius.
- Stratified distortion at the tip affecting 50% of the inlet radius.
- Circumferential distortion affecting a sector of 60 degrees.

The general findings of this investigation are shown in Table 9.3.2.4.

	W [kg/s]	$P_{o,in}$ [Pa]	$T_{o,out}$ [K]	PR	$\eta_{is}$
Undistorted	39.82	54426.72	332.00	1.655	0.8149
Radial (25%)	39.05	53440.37	333.91	1.677	0.8087
Stratified (50%)	39.48	53774.67	333.26	1.674	0.8157
Circumferential (60 deg)	39.36	53855.67	333.21	1.669	0.8115

	% change in W	% change in $P_{o,in}$	% change in $T_{o,out}$	% change in PR	% change in $\eta_{is}$
Radial (25%)	-1.934	-1.812	0.575	1.329	-0.761
Stratified (50%)	-0.854	-1.198	0.379	1.148	0.098
Circumferential (60 deg)	-1.155	-1.049	0.364	0.845	-0.417

Table 9.3.2.4: Results for different types of distortion with the same extent and the same distortion magnitude

Although the distortion magnitude, as defined previously, and the affected area were similar in all three cases, different types of distortion resulted in different average inlet total pressure drops, with the radial distortion resulting in the largest change in inlet total pressure. Consequently, this type of distortion caused the largest reduction in mass flow and the largest increase in stage pressure ratio and temperature ratio compared to the other two distortion cases examined. From the 3D CFD analysis it became apparent that since an already highly loaded region of the blade (tip) experienced a further increase in loading due to the incidence change, although the overall pressure ratio of the blade increased, the flow began to separate at the tip decreasing the efficiency as shown above. The radial and circumferential distortions seemed to follow this general trend just described.

It is worth pointing out however that the stratified distortion deviated slightly from the general rule, with the mass flow through the stage dropping less than in the other two cases and the efficiency increasing slightly. This is justified by the fact that in the case of stratified distortion, only a small portion of the blade and for a limited period of time experiences the lowest value of the total pressure profile imposed at the inlet. In this case, although the overall extent and lowest total pressure value imposed were similar to the other two cases, the overall effect on the blade was much less pronounced, mainly affecting a small region close to the tip and for a very short period of time (see Figure 9.3.2.8).

#### Different Types of Distortion with Similar Inlet Average Total Pressure Drops

This case study looked into different types of inlet distortion of the same magnitude and similar average total pressure drops, but different extents. The minimum total



pressure imposed at the inlet was 10% of the design undistorted total pressure as in previous studies. The three cases simulated at design point operating conditions were:

- Radial distortion at the tip affecting 25% of the inlet radius approximately.
- Stratified distortion affecting 70% of the inlet radius approximately.
- Circumferential distortion affecting a sector of 90 degrees approximately.

Through an iterative approach, different distortion extents were simulated for respective distortion types in order to achieve similar average total pressure drops in all three cases examined. The reader needs to be reminded at this stage that every unsteady simulation took approximately 2 to 3 days to converge and therefore it was extremely tedious and time consuming to achieve an exact match in overall total pressure drop at the inlet as Table 9.3.2.5 shows. Moreover, in order to reach the same average pressure decrease at the inlet in the case of the stratified distortion, an unrealistically large portion of the compressor annulus had to be affected (70%), without this however invalidating the comparison with the other cases.

	W [kg/s]	$P_{o,in}$ [Pa]	$T_{o,out}$ [K]	PR	$\eta_{is}$
Undistorted	39.82	54426.72	332.00	1.655	0.8149
Radial (25%)	39.05	53440.37	333.91	1.677	0.8087
Stratified (70%)	39.27	53479.67	333.56	1.681	0.8177
Circumferential (90 deg)	39.07	53484.82	333.59	1.677	0.8138

	% change in W	% change in $P_{o,in}$	% change in $T_{o,out}$	% change in PR	% change in $\eta_{is}$
Radial (25%)	-1.934	-1.812	0.575	1.329	-0.761
Stratified (70%)	-1.381	-1.740	0.470	1.571	0.344
Circumferential (90 deg)	-1.883	-1.731	0.478	1.329	-0.135

Table 9.3.2.5: Results for different types of distortion with similar inlet average total pressure drops

Basically, what this case study examined was the effect of different shapes of distortion on stage performance. From the above table it is evident that radial and circumferential distortions result in similar trends as before, especially as far as percentage change in mass flow and pressure ratio are concerned. The change in mass flow in the case of radial distortion appears slightly higher than in the case of the circumferential, but that is due to the slightly larger reduction in average total pressure at the inlet. Both distortion patterns seem to be causing similar changes in pressure ratio with the radial distortion causing a slightly higher temperature ratio change due to the higher loading at the tip. However, the change in efficiency in the case of the radial distortion appears to be much larger. This was due to the reduction in efficiency at the affected tip region caused by the flow separating due to excessive blade loading. Although the same is true for the circumferential distortion as well, in this case the whole of the blade span experiences the same levels of distortion which causes the efficiency at the highly loaded regions of the blade (hub and tip) to drop, but the rest of the blade to operate at slightly higher efficiencies than before, resulting in a smaller overall reduction.

The stratified distortion, which is actually a combination of the other two, despite the similar reduction in average inlet total pressure, causes a smaller reduction in mass



flow and a large increase in pressure ratio and efficiency. This is actually in line with the findings of the previous case study for distortions of different type with same extent and magnitude and could be explained in a similar way. In the case of stratified distortion, only the tip of the blade and for a limited period of time experiences the lowest value of total pressure at the inlet. Despite the reduction in efficiency at the tip, the rest of the blade span which is less loaded operates at higher incidences and hence more deflection is imposed to the flow resulting in higher pressure ratios and efficiencies without the blade stalling. The hub of the blade is not affected by the distortion in this case.

The overall findings of the 3D CFD analysis are in a very good agreement with the results and trends obtained by the 2D SLC analysis of compressor inlet radial distortion discussed previously. Obviously, the above observations are valid for the particular compressor geometry under investigation and the operating conditions under which the simulations took place and can only be taken qualitatively. Generally speaking, this investigation showed that apart from the circumferential distortion which usually degrades the performance of the compressor by affecting the whole of the blade span, stratified and radial distortions can have a positive or negative effect on compressor performance. For example, if they act over the portion of the blade which is already highly loaded, producing most of the work and pressure rise, they can lead to severe compressor performance deterioration. On the other hand, depending on the design, they may actually improve the performance of the compressor by setting more favourable incidences than the nominal.

### Engine Performance Simulation

According to the de-coupled approach to high-fidelity analysis, a series of 3D CFD simulations with a uniform inlet pressure profile were first carried out to establish the baseline characteristic map for the first stage of the LP compressor. This map was subsequently used as the base for evaluating the deviation in stage and engine performance due to stratified and radial total pressure distortions. To minimize running times only one stage passage was simulated as before.

### Stage Performance under Uniform Inlet Conditions

Changing the rotational speed of the compressor, in total six relative to design point non-dimensional speed lines were generated from the averaged, 3D flow solutions, between 0.6 (60%) and 1.1 (110%), 1.0 representing the design point speed line. The simulations were carried out by imposing rotational speed, inlet total pressure, total temperature and direction of flow and the average static pressure at the stage outlet as boundary conditions. Changing the outlet static pressure gave the different compressor operating points on every relative non-dimensional speed line. To ensure stable conditions at the rotor face, all boundary conditions were imposed one blade cord length upstream the inlet of the stage. The various operating points on the stage map each required an average of 8 to 15 hours to converge.

The shape of the constant speed lines, obtained from the averaged, 3D CFD flow solutions, demonstrated a typical stage characteristic at low and high speeds, covering



a satisfactory range of stage operating conditions. The above method for simulating the compressor stage performance gave satisfactory results at operating points close to design point where the incidence of the flow on the blade was low enough to give small separations. At near-stall conditions, however, the use of a steady state simulation to analyze a stalled flow produced an unstable computational behaviour as reported earlier on. The performance of the compressor was therefore ‘captured’ until the very last point where the method showed convergence, assuming stall to be located close to where the convergence stopped.

**LP Compressor First Stage Characteristic  
Uniform Inlet Conditions**

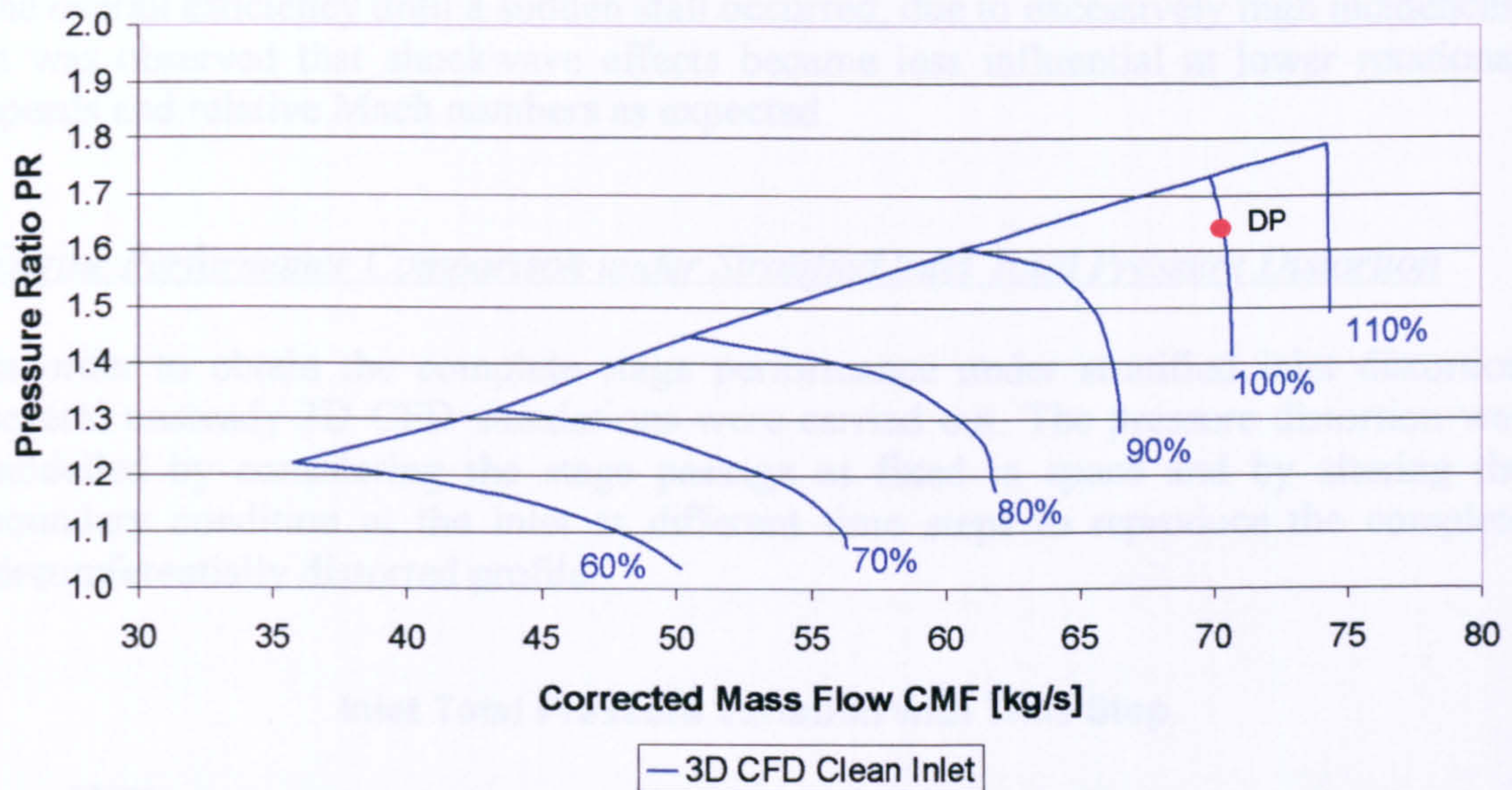


Figure 9.3.2.13: CFD derived LP compressor first stage characteristic for uniform inlet conditions – Pressure Ratio vs Corrected Mass Flow

**LP Compressor First Stage Characteristic  
Uniform Inlet Conditions**

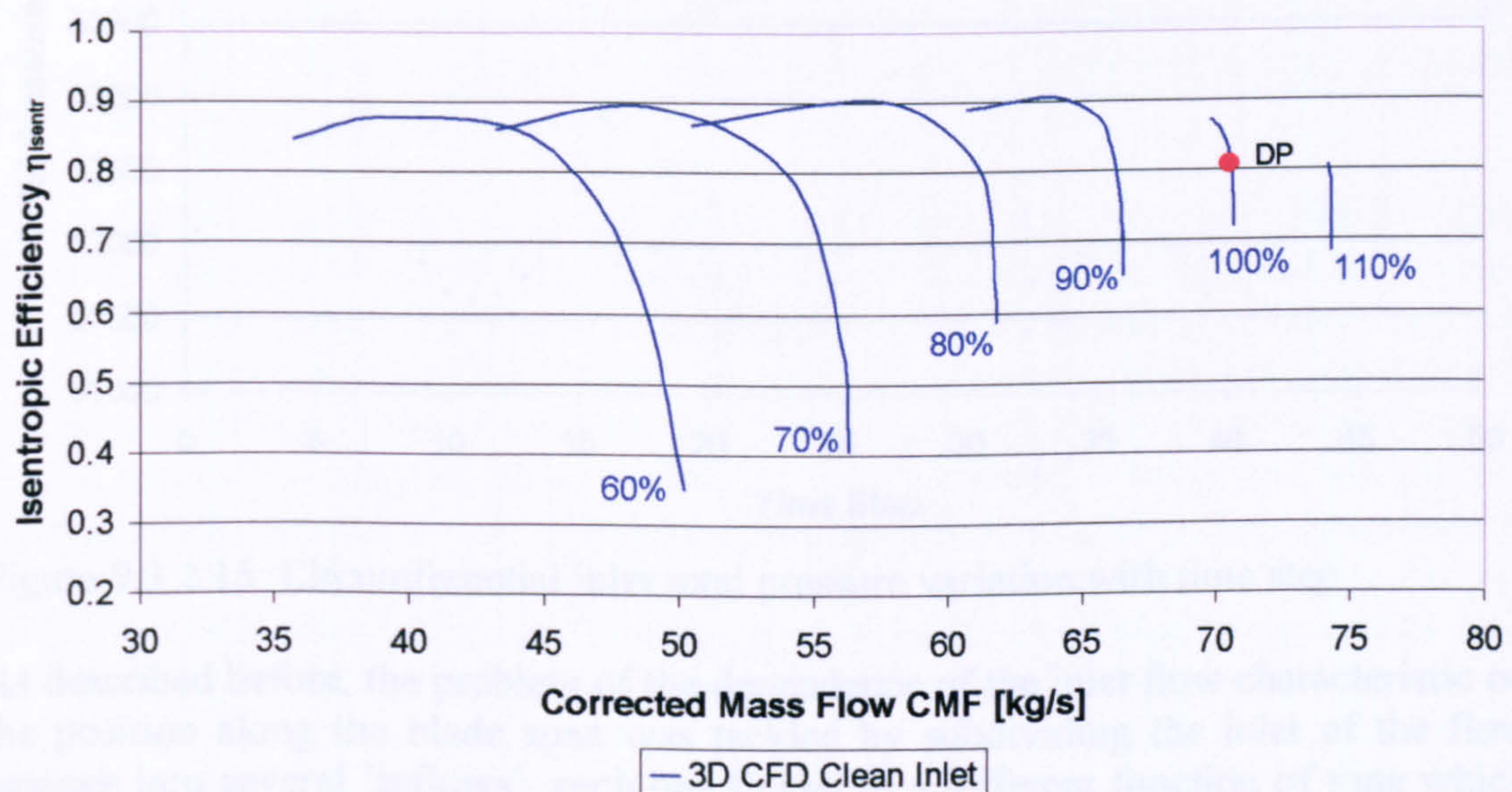


Figure 9.3.2.14: CFD derived LP compressor first stage characteristic for uniform inlet conditions – Isentropic Efficiency vs Corrected Mass Flow



The stage characteristics obtained after mass-averaging the high-fidelity 3D CFD flow solutions, are illustrated in Figures 9.3.2.13 and 9.3.2.14 in the form of pressure ratio and isentropic efficiency plotted against corrected mass flow for different relative non-dimensional speed lines. The surge line in Figure 9.3.2.13 is only an approximate one. From these figures it can also be observed that the compressor efficiency at high rotational speeds increases without exhibiting the usual ‘point of maximum compressor efficiency’, as at lower compressor speeds. The combination of very high relative Mach numbers and the use of Double Circular Arc (DCA) blade profiles resulted in very strong shock waves, especially at the tip of the rotor blades, which were the main cause of efficiency loss at high rotational speeds. An increase in pressure ratio accompanied by a reduction in mass flow had the effect of increasing the overall efficiency until a sudden stall occurred, due to excessively high incidences. It was observed that shockwave effects became less influential at lower rotational speeds and relative Mach numbers as expected.

### Engine Performance Comparison under Stratified Inlet Total Pressure Distortion

In order to obtain the complete stage performance under stratified inlet distortion several unsteady 3D CFD simulations were carried out. The pressure distortion was modelled by considering the stage passage as fixed in space and by altering the boundary condition at the inlet at different time steps to reproduce the complete circumferentially distorted profile.

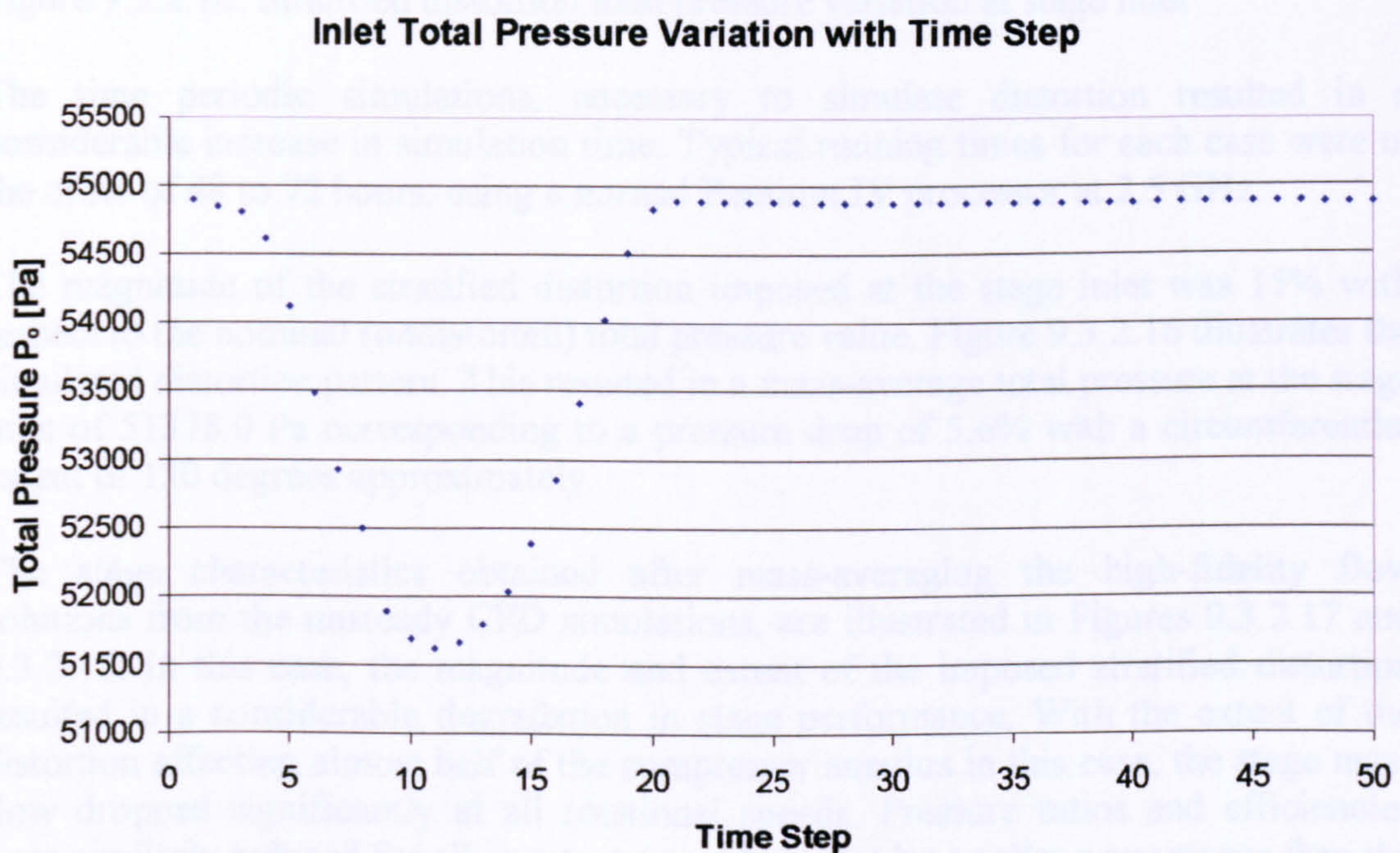


Figure 9.3.2.15: Circumferential inlet total pressure variation with time step

As described before, the problem of the dependence of the inlet flow characteristic on the position along the blade span was tackled by subdividing the inlet of the flow passage into several ‘inflows’, each one linked to a different function of time which was proportional to the angular position of the blade. In this case the fan face was divided into 50 sections, resulting in a CFD simulation of 50 time steps, each one with



a different inlet boundary condition equal to one fiftieth of the revolution period at the design rotational speed. The following figure shows the inlet mass-averaged values of total pressure for all time steps which were also related to different circumferential positions.

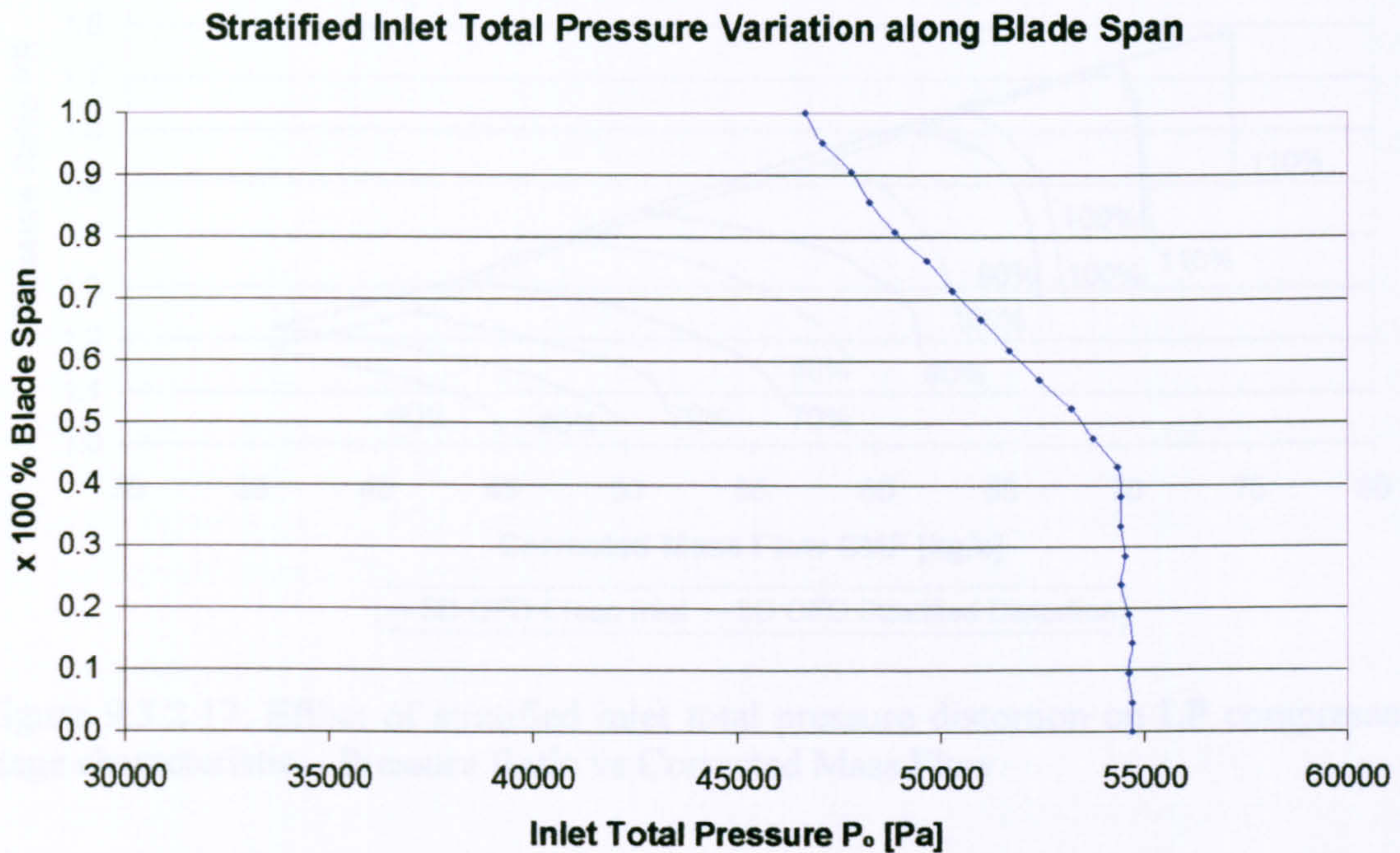


Figure 9.3.2.16: Stratified distortion total pressure variation at stage inlet

The time periodic simulations, necessary to simulate distortion resulted in a considerable increase in simulation time. Typical running times for each case were of the order of 48 to 72 hours, using a normal Pentium IV processor at 2.5 GHz.

The magnitude of the stratified distortion imposed at the stage inlet was 15% with respect to the nominal (undistorted) total pressure value. Figure 9.3.2.16 illustrates the simulated distortion pattern. This resulted in a mass-average total pressure at the stage inlet of 51378.0 Pa corresponding to a pressure drop of 5.6% with a circumferential extent of 130 degrees approximately.

The stage characteristics obtained after mass-averaging the high-fidelity flow solutions from the unsteady CFD simulations, are illustrated in Figures 9.3.2.17 and 9.3.2.18. In this case, the magnitude and extent of the imposed stratified distortion resulted in a considerable degradation in stage performance. With the extent of the distortion affecting almost half of the compressor annulus in this case, the stage mass flow dropped significantly at all rotational speeds. Pressure ratios and efficiencies were similarly reduced for all constant speed lines but by smaller percentages than the mass flow due to the distortion affecting a larger portion of the blade span than in previous case studies. The overall trends presented here are in a good agreement with the conclusions of the preliminary investigations discussed previously.



LP Compressor First Stage Characteristic  
Effect of Inlet Total Pressure Distortion

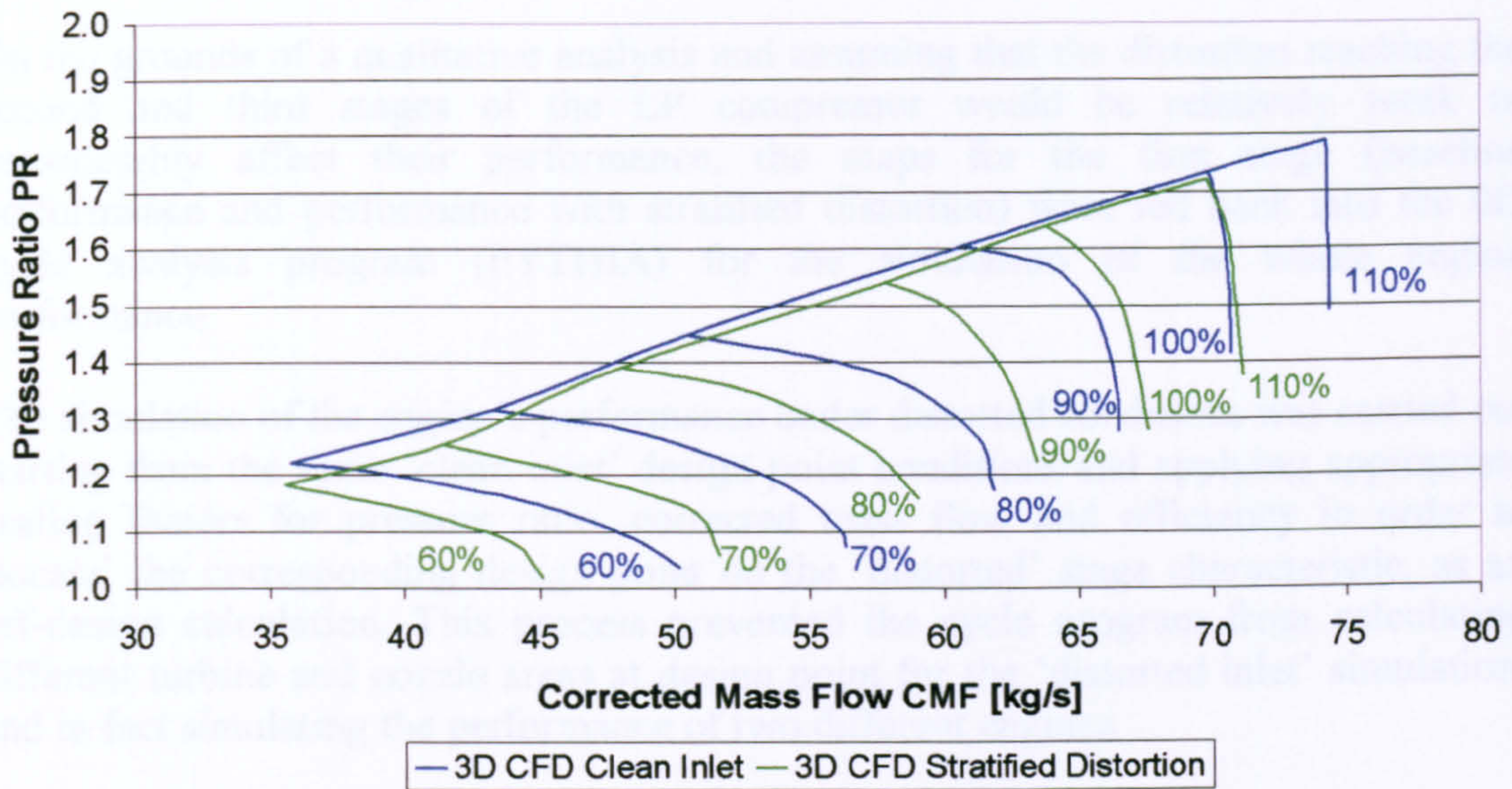


Figure 9.3.2.17: Effect of stratified inlet total pressure distortion on LP compressor stage characteristic – Pressure Ratio vs Corrected Mass Flow

LP Compressor First Stage Characteristic  
Effect of Inlet Total Pressure Distortion

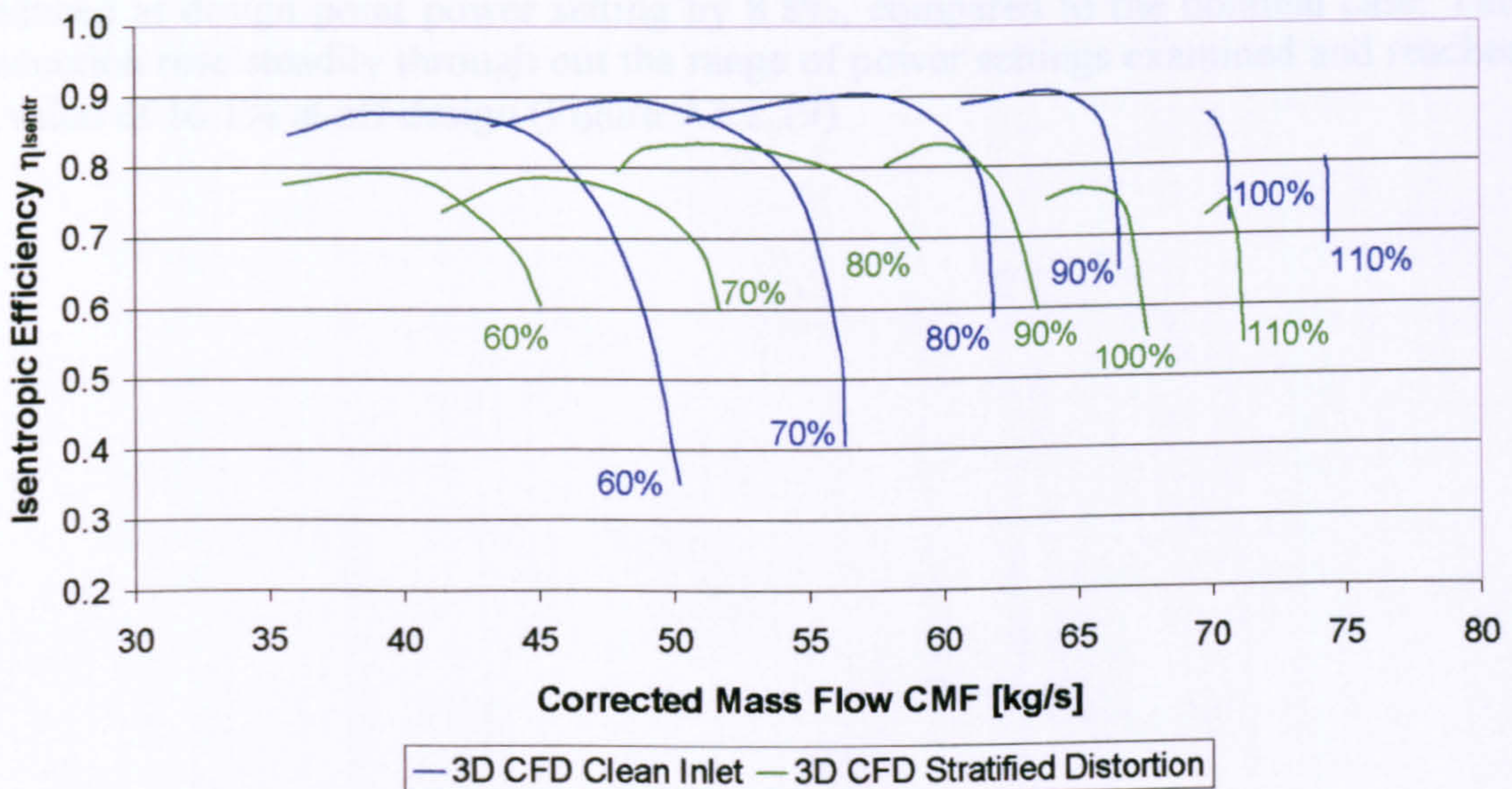


Figure 9.3.2.18: Effect of stratified inlet total pressure distortion on LP compressor stage characteristic – Isentropic Efficiency vs Corrected Mass Flow

During the CFD runs it was also observed that the pressure distortion imposed at the inlet largely attenuated through out the stage (Melloni, et al., 2006). The pressure variation measured at the outlet of the stage was remarkably less than the one imposed at the inlet, due to the effects of the increase in work done on the flow. That proved to



be in a good agreement with the published literature (Longley, 1990) and partially justified the use of PYTHIA's default maps for the second and third stages of the LP compressor, in the subsequent engine cycle simulations.

On the grounds of a qualitative analysis and assuming that the distortion reaching the second and third stages of the LP compressor would be relatively weak to considerably affect their performance, the maps for the first stage (baseline performance and performance with stratified distortion) were fed back into the OD cycle analysis program (PYTHIA) for the simulation of the whole engine performance.

The simulation of the engine's performance under distorted conditions was carried out starting from the same 'clean-inlet' design point conditions and applying appropriate scaling factors for pressure ratio, corrected mass flow and efficiency in order to 'locate' the corresponding design point on the 'distorted' stage characteristic, as an off-design calculation. This process prevented the cycle program from calculating different turbine and nozzle areas at design point for the 'distorted inlet' simulation, and in fact simulating the performance of two different engines.

The performance of the engine at cruise conditions with uniform and distorted inlet conditions was established for a range of engine power settings by varying the Turbine Entry Temperature (TET) from the design point value down to 1550.0 K. Figures 9.3.2.19 to 9.3.2.22 illustrate the effect of the imposed stratified distortion on engine performance. As expected, the performance of the engine was severely affected by the reduction in LP compressor stage pressure ratio, efficiency and engine mass flow due to the distortion. More analytically, the engine's gross thrust was reduced at design point power setting by 8.8%, compared to the nominal case. This reduction rose steadily through out the range of power settings examined and reached a value of 16.1% at off-design (Figure 9.3.2.19).



**LBR Military Turbofan Engine Performance Comparison  
Effect of LP Compressor Inlet Total Pressure Distortion**

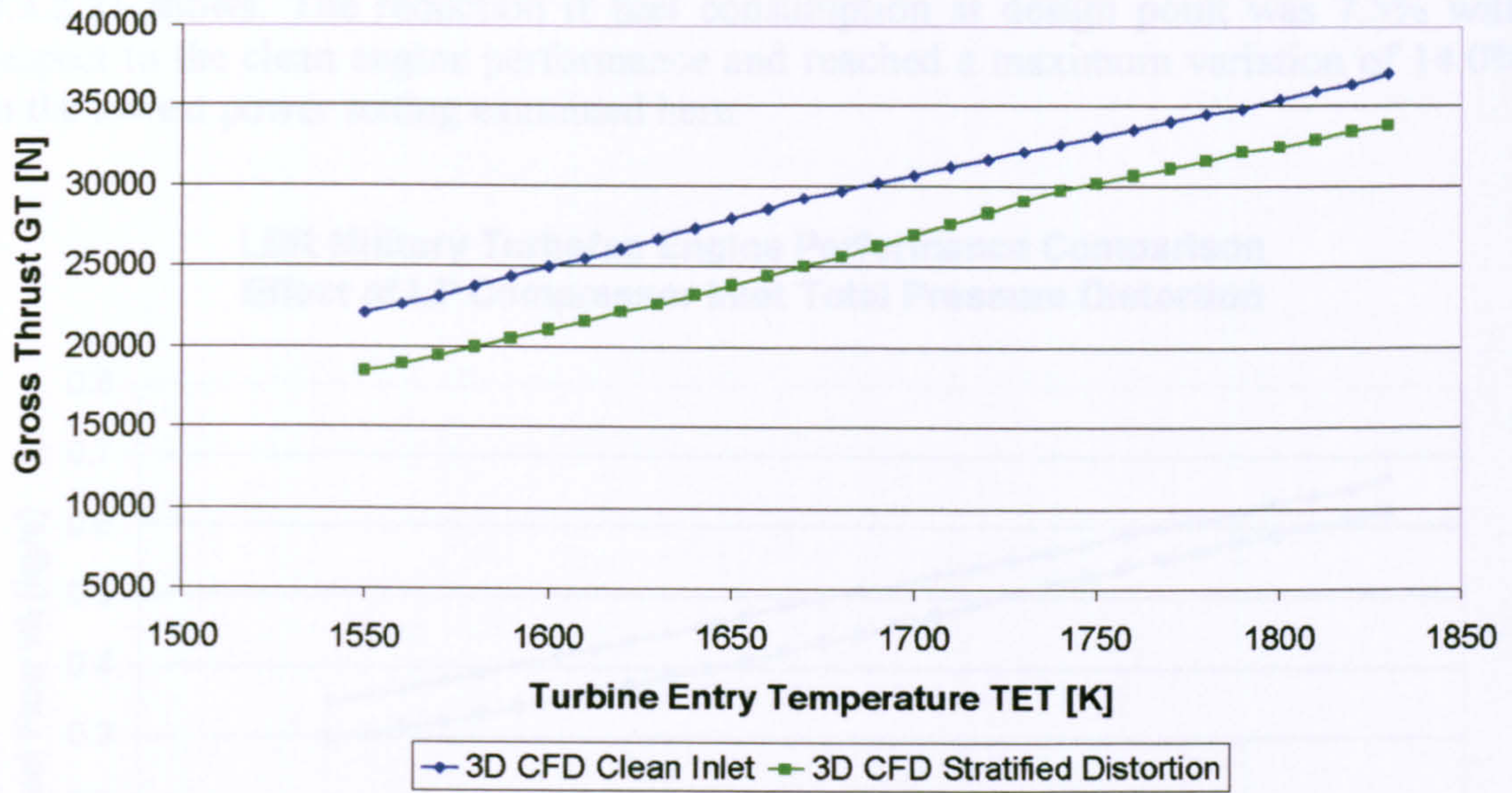


Figure 9.3.2.19: Effect of inlet stratified distortion on LBR military engine performance – Gross Thrust vs Turbine Entry Temperature

**LBR Military Turbofan Engine Performance Comparison  
Effect of LP Compressor Inlet Total Pressure Distortion**

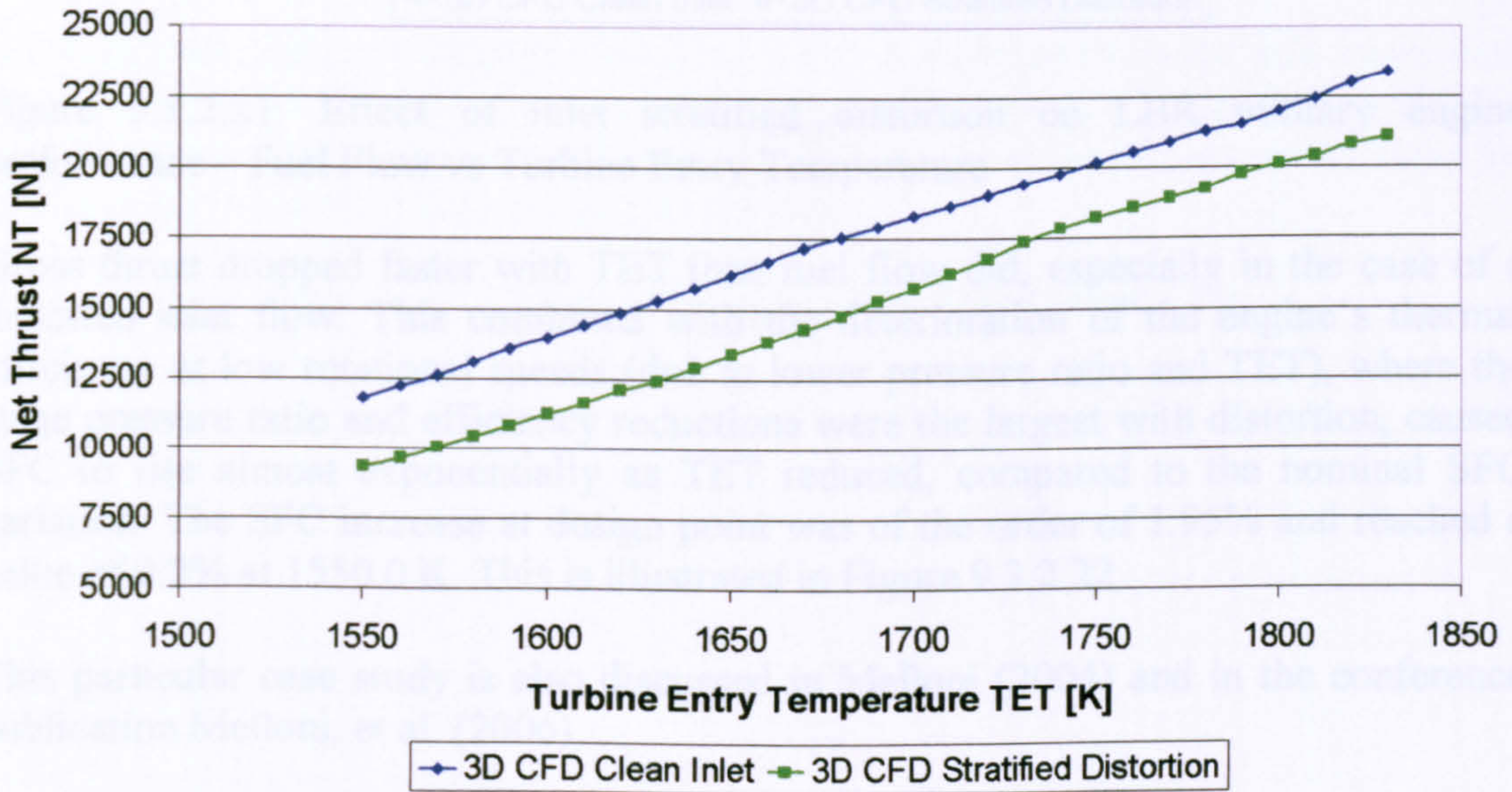


Figure 9.3.2.20: Effect of inlet stratified distortion on LBR military engine performance – Net Thrust vs Turbine Entry Temperature

At a constant altitude and flight Mach number, the engine’s net thrust exhibited similar trends to the gross thrust and was reduced by 9.8% compared to the nominal case at design point and by 20.1% at 1550.0 K of TET (Figure 9.3.2.20).



Since gross thrust under stratified distortion reduced almost linearly with respect to power setting and the nominal gross thrust variation with TET, the fuel flow requirement of the engine also reduced with distortion in a similar manner as Figure 9.3.2.21 shows. The reduction in fuel consumption at design point was 7.5% with respect to the clean engine performance and reached a maximum variation of 14.0% at the lowest power setting examined here.

**LBR Military Turbofan Engine Performance Comparison  
Effect of LP Compressor Inlet Total Pressure Distortion**

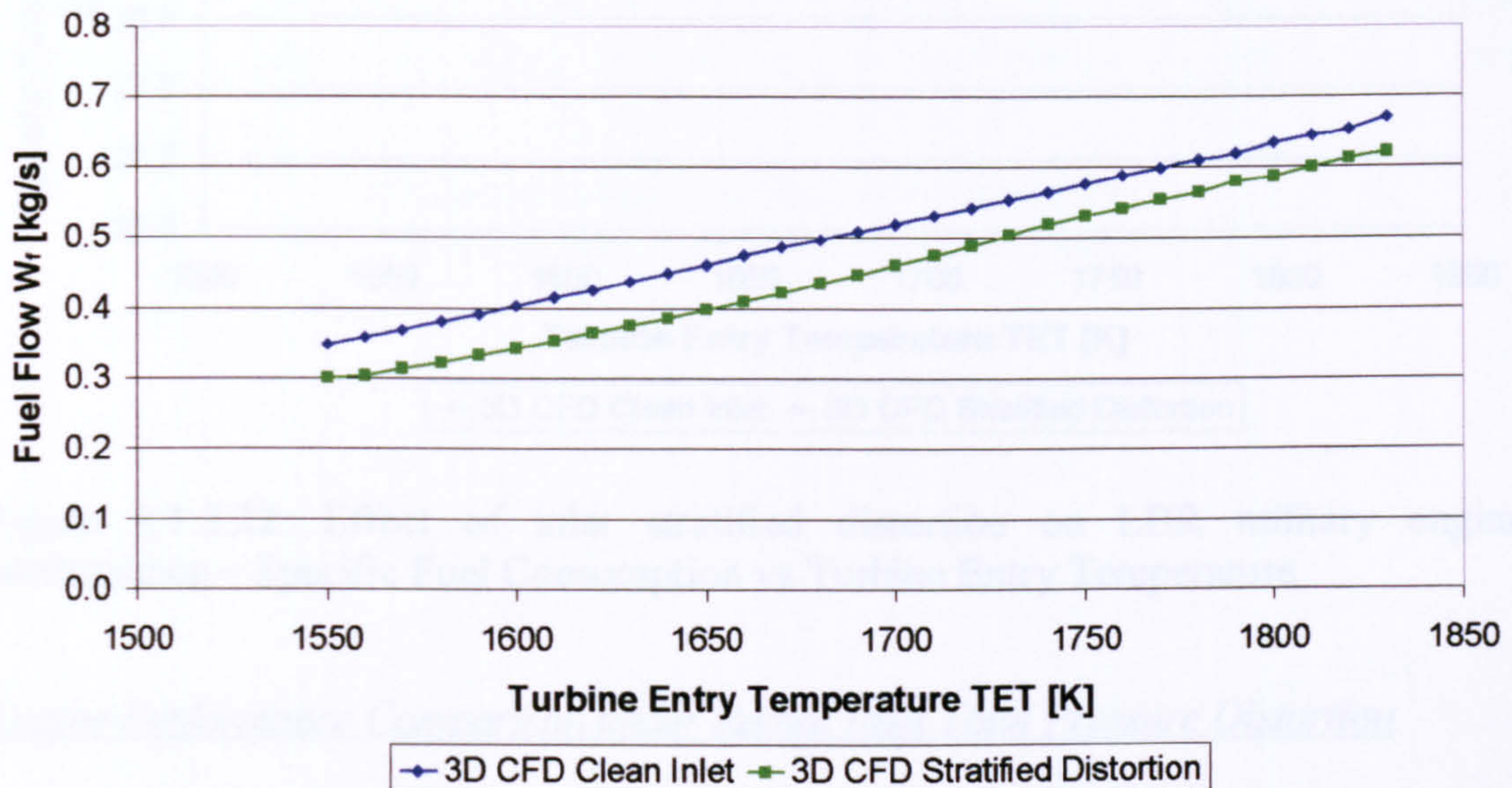


Figure 9.3.2.21: Effect of inlet stratified distortion on LBR military engine performance – Fuel Flow vs Turbine Entry Temperature

Gross thrust dropped faster with TET than fuel flow did, especially in the case of a distorted inlet flow. This combined with the deterioration of the engine's thermal efficiency at low rotational speeds (due to lower pressure ratio and TET), where the stage pressure ratio and efficiency reductions were the largest with distortion, caused SFC to rise almost exponentially as TET reduced, compared to the nominal SFC variation. The SFC increase at design point was of the order of 1.95% and reached a value of 9.2% at 1550.0 K. This is illustrated in Figure 9.3.2.22.

This particular case study is also discussed in Melloni (2004) and in the conference publication Melloni, et al. (2006).



**LBR Military Turbofan Engine Performance Comparison  
Effect of LP Compressor Inlet Total Pressure Distortion**

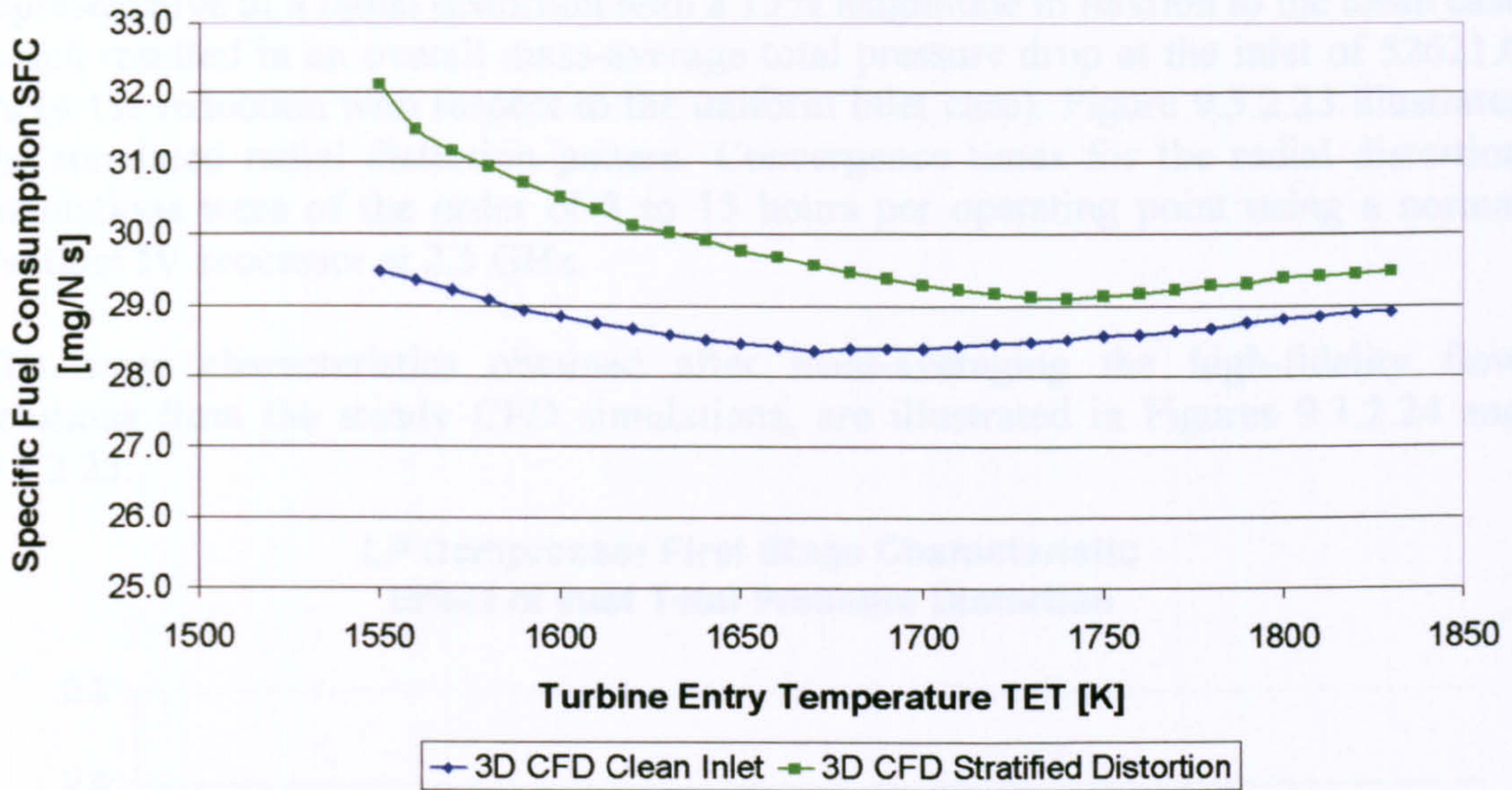


Figure 9.3.2.22: Effect of inlet stratified distortion on LBR military engine performance – Specific Fuel Consumption vs Turbine Entry Temperature

Engine Performance Comparison under Radial Inlet Total Pressure Distortion

To obtain the complete stage performance under conditions of radial inlet distortion, several steady 3D CFD simulations were carried out, supported by the fact that in this case the imposed reduction in total pressure near the tip of the blade was the same for all circumferential positions around the annulus.

**Radial Inlet Total Pressure Variation along Blade Span**

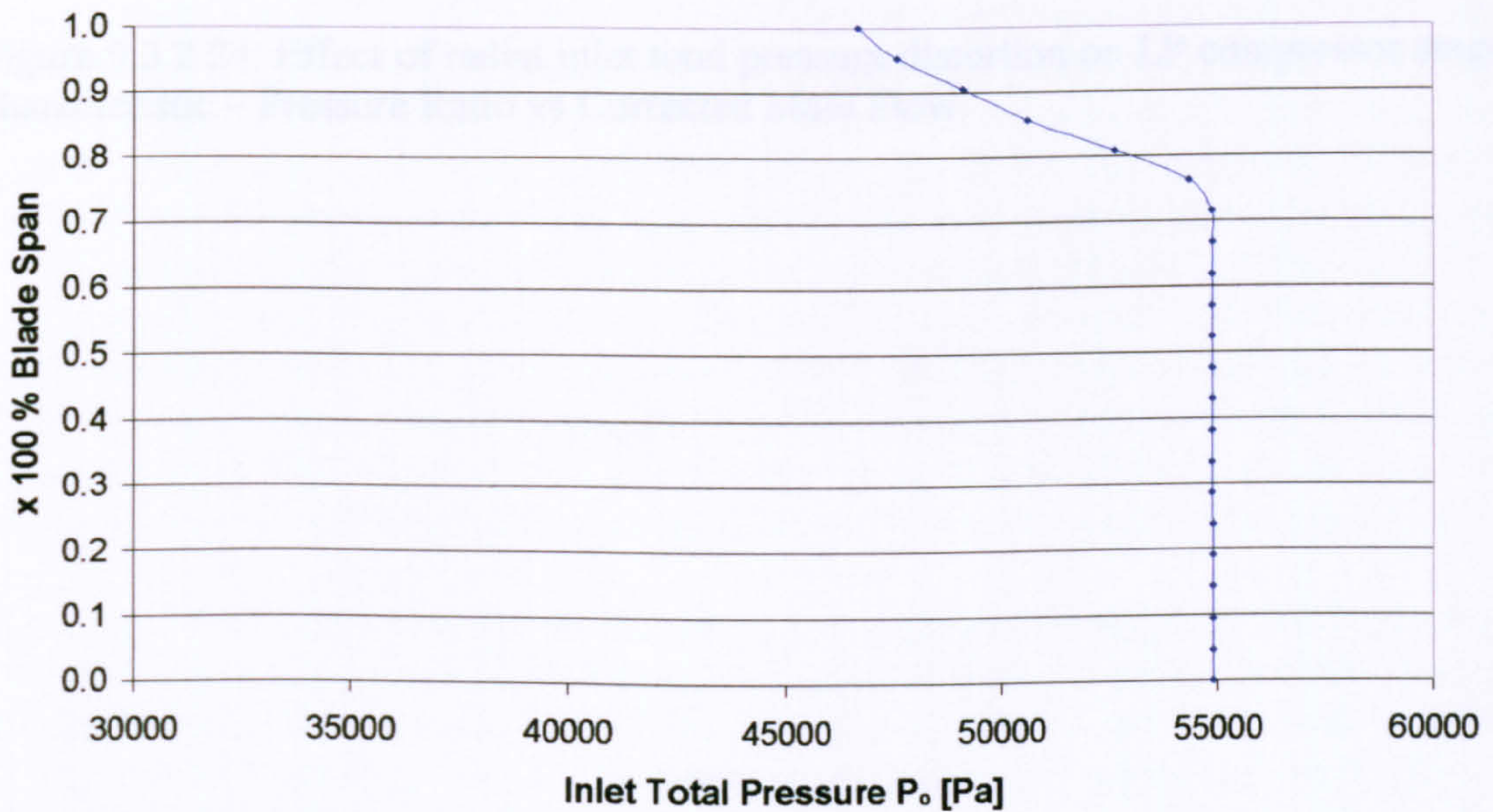


Figure 9.3.2.23: Radial distortion total pressure variation at stage inlet



The rotor-stator passage was subdivided at the inlet plane into 9 annular sectors, each one having a different value of total pressure imposed, ranging from 54895.0 Pa at the hub to 46661.0 Pa at the tip approximately. This total pressure profile was representative of a radial distortion with a 15% magnitude in relation to the clean case which resulted in an overall mass-average total pressure drop at the inlet of 52621.0 Pa (4.1% reduction with respect to the uniform inlet case). Figure 9.3.2.23 illustrates the simulated radial distortion pattern. Convergence times for the radial distortion simulations were of the order of 8 to 15 hours per operating point using a normal Pentium IV processor at 2.5 GHz.

The stage characteristics obtained after mass-averaging the high-fidelity flow solutions from the steady CFD simulations, are illustrated in Figures 9.3.2.24 and 9.3.2.25.

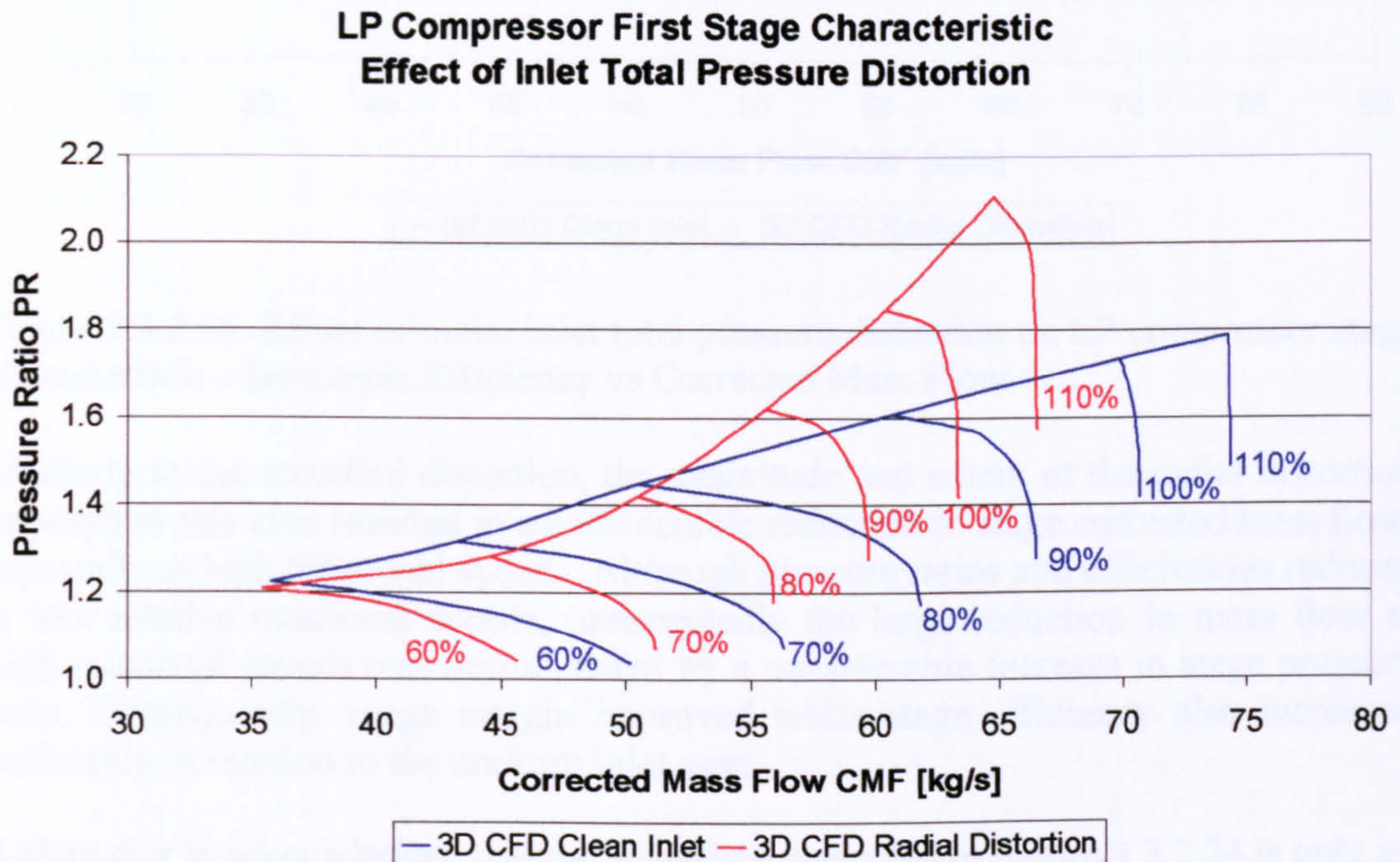


Figure 9.3.2.24: Effect of radial inlet total pressure distortion on LP compressor stage characteristic – Pressure Ratio vs Corrected Mass Flow



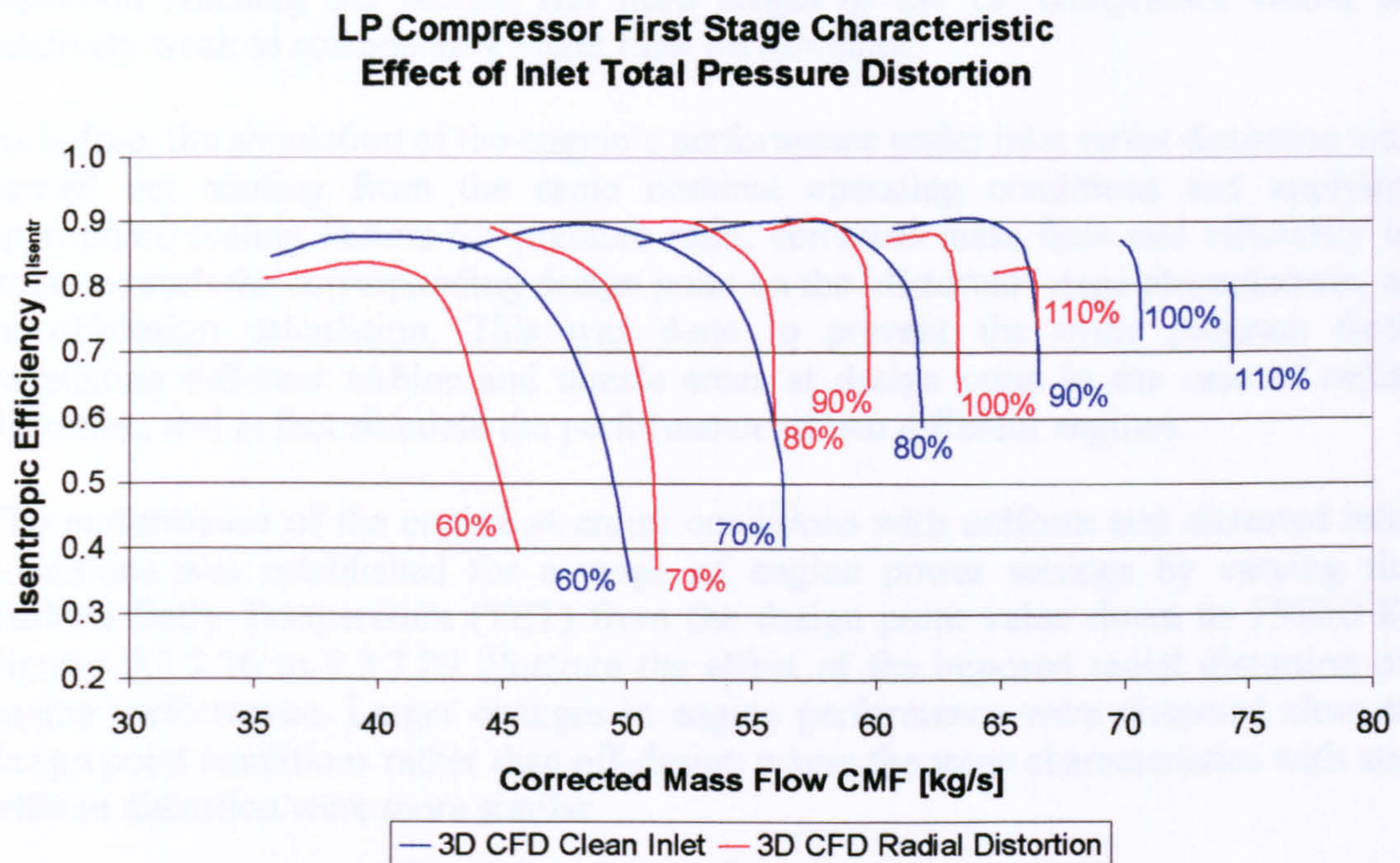


Figure 9.3.2.25: Effect of radial inlet total pressure distortion on LP compressor stage characteristic – Isentropic Efficiency vs Corrected Mass Flow

Similarly to the stratified distortion, the magnitude and extent of the radial distortion imposed in this case resulted in a considerable reduction in stage corrected mass flow, especially at high rotational speeds. Although pressure ratios and efficiencies reduced at low relative rotational speeds, unexpectedly the large reduction in mass flow at high rotational speeds was accompanied by a considerable increase in stage pressure ratio. Consequently, surge margin improved while stage efficiency also increased noticeably in relation to the uniform inlet case.

Although it is acknowledged that the surge line presented in Figure 9.3.2.24 is only an approximate one due to the steady type of CFD simulations carried out in this case, the increase in pressure ratio and efficiency at high rotational speeds is quite evident. This was justified by the fact that the large reduction in mass flow affecting the upper quarter of the blade span reduced the meridional velocity in that region considerably and at the same time increased the incidence of the flow on the blade. The reduction in meridional velocity resulted in a reduction in the relative velocity and local relative Mach number and hence shock wave losses were also reduced. This increased the blade efficiency at the tip and in combination with the higher blade loading resulted in higher pressure ratios and stall margins. The above observations were also verified by temperature profile plots at the exit of the rotor which showed an increase in temperature ratio towards the tip due to the larger flow turning and hence work input.

Similarly to the case of stratified distortion, the high-fidelity maps for the first stage (baseline performance and performance with radial distortion) were fed back into the OD cycle analysis program (PYTHIA) for the simulation of the whole engine performance according to the de-coupled approach to advanced performance simulation. PYTHIA's default maps were used for the second and third stages of the LP compressor on the grounds of a qualitative analysis and assuming that the



distortion reaching the second and third stages of the LP compressor would be relatively weak to considerably affect their performance.

As before, the simulation of the engine's performance under inlet radial distortion was carried out starting from the same nominal operating conditions and applying appropriate scaling factors for pressure ratio, corrected mass flow and efficiency in order to reach the corresponding design point on the 'distorted' stage characteristic, as an off-design calculation. This was done to prevent the cycle program from calculating different turbine and nozzle areas at design point in the case of radial distortion, and in fact simulate the performance of two different engines.

The performance of the engine at cruise conditions with uniform and distorted inlet conditions was established for a range of engine power settings by varying the Turbine Entry Temperature (TET) from the design point value down to 1550.0 K. Figures 9.3.2.26 to 9.3.2.29 illustrate the effect of the imposed radial distortion on engine performance. Larger changes in engine performance were observed close to design point conditions rather than off-design where the stage characteristics with and without distortion were more similar.

At conditions close to design point with radial distortion, despite the significant increase in stage pressure ratio (and hence engine overall pressure ratio) and efficiency, the performance of the engine was mainly affected by the relatively larger reduction in engine mass flow. More analytically, the engine's gross thrust was reduced at design point power setting by 11.1%, compared to the nominal case. This relative reduction in engine gross thrust gradually decreased through out the range of power settings examined, and actually reversed at a TET of 1550.0 K by 2.2% (Figure 9.3.2.26).

At a constant altitude and flight Mach number, the engine's net thrust exhibited similar trends to the gross thrust and was reduced by 11.7% compared to the nominal case at design point and increased slightly by 3.6% at 1550.0 K of TET (Figure 9.3.2.27).

Since gross thrust under radial distortion reduced almost linearly with respect to power setting and the nominal gross thrust variation with TET, the fuel flow requirement of the engine also reduced with distortion in a similar manner as Figure 9.3.2.28 shows. The reduction in fuel consumption at design point was 7.7% with respect to the clean engine performance and increased by 3.9% at the lowest power setting examined here.



**LBR Military Turbofan Engine Performance Comparison  
Effect of LP Compressor Inlet Total Pressure Distortion**

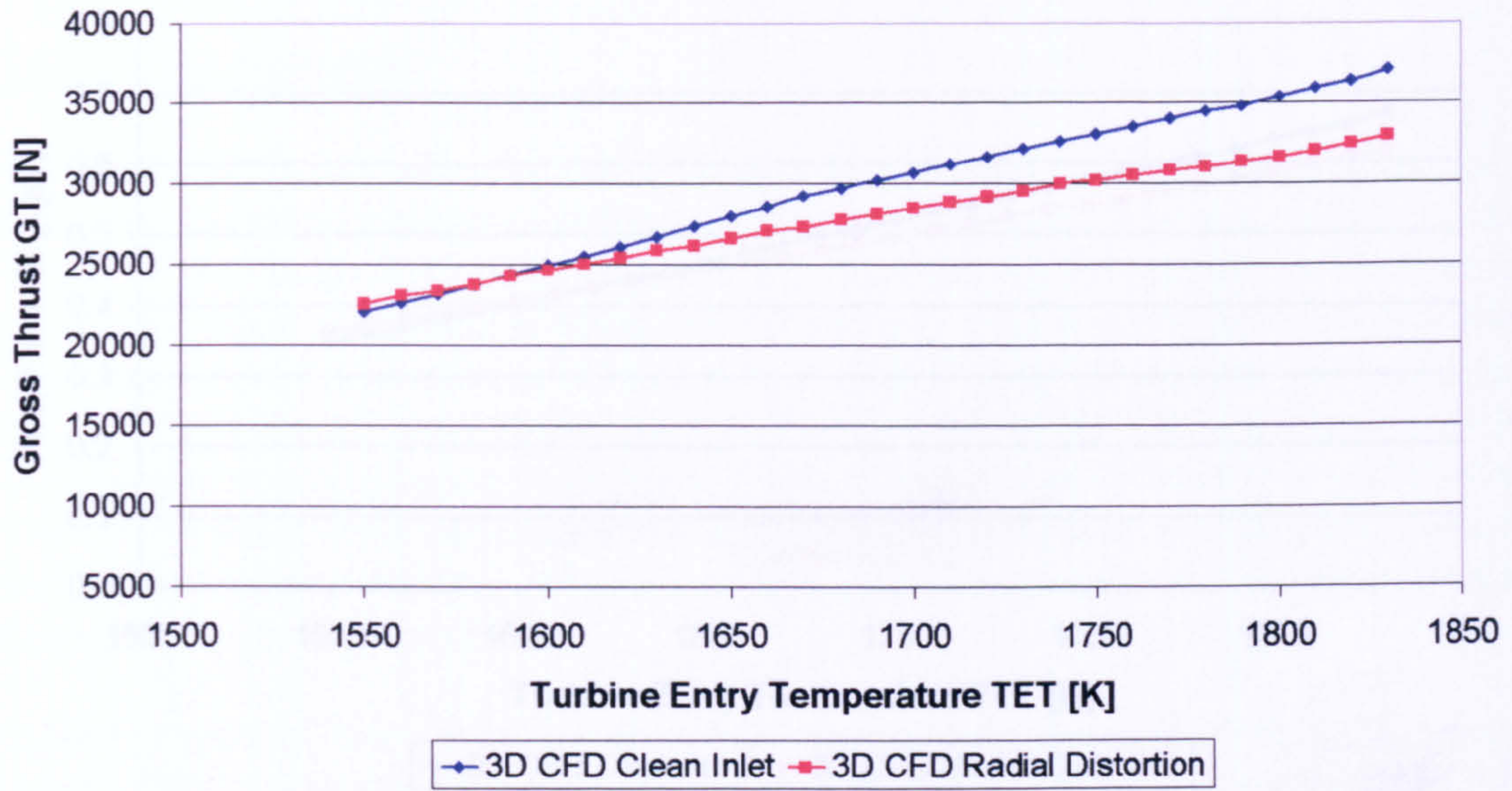


Figure 9.3.2.26: Effect of inlet radial distortion on LBR military engine performance – Gross Thrust vs Turbine Entry Temperature

**LBR Military Turbofan Engine Performance Comparison  
Effect of LP Compressor Inlet Total Pressure Distortion**

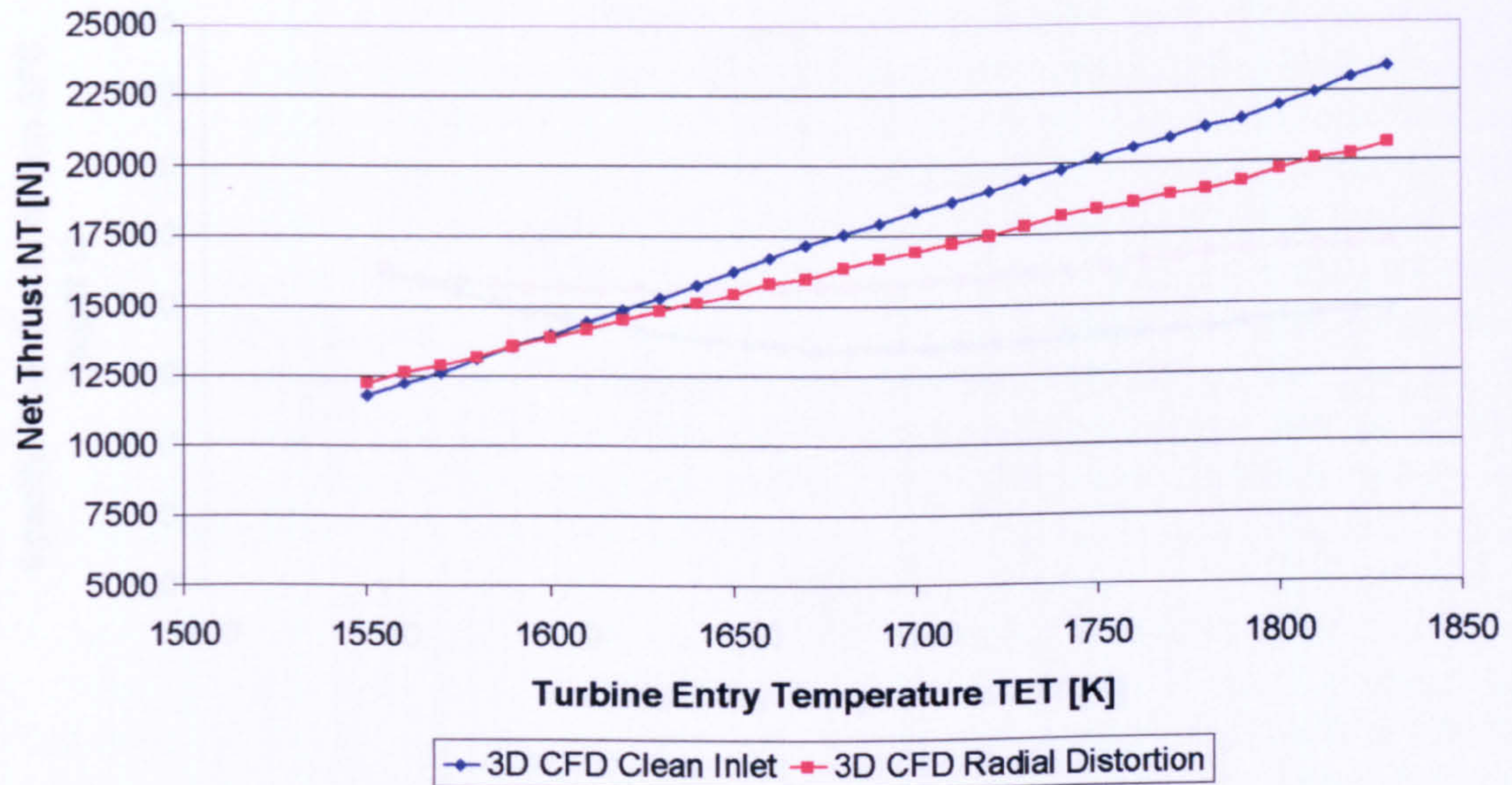


Figure 9.3.2.27: Effect of inlet radial distortion on LBR military engine performance – Net Thrust vs Turbine Entry Temperature



**LBR Military Turbofan Engine Performance Comparison  
Effect of LP Compressor Inlet Total Pressure Distortion**

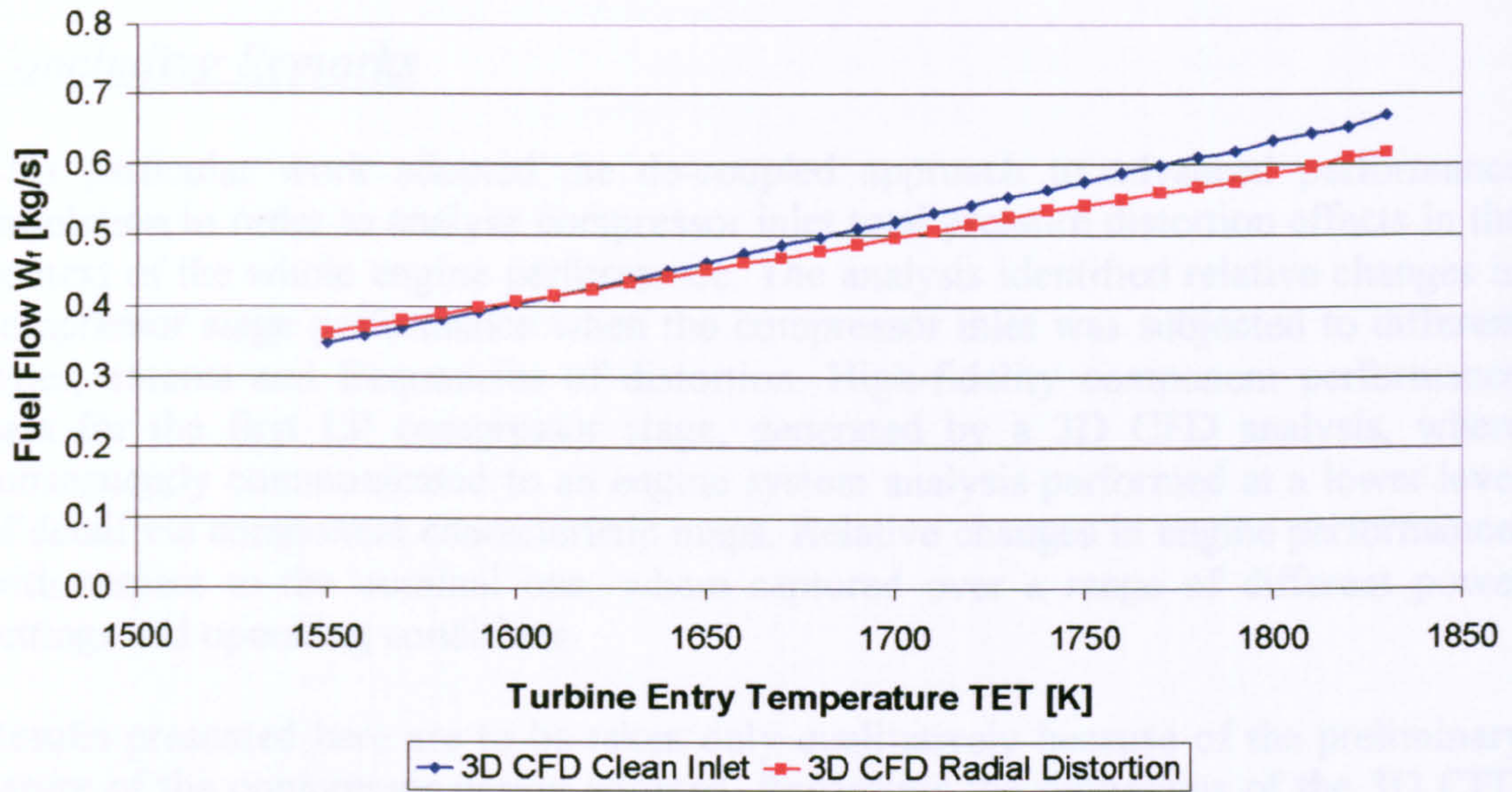


Figure 9.3.2.28: Effect of inlet radial distortion on LBR military engine performance – Fuel Flow vs Turbine Entry Temperature

**LBR Military Turbofan Engine Performance Comparison  
Effect of LP Compressor Inlet Total Pressure Distortion**

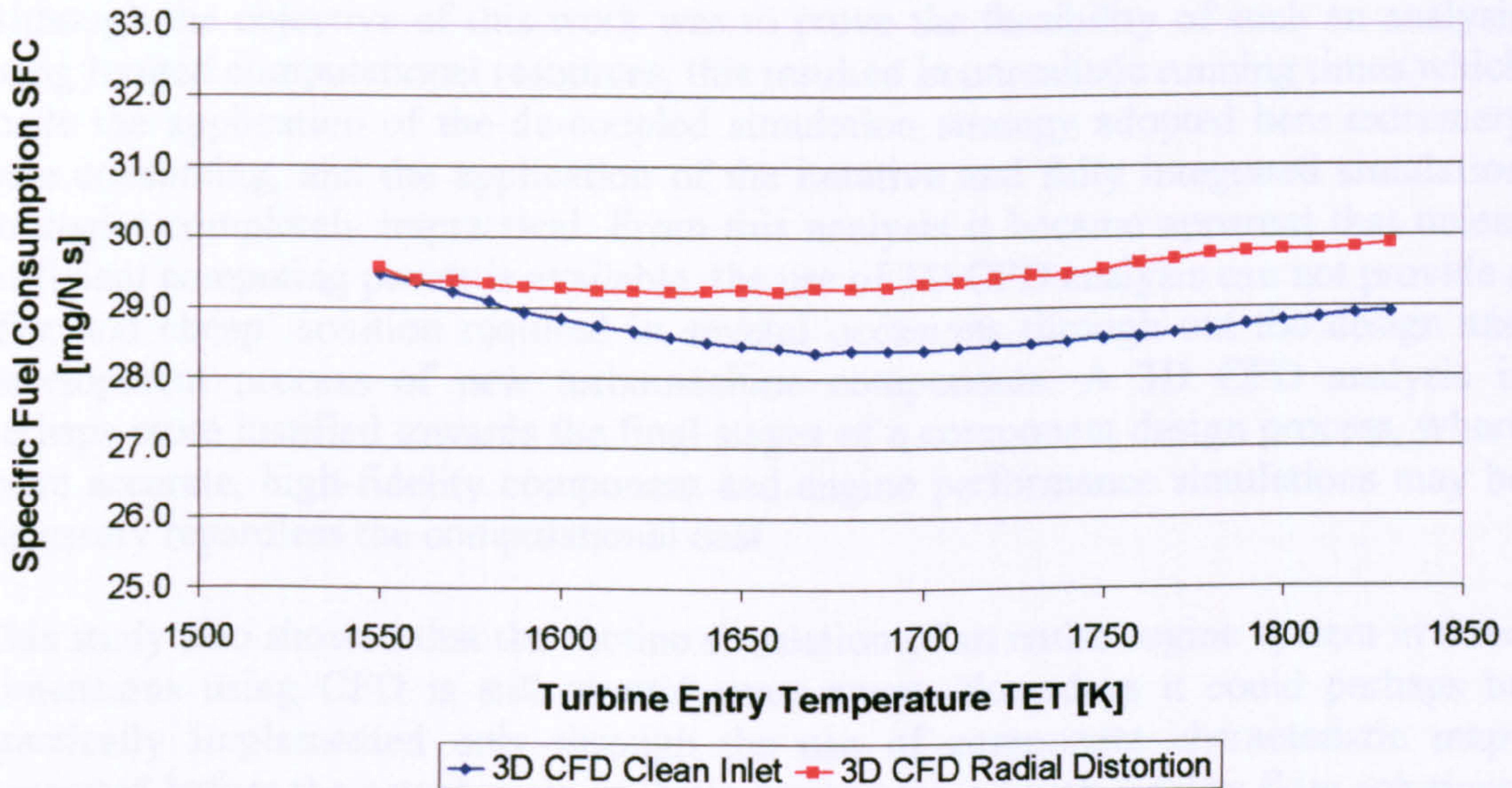


Figure 9.3.2.29: Effect of inlet radial distortion on LBR military engine performance – Specific Fuel Consumption vs Turbine Entry Temperature

Specific fuel consumption in this case remained at similar levels with radial inlet distortion for all power settings. The SFC increase at design point was of the order of 3.4% and reached more or less the same value with the nominal SFC at 1550.0 K.



This is illustrated in Figure 9.3.2.29. This case study is also discussed in more detail in Melloni (2004).

### Concluding Remarks

This particular work adopted the de-coupled approach to advanced performance simulation in order to analyse compressor inlet total pressure distortion effects in the context of the whole engine performance. The analysis identified relative changes in compressor stage performance when the compressor inlet was subjected to different types, extents and frequencies of distortion. High-fidelity component performance data for the first LP compressor stage, generated by a 3D CFD analysis, were subsequently communicated to an engine system analysis performed at a lower level of detail via component characteristic maps. Relative changes in engine performance, with respect to the nominal one, were captured over a range of different power settings and operating conditions.

Results presented here are to be taken only qualitatively because of the preliminary nature of the compressor design adopted. Regardless the limitations of the 3D CFD model itself (i.e. tip clearance effects ignored, adiabatic walls, property mass-averaging between rotor and stator), the analysis carried out by this study demonstrated relative changes in the simulated engine performance larger than 1%. More importantly, it managed to extend the limited capability of the 0D cycle analysis by taking into account the effects of complex, three-dimensional flow phenomena such as inlet flow distortion.

Although the objective of this work was to prove the feasibility of such an analysis using limited computational resources, this resulted in unrealistic running times which made the application of the de-coupled simulation strategy adopted here extremely time consuming, and the application of the iterative and fully integrated simulation strategies completely impractical. From this analysis it became apparent that unless sufficient computing power is available, the use of 3D CFD analysis can not provide a 'fast and cheap' solution required in several occasions through out the design and development process of new turbomachine components. A 3D CFD analysis is perhaps more justified towards the final stages of a component design process, where more accurate, high-fidelity component and engine performance simulations may be necessary regardless the computational cost.

This study also showed that the routine simulation of an entire engine system in three dimensions using CFD is still several years away. Nowadays it could perhaps be practically implemented only through the use of component characteristic maps generated before the actual cycle analysis from averaged high-fidelity flow solutions, as it was demonstrated in this case.

### ***9.3.3. Effect of 3D CFD Turbine Inlet Total Temperature Distortion***

Inlet total pressure distortion may be common in intakes, fans and compressors it is less common however in turbines. On the other hand, turbine inlet total temperature distortion is a far more realistic scenario, certainly worth investigating. The



combustor exit flow exhibits large spatial variations in temperature, both radially and circumferentially. Although it has been established that turbine performance is not greatly affected by temperature distortion, the third case study discussed here looked into the effects of inlet total temperature distortion on the performance of the HP and LP turbines of a LBR military engine. In military engines, due to the higher temperatures involved, combustor outlet total temperature profiles can be significantly amplified in all three dimensions, and could potentially affect the performance of downstream, highly-loaded turbines.

The main objective of this work was the development of a tool using CFD that could carry out turbine performance analysis at high-fidelity, and could subsequently be used in whole-engine performance simulations. This involved the investigation of the performance of high-pressure and low-pressure axial turbines when subjected to different kinds of inlet temperature distortion and the validation of the models by comparing results with published data.

This particular case study is also discussed here as an example of how advanced performance simulation can contribute to the design of new engine components, as well as to the analysis of the impact of design changes in existing components. Moreover, the findings of this investigation are presented here as an example of the kind of detailed, high-resolution analysis that can be carried out in the context of the whole engine performance using 3D CFD tools.

### Introduction

As mentioned above, in gas turbine engines, flows exiting the combustion chamber can present large circumferential and radial gradients in temperature. Typically, the radial variation is the result of the combustor cooling while the circumferential variation is associated with the location and number of the individual fuel injectors. These temperature gradients result in hot spots, and when these hot spots migrate through the first stage turbine they result in hot streaks. Hot streaks, which can have stagnation temperatures double that of the free stream, increase the extent of the secondary flows in the first stage rotor and significantly alter the rotor surface temperature distribution compared to that with no hot streaks.

Three main theoretical models have been utilized over the years to guide the physical and computational studies on turbine inlet temperature distortion. The first model is called the 'substitution principle' and was firstly introduced by Munk and Prim (1947). This model supports that inflow temperature gradients do not alter the streamline patterns in a stationary blade row as long as the inflow stagnation pressure is constant. The local velocity vector can be shown to be proportional to the square root of the local total temperature and therefore the Mach number distribution would be similar for flows with different stagnation temperature distributions but the same total pressure distribution. The second theoretical model however, introduced by Hawthorne (1951) and subsequently extended by Lakshminarayana (1975), indicates that inflow temperature non-uniformities can lead to secondary flows in the rotating blade rows. In addition to the generation of secondary flows, a third effect of non-uniform inlet temperature was demonstrated both theoretically and experimentally by Kerrebrock and Mikolajczak (1970). They showed that in an axial flow compressor, a



non uniform inflow total temperature leads to a segregation of hot and cold gases in the stators, which is caused by a difference in stator inlet flow angle between the hot and cold gas. This effect is even more pronounced in turbines due to larger circumferential temperature gradients.

Low-speed turbine experimental results have provided important information on the flow physics governing the migration of the hot gases. In particular, they have established that:

- A distorted temperature profile has a significant effect on rotor secondary flows, while the vane flow field remains unaffected.
- Segregation of hot and cold gas results in a higher temperature on the rotor pressure side which is also found to be a strong function of the turbine flow coefficient  $V_a/U$ . This is also known as the ‘Kerrebrock’s’ effect (Sharma and Stetson, 1998).
- The effect of hot streaks can be controlled by indexing (clocking) them on the NGV leading edge. This has been found to reduce their velocity and hence incidence angle for the downstream rotor (Sharma and Stetson, 1998).

Over the years, several researchers have studied the effects of turbine inlet total temperature distortion. CFD codes based on Euler and RANS equations have been extensively used by researchers to perform two- and three-dimensional, steady and unsteady flow simulations. Among these, significant enhancement in the understanding of the phenomenon has been achieved as a result of simulations conducted by Takahashi and Ni (1990) and Dorney, et al. (1996). One of the first numerical simulations of hot streak migration was performed by Rai and Dring (1987) using a 2D Navier-Stokes analysis. For reasons that become more evident later on in the discussion, of particular interest are the results obtained by Staubach (1998) published in Sharma and Stetson (1998). In his work, Staubach conducted a series of computations using the unsteady RANS code adopted by Takahashi and Ni (1990).

With the assistance of Thermal Power MSc students and under the technical leadership of the author, both the HP and LP turbines of a LBR military engine were investigated under conditions of inlet total temperature distortion. Due to the great similarities between the two separate investigations, only the HP turbine simulation is discussed here in detail, since this also turned out to be the most interesting case examined from a turbine performance point of view.

It is worth mentioning however that contrary to the HP turbine simulation, the LP turbine investigation managed to capture the ‘Kerrebrock’s’ effect. This being essentially a flow phenomenon and hence outside the general scope of this PhD Thesis it is only briefly described in the following discussion in the context of the HP turbine simulation. A complete account of the LP turbine investigation and a full description of the ‘Kerrebrock’s’ effect can be found in Buono (2004).

### *HP Turbine Inlet Temperature Distortion*

First of all, this particular work dealt with the steady-state simulation of the performance of a single-stage, high-pressure turbine at design point and along two constant speed lines. This study also examined the behaviour of the turbine when



subjected to uneven inlet total temperature distribution. In addition to the ideal case (uniform inlet temperature), the effects of three different types of distorted conditions were investigated at design point. More analytically, during this particular investigation the following cases were examined:

- A clean-inlet simulation with constant inlet stagnation properties to represent an ‘idealized’ design, consistent with the assumptions used in current design processes.
- Radial temperature distortion at design point.
- Combined radial and circumferential temperature distortion (hot spot) at design point. For this kind of distortion two cases were simulated:
  - Hot spots aligned to the mid-passage of the stator, in order to represent a ‘conventional’ design approach (Un-clocked position).
  - Hot spots aligned to the stator LE, in order to represent a ‘managed hot streak’ design approach (Clocked position).

The clean inlet simulation was performed for two reasons, firstly for the validation of the turbine design and its performance at design point conditions, and secondly for the calculation of two non-dimensional speed lines on the HP turbine map for a more complete evaluation of the stage performance at off-design. As mentioned before, distorted inlet temperature profiles were simulated only at design point conditions and then a performance comparison between the different distortion patterns was carried out in relation to the clean case.

The present study looked into the above cases of turbine inlet total temperature distribution which were also examined by Staubach (1998) in the past, for validation and comparative purposes. In his study, Staubach found that the best overall efficiency was achieved with a uniform inlet temperature (i.e. ‘idealized’ design), while the worst efficiency (0.8% lower than the idealized design) was obtained with the ‘conventional’ design (i.e. with the hot-streak passing through the middle of the stator airfoils). He also found that the ‘managed hot streak’ design (i.e. with the hot streaks clocked towards the NGV leading edge) gives a 0.4% higher efficiency than the conventional design and lower efficiency than the idealized design by the same amount.

### Simulation Tools

This work utilized exactly the same simulation software as in the previous case study reported in sub *Section 9.3.2. Effect of 3D CFD Fan Inlet Total Pressure Distortion*: i) a 0D gas turbine modelling and performance simulation code – PYTHIA, and ii) the commercial CFD package CFX-TASCflow/TurboGrid by AEA Technology.

For the purposes of this investigation, PYTHIA’s engine model of the EJ200 was used again (Figure 9.3.3.1). The overall design performance of the engine is illustrated in Table 9.3.3.1. Other engine performance parameters can be found in PYTHIA’s engine input data files which have been included in this thesis as *Appendix J - PYTHIA Engine Input Data Files*.



OPR		25.0:1.0
BPR		0.4:1.0
W	[kg/sec]	77.0
TET	[K]	1800.0
GT with AB	[kN]	90.0
GT w/o AB	[kN]	60.0
SFC	[mg/N sec]	23.0

Table 9.3.3.1: Two-shaft, LBR, military turbofan engine design performance parameters

PYTHIA - 0D Engine Cycle Simulation

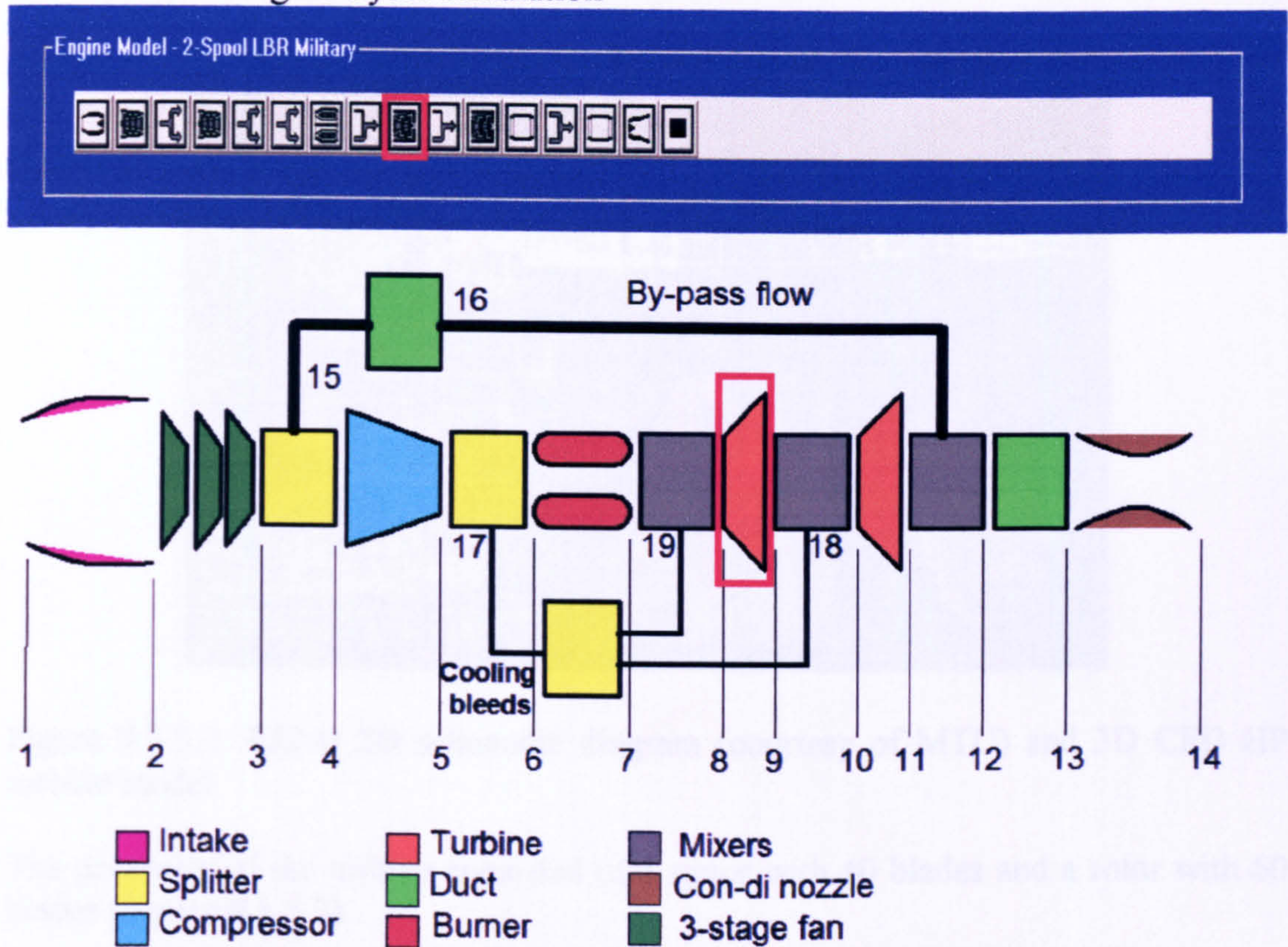


Figure 9.3.3.1: Schematic representation of PYTHIA’s model of the, two-spool, LBR, mixed-exhaust, military turbofan engine

The geometry and 3D CFD model of the investigated high-pressure (Figure 9.3.3.2), single-stage, transonic turbine had to be especially developed for this study due to the lack of published, detailed geometric data for this particular turbine. The turbine duty requirements were obtained by carrying out a PYTHIA 0D simulation of the performance of the engine at its design point (taken at 11000.0 m of altitude and at a flight Mach number of 1.2). The 0D analysis was used alongside the 3D CFD analysis to produce the following turbine performance:



Pressure Ratio		3.250
Isentropic Efficiency		0.870
Non-Dimensional Mass Flow		0.674
Stage Loading Factor ( $\Delta H/U^2$ )		2.290
Flow Factor ( $V_a/U$ )		0.790
Rotational Speed	[rpm]	16786.000
Mean Diameter	[m]	0.512
Hub to Tip Ratio		0.830
Blade Mid-Height Reaction	[%]	50.000

Table 9.3.3.2: LBR military turbofan HP turbine performance

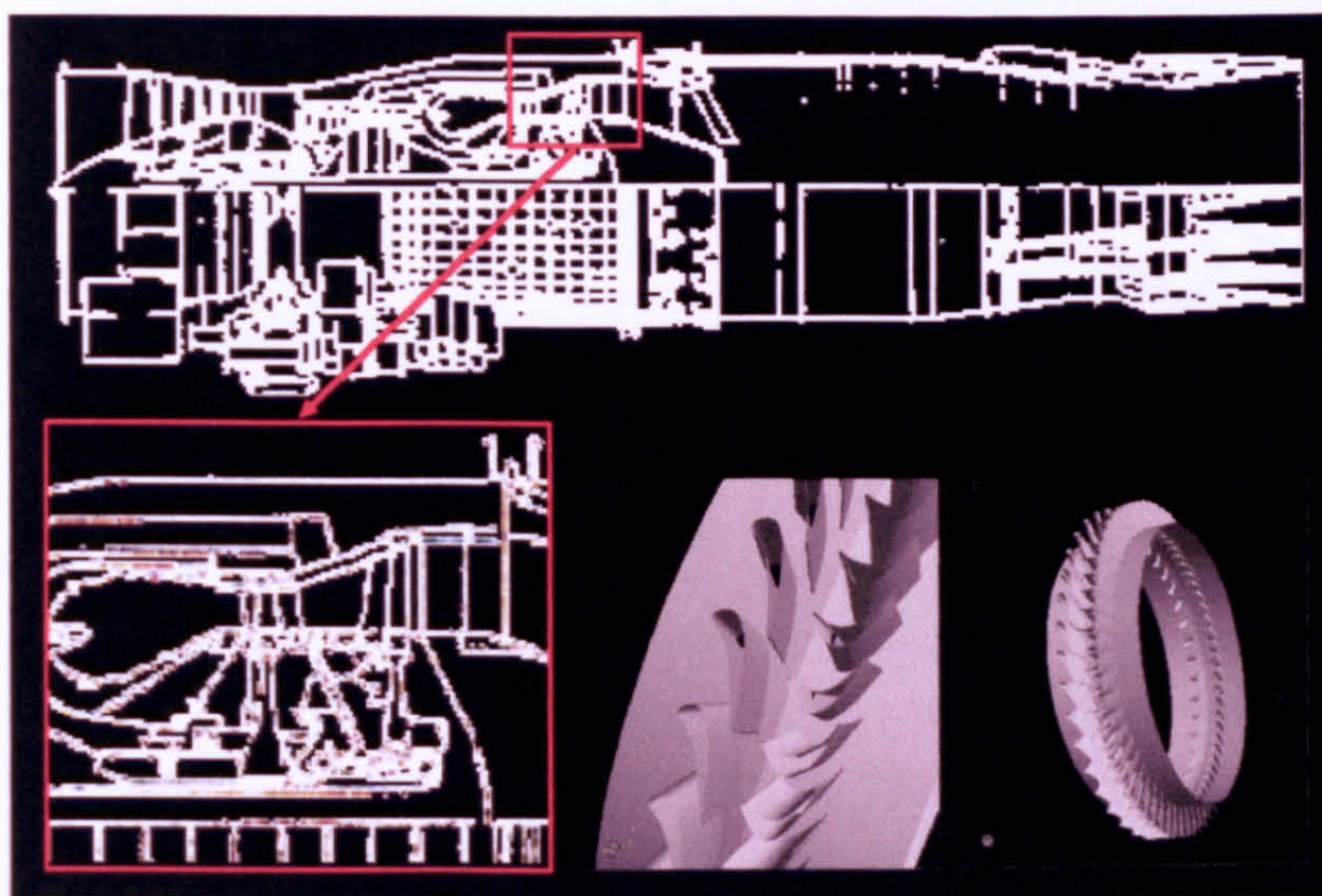


Figure 9.3.3.2: EJ200 2D schematic diagram (courtesy of MTU) and 3D CFD HP turbine model

The geometry of the turbine consisted of a stator with 40 blades and a rotor with 60 blades (Figure 9.3.3.3).



Figure 9.3.3.3: HP turbine stator and rotor blades



Designing the 3D turbine geometry from scratch, obviously involved an iterative process. After establishing the overall engine performance from PYTHIA's 0D solutions, and also the operating conditions of the HP turbine at design point, a turbine preliminary design exercise took place using Cranfield's CASSANDRA software for turbomachinery. Based on the outcome of the preliminary design a 3D CFD turbine geometry was created to meet the same performance requirements. Fine tuning the model at design point involved an iterative process where small changes and adjustments had to be done to the original design until the averaged, 3D CFD turbine performance matched the 0D cycle predictions. For the blade design, a parametric technique was followed based on a composite curve approach. Both NGV and rotor blade suction and pressure surfaces were defined analytically via quadratic Bezier splines. Each blade surface was defined by eight independent parameters and for the radial stacking the centroid of the area was used (Figure 9.3.3.4).

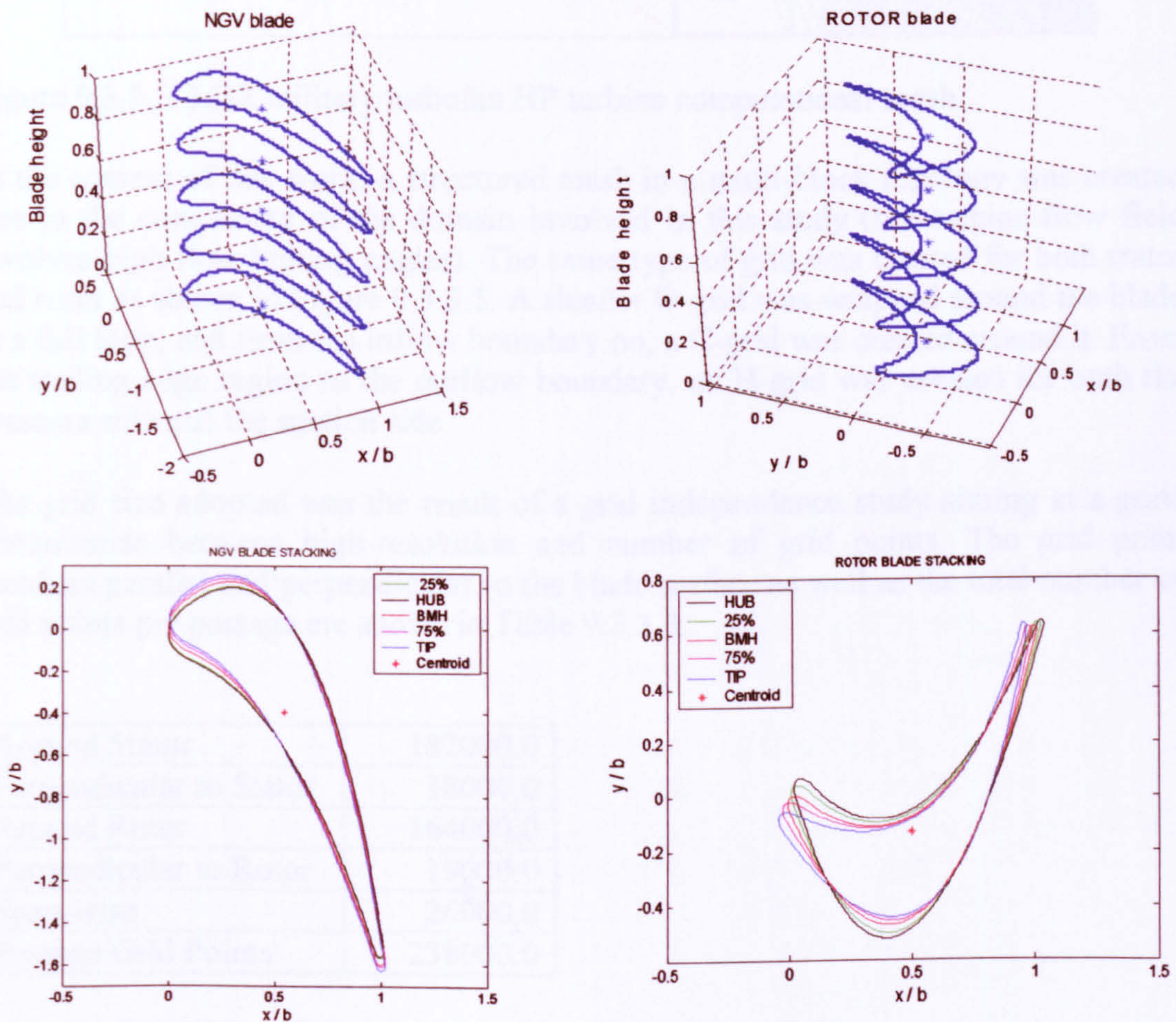


Figure 9.3.3.4: HP turbine stator and rotor blade stacking

In order to reduce the computational cost and to simplify the model, the effects of tip clearance and cooling flows were ignored. Further details of the complete design process and of the final turbine characteristics are reported in Zilli (2004).

In this study the computational mesh was created using the commercial software CFX-TurboGrid as in the case of the 3D CFD compressor discussed previously.



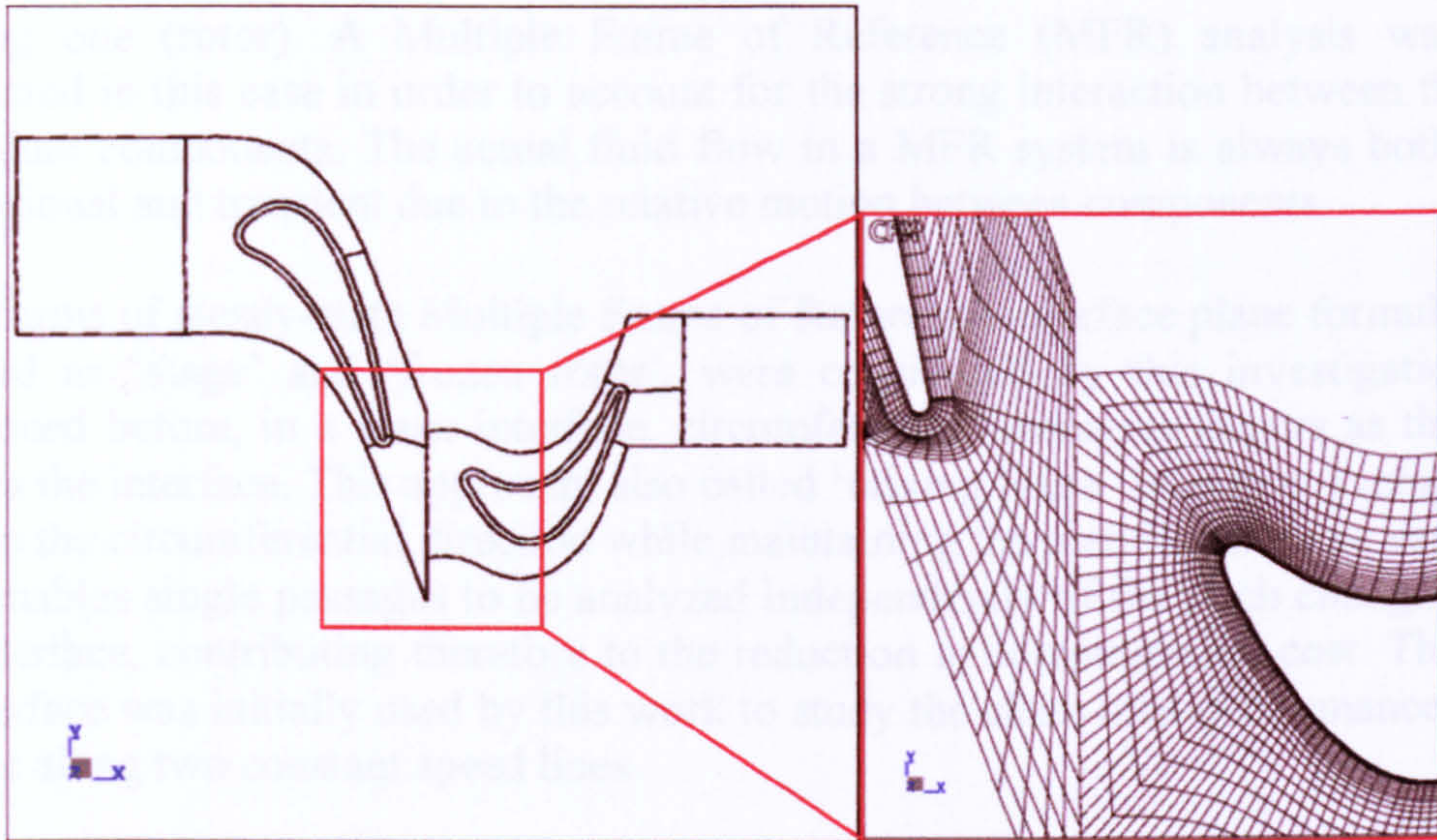


Figure 9.3.3.5: LBR military turbofan HP turbine computational mesh

In the context of this work, a structured mesh in a multi-block topology was created due to the complexity of the domain involved in this study (the turbine flow field involves high flow turning angles). The same type of grid was created for both stator and rotor as shown in Figure 9.3.3.5. A slender O-grid was wrapped around the blade in a full loop, and from the inflow boundary on, a C-grid was created around it. From the trailing edge region to the outflow boundary, an H-grid was created for both the pressure side and the suction side.

The grid size adopted was the result of a grid independence study aiming at a good compromise between high-resolution and number of grid points. The grid point numbers parallel and perpendicular to the blade surface as well as the total number of grid points per passage are shown in Table 9.3.3.3.

Around Stator	182000.0
Perpendicular to Stator	18000.0
Around Rotor	164000.0
Perpendicular to Rotor	19000.0
Span-wise	26000.0
Passage Grid Points	238000.0

Table 9.3.3.3: LBR military turbofan HP turbine grid resolution

Moreover, the software CFX-TASCflow was used as before as the CFD flow solver, together with the standard k- $\epsilon$  model to account for the effects of turbulence (see sub Section 9.3.2. *Effect of 3D CFD Fan Inlet Total Pressure Distortion*).

### Interface Plane

The single-stage, high-pressure turbine of the LBR military engine under investigation consists of two components, a stationary row of blades (stator) and a



rotating one (rotor). A Multiple Frame of Reference (MFR) analysis was also conducted in this case in order to account for the strong interaction between the two individual components. The actual fluid flow in a MFR system is always both three dimensional and transient due to the relative motion between components.

Both forms of steady-state Multiple Frame of Reference interface plane formulations, denoted as 'stage' and 'frozen rotor', were considered by this investigation. As mentioned before, in a stage interface, circumferential averaging occurs as the flow crosses the interface. This approach, also called 'mixing plane' interface, averages the flow in the circumferential direction while maintaining the meridional plane variation. This enables single passages to be analyzed independently of the pitch change across the interface, contributing therefore to the reduction in computational cost. This type of interface was initially used by this work to study the clean inlet performance of the turbine along two constant speed lines.

In a frozen rotor interface, the frame change occurs as the flow crosses the interface without imposing any circumferential averaging and the relative pitch-wise position of the two components remains fixed for the entire simulation (a quasi-steady approximation where the wake/core profile is preserved across the interface). This means that the flow can freely re-circulate across the interface, thus enabling local flow features to be transported across the sliding interface. The flow field obtained from such a simulation corresponds to a snapshot of the dynamic interaction process and is hence, nearly equivalent to the situation where the rotor angular motion is frozen.

In TASCflow, the frozen rotor method is often employed as the starting point for a transient simulation or as a method of investigation of a particular flow condition regarding the relative pitch-wise positioning of two adjacent blade rows. The ability to examine the effects of the pitch-wise positioning of rotors and stators enables the investigation of aspects of unsteady interaction, such as the impingement of upstream wakes onto downstream components, while incurring steady-state simulation costs.

As mentioned above, although the mixing plane interface was initially used in this work to study the clean inlet performance of the turbine, the frozen rotor interface formulation was finally adopted by this work. In order to compare the results obtained with the two different temperature distortion patterns (i.e. radial and radial plus circumferential) and the clean case, it was found necessary to keep the same grid interface model. The mixing plane interface is unable to capture the hot streak migration across the stage. Since hot spots are a combination of radial and circumferential temperature distortions, the circumferential averaging at the interface introduced by the stage mixing plane leads to an incorrect representation of the phenomenon. Using that approach only the radial distortion, besides of course the clean case, could have been studied.

Given that the frozen rotor is a steady-state method where no relative position change takes place over time, the generality of the analysis depends upon the relative pitch-wise clocking between the stator and rotor. The flow solutions presented here are thus the average of the solutions obtained by varying the clocking position of the two components until a complete stator passage has been swept by a rotor blade.



### Boundary Conditions

For the 3D CFD simulations all solid walls (i.e. blade surfaces and annulus walls) were assumed to be adiabatic and perfectly smooth. The flow at the inlet was assumed to be parallel to the machine axis. At the inflow, total pressure and total temperature were used as boundary conditions. Turbulence intensity and eddy length scale were also defined at the inflow boundary as follows:

Inlet Total Temperature	[K]	1737.14
Inlet Total Pressure	[kPa]	139.08
Turbulence Intensity	[%]	15.00
Eddy Length Scale	[mm]	3.00

Table 9.3.3.4: LBR military turbofan HP turbine inflow boundary conditions

At the outflow boundary the grid face averaged value of static pressure was imposed. For the clean inlet simulation inlet stagnation properties were set at the constant values given by PYTHIA's design point simulation results. The performance of the turbine under uniform inlet conditions was investigated at two relative to design rotational speeds, for 100% (16786.0 rpm) and 60% (10070.0 rpm) approximately. The various points on the map, along the two constant speed lines, were obtained by changing the turbine outlet static pressure using approximate data obtained from PYTHIA's 0D simulations, according to the de-coupled approach to high-fidelity analysis. This was equivalent to allowing more or less mass flow to pass through the stage, thus changing the operating point of the turbine.

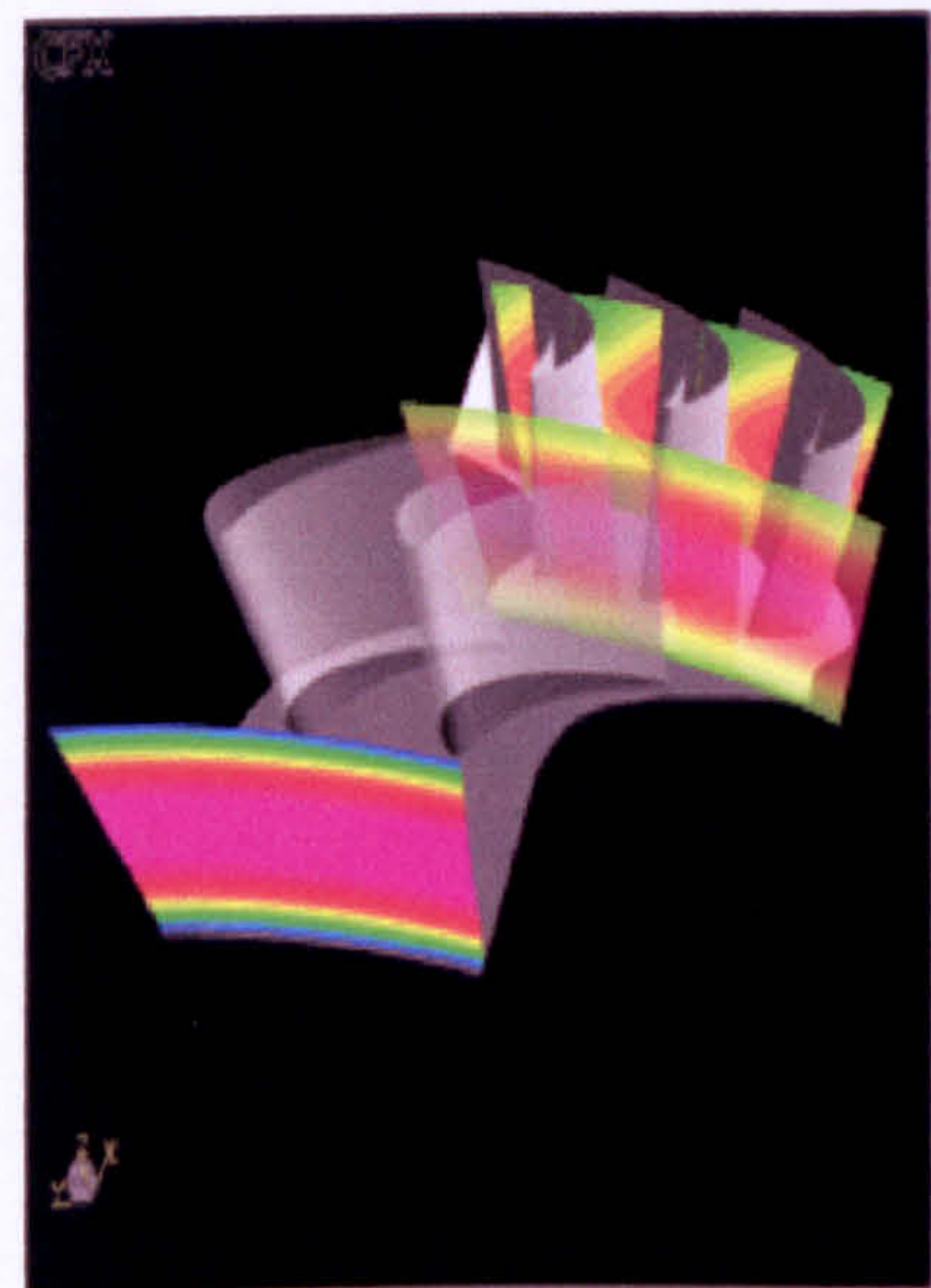
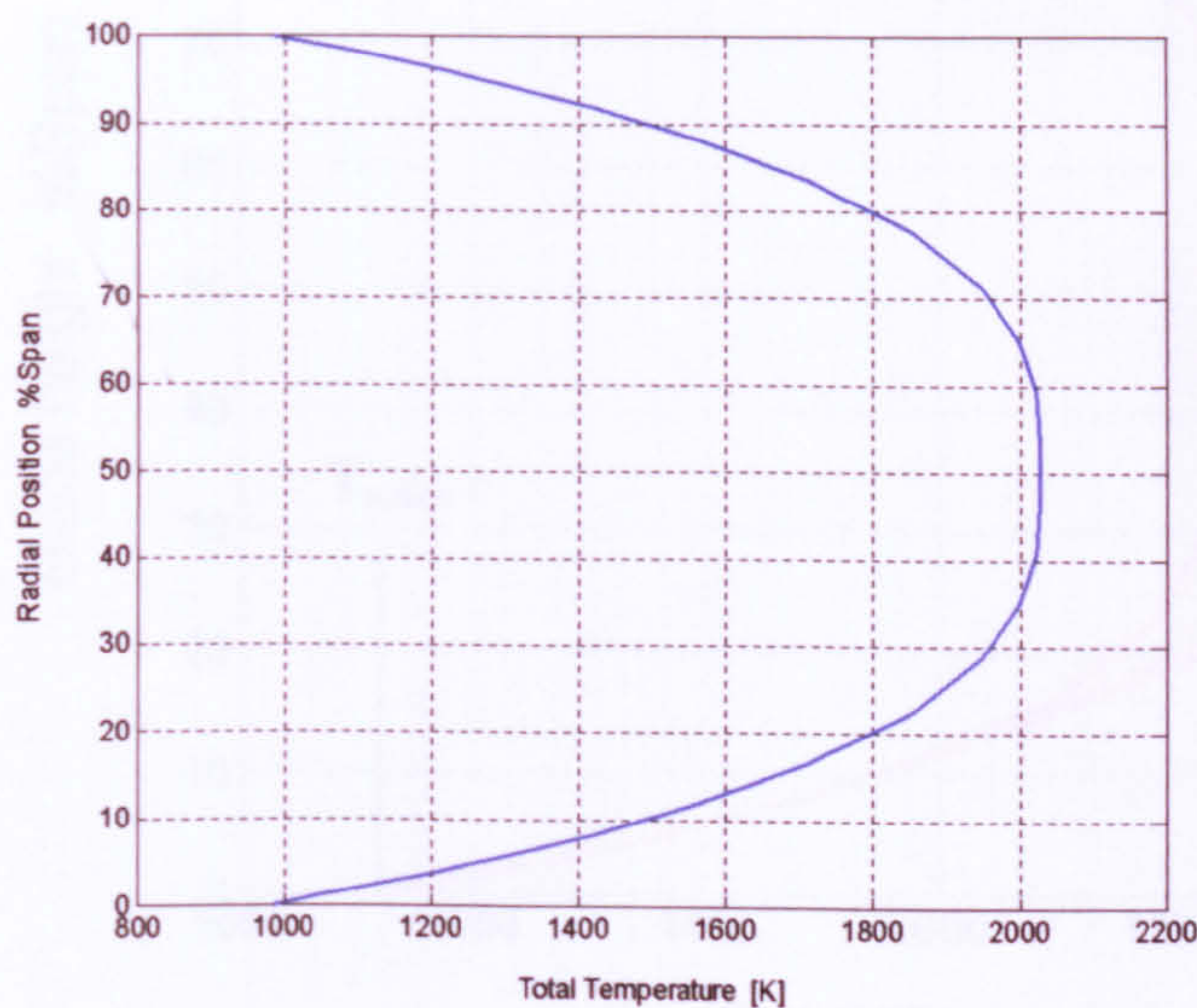


Figure 9.3.3.6: HP turbine radial total temperature distortion inlet profile

Two different patterns of total temperature distortion were examined at design point, one radial and one mixed (combination of radial and circumferential) in an attempt to simulate a combustor exit profile that was as realistic as possible. In both cases, the temperature profile imposed at the inlet was determined in such a way that the mass-averaged total temperature was the same as in the clean case (i.e. design point TET).



This was done in order to show the relative variations in turbine performance with respect to design point.

The imposed profile of radial total temperature distortion is illustrated in Figure 9.3.3.6 and gives a peak temperature at blade mid-height of 2028.0 K and a minimum at hub and tip of 985.0 K where the cooling flow comes from the combustor dilution holes. This corresponds to a relatively severe Pattern Factor (PF) of 0.39, given by the following relationship:

$$PF = \frac{T_{o,max} - \overline{T_o}}{\overline{T_o} - T_{o,min}} \quad [Eq. 9.3.3.1]$$

The second temperature pattern represented a circular hot spot in an attempt to simulate the presence of the fuel injectors. Twenty fuel injectors were considered, therefore the computational domain examined had to be one twentieth of the annulus area, corresponding to two NGV and three rotor passages. The temperature profile, combination between a radial and a circumferential temperature gradient was modelled by a Gaussian distribution superimposed on a radial profile. This is shown in Figure 9.3.3.8.

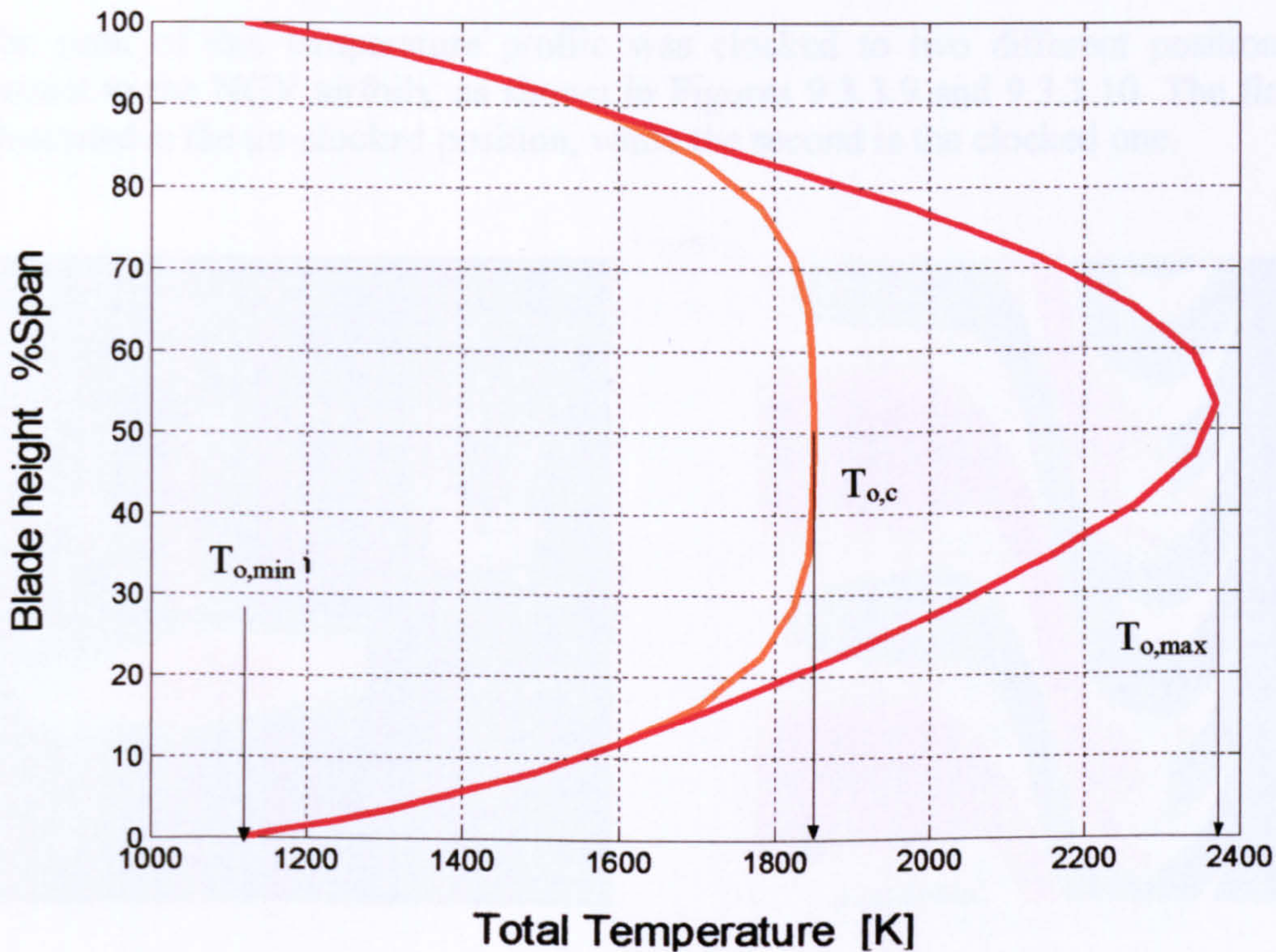


Figure 9.3.3.7: Meridional view of the hot spot temperature profile

As far as the hot spot temperature profile is concerned, a temperature ratio of 1.28 was used, between the peak temperature and the temperature of the flow immediately surrounding the hot streak, according to the following relationship and Figure 9.3.3.7.



$$\lambda = \frac{T_{o,max}}{T_{o,c}} \quad [\text{Eq. 9.3.3.2}]$$

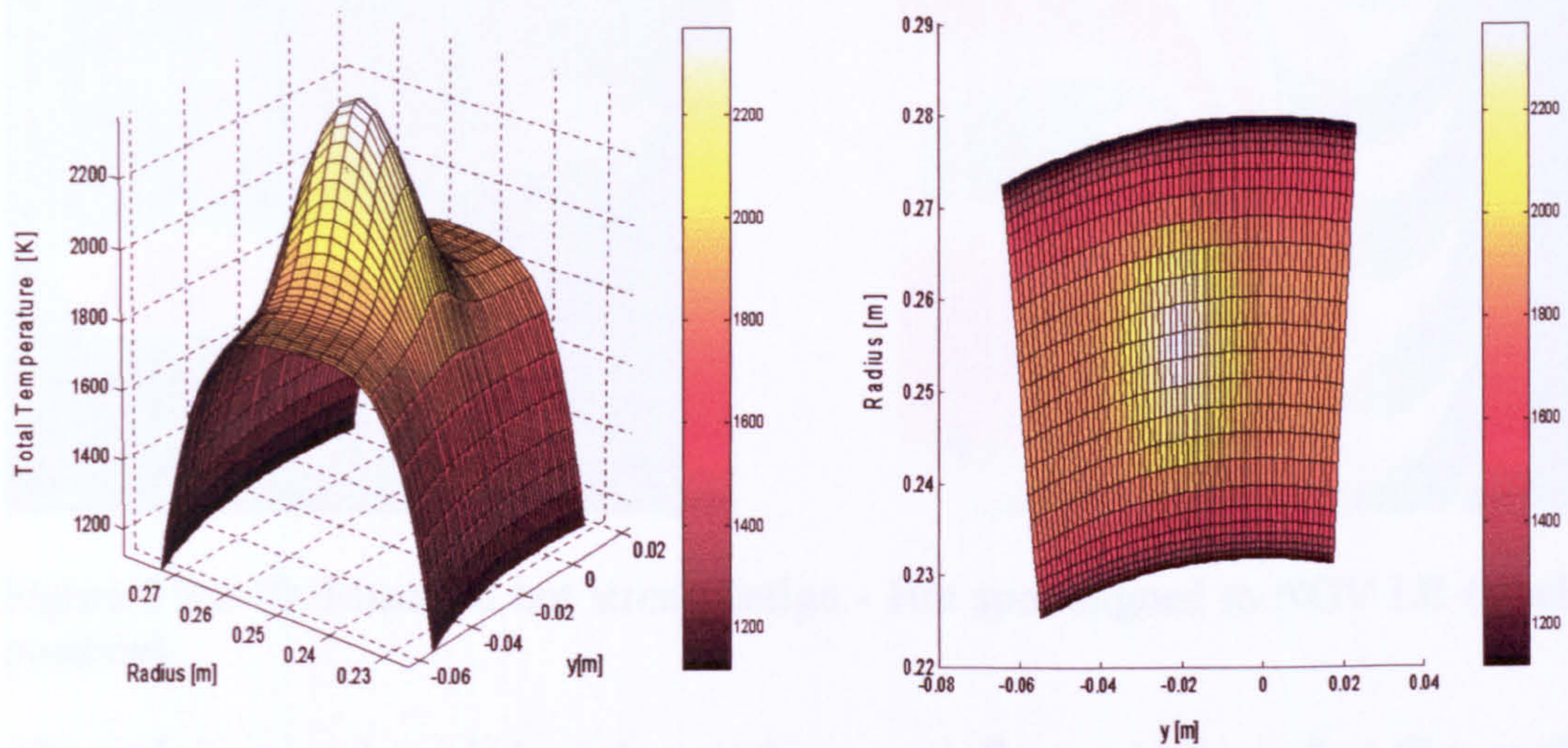


Figure 9.3.3.8: Hot spot temperature profile over 1/20<sup>th</sup> of annulus area

The peak of this temperature profile was clocked to two different positions with respect to the NGV airfoils, as shown in Figures 9.3.3.9 and 9.3.3.10. The first case illustrated is the un-clocked position, while the second is the clocked one.

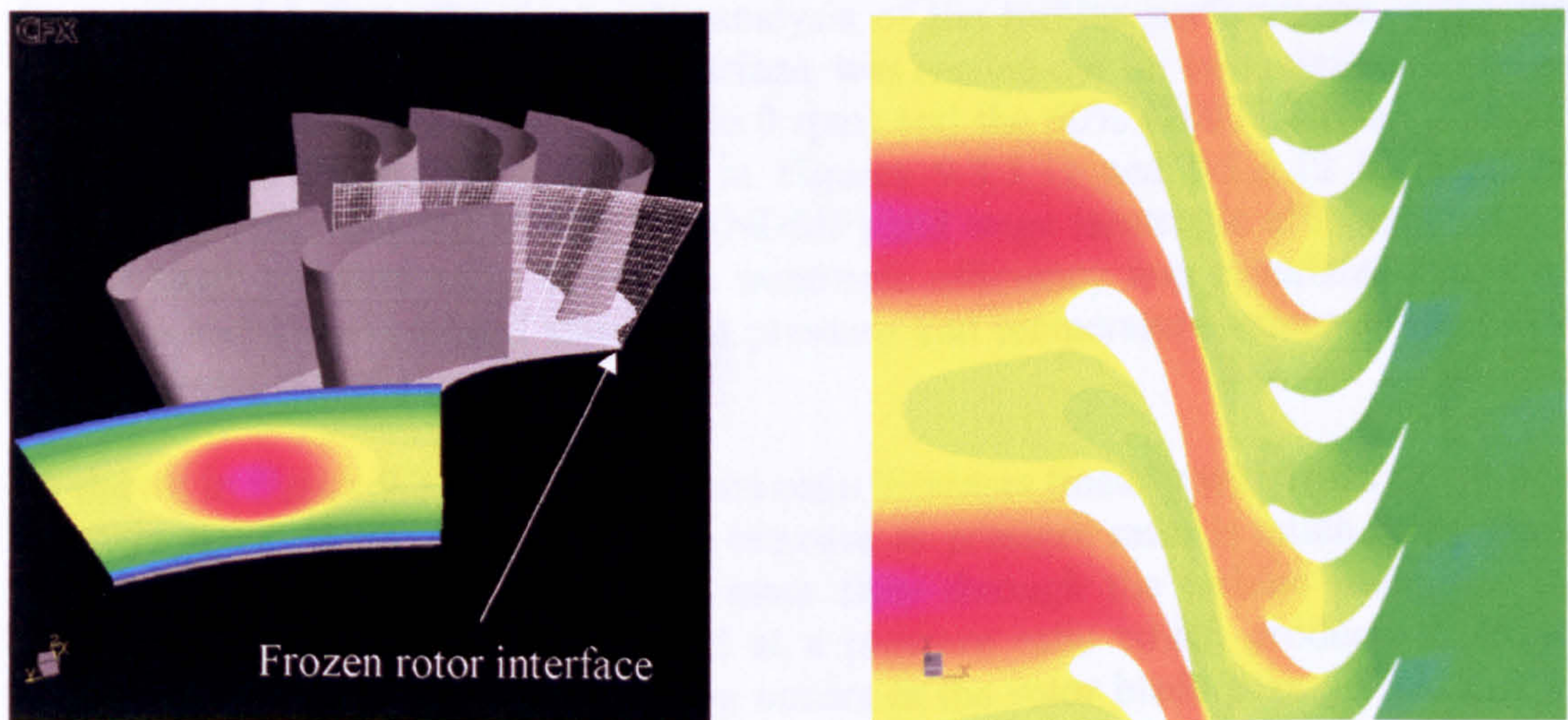


Figure 9.3.3.9: Conventional design - Hot spot aligned to NGV mid-passage (un-clocked position)



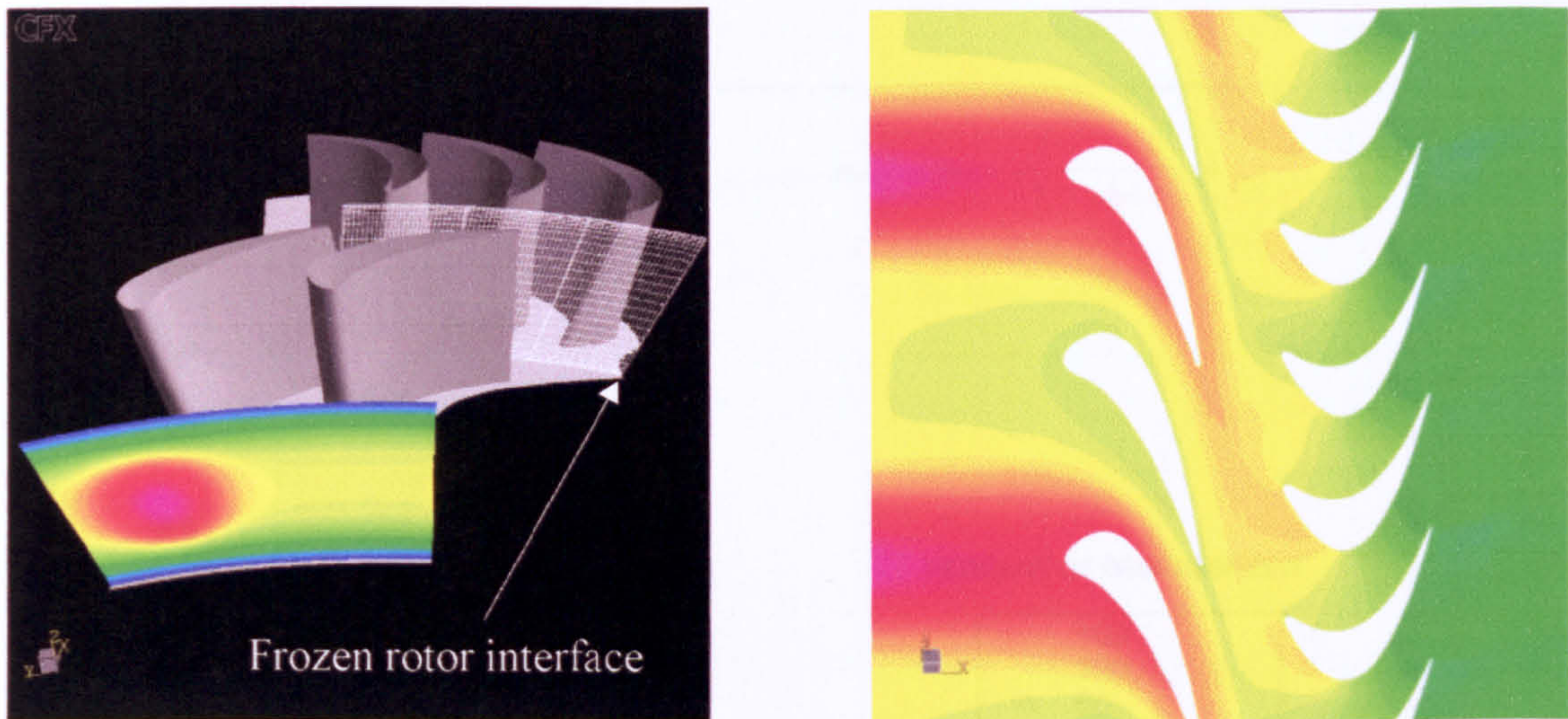


Figure 9.3.3.10: Managed hot streak design - Hot spot aligned to NGV LE (clocked position)

Although it was acknowledged that clocking can influence blade surface film cooling and hence turbine efficiency, it was outside the scope of this investigation to carry out a more detailed study of cooling flow effects. However, the profiles of total temperature adopted by this study were consistent with there being some cooling flows from the combustor annulus.

### Clean Inlet Performance

As mentioned before, the clean inlet analysis of the turbine performance, using the mixing plane approach as a sliding interface, was carried out for two relative to design rotational speeds, namely 100% (16786.0 rpm) and the 60% (10070.0 rpm). The 3D CFD averaged results are presented in Figures 9.3.3.11 and 9.3.3.12 in terms of turbine Non-Dimensional Mass Flow (NDMF) and stage isentropic efficiency versus overall stage pressure ratio. The stage isentropic efficiency was calculated based on the mass and time averaged stagnation pressure and temperature values at the NGV inlet and rotor outlet planes.

As shown in Figure 9.3.3.11, the pressure ratio increases linearly with mass flow up to a certain point. Beyond this point the increase in pressure ratio is much more rapid and compressibility effects limit the mass flow through the turbine passage. The maximum value of NDMF is reached at a pressure ratio which produces choking conditions. In the present case choking occurs in the rotor blade passage and this is why the maximum mass flow varies slightly with relative rotational speed.

As shown in Figure 9.3.3.12, along the design speed line, the efficiency is sensibly constant over a wide range of pressure ratios. This is because the favourable pressure gradient, which controls the boundary layer growth, allows the turbine blading to operate over a wide range of incidence without much increase in the loss coefficient. The higher pressure ratios give rise to a large acceleration of relative flow and the presence of supersonic exit flow. Therefore, both the shock losses and viscous losses increase with an increase in pressure ratio.



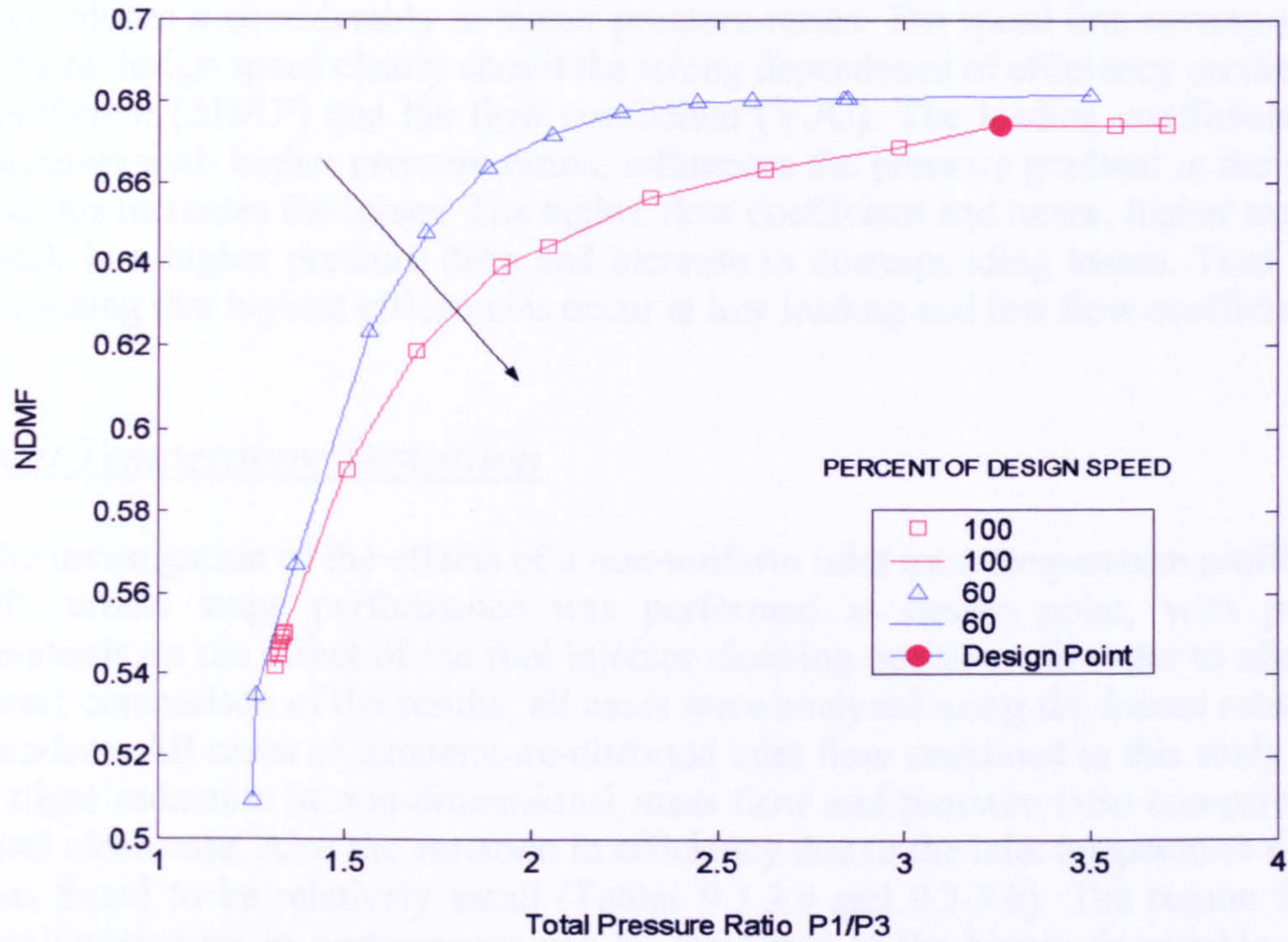


Figure 9.3.3.11: 3D CFD HP turbine characteristic for two constant speed lines – Non Dimensional Mass Flow vs Stage Overall Pressure Ratio

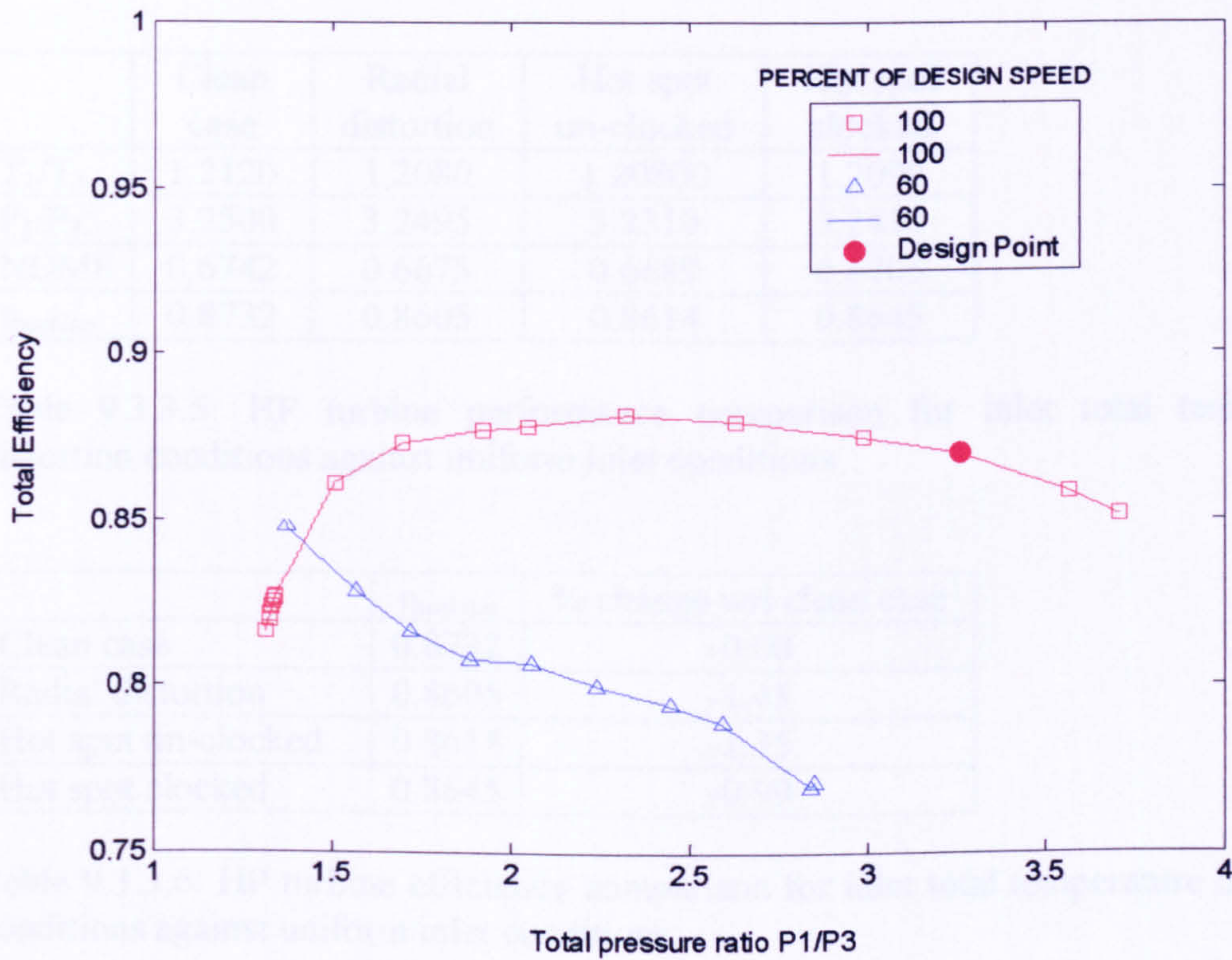


Figure 9.3.3.12: 3D CFD HP turbine characteristic for two constant speed lines – Stage Isentropic Efficiency vs Stage Overall Pressure Ratio



The reduction in rotational speed increases the stage efficiency at low pressure ratios and reduces it considerably at higher pressure ratios. The speed line corresponding to 60% of design speed clearly shows the strong dependence of efficiency on the loading coefficient ( $\Delta H/U^2$ ) and the flow coefficient ( $V_a/U$ ). The loading coefficient, which increases with higher pressure ratios, influences the pressure gradient in the passage, and this increases the losses. The higher flow coefficient and hence, higher mass flow, result in a higher pressure drop and increase in corresponding losses. Thus it is not surprising that highest efficiencies occur at low loading and low flow coefficient.

### Inlet Temperature Distortion

The investigation of the effects of a non-uniform inlet total temperature profile on the HP turbine stage performance was performed at design point, with particular emphasis on the effect of the fuel injector clocking positions. In order to allow for a direct comparison of the results, all cases were analysed using the frozen rotor sliding interface. All cases of temperature-distorted inlet flow examined in this study showed a slight reduction in non-dimensional mass flow and pressure ratio compared to the ideal clean case. Also the variation in efficiency due to the inlet temperature distortion was found to be relatively small (Tables 9.3.3.5 and 9.3.3.6). The reason for these small variations in performance can be attributed to the highly favourable pressure gradient that characterises a turbine, in particular, the one examined in this study. In fact, the favourable pressure gradient allowed a better control over the boundary layer growth, making it more tolerant to flow non-uniformities.

	Clean case	Radial distortion	Hot spot un-clocked	Hot spot clocked
$T_1/T_3$	1.2120	1.2080	1.20800	1.2090
$P_1/P_3$	3.2500	3.2495	3.2310	3.2410
NDMF	0.6742	0.6675	0.6689	0.6705
$\eta_{\text{turbine}}$	0.8732	0.8605	0.8614	0.8645

Table 9.3.3.5: HP turbine performance comparison for inlet total temperature distortion conditions against uniform inlet conditions

	$\eta_{\text{turbine}}$	% change wrt clean case
Clean case	0.8732	-0.00
Radial distortion	0.8605	-1.45
Hot spot un-clocked	0.8614	-1.35
Hot spot clocked	0.8645	-0.99

Table 9.3.3.6: HP turbine efficiency comparison for inlet total temperature distortion conditions against uniform inlet conditions



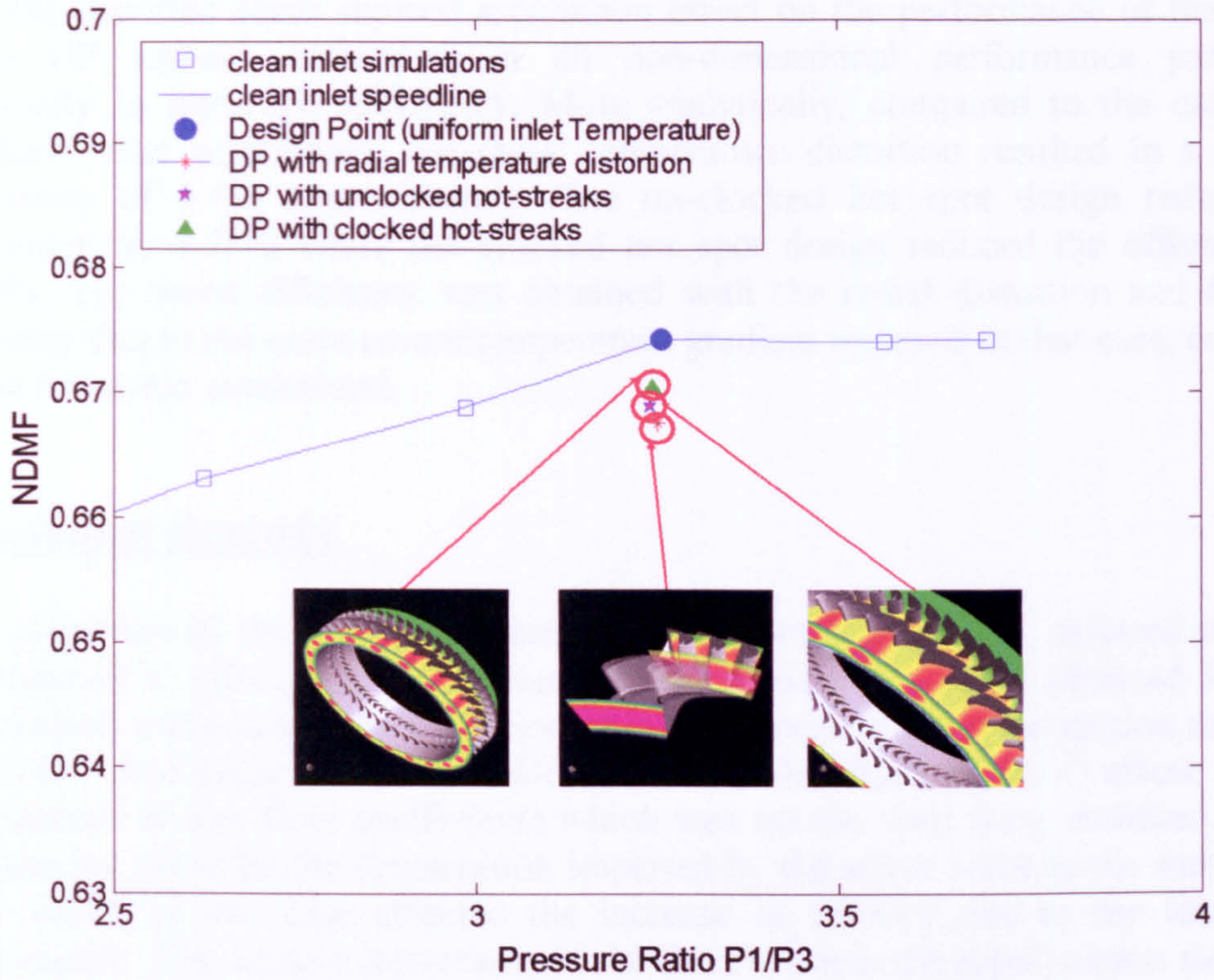


Figure 9.3.3.13: Design point HP turbine performance comparison for inlet total temperature distortion conditions against uniform inlet conditions – Non-Dimensional Mass Flow vs Stage Pressure Ratio

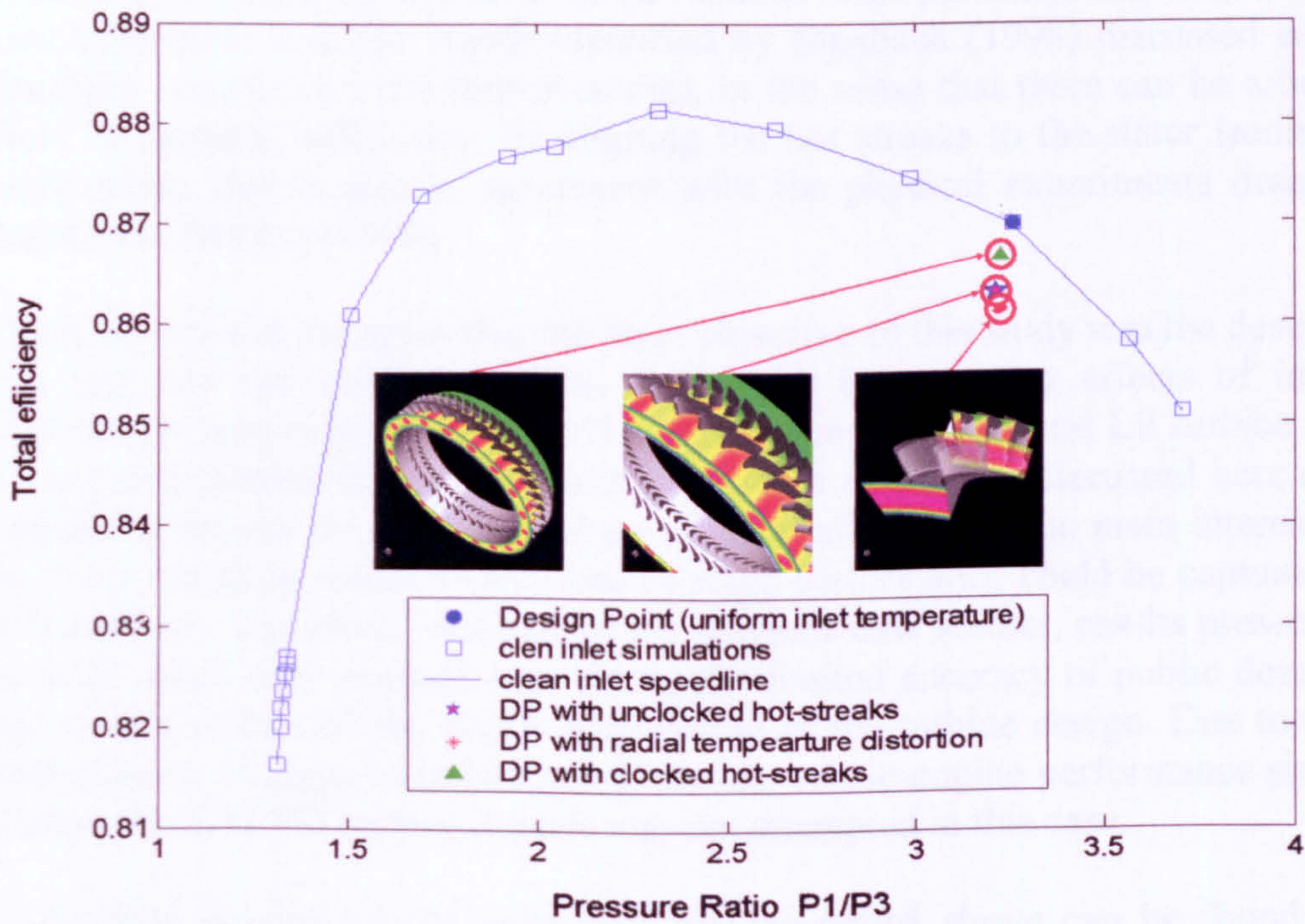


Figure 9.3.3.14: Design point HP turbine performance comparison for inlet total temperature distortion conditions against uniform inlet conditions – Stage Isentropic Efficiency vs Stage Pressure Ratio



From Tables 9.3.3.5 and 9.3.3.6 and Figures 9.3.3.13 and 9.3.3.14, it becomes evident that the distorted cases showed a common effect on the performance of the single-stage HP turbine, reductions in all non-dimensional performance parameters especially in isentropic efficiency. More analytically, compared to the clean case (uniform inlet conditions), the radial temperature distortion resulted in a drop in efficiency of 1.4% approximately. The un-clocked hot spot design reduced the efficiency by 1.35% while the clocked hot spot design reduced the efficiency by 0.99%. The worst efficiency was obtained with the radial distortion and this was probably due to the more severe temperature gradient imposed in that case, compared to the hot streak simulations.

### Concluding Remarks

The migration of the hot gas towards the rotor pressure surface, referred to as the 'Kerrebrock's' effect, was not captured by this study. The result obtained from the simulations was actually the migration of the hot streak towards the suction surface of the rotor. According to Rai and Dring (1987), the 'Kerrebrock's' effect is more pronounced at low flow coefficients which was not the case here. Another possible explanation could be the deceleration imparted by the stator wake to the surrounding flow which in this case affected the increase in velocity due to the increase in temperature. The relative movement of the fluid towards the rotor suction side could be cinematically explained by the so called 'negative jet' effect induced by the stator wake (Hodson, 1998).

However, what is of a great importance here is the fact that this study captured and demonstrated a 0.36% improvement in stage performance, with respect to the conventional design, by indexing the hot streaks. This particular outcome is in a very good agreement with the trends identified by Staubach (1998) discussed earlier on (Staubach reported a 0.4% improvement), in the sense that there can be a beneficial effect, in terms of efficiency, by aligning the hot streaks to the stator leading edge. Furthermore, this is also in agreement with the physical experiments described in Sharma and Stetson (1998).

It must be pointed out again that the main objective of this study was the development of a tool and the validation of its fidelity by investigating effects of inlet total temperature distortion on the overall performance of an HP and LP turbine stage. It can not be expected that a CFD calculation such as the one discussed here can give trustworthy results for absolute values of stage efficiency. The main interest was to see if any trends in relative variations of stage performance could be captured by the CFD analysis. Therefore, similarly to the previous case studies, results presented here are to be taken only qualitatively, due to the limited accuracy of public domain data used in this study and the preliminary nature of the turbine design. Due to the very small relative changes in turbine performance, whole-engine performance simulation utilising the 3D CFD turbine models was not attempted in this case.

A complete account of the work that was described above can be found in Zilli (2004). The above work also resulted in a conference publication (Zilli, et al., 2005).



## CHAPTER X

# **CONCLUSIONS AND FUTURE WORK**

This chapter outlines the main achievements of the work presented in this Thesis, summarises the main conclusions of the investigation and finally lists a number of recommendations for the potential future expansion of the software tools and methodologies developed in the context of this study.

### ***10.1. Achievements***

This work investigated different simulation strategies for communicating the performance characteristics of an isolated gas turbine engine component, resolved from a detailed, high-fidelity analysis, to an engine system analysis carried out at a lower level of resolution.

The findings of this investigation will hopefully allow component-level, complex physical processes to be captured and analyzed in the context of the whole engine performance, at a more affordable computing resource and time than before.

In the context of this study, three methods of advanced performance simulation, i.e. the de-coupled, the iterative and the fully integrated simulation strategies, were thoroughly investigated in terms of their actual implementation and potential, by utilising 2D SLC and 3D CFD engine component models.

The analysis carried out by this work demanded the development of robust SLC software. A *2D Intake SLC Software* was developed to handle the modelling and performance of conical and annular intakes and ducts, and a *2D Compressor SLC Software* was developed to handle the modelling and performance of compressors.

The three advanced simulation strategies were also investigated in terms of their actual implementation and potential by looking into relative changes in engine performance after integrating CFD-generated, high-fidelity component performances back into the 0D engine analysis. For this purpose, several case studies were carried out, such as different types, extents and frequencies of compressor inlet pressure distortion and of turbine inlet temperature distortion, utilising 3D CFD engine component models.

The CFD and SLC software tools developed in the context of this work can be now used as:

- Performance prediction tools for components of a known design
- Development tools to assess the changes in performance of a known component after implementing small geometry changes
- Design tools to verify and refine the outcome of a preliminary design analysis
- Plug-in tools that can be integrated into a conventional 0D gas turbine engine simulation code for high-fidelity studies



Perhaps the most important outcome of this research effort was the successful, full integration of 2D SLC component models into a 0D engine cycle analysis at an affordable computational cost. This has opened the way towards a full 2D engine cycle analysis in the very near future, by establishing the necessary methodology and technology for such an undertaking.

The work presented in this Thesis covered the full spectrum of high-fidelity analysis from 0D to 3D, included both CFD and through-flow analysis tools, discussed all three high-fidelity simulation strategies in detail (de-coupled, iterative, fully integrated) and looked into several different aspects of engine performance such as compressor inlet flow distortion and turbine inlet temperature distortion.

In total, 16+ different analyses were carried out in the context of this work. Moreover, this author's research work in the area of high-fidelity analysis, supported by visiting and Thermal Power MSc students, resulted in 12+ conference and journal publications.

## ***10.2. Main Conclusions***

This section focuses on the main conclusions and observations of this study. The various concluding remarks made throughout the Thesis are discussed and summarised below.

### ***De-Coupled Approach***

This work demonstrated through several case studies that the de-coupled approach to high-fidelity analysis can be successfully applied to all engine components which can be modelled in 2D and 3D, either by means of a through-flow analysis method or by the use of CFD tools.

Utilising 2D SLC component models, this approach proved to be a fast and inexpensive in terms of computational resources method, for integrating into a 0D engine cycle analysis the full geometric characteristics of a component and its actual performance.

Utilising 3D CFD component models, certainly offers greater accuracy compared to the 2D SLC analysis, at the expense of a more time consuming process to establish the component characteristic map. In those cases however, where more accurate, high-fidelity engine performance simulation is required, the extra time and effort that is required to create and run a 3D CFD engine component is perhaps justifiable if not necessary.

More analytically, despite the automatic scaling of default component maps at design point, the analysis carried out by this work demonstrated large differences in off-design engine performance arising from the use of default component characteristics, compared to the engine performance obtained after integrating the characteristics of the high-fidelity components into the 0D cycle analysis. In the case of the 2D SLC compressor for example, the analysis showed that although 'default' and 'high-



fidelity' engine equilibrium running lines appeared to be in a good agreement, operating points along these lines actually corresponded to different thermodynamic balances in the engine and hence, different engine power settings, for the same relative rotational speed and corrected mass flow.

Moreover, this particular work adopted the de-coupled approach to advanced performance simulation in order to analyse compressor inlet total pressure distortion effects in the context of the whole engine performance using CFD. The analysis identified relative changes in compressor performance when the compressor inlet was subjected to different types, extents and frequencies of distortion. High-fidelity component performance data generated by the 3D CFD analysis, where subsequently communicated to an engine system analysis performed at a lower level of detail via component characteristic maps. Relative changes in engine performance, with respect to the nominal one, were captured over a range of different power settings and operating conditions.

The analysis carried out by this study demonstrated relative changes in the simulated engine performance larger than 1%, but more importantly managed to demonstrate the extension of the limited capability of the 0D cycle analysis by taking into account the effects of complex, three-dimensional flow phenomena such as inlet flow distortion.

In the case of the 3D CFD high-fidelity simulations, this work attempted to prove the feasibility of such an analysis using computational resources similar to the ones used in the 2D SLC analysis. This however resulted in very long running times which made the application of the de-coupled simulation strategy extremely time consuming, and the application of the iterative and fully integrated simulation strategies completely impractical.

From this analysis it became apparent that unless sufficient computing power is available, the use of 3D CFD analysis can not provide a 'fast and cheap' solution required in several occasions throughout the design and development process of new turbomachine components. A 3D CFD analysis is perhaps more justified towards the final stages of a component design process, where more accurate, high-fidelity component and engine performance simulations may be necessary regardless the computational cost.

This study also showed that the routine simulation of an entire engine system in three dimensions using CFD is still several years away. Nowadays it could perhaps be practically implemented only through the use of component characteristic maps generated before the actual cycle analysis from averaged high-fidelity flow solutions.

Generally speaking, the de-coupled approach to advanced performance simulation is limited by the fact that the generated component map is only applicable to the component geometry and operating conditions for which the simulations were carried out. If the component geometry changes or particular flow phenomena need to be investigated, this would demand the repetition of the whole process.

Another limitation of this simulation strategy is the accurate resolution of 2D and 3D boundary profiles from the 1D values supplied by the 0D cycle analysis. This could



be overcome by looking into particular cases of component inlet conditions or by employing previous in-house empiricism and expertise.

### Iterative Approach

Similarly to the de-coupled simulation, this work demonstrated through several case studies that the iterative approach to high-fidelity analysis could be applied to all engine components which can be modelled in 2D and 3D, either by means of a through-flow analysis method or by the use of CFD tools.

At the beginning it was the author's expectation that this particular simulation strategy could save a lot of simulation time compared to the de-coupled method, since the generation of the whole component map was not required and only a narrow region of component performance of interest had to be established through the iterative process.

Utilising a 2D SLC compressor model, the analysis conducted by this study revealed that the iterative simulation approach, although it offered a faster solution close to design point conditions, it could not have a real benefit off-design, unless it was programmed in a PC and the iterative scaling of the default map was carried out completely automatically. This was not attempted by the current study and is recommended for future work.

In those cases where the default and actual component characteristics are too far apart, it is perhaps more time effective to actually establish the high-fidelity component map and engine performance through the de-coupled simulation strategy rather than carry out the iterative process manually. The above conclusions apply also to the case of high-fidelity CFD components.

Moreover, the analysis carried out by this study in the case of a 3D CFD intake model demonstrated that generating map points through this iterative process successfully, depends strongly on the quality of the CFD model geometry, grid fidelity and the soundness of the boundary conditions selected. As a direct result of this, a huge amount of time may be spend in adjusting and fine-tuning the model while actually trying to establish the component map. The de-coupled approach, although affected, does not seem to be as much limited by the same drawback as the iterative method is, since the map is essentially established independently, perhaps at a reduced accuracy.

Although a direct comparison between the de-coupled and iterative strategies was not attempted by this work, it is the author's view that any errors arising from the independent generation of the map via the de-coupled approach could in fact be easily treated by appropriate scaling of the map. This needs to be further investigated and demonstrated in the future.

As far as the simulation of a whole engine at high-resolution is concerned, similarly to the de-coupled approach, the iterative simulation strategy can be employed in high-fidelity studies involving the analysis of one or more engine components with CFD, where simulation times can be extremely long.



The iterative approach to high-fidelity analysis utilising 3D CFD component models, offers greater accuracy compared to the 2D SLC analysis, at the expense of a much more complex and time consuming process to match the correct component operating point. In those cases however, where more accurate, high-fidelity engine performance simulation is required, the extra time and complexity are perhaps justified.

This strategy suffers from the same limitations that the de-coupled approach does. The generated component map is only applicable to the component geometry and operating conditions for which the simulations were carried out. If the component geometry changes or particular flow phenomena need to be investigated, this would demand the repetition of the whole process. The accurate resolution of 2D and 3D boundary profiles from the 1D values supplied by the 0D cycle analysis is also an issue here, unless particular cases of component inlet conditions are examined or previous in-house empiricism can be employed.

### Fully Integrated Approach

This work demonstrated through several case studies that the fully integrated approach to high-fidelity analysis can be successfully applied to all engine components which can be modelled in 2D and 3D, either by means of a through-flow analysis method or by the use of CFD tools.

The fully integrated type of analysis requires the execution of the high-fidelity component simulation every time the 0D cycle iterates in order to reach a thermodynamic balance throughout the engine. This is usually achieved within 2 to 4 engine cycle loops depending on the selected step size and number of off-design cases to calculate and converge on. Obviously there is a trade-off between step size and number of calculated operating points. A sensitivity analysis would be useful establishing the optimum step size with respect to the number of calculated off-design cases. This was not attempted by the current study and is recommended for future work.

The fully integrated type of analysis, by directly embedding the high-fidelity model into the 0D cycle analysis, allows high-resolution engine performance simulations to be readily carried out regardless the particular flow phenomena under study. This technique can be applied to all engine components and proved to be more suitable for analysis involving several high-fidelity components which do not require long execution times. Moreover, the fully integrated analysis has the potential to effectively address the limitation of the other two strategies to accurately generate 2D or 3D boundary profiles by employing several high-fidelity components, at least in the crucial flow paths of the engine such as intake, fan, bypass duct, compressor, turbine etc.

This work demonstrated the potentials of the fully integrated approach by using a 2D SLC compressor model, directly coupled to a 0D engine performance simulation software. The high-fidelity compressor model fully defined the performance characteristics of that particular compressor geometry, at the simulated operating conditions, and was then used to provide a more accurate, physics-based estimate of



compressor performance and hence, engine performance, under clean and distorted inlet conditions.

The subsequent integration of two high-fidelity SLC components (intake and compressor) into a 0D cycle analysis facilitated engine performance calculations taking into account the full geometry and performance of two engine components within realistic and practical computational resources. What was demonstrated in this case is of paramount importance since it has the potential to evolve into a full engine 2D analysis with the addition of more 2D components in the very near future.

This work demonstrated that the fully integrated type of analysis utilising 2D SLC components provided in this case the faster solution amongst the methods tested and the less tedious one. This of course necessitated the programming of an explicit interface between the 0D cycle code and the high-fidelity component models which however required only basic programming skills.

Generally speaking the above analysis proved the potential of the fully integrated simulation strategy to investigate relevant physical processes occurring in an engine component in a direct and more detailed way, and to assess the effects of various isolated flow phenomena on overall engine performance in a timely and affordable manner.

In the case of the CFD analysis, the high-fidelity component communicated with the lower fidelity cycle via an iterative, manual process for the determination of the correct operating point. Although this process could have been fully automated through the use of a standard API (Application Program Interface) such as CORBA, this was not attempted by this study. The fully integrated approach to high-fidelity analysis utilising 3D CFD component models, despite offering greater accuracy compared to the fully integrated 2D SLC analysis, is limited by the long running times required.

This analysis showed that in the case of simple 3D CFD models such as intakes, execution times are of the order of 2 to 3 hours approximately per operating point. An unsteady 3D CFD analysis of a compressor or turbine can easily reach 2 to 3 days of convergence time approximately. Given that 2 to 4 engine cycle convergence loops are normally required to establish a thermodynamic balance at off-design conditions, the fully integrated simulation strategy utilising 3D CFD components certainly can not be implemented at this stage with conventional computational power.

Moreover, the above work indicated that prior to running a high-resolution engine simulation, the quality of the CFD model geometry, grid fidelity and the soundness of the selected operating conditions need to be established and verified. Otherwise a huge amount of time may be lost by realising too late that the high-fidelity model needs to be further adjusted and fine-tuned.

In those cases however, where more accurate, high-fidelity engine performance simulation is required, the detailed, high-resolution results of this work perhaps justify: i) the extra computational effort required for a more automatic link between the high-fidelity component and the 0D cycle, ii) the extra time and effort that is usually required to create and run a 3D CFD engine component.



### Summary of Conclusions

This work demonstrated through several case studies that the 3D CFD analysis can successfully capture extremely complex flow phenomena and their effects on component performance in detail, and that it will probably become the standard in high-resolution gas turbine modelling and performance simulation in the future.

For the time being however, the detailed, three-dimensional CFD analysis of an entire propulsion system is still impractical and cost-prohibitive. CFD analysis suffers from the fact that it requires a very high amount of manual intervention and long execution times. Moreover, commercially available CFD tools do not allow in-house empiricism and expertise to be incorporated in the flow-field solution in the form of deviation and loss models. In those cases where CFD results differ from experiments there is really little the user can do in order to calibrate the model, as it was demonstrated in the case of the 2D SLC compressor.

For the above reasons, a high-fidelity CFD analysis is more appropriate for the decoupled and iterative types of advanced simulation which both involve the generation of a standard component characteristic map that can be used at a later stage by a zero-dimensional cycle analysis.

On the other hand, this work demonstrated that a two-dimensional through-flow analysis of the whole engine is quite feasible even nowadays utilising 'conventional' computational tools. By incorporating in-house expertise, two-dimensional through-flow component models can be used directly by a low-fidelity engine simulation code, to provide a more accurate performance prediction for individual engine components, based on actual component geometries. A full, two-dimensional engine analysis program, can avoid errors associated with averaging of performance data by linking together several high-fidelity components, and can overcome the long execution times, complexity and impracticality associated with the use of three-dimensional CFD software.

A flexible, two-dimensional through-flow analysis code, based on a fast and robust computational technique such as streamline curvature, can provide a fairly accurate representation of the flow field, as well as the ability to study complex phenomena and their effects on engine performance, in a more cost- and time-effective manner than CFD.

### *10.3. Recommendations for Future Work*

This section briefly discusses a number of recommendations for the potential future expansion of the software tools and methodologies developed in the context of this study.



## Methodology

This subsection focuses on the potential improvement of the simulation strategies developed in the context of this work:

- As far as methodology is concerned, a more automatic execution of the iterative high-fidelity simulation strategy needs to be attempted in the future and the calculated component map needs to be compared against the characteristics obtained through the de-coupled approach.
- For the fully integrated simulation strategy, there is a trade-off between step size and number of calculated operating points. An optimisation analysis needs to be carried out in order to establish the optimum step size with respect to the number of calculated off-design cases.
- Moreover, more 2D SLC components, especially the combustor and turbine need to be developed and integrated into the 0D cycle analysis for a full 2D engine simulation. The *2D SLC Compressor Software* could be easily converted into a turbine software for this purposes, with the adoption of appropriate turbine loss models. Similarly, *2D SLC Intake Software* could be used as the basis for the development of a 2D SLC combustor model.
- Finally, the use of distributed and parallel computing architecture utilising standard API's should be thoroughly investigated for the future, fully integrated, three-dimensional CFD analysis of an entire propulsion system.

## 2D SLC Compressor Software

This subsection focuses on the potential expansion of the *2D SLC Compressor Software*. The various recommendations for the potential development of the software made throughout the Thesis are summarised and listed below:

- As explained before, in the derived expression of the full radial equilibrium equation, blade and dissipative force terms were neglected. Although dissipative force terms can be considered negligible if the direction of the calculating station is nearly perpendicular to the streamline direction, blade force terms should be included in the radial equilibrium equation. This will allow compressor geometries exhibiting appreciable leaning to be simulated more accurately.
- The subroutine for calculating the minimum-loss incidence can be expanded to include a correlation for the calculation of the 'unique' incidence angle  $i_{\text{unique}}$ . It has been experimentally proven that at sonic and supersonic conditions, when the bow oblique shock is attached onto the blade leading edge, the cascade operates with minimum losses only at one incidence, the 'unique' incidence. The basic correlation adopted by this study for calculating the minimum-loss incidence is limited to low inlet Mach numbers below 0.5. The



basic correlation could be also extended to include three-dimensional flow effects by adding extra experimental-corrective terms.

- Lieblein's and Cetin's models for the calculation of the minimum-loss deviation give more accurate results at high inlet Mach numbers. Moreover, Creveling's correlation for the calculation of the deviation angle does not take into account the inlet Mach number as well as the level of blade loading. Consequently, at high Mach numbers and increased blade loadings, the calculated deviation angles are expected to deviate considerably from experimental results. An independent potential flow solution could be used at low inlet Mach numbers and low blade loadings, for the calculation of the deviation and minimum-loss deviation angles. It would be advisable to check whether the level of inlet Mach number is such as to cause the formation of a shock wave within the blade passage and thus apply a correlation that takes into account the effect of such a flow regime on the air flow outlet direction. It would also be useful to include a correlation as an option to the user that calculates the flow deviation based on the equivalent diffusion factor. This solution may require more computational power since an iterative calculation procedure would need to be established between the two, but it would give more accurate results at high blade loadings. As in the case of the minimum-loss incidence, reduced accuracy is also expected on the grounds that three dimensional effects are not taken into account. Deviation and minimum-loss deviation correlations could be extended to include three-dimensional flow effects by adding extra experimental-corrective terms, as shown before.
- The current model for the calculation of blade passage choking identifies conditions likely to cause a choked passage throat at various locations along the blade span but makes no attempt to identify complete annulus choking. The possibility of one or more stream tubes being choked needs to be taken carefully into account in the solution of the full radial equilibrium equation and particularly in the execution of the meridional velocity convergence algorithm. This will allow the software to produce more realistic flow profiles after the onset of passage choking and also detect complete annulus choking.
- Similarly, the compressor surge model adopted is only useful indicating stall conditions in individual stream tubes at various locations along the blade span, but not complete compressor surge. A limit needs to be defined as to how much of the blade span can be allowed to operate under stalled conditions before it is assumed that complete compressor surge has taken place. Obviously this could not be set universally for all compressor geometries and probably the user would need to decide for each case individually based on experimental or statistical data if available. Alternative or additional surge prediction models could easily be programmed within the appropriate subroutine, such as the one proposed by Greitzer. In this way, when experimental data for the compressor under simulation are available, the user will have the option to select the most appropriate stall prediction model.
- The current model for the calculation of the blade passage throat width can calculate the throat width of DCA cascades fairly accurately and can also be used for other blade profiles on a circular camber line to a good



approximation. Extending the model to handle a wider range of blade profiles will improve the accuracy in identifying choking conditions and also improve the versatility of the software.

- The correct calculation of the flow blockage is critical for the accurate simulation of the compressor flow field. The boundary layer model adopted in this study does not take into account boundary layer growth within bladed regions. The corresponding subroutine could be extended to include a three-dimensional boundary layer calculation inside bladed regions. A sensitivity analysis should also be performed in order to determine the optimum number of auxiliary points required in the calculation of the boundary layer to achieve sufficient accuracy at minimum computational time. A similar sensitivity analysis is also necessary to establish a reasonable convergence tolerance for the boundary layer blockage factors. Finally, the subroutine could be expanded to include boundary layer models for the blade surfaces. This would be very useful in the more precise calculation of the blade passage throat area, choking conditions and entropy generation across the blade row.
- As it was thoroughly discussed before, there is no loss model without limitations or at least without a given restricted range of applicability. The empirical correlations used in the calculation of blade losses are usually derived from experimental results and are therefore very dependent on the experiment's conditions. It needs to be pointed out again that one should be very cautious when applying these correlations to different geometries. It would be an advantage for the software to offer the user several more alternative correlations, which could then be compared against experimental data (if available) to find the most adequate, given the application. Perhaps combining different loss models together would be sufficient to predict the flow field reasonably accurate. However, even this approach would need to be thoroughly experimentally tested before put in practical use.
- The traditional, two-dimensional approach can overestimate in some cases the magnitude of losses generated by shock waves that appear to be nearly normal to the blade suction surface. Therefore, a potential improvement would be the implementation of an iterative procedure with the intention to determine more accurately the position and the inclination of the normal shock, according to the cascade solidity, camber, staggering and inlet flow conditions. Although losses attributed to bow oblique shock waves are considered to be comparatively small, they should be included in the calculations for a more accurate loss prediction at any operating condition. As mentioned before, more correlations should be programmed and be given as potential options to the user. In the case where experimental data are available, the user should be able to select the most appropriate model, for the specific compressor under simulation, or even switch between different loss models according to the operating conditions.
- Expressing losses due to secondary flows mathematically has been extremely difficult and empirical correlations developed over the years have been restricted to predicting 'orders of magnitude' of the various quantitative aspects of the flow. The corresponding subroutine may be expanded to include



a potential flow calculation in the case of lightly loaded blades, in order to predict the vorticity transport within the blade row passage and thus determine more accurately the secondary velocities. Alternatively, secondary losses could be broken down to the various different causes of loss described before such as rotor tip clearance etc.

- A potential expansion of the Reynolds-effects subroutine could be to include the effect of aerodynamic roughness. It has been experimentally established that losses vary with Reynolds number up to a critical value which is a function of roughness height. Above this value the effect of Reynolds on compressor efficiency remains relatively constant. Consequently, the implementation of a correlation to determine the value of the critical Reynolds number is strongly suggested.
- In the current version of the *2D SLC Compressor Software*, downstream blade rows interpolate between the outlet boundary conditions and geometric data of the previous blade row to establish inlet boundary conditions and streamline locations. In reality, the flow profiles within the bladeless space between adjacent blade rows do not remain constant. The flow is slightly redistributed and that should be taken into account. The current version of the software treats this phenomenon rather simplistically but future versions should incorporate this in the calculations for greater accuracy.
- In the case when data are not monotonically increasing or decreasing, cubic spline interpolation can be carried out if the function of the interpolated curve is known before hand and local minima and maxima can be readily identified. In the case of streamlines however, whose position, slope and curvature change in every iteration, local minima and maxima are very difficult to establish. This can introduce numerical instabilities and may result in the software crashing. For this reason the cubic spline interpolation routine currently programmed in the code can only handle monotonically increasing or decreasing data. A mathematical solution around this problem should be found in the future.

### 2D SLC Intake Software

This subsection focuses on the potential expansion of the *2D SLC Intake Software*. The various recommendations for the potential development of the software made throughout the Thesis are summarised and listed below:

- First of all, the streamline curvature intake model adopted by this study does not account for inlet swirl. The effects of swirl on intake flow angle, pressure recovery and boundary layer stability could potentially be incorporated by means of separate models, as in the case of intake pressure losses.
- As discussed previously, the subdivision of the overall intake pressure loss into two parts, based on the boundary layer displacement thicknesses of the cone and lip, is a rather simple approach. An iterative loop should be employed in order to take into account the progressive drop in pressure along



the length of the boundary layer and how this would in turn affect the displacement thickness of the boundary layer and overall pressure loss. This however, would probably increase the computational demand enormously, without really changing the intake's performance considerably, given that typical intake pressure recovery values change very little at off-design conditions.

- The current model assumes that the skin friction coefficient  $C_F$ , calculated based on throat conditions, remains unchanged throughout the intake. Although it has been reported in literature that the adopted model agrees with experimental data satisfactorily, a more versatile model should be programmed to estimate the changes in  $C_F$  throughout the diffuser based on boundary layer development and pressure gradient effects.
- Similarly, losses due to entry-diffuser interactions are treated by the current analysis empirically only. Although the adopted model is applicable to a large range of flow conditions and diffuser geometries, for a quantitative type of analysis the user needs to compare the results against experimental data and calibrate the model accordingly.
- The loss model adopted for the calculation of the intake pressure loss due to incidence effects assumes that interaction effects are independent of how the lip loss is calculated i.e. at incidence or at zero-incidence. There are no sufficient data in literature to verify the validity of this assumption although there is evidence that it is the overall loss in pressure at entry which determines the magnitude of the diffuser loss rather than the detailed asymmetric distribution of it. This should be thoroughly investigated and verified in the future.
- An improved method for establishing the effective area at the throat for conditions above choking needs to be established. This would allow the pressure recovery for conditions above intake choking to be calculated more accurately. Moreover, the estimation of the choking limit obtained from the current models is only approximate since the flow conditions at choking are in reality very sensitive to small changes in flow parameters and geometry.
- As in the case of the *2D SLC Compressor Software*, the applicability of the loss models for intakes and ducts adopted by this study is limited by the range of application of the various empirical correlations and the boundaries of the tabulations and charts used. The objective here was to establish the methodology and create a software tool that could incorporate any type of loss model for a more accurate analysis. It is really up to the end user to assess the adequacy of these loss models, according to the application, and adopt additional or alternative ones.



## REFERENCES

### [A]

Adler, D. and Krimerman, Y., "The numerical calculation of the meridional flow field in turbomachines using the finite elements method", *Israel Journal of Technology*, Vol. 12, 1974, p. 268-274.

Aungier, R. H., "Axial-flow compressors: A strategy for aerodynamic design and analysis", ASME Press, Three Park Avenue, New York, NY 10016, 2003.

### [B]

Barbosa, J. R., "A streamline curvature computational program for axial compressor performance prediction", PhD Thesis, Vol. 1, School of Mechanical Engineering, Cranfield Institute of Technology, 1987.

Bardina, J., Kline, S. J. and Ferziger, J. H., "Computation of straight diffuser at low Mach number incorporating an improved correlation for turbulent detachment and reattachment", Mechanical Engineering Department, Stanford University, Thermo-Sciences Division, Report PD-22, 1982.

Barger, R. L., "Streamline curvature design procedure for subsonic and transonic ducts", Langley Research Centre, NASA Technical Note, TN D-7368, Washington DC, December 1973.

Blackaby, J. R., "Low-speed investigation of the effects of angle of attack on the pressure recovery of a circular nose inlet with several lip shapes", NACA Technical Note, TN 3394, 1955.

Blackaby, J. R. and Watson, E. C., "An experimental investigation at low speeds of the effects of lip shape on the drag and pressure recovery of a nose inlet in a body of revolution", NACA Technical Note 3170, 1954.

Bosman, C. and El-Shaarawi, M., "Quasi-three-dimensional numerical solution of flow in turbomachines", *Transactions of the ASME, Journal of Fluids Engineering*, Vol. 99, 1977, p. 132-140.

Bosman, C. and Marsh, H., "An improved method for calculating the flow in turbomachines, including a consistent loss model", *Journal of Mechanical Engineering Science*, Vol. 16, 1974, p. 25-31.

Bullock, R. O., "Critical highlights in the development of the transonic compressor", *Transactions of the ASME, Journal of Engineering for Power, Series D*, Vol. 83, 1961, p. 243-257.



Bullock, R. O. and Johnsen I. A., "Chapter III – Compressor design system", of "NASA SP 36 - Aerodynamic design of axial flow compressors", Scientific and Technical Information Division, National Aeronautics and Space Administration, Washington DC, 1965.

Buono, F., "Influence of inlet temperature distortion on an axial flow LP turbine by a CFD analysis", Cranfield University, School of Engineering, MSc Thesis, 2004.

## [C]

Carter, A. D. S., "The low speed performance of related aerofoils in cascade", National Gas Turbine Establishment, Report No. R55, September 1949, Re-printed by the Aeronautical Research Council, CP29, 1950.

Carter, A. D. S., Moss, C. E., Green, G. R. and Annear G. G., "The effect of Reynolds number on the performance of a single-stage compressor", Ministry of Aviation, Aeronautical Research Council, Reports and Memorandum, R&M No. 3184, May 1957.

Casey, M. V., "A mean line prediction method for estimating the performance characteristic of an axial compressor stage", Transactions of the IMechE, C264/87, 1987, p. 273-285.

Cetin, M., Hirsch, C., Serovy, G. K. and Ucer, A. S., "An off-design loss and deviation prediction study for transonic axial compressors", ASME Paper publication, ASME 89-GT-324, Presented at the 34th International Gas Turbine and Aeroengine Congress and Exposition, Toronto, Ontario, Canada, June 1989.

Charalambous, N., "Axial compressor response to inlet flow distortion by CFD analysis – Effect of different frequencies of circumferential distortion", Cranfield University, School of Engineering, MSc Thesis, 2003.

Charalambous, N., Ghisu T., Iurisci G., Pachidis V. and Pilidis P., "Axial compressor response to inlet flow distortion by a CFD analysis", Proceedings of ASME Turbo Expo 2004, GT2004-53846, Vienna, Austria, June 2004.

Cockrell, D. J., Diamond, M. J. and Jones, G. D., "The diffuser inlet flow parameter", Journal of Aeronautical Society, Vol. 69, May 1965, p. 350-352.

Cockrell, D. J. and Markland, E., "A review of incompressible diffuser flow", Aircraft Engineering, Vol. 35, October 1963, p. 286.

Cumpsty, N. A., "Compressor aerodynamics", Longman Scientific & Technical, Longman Group UK Limited, 1989.

Cunningham, T. G., Medlock, A., Sandefur, M. H. and McKeever, C. W., "Integrated preliminary design software for gas turbine engines", Transactions of the ASME, Paper GT2006-90271, 2006.



Creveling, H. F. and Carmody, R. H., "Axial flow compressor computer program for calculating off-design performance (Program IV)", General Motors, Allison Division, Indianapolis, Prepared for NASA, Report CR-72427, August 1968.

## [D]

Davis, M., Hale, A. and Beale, D., "An argument for enhancement of the current inlet distortion ground test practice for aircraft gas turbine engines", Transactions of the ASME, Journal of Turbomachinery, 2002.

Davis, W. R. and Millar, D. A. J., "A comparison of the matrix and streamline curvature methods of axial-flow turbomachinery analysis, from a user's point of view", Transactions of the ASME, Journal of Engineering for Power, Vol. 97, 1974, p. 549-560.

Denton, J. D., "Through-flow calculations for transonic axial flow turbines", Transactions of the ASME, Journal of Engineering for Power, Vol. 100, 1978, p. 212-218.

Denton, J. D. and Singh, U. K., "Time marching methods for turbomachinery flow calculations", Application of Numerical Methods to Flow Calculations in Turbomachines, VKI 15 1979-7, April 1979.

Dolan, F. X. and Runstadler, P. W., "Pressure recovery performance of conical diffusers at high subsonic Mach numbers", NASA Contractor Report, NASA CR – 2299, August 1973.

Dorney, D. J. and Sondak, D. L., "Study of the effects of hot streaks on heat transfer in subsonic and transonic flows", Conference Publication, AIAA 96-2923, 1996.

Dransfield, D. C. and Calvert, W. J., "Detailed flow measurements in a four stage axial compressor", Conference Publication, ASME Paper No. 76-GT-46, ASME, New York, NY, 1976.

## [E]

ESDU, "Performance of conical diffusers in incompressible flow", Item No. 73024, Engineering Sciences Data Unit, London, October 1973.

ESDU, "Introduction to design and performance data for diffusers", Item No. 76027, Engineering Sciences Data Unit, London, November 1976.

ESDU, "Pressure recovery of axi-symmetric intakes at subsonic speeds", Item No. 80037, Engineering Sciences Data Unit, London, November 1980.



**[F]**

Follen, G. and auBuchon, M., "Numerical zooming between a NPSS engine system simulation and a one-dimensional high compressor analysis code", Prepared for the Computational Aerosciences Workshop sponsored by the High Performance Computing and Communications Program, Moffett Field, California, NASA/TM-2000-209913, February 2000.

Fradenburgh, E. A. and Wyatt, D. D., "Theoretical performance characteristics of sharp-lip inlets at subsonic speeds", NACA Report 1193, 1954.

Frost, D. H., "A streamline curvature through-flow computer program for analysing the flow through axial-flow turbomachines", National Gas Turbine Establishment, Reports and Memoranda, NGTE RM 3687, August 1970.

**[G]**

Gallus, H. E., Zeschky, J. and Hah, C., "End-wall and unsteady flow phenomena in an axial turbine stage", Conference Publication, ASME Paper 94-GT-143, 1994.

Ghisu, T., "Axial compressor response to inlet flow distortion by CFD analysis – Effect of different levels of distortion", Cranfield University, School of Engineering, MSc Thesis, 2003.

Giamati, G. C. and Finger, B., "Design velocity distribution in meridional plane", NASA SP-36, Chapter VIII - Aerodynamic design of axial-flow compressors, 1965.

Glenny, D. E., "An application of streamline curvature methods to the calculation of flow in a multistage axial compressor", Department of Supply, Australian Defence Scientific Service, Aeronautical Research Laboratories, Mechanical Engineering Note, ARL/M.E. 346, April 1974.

Greitzer, E. M., "Surge and rotating stall in axial flow compressors, Parts I: Theoretical compression system model", Transactions of the ASME, Journal of Engineering For Power, Vol. 98, April 1976, p. 190-198.

Griepentrog, H. R., "Secondary flow losses in axial compressors", AGARD LS 39.

Guindeuil, G., Pachidis, V. and Pilidis, P., "Iterative approach to 2D component zooming applied to a turbofan intake", Cranfield Technical Report, Cranfield University, School of Engineering, Department of Power, Propulsion and Aerospace Engineering, Gas Turbine Engineering Group, July 2004.



**[H]**

Hatch, J. E., Ciamati, G. and Jackson, R. J., "Application of radial-equilibrium condition to axial-flow turbomachine design including consideration of change of entropy with radius downstream of blade row", NACA RM L54A20, 1954.

Hamrick, J. T., Ginsburg, A. and Osborn, W. M., "Method of analysis for compressible flow through mixed flow centrifugal impellers of arbitrary design", NACA Report 1082, 1951.

Hawthorne, W. R., "Secondary circulation in fluid flow", Proceedings of the Royal Society Series A, Vol. 206, 1951, p. 374-387.

Hawthorne, W. R., "The secondary flow about struts and aerofoils", Fluid Motion Sub-Committee, Aeronautical Research Council, ARC - 16,236, October 1953.

Hirai, K., Kodama, H., Nozaki, K. and Tamura, M., "A steady three-dimensional analysis of inlet distortion in turbomachinery", Transactions of the AIAA, AIAA-97/2735, 1997.

Hirsch, C. and Warzee, G., "A finite element method for through-flow calculations in turbomachines", Transactions of the ASME, Paper 76 FE 12, 1976.

Hirsch, C. and Warzee, G., "An integrated quasi-3D finite element calculation program for turbomachinery flows", Transactions of the ASME, Journal of engineering for Power, Vol. 101, 1979, p. 141-148.

Hodson, H. P., "Blade row interactions in low pressure turbines", Von Karman Institute for Fluid Dynamics, Lecture series 1998-02, 1998.

Horlock, J. H. and Marsh, H., "Flow models for turbomachinery", Journal of Mechanical Engineering Science, Vol. 13, 1971, p. 358-368.

Horlock, J. H. and Perkins, H. J., "Annulus wall boundary layers in turbomachines", North Atlantic Treaty Organization, Advisory Group for Aerospace Research and Development, AGARD-AG-185, May 1974.

Howell, A. R., "Fluid dynamics of axial compressors." Proceedings of the IMechE, Vol. 153, 1945, p. 441-82.

Howell, A. R. and Calvert, W. J., "A new stage stacking technique for axial-flow compressor performance prediction", Transactions of the ASME, Journal of Engineering for Power, Vol. 100, 1978, p. 698-703.

Hoynigen-Huene, M.V. and Hermeler, J., "Comparison of three approaches to model stator-rotor interaction in the turbine front stage of an industrial gas turbine", Third European Conference on Turbomachinery: Fluid Dynamics and Thermodynamics, 2-5 March 1999, Royal National Hotel London, UK, Volume A, 1999.



**[I]**

Iurisci, G., F., "Axial compressor response to inlet flow distortion by CFD analysis – Effect of different types and extents of distortion", Cranfield University, School of Engineering, MSc Thesis, 2003.

Ivanov, M. and Kimasov, I., "Numerical solution of the problem of determining the average, axi-symmetric flow of an ideal gas through turbomachine stages", Fluid Mechanics, Soviet Research, July-August, 1978, p. 143-152.

**[J]**

Jansen, W., "The application of end-wall boundary layer effects in the performance analysis of axial compressors", Conference Publication, ASME Paper No. 67-WA/GT-11, ASME, New York, NY, 1967.

Jansen, W. and Moffatt, W. C., "The off-design analysis of axial flow compressors", Transactions of the ASME, Journal of Engineering for Power, Vol. 89, October 1967, p. 453-462.

Jennions, I. K. and Stow, P., "The quasi-three-dimensional turbomachinery blade design system, Part I: Through-flow analysis, Part II: Computerised system, Transactions of the ASME, Journal of Engineering for Gas turbines and Power, Vol. 107, 1985, p. 308-316.

Jennions, I. K. and Stow, P., "The importance of circumferential non-uniformities in a passage-averaged quasi-three-dimensional turbomachinery design system", Transactions of the ASME, Journal of Engineering for Gas turbines and Power, Vol. 108, 1986, p. 240-245.

Jennions, I. K. and Turner, M.G., "Three dimensional computations of a transonic fan using an explicit flow solver and an implicit k- $\epsilon$  solver", Transactions of the ASME, Journal of Turbomachinery, Vol. 115, 1993.

**[K]**

Katsanis, T. and McNally, W., "Revised FORTRAN program for calculating velocities and streamlines on the hub-shroud mid-channel stream surface of an axial-, radial-, or mixed-flow turbomachine or annular duct", User's Manual, NASA TN D-8430, 1977.

Kerrebrock, J. L. and Mikolajczak, A. A., "Intra-stator transport of rotor wakes and its effect on compressor performance", Transactions of the ASME, ASME Journal of Engineering for Power, Vol. 92, October 1970, p. 359-369.



Koch, C. C., "Stalling pressure rise capability of axial flow compressor stages", Transactions of the ASME, Journal of Engineering For Power, Vol. 103, October 1981, p. 645-656.

Koch, C. C. and Smith, L. H., "Loss sources and magnitudes in axial-flow compressors", Transactions of the ASME, Journal of Engineering for Power, Vol. 98, 1976, p. 411-424.

## [L]

Lakshminarayana, B., "Effect of inlet temperature gradients on turbomachinery performance", ASME Journal of Engineering for Power, Vol. 97, 1975, p. 64-74.

Levine, P., "The two-dimensional inflow conditions for a supersonic compressor with curved blades", Wright Air Development Center, Air Research and Development Command, United States Air Force, Wright-Patterson Air Force Base, Ohio, WADC TR 55-387, May 1956.

Lieblein, S., "Analysis of experimental low-speed loss and stall characteristics of two-dimensional compressor blade cascades", National Advisory Committee for Aeronautics, Research Memorandum, NACA RM E57A28, Washington, March 1957.

Lieblein, S., "Loss and stall analysis of compressor cascades", Transactions of the ASME, Journal of Basic Engineering, Series D, Vol. 81, September 1959, p. 387-400.

Lieblein, S., "Incidence and deviation angle correlations for compressor cascades", Transactions of the ASME, Journal of Basic Engineering, Vol. 82, September 1960, p. 575-587.

Lieblein, S., "Chapter VI - Experimental flow in two-dimensional cascades", of "NASA SP 36 - Aerodynamic design of axial flow compressors", Scientific and Technical Information Division, National Aeronautics and Space Administration, Washington DC, 1965.

Lieblein, S. and Roudebush, W. H., "Theoretical loss relations for low-speed two-dimensional-cascade flow", National Advisory Committee for Aeronautics, Technical Note, NACA TN 3662, 1956.

Lieblein, S. and Johnsen, I. A., "Resume of transonic compressor research at NACA Lewis Laboratory", Transactions of the ASME, Journal of Engineering for Power, Vol. 83, 1961, p. 219-234.

Longley, J. P., "Measured and predicted effects of inlet distortion on axial compressors", Transactions of the ASME, ASME Journal 90-GT-214, 1990.

Lytle, J. K., "The numerical propulsion system simulation: An overview", NASA/TM-2000-209915, 2000.



**[M]**

Markowski, S. J., Lohmann, R. P. and Brookman, R. P., "The performance of conical wall annular diffusers with swirling inlet flow", Proceedings of the IAHR/ASME/ASCE Meeting, Ft. Collins, CO, June 1978, p. 235-246.

Marsh, H., "A digital computer program for the through-flow fluid mechanics in an arbitrary turbomachine using a matrix method", Aeronautical Research Council, ARC RM 3509, 1968.

Marsh, H., "The uniqueness of turbomachinery flow calculations using the streamline curvature and matrix through-flow methods", Transactions of the I.Mech.E., Journal of Mechanical Engineering and Science, Vol. 13, No. 6, 1971.

Melloni, L., "Low BPR military engine performance investigation under radial and stratified inlet flow distortion", Cranfield University, School of Engineering, MSc Thesis, 2004.

Melloni, L., Kotsiopoulos, P., Jackson, A. J. B., Pachidis, V. and Pilidis, P., "Military engine response to compressor inlet stratified pressure distortion by an integrated CFD analysis", GT2006-90805, ASME Turbo Expo, Power For Land, Sea and Air, Barcelona, Spain, May 2006.

Miller, D. C., "The performance prediction of scaled axial compressors from model tests", IMechE, 1977.

Miller, G. R., Lewis, G. W. and Hartmann, M. J., "Shock losses in transonic rotor rows", Transactions of the ASME, Journal of Engineering for Power, Vol. 83, 1961, p. 235-242.

Milillo, J. R., "Some internal-flow characteristics at zero flight speed of an annular supersonic inlet and an open-nose inlet with sharp and rounded lips", NACA Research Memorandum, RM L54E19 (NASA TIB 4294), July 1954.

Mossman, E. A. and Anderson, W. E., "The effect of lip shape on a nose inlet. Installation at Mach numbers from 0.0 to 1.5 and a method for optimising engine-inlet combinations", NACA Research Memorandum, RM A54B08 (NASA TIL 6547), May 1954.

Munk, M. and Prim, R.C., "On the multiplicity of steady gas flows having the same streamline pattern", Proceedings of the National Academy of Sciences, U.S Vol. 33, 1947, p. 137-141.

**[N]**

Nantua, N., Pachidis, V. and Pilidis, P., "De-coupled approach to component zooming applied to a HBR turbofan engine intake", Cranfield Technical Report, Cranfield



University, School of Engineering, Department of Power, Propulsion and Aerospace Engineering, Gas Turbine Engineering Group, July 2004.

Novak, R. A., "Streamline curvature computing procedures for fluid-flow problems", Transactions of the ASME, Journal of Engineering for Power, Vol. 89, 1967, p. 478-490.

Novak, R. A. and Hearsey, R. M., "A nearly three-dimensional intra-blade computing system for turbomachinery", Transactions of the ASME, Journal of Fluid Engineering, Vol. 99, 1977, p. 154-66.

## **[O]**

Oldham, R. K., "Some design data for double circular arc compressor blading", Ministry of Aviation, NGTE Note No. NT. 589, December 1965.

## **[P]**

Pachidis, V., "Gas turbine simulation – PYTHIA workshop guide", Part I and II, Cranfield University, Department of Power, Propulsion and Aerospace Engineering, ASME/IGTI Aero Engine Life Management Conference, London, March 2004.

Pachidis, V., Pilidis, P., Guindeuil, G., Kalfas, A. and Templalexis, I., "A partially integrated approach to component zooming using computational fluid dynamics", GT2005-68457, ASME Turbo Expo, Power For Land, Sea and Air, Reno-Tahoe, Nevada, USA, June 2005a.

Pachidis, V., Pilidis, P., Talhouarn, F., Kalfas, A. and Templalexis, I., "A fully integrated approach to component zooming using computational fluid dynamics", GT2005-68458, ASME Turbo Expo, Power For Land, Sea and Air, Reno-Tahoe, Nevada, USA, June 2005b.

Pachidis, V., Pilidis, P., Alexander, T., Kalfas, A. and Templalexis, I., "Advanced performance simulation of a turbofan engine intake", Log No B5062, Transactions of the AIAA, Journal of Propulsion and Power, Vol. 22, No. 1, January-February, 2006a.

Pachidis, V., Pilidis, P., Talhouarn, F., Kalfas, A. and Templalexis, I., "A fully integrated approach to component zooming using computational fluid dynamics", Transactions of the ASME, Journal of Engineering for Gas Turbines and Power, Vol. 128, April 2006b.

Pachidis, V., Pilidis, P., Templalexis, I. and Kotsiopoulos, P., "Prediction of engine performance under compressor inlet flow distortion using streamline curvature", GT2006-90806, ASME Turbo Expo, Power For Land, Sea and Air, Barcelona, Spain, May 2006c.



Pollard, D. and Gostelow, J. P., "Some experiments at low speed on compressor cascades", Transactions of the ASME, Journal of Engineering for Power, Vol. 89, July 1967, p. 427-436.

**[R]**

Rai, M. M. and Dring, R. P., "Navier-Stokes analyses of the redistribution of inlet temperature distortions in a turbine", AIAA 87- 2146, 1987.

Raw, J. A. and Weir, G. C., "The prediction of off-design characteristic of axial-centrifugal compressors", SAE paper No 800628, Turbine Power for Executive Aircraft Meeting, Arizona, 1980.

Riegler, C., Batier, M. and Kurzke, J., "Some aspects of modelling compressor behaviour in gas turbine performance calculations", Transactions of the ASME, Journal of Engineering for Gas Turbines and Power, Vol. 123, 2001, p. 372-78.

Reed, J. A. and Afjeh, A. A., 'Development of an interactive graphical propulsion system simulator', 30th AIAA/ASME/SAE/ASEE Joint Propulsion Conference, AIAA 94-3216, Indianapolis, June 1994.

Reed, J. A., and Afjeh, A. A., "Distributed and parallel programming in support of zooming in numerical propulsion system simulation", NASA Proceeding of Symposium on Applications of Parallel and Distributed Computing, Columbus OH, USA, April 1994.

Reed, J. A. and Afjeh, A. A., "An interactive graphical system for engine component zooming in a numerical propulsion system simulation", 33rd Aerospace Sciences Meeting and Exhibit, AIAA 95-0118, Reno-Nevada, January 1995.

Reed, J. A., and Afjeh, A. A., "A comparative study of high and low fidelity fan models for turbofan engine system simulation", Proceeding of the IASTED International Conference on Applied Modelling and Simulation, Banff, Canada, July 1997.

Reed, J. A., Turner, M. G., Norris, A. and Veres, J. P., "Towards an automated full-turbofan engine numerical simulation", ISABE Paper No. 2003-1235, 2003.

Reneau, L. R., Johnston, J. P. and Kline, S. J., "Performance and design of straight, two dimensional diffusers", Transactions of the ASME, Journal of Basic Engineering, Vol. 89, March 1967, p. 141-150.

Robbins, W. H., Jackson, R. J. and Lieblein, S., "Chapter VII – Blade element flow in annular cascades", of "NASA SP 36 - Aerodynamic design of axial flow compressors", Scientific and Technical Information Division, National Aeronautics and Space Administration, Washington DC, 1965.



## [S]

Sandercock, D. M., Kovach, K. and Lieblein, S., "Experimental investigation of a five-stage axial-flow research compressor with transonic rotors in all stages; I - Compressor design", NACA Research Memorandum, RM E54F24, NACA, Washington DC, 1954.

Saxer, A. P. and Giles, M. B., "Predictions of three dimensional steady and unsteady inviscid transonic stator/rotor interaction with inlet radial temperature non-uniformity", Transactions of the ASME, ASME Journal of Turbomachinery, Vol. 116, 1994, p. 347-357.

Schaffler, P. C., "Experimental and analytical investigation of the effects of Reynolds number and blade surface roughness on multistage axial compressors", ASME paper 79-GT-2, 1979.

Scherrer, R. and Anderson, W. E., "Preliminary investigation of a family of diffusers designed for near sonic inlet velocities", NACA Technical Note, TN 3668, 1956.

Schlichting, H., "Boundary layer theory", Mc-Graw-Hill Book Co., Inc., NY, 1960.

Schmidt, J. F. and Ruggeri, R. S., "Performance with and without inlet radial distortion of a transonic fan stage designed for reduced loading in the tip region", NASA Technical Paper 1294, August 1978.

Schwenk, F. C., Lewis, G. W. and Hartman, M. J., "A preliminary analysis of the magnitude of shock losses in transonic compressors", NACA RM E57A30, 1957.

Sharma, O. P. and Stetson, G. M., "Impact of combustor generated temperature distortions on the performance, Durability and Structural Integrity of Turbines", Von Karman Lecture Series 1998-02, 1998.

Smith, L. H., "NASA/GE fan and compressor research accomplishments", Transactions of the ASME, Journal of Turbomachinery, Vol.116, No.4, p. 554-568, 1994.

Smith, L. H., "The radial-equilibrium equation of turbomachinery", Transactions of the ASME, Journal of Engineering for Power, Vol. 88, 1966, p. 1-12.

Squire, H. B. and Winter, K. G., "The secondary flow in a cascade of airfoils in a non-uniform stream", Royal Aircraft Establishment, Report No. RAE Aero 2317, March 1949.

Srinath, T., "An investigation of the effects of swirl on the flow regimes and performance of annular diffusers with equal inner and outer core angles", MSc Thesis, Mechanical Engineering, University of Waterloo, Canada, 1968.

Stratford, B. S., "The use of boundary layer technique to calculate the blockage from the annulus boundary layer in a compressor", Conference Publication, ASME Paper No. 67-WA/GT-7, ASME, New York, NY, 1967.



Swan, W. C., "A practical method of prediction transonic compressor performance", Transactions of the ASME, Journal of Engineering for Power, Vol. 86, July 1961, p. 322-330.

## [T]

Takahashi, R. K. and Ni, R. H., "Unsteady Euler analysis of the redistribution of an inlet temperature distortion in a turbine", AIAA 90-2262, 1990.

Talhouarn, F., Pachidis, V. and Pilidis, P., "Partially integrated approach to 3-D component zooming applied to the intake", Cranfield Technical Report, Cranfield University, School of Engineering, Department of Power, Propulsion and Aerospace Engineering, Gas Turbine Engineering Group, July 2004.

Templalexis, I., Pilidis, P., Guindeuil, G., Lekkas, T. and Pachidis, V., "3D simulation of a convergent-divergent aero engine intake using two different CFD methods", GT2005-68526, ASME Turbo Expo, Power For Land, Sea and Air, Reno-Tahoe, Nevada, USA, June 2005a.

Templalexis, I., Pilidis, P., Guindeuil, G., Kotsiopoulos, P. and Pachidis, V., "Aero engine axi-symmetric convergent-constant area intake 3D simulation using a panel method approach", GT2005-68528, ASME Turbo Expo, Power For Land, Sea and Air, Reno-Tahoe, Nevada, USA, June 2005b.

Templalexis, I., Pilidis, P., Pachidis, V. and Kotsiopoulos, P., "Development of a 2D compressor streamline curvature code", GT2006-90867, ASME Turbo Expo, Power For Land, Sea and Air, Barcelona, Spain, May 2006a.

Templalexis, I., Pilidis, P., Pachidis, V. and Kotsiopoulos, P., "Quasi-three-dimensional compressor performance simulation using streamline curvature and multi-parallel compressor theory", GT2006-90812, ASME Turbo Expo, Power For Land, Sea and Air, Barcelona, Spain, May 2006b.

Turner, M. G., Reed, J. A., Ryder R. and Veres, J. P., "Multi-fidelity simulation of a turbofan engine with results zoomed into mini-maps for a 0D cycle simulation", Proceedings of ASME Turbo Expo 2004, GT2004-53956, Vienna-Austria, June 2004.

Tyler, R. A. and Williamson, R. G., "Pressure loss and flow distortion measurements on circular compressor intakes in inclined flow", National Research Council of Canada, Aeronautical Report LR-401, 1964.

## [U]

Ursek, D. C., Gorell, W. T. and Cunnan, W. S., "Performance of two-stage fan having low-aspect-ratio, first stage rotor blading", NASA Technical Paper 1493, 1979.



**[V]**

Voit, C. H., "Investigation of a high-pressure-ratio eight-stage axial-flow research compressor with two transonic inlet stages", I - Aerodynamic Design, NACA RM E53124, 1953.

**[W]**

Walker, G. J., "The role of laminar-turbulent transition in gas turbine engines: A discussion", Transactions of the ASME, Journal of Turbomachinery, Vol. 115, 1993.

Walsh, P. and Fletcher P., "Gas turbine performance", Blackwell Science Ltd, 1998.

Wassel, A. B., "Reynolds number effects in axial compressors", Transactions of the ASME, Journal of Engineering For Power, Vol. 90, April 1968, p. 149-156.

Wilkinson, D. H., "Calculation of blade-to-blade flow in a turbomachine by streamline curvature", Aeronautical Research Council, ARC 32 878, Turbo 157, December 1970.

Winternitz, F. A. L. and Ramsay, W. J., "Effects of inlet boundary layer on pressure recovery, energy conversion and losses in conical diffusers", Journal of Aeronautical Society, Vol. 61, February 1957, p. 116-124.

Wright, C. and Kovach, K., "Design procedure and limited test results for a high solidity, 12-inch transonic impeller with axial discharge", NACA RM E53B09, 1953.

Wright, P. I. and Miller, D. C., "An improved compressor performance prediction model", Transactions of the IMechE, C423/028, 1991, p. 69-82.

Wu, C. H., "A general theory of three-dimensional flow in subsonic or supersonic turbomachines of axial-, radial- and mixed-flow type", NACA TN 2604, 1952.

Wu, C. H. and Wolfenstein, L., "Application of radial equilibrium condition to axial-flow compressor and turbine design", NACA TN 1795, 1949.

**[Y]**

Yin, J., Hales, R., Pilidis, P. and Curnock, B., "Two-shaft high-bypass ratio turbofan performance calculation using a new 2D fan model", 37<sup>th</sup> AIAA/ASME/SAE/ASEE Joint Propulsion Conference, AIAA 2001-3302, Salt Lake City-Utah, July 2001.



**[Z]**

Zilli, A., “Computational investigation of the performance of a military HP axial turbine subjected to realistic inlet temperature profiles”, Cranfield University, School of Engineering, MSc Thesis, 2004.

Zilli, A., Pachidis, V., Jackson, A. J. B. and Pilidis, P., “CFD Investigation of the performance of a military HP axial turbine subjected to inlet temperature distortion”, GT2005-68503, ASME Turbo Expo, Power For Land, Sea and Air, Reno-Tahoe, Nevada, USA, June 2005.



**APPENDIX A**

**0D PERFORMANCE SIMULATION SOFTWARE MATRIX**

													Active Features
<b>Application</b>	<b>Thermoflex</b>	<b>GT PRO</b>	<b>GT MASTER</b>	<b>STEAM PRO</b>	<b>STEAM MASTER</b>	<b>GasTurb</b>	<b>GSP</b>	<b>GateCycle</b>	<b>TurboMatch</b>	<b>PYTHIA</b>	<b>VARIFLOW</b>		
Design													
Simulation													
Aero													
Industrial													
Application Specific													
Fully Flexible													
	<b>TurboTrans</b>	<b>TurboFlexi</b>	<b>TurboTest</b>	<b>PEPSE-GT</b>	<b>NEPP</b>	<b>GTS</b>	<b>GECAT</b>	<b>RRAP-BB16</b>	<b>TESS</b>	<b>NCP</b>	<b>STEAMOMATCH</b>		
Design													
Simulation													
Aero													
Industrial													
Application Specific													
Fully Flexible													
<b>Configuration</b>	<b>Thermoflex</b>	<b>GT PRO</b>	<b>GT MASTER</b>	<b>STEAM PRO</b>	<b>STEAM MASTER</b>	<b>GasTurb</b>	<b>GSP</b>	<b>GateCycle</b>	<b>TurboMatch</b>	<b>PYTHIA</b>	<b>VARIFLOW</b>		
Fixed													
Modular													
	<b>TurboTrans</b>	<b>TurboFlexi</b>	<b>TurboTest</b>	<b>PEPSE-GT</b>	<b>NEPP</b>	<b>GTS</b>	<b>GECAT</b>	<b>RRAP-BB16</b>	<b>TESS</b>	<b>NCP</b>	<b>STEAMOMATCH</b>		
Fixed													
Modular													
<b>Performance Modelling</b>	<b>Thermoflex</b>	<b>GT PRO</b>	<b>GT MASTER</b>	<b>STEAM PRO</b>	<b>STEAM MASTER</b>	<b>GasTurb</b>	<b>GSP</b>	<b>GateCycle</b>	<b>TurboMatch</b>	<b>PYTHIA</b>	<b>VARIFLOW</b>		
Design Point													
Off Design													
Transient													
	<b>TurboTrans</b>	<b>TurboFlexi</b>	<b>TurboTest</b>	<b>PEPSE-GT</b>	<b>NEPP</b>	<b>GTS</b>	<b>GECAT</b>	<b>RRAP-BB16</b>	<b>TESS</b>	<b>NCP</b>	<b>STEAMOMATCH</b>		
Design Point													
Off Design													
Transient													
<b>Cycle</b>	<b>Thermoflex</b>	<b>GT PRO</b>	<b>GT MASTER</b>	<b>STEAM PRO</b>	<b>STEAM MASTER</b>	<b>GasTurb</b>	<b>GSP</b>	<b>GateCycle</b>	<b>TurboMatch</b>	<b>PYTHIA</b>	<b>VARIFLOW</b>		
Gas Turbines													
Steam Turbines													
Combined-Cycle/Cogeneration													
Steam Power Plants													
Coal Gasification													
Waste-to-Energy													
Recuperative Cycle													
Intercooled Cycle													
Biomass-Gasifier													
Heat Recovery Steam Generators													
	<b>TurboTrans</b>	<b>TurboFlexi</b>	<b>TurboTest</b>	<b>PEPSE-GT</b>	<b>NEPP</b>	<b>GTS</b>	<b>GECAT</b>	<b>RRAP-BB16</b>	<b>TESS</b>	<b>NCP</b>	<b>STEAMOMATCH</b>		
Gas Turbines													
Steam Turbines													
Combined-Cycle/Cogeneration													
Steam Power Plants													
Coal Gasification													
Waste-to-Energy													
Recuperative Cycle													
Intercooled Cycle													
Biomass-Gasifier													
Heat Recovery Steam Generators													

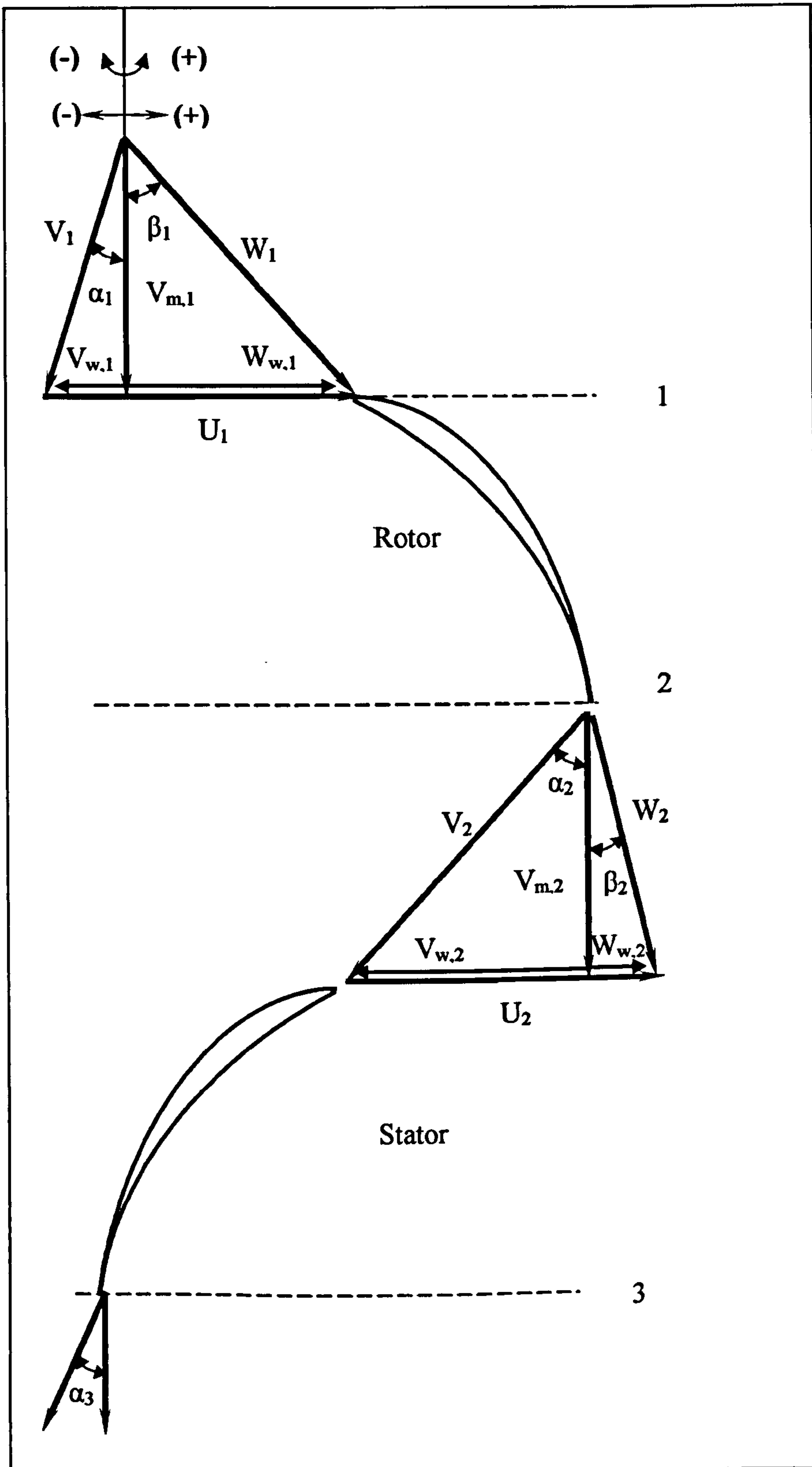


Performance features	Thermoflex	GT PRO	GT MASTER	STEAM PRO	STEAM MASTER	GasTurb	GSP	GateCycle	TurboMatch	PYTHIA	VARIFLOW
Alternative Working Fluids											
Alternative Working Fuels											
Effects of Deterioration											
Effects of Inlet Flow Distortion											
Small Effects											
Monte Carlo											
Flight Envelope											
Exhaust Gas Emissions											
Installation losses											
Reynolds											
Chemical Dissociation											
Rig Test Analysis											
Engine Diagnostics											
Optimisation											
Engine Limiters											
Multimode VSE Simulation											
Combustor Blowout											
Relight											
Advanced (2D/3D) Simulation											
	TurboTrans	TurboFlexi	TurboTest	PEPSE-GT	NEPP	GTS	GECAT	RRAP-BB16	TESS	NCP	STEAMOMATCH
Alternative Working Fluids											
Alternative Working Fuels											
Effects of Deterioration											
Effects of Inlet Flow Distortion											
Small Effects											
Monte Carlo											
Flight Envelope											
Exhaust Gas Emissions											
Installation losses											
Reynolds											
Chemical Dissociation											
Rig Test Analysis											
Engine Diagnostics											
Optimisation											
Engine Limiters											
Multimode VSE Simulation											
Combustor Blowout											
Relight											
Advanced (2D/3D) Simulation											
Control	Thermoflex	GT PRO	GT MASTER	STEAM PRO	STEAM MASTER	GasTurb	GSP	GateCycle	TurboMatch	PYTHIA	VARIFLOW
Open Loop											
Closed Loop											
	TurboTrans	TurboFlexi	TurboTest	PEPSE-GT	NEPP	GTS	GECAT	RRAP-BB16	TESS	NCP	STEAMOMATCH
Open Loop											
Closed Loop											
Software features	Thermoflex	GT PRO	GT MASTER	STEAM PRO	STEAM MASTER	GasTurb	GSP	GateCycle	TurboMatch	PYTHIA	VARIFLOW
Control Loop											
Parameter Matching											
Macro											
Fix-a-Flow											
Fix-a-Pressure											
Dynamic Convergence Control											
Multiple Model Simulation											
OLE Automation											
GUI											
	TurboTrans	TurboFlexi	TurboTest	PEPSE-GT	NEPP	GTS	GECAT	RRAP-BB16	TESS	NCP	STEAMOMATCH
Control Loop											
Parameter Matching											
Macro											
Fix-a-Flow											
Fix-a-Pressure											
Dynamic Convergence Control											
Multiple Model Simulation											
OLE Automation											
GUI											



APPENDIX B

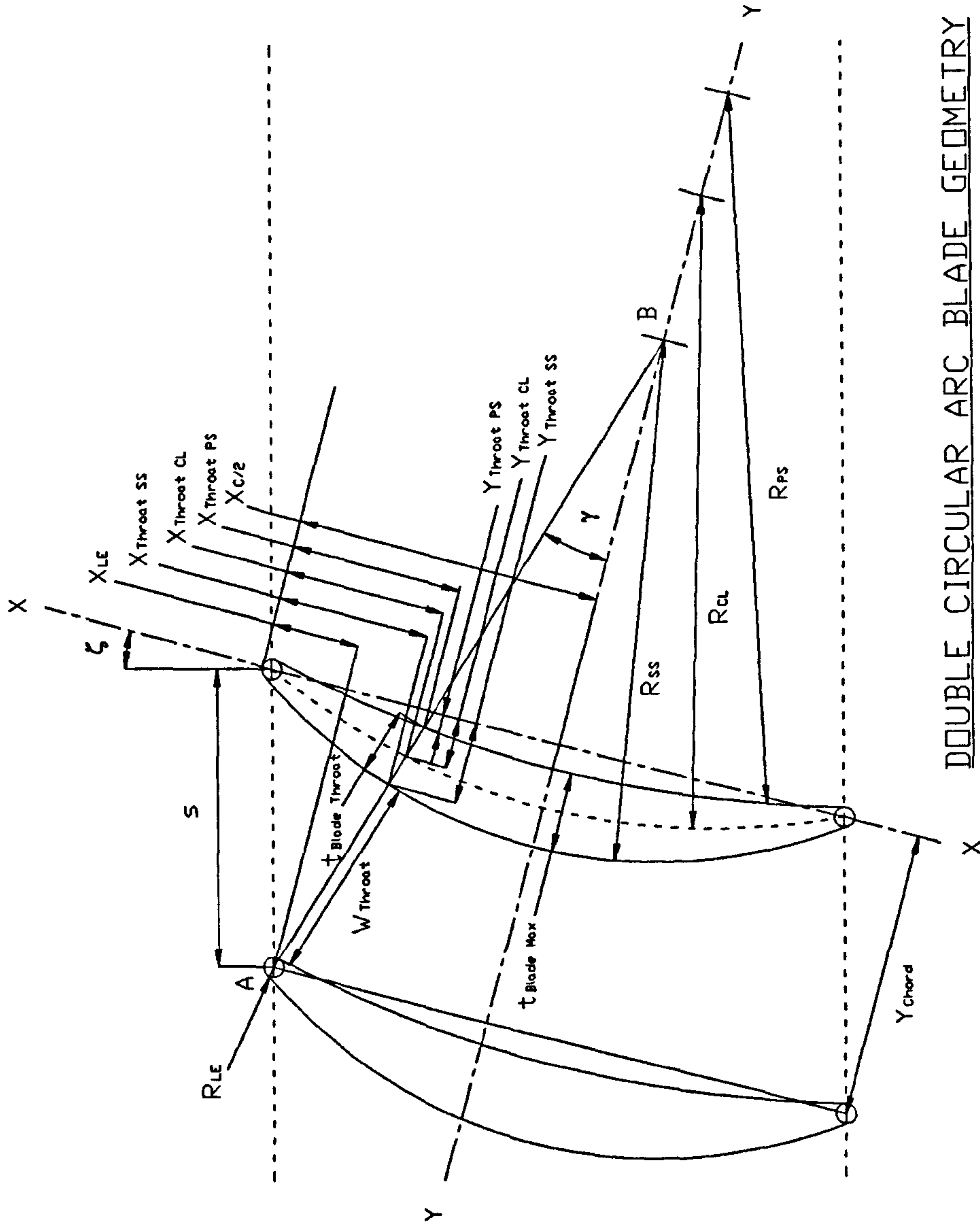
**SIGN CONVENTION AND VELOCITY TRIANGLES**





APPENDIX C

DOUBLE CIRCULAR ARC BLADE GEOMETRY

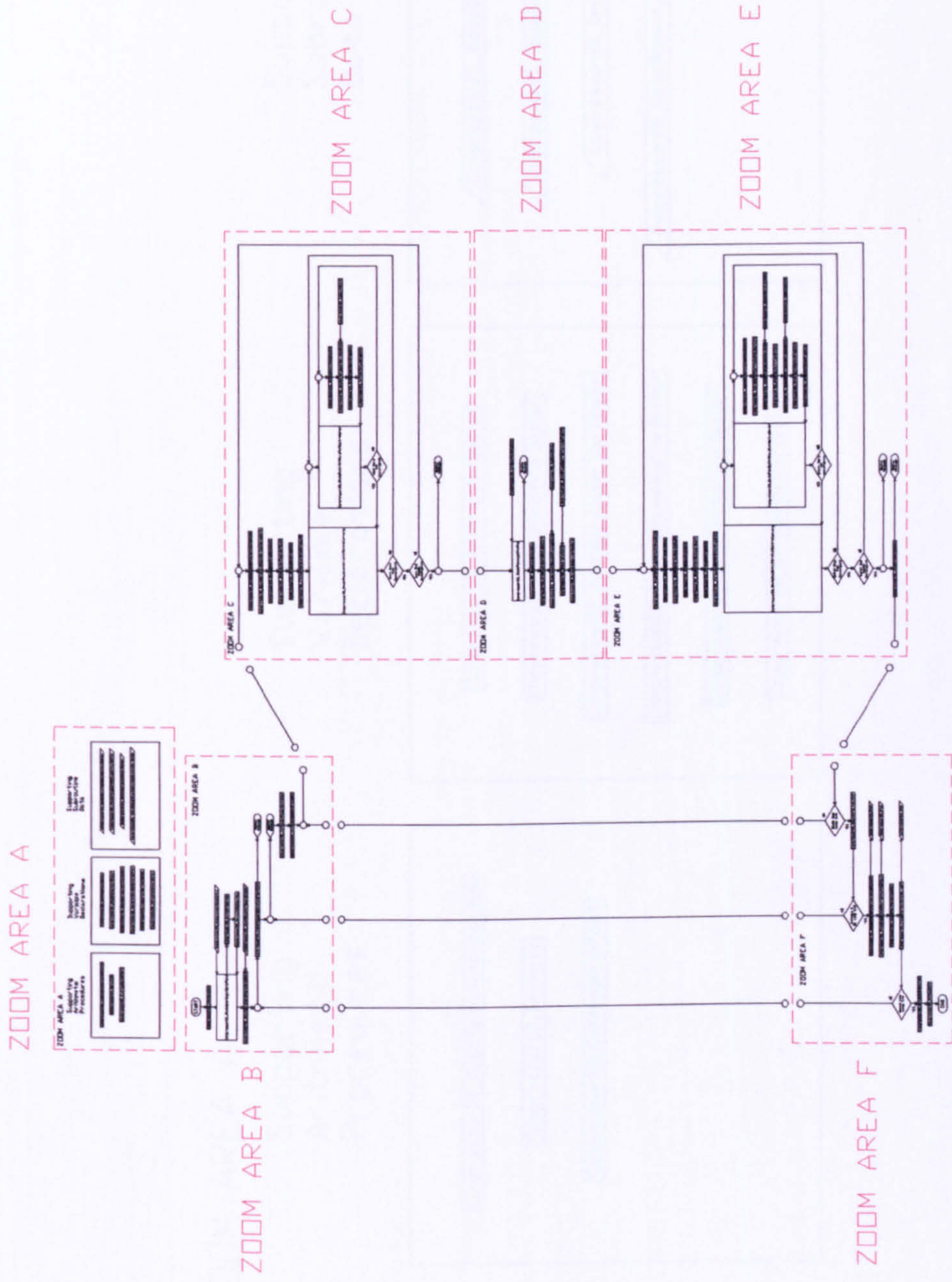


DOUBLE CIRCULAR ARC BLADE GEOMETRY



APPENDIX D

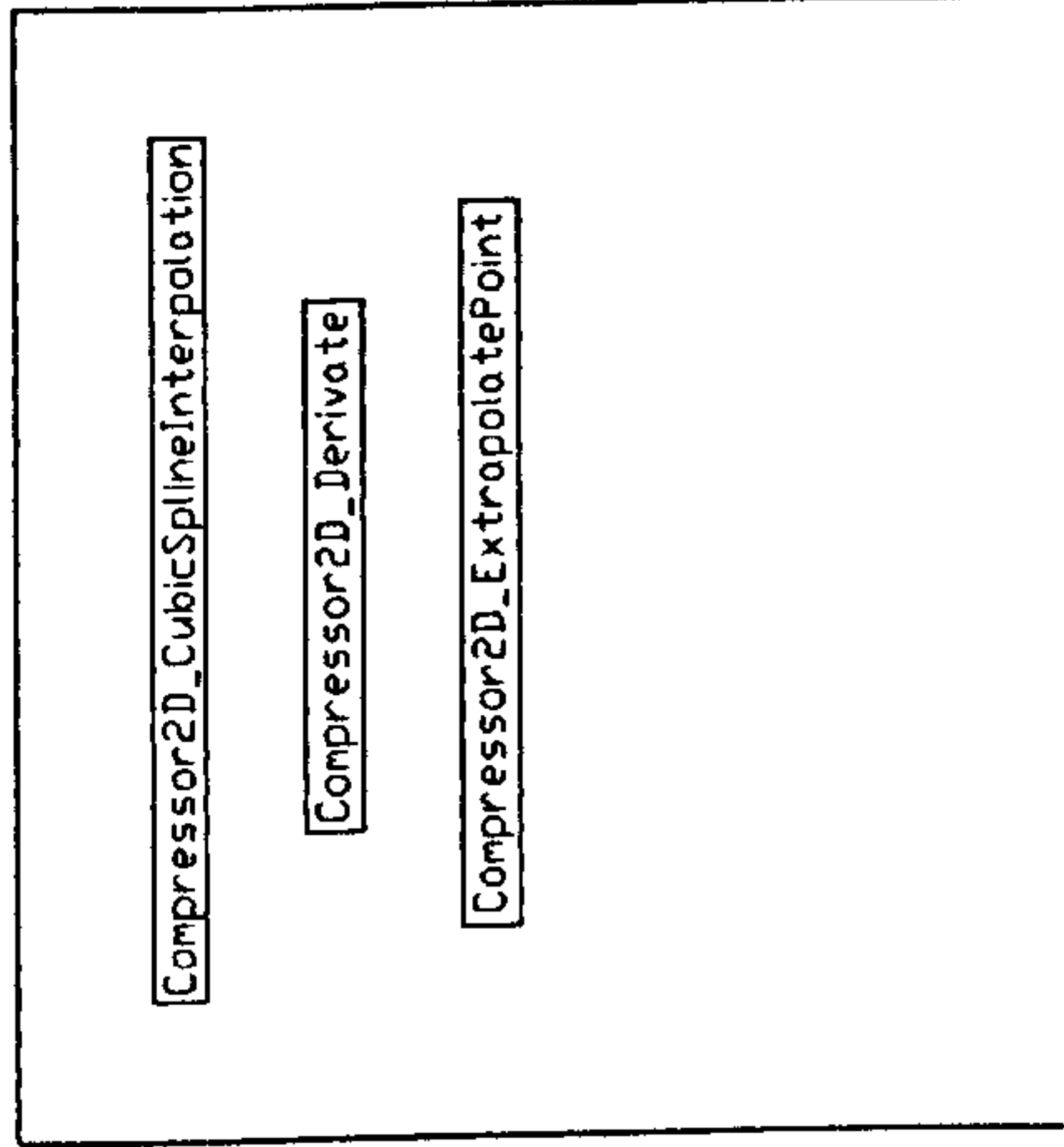
**2D COMPRESSOR SLC SOFTWARE FLOW CHART**



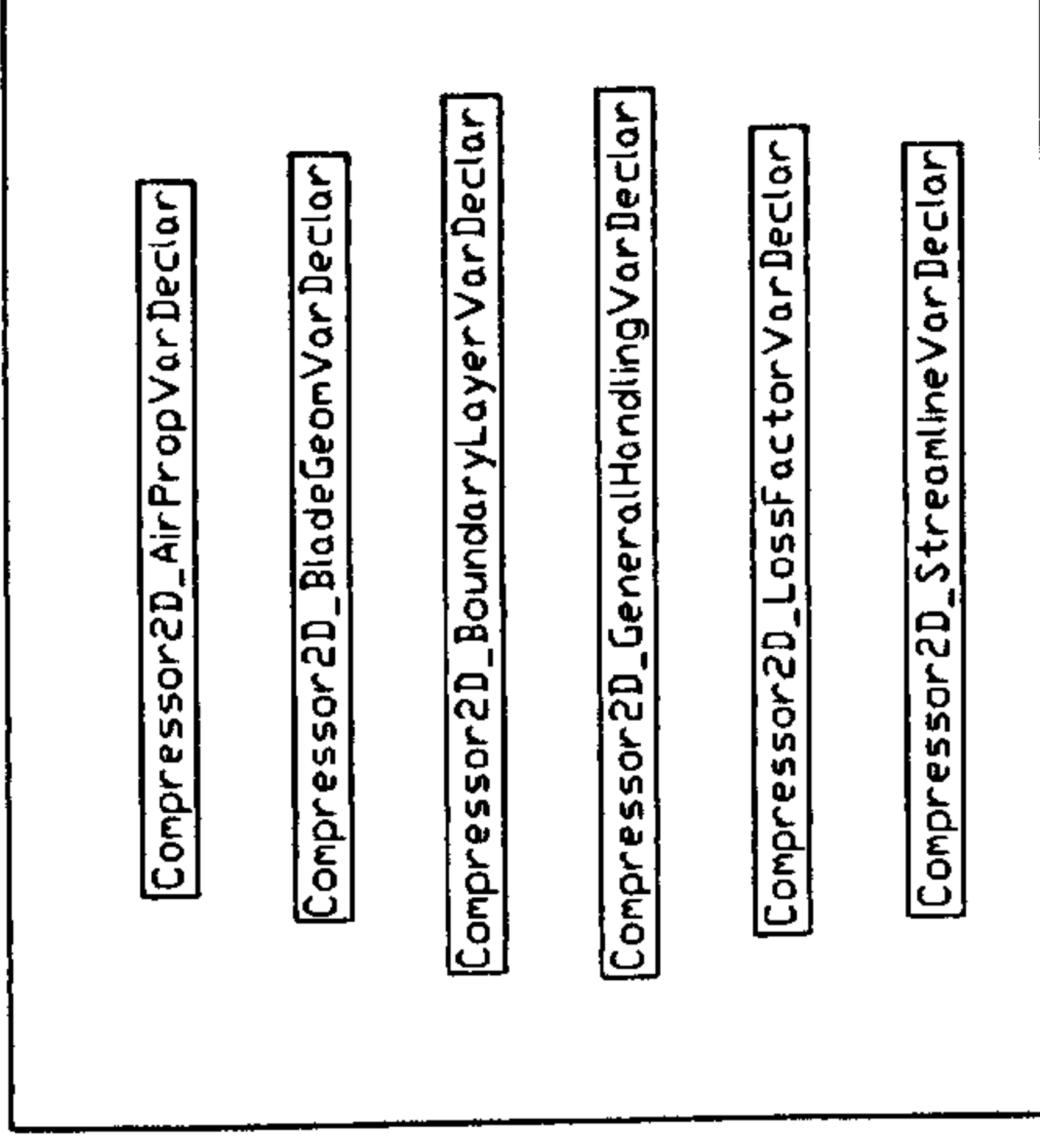


ZOOM AREA A

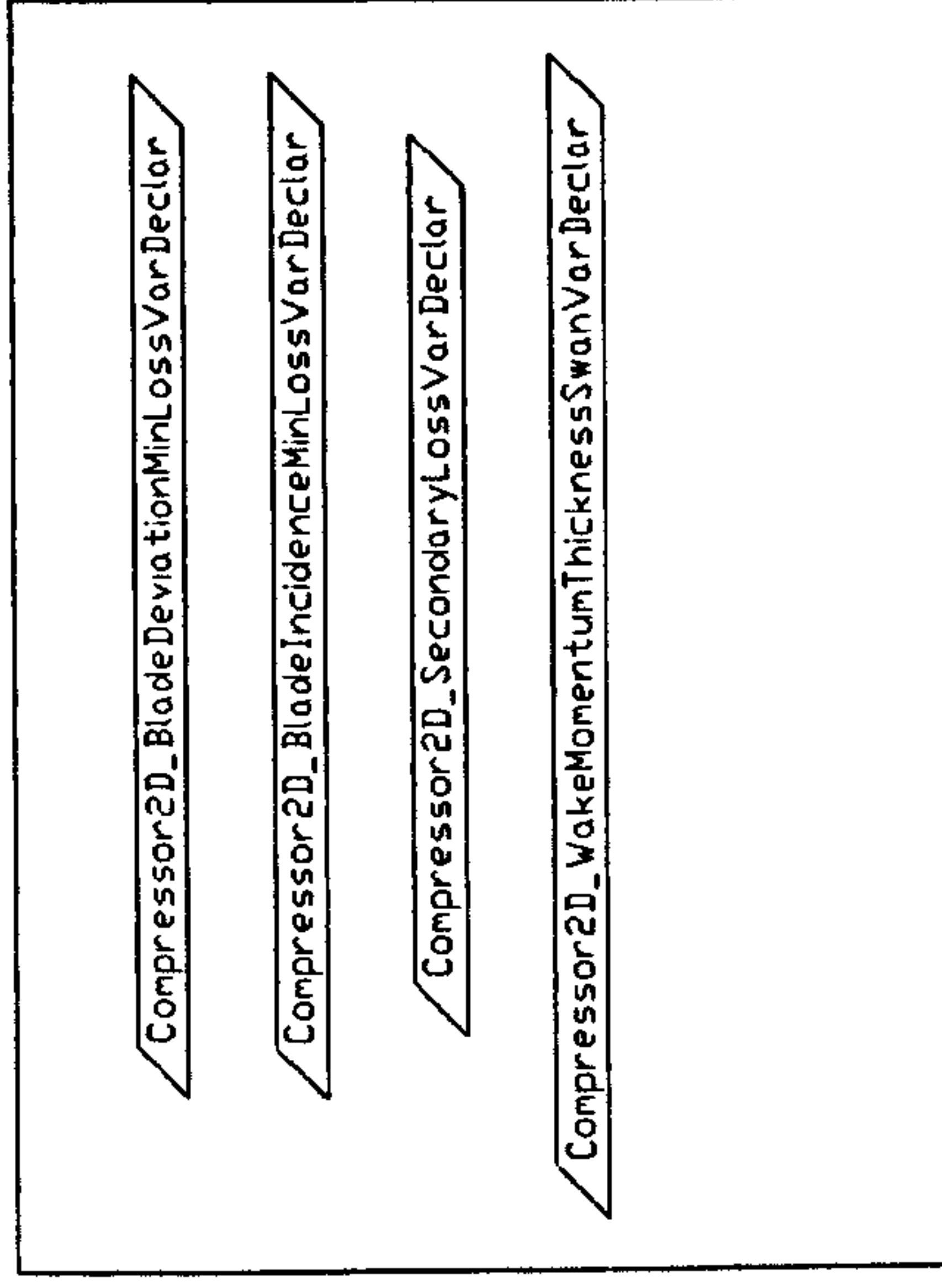
Supporting  
Arithmetic  
Procedures



Supporting  
Variable  
Declarations

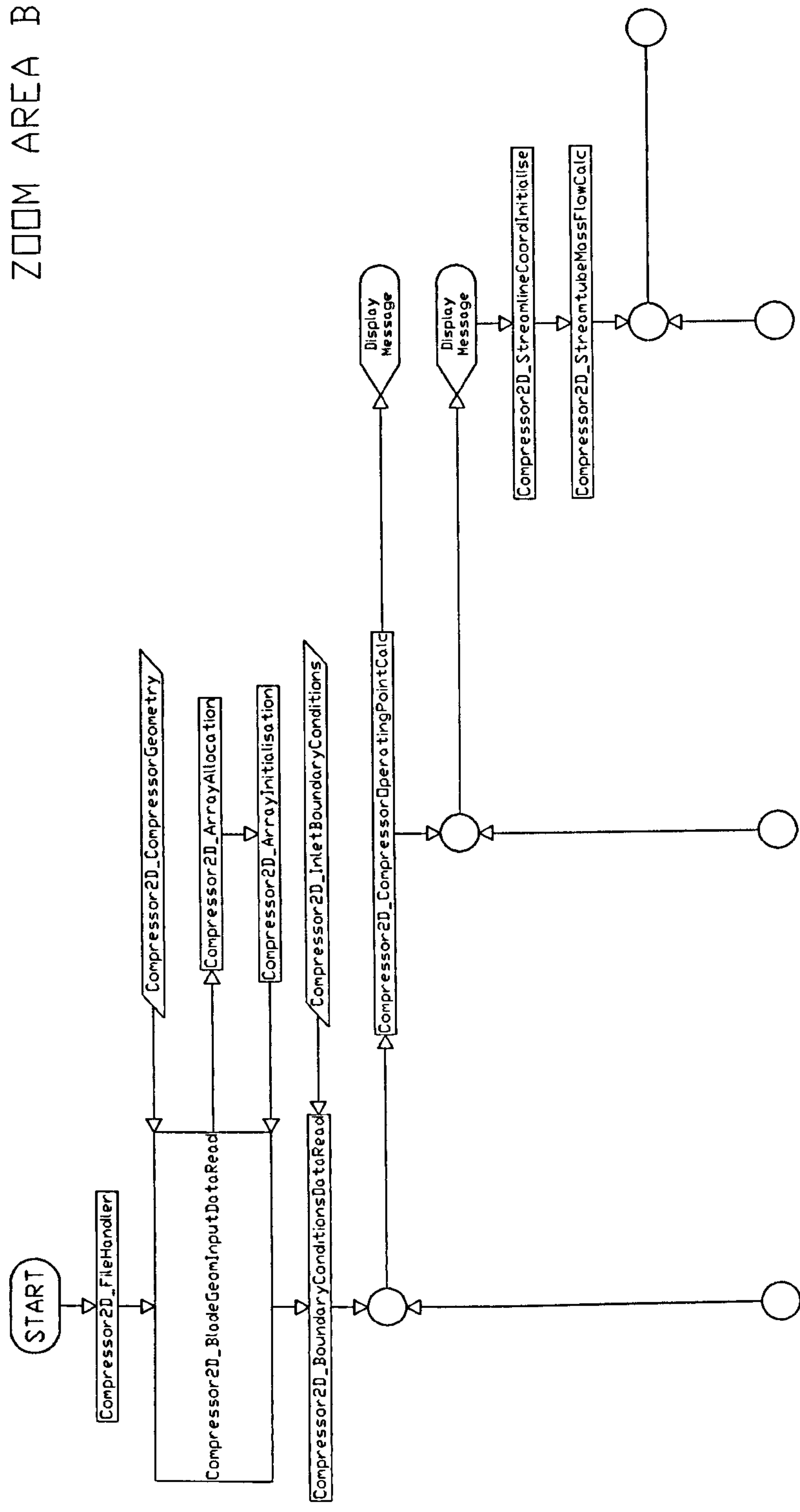


Supporting  
Subroutine  
Data



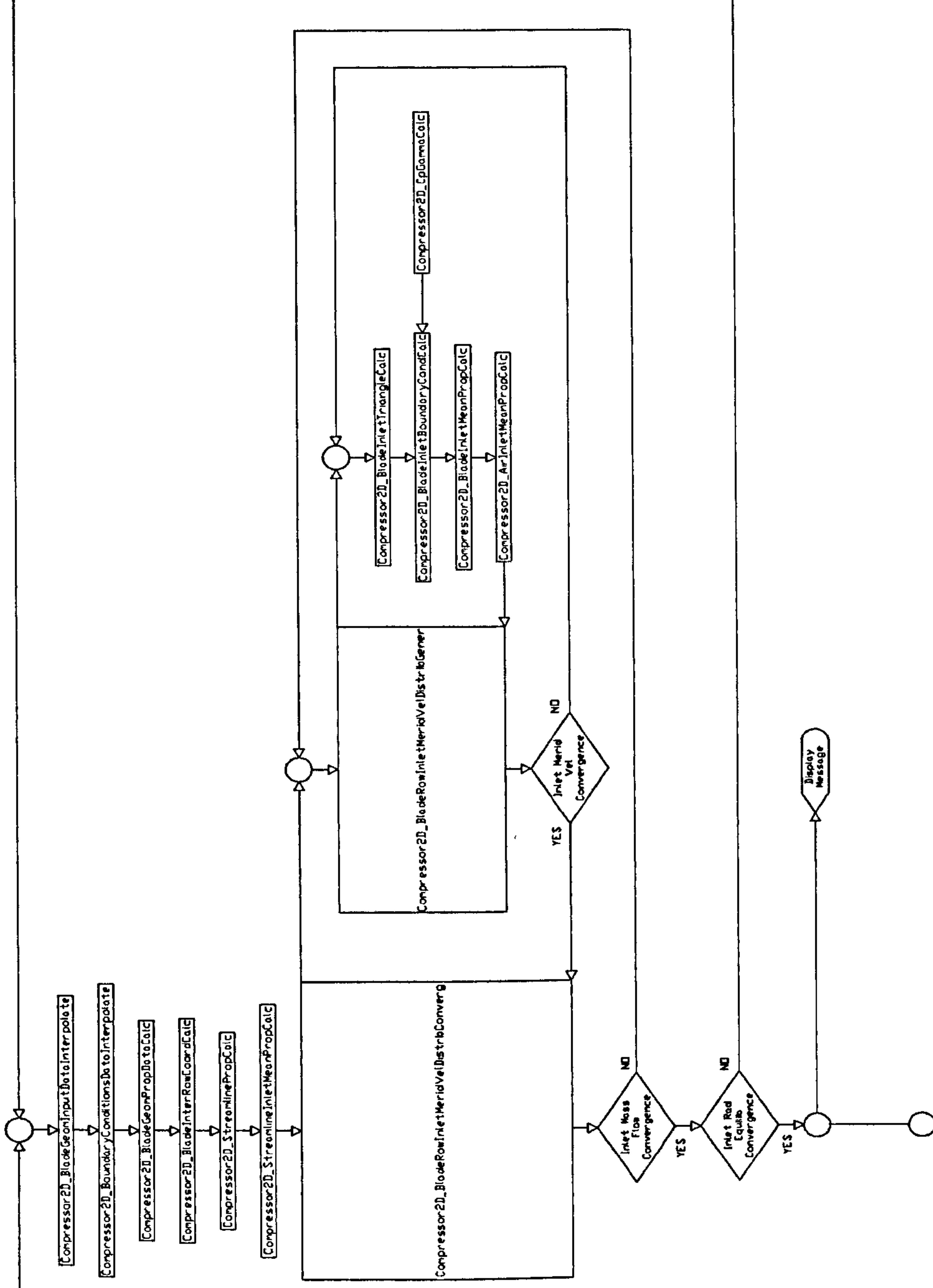


ZOOM AREA B



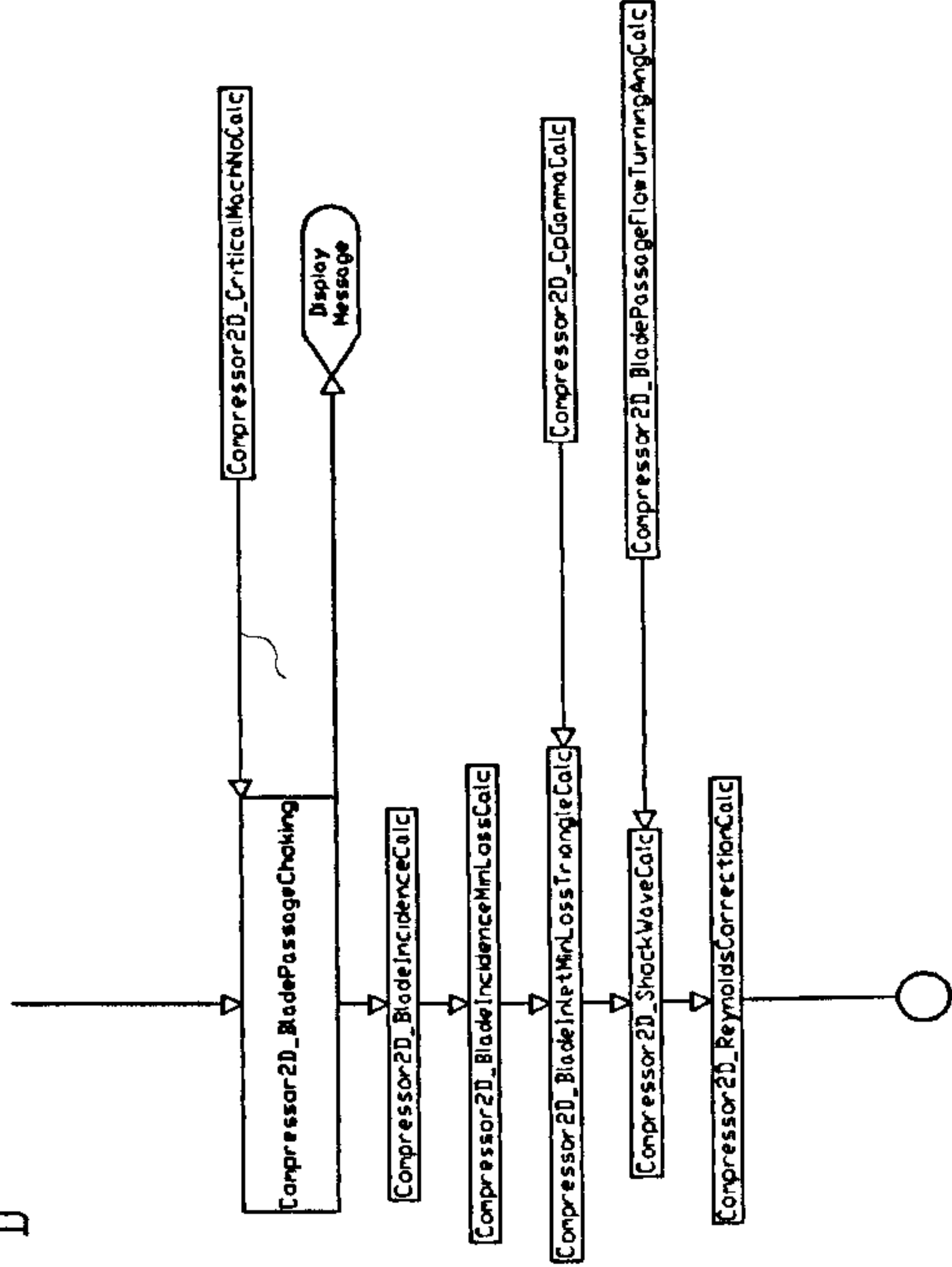


ZOOM AREA C

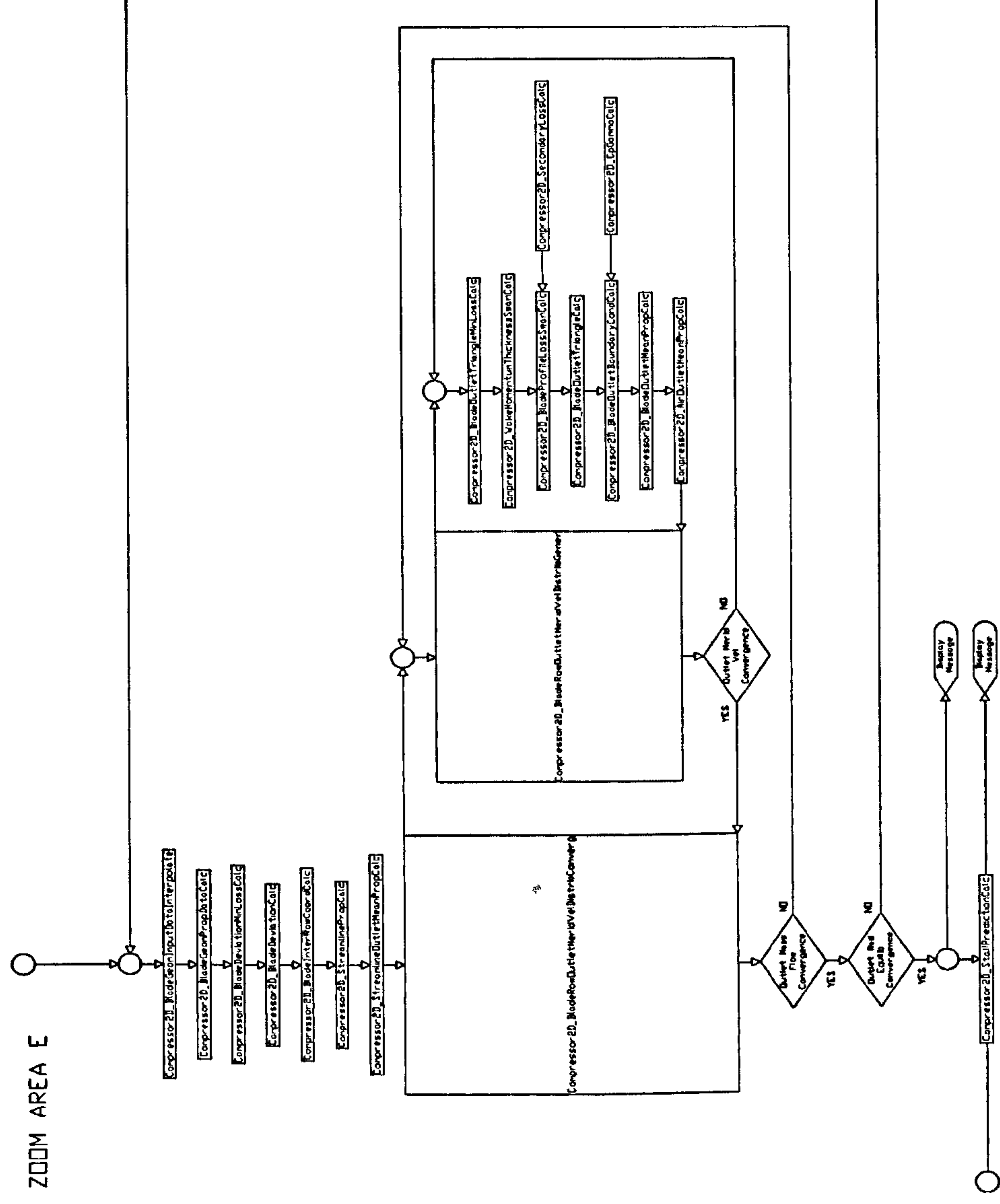




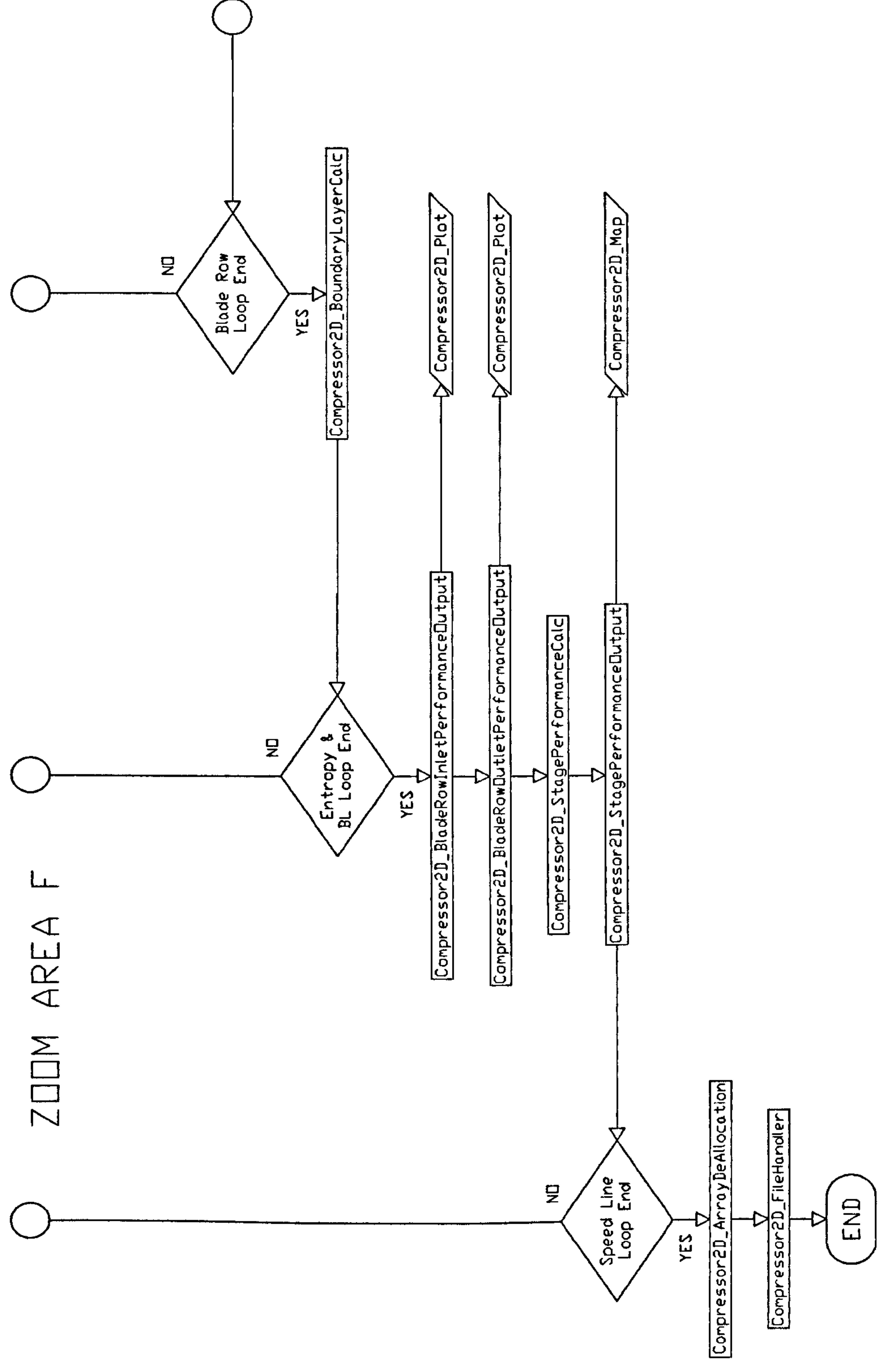
ZOOM AREA D







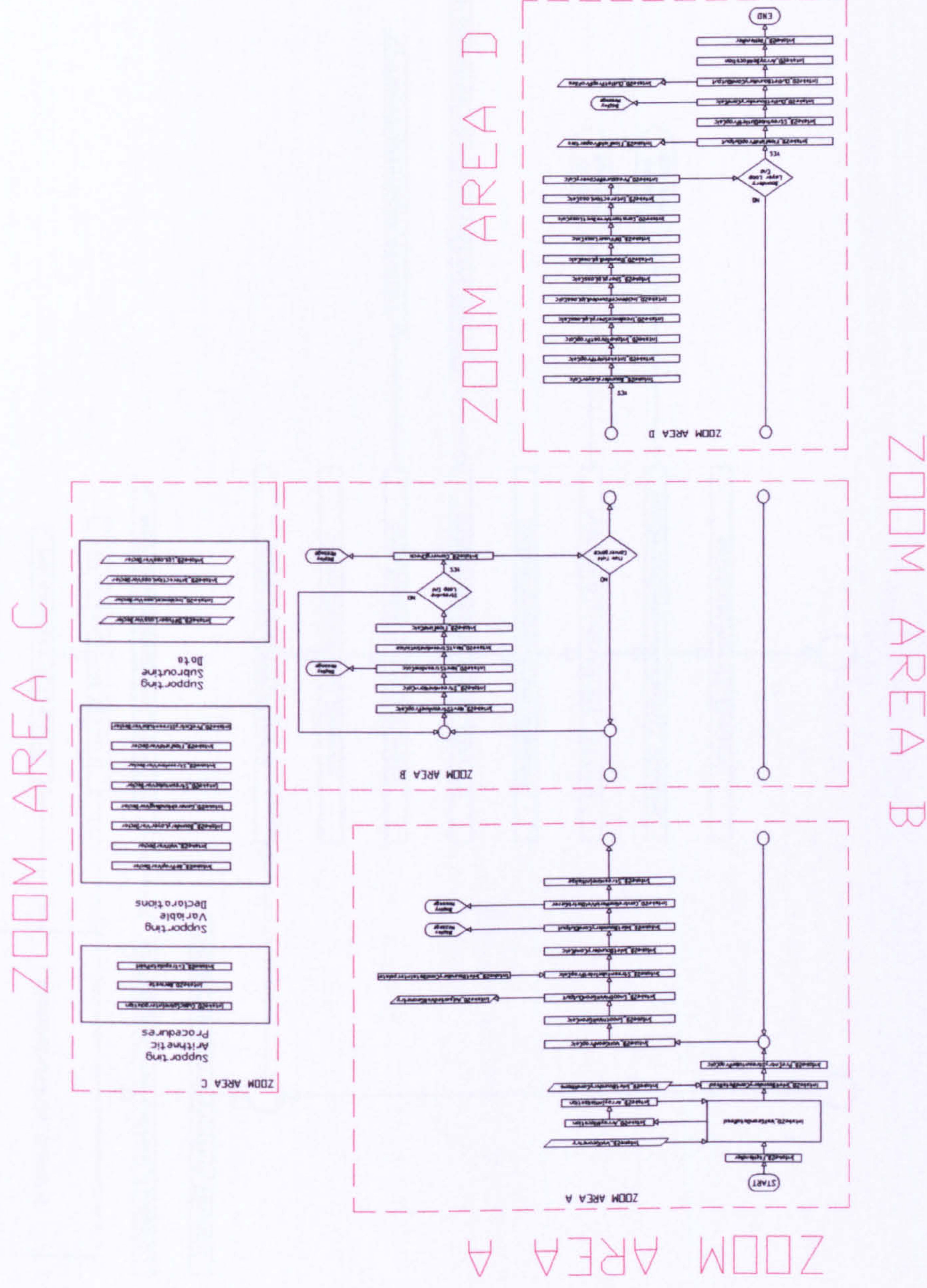






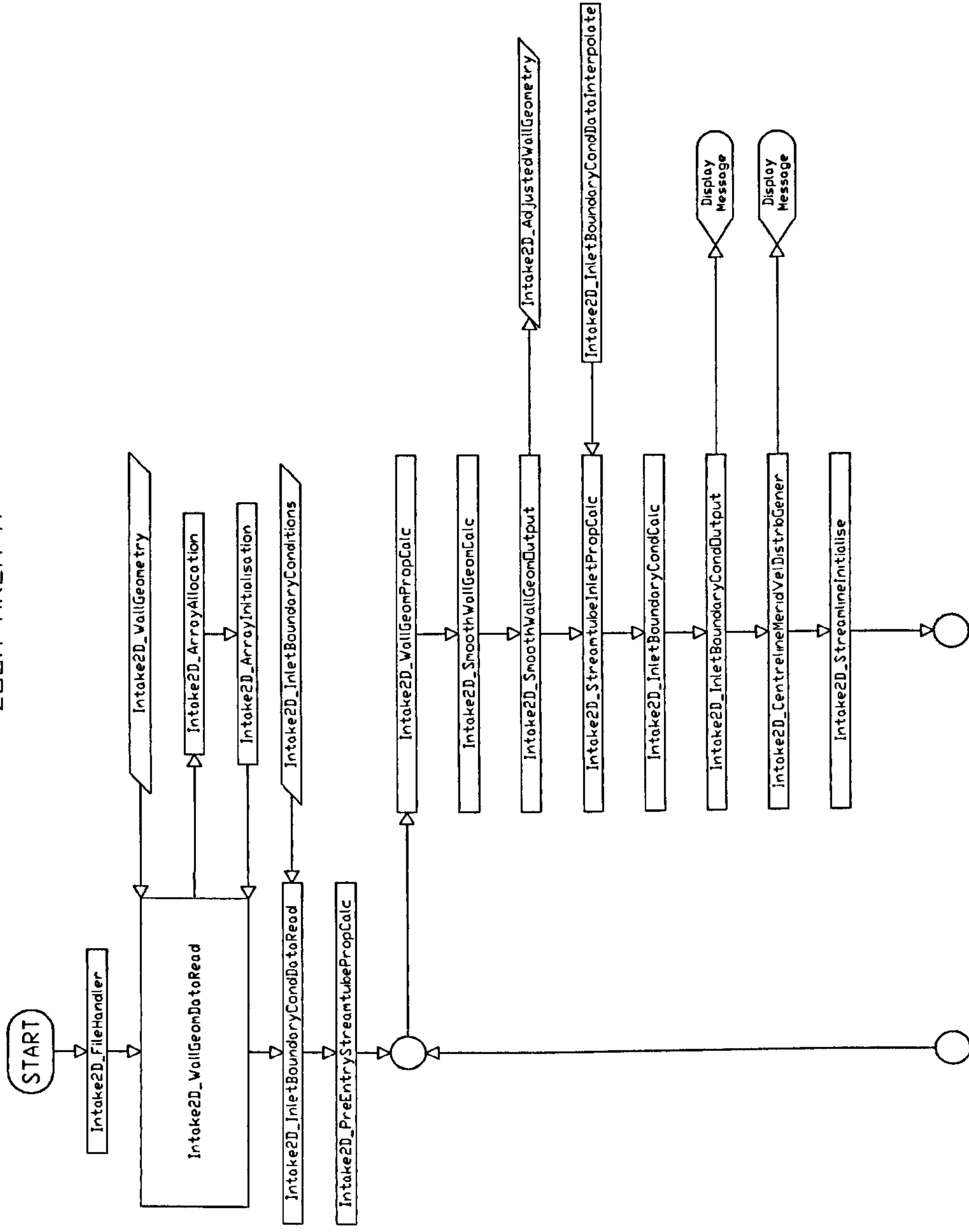
APPENDIX E

2D INTAKE SLC SOFTWARE FLOW CHART

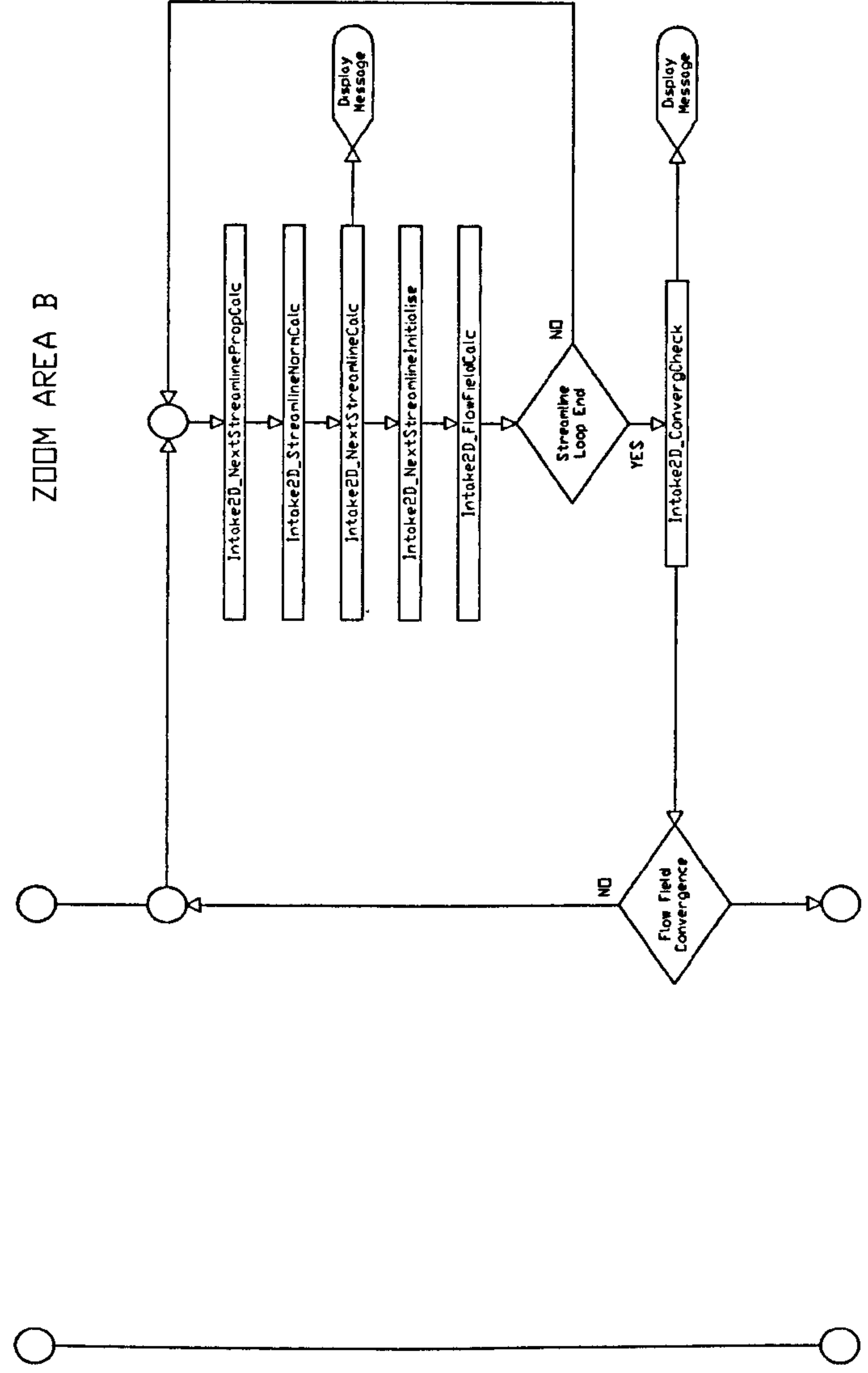




ZOOM AREA A



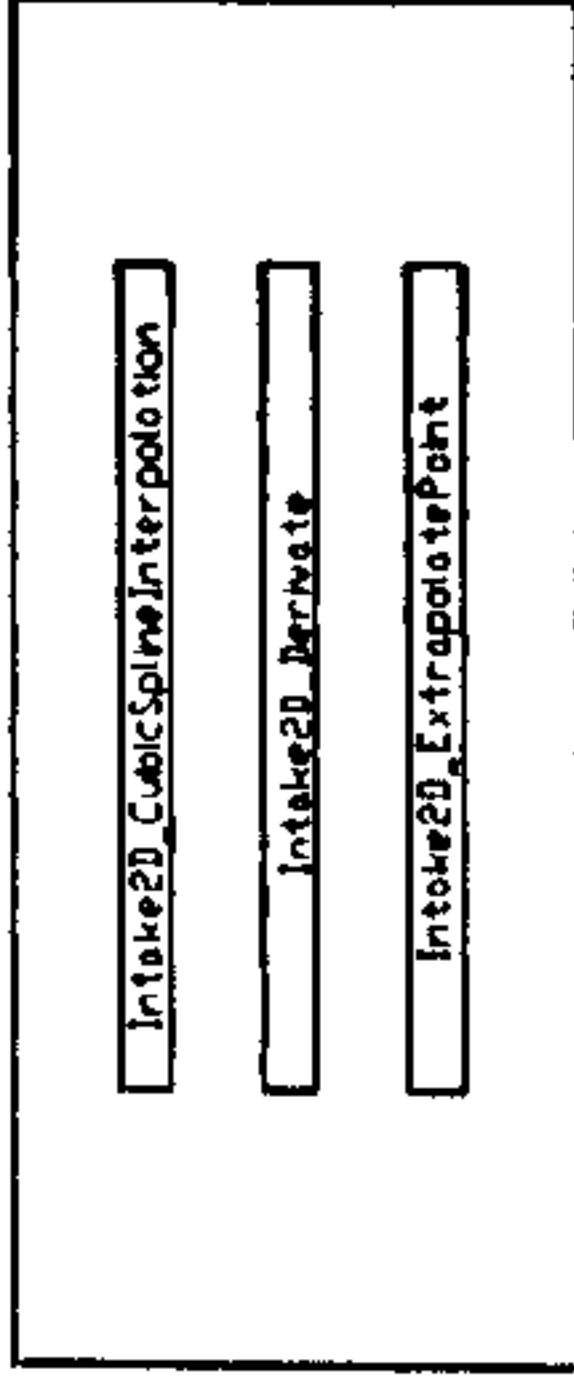




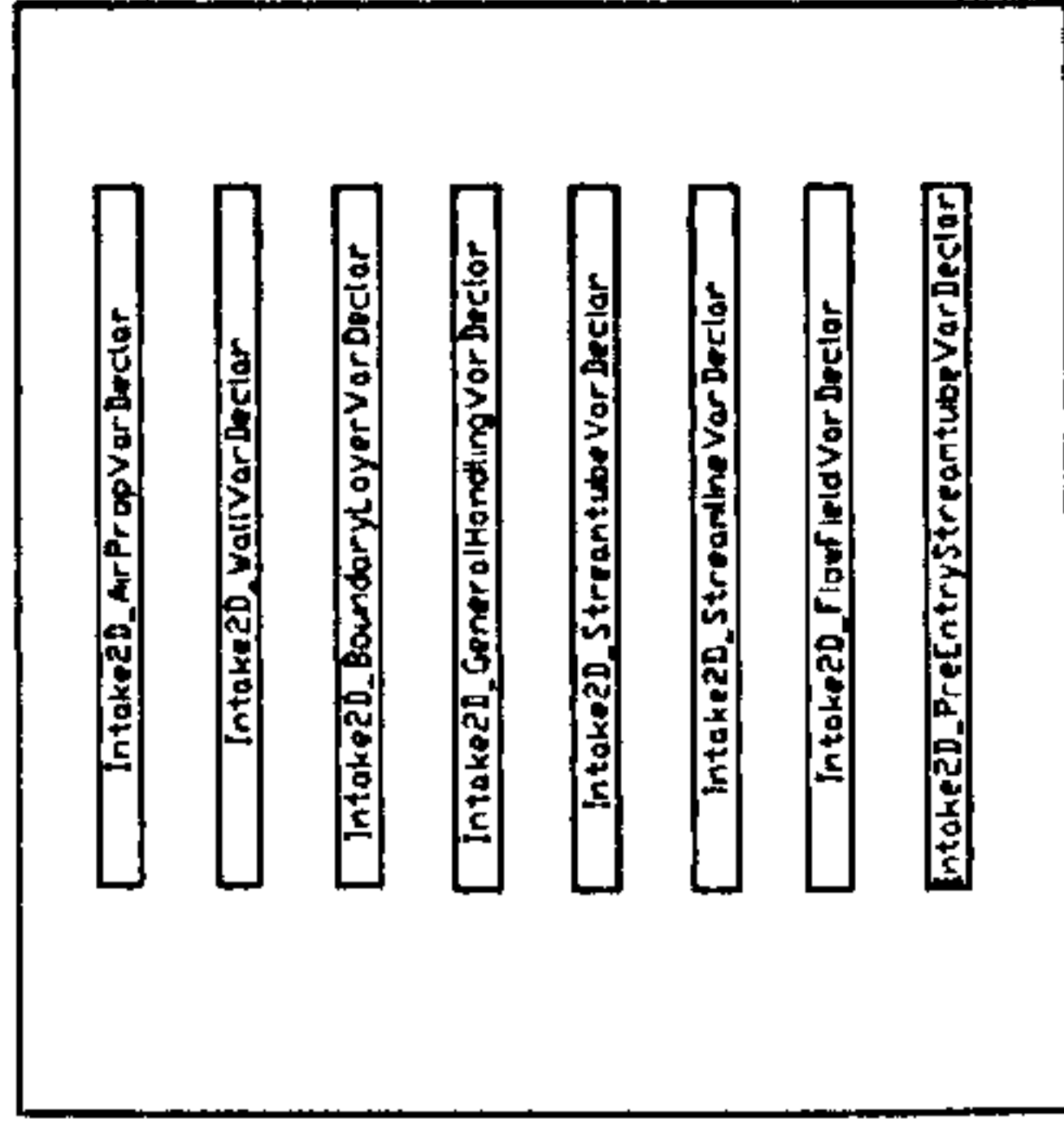


ZOOM AREA C

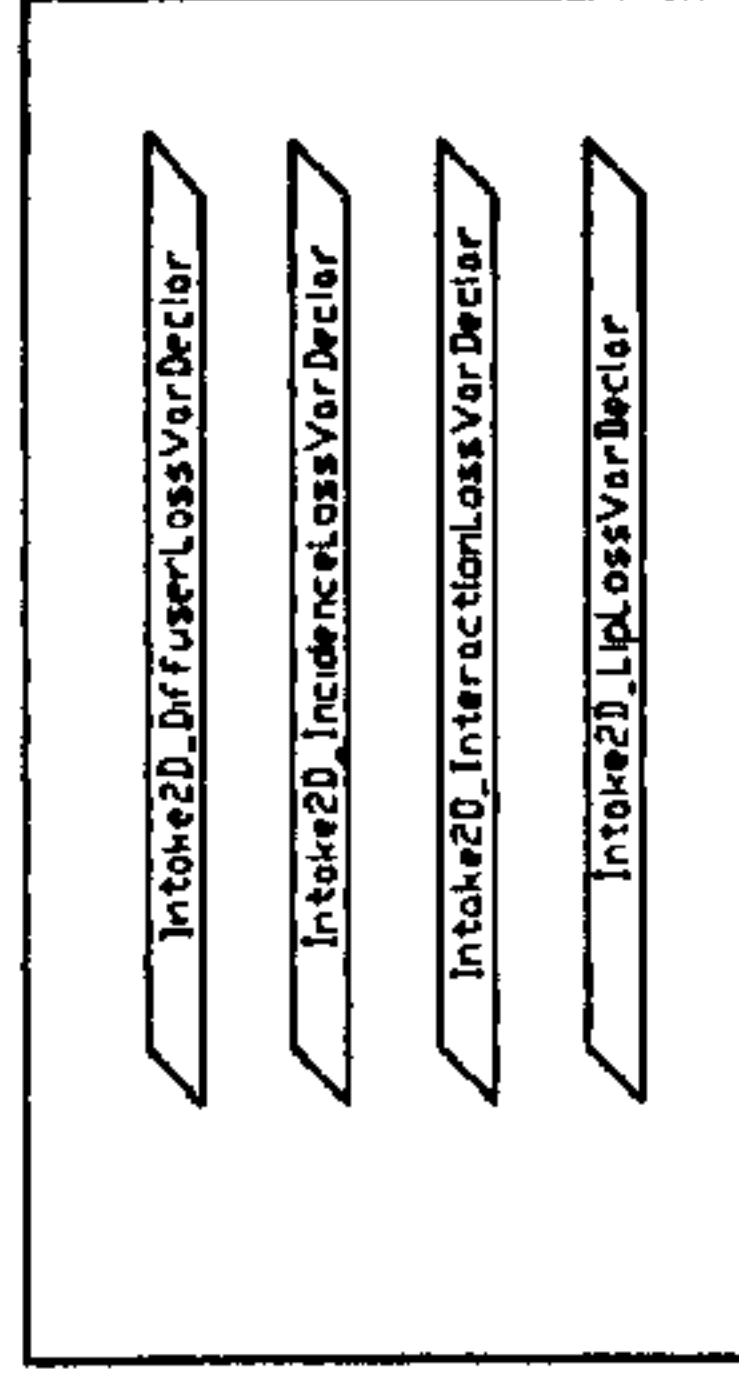
Supporting  
Arithmetic  
Procedures



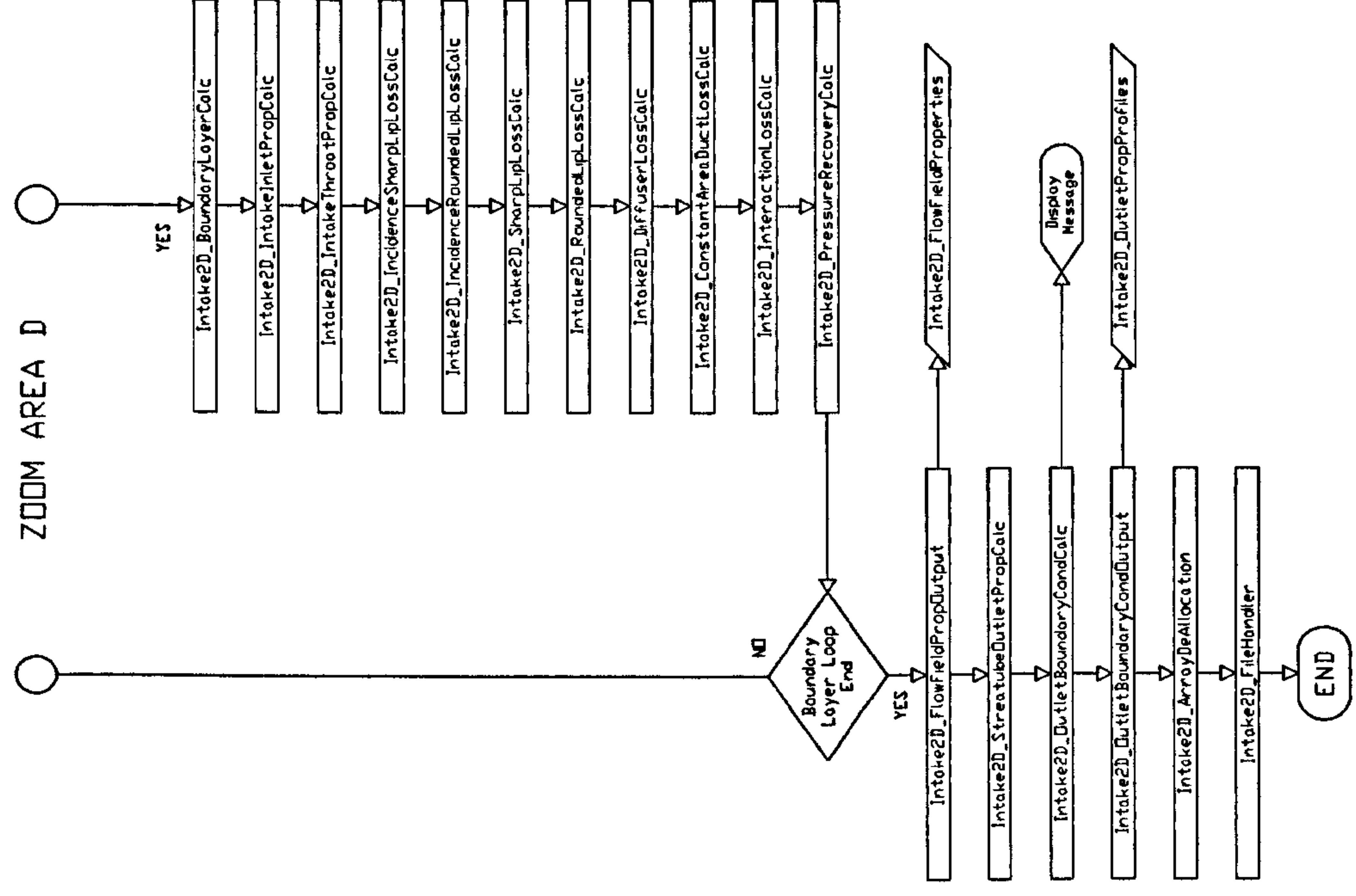
Supporting  
Variable  
Declarations



Supporting  
Subroutine  
Data









APPENDIX F**TWO-STAGE COMPRESSOR GEOMETRY**

\*\*\*\*\*Axial-Flow Compressor and Blade Geometry Input Data\*\*\*\*\*

NoofBladeRows : 4  
 NoofStrlines : 13  
 NoofBladeChordLocations : 26  
 NoofBoundLayerAuxPoints : 40

1st Stage Rotor(Clockwise Rotation)

-----

BladeRowType : 2  
 NoofBlades : 22  
 AirInletBlockageFactor : 1.000  
 AirOutletBlockageFactor : 0.998  
 BladeProfile : 65s

%Chord	T/C
0.00	0.0000
0.50	1.5440
0.75	1.2427
1.25	0.9352
2.50	0.6296
5.00	0.4354
7.50	0.3529
10.00	0.3040
15.00	0.2444
20.00	0.2072
25.00	0.1801
30.00	0.1587
35.00	0.1407
40.00	0.1249
45.00	0.1103



	InRCoord	OutRCoord	InZCoord	OutZCoord	Pitch/Chord	StaggerAng	InletAng	OutletAng	Tmax/C	TipRadius/Tmax
	50.00	0.0962								
	55.00	0.0824								
	60.00	0.0691								
	65.00	0.0566								
	70.00	0.0451								
	75.00	0.0345								
	80.00	0.0248								
	85.00	0.0163								
	90.00	0.0090								
	95.00	0.0032								
	100.00	0.0000								
	InRCoord	OutRCoord	InZCoord	OutZCoord	Pitch/Chord	StaggerAng	InletAng	OutletAng	Tmax/C	TipRadius/Tmax
	25.5300	25.5300	2.4562	6.3986	0.7700	-63.8600	-66.6100	-53.0600	2.9037	6.2174
	24.2223	24.3883	2.2515	6.6339	0.7536	-61.5900	-64.5600	-53.1500	2.9301	6.1617
	22.9146	23.2465	2.0468	6.8692	0.7270	-59.6300	-62.8300	-52.5000	3.0800	6.1070
	21.6069	22.1048	1.8421	7.1045	0.6916	-56.9400	-60.8500	-50.8000	3.3301	6.0502
	20.2992	20.9630	1.6375	7.3398	0.6498	-54.0100	-59.0100	-48.2500	3.8835	5.9945
	18.9915	19.8213	1.4328	7.5751	0.6075	-50.3500	-56.8100	-43.2400	4.5666	5.9388
	17.6839	18.6795	1.2281	7.8104	0.5643	-45.8400	-54.2700	-36.7000	5.3564	5.8831
	16.3762	17.5378	1.0234	8.0457	0.5200	-40.4500	-51.4000	-29.0500	6.1960	5.8273
	15.0685	16.3960	0.8187	8.2810	0.4739	-33.6500	-47.4400	-19.5300	7.0397	5.7716
	13.7608	15.2543	0.6140	8.5163	0.4259	-25.9800	-43.7900	-7.6000	7.7873	5.7159
	12.4531	14.1125	0.4094	8.7516	0.3841	-19.4000	-41.4000	4.8000	8.2698	5.6602
	11.1454	12.9708	0.2047	8.9869	0.3490	-14.0200	-40.3000	13.8200	8.4674	5.6045
	9.8377	11.8290	0.0000	9.2222	0.3211	-10.0600	-39.3500	21.3800	8.5486	5.5487

1st Stage Stator  
-----

BladeRowType : 3  
 NoOfBlades : 34  
 AirInletBlockageFactor : 0.996  
 AirOutletBlockageFactor : 0.994  
 BladeProfile : 65s

%Chord T/C  
 0.00 0.0000  
 0.50 1.5440



0.75	1.2427	InRCoord	OutRCoord	InZCoord	OutZCoord	Pitch/Chord	staggerAng	InletAng	OutletAng	Tmax/C	Tipradius/Tmax
1.25	0.9352	25.5300	25.5300	12.5927	18.2613	0.7868	10.9700	38.8300	-16.9800	8.0324	16.3043
2.50	0.6296	24.4183	24.4801	12.6096	18.2607	0.7675	10.9800	36.1100	-14.1000	7.9274	16.0793
5.00	0.4354	23.3065	23.4302	12.6265	18.2600	0.7422	11.2300	34.4700	-12.0400	7.8026	15.6411
7.50	0.3529	22.1948	22.3803	12.6434	18.2594	0.7117	12.1600	34.4000	-10.3900	7.6284	15.1030
10.00	0.3040	21.0830	21.3303	12.6603	18.2588	0.6743	12.7500	34.8100	-9.4000	7.4346	14.4366
15.00	0.2444	19.9713	20.2804	12.6772	18.2582	0.6369	13.4600	35.7300	-8.8600	7.2226	13.6304
20.00	0.2072	18.8595	19.2305	12.6941	18.2576	0.5988	14.2700	37.0900	-8.6300	7.0107	12.8060
25.00	0.1801	17.7478	18.1806	12.7110	18.2569	0.5609	15.0300	38.6500	-8.6700	6.8149	11.9066
30.00	0.1587	16.6360	17.1307	12.7279	18.2563	0.5222	15.9000	40.5500	-8.9500	6.6006	11.1016
35.00	0.1407	15.5243	16.0808	12.7448	18.2557	0.4833	16.7900	42.9700	-9.8600	6.3828	10.2861
40.00	0.1249	14.4125	15.0308	12.7617	18.2551	0.4485	17.4700	46.0800	-11.2900	6.1979	9.5238
45.00	0.1103	13.3008	13.9809	12.7786	18.2545	0.4241	17.7000	47.9400	-13.1200	6.0680	8.7143
50.00	0.0962	12.1890	12.9310	12.7955	18.2538	0.4024	17.8400	50.0400	-15.0400	5.9592	7.9942
55.00	0.0824										
60.00	0.0691										
65.00	0.0566										
70.00	0.0451										
75.00	0.0345										
80.00	0.0248										
85.00	0.0163										
90.00	0.0090										
95.00	0.0032										
100.00	0.0000										



## 2nd Stage Rotor(Clockwise Rotation)

-----

```

BladeRowType      : 2
NoofBlades       : 39
AirInletBlockageFactor : 0.992
AirOutletBlockageFactor : 0.990
BladeProfile     : 65s

```

%Chord	T/C	InRCoord	OutRCoord	InZCoord	OutZCoord	Pitch/Chord	StaggerAng	InletAng	OutletAng	Tmax/C	TipRadius/Tmax
0.00	0.0000										
0.50	1.5440										
0.75	1.2427										
1.25	0.9352										
2.50	0.6296										
5.00	0.4354										
7.50	0.3529										
10.00	0.3040										
15.00	0.2444										
20.00	0.2072										
25.00	0.1801										
30.00	0.1587										
35.00	0.1407										
40.00	0.1249										
45.00	0.1103										
50.00	0.0962										
55.00	0.0824										
60.00	0.0691										
65.00	0.0566										
70.00	0.0451										
75.00	0.0345										
80.00	0.0248										
85.00	0.0163										
90.00	0.0090										
95.00	0.0032										
100.00	0.0000										
		InRCoord	OutRCoord	InZCoord	OutZCoord	Pitch/Chord	StaggerAng	InletAng	OutletAng	Tmax/C	TipRadius/Tmax
		25.5300	25.5300	24.3271	26.5261	0.8190	-60.5789	-64.6500	-54.4000	3.4100	17.3410
		24.5102	24.6069	24.2470	26.6366	0.7876	-59.6284	-63.0600	-54.2200	3.4500	18.5714
		23.4903	23.6838	24.1670	26.7470	0.7562	-58.3289	-61.3300	-54.0000	3.5330	19.3820



22.4705	22.7608	24.0869	26.8575	0.7248	-56.6804	-59.8600	-53.1800	3.7790	20.0000
21.4507	21.8377	24.0069	26.9680	0.6934	-54.6828	-58.2600	-51.5200	4.2700	19.9095
20.4308	20.9146	23.9268	27.0785	0.6620	-52.3362	-56.4800	-49.0600	4.8503	19.2460
19.4110	19.9915	23.8468	27.1890	0.6306	-49.6406	-54.7000	-46.0500	5.4600	18.4669
18.3912	19.0684	23.7667	27.2995	0.5991	-46.5958	-53.1000	-42.0500	6.1070	17.8571
17.3713	18.1453	23.6866	27.4100	0.5677	-43.2021	-51.8100	-37.0800	6.7400	17.5562
16.3515	17.2223	23.6066	27.5205	0.5363	-39.4593	-50.7000	-30.9300	7.3073	17.5325
15.3317	16.2992	23.5265	27.6310	0.5049	-35.3675	-50.4600	-23.8000	7.7572	17.9803
14.3118	15.3761	23.4465	27.7415	0.4735	-30.9266	-51.5000	-12.5500	8.0377	18.4019
13.2920	14.4530	23.3664	27.8520	0.4421	-26.1366	-53.6241	-2.0800	8.0970	18.9737

2nd stage stator  
-----

BladeRowType : 3  
 NoofBlades : 42  
 AirInletBlockageFactor : 0.988  
 AirOutletBlockageFactor : 0.986  
 BladeProfile : 65s

%Chord	T/C
0.00	0.0000
0.50	1.5440
0.75	1.2427
1.25	0.9352
2.50	0.6296
5.00	0.4354
7.50	0.3529
10.00	0.3040
15.00	0.2444
20.00	0.2072
25.00	0.1801
30.00	0.1587
35.00	0.1407
40.00	0.1249
45.00	0.1103
50.00	0.0962
55.00	0.0824
60.00	0.0691



InRCoord	outRCoord	InZCoord	outZCoord	Pitch/Chord	staggerAng	InletAng	outletAng	Tmax/C	TipRadius/Tmax
65.00	0.0566								
70.00	0.0451								
75.00	0.0345								
80.00	0.0248								
85.00	0.0163								
90.00	0.0090								
95.00	0.0032								
100.00	0.0000								
InRCoord	outRCoord	InZCoord	outZCoord	Pitch/Chord	staggerAng	InletAng	outletAng	Tmax/C	TipRadius/Tmax
25.5300	25.5300	32.2436	36.6521	0.8617	6.4600	37.5000	-16.1600	8.4916	17.5562
24.6418	24.6725	32.2577	36.6487	0.8322	8.2600	36.0700	-13.8500	8.2794	17.2365
23.7537	23.8150	32.2717	36.6453	0.8026	9.9200	35.0300	-11.9100	8.0673	16.9075
22.8655	22.9575	32.2857	36.6418	0.7730	11.3100	34.4800	-10.4500	7.8551	16.2202
21.9773	22.1000	32.2998	36.6384	0.7434	12.2600	34.3200	-9.5600	7.6429	15.5963
21.0892	21.2425	32.3138	36.6350	0.7139	12.9000	34.4800	-9.2300	7.4307	14.9842
20.2010	20.3850	32.3278	36.6315	0.6843	13.3800	34.9700	-9.1100	7.2185	14.2857
19.3128	19.5275	32.3419	36.6281	0.6547	13.9000	35.7900	-9.2300	7.0063	13.3779
18.4247	18.6700	32.3559	36.6247	0.6251	14.5400	37.1000	-9.5200	6.7942	12.5862
17.5365	17.8125	32.3699	36.6213	0.5956	15.2300	38.6900	-10.6700	6.5820	11.7021
16.6483	16.9550	32.3840	36.6178	0.5660	16.0000	41.2000	-12.3600	6.3698	10.8059
15.7602	16.0975	32.3980	36.6144	0.5364	16.6400	44.2000	-14.4000	6.1576	10.2230
14.8720	15.2400	32.4120	36.6110	0.5068	17.0900	47.9000	-17.0400	5.9454	9.6591



APPENDIX G**INTAKE GEOMETRY**

\*\*\*\*\*Axial-Flow Intake Geometry Input Data\*\*\*\*\*

NoofStrLines : 13  
 NoofStrLinePoints : 23  
 NoofConeStrLinePoints : 10

WallZCoord	WallRCoord
0.0000	24.0500
2.2727	21.6300
4.5454	20.7000
6.8182	20.4700
9.0909	20.6400
11.3636	20.9400
13.7500	21.3600
15.9091	21.7100
18.1818	22.0100
20.4545	22.3200
22.7273	22.6300
25.0000	22.9400
27.2727	23.2500
29.5454	23.5500
31.8182	23.8600
34.0909	24.1700
36.3636	24.4800
38.6364	24.7900
40.9091	25.0900
43.1818	25.4000
45.4545	25.5300
47.7273	25.5300
50.0000	25.5300



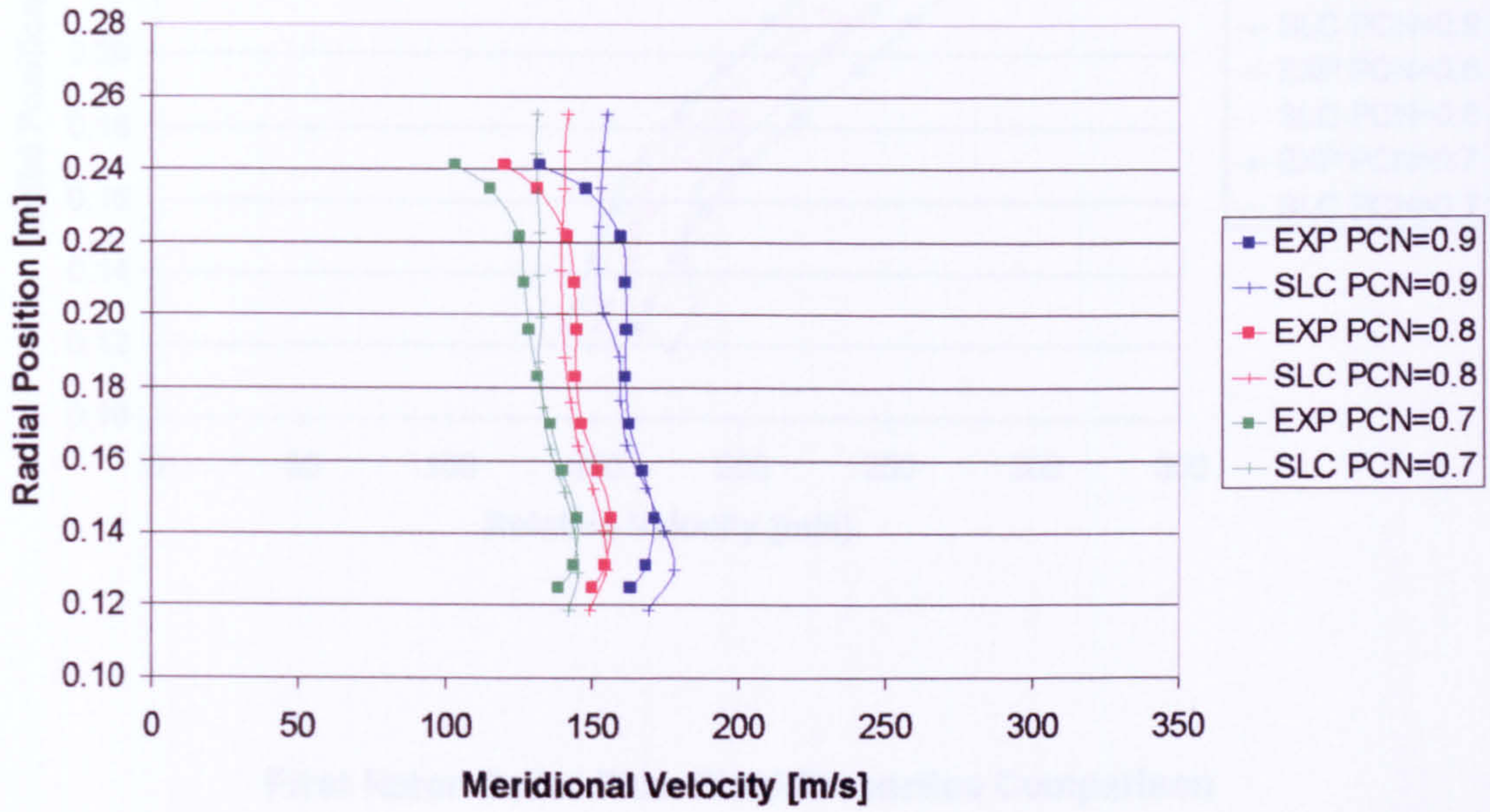
ConeZCoord	ConeRCoord
29.5454	0.0000
31.8182	1.4414
34.0909	2.8828
36.3636	4.3241
38.6364	5.7655
40.9091	7.2069
43.1818	8.0000
45.4545	8.6400
47.7273	9.2500
50.0000	9.8377



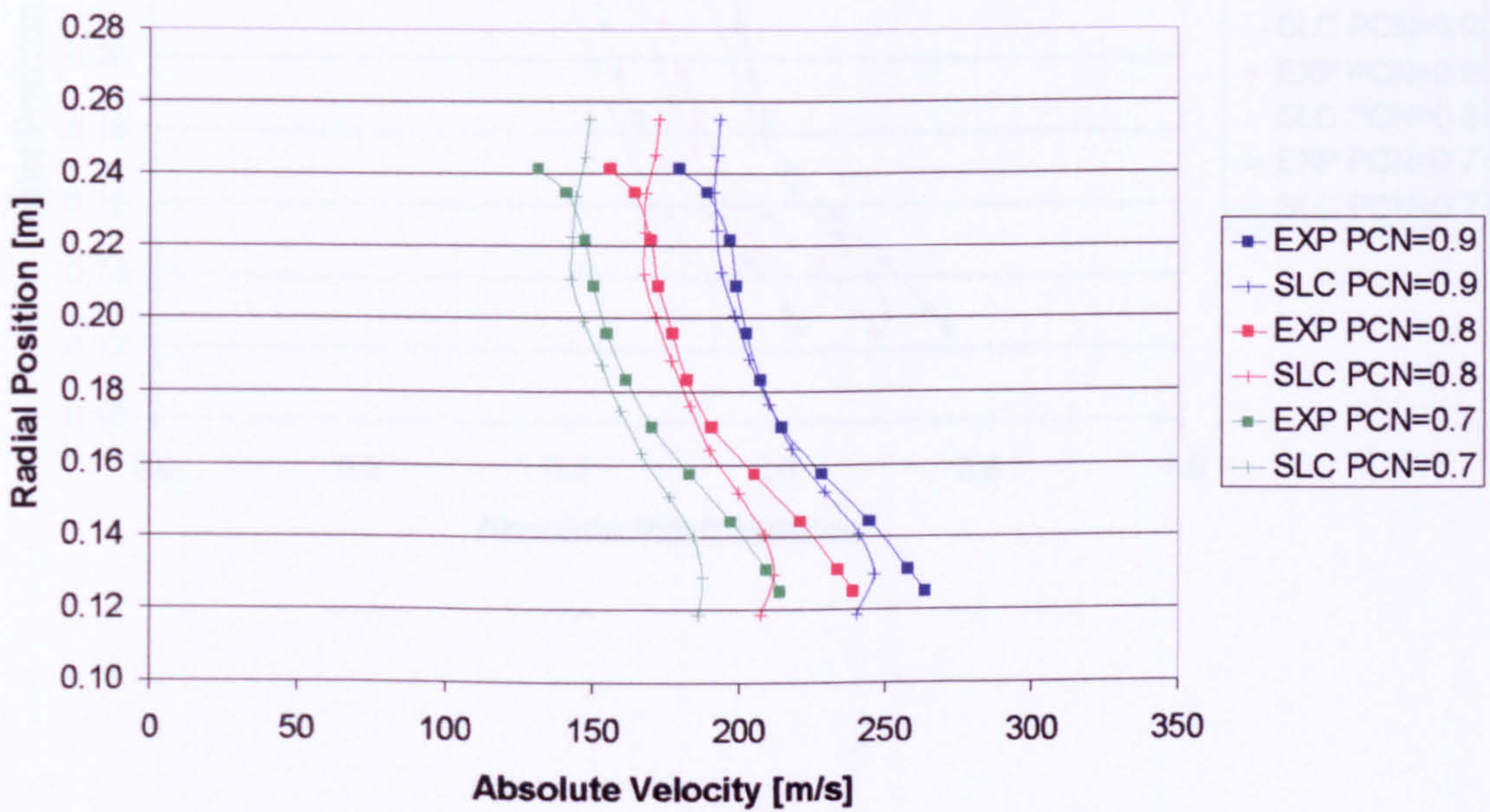
APPENDIX H

**2D PROFILE COMPARISON**

**First Rotor Outlet Flow Field Properties Comparison**

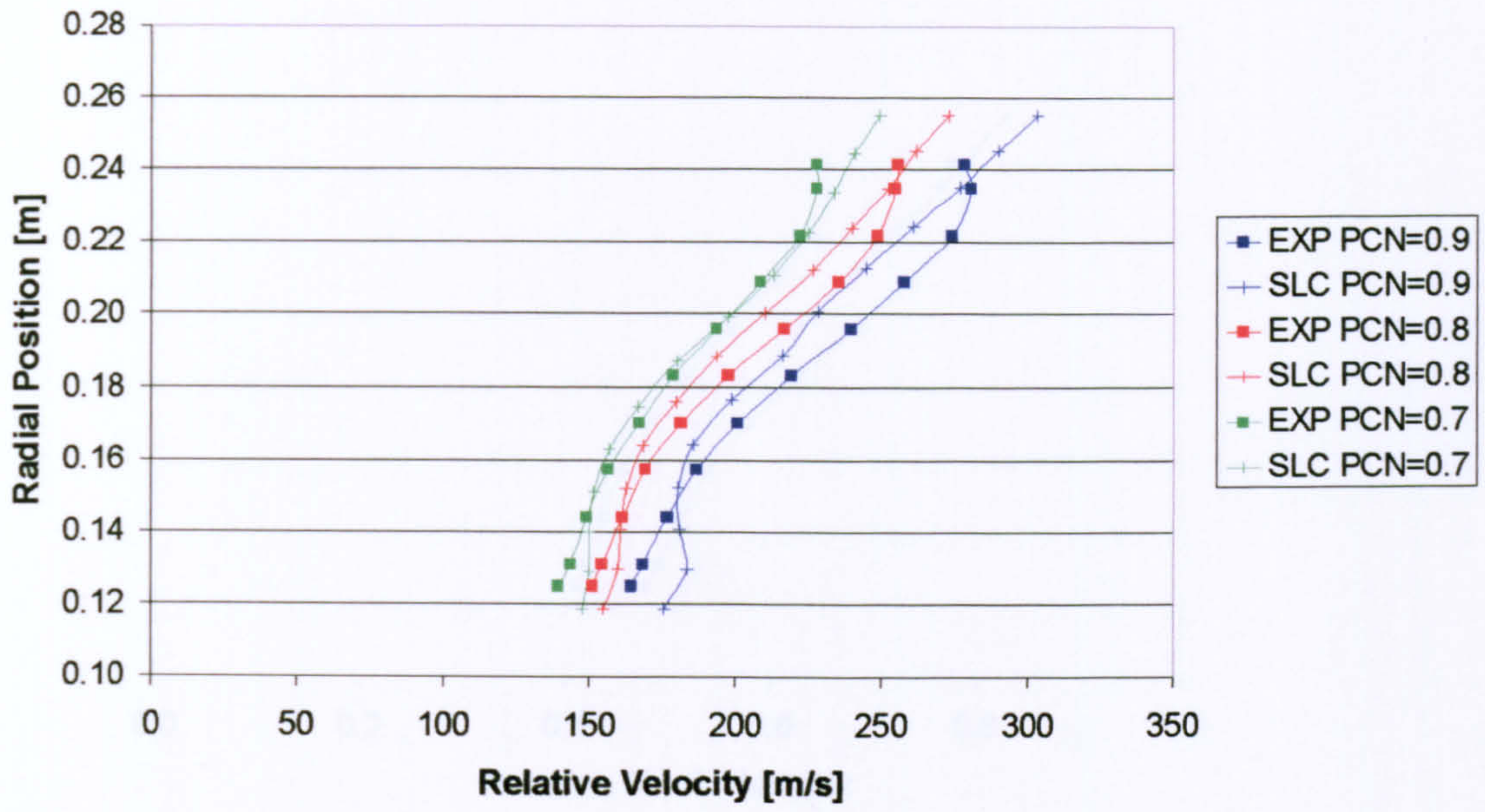


**First Rotor Outlet Flow Field Properties Comparison**

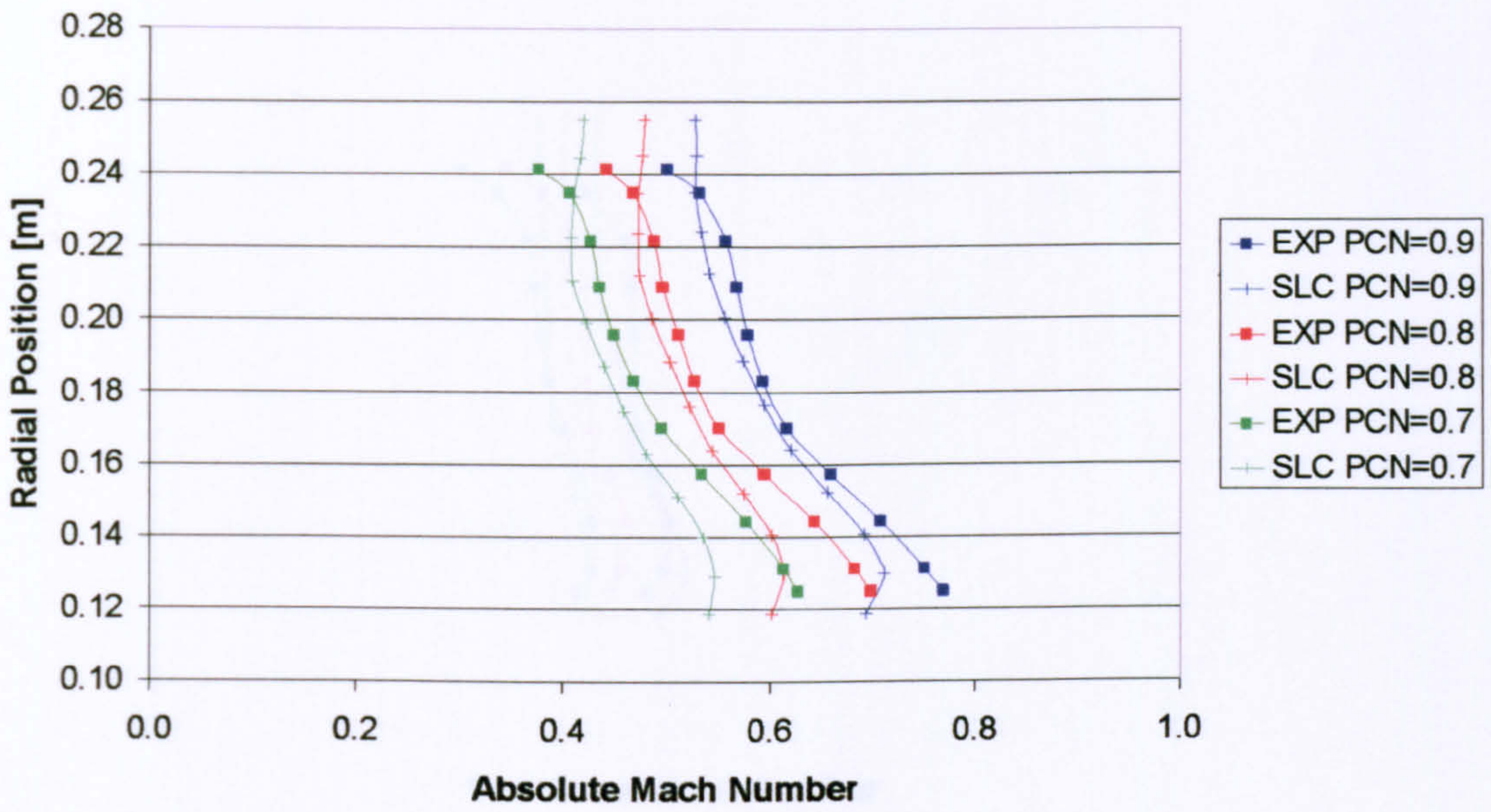




First Rotor Outlet Flow Field Properties Comparison

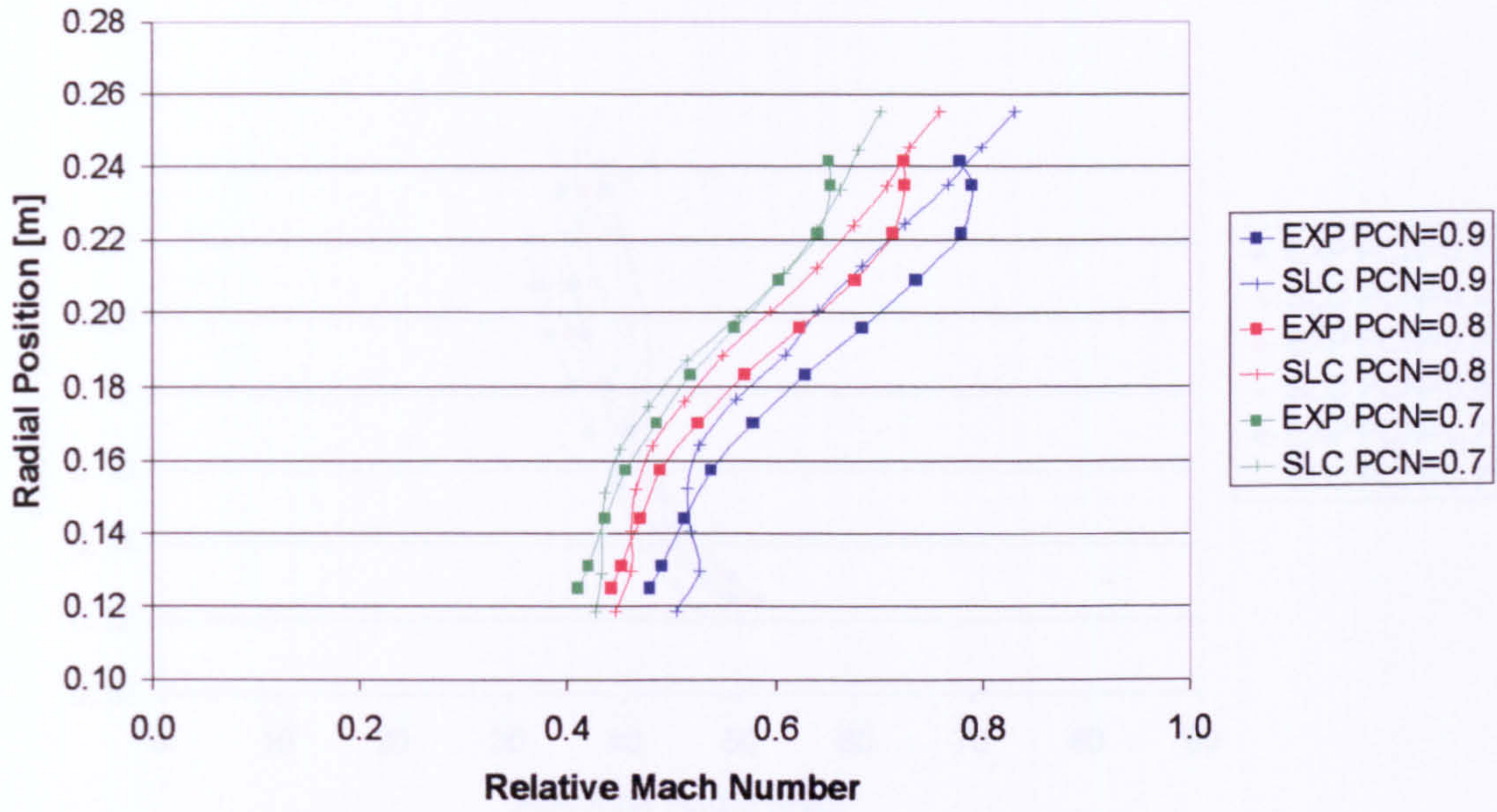


First Rotor Outlet Flow Field Properties Comparison

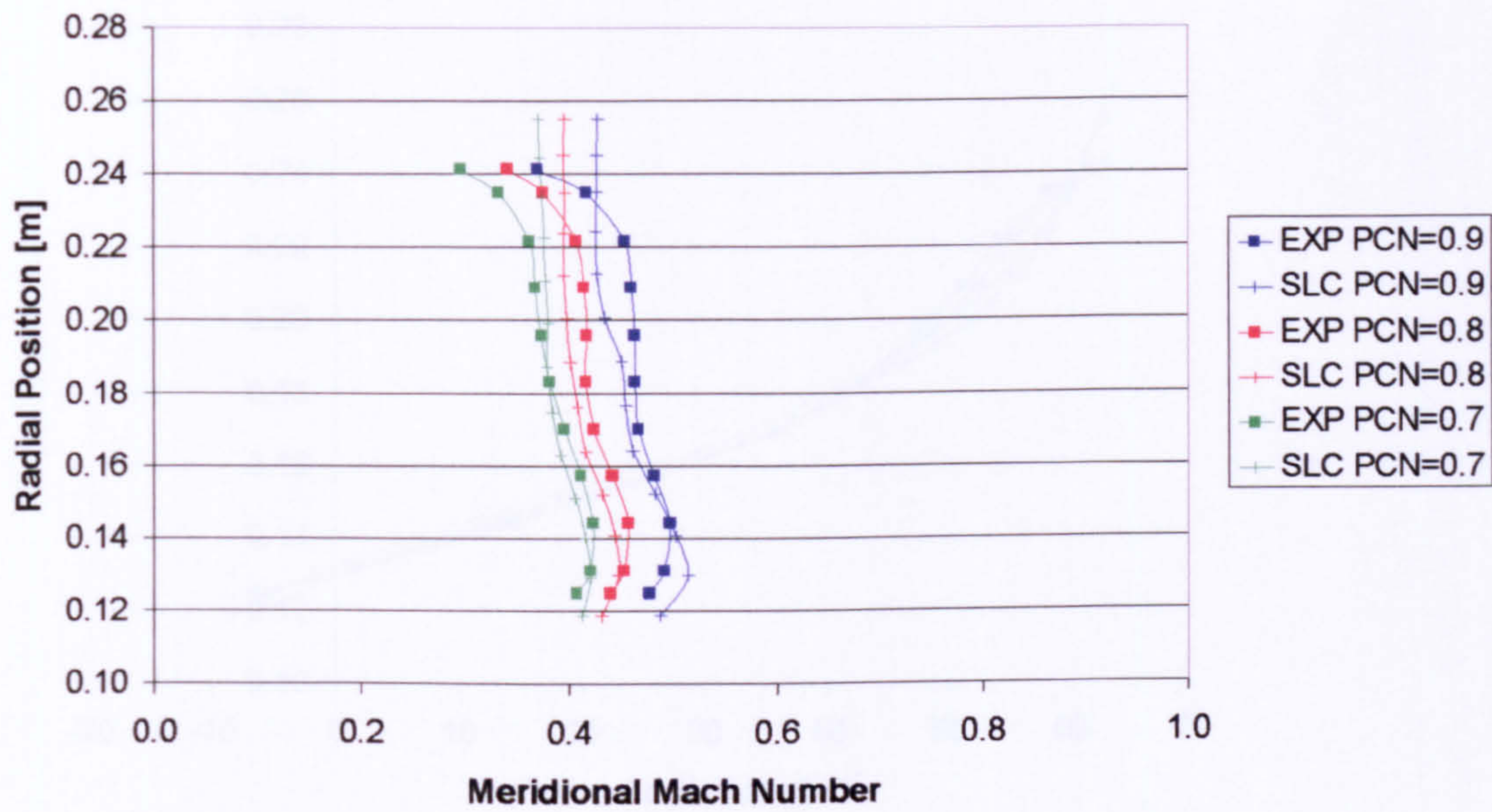




First Rotor Outlet Flow Field Properties Comparison

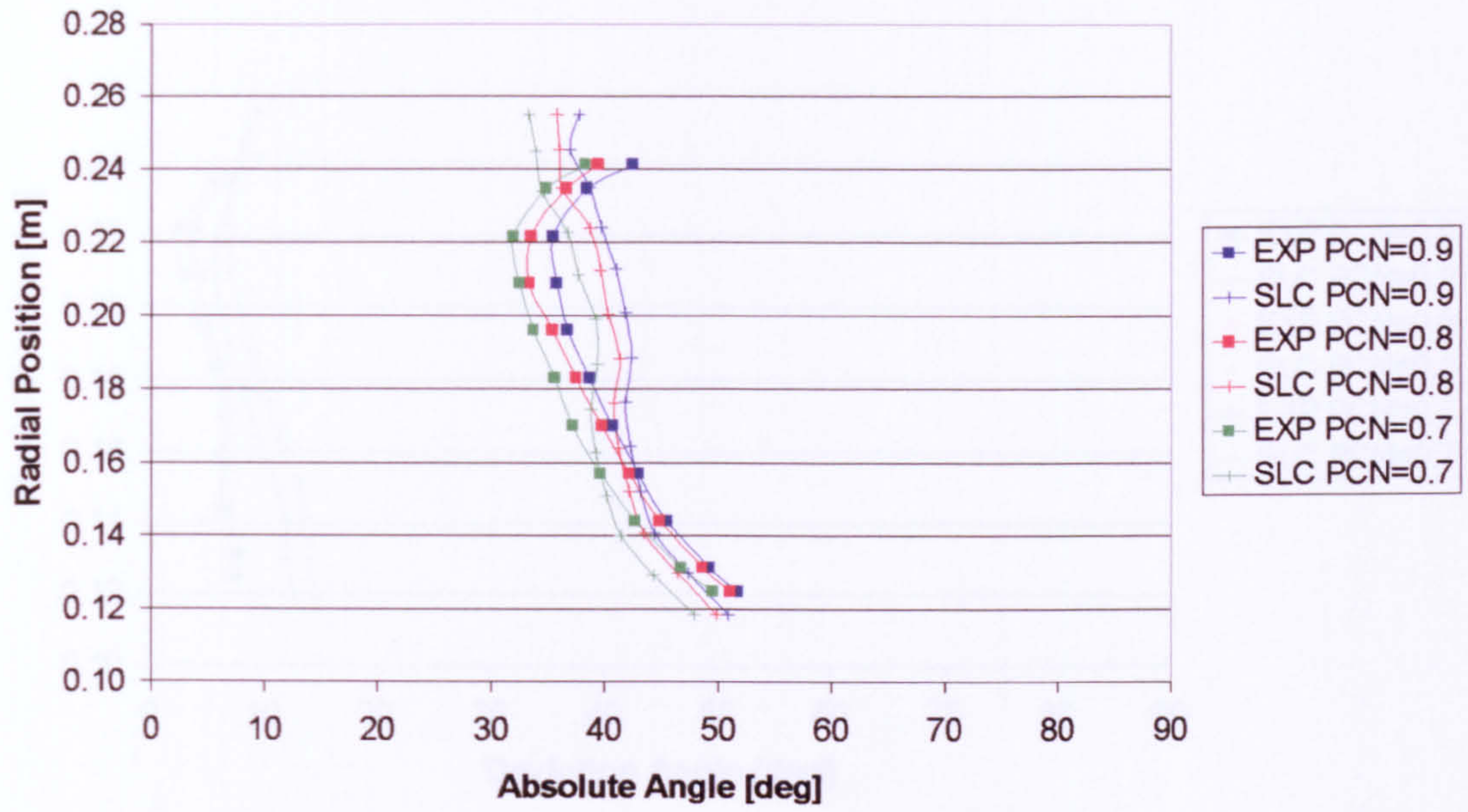


First Rotor Outlet Flow Field Properties Comparison

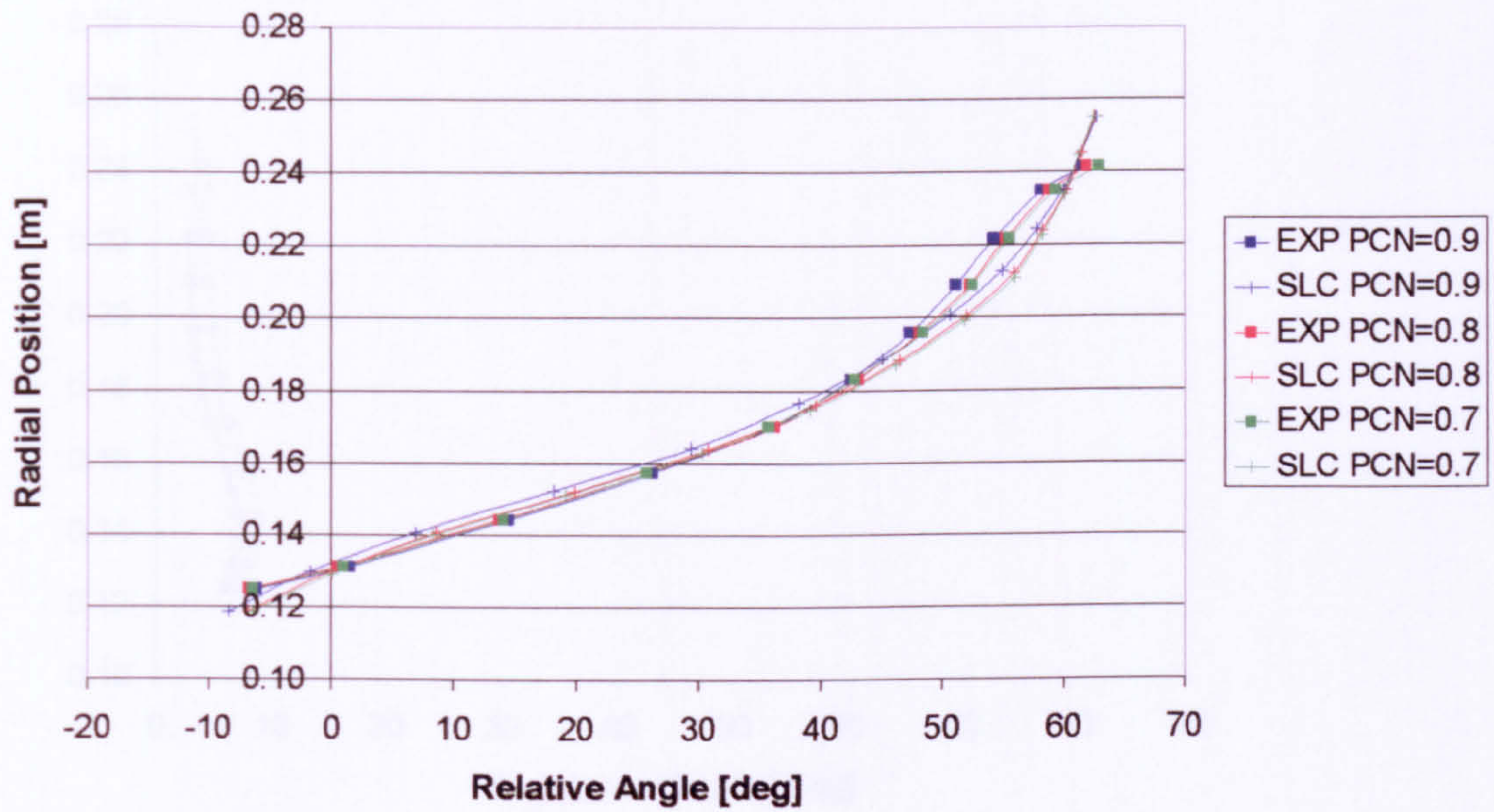




First Rotor Outlet Flow Field Properties Comparison

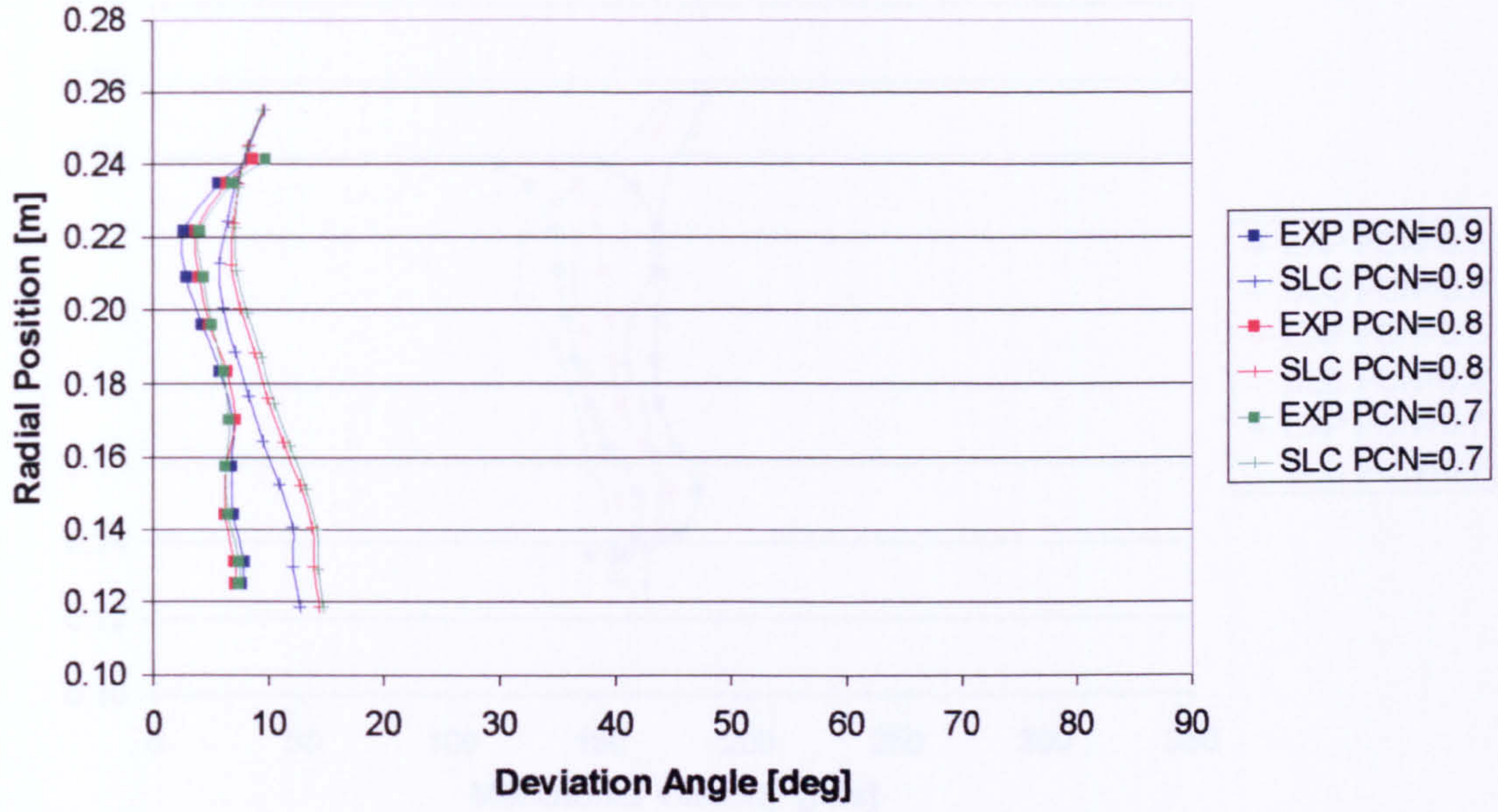


First Rotor Outlet Flow Field Properties Comparison

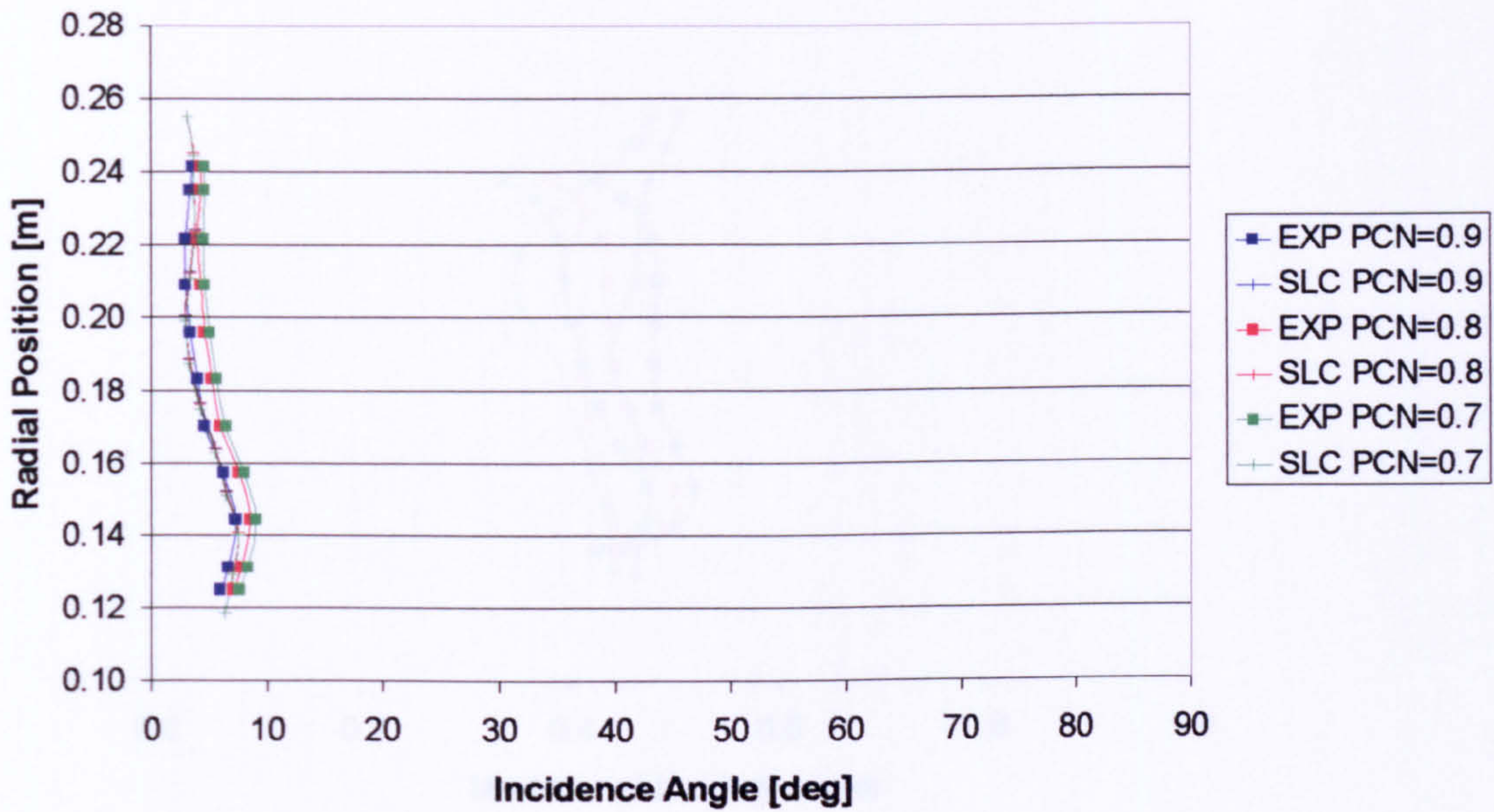




First Rotor Outlet Flow Field Properties Comparison

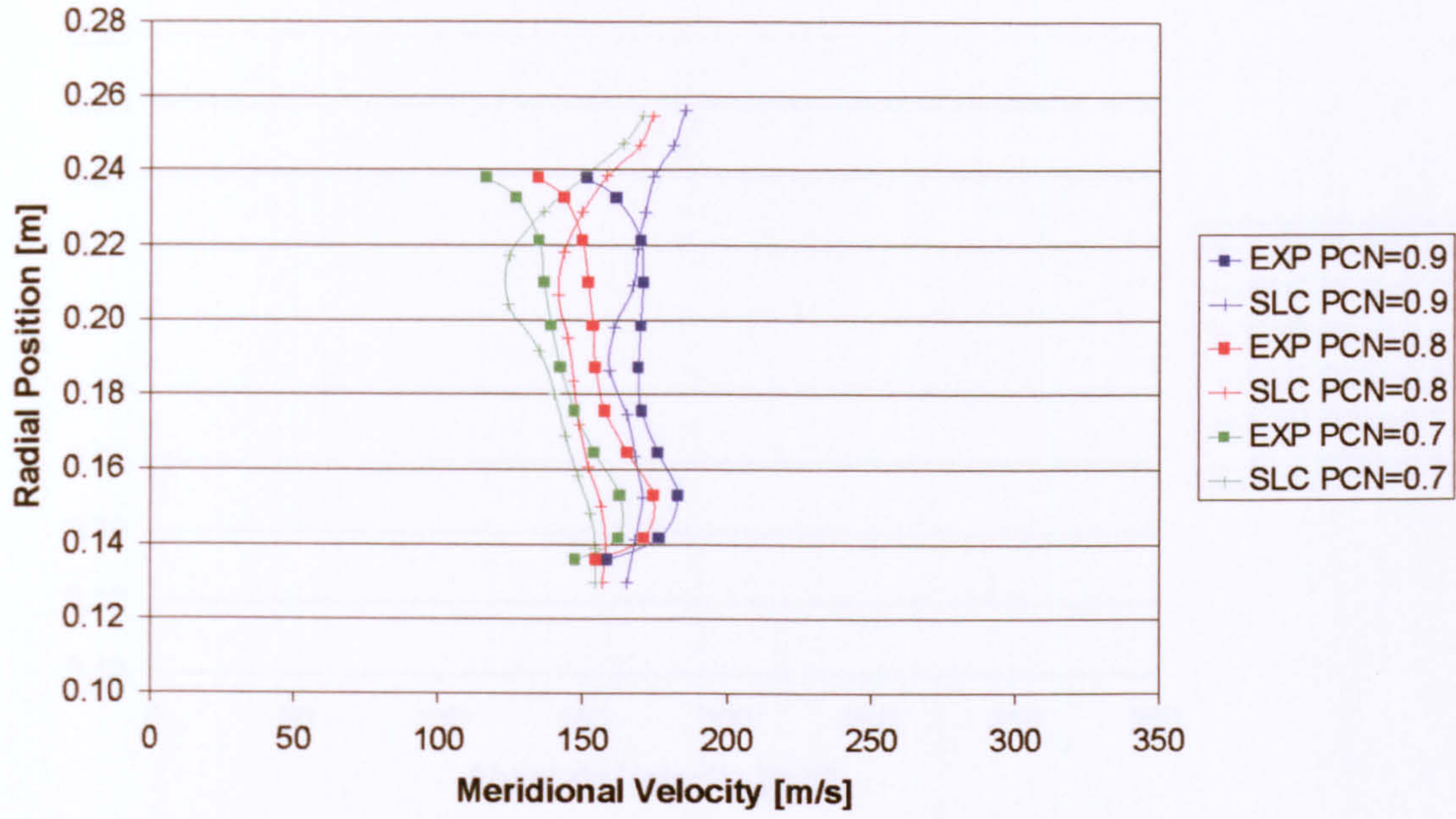


First Rotor Inlet Flow Field Properties Comparison

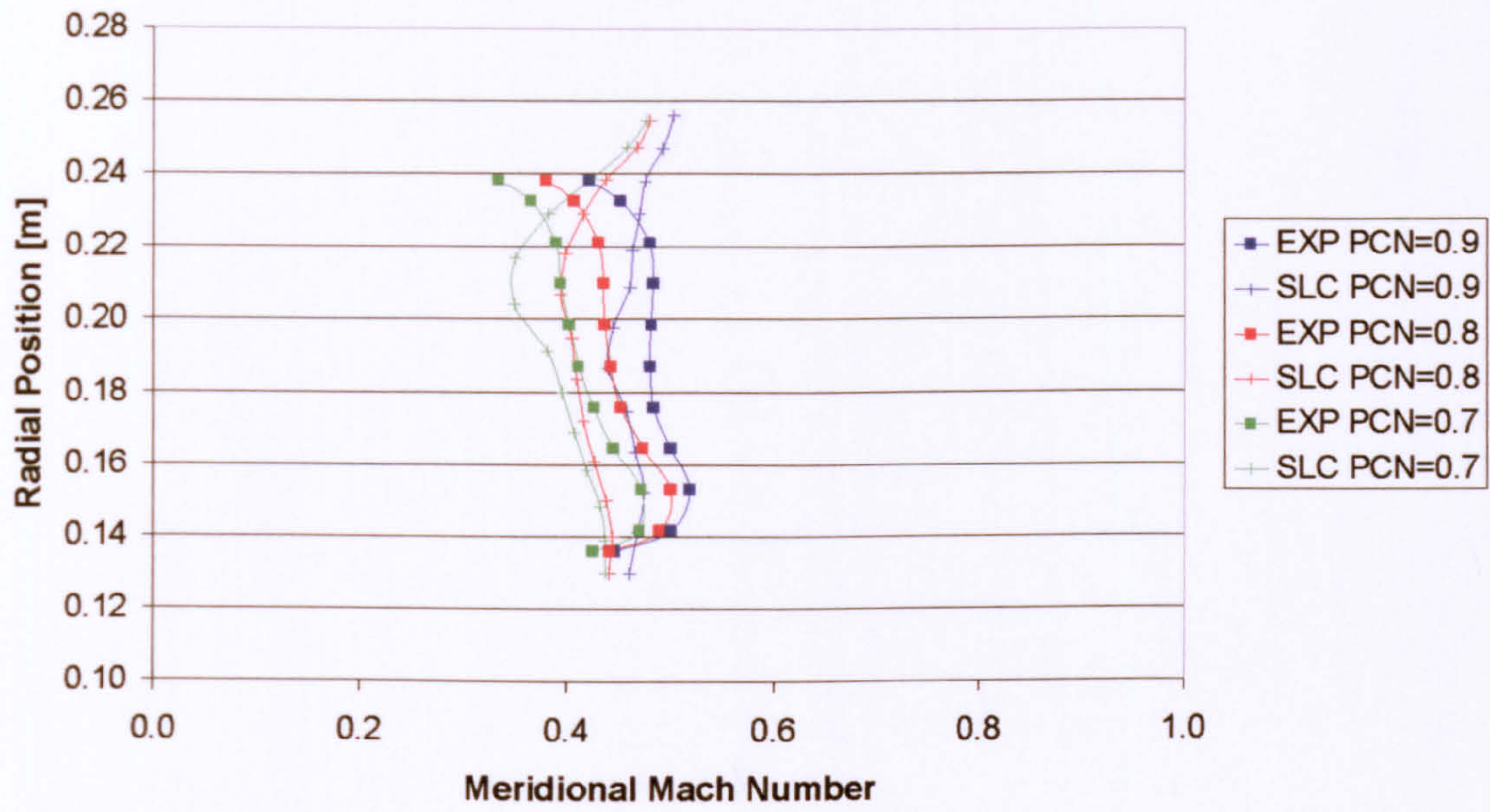




First Stator Outlet Flow Field Properties Comparison

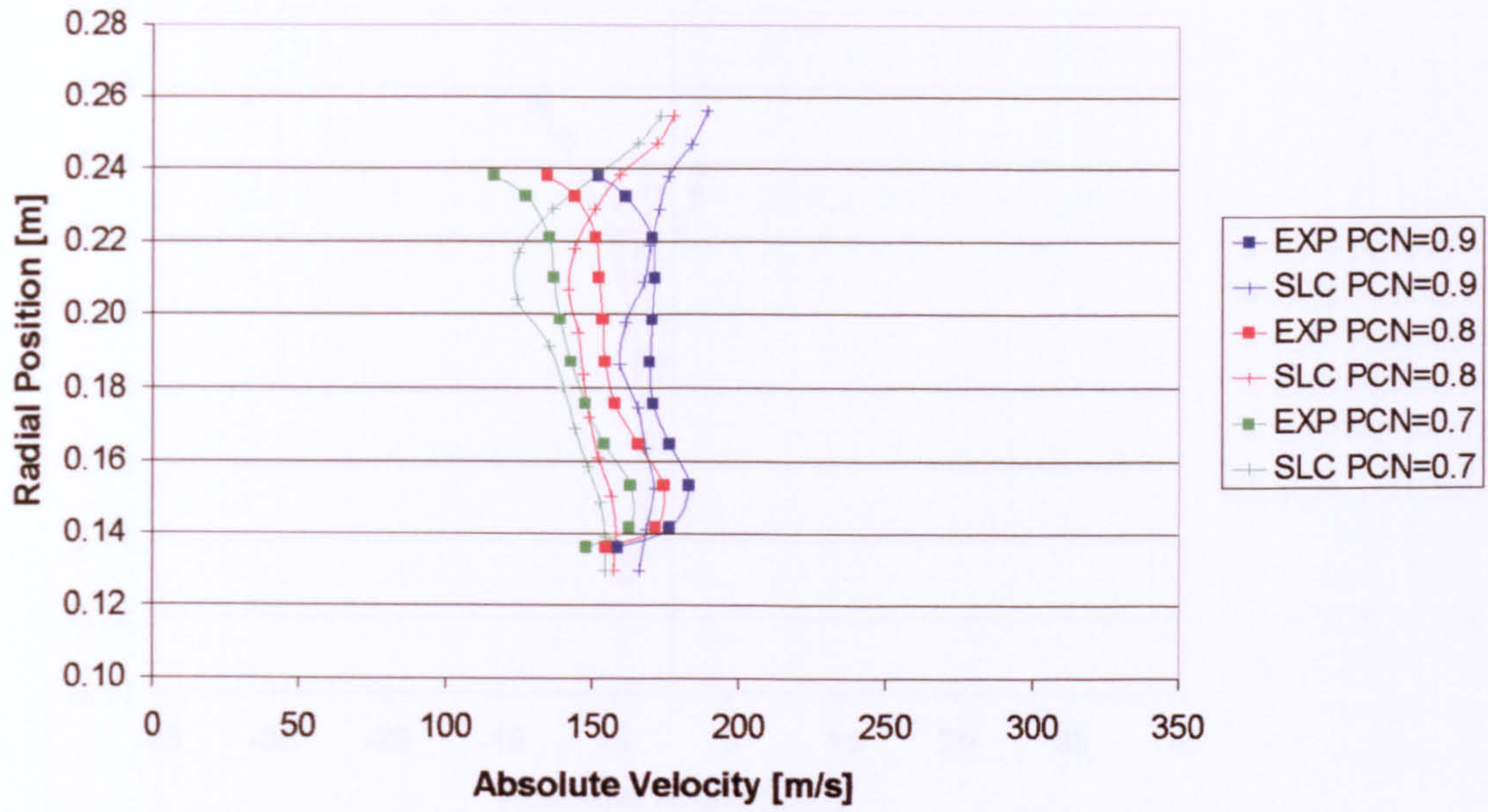


First Stator Outlet Flow Field Properties Comparison

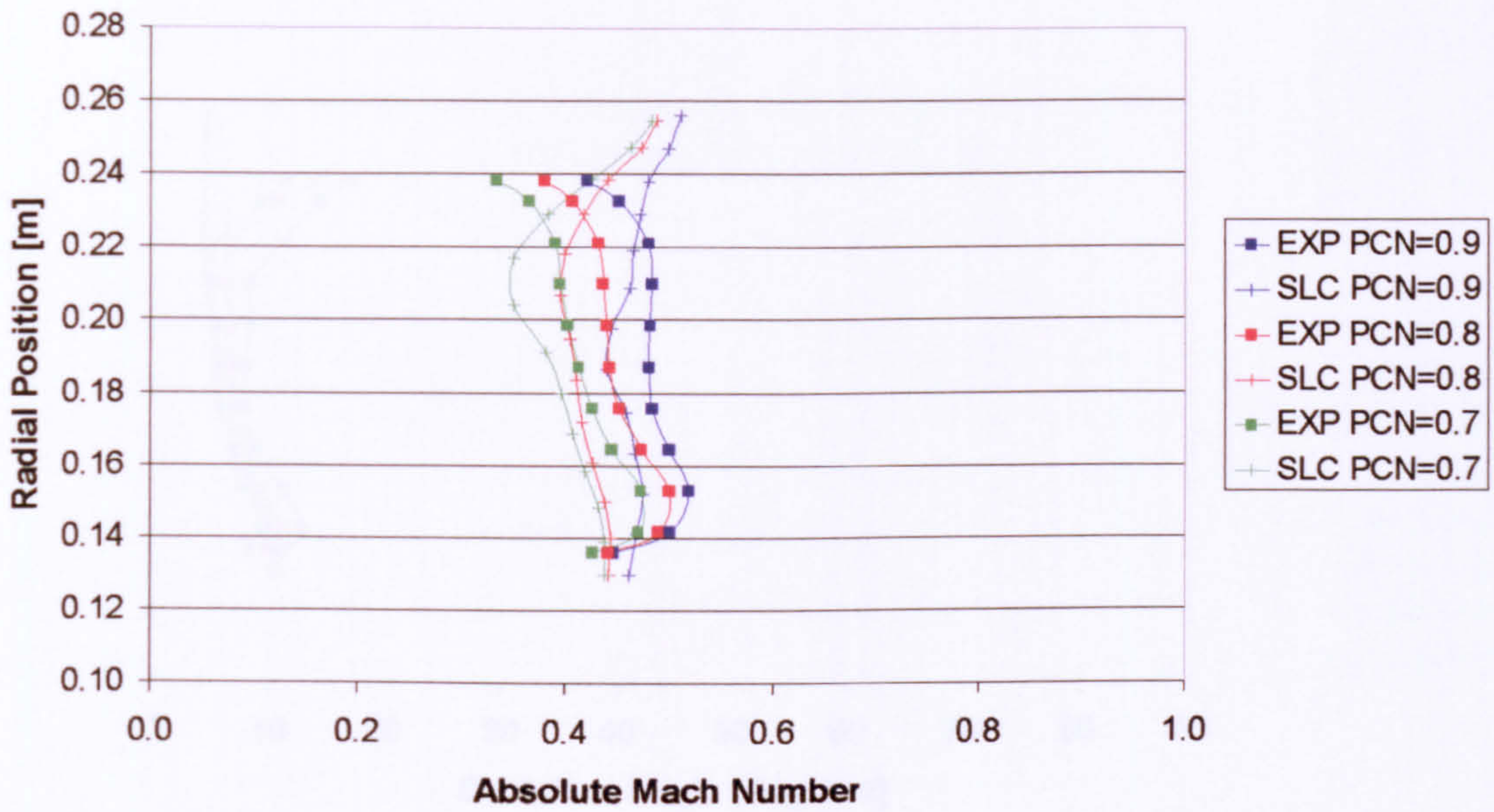




First Stator Outlet Flow Field Properties Comparison

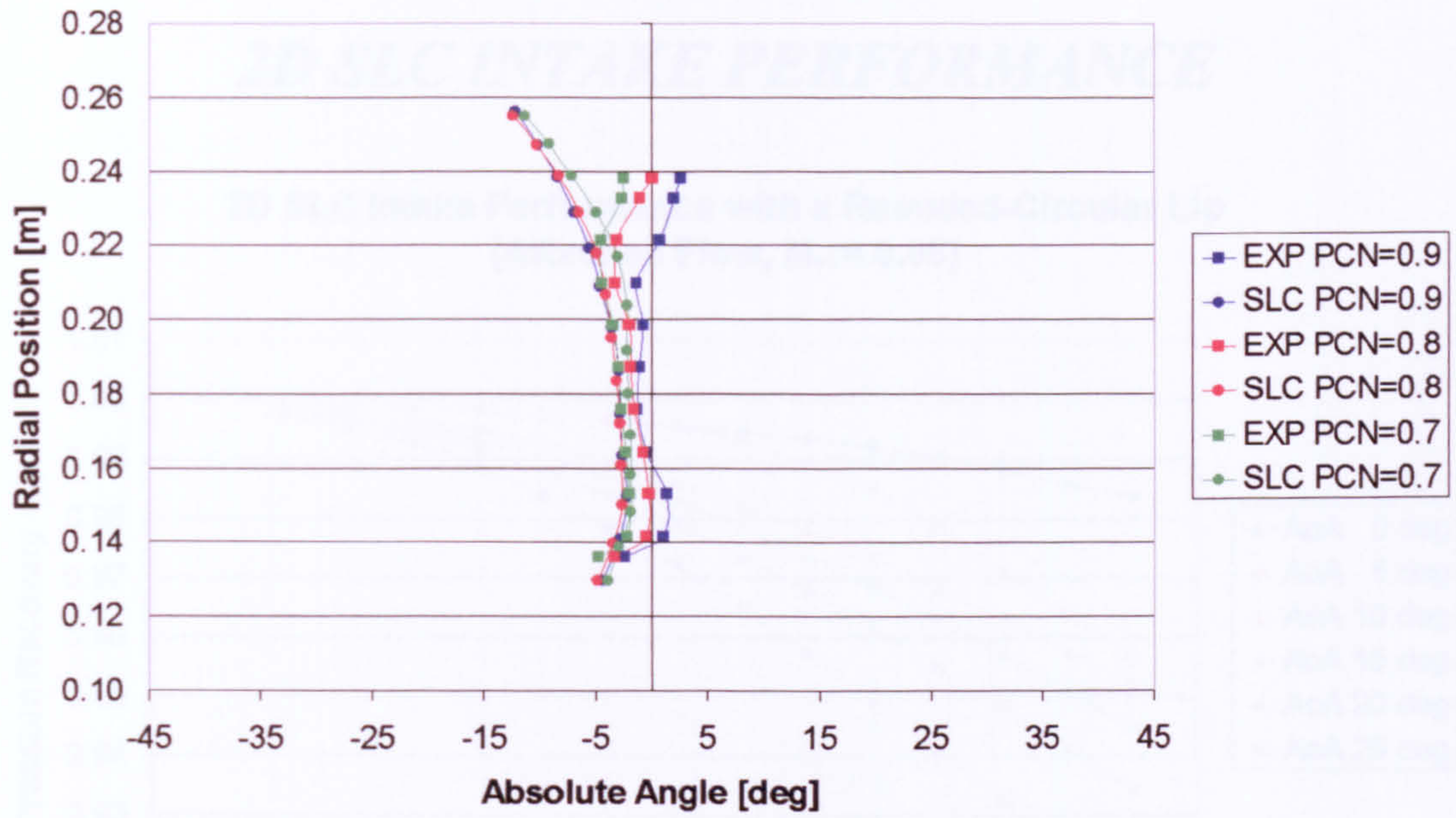


First Stator Outlet Flow Field Properties Comparison

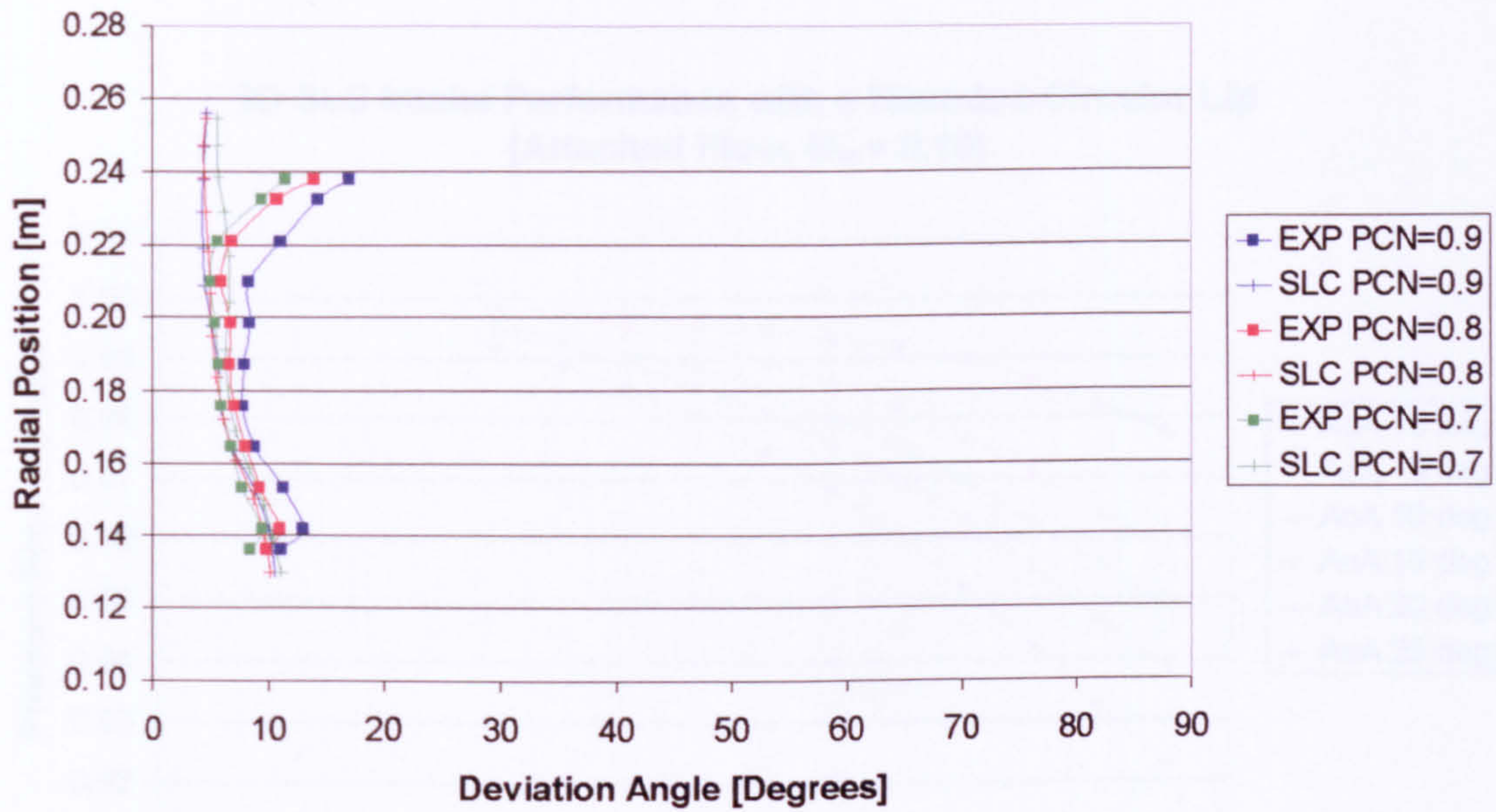




First Stator Outlet Flow Field Properties Comparison



First Stator Outlet Flow Field Properties Comparison

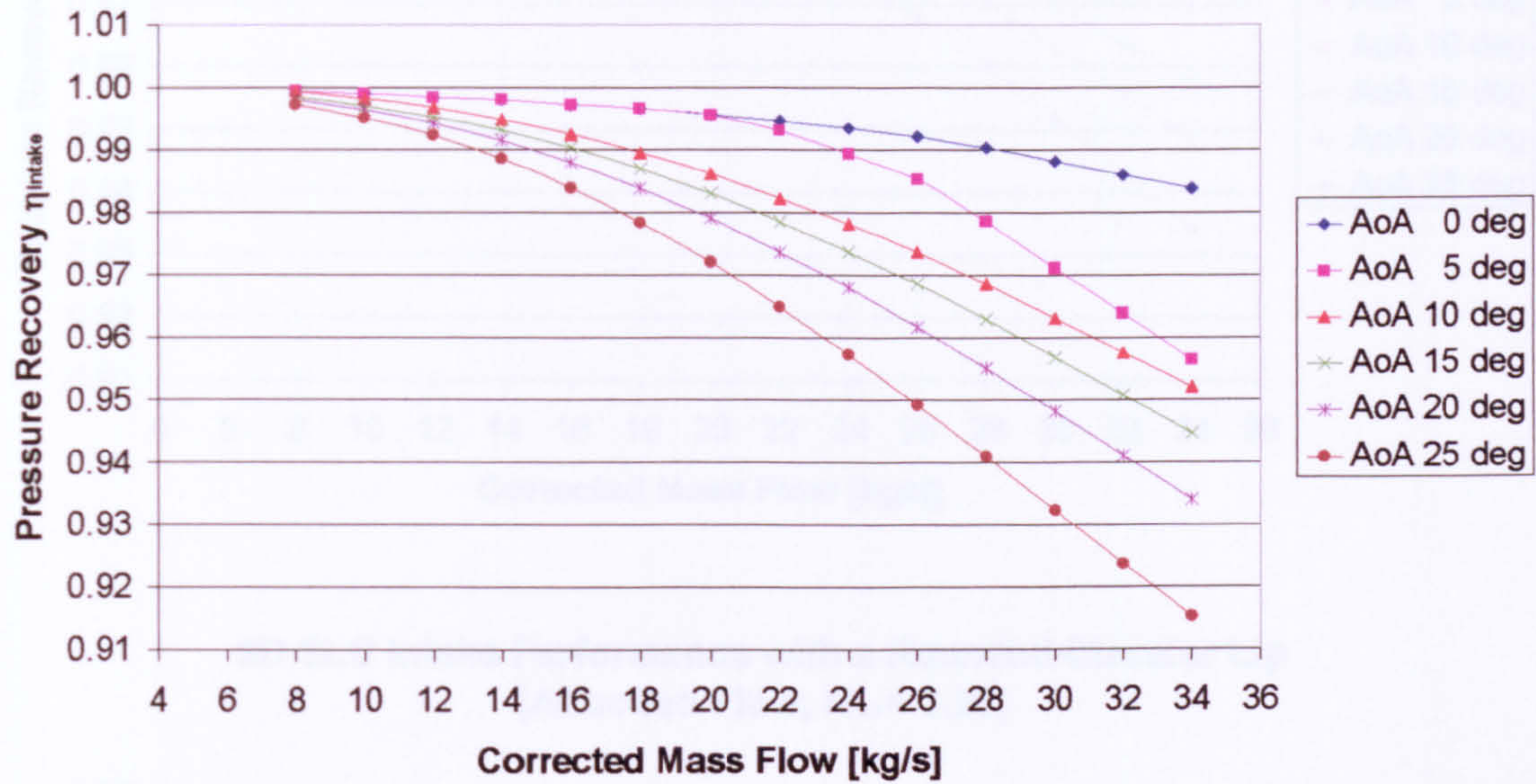




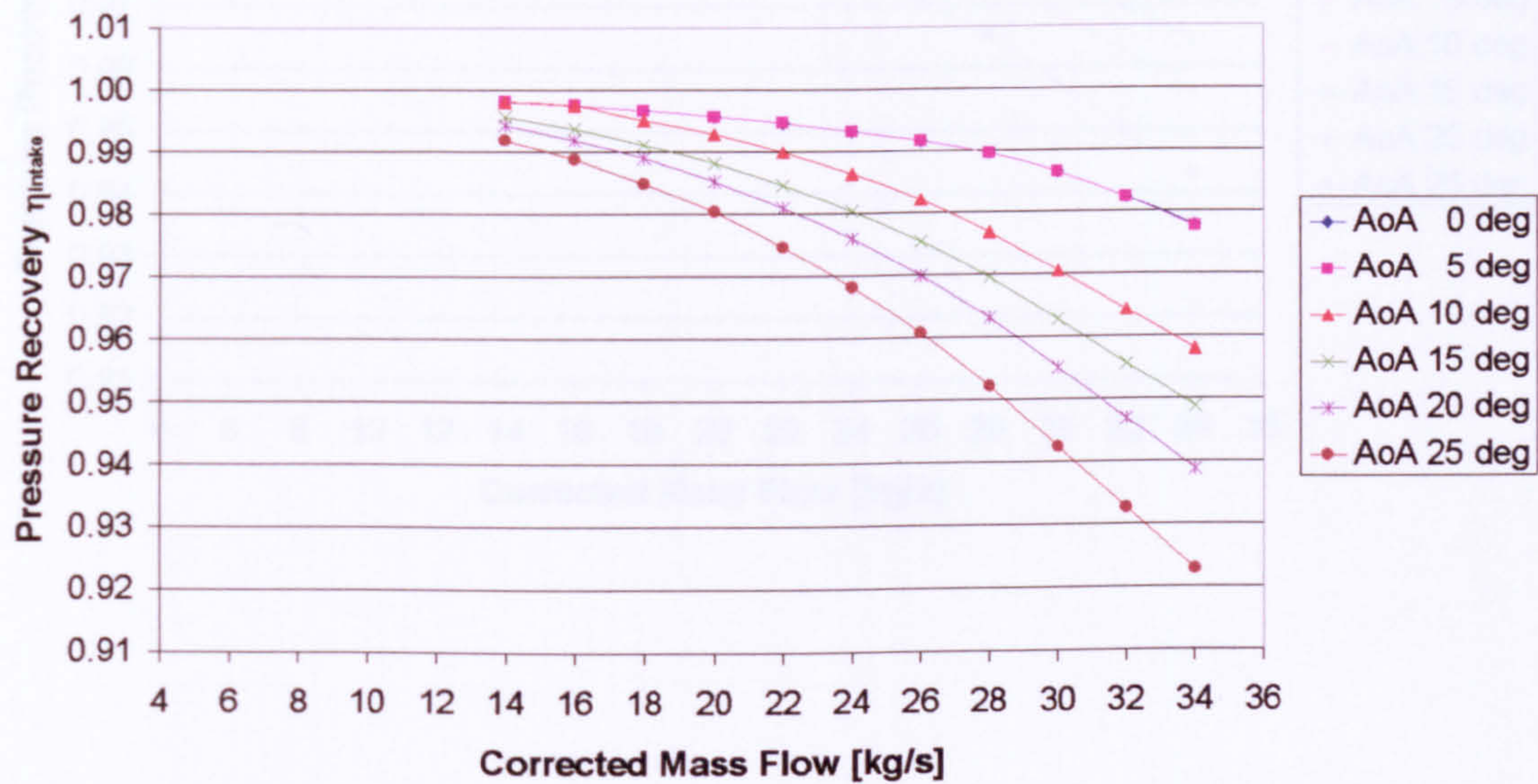
APPENDIX I

**2D SLC INTAKE PERFORMANCE**

**2D SLC Intake Performance with a Rounded-Circular Lip  
(Attached Flow,  $M_{\infty} = 0.05$ )**

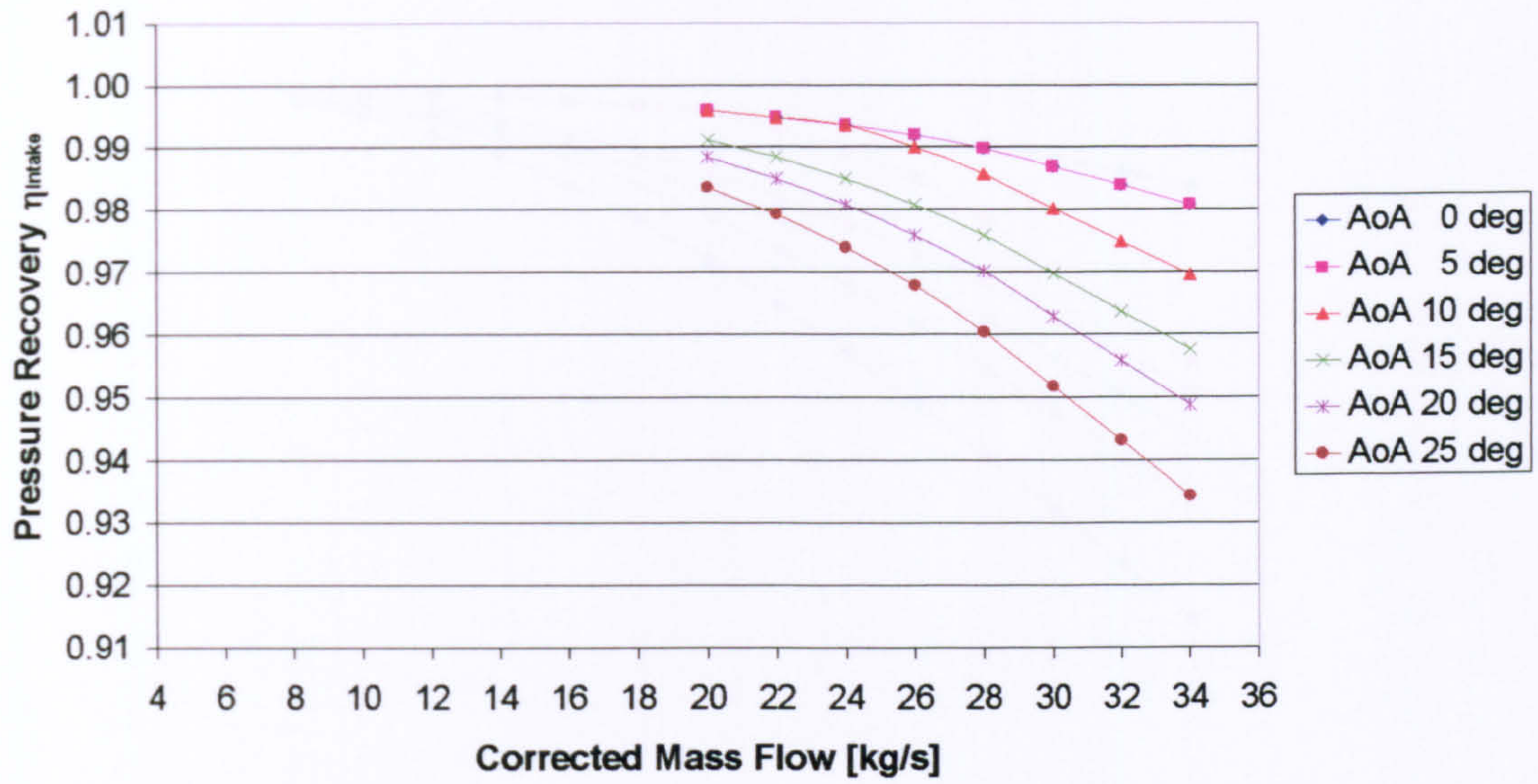


**2D SLC Intake Performance with a Rounded-Circular Lip  
(Attached Flow,  $M_{\infty} = 0.10$ )**

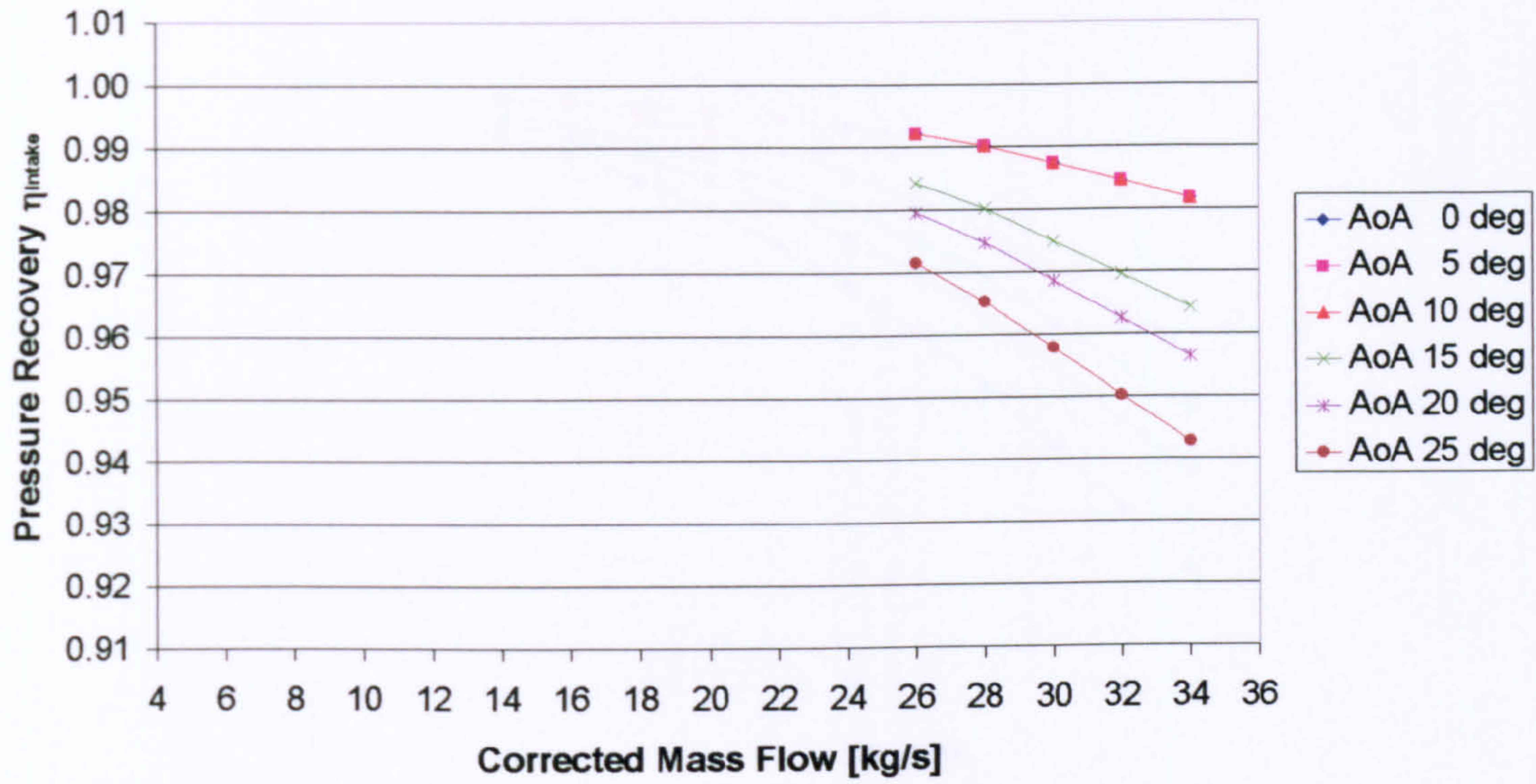




**2D SLC Intake Performance with a Rounded-Circular Lip  
(Attached Flow,  $M_{\infty} = 0.15$ )**

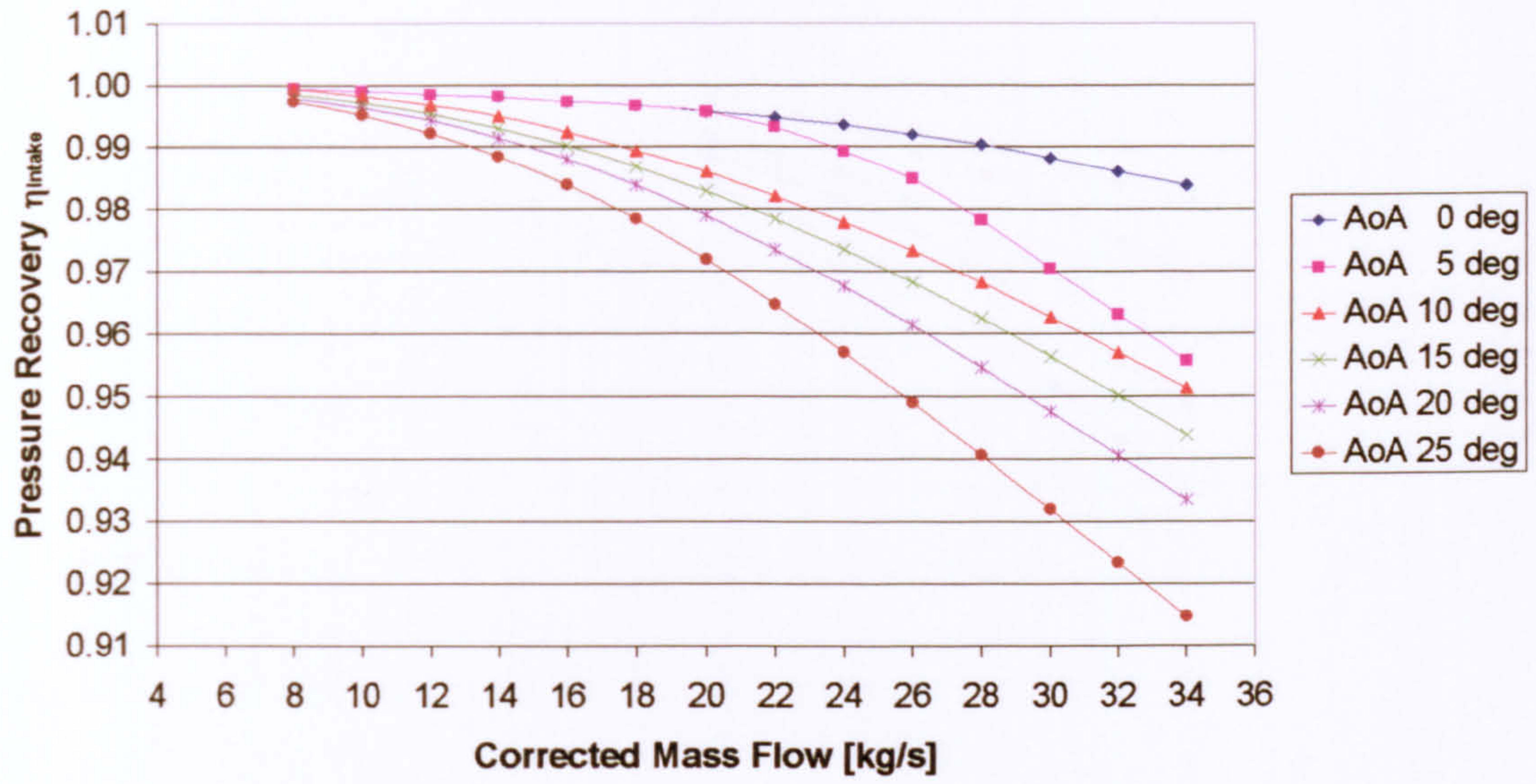


**2D SLC Intake Performance with a Rounded-Circular Lip  
(Attached Flow,  $M_{\infty} = 0.20$ )**

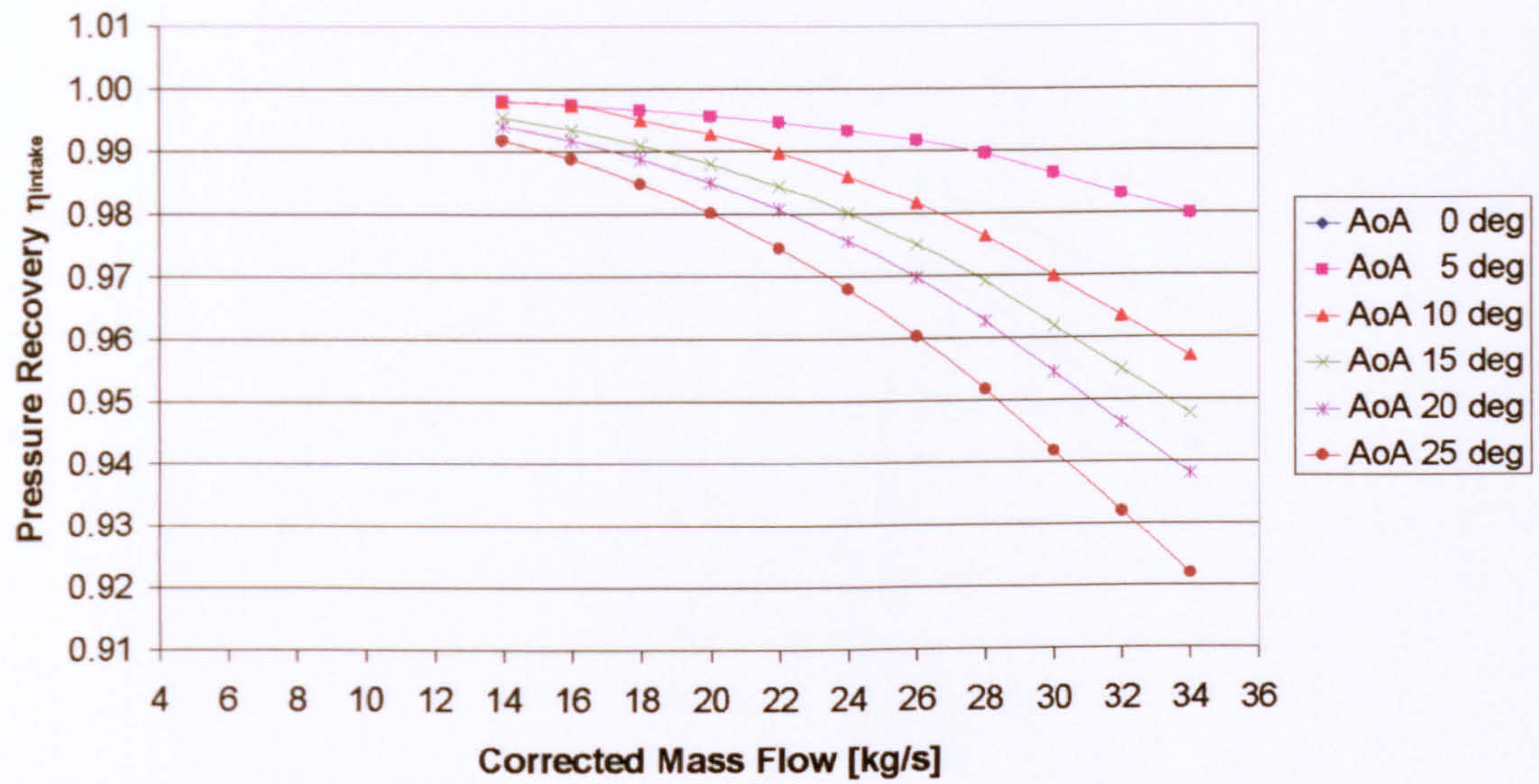




2D SLC Intake Performance with a Rounded-Circular Lip  
(Separated Flow,  $M_{\infty} = 0.05$ )

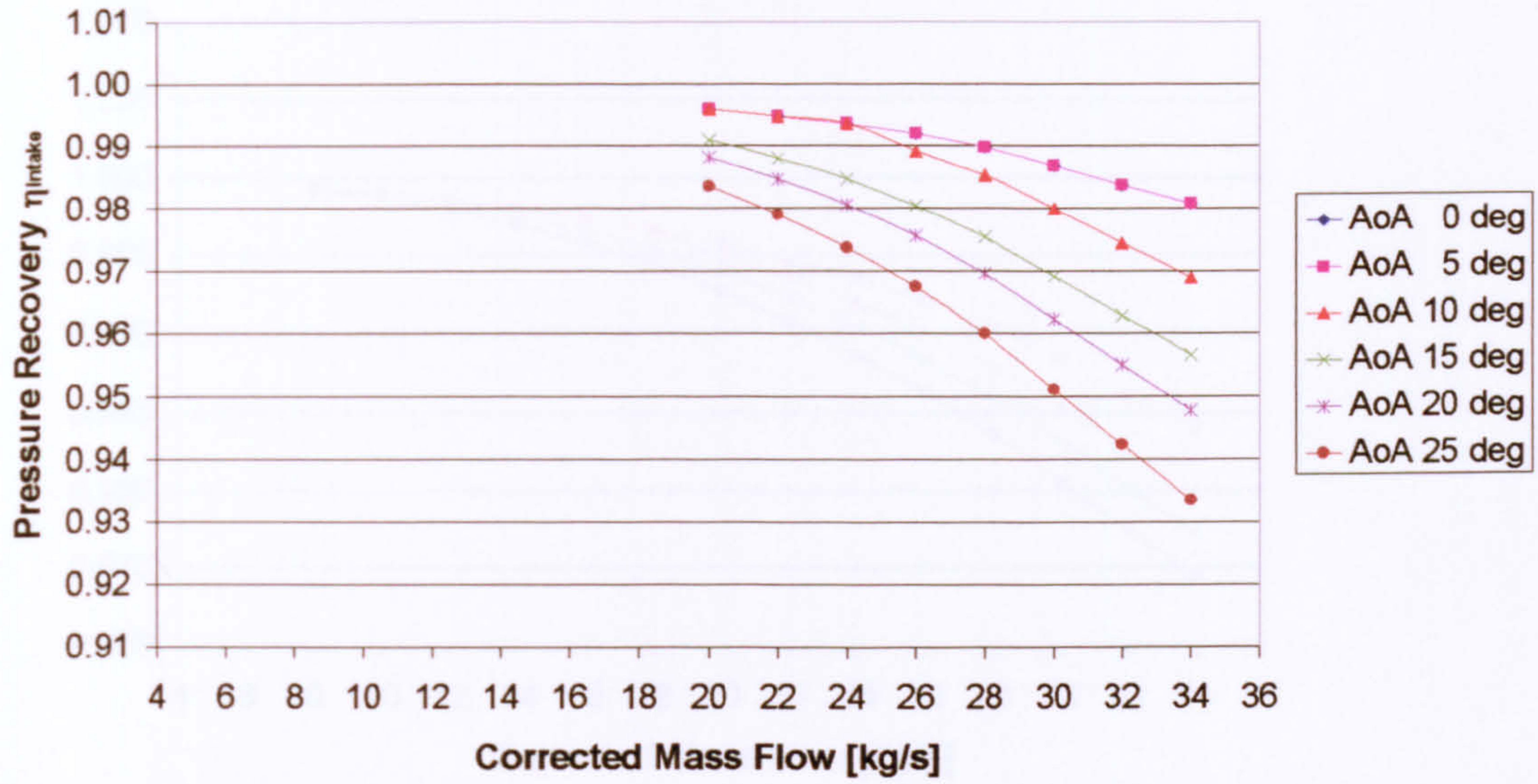


2D SLC Intake Performance with a Rounded-Circular Lip  
(Separated Flow,  $M_{\infty} = 0.10$ )

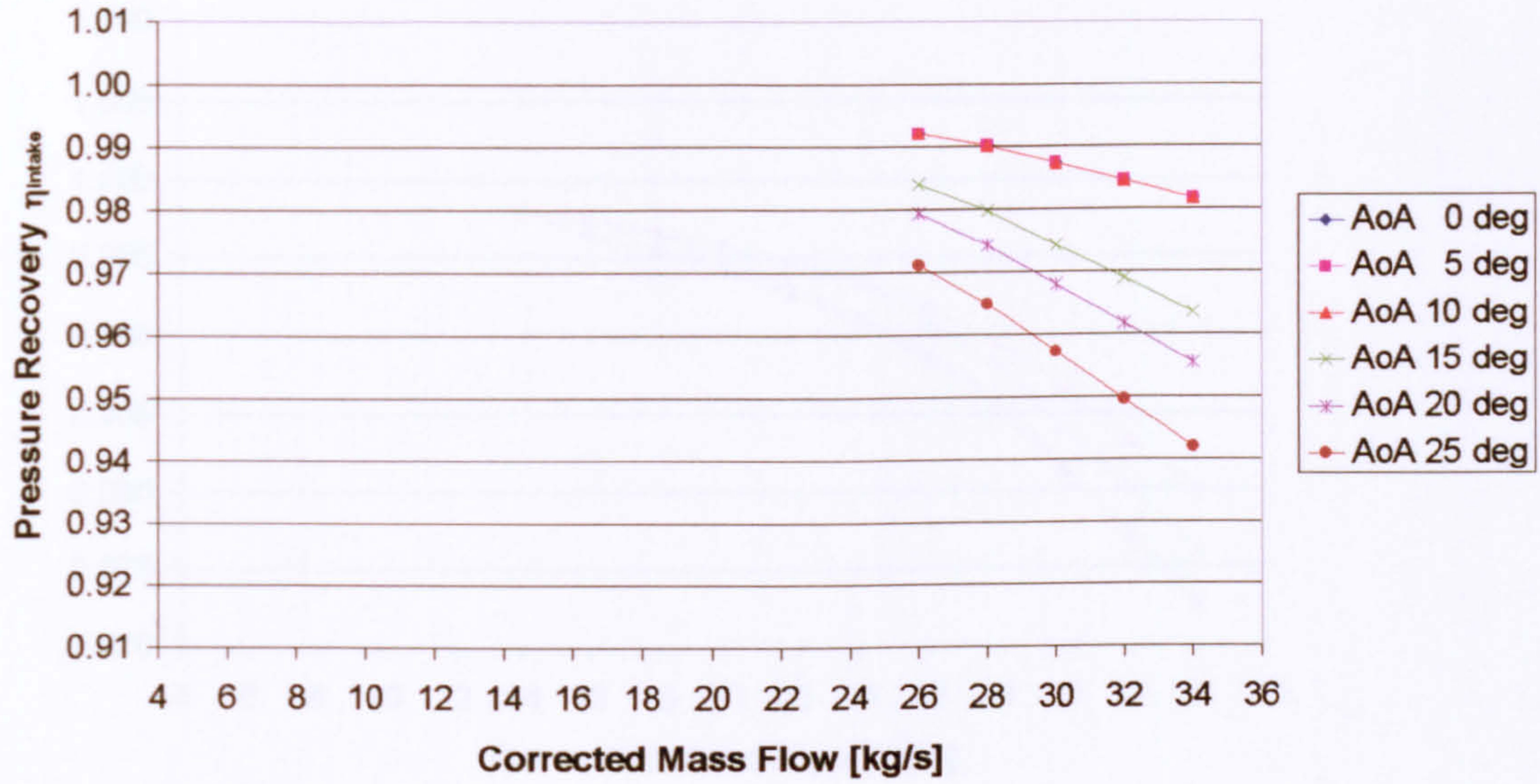




2D SLC Intake Performance with a Rounded-Circular Lip  
(Separated Flow,  $M_{oo} = 0.15$ )

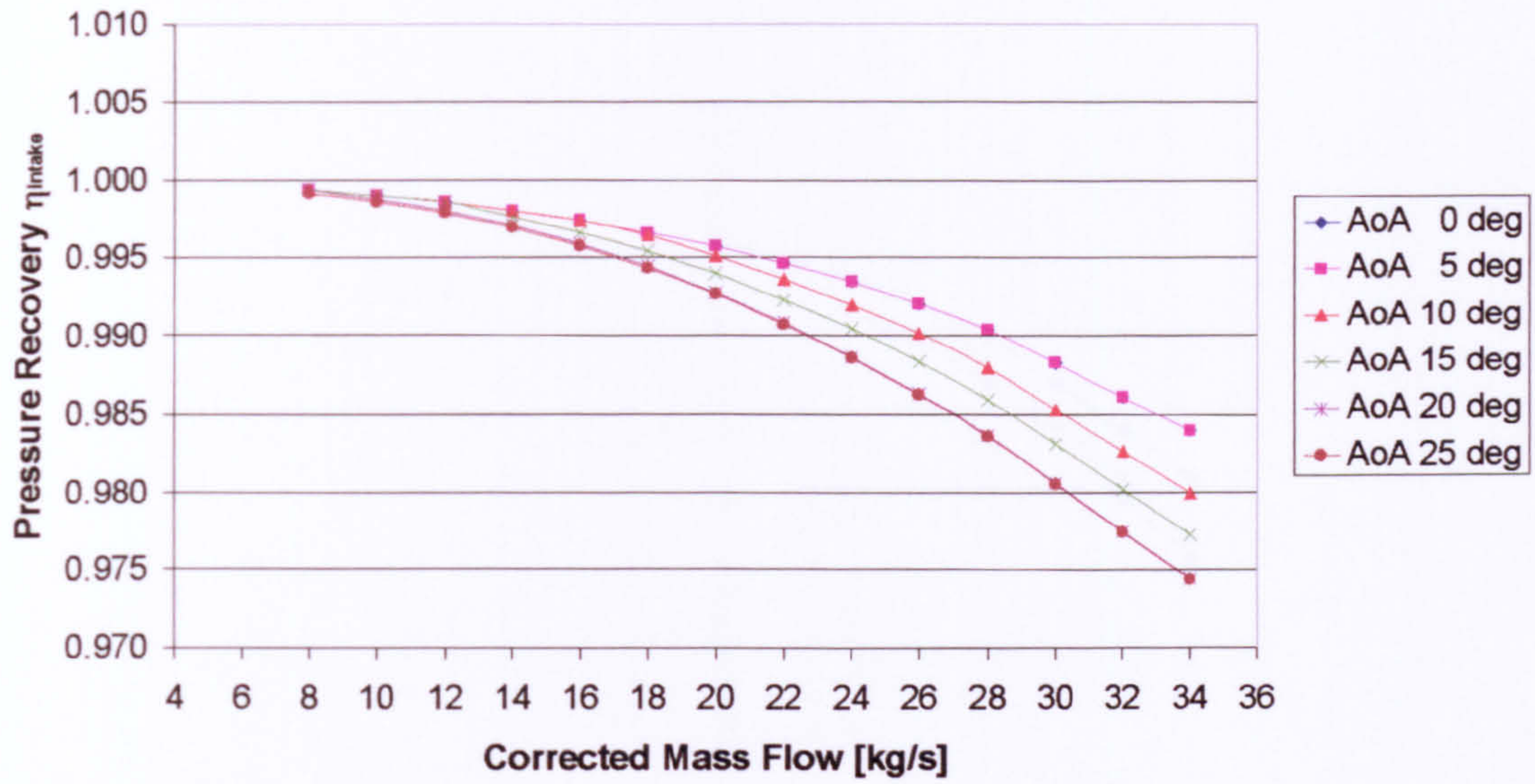


2D SLC Intake Performance with a Rounded-Circular Lip  
(Separated Flow,  $M_{oo} = 0.20$ )

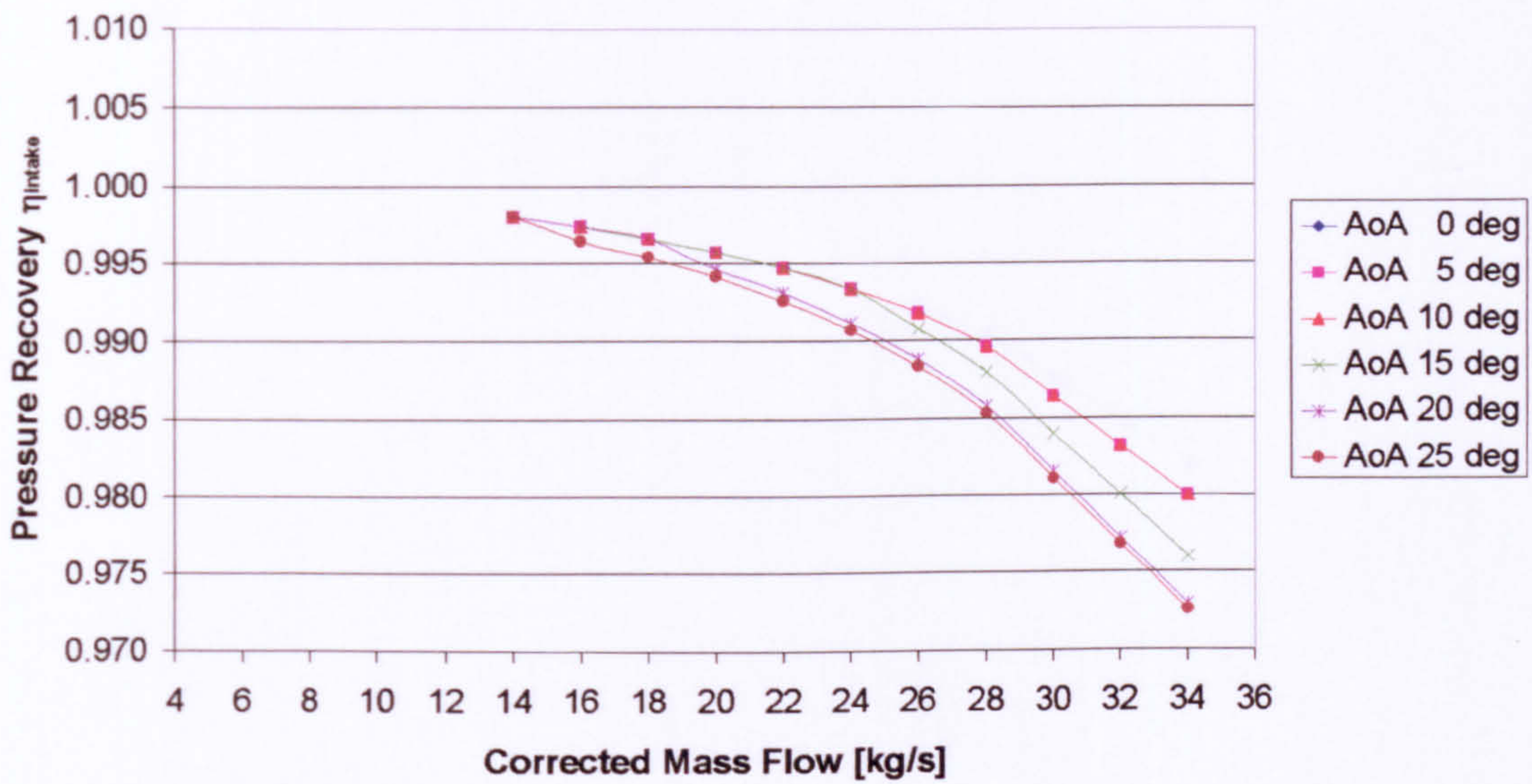




2D SLC Intake Performance with a Rounded-Elliptical Lip  
(Attached Flow,  $M_{\infty} = 0.05$ )

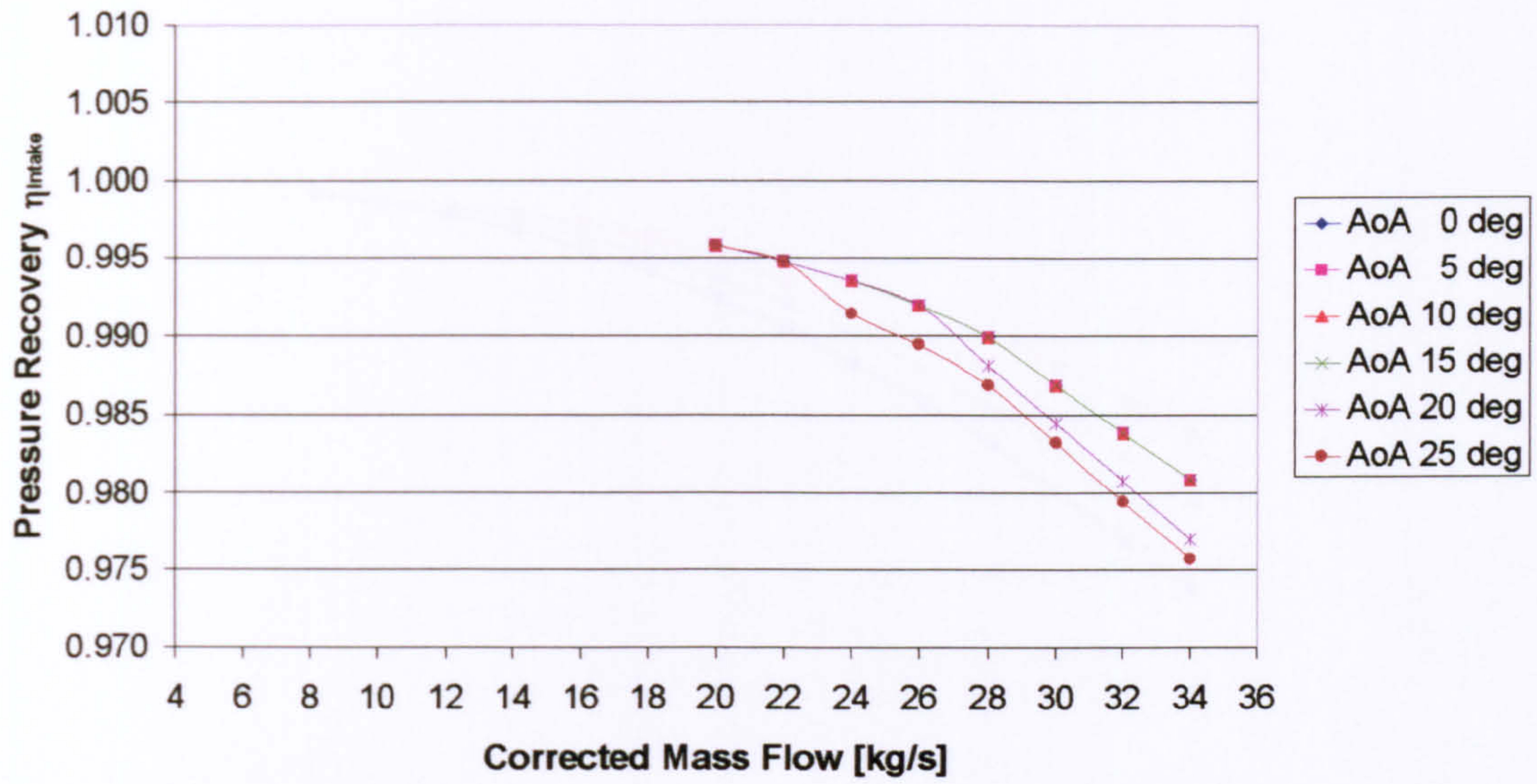


2D SLC Intake Performance with a Rounded-Elliptical Lip  
(Attached Flow,  $M_{\infty} = 0.10$ )

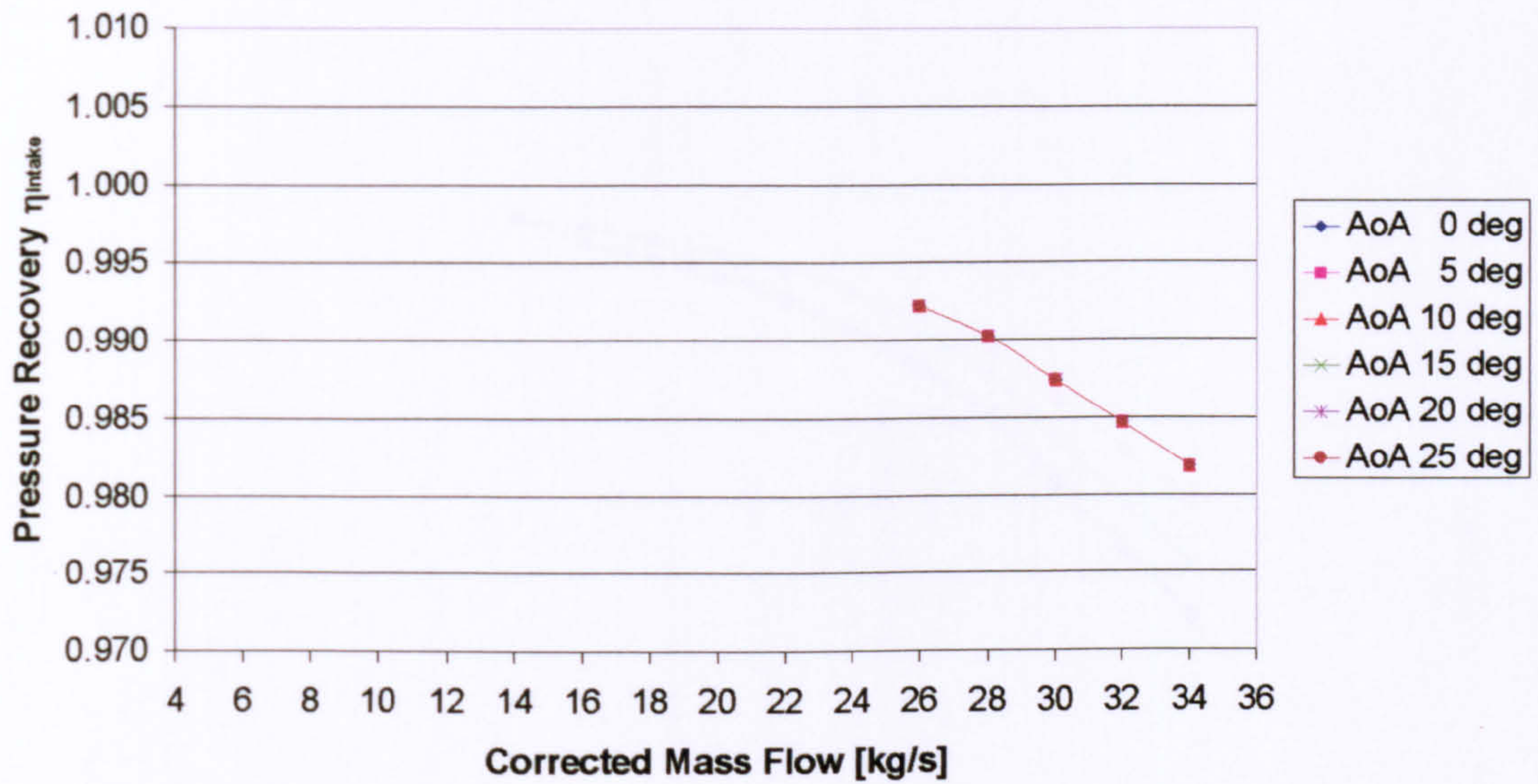




2D SLC Intake Performance with a Rounded-Elliptical Lip  
(Attached Flow,  $M_{\infty} = 0.15$ )

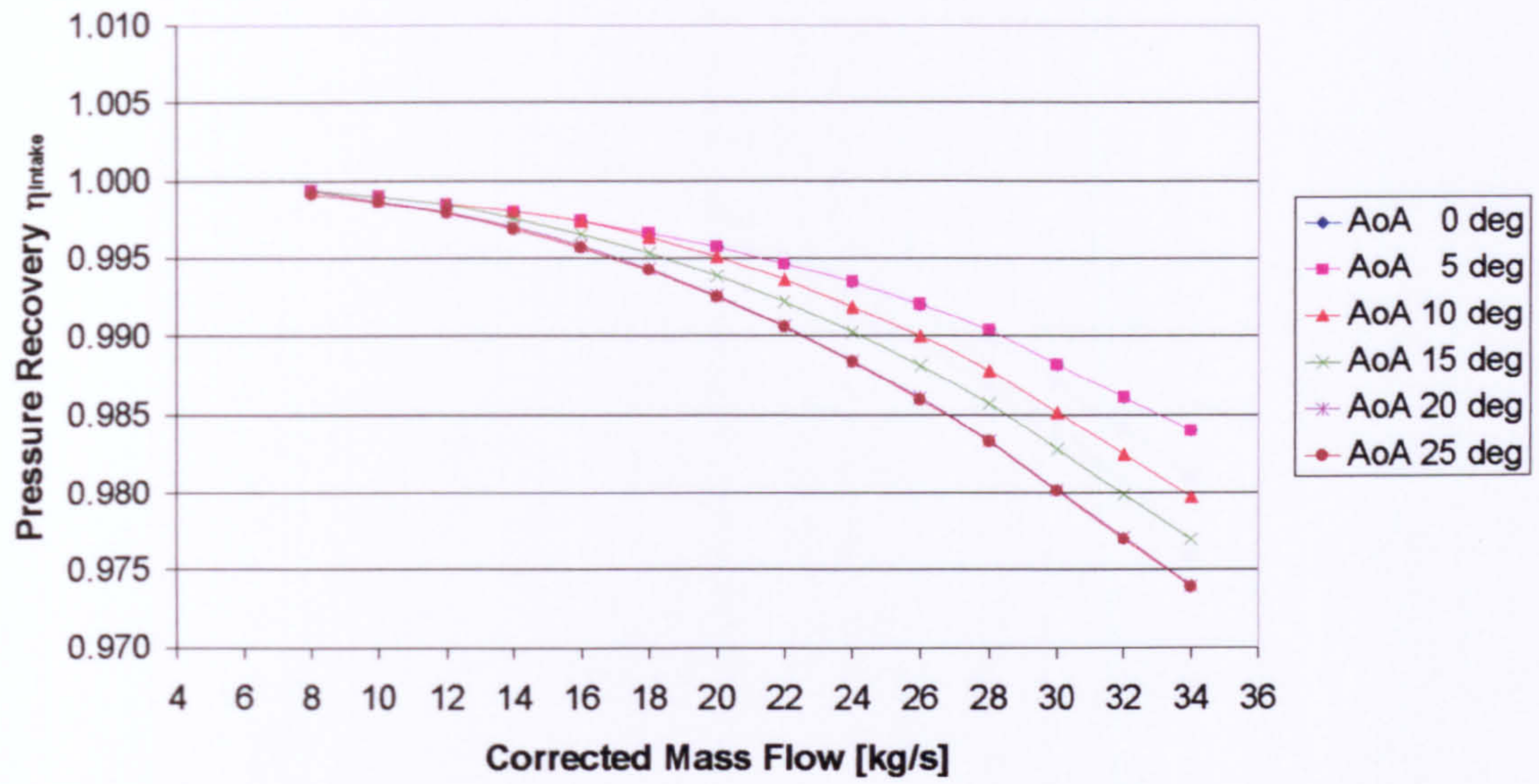


2D SLC Intake Performance with a Rounded-Elliptical Lip  
(Attached Flow,  $M_{\infty} = 0.20$ )

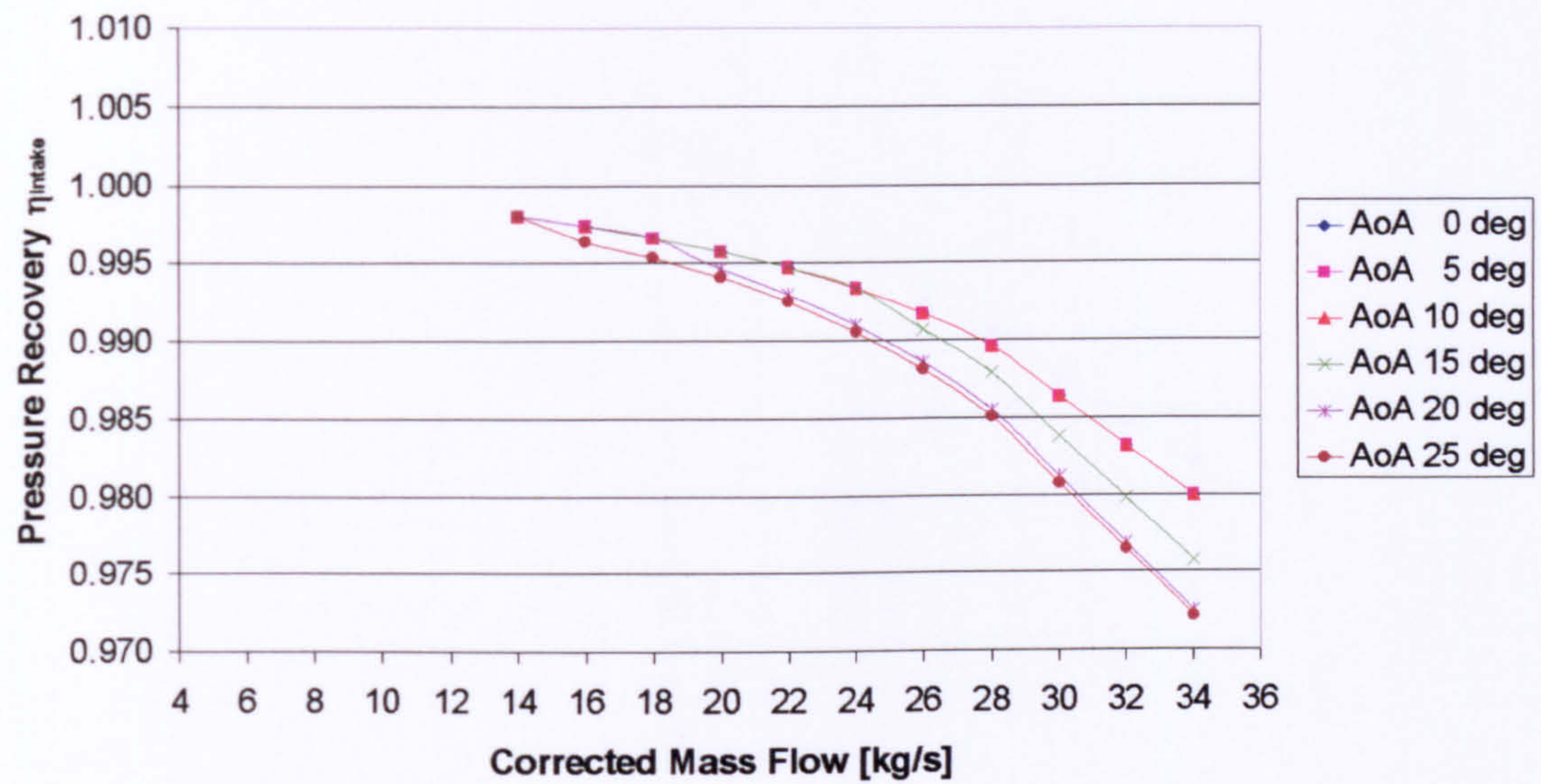




2D SLC Intake Performance with a Rounded-Elliptical Lip  
(Separated Flow,  $M_{\infty} = 0.05$ )

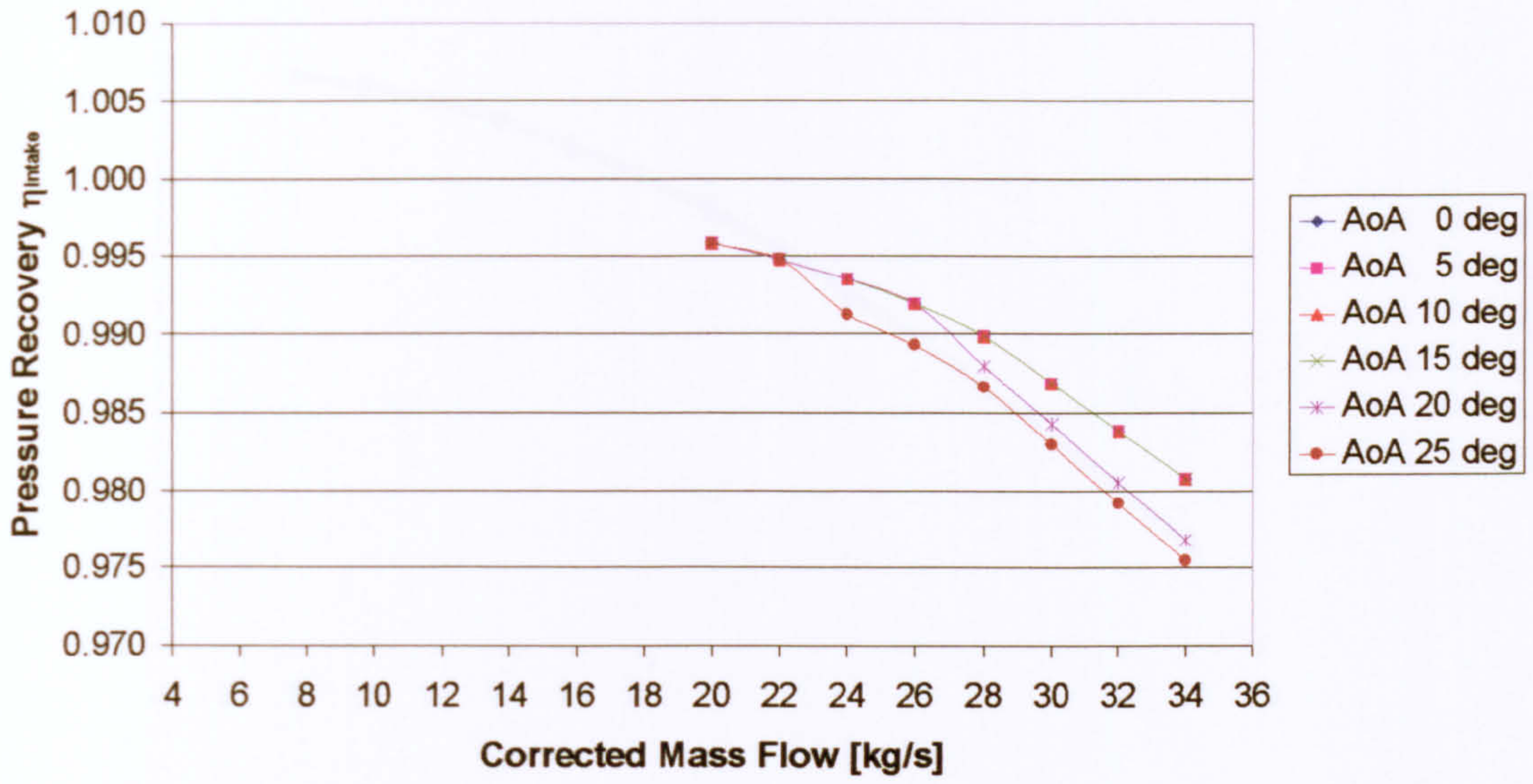


2D SLC Intake Performance with a Rounded-Elliptical Lip  
(Separated Flow,  $M_{\infty} = 0.10$ )

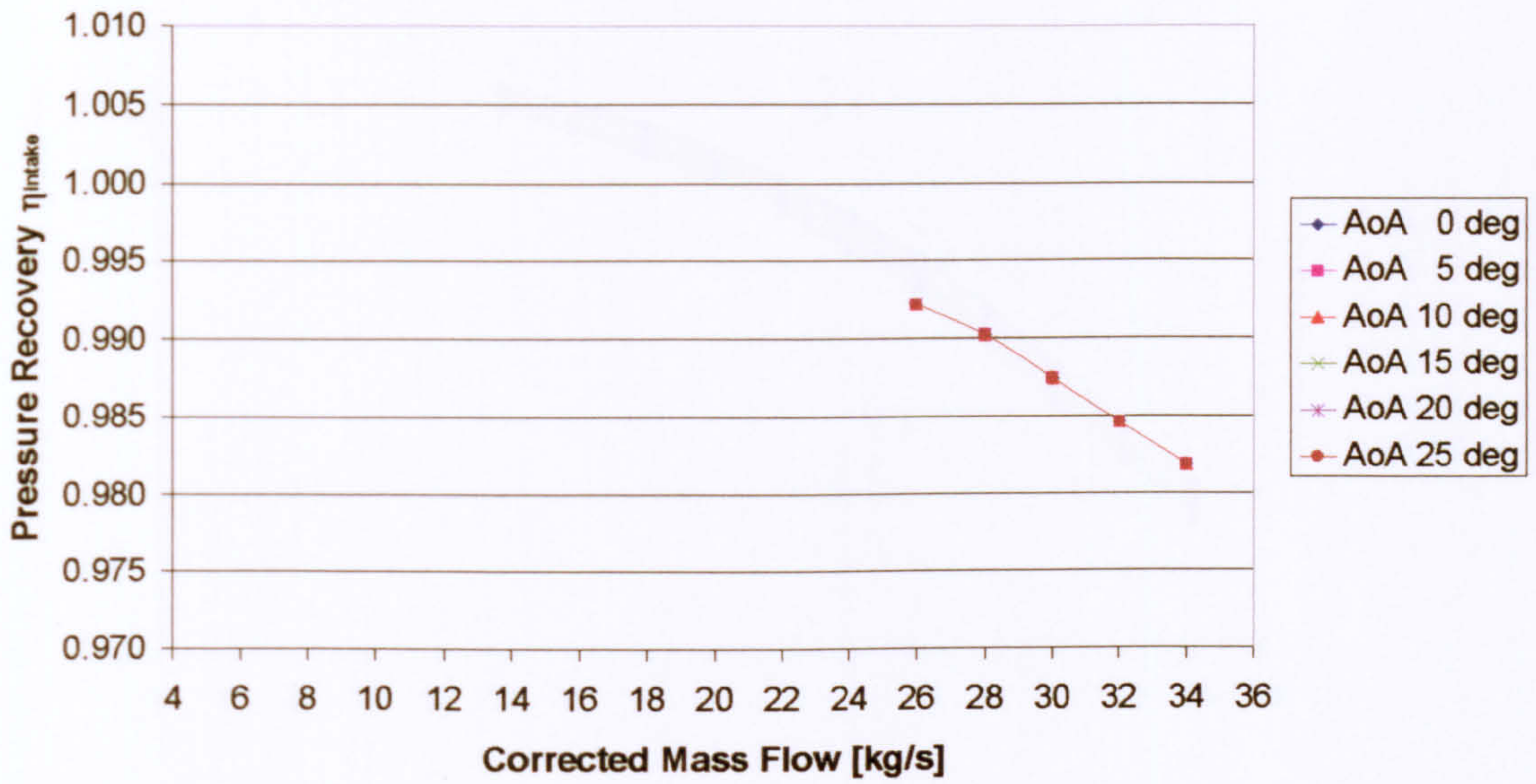




2D SLC Intake Performance with a Rounded-Elliptical Lip  
(Separated Flow,  $M_{\infty} = 0.15$ )

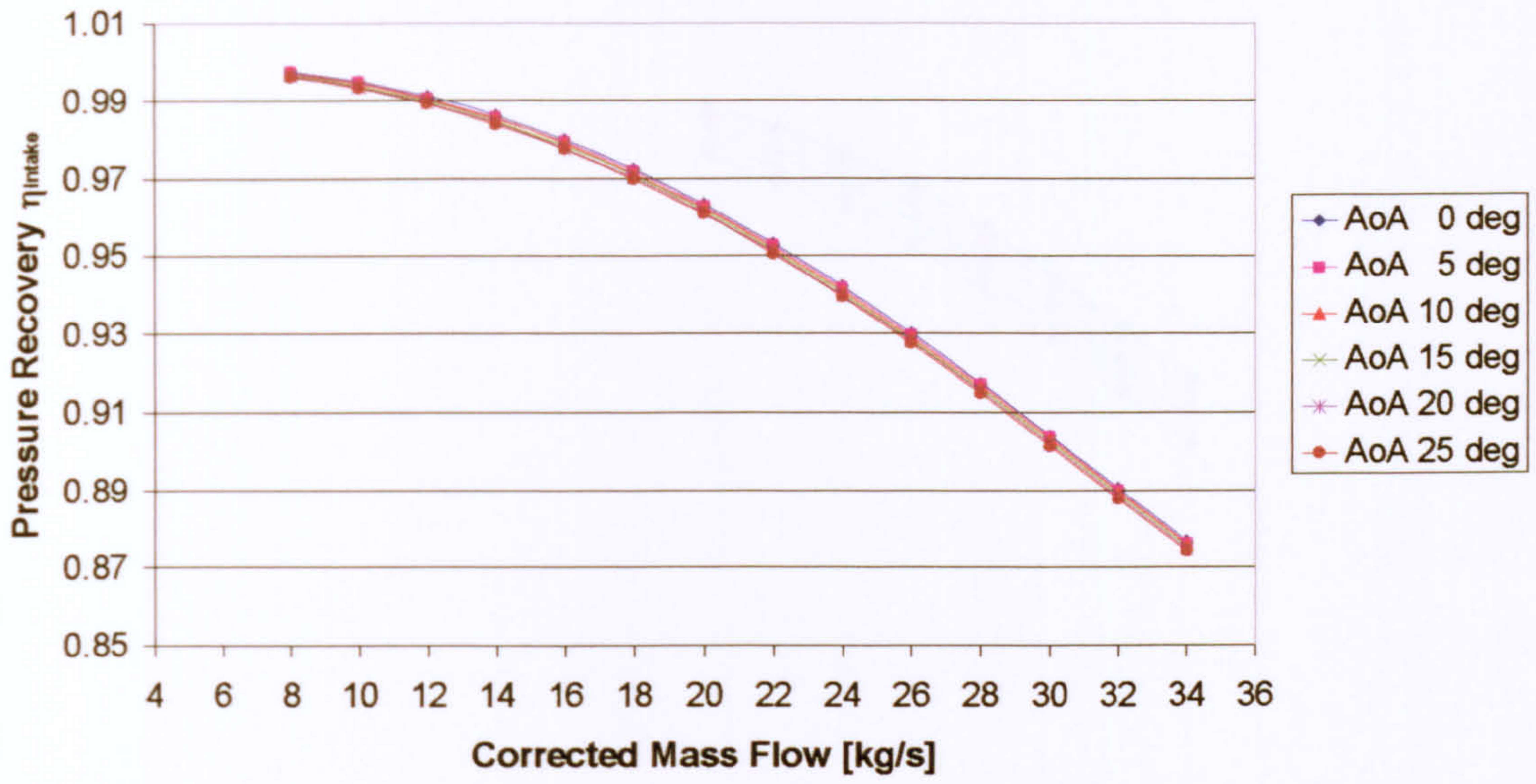


2D SLC Intake Performance with a Rounded-Elliptical Lip  
(Separated Flow,  $M_{\infty} = 0.20$ )

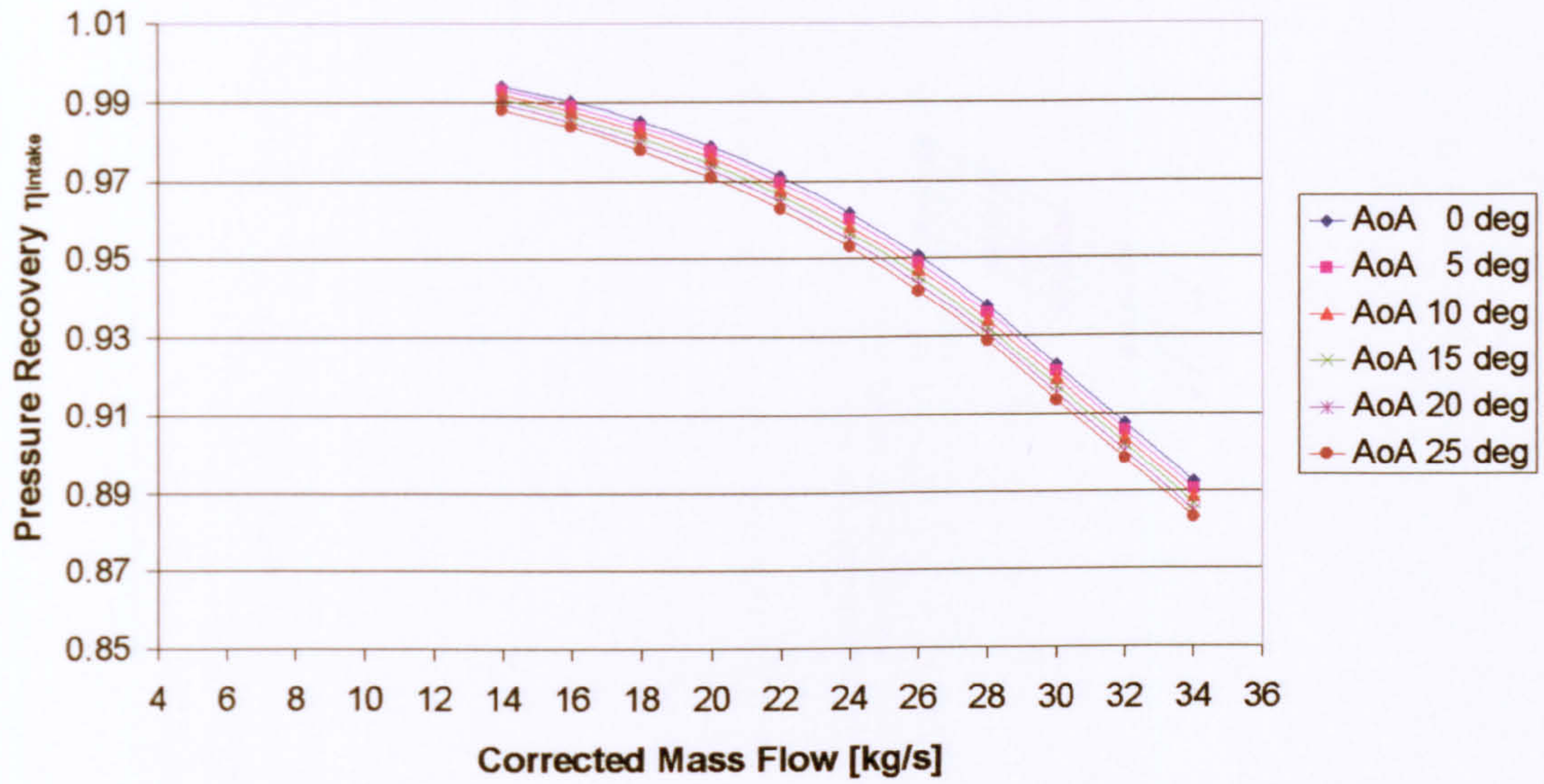




2D SLC Intake Performance with a Sharp Lip  
(Attached Flow,  $M_{\infty} = 0.05$ )

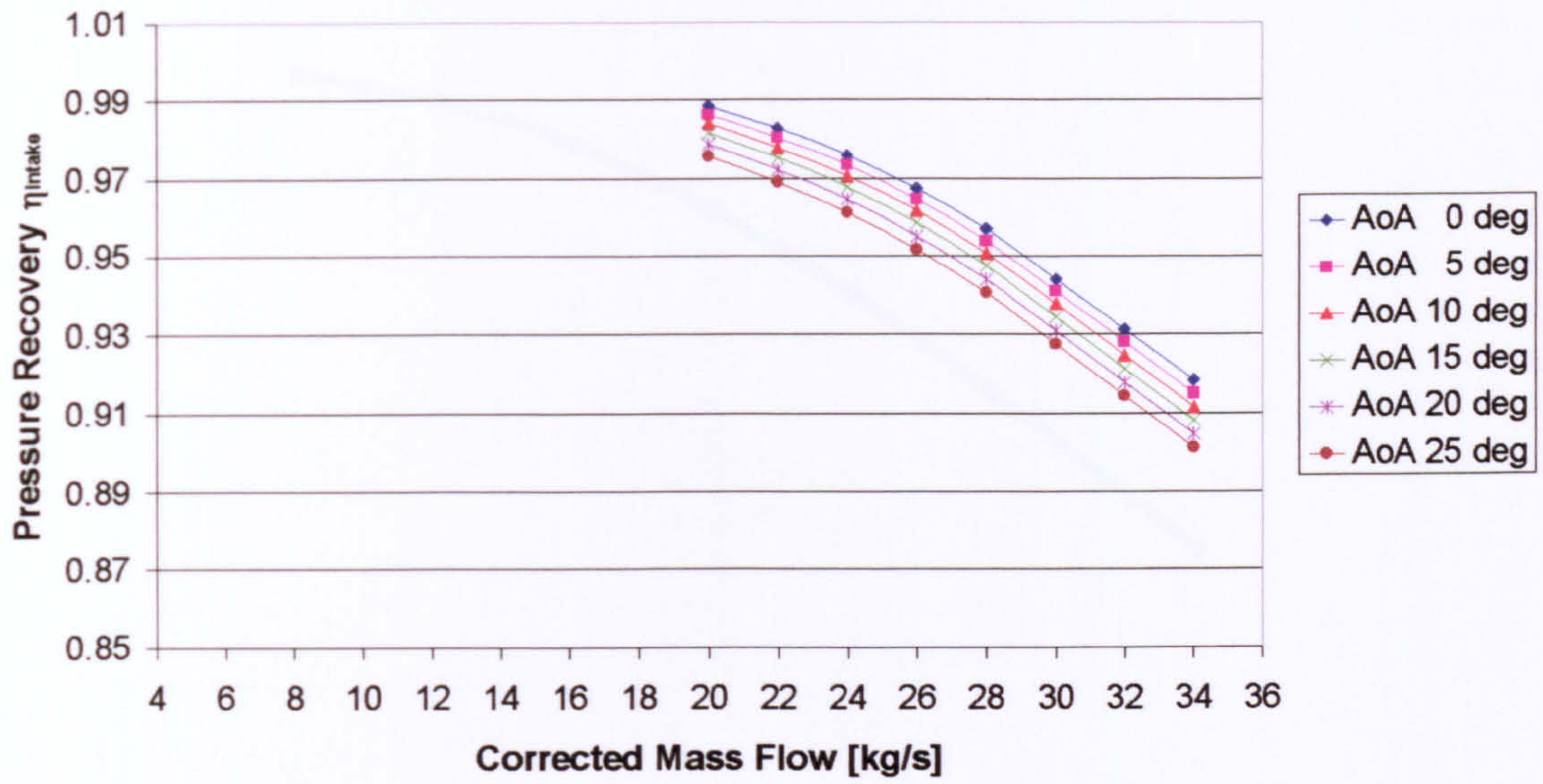


2D SLC Intake Performance with a Sharp Lip  
(Attached Flow,  $M_{\infty} = 0.10$ )

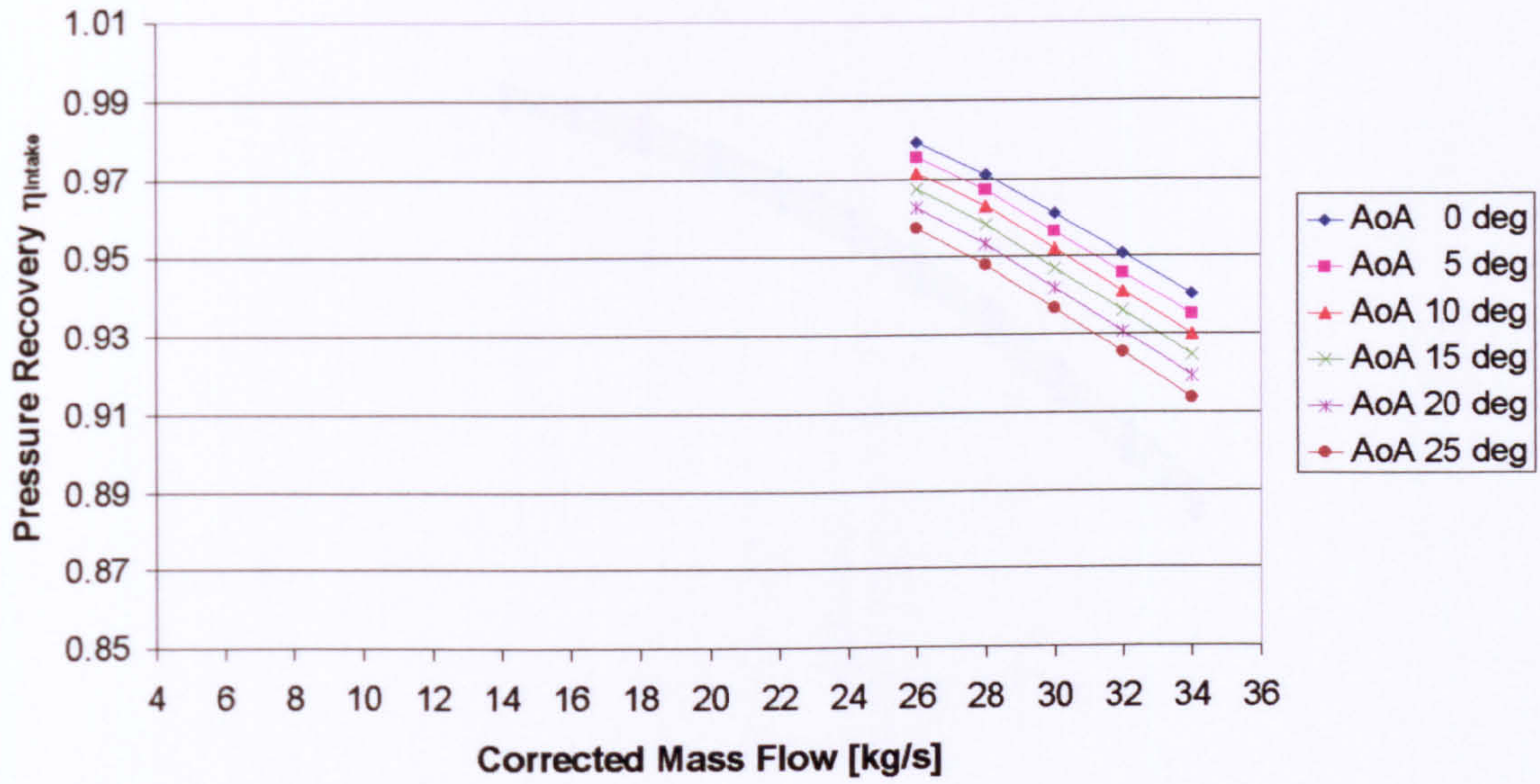




2D SLC Intake Performance with a Sharp Lip  
(Attached Flow,  $M_{\infty} = 0.15$ )

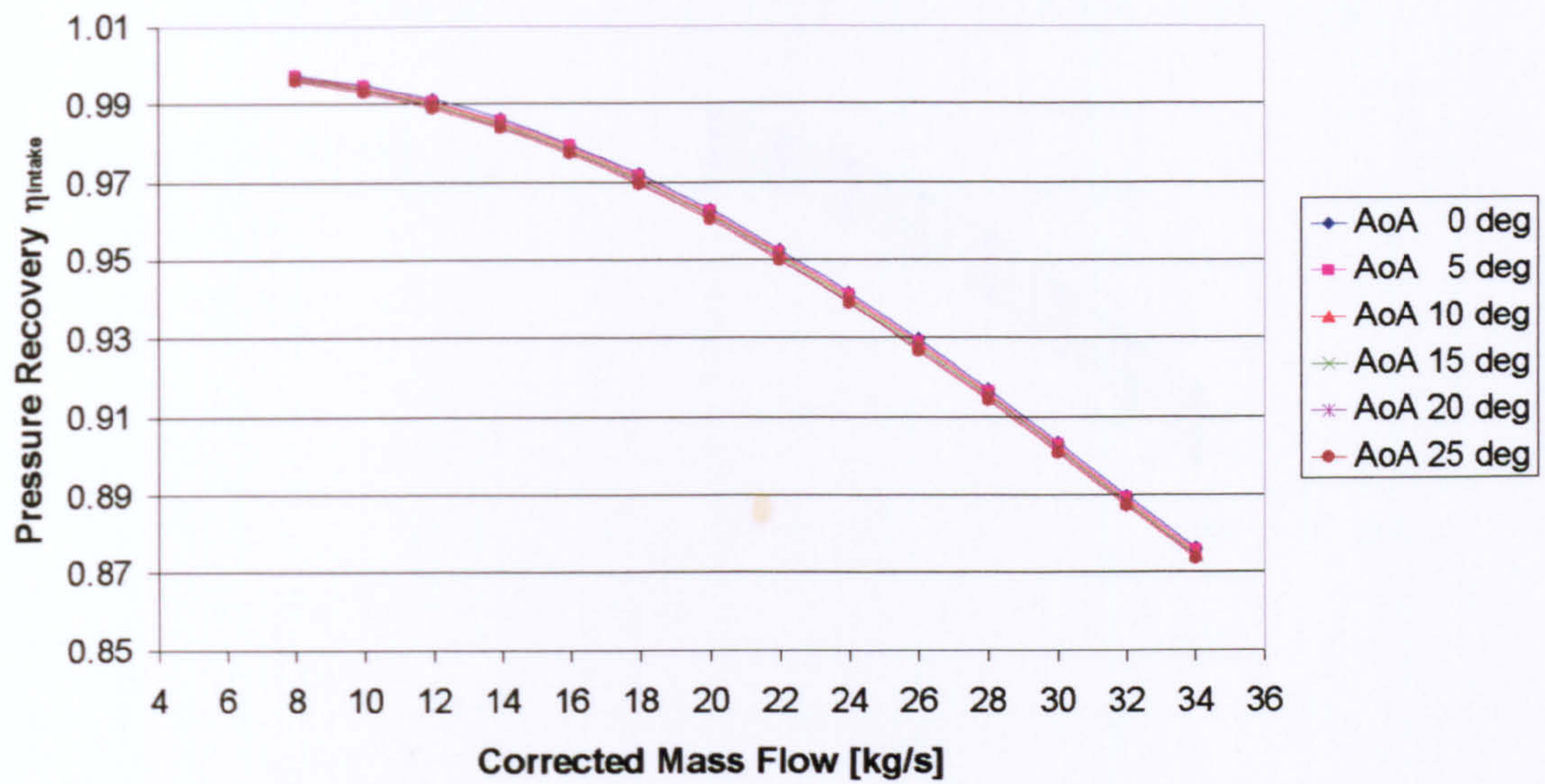


2D SLC Intake Performance with a Sharp Lip  
(Attached Flow,  $M_{\infty} = 0.20$ )

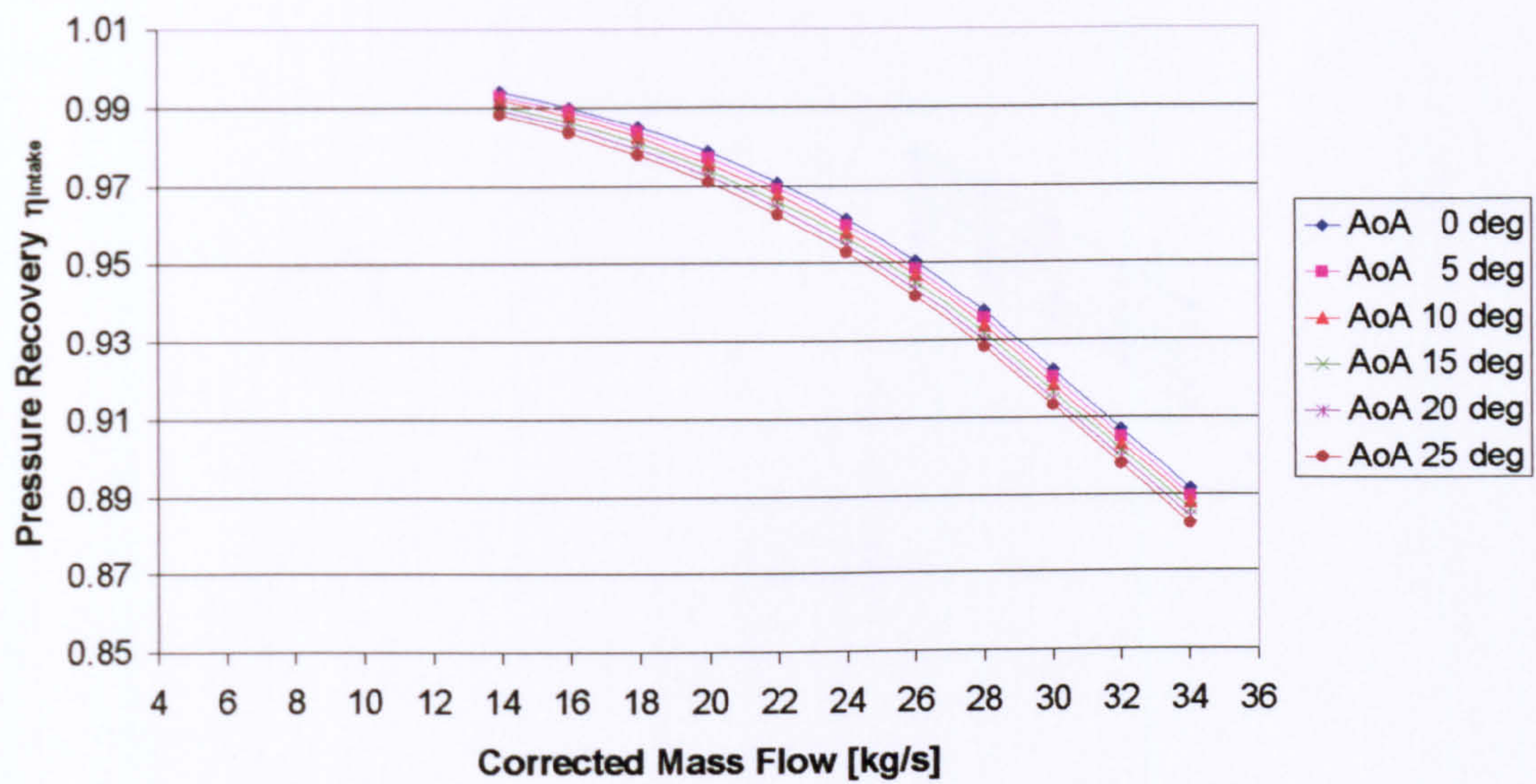




2D SLC Intake Performance with a Sharp Lip  
(Separated Flow,  $M_{oo} = 0.05$ )

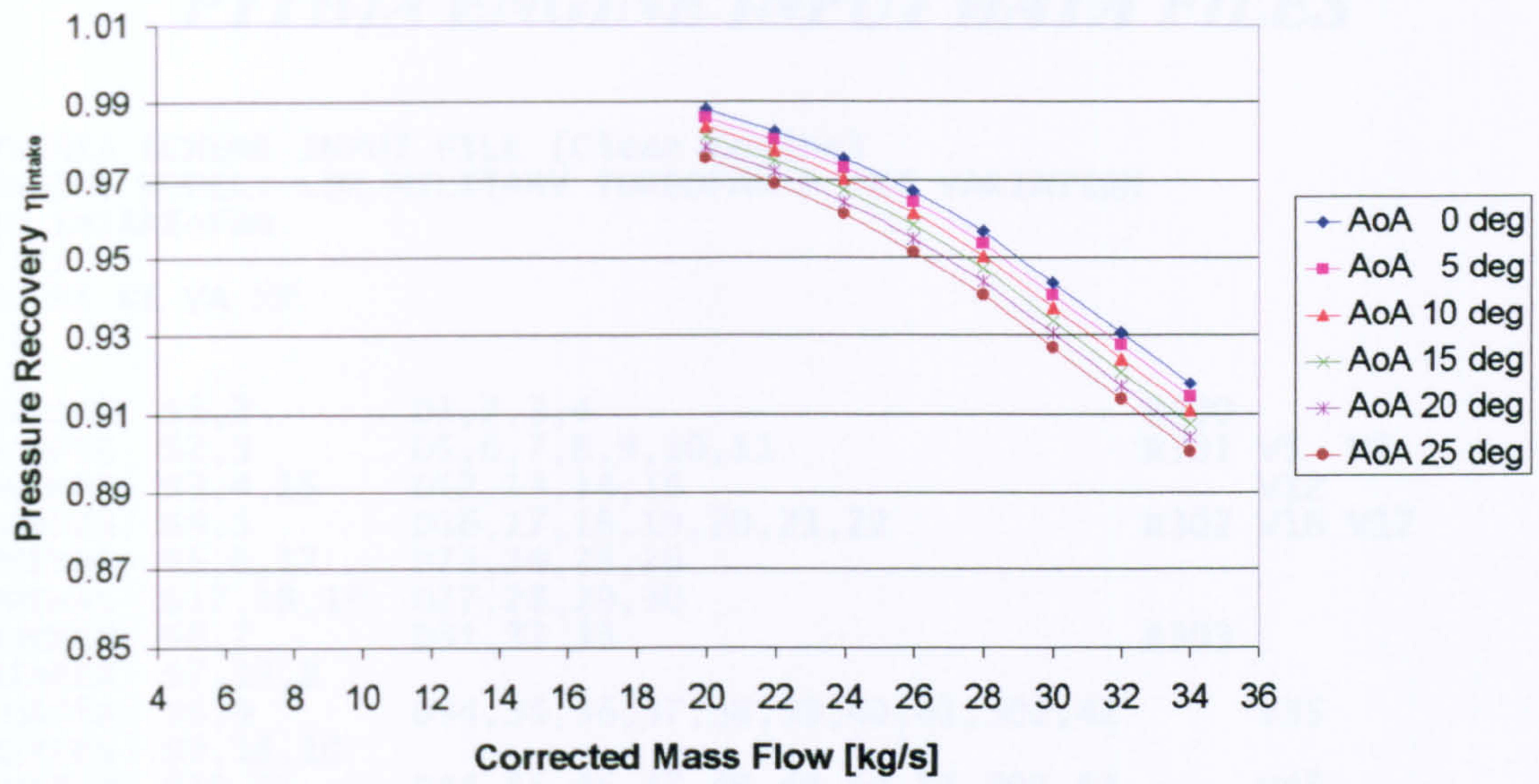


2D SLC Intake Performance with a Sharp Lip  
(Separated Flow,  $M_{oo} = 0.10$ )

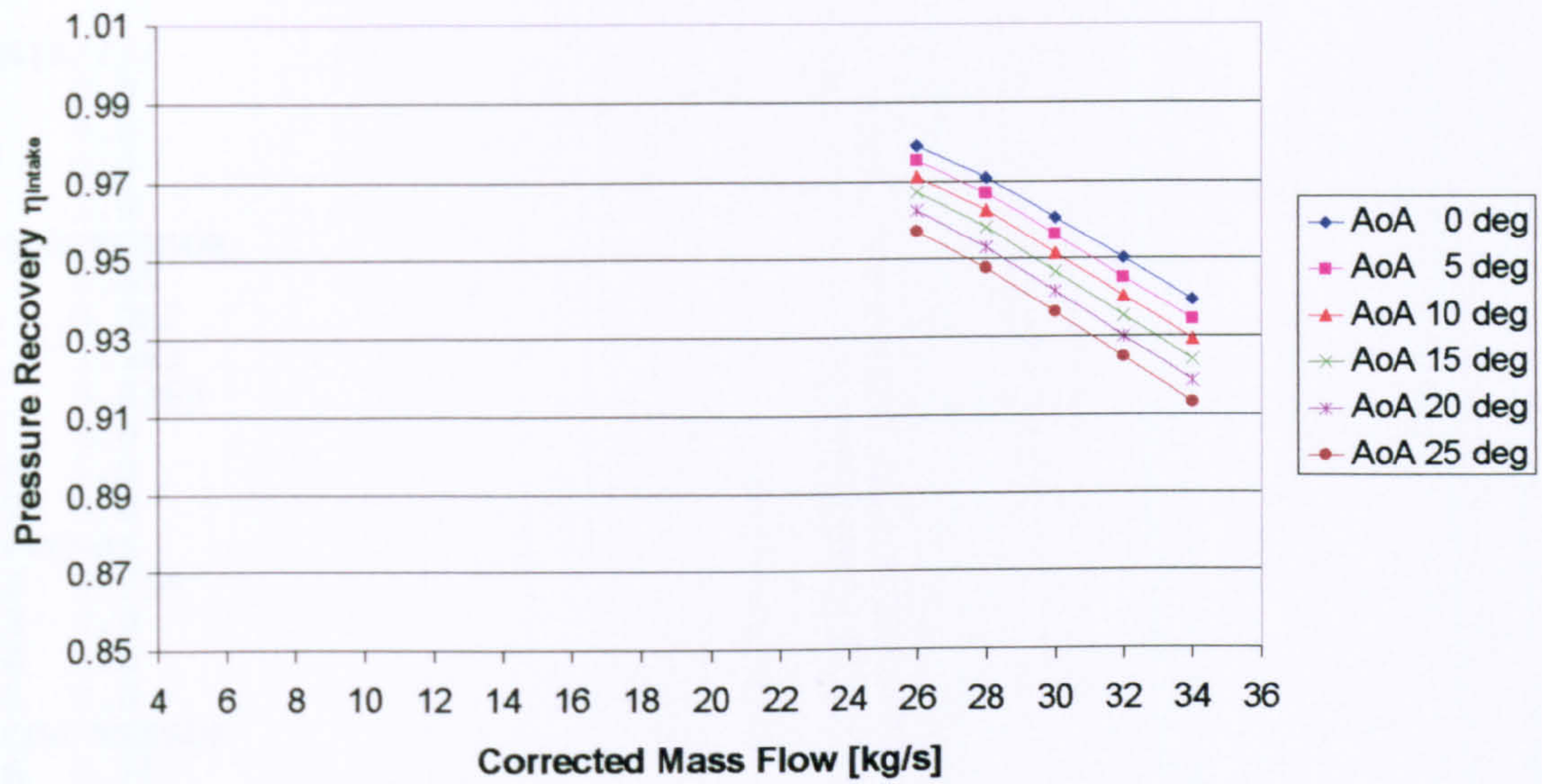




2D SLC Intake Performance with a Sharp Lip  
(Separated Flow,  $M_{\infty} = 0.15$ )



2D SLC Intake Performance with a Sharp Lip  
(Separated Flow,  $M_{\infty} = 0.20$ )





APPENDIX J**PYTHIA ENGINE INPUT DATA FILES**

```

PYTHIA SCHEME INPUT FILE (Clean Engine)
ENGINE MODEL: LBR MILITARY TURBOFAN - TET VARIATION
OD INTAKE+Fan
////
OD SI KE VA XP
-1
-1
INTAKE S1,2 D1,2,3,4 R300
COMPRES S2,3 D5,6,7,8,9,10,11 R301 V5 V6
PREMAS S3,4,15 D12,13,14,15 V12
COMPRES S4,5 D16,17,18,19,20,21,22 R302 V16 V17
PREMAS S5,6,17 D23,24,25,26
PREMAS S17,18,19 D27,28,29,30
BURNER S6,7 D31,32,33 R303
MIXEES S7,19,8
TURBIN S8,9 D34,35,36,37,38,39,40,41,302,42 V35
MIXEES S9,18,10
TURBIN S10,11 D44,45,46,47,48,49,50,51,301,52 V45
DUCTER S15,16 D54,55,56,57 R304
MIXFUL S11,16,12 D58,59,60
DUCTER S12,13 D61,62,63,64 R305
NOZDIV S13,14,1 D65,66 R306
PERFOR S1,0,0 D67,68,69,70,306,300,303,0,0,305,0,0,0
CODEND

```

```

DATA////
1 0.0
2 0.0
3 0.0
4 -1.0
!COMPRESSOR
5 0.65
6 0.967
7 1.593
8 0.8363
9 0.0
10 1.0
11 0.0
!PREMAS
12 0.714
13 0.0
14 1.0
15 0.0
!COMPRESSOR
16 0.75
17 1.0
18 2.28
19 0.84
20 0.0
21 1.0
22 0.0
!PREMAS
23 0.82
24 0.0
25 1.0
26 0.0
!PREMAS
27 0.3
28 0.0
29 1.0
30 0.0

```



```
!BURNER
31 0.05
32 0.99
33 -1.0
!TURBINE
34 0.0
35 0.7
36 0.7
37 0.86
38 -1.0
39 2.0
40 1.0
41 -1.0
42 0.0
!TURBINE
44 0.0
45 0.7
46 0.5
47 0.89
48 -1.0
49 1.0
50 1.0
51 -1.0
52 0.0
!DUCTER
54 0.0
55 0.05
56 0.0
57 0.0
!MIXFUL
58 1.0
59 1.0
60 0.275
!DUCTER
61 1.0
62 0.05
63 0.90
64 100000.0
!NOZDIV
65 -1.0
66 -1.0
!PERFOR
67 -1.0
68 -1.0
69 0.0
70 0.0
-1
1 2 33.248
7 6 1000.0
-1
-1
7 6 975.0
-1
-1
7 6 950.0
-1
-1
7 6 925.0
-1
-1
7 6 900.0
-1
-1
7 6 875.0
-1
-1
7 6 850.0
-1
-1
```



7 6 825.0  
 -1  
 -1  
 7 6 800.0  
 -1  
 -1  
 7 6 775.0  
 -1  
 -1  
 7 6 750.0  
 -1  
 -1  
 7 6 725.0  
 -1  
 -1  
 7 6 700.0  
 -1  
 -1  
 7 6 675.0  
 -1  
 -1  
 7 6 650.0  
 -1  
 -1  
 7 6 625.0  
 -1  
 -1  
 7 6 600.0  
 -1  
 -1  
 7 6 575.0  
 -1  
 -1  
 7 6 550.0  
 -1  
 -1  
 7 6 525.0  
 -1  
 -1  
 7 6 500.0  
 -1  
 -3

---

PYTHIA SCHEME INPUT FILE (Clean Engine)  
 ENGINE MODEL: LBR MILITARY TURBOFAN - TET VARIATION  
 2D INTAKE+FAN  
 ////  
 OD SI KE CT FP  
 -1  
 -1  
 INTA2D S1,2 D1,2,3,4 R300  
 COMP2D S2,3 D5,6,7,8,9,10 R301 V5 V6  
 PREMAS S3,4,15 D12,13,14,15 V12  
 COMPRE S4,5 D16,17,18,19,20,21 R302 V16 V17  
 PREMAS S5,6,17 D23,24,25,26  
 PREMAS S17,18,19 D27,28,29,30  
 BURNER S6,7 D31,32,33 R303  
 MIXEES S7,19,8  
 TURBIN S8,9 D34,35,36,37,38,39,40,41,302 V35  
 MIXEES S9,18,10  
 TURBIN S10,11 D44,45,46,47,48,49,50,51,301 V45  
 DUCTER S15,16 D54,55,56,57 R304  
 MIXFUL S11,16,12 D58,59,60  
 DUCTER S12,13 D61,62,63,64 R305  
 NOZDIV S13,14,1 D65,66 R306  
 PERFOR S1,0,0 D67,68,69,70,306,300,303,0,0,305,0,0,0  
 CODEND



```
DATA////
1 0.0
2 0.0
3 0.0
4 -1.0
!COMPRESSOR
5 1.0
6 0.967
7 0.0
8 0.0
9 0.0
10 0.0
!PREMAS
12 0.714
13 0.0
14 1.0
15 0.0
!COMPRESSOR
16 0.75
17 1.0
18 2.28
19 0.84
20 0.0
21 1.0
!PREMAS
23 0.82
24 0.0
25 1.0
26 0.0
!PREMAS
27 0.3
28 0.0
29 1.0
30 0.0
!BURNER
31 0.05
32 0.99
33 -1.0
!TURBINE
34 0.0
35 0.7
36 0.7
37 0.86
38 -1.0
39 2.0
40 1.0
41 -1.0
!TURBINE
44 0.0
45 0.7
46 0.5
47 0.89
48 -1.0
49 1.0
50 1.0
51 -1.0
!DUCTER
54 0.0
55 0.05
56 0.0
57 0.0
!MIXFUL
58 1.0
59 1.0
60 0.275
!DUCTER
61 1.0
62 0.05
63 0.90
```



```
64 100000.0
!NOZDIV
65 -1.0
66 -1.0
!PERFOR
67 -1.0
68 -1.0
69 0.0
70 0.0
-1
1 2 33.248
7 6 1000.0
-1
-1
7 6 975.0
-1
-1
7 6 950.0
-1
-1
7 6 925.0
-1
-1
7 6 900.0
-1
-1
7 6 875.0
-1
-1
7 6 850.0
-1
-1
7 6 825.0
-1
-1
7 6 800.0
-1
-1
7 6 775.0
-1
-1
7 6 750.0
-1
-1
7 6 725.0
-1
-1
7 6 700.0
-1
-1
7 6 675.0
-1
-1
7 6 650.0
-1
-1
7 6 625.0
-1
-1
7 6 600.0
-1
-1
7 6 575.0
-1
-1
7 6 550.0
-1
-1
7 6 525.0
```



-1  
 -1  
 7 6 500.0  
 -1  
 -3

PYTHIA SCHEME INPUT FILE (Clean Engine)  
 ENGINE MODEL: LBR MILITARY TURBOFAN - PCN VARIATION  
 2D INTAKE+FAN

////

OD SI KE CT FP

-1

-1

INTA2D	S1,2	D1,2,3,4	R300
COMP2D	S2,3	D5,6,7,8,9,10	R301 V5
PREMAS	S3,4,15	D12,13,14,15	V12
COMPRES	S4,5	D16,17,18,19,20,21	R302 V16 V17
PREMAS	S5,6,17	D23,24,25,26	
PREMAS	S17,18,19	D27,28,29,30	
BURNER	S6,7	D31,32,33	R303 W7,6
MIXEES	S7,19,8		
TURBIN	S8,9	D34,35,36,37,38,39,40,41,302	V35
MIXEES	S9,18,10		
TURBIN	S10,11	D44,45,46,47,48,49,50,51,301	V45
DUCTER	S15,16	D54,55,56,57	R304
MIXFUL	S11,16,12	D58,59,60	
DUCTER	S12,13	D61,62,63,64	R305
NOZDIV	S13,14,1	D65,66	R306
PERFOR	S1,0,0	D67,68,69,70,306,300,303,0,0,305,0,0,0	
CODEND			

DATA////

1 0.0  
 2 0.0  
 3 0.0  
 4 -1.0  
 !COMPRESSOR  
 5 1.0  
 6 0.967  
 7 0.0  
 8 0.0  
 9 0.0  
 10 0.0  
 !PREMAS  
 12 0.714  
 13 0.0  
 14 1.0  
 15 0.0  
 !COMPRESSOR  
 16 0.75  
 17 1.0  
 18 2.28  
 19 0.84  
 20 0.0  
 21 1.0  
 !PREMAS  
 23 0.82  
 24 0.0  
 25 1.0  
 26 0.0  
 !PREMAS  
 27 0.3  
 28 0.0  
 29 1.0  
 30 0.0  
 !BURNER  
 31 0.05  
 32 0.99  
 33 -1.0



```
!TURBINE
34 0.0
35 0.7
36 0.7
37 0.86
38 -1.0
39 2.0
40 1.0
41 -1.0
!TURBINE
44 0.0
45 0.7
46 0.5
47 0.89
48 -1.0
49 1.0
50 1.0
51 -1.0
!DUCTER
54 0.0
55 0.05
56 0.0
57 0.0
!MIXFUL
58 1.0
59 1.0
60 0.275
!DUCTER
61 1.0
62 0.05
63 0.90
64 100000.0
!NOZDIV
65 -1.0
66 -1.0
!PERFOR
67 -1.0
68 -1.0
69 0.0
70 0.0
-1
1 2 33.248
7 6 1000.0
-1
6 0.94
-1
-1
6 0.92
-1
-1
6 0.90
-1
-1
6 0.88
-1
-1
6 0.86
-1
-1
6 0.84
-1
-1
6 0.82
-1
-1
6 0.80
-1
-1
6 0.78
```



-1  
-1  
6 0.76  
-1  
-1  
6 0.74  
-1  
-1  
6 0.72  
-1  
-1  
6 0.70  
-1  
-1  
6 0.68  
-1  
-1  
6 0.66  
-1  
-1  
6 0.64  
-1  
-1  
6 0.62  
-1  
-1  
6 0.60  
-1  
-1  
6 0.58  
-1  
-1  
6 0.56  
-1  
-1  
6 0.54  
-1  
-1  
6 0.52  
-1  
-1  
6 0.50  
-1  
-1  
6 0.48  
-1  
-1  
6 0.46  
-1  
-1  
6 0.44  
-1  
-1  
6 0.42  
-1  
-1  
6 0.40  
-1  
-1  
6 0.38  
-1  
-1  
6 0.36  
-1  
-1  
6 0.34  
-1  
-1  
6 0.32



-1  
 -1  
 6 0.30  
 -1  
 -1  
 -3

!!  
 CFM56-5B2  
 !!!

HIGH BYPASS TURBO-FAN ENGINE (2 SPOOL)

DESIGN POINT : CRUISE  
 ALT 10670 m  
 MACH 0.8  
 OPR 35.5  
 THRUST 25.8 kN

OTHER PARAMATERS OBTAINED BY MATCHING TAKE-OFF CONDITIONS

THRUST 136.8 kN  
 BPR 5.5  
 MASS FLOW 433 kg/s

PROGRAMMED BY N. NANTUA 05/11/04

////

OD SI KE VA FP

-1

-1

INTAKE	S1-2	D1-4	R200		
COMPRES	S2-3	D5-11	R210	V5	V6
PREMAS	S3,16,4	D12-15		V12	
ARITHY		D80-84			
COMPRES	S4-5	D16-22	R230	V16	
PREMAS	S5,17,6	D23-26			
MIXEES	S16,17,18				
DUCTER	S18-19	D27-30	R220		
NOZCON	S19-20,1	D31	R290		
COMPRES	S6-7	D32-38	R240	V32	V33
PREMAS	S7,22,8	D39-42			
PREMAS	S8,21,9	D43-46			
BURNER	S9-10	D47-49	R250		
MIXEES	S10,21,11				
TURBIN	S11-12	D50-57,240,97		V51	
ARITHY		D85-91			
TURBIN	S12-13	D58-65,260,98		V59	
DUCTER	S13-14	D66-69			
NOZCON	S14-15,1	D70	R280		
PERFOR	S1,0,0	D71-74,280,200,250,290,0,0			

CODEND

BRICK DATA////

! INLET

1 10670.0 ! ALTITUDE  
 2 0.0 ! ISA DEVIATION  
 3 0.8 ! MACH NO  
 4 0.964026771 ! PRESSURE RECOVERY

! FAN

5 0.85 ! SURGE MARGINE  
 6 1.0 ! ROTATIONAL SPEED,N1  
 7 1.7 ! FAN PRESSURE RATIO  
 8 0.87 ! EFFICIENCY  
 9 0.0 ! ERROR SELECTOR  
 10 1.0 ! MAP NUMBER  
 11 0.0 ! VSV ANGLE

! BYPASS-MAIN

12 0.84615 ! LAMDA (BYPASS RATIO 5.5)  
 13 0.0 ! MASS FLOW LOSS  
 14 1.0 ! PRESSURE FACTOR



```

15  0.0          ! PRESSURE LOSS
! BOOSTER
16  0.75         ! SURGE MARGIN
17  1.0          ! ROTATIONAL SPEED
18  1.8          ! PRESSURE RATIO
19  0.86         ! EFFICIENCY
20  1.0          ! ERROR SELECTOR
21  1.0          ! MAP NUMBER
22  0.0          ! VSV ANGLE
! AIR BLEED
23  0.01         ! LAMDA (1%)
24  0.0          ! MASS FLOW LOSS
25  1.0          ! PRESSURE FACTOR
26  0.0          ! PRESSURE LOSS
! BYPASS-DUCT
27  0.0          ! REHEAT SELECTOR
28  0.01         ! PRESSURE LOSS 1%
29  0.0          ! REHEAT COMB.EFFICIENCY
30  1.E6         ! MAX REHEAT FUEL FLOW
! FAN NOZZLE
31 -1.0         ! SWITCH, AREA FIXED
! HPC COMPRESSOR
32  0.85         ! SURGE MARGIN
33  1.0          ! ROTATIONAL SPEED
34  11.6         ! PRESSURE RATIO
35  0.86         ! EFFICIENCY
36  1.0          ! ERROR SELECTOR
37  3.0          ! MAP NUMBER
38  0.0          ! VSV ANGLE
! ACCESSORY BYPASS
39  0.01         ! BYPASS RATIO
40  0.0          ! MASS FLOW LOSS
41  1.0          ! PRESSURE FACTOR
42  0.0          ! PRESSURE LOSS
! HPT COOLING BYPASS
43  0.13         ! BYPASS RATIO
44  0.0          ! MASS FLOW LOSS
45  1.0          ! PRESSURE FACTOR
46  0.0          ! PRESSURE LOSS
! BURNER
47  0.06         ! PRESSURE LOSS
48  0.99         ! COMBUSTION EFFICIENCY
49  -1.0         ! FUEL FLOW
! TURBINE-HPT
50  100000.0     ! AUX.WORK
51 -1.0         ! REL NON-D MASS FLOW
52 -1.0         ! REL NON-D SPEED
53  0.88         ! EFFICIENCY
54 -1.0         ! REL ROT.SPEED(COMP TURB=-1)
55  3.0          ! COMP NO. FROM LOW END
56  5.0          ! TURBINE MAP
57 -1.0         ! POWER LAW
! TURBINE-LPT
58  0.0          ! AUX.WORK
59 -1.0         ! REL NON-D MASS FLOW
60 -1.0         ! REL NON-D SPEED
61  0.88         ! EFFICIENCY
62 -1.0         ! REL ROT.SPEED
63  1.0          ! COMP NO. FROM LOW END
64  5.0          ! TURBINE MAP
65 -1.0         ! POWER LAW
! CORE DUCT
66  0.0          ! REHEAT SELECTOR
67  0.0          ! PRESSURE LOSS 1%
68  0.0          ! REHEAT COMB.EFFICIENCY
69  1.E6         ! MAX REHEAT FUEL FLOW
! CONVERGENT NOZZLE
70 -1.0         ! SWITCH, AREA FIXED

```



```

! PERFORMANCE
71 -1.0      ! POWER (-1=TURBOJET/FAN)
72 -1.0      ! PROPELLER EFFICIENCY(")
73  0.0      ! SCALING INDEX
74  0.0      ! REQ'D D.P. THRUST
! ARITHY : BOOSTER SPEED = FAN SPEED
80  5.0      ! COPY
81 -1.0
82 17.0      ! BOOSTER SPEED
83 -1.0
84  6.0      ! FAN SPEED
! ARITHY : LPT WORK = BOOSTER WORK + FAN WORK
85  1.0      ! ADD
86 -1.0
87 260.0     ! LPT WORK
88 -1.0
89 210.0     ! FAN WORK
90 -1.0
91 230.0     ! BOOSTER WORK
97  0.0
98  0.0
-1
1  2 170.0   ! INLET MASS FLOW
10 6 1483.0  ! TET
-3

```

---

**PYTHIA SCHEME INPUT FILE (Clean Engine)**
**ENGINE MODEL: 2-SPOOL LBR MILITARY BASED ON THE EJ200**
**////**
**OD SI KE VA XP**
**-1**
**-1**

INTAKE	S1,2	D1,2,3,4	R300
COMPRES	S2,3	D5,6,7,8,9,10,11	R301 V5 V6
PREMAS	S3,4,15	D12,13,14,15	V12
COMPRES	S4,5	D16,17,18,19,20,21,22	R302 V16 V17
PREMAS	S5,6,17	D23,24,25,26	
PREMAS	S17,18,19	D27,28,29,30	
BURNER	S6,7	D31,32,33	R303
MIXEES	S7,19,8		
TURBIN	S8,9	D34,35,36,37,38,39,40,41,302,43	V35
MIXEES	S9,18,10		
TURBIN	S10,11	D44,45,46,47,48,49,50,51,301,53	V45
DUCTER	S15,16	D54,55,56,57	R304
MIXFUL	S11,16,12	D58,59,60	
DUCTER	S12,13	D61,62,63,64	R305
NOZDIV	S13,14,1	D65,66	R306
PERFOR	S1,0,0	D67,68,69,70,306,300,303,0,0,305,0,0,0	

**CODEND**
**DATA////**

```

1  0.0
2  0.0
3  0.5
4 -1.0
5  0.6
6  1.2
7  4.21
8  0.86
9  0.0
10 2.0
11 0.0
12 0.6
13 0.0
14 1.0
15 0.0
16 0.75
17 1.2
18 6.1758
19 0.84
20 0.0

```



21 3.0  
22 0.0  
23 0.82  
24 0.0  
25 1.0  
26 0.0  
27 0.3  
28 0.0  
29 1.0  
30 0.0  
31 0.05  
32 0.99  
33 -1.0  
34 100000.0  
35 0.8  
36 -1.0  
37 0.89  
38 -1.0  
39 2.0  
40 3.0  
41 -1.0  
43 0.0  
44 0.0  
45 0.8  
46 -1.0  
47 0.89  
48 -1.0  
49 1.0  
50 2.0  
51 -1.0  
53 0.0  
54 0.0  
55 0.05  
56 0.0  
57 0.0  
58 1.0  
59 1.0  
60 0.275  
61 1.0  
62 0.05  
63 0.90  
64 100000.0  
65 -1.0  
66 -1.0  
67 -1.0  
68 -1.0  
69 0.0  
70 0.0  
-1  
1 2 76.0  
7 6 1820  
13 6 1990.0  
-1  
-3